The international journal of science / 7 January 2021

nature

ATOMIC INSIGHTS

Machine learning offers mechanistic view of transitions in disordered silicon

Fast-track research
How the hunt for a COVID jab could change vaccine science

Structured movies
Anti-tuberculosis drug imaged in action at its cellular target

Coronavirus
Mobile-phone data help model infection dynamics for COVID-19

Vol. 589, No. 7840
nature.com

Nature.2021.01.09

[Sat, 09 Jan 2021]

- Donation
- This Week
- News in Focus
- Opinion
- Work
- Research
- Amendments & Corrections

Donation

- **-> 打赏 - Donation**

打赏 - JUST FOR FUN

支持分享! 一杯咖啡钱, 打赏金额随意，感谢大家~ :)

经济学人2020年全集(含epub、mobi、高清pdf, 音频下载地址)已经整理完毕, 有需要的同学可以点击 emagazines.site 查看.

本书来自: www.github.com/hehonghui

This article was downloaded by **calibre** from https://emagazines.site/donate.html

This Week

- **Global climate action needs trusted finance data** [06 January 2021]
  Editorial • An agreed system for measuring funding of green projects in poorer nations will be vital to achieving action on climate change in 2021.
- **Beyond past due: data to guide US school reopenings** [05 January 2021]
  World View • President-elect Joe Biden must coordinate efforts to gather COVID-19 infection data.

EDITORIAL
06 January 2021

- Correction 08 January 2021

Global climate action needs trusted finance data

An agreed system for measuring funding of green projects in poorer nations will be vital to achieving action on climate change in 2021.

UN secretary-general António Guterres (pictured) has said developed countries are lagging in their pledge to provide US$100 billion a year in climate funding for poorer countries by 2020.Credit: Pedro Fiúza/NurPhoto/Getty

A fortnight before the adoption of the 2015 Paris climate agreement, India's government published a report that could have imperilled the talks.

Developing countries were being asked to commit to reducing their greenhouse-gas emissions. In exchange, they expected developed nations to provide climate funding totalling US$100 billion a year by 2020. Data published by the Organisation for Economic Co-operation and Development (OECD), a body that represents many of the world's richer nations, said that developed countries were on their way to meeting this target — providing around $50 billion annually to low- and middle-income countries. But India said that the real figure was nearer $2.2 billion, and that the numbers reported by the OECD were open to '"gaming' and exaggeration", adding to tensions between the two sides.

The Paris meeting was rescued. Developed and developing countries alike pledged to reduce greenhouse-gas emissions, and to come back in 2020 with more-ambitious commitments. But arguments over funding data have endured. Five years on, they are casting a shadow over the next United Nations climate conference (COP26), scheduled for November, when nations are expected to meet in Glasgow, UK, to take stock of their climate commitments.

This is a crucial year for efforts to combat climate change. A number of countries are pledging to work towards achieving net-zero emissions. And the United Kingdom is making a determined effort to get the worlds of banking, other private finance and industry to commit to greening their processes and operations. But there's been little progress in resolving disagreements over public climate-finance provision. According to the OECD's latest data, developed countries mobilized nearly $80 billion in 2018 — $62.2 billion of it from public sources and $14.6 billion in private finance. If increases continue at the same rate, these nations are within touching distance of the $100-billion target by 2020.

But other studies do not support these findings. According to a report released by the aid group Oxfam last October, climate-specific assistance provided by developed countries came to no more than $22.5 billion in 2017–18. And last month, researchers commissioned by the UN secretary-

general António Guterres found that donors were over-reporting climate-funding data by $3 billion to $4 billion.

Such disagreements are not new, but they are once again fuelling mistrust ahead of a crucial climate meeting, says Saleemul Huq, director of the International Centre for Climate Change and Development, which is based in Dhaka. Ideally, verification should fall to organizations or processes that all sides can trust. Only then will there be any hope of resolving these disagreements.

A helping hand

Climate finance has been a point of contention since at least 1992, when the Earth Summit was held in Rio de Janeiro, Brazil. Because richer countries are overwhelmingly the source of the emissions responsible for global warming, they agreed — albeit reluctantly — to help more-vulnerable countries to protect themselves from the effects of climate change. The Global Environment Facility was created, headquartered at the World Bank in Washington DC. But its complicated rules made it hard for some of the most vulnerable developing nations to obtain funding — especially for climate-adaptation projects.

Over time, developing countries worked hard to persuade the international community to establish funding bodies, such as the Green Climate Fund and the Adaptation Fund, that were more able to respond to their specific needs. But donor nations have mostly avoided providing climate finance through these channels, preferring to fund countries directly, or through multilateral development banks such as the World Bank.

A major point of contention is the fact that more than 80% of climate finance supplied to developing countries comprises loans. The proportion of climate funding given as grants has been falling — between 2013 and 2018, for example, it dropped from 27% to 20%. The trend towards loans is problematic, both because loans need to be repaid, with interest, and because they tend to be provided for projects that can demonstrate a return on the investment, such as power generation. Loans are less likely to be obtained

for projects, such as the building of flood defences, that are designed to help countries become more resilient but do not make money.

The pandemic has also resulted in cuts to many nations' credit ratings, and the subsequent reduction in borrowing capacity has hit the poorest countries hard. Ultimately, the nature of loan financing means that these countries will end up in increasing amounts of debt — as the costs of the damage done by climate change rise alongside temperatures.

But it is the lack of agreed and trusted accounting rules for climate finance that fuels mistrust. The absence of such rules is a major oversight in climate diplomacy, say Romain Weikmans at the Université Libre de Bruxelles and Timmons Roberts at Brown University in Providence, Rhode Island[1].

The authors of India's 2015 report arrived at the $2.2-billion figure by counting money that they said had been disbursed. By contrast, the data from donors include all pledged funding, whether or not the money has reached the recipients. The OECD data also count funding for projects with only a partial link to climate mitigation.

Another complicating factor is that the OECD's researchers are working to a rule book agreed at a previous climate meeting, COP24, held in Poland in 2018. UN member states are looking at how to improve data accuracy. But even with clear criteria and better reporting, one thing will not change: the OECD is an intergovernmental body whose leadership does not represent the majority of nations. If recurring arguments are to be avoided, a climate-finance verification mechanism needs to be found that fully incorporates the perspectives of OECD non-members.

'Meeting of minds' needed

To agree on new accounting rules, both developed and developing countries should consider taking advice from a trusted third party that already has a role in setting data standards, but is not involved in international diplomacy. That could be the UN Statistical Commission or the International Organization for Standardization. "Countries should come up with proposals," says Selwin Hart, who advises Guterres on climate finance.

“There needs to be a meeting of minds so that all sides can be confident there is accuracy and accountability,” he adds.

The COP26 meeting is less than a year away. Widely seen as the world’s last chance to take meaningful, unified action on climate change, it must succeed. That means developed and developing countries must agree on more-ambitious targets to reduce emissions, and ensure that the poorest countries, and those most vulnerable to climate change, receive support as they develop their economies in a more sustainable manner and prepare for the inevitable effects of global warming. The $100-billion pledge is a fraction of what is needed. Ultimately, investments around the world must shift to support sustainable development. If global leaders can accomplish that, Earth might yet have a chance.

Nature **589**, 7 (2021)

doi: https://doi.org/10.1038/d41586-020-03646-x

Updates & Corrections

- **Correction 08 January 2021**: An earlier version of this editorial erroneously stated that the OECD climate-finance data count funding for more-efficient coal-fired power.

References

1. 1.

   Weikmans, R. & Roberts, J. T. *Clim. Dev.* **11**, 97–111 (2017).

Jobs from Nature Careers

-
  -
    - All jobs
  -

- **Aushilfe / Studentische Hilfskraft (m/w/d) im Abteilungssekretariat für 15 Std. / Woche**

  German Cancer Research Center in the Helmholtz Association (DKFZ)

  Heidelberg, Germany

  JOB POST

- **Hochfrequenz Technikerin I Hochfrequenz Techniker (w/m/d)**

  Helmholtz-Zentrum Berlin for Materials and Energy (HZB)

  Berlin, Germany

  JOB POST

- **PhD position – Genetics of neuropathological changes in Alzheimer's disease**

  Flanders Institute for Biotechnology (VIB)

  Antwerp, Belgium

  JOB POST

- **53541: Physicist, Engineer or similar - Laser-spectroscopic methods for the protection of terrestrial infrastructures**

  German Aerospace Center (DLR)

  Köln, Germany

  JOB POST

This article was downloaded by **calibre** from https://www.nature.com/articles/d41586-020-03646-x

WORLD VIEW
05 January 2021

Beyond past due: data to guide US school reopenings

President-elect Joe Biden must coordinate efforts to gather COVID-19 infection data.

Emily Oster

Emily Oster is an economics professor at Brown University in Providence, Rhode Island. Twitter: @ProfEmilyOster
Contact

Search for this author in:

- Pub Med
- Nature.com
- Google Scholar

As we stare into the dawn of 2021, children in the United States face a stark reality. Many have been out of classrooms since March 2020. Online educational alternatives are spotty. Grades and achievement scores are slumping, with the biggest losses for the most vulnerable students. An analysis by consultancy McKinsey & Company, based in New York City, estimates that white students could lose 4–8 months of learning in mathematics, and students of colour 6–12. It's unclear when many US schools should reopen for in-person learning. Tragically, the country still lacks data that show what's safe. The fragmented data collection in schools echoes the country's slipshod approach to tracking COVID-19 in care homes and hospitals, and even basic case- and death-rate information.

Other countries have handled school decisions differently. In the United Kingdom, Public Health England enhanced its national COVID-19 surveillance when schools reopened for a mini-term in June. That month, it found, only around 70 children out of roughly 1.6 million who attended school were infected — and infection rates mostly depended on the infection prevalence in the community. Although the country has stumbled in other aspects of its response, this organized data effort generated confidence in allowing UK schools to reopen nationally in the autumn.

School officials in the United States could probably learn something from foreign data — but US-based data would be more powerful. Alongside many differences, most developed countries have much lower community rates of infection than does the United States (as I write, the UK rate is about half the US rate). However, the US education system is extremely fragmented and mainly under the control of local governments. So decisions are rarely centralized, and data-collection systems are even less so. There have been several efforts to make systematic school COVID-19 dashboards, but all are run by non-governmental entities.

Regional differences in progression of the pandemic across the country, and the times at which schools re-opened, should have provided excellent learning opportunities. A number of states in heavily affected areas of the country opened their schools first, some as early as August. By September, data from these schools could have informed actions elsewhere. However, with no systematic data collection, the learning opportunity was lost.

Take the key question of appropriate distancing in classrooms. Evidence on aerosol transmission pointed to 2 metres as the best distance, but some studies argued that 1 metre is sufficient to reduce infection risk. That would make a big difference in how many students could fit in a classroom. The information to answer this question existed, in principle. It's true that schools with greater distancing probably take other precautions and probably have more space and better ventilation. Still, with enough reliable data, analyses might have clearer answers on how well various precautions work.

The data collected by states can be hard to learn from. Several states (including Kentucky and Massachusetts) report counts of COVID-19 cases by school district, which can be useful — but they do not report information on numbers of children and staff at school, which are necessary to know rates of infection. Texas and New York both produce information on COVID-19 cases by school, alongside information on numbers of students and staff. Texas, however, does not report for schools with fewer than five cases, and because most schools have few infections, many data are lost.

Some states report only school outbreaks, which could be defined as more than 2 cases — or more than 3, or more than 5 — in a school over 14 days. Sometimes, an outbreak is reported only if the cases were confirmed to be spread at school. Some states will test asymptomatic staff or students — but this information is not typically systematically reported or integrated with other data, such as in-person attendance rates or community testing and case rates.

I'm an economist studying health-related behaviours but, like many scholars during the pandemic, I pivoted my focus to try to be of use. I've developed the COVID-19 School Response Dashboard (see go.nature.com/3auxx1e), which seeks to collect data from districts all across the country and to aggregate state-level data. But it relies on schools participating voluntarily, and it leaves many out, including many districts with fewer resources. The mismatched nature of data collection means such efforts cannot be fully representative. Individuals cannot compel data provision and participation as a government could.

I would like to see US president-elect Joe Biden's administration bring together the Centers for Disease Control and Prevention and the Department of Education to develop a stronger system for tracking COVID-19 in schools. A good first step would be to set up a coordinated data-entry system and to strongly encourage schools to participate. The administration should also create centralized guidance for opening plans and what information on COVID-19 infections schools should produce. We need to be able to identify the virus spreading in schools and work out what went wrong. The data we do have suggest that outbreaks in schools are not common, but they do happen. We need a way to find them systematically.

Certainty might be impossible, but decisions driven by reliable, relevant data shouldn't be. If we can get those data, we can use these insights to guide schools reopening.

Nature **589**, 8 (2021)

doi: https://doi.org/10.1038/d41586-020-03647-w

Jobs from Nature Careers

-
  -
    - All jobs
  -
    - **Aushilfe / Studentische Hilfskraft (m/w/d) im Abteilungssekretariat für 15 Std. / Woche**

      German Cancer Research Center in the Helmholtz Association (DKFZ)

      Heidelberg, Germany

      JOB POST
    -

Hochfrequenz Technikerin I Hochfrequenz Techniker (w/m/d)

Helmholtz-Zentrum Berlin for Materials and Energy (HZB)

Berlin, Germany

JOB POST

- **PhD position – Genetics of neuropathological changes in Alzheimer's disease**

  Flanders Institute for Biotechnology (VIB)

  Antwerp, Belgium

  JOB POST

- **53541: Physicist, Engineer or similar - Laser-spectroscopic methods for the protection of terrestrial infrastructures**

  German Aerospace Center (DLR)

  Köln, Germany

  JOB POST

This article was downloaded by **calibre** from https://www.nature.com/articles/d41586-020-03647-w

News in Focus

- **COVID lockdowns and Europe's science spending** [06 January 2021]
  News Round-Up • The latest science news, in brief.
- **Is lightning striking the Arctic more than ever before?** [17 December 2020]
  News • Team detects a huge increase and says it could be due to climate change, but others can't confirm the findings.
- **Prestigious AI meeting takes steps to improve ethics of research** [23 December 2020]
  News • For the first time, the organizers of NeurIPS required speakers to consider the societal impact of their work.
- **Surprise! First peek inside Mars reveals a crust with cake-like layers** [15 December 2020]
  News • NASA's InSight mission yields the first data on the internal structure of a planet other than Earth.
- **The science events to watch for in 2021** [22 December 2020]
  News • Climate change and COVID-19 vaccines are among the themes set to shape research.
- **The lightning-fast quest for COVID vaccines — and what it means for other diseases** [18 December 2020]
  News Feature • The speedy approach used to tackle SARS-CoV-2 could change the future of vaccine science.

NEWS ROUND-UP
06 January 2021

COVID lockdowns and Europe's science spending

The latest science news, in brief.

Restaurants and pubs closed in London as part of an effort to halt a spike in COVID-19 cases.Credit: Kate Green/Anadolu Agency/Getty

Stay-at-home orders do little to curb covid spread

An analysis of COVID-19 data from 41 countries has identified 3 measures that each substantially cut viral transmission: school and university closures, restricting gatherings to no more than 10 people, and shutting businesses. But adding stay-at-home orders to those actions brought only marginal benefit.

Questions linger about the relative effectiveness of specific measures to reduce the spread of SARS-CoV-2. To pinpoint the most useful ones, Jan Brauner at the University of Oxford, UK, and his colleagues modelled the number of new infections in 41 countries between 22 January last year and either 30 May or, if restrictions were lifted sooner, the date when they were first eased (J. M. Brauner *et al. Science* https://doi.org/ghp2p7; 2020). The team also examined when each country implemented seven common anti-transmission approaches.

By combining the two data sets, the researchers found that closing schools and universities had a "large effect" on dampening viral spread. Most countries closed schools and universities in quick succession, making it impossible to disentangle the effects of each type of closure. In countries that closed schools and businesses and restricted gatherings, a stay-at-home order did little more to curb transmission, the team found.

Horizon 2020 ends: UK among largest beneficiaries

The end of 2020 marked the close of the European Union's massive 2014–20 research programme, Horizon 2020. Over the past 7 years, more than 150,000 participants — including research institutes, companies and individual scientists — collectively received almost €60 billion (US$73.5 billion) in research funding.

Between them, the EU's three biggest economies got almost 40% of the funds: researchers in Germany, France and the United Kingdom received a combined total of more than €22 billion.

The United Kingdom received 12.1% (more than €7 billion) of the Horizon 2020 funding; by comparison, the country's average contribution to the

overall EU budget is around 11.4% of the total. Germany took home the biggest percentage of Horizon 2020 funding (14.9%), but it contributes a higher percentage to the overall EU budget (20.9%). Likewise, France's funding share (11.1%) was lower than its average contribution percentage to the EU budget (17%; see 'Gains and losses').

GAINS AND LOSSES

The percentage of Horizon 2020 funding that some countries received was in some cases lower than their percentage contribution to the overall EU budget.

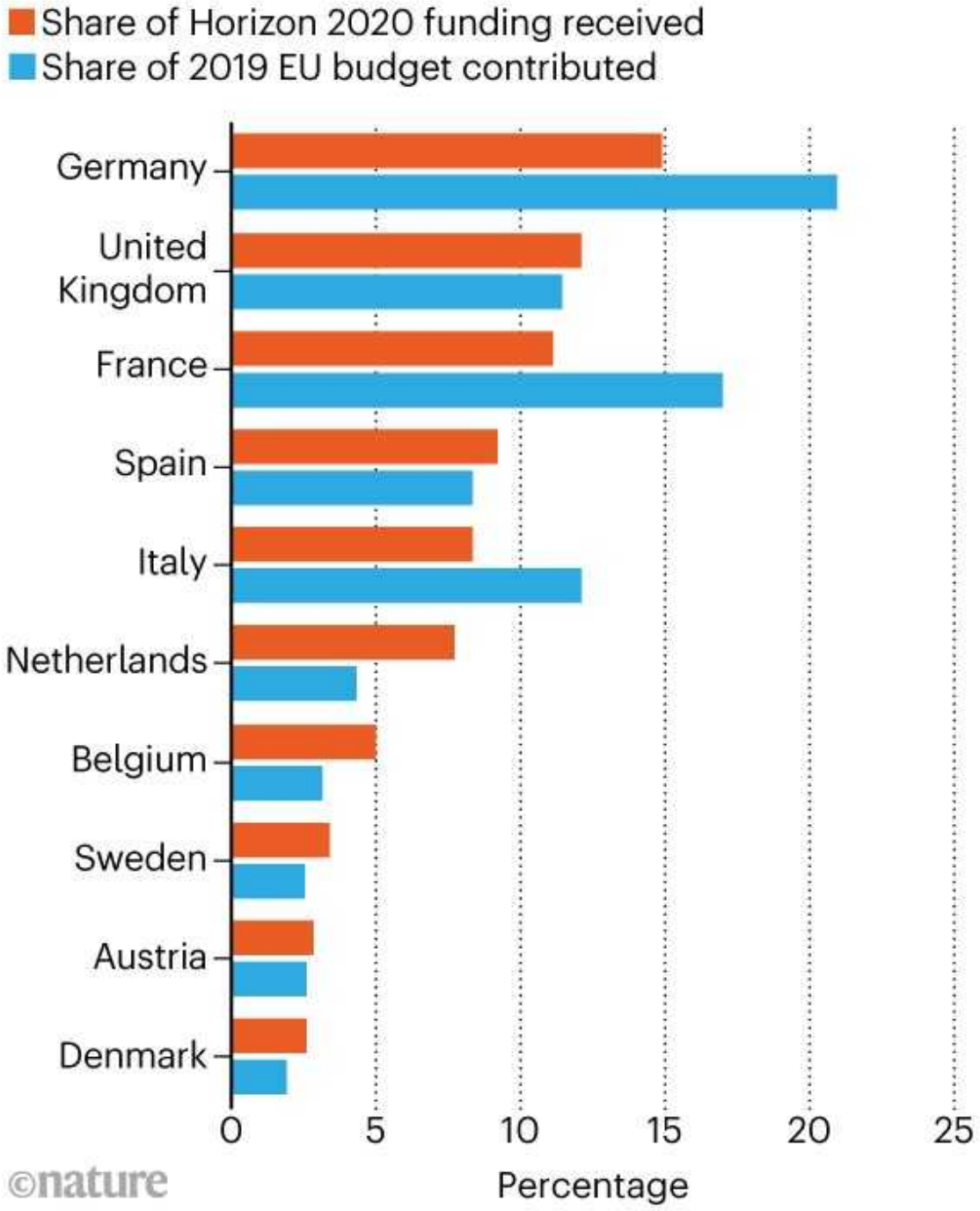

©nature

Source: European Commission/Horizon 2020 dashboard/Eurostat

The United Kingdom has officially left the EU, but will continue to participate in Horizon 2020 until all projects are completed. And the country will join the next EU research programme, Horizon Europe, which is worth €85 billion, as part of a post-Brexit trade deal.

Nature **589**, 9 (2021)

doi: https://doi.org/10.1038/d41586-020-03648-9

Jobs from Nature Careers

-
  -
    - All jobs
  -
    - **Aushilfe / Studentische Hilfskraft (m/w/d) im Abteilungssekretariat für 15 Std. / Woche**

      German Cancer Research Center in the Helmholtz Association (DKFZ)

      Heidelberg, Germany

      JOB POST

    - **Hochfrequenz Technikerin I Hochfrequenz Techniker (w/m/d)**

      Helmholtz-Zentrum Berlin for Materials and Energy (HZB)

      Berlin, Germany

      JOB POST

    -

PhD position – Genetics of neuropathological changes in Alzheimer's disease

Flanders Institute for Biotechnology (VIB)

Antwerp, Belgium

JOB POST

- **53541: Physicist, Engineer or similar - Laser-spectroscopic methods for the protection of terrestrial infrastructures**

  German Aerospace Center (DLR)

  Köln, Germany

  JOB POST

This article was downloaded by **calibre** from https://www.nature.com/articles/d41586-020-03648-9

NEWS
17 December 2020

Is lightning striking the Arctic more than ever before?

Team detects a huge increase and says it could be due to climate change, but others can't confirm the findings.

Alexandra Witze

Search for this author in:

- Pub Med
- Nature.com
- Google Scholar

Lightning typically forms with the aid of warm air, which is why it has historically been rare in the Arctic.Credit: Tommy Eliassen/Science Photo Library

Lightning is striking the Arctic many times more often than it did a decade ago, a study suggests — and the rate could soon double. The findings demonstrate yet another way Earth's climate could be changing as the planet warms, although not all researchers agree that the trend is real.

Robert Holzworth, an atmospheric physicist at the University of Washington in Seattle and leader of the study, defends the findings. "We're seeing a symptom of global climate change," he says. Holzworth is director of the World Wide Lightning Location Network (WWLLN), the collection of ground-based sensors that measured the data. He reported the results on 8 December at a virtual meeting of the American Geophysical Union (and published them before peer review as a preprint[1]).

The Arctic is burning like never before — and that's bad news for climate change

Another lightning-detection network, whose records do not extend as far back as those Holzworth studied, does not find the same increase.

Whether or not lightning is increasing in the Arctic could have a significant impact on the region. The past two years have set records for the largest area of land burnt by wildfires — some of them ignited by lightning — and the most carbon dioxide emitted in the Arctic since records began. More lightning would mean even more chances that wildfires will start, which could in turn put even more climate-altering soot and gases into the air.

Polar lightning

Lightning forms when ice crystals inside convecting storm clouds — those filled with roiling air currents fed by warm air — collide and transfer electrical charge. A charge separation builds up until it hits a threshold, and a lightning stroke is released. Some researchers have predicted that global warming will lead to more convective storms and lightning worldwide as air and ocean temperatures rise[2]. However, some modelling studies suggest the opposite[3].

Nonetheless, the World Meteorological Organization in Geneva, Switzerland, added lightning to its list of 'essential climate variables' in 2016, meaning that observations of lightning could help researchers to track the changing global climate.

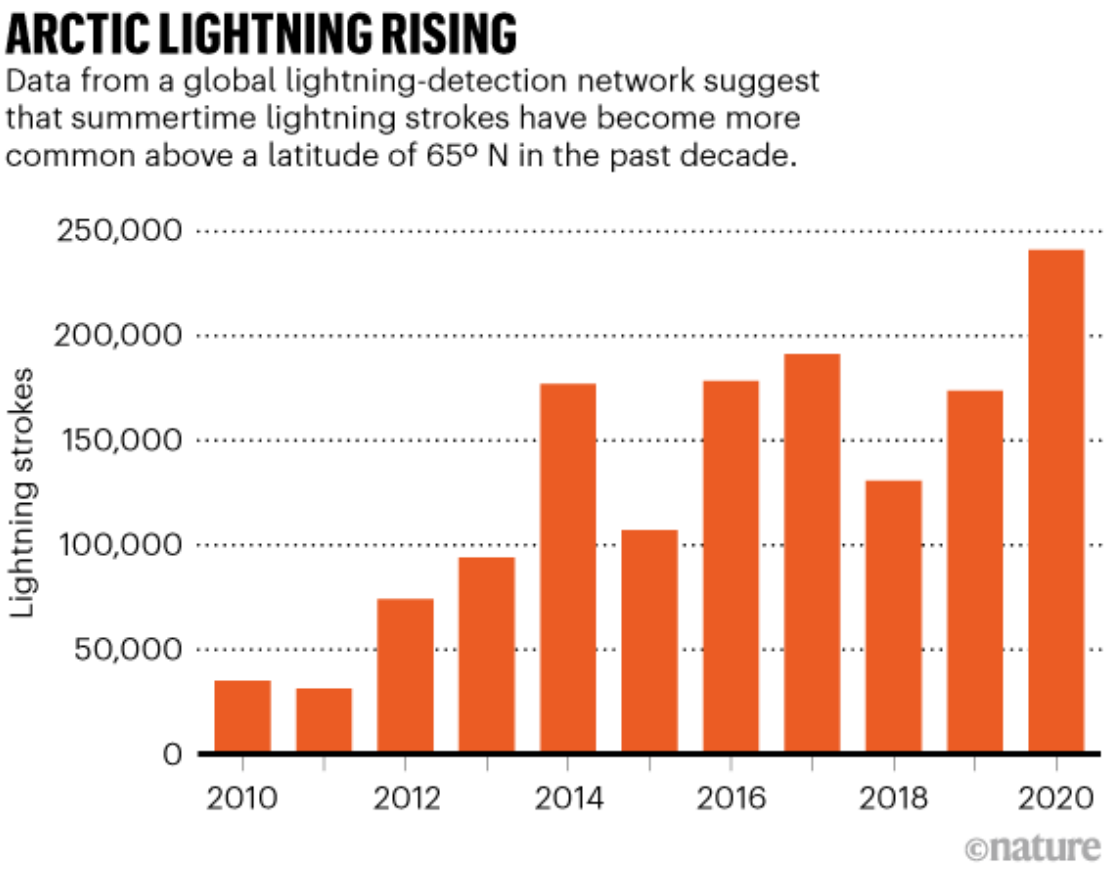

Source: Robert Holzworth/University of Washington

The Arctic is warming faster than the rest of the planet, so changes in lightning might be most apparent there. August 2019 saw the most northerly stroke ever detected — just 52 kilometres from the North Pole — according to the Finnish company Vaisala, headquartered in Vantaa, which runs a lightning-detection network. And a July 2014 storm over the Canadian Arctic caused more than 15,000 lightning strokes north of the Arctic Circle[4].

Lightning in the Arctic is normally rare, accounting for around 0.5% of all global strokes detected by the WWLLN.

But Holzworth and his colleagues found that the number of annual summertime lightning strokes above a latitude of 65° N rose from around 35,000 in 2010 to nearly 250,000 this year (see 'Arctic lightning rising'). The scientists studied the months of June, July and August, when nearly all Arctic lightning occurs. They found increasing numbers of lightning strokes

across the Arctic, with most of the activity happening around northern Siberia.

Verifying a trend

Tracking trends in lightning can be difficult because detection networks grow more efficient over time, as advanced sensors are added. So Holzworth and his colleagues ran several analyses to confirm that there was more Arctic lightning happening, not just more being detected. “There’s no question about it,” he says.

Scientists probe lightning hotspot to predict future strikes

Vaisala’s network has not recorded the same trend. Its data go back only to 2012, rather than to 2010. But “we don’t see an unambiguous trend toward more lightning at more extreme latitudes”, says Ryan Said, a meteorologist and lightning analyst in Vaisala’s office in Louisville, Colorado.

In places that see relatively little lightning, such as the Arctic, just a couple of intense thunderstorms can cause a proportionally huge rise in the total number of lightning strokes detected in a given year, Said notes. With so much year-to-year variability, it can be hard to isolate long-term trends.

Some researchers in the community say Holzworth's findings make sense. The work "supports the wider view of a lightning-richer future for the Arctic", says Sander Veraverbeke, an Earth-systems scientist at the Free University of Amsterdam. In 2017, Veraverbeke and his colleagues reported that lightning was igniting more wildfires, farther north, than in the past in parts of Alaska and Canada[5].

Arctic sea ice hits second-lowest level on record

One way to verify Holzworth's work would be to survey Indigenous and other communities living at high latitudes, says Jessica McCarty, a geographer at Miami University in Oxford, Ohio, who studies Arctic wildfire.

Another way is to follow up with further lightning-detection studies. Holzworth's work shows "an interesting correlation" with changes in global temperature, says Antti Mäkelä, a lightning specialist at the Finnish Meteorological Institute in Helsinki. By next year, Mäkelä and his colleagues will have 20 years of data from a lightning-detection system that spans Norway, Sweden, Finland and Estonia[6] — and they plan to analyse the data set to see whether there has been an increase in lightning in northern Scandinavia.

Nature **589**, 11-12 (2021)

doi: https://doi.org/10.1038/d41586-020-03561-1

References

1. 1.

   Holzworth, R. H. *et al.* Preprint at ESSOAr https://doi.org/10.1002/essoar.10504658.1 (2020).

2. 2.

   Price, C. & Rind, D. *J. Geophys. Res.* **99**, 10823–10831 (1994).

3. 3.

   Finney, D. L. *et al. Nature Clim. Change* 8, 210–213 (2018).

4. 4.

   Brown, D. M., Kochtubajda, B. & Said, R. K. *Atmos.–Ocean* **58**, 231–242 (2020).

5. 5.

   Veraverbeke, S. *et al. Nature Clim. Change* **7**, 529-534 (2017).

6. 6.

Mäkelä, A., Enno, S.-E. & Haapalainen, J. *Atmos. Res.* **139**, 46–61 (2014).

Jobs from Nature Careers

-
  -
    - All jobs
  -
    - **Aushilfe / Studentische Hilfskraft (m/w/d) im Abteilungssekretariat für 15 Std. / Woche**

      German Cancer Research Center in the Helmholtz Association (DKFZ)

      Heidelberg, Germany

      JOB POST

    - **Hochfrequenz Technikerin I Hochfrequenz Techniker (w/m/d)**

      Helmholtz-Zentrum Berlin for Materials and Energy (HZB)

      Berlin, Germany

      JOB POST

    - **PhD position – Genetics of neuropathological changes in Alzheimer's disease**

      Flanders Institute for Biotechnology (VIB)

      Antwerp, Belgium

      JOB POST

- **53541: Physicist, Engineer or similar - Laser-spectroscopic methods for the protection of terrestrial infrastructures**

  German Aerospace Center (DLR)

  Köln, Germany

  JOB POST

This article was downloaded by **calibre** from https://www.nature.com/articles/d41586-020-03561-1

NEWS
23 December 2020

- Correction 23 December 2020

Prestigious AI meeting takes steps to improve ethics of research

For the first time, the organizers of NeurIPS required speakers to consider the societal impact of their work.

Davide Castelvecchi

Search for this author in:

- Pub Med
- Nature.com
- Google Scholar

Artificial-intelligence research is coming under increasing ethical scrutiny.Credit: Michael Cohen/Getty

After a year of heavy scrutiny and seemingly endless controversy around artificial-intelligence (AI) technologies, the field's most prestigious conference has tried to set a good example. For the first time, the Neural Information Processing Systems (NeurIPS) meeting, which took place completely online this month, required presenters to submit a statement on the broader impact their research could have on society, including any possible negative effects.

The organizers also appointed a panel of reviewers to scrutinize papers that raised ethical concerns — a process that could lead to their rejection.

"I think there's a lot of value even in getting people to think about these things," says Jack Poulson, founder of the industry watchdog Tech Inquiry in Toronto, Canada. He adds that the policy could help to shift culture in the field.

Researchers who work on machine learning are increasingly aware of the challenges posed by harmful uses of the technology, from the creation of falsified videos, or 'deepfakes', to mistakes by police who rely on facial-recognition algorithms in deciding who to arrest.

"There was previously a period of techno optimism," says Iason Gabriel, an ethicist at the AI powerhouse DeepMind, a sister company of Google based in London. "Clearly, that has changed in recent years."

Unintended uses

The idea of conference participants writing an impact statement was inspired by the Future of Computing Academy, a group led by Brent Hecht, a specialist in the human impacts of technology at Microsoft and at Northwestern University in Evanston, Illinois. In 2018, Hecht and his collaborators proposed that computer-science publications be required to state the potential side effects and unintended uses of their research. Unlike in other scientific disciplines, most peer review in computer science happens when manuscripts are submitted to conferences, rather than to scholarly journals. As the field's largest and most prestigious conference, NeurIPS was a natural choice to test this proposal.

This year's conference attracted 9,467 paper submissions. The reviewers assessed submissions mainly on their scientific value, but papers with potential to be accepted could be flagged for a full review by a separate ethics committee led by Gabriel. Of 290 papers that were flagged, 4 were ultimately rejected by the programme chairs because of ethical considerations, says Marc'Aurelio Ranzato, a computer scientist at Facebook AI Research in New York City who was one of the conference's programme chairs.

"In general, I would say the ethics process has done well," says Katherine Heller, a computer scientist at Google in Mountain View, California, who was the conference's co-chair of diversity and inclusion.

Gabriel says that most problematic issues should have been caught, because any of the three anonymous peer reviewers could flag a paper, as could the

subject-area chair. “A signal from any one of them would be enough to engage the review process,” he says. Still, he admits that the process was not infallible. For example, if all the reviewers happened to be men — not unusual in a male-dominated field — they might not be able to adequately assess whether an algorithm could affect women negatively. “I can’t rule out the possibility that there would be blind spots of this kind,” Gabriel says.

In addition, reviewers were not given specific guidance on what constitutes harm to society. For example, says Ranzato, some reviewers flagged papers that made use of databases containing personal information or photographs that were collected without explicit consent. The use of such databases has come under heavy criticism, but the conference organizers did not single out this issue to reviewers or provide a list of problematic databases. Still, Ranzato adds that the review policy is a step in the right direction. “Nothing is perfect, but it’s better than before.”

Policing AI

The last day of the conference featured a special session focused on the broader impact of AI on society. Hecht, Gabriel and other panellists discussed ways to address the industry’s problems. Hanna Wallach, a researcher at Microsoft in New York City, called for researchers to assess and mitigate any potential harm to society from the early stages of research, without assuming that their colleagues who develop and market end products will do that ethical work. Ethical thinking should be built into the machine-learning field rather than simply being outsourced to ethics specialists, she said, otherwise, “other disciplines could become the police while programmers try to evade them”.

Wallach and others, such as Donald Martin, a technical programme manager at Google in San Francisco, California, are working to redesign the product-development process at their companies so that it incorporates awareness of social context. AI ethics, Martin says, “is not a crisis in the public understanding of science, but a crisis in science’s understanding of the public”.

The revamped review process and the ethics-focused discussions are the latest in a series of efforts by NeurIPS organizers to improve practices in machine learning and AI. In 2018, the conference dropped an acronym that many people found offensive, and began a crackdown on sexist behaviour by participants. And last year's meeting featured robust discussions of AI ethics and inclusivity.

The mood of this year's conference was affected by events that occurred on its eve. On 2 December, Timnit Gebru, a leading researcher on racial bias in machine-learning algorithms, said that after a dispute over the publication of a paper she had co-authored, she had been dismissed from Google, where she co-led a team working on ethics in AI. Google has stated that it accepted her resignation; Gebru has said that she never resigned, but had merely threatened to do so at a later date if her conditions on the paper's internal review were not met.

The situation has led many researchers to publicly question Google's commitment to ethical AI. Thousands both at Google and elsewhere have signed a letter of solidarity, pointing out that Gebru was "one of very few Black women Research Scientists at the company, which boasts a dismal 1.6% Black women employees overall".

On 16 December, members of the US Congress wrote to Google chief executive Sundar Pichai, saying that "the incident raises broader questions, the answers to which may meaningfully impact our work as legislators". Google did not respond to a request for comment from *Nature*'s news team.

Nature **589**, 12-13 (2021)

doi: https://doi.org/10.1038/d41586-020-03611-8

Updates & Corrections

- **Correction 23 December 2020**: This story was updated to clarify that the ethics committee didn't have the power to reject a submission. It was the programme chairs who ultimately rejected submissions because of ethical considerations.

Jobs from Nature Careers

-
  -
    - All jobs
  -
    - **Aushilfe / Studentische Hilfskraft (m/w/d) im Abteilungssekretariat für 15 Std. / Woche**

      German Cancer Research Center in the Helmholtz Association (DKFZ)

      Heidelberg, Germany

      JOB POST

    - **Hochfrequenz Technikerin I Hochfrequenz Techniker (w/m/d)**

      Helmholtz-Zentrum Berlin for Materials and Energy (HZB)

      Berlin, Germany

      JOB POST

    - **PhD position – Genetics of neuropathological changes in Alzheimer's disease**

      Flanders Institute for Biotechnology (VIB)

      Antwerp, Belgium

      JOB POST

    - **53541: Physicist, Engineer or similar - Laser-spectroscopic methods for the protection of**

terrestrial infrastructures

German Aerospace Center (DLR)

Köln, Germany

JOB POST

This article was downloaded by **calibre** from https://www.nature.com/articles/d41586-020-03611-8

NEWS
15 December 2020

Surprise! First peek inside Mars reveals a crust with cake-like layers

NASA's InSight mission yields the first data on the internal structure of a planet other than Earth.

Alexandra Witze

Search for this author in:

- Pub Med
- Nature.com
- Google Scholar

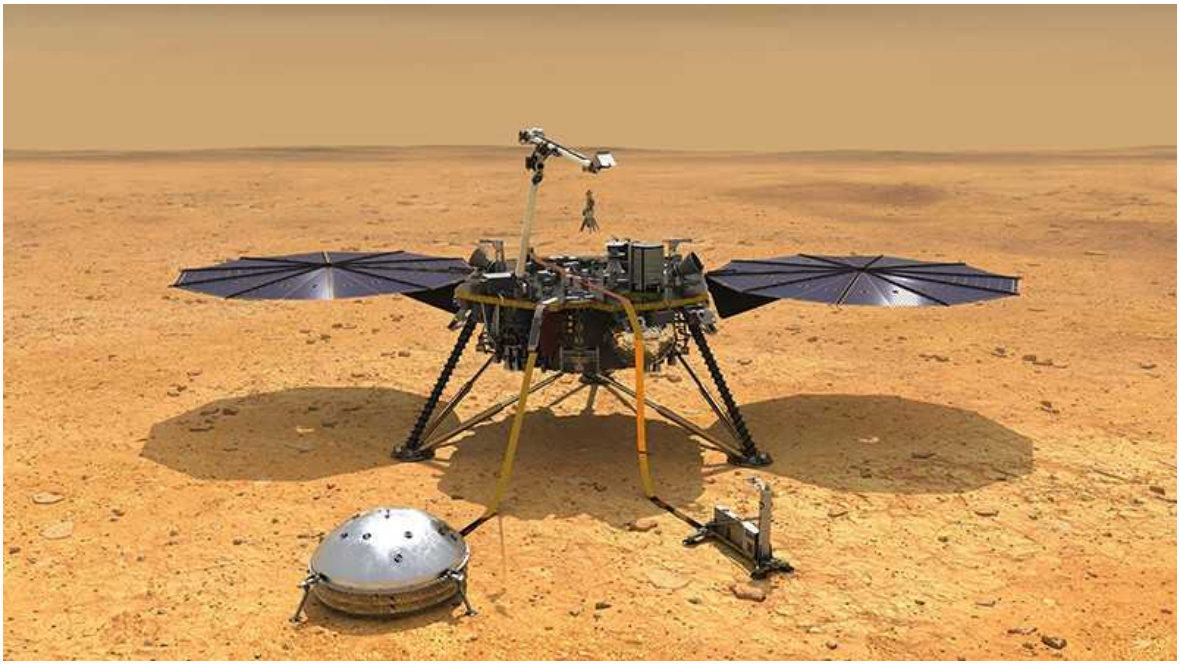

The Mars InSight lander is equipped with a domed seismometer (left) and a probe for measuring heat flow (right).Credit: NASA/JPL-Caltech

NASA's InSight mission has finally peered inside Mars — and discovered that the planet's crust might be made of three layers. This is the first time scientists have directly probed the inside of a planet other than Earth, and will help researchers to unravel how Mars formed and evolved over time.

Before this mission, researchers had measured only the interior structures of Earth and the Moon. "This information was missing, until now, from Mars," said Brigitte Knapmeyer-Endrun, a seismologist at the University of Cologne in Germany, in a prerecorded talk played at the virtual American Geophysical Union meeting on 15 December. She declined an interview with *Nature*, saying that the work is under consideration for publication in a peer-reviewed journal.

‘Marsquakes’ reveal red planet’s hidden geology

It is a major finding for InSight, which landed on Mars in November 2018 with a goal of working out the planet's internal structure[1]. The InSight

lander squats near the Martian equator, on a smooth plain known as Elysium Planitia, and uses an exquisitely sensitive seismometer to listen to geological energy thrumming through the planet[2]. So far, the mission has detected more than 480 ‘marsquakes’, says Bruce Banerdt, the mission’s principal investigator and a scientist at the Jet Propulsion Laboratory in Pasadena, California. Mars is less seismically active than Earth, but more so than the Moon.

Just as they do with earthquakes on Earth, seismologists are using marsquakes to map the red planet’s interior structure. Seismic energy travels through the ground in two types of wave; by measuring the differences in how those waves move, researchers can calculate where the planet’s core, mantle and crust begin and end, and the general make-up of each one. Those fundamental geological layers reveal how the planet cooled and formed billions of years ago at the fiery birth of the Solar System. Now, “we have enough data to start answering some of these big questions”, says Banerdt.

Earth’s continental crust is generally divided into sublayers of different types of rock. Researchers had suspected, but didn't know for sure, that the Martian crust was also layered, says Justin Filiberto, a planetary geologist at the Lunar and Planetary Institute in Houston, Texas. Now, InSight’s data show that it is made up of either two or three layers.

A three-layered crust would fit best with geochemical models[3] and studies of Martian meteorites, says Julia Semprich, a planetary scientist at the Open University in Milton Keynes, UK.

‘Marsquake’ hunter prepares to land on the red planet

Depending on whether the crust actually has two or three layers, it is either 20 or 37 kilometres thick, Knapmeyer-Endrun said during her talk. That thickness probably varies at different locations around the planet, but is likely to be no greater than 70 kilometres on average, she added. On Earth,

the crustal thickness varies from around 5 to 10 kilometres beneath the oceans, to around 40 to 50 kilometres beneath the continents.

In the coming months, InSight scientists plan to report measurements taken even deeper in Mars, says Banerdt — ultimately revealing information about the planet's core and mantle.

Along with listening to marsquakes, InSight's other big scientific goal is to measure heat flow through the Martian ground using a probe dubbed the mole. It was meant to bury itself deep in the soil, but has struggled to do so — at one point even popping out of the ground altogether. The mole has finally managed to get itself several centimetres deep, says Banerdt, and will try digging one final time in the coming weeks before giving up. "We're at what we consider to be the end game now," he says.

Nature **589**, 13 (2021)

doi: https://doi.org/10.1038/d41586-020-03562-0

References

1. 1.

   Knapmeyer-Endrun, B. & Kawamura, T. *Nature Commun.* **11**, 1451 (2020).

2. 2.

   Banerdt, W. B. *et al. Nature Geosci.* **13**, 183-189 (2020).

3. 3.

   Semprich, J. & Filiberto, J. *Meteorit. Planet. Sci.* **55**, 1600-1614 (2020).

Jobs from Nature Careers

-

- All jobs

- **Aushilfe / Studentische Hilfskraft (m/w/d) im Abteilungssekretariat für 15 Std. / Woche**

  German Cancer Research Center in the Helmholtz Association (DKFZ)

  Heidelberg, Germany

  JOB POST

- **Hochfrequenz Technikerin I Hochfrequenz Techniker (w/m/d)**

  Helmholtz-Zentrum Berlin for Materials and Energy (HZB)

  Berlin, Germany

  JOB POST

- **PhD position – Genetics of neuropathological changes in Alzheimer's disease**

  Flanders Institute for Biotechnology (VIB)

  Antwerp, Belgium

  JOB POST

- **53541: Physicist, Engineer or similar - Laser-spectroscopic methods for the protection of terrestrial infrastructures**

  German Aerospace Center (DLR)

Köln, Germany

JOB POST

This article was downloaded by **calibre** from https://www.nature.com/articles/d41586-020-03562-0

NEWS
22 December 2020

The science events to watch for in 2021

Climate change and COVID-19 vaccines are among the themes set to shape research.

Holly Else

Search for this author in:

- Pub Med
- Nature.com
- Google Scholar

The large blackened and decapitated trunk of a giant Sequoia surrounded by other fire-damaged trees in a forest in the hills

Climate change could make wildfires like the one that decapitated this giant sequoia in California more frequent. Credit: Al Seib/Los Angeles Times/Getty

Climate comeback

2021 looks set to be a pivotal year for the fight against climate change. US president-elect Joe Biden has made clear that he will move to restore the country's leadership in that regard, including by rejoining the Paris climate agreement to fight global warming. (President Donald Trump pulled the United States out of the accord, and the nation officially left the day after the 2020 election.) A key moment for climate negotiations will come at the United Nations' climate conference in Glasgow, UK, in November.

Countries will make a new round of pledges on cuts to greenhouse-gas emissions — the first since they signed the Paris agreement in 2015. The European Union and China have ambitious plans to become carbon neutral by 2050–60; scientists are waiting to see whether Biden will set similar goals for the United States.

COVID detectives

A task force established by the World Health Organization will head to China in January 2021 to try to identify the source of the COVID-19 pandemic. The group, which includes epidemiologists, virologists and public- and animal-health researchers, will begin their search in Wuhan, the Chinese city where infections with the coronavirus SARS-CoV-2 were first identified in 2019. The initial stages of the project will look at meat and animals sold at the Huanan market — visited by many of the first people reported to have COVID-19 — and trace their journeys through China and across borders. Discovering the origins of the virus could take years, but experts think some new information will come to light by the end of the year.

It is unclear whether the Huanan market in Wuhan, China, was ground zero for SARS-CoV-2.Credit: Hector Retamal/AFP/Getty

Vaccines and the pandemic

2020 saw the roll-out of the first vaccines authorized for use against COVID-19. The effectiveness of several new vaccines will become clearer in early 2021. Of particular interest will be the results of phase III clinical trials of immunizations developed by the US pharmaceutical companies Novavax and Johnson & Johnson. These jabs are likely to be easier to distribute than the RNA-based vaccines made by Pfizer–BioNTech and Moderna, which have already returned phase III results but must be stored at very low temperatures. As *Nature* went to press, the Pfizer vaccine already had emergency authorization for use in some countries. Late last year, Novavax launched two large trials of its viral-spike-protein vaccine in the United Kingdom and the United States, which will report in early 2021. The company could produce as many as two billion vaccine doses per year. Johnson & Johnson is testing a single-shot version of its vaccine; by contrast, those from Pfizer and Moderna require two.

Open-access drive

All eyes will be on science publishing in 2021 as a two-year open-access project organized by some of the world's largest research funders comes to fruition. More than 20 organizations, including Wellcome in London, the Bill & Melinda Gates Foundation in Seattle, Washington, and Dutch national funder NWO, will from January start stipulating that scholarly papers published from the work they fund must be immediately free to read. The initiative, called Plan S, could spell the end of journal subscriptions and allow anyone to read the scientific literature. Plan S has already prompted several titles — including *Nature* — to offer open-access publishing for the first time. (*Nature* is editorially independent from its publisher, Springer Nature.)

Stem-cell revamp

Stem-cell scientists will be eagerly awaiting updated guidelines for research from the International Society for Stem Cell Research (ISSCR). The ISSCR, a membership oganization, last issued guidelines four years ago. The revamp, which will include guidance on studies of human 'embryo-like structures' grown from stem cells *in vitro*, could provide ammunition for lengthening the '14-day rule', which dictates that researchers cannot work with a human embryo produced *in vitro* for more than two weeks after fertilization and is enshrined in law in many countries. Extending the limit could allow scientists to better understand why so many early pregnancies end in miscarriage.

Crunch time for Alzheimer's drug

US regulators are slated to decide whether the first drug reported to slow down the progression of Alzheimer's disease can be used as a treatment. The drug, aducanumab, made by pharmaceutical company Biogen, is an antibody that binds to a sticky brain protein called amyloid, which most scientists think could be the main trigger for the disease. Evidence that the drug works is mixed. Two phase III clinical trials have offered conflicting results, and an independent advisory panel convened by the US Food and Drug Administration to assess the drug's effectiveness says that the data do not support its use. The only Alzheimer's drugs approved so far treat cognitive symptoms such as memory loss, rather than the progression of the disease.

Mars gets busy

China's ambitious agenda for space science continues in 2021. A Chinese probe destined for Mars should touch down there in February. The Tianwen-1 mission will look for water and signs of life using 13 instruments, including cameras, radar and particle analysers. If successful, it will be the country's first exploration of the red planet and the only time a probe carrying an orbiter, lander and rover has touched down there. Craft from the United Arab Emirates and the United States should also arrive at the red planet around the same time.

The James Webb telescope. Its mirror and sunshield will be folded up during launch.Credit: NASA

Long-awaited telescope launch

October will see the long-awaited launch of the James Webb Space Telescope — which its developer, NASA, calls the “largest, most powerful and complex space telescope ever built”. The US$8.8-billion Webb will seek to repeat the success of the Hubble Telescope, which revolutionized astronomy when it launched in 1990 and has made more than 1.3 million observations since. Webb will cover more wavelengths than Hubble, enabling scientists to peer deeper into the Universe.

Ripple effect

Radio astronomers could be on the verge of demonstrating a new way of detecting gravitational waves by harnessing pulsating neutron stars as beacons. By precisely timing the signals from these pulsars, teams in

Europe, North America and Australia seek to detect long-wavelength ripples produced by pairs of supermassive black holes as they orbit each other at the centres of distant galaxies.

Brexit unknowns

As *Nature* went to press, the European Union and the United Kingdom were still attempting to negotiate a trade deal ahead of the scheduled expiry of the Brexit transition agreement on 31 December. Deal or no deal, Brexit creates uncertainty around research funding and many other issues for scientists, and this will continue into 2021.

Nature **589**, 14-15 (2021)

doi: https://doi.org/10.1038/d41586-020-03651-0

Jobs from Nature Careers

-
  -
    - All jobs
  -
    - **Aushilfe / Studentische Hilfskraft (m/w/d) im Abteilungssekretariat für 15 Std. / Woche**

      German Cancer Research Center in the Helmholtz Association (DKFZ)

      Heidelberg, Germany

      JOB POST

    - **Hochfrequenz Technikerin I Hochfrequenz Techniker (w/m/d)**

      Helmholtz-Zentrum Berlin for Materials and Energy (HZB)

Berlin, Germany

JOB POST

- **PhD position – Genetics of neuropathological changes in Alzheimer's disease**

  Flanders Institute for Biotechnology (VIB)

  Antwerp, Belgium

  JOB POST

- **53541: Physicist, Engineer or similar - Laser-spectroscopic methods for the protection of terrestrial infrastructures**

  German Aerospace Center (DLR)

  Köln, Germany

  JOB POST

This article was downloaded by **calibre** from https://www.nature.com/articles/d41586-020-03651-0

NEWS FEATURE
18 December 2020

The lightning-fast quest for COVID vaccines — and what it means for other diseases

The speedy approach used to tackle SARS-CoV-2 could change the future of vaccine science.

Philip Ball

Search for this author in:

- Pub Med
- Nature.com
- Google Scholar

Workers in hi-vis vests move a large shipping container across the floor of a warehouse

The first US shipments of the joint Pfizer–BioNTech COVID-19 vaccine were ready by mid-December. Credit: Michael Clevenger/Getty

When scientists began seeking a vaccine for the SARS-CoV-2 coronavirus in early 2020, they were careful not to promise quick success. The fastest any vaccine had previously been developed, from viral sampling to approval, was four years, for mumps in the 1960s. To hope for one even by the summer of 2021 seemed highly optimistic.

But by the start of December, the developers of several vaccines had announced excellent results in large trials, with more showing promise. And on 2 December, a vaccine made by drug giant Pfizer with German biotech

firm BioNTech, became the first fully-tested immunization to be approved for emergency use.

That speed of advance "challenges our whole paradigm of what is possible in vaccine development", says Natalie Dean, a biostatistician at the University of Florida in Gainesville. It's tempting to hope that other vaccines might now be made on a comparable timescale. These are sorely needed: diseases such as malaria, tuberculosis and pneumonia together kill millions of people a year, and researchers anticipate further lethal pandemics, too.

The COVID-19 experience will almost certainly change the future of vaccine science, says Dan Barouch, director of the Center for Virology and Vaccine Research at Harvard Medical School in Boston, Massachusetts. "It shows how fast vaccine development can proceed when there is a true global emergency and sufficient resources," he says. New ways of making vaccines, such as by using messenger RNA (mRNA), have been validated by the COVID-19 response, he adds. "It has shown that the development process can be accelerated substantially without compromising on safety."

The first UK injections of a fully tested COVID-19 vaccine were given in early December.Credit: Dan Charity/AFP/Getty

The world was able to develop COVID-19 vaccines so quickly because of years of previous research on related viruses and faster ways to manufacture vaccines, enormous funding that allowed firms to run multiple trials in parallel, and regulators moving more quickly than normal. Some of those factors might translate to other vaccine efforts, particularly speedier manufacturing platforms.

But there's no guarantee. To repeat such rapid success will require similar massive funding for development, which is likely to come only if there is a comparable sense of social and political urgency. It will depend, too, on the nature of the pathogen. With SARS-CoV-2, a virus that mutates relatively slowly and that happens to belong to a well-studied family, scientists might — strange as it sounds — have got lucky.

Years of advance research

The research that helped to develop vaccines against the new coronavirus didn't start in January. For years, researchers had been paying attention to related coronaviruses, which cause SARS (severe acute respiratory syndrome) and MERS (Middle East respiratory syndrome), and some had been working on new kinds of vaccine — an effort that has now paid off spectacularly.

Vials of Sinovac Biotech's COVID-19 vaccine on a production line in Beijing.Credit: Kevin Frayer/Getty

Conventional vaccines contain viral proteins or disabled forms of the virus itself, which stimulate the body's immune defences against infection by a live virus. But the first two COVID-19 vaccines for which efficacy was announced in large-scale (phase III) clinical trials used just a string of mRNA inside a lipid coat. The mRNA encodes a key protein of SARS-CoV-2; once the mRNA gets inside our cells, our bodies produce this protein. That acts as the antigen — the foreign molecule that triggers an immune response. The vaccines made by Pfizer and BioNTech and by the US pharmaceutical company Moderna both use mRNA that encodes the spike protein, which docks to human cell membranes and allows the coronavirus to invade the cell.

"A lot went into the mRNA platform that we have today," says immunologist Akiko Iwasaki at the Yale School of Medicine in New Haven, Connecticut, who has worked on nucleic-acid vaccines — those based on lengths of DNA or RNA — for more than two decades. The basic research

on DNA vaccines began at least 25 years ago, and RNA vaccines have benefited from 10–15 years of strong research, she says, some aimed at developing cancer vaccines. The approach has matured just at the right time; five years ago, the RNA technology would not have been ready.

For instance, researchers at the US National Institute of Allergy and Infectious Diseases (NIAID) in Bethesda, Maryland, knew from their research on MERS and SARS that it was best to tune the RNA sequence to stabilize the resulting spike protein in the form it adopts before it docks with a host cell. “If you can trap it in its original pre-fusion state, it becomes a much better vaccine antigen,” says Barney Graham, deputy director of NIAID’s vaccine research centre. That work gave the NIAID team, which worked with Moderna, a head start once SARS-CoV-2 was sequenced in January. “The fact that people had been paying close attention to coronaviruses really allowed this whole process to accelerate,” says Dean.

Barney Graham, deputy director of the NIAID Vaccine Research Center (VRC; left), talks to US President Donald Trump (second from right) during a visit in March. VRC scientists at the centre, co-led by researcher Kizzmekia Corbett (far right), created RNA sequences for COVID-19

vaccines in early January. Also pictured are NIH director Francis Collins (second from left) and VRC director John Mascola (third from left).Credit: Evan Vucci/AP/Shutterstock

The third vaccine to show efficacy in phase III clinical trials in November, made by the pharmaceutical firm AstraZeneca with the University of Oxford, UK, does not use mRNA. Instead, a viral vector (or carrier) holds extra genetic material that codes for the SARS-CoV-2 spike protein. This, too, benefited from years of research to select the vector; in this case, the firm chose a modified form of adenovirus isolated from chimpanzee stool. Advances in conventional vaccines such as these have also come from research on SARS, MERS, Ebola and malaria, says Beate Kampmann, director of the Vaccine Centre at the London School of Hygiene & Tropical Medicine, and such approaches remain cheaper than using mRNA.

Vaccine researchers were fortunate with SARS-CoV-2 in many respects, says Iwasaki. The virus doesn't mutate a lot or have effective strategies for foiling the human immune system, she says, unlike HIV, herpes or even influenza. The herpes virus, by contrast, has more evasion capability — it actively blocks antibodies from binding, which makes it harder to find an effective agent against it. And the fast mutation of flu viruses requires a different vaccine formulation for every flu season.

Supercharged with funding

The slowest part of vaccine development isn't finding candidate treatments, but testing them. This often takes years (see 'Vaccine innovation'), with companies running efficacy and safety tests on animals and then in humans. Human testing requires three phases that involve increasing numbers of people and proportionately escalating costs. The COVID-19 vaccines went through the same trials, but the billions poured into the process made it possible for companies to take financial risks by running some tests at the same time (see 'A vaccine in a year').

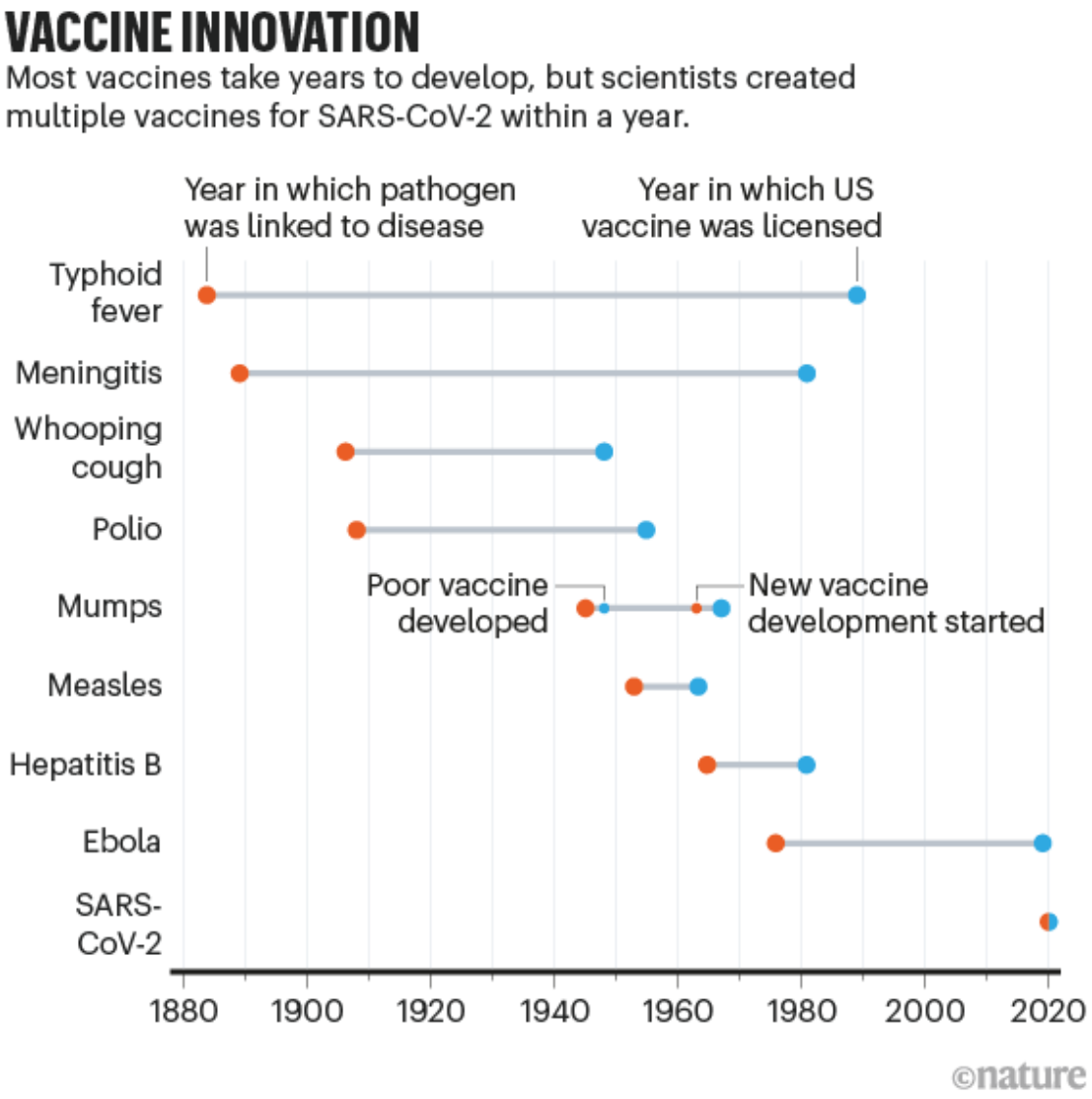

Sources: Our World in Data; *Nature* analysis

With large sums given to vaccine firms by public funders and private philanthropists, "they could do preclinical and phase I, II and III trials, as well as manufacturing, in parallel instead of sequentially", says Rino Rappuoli, chief scientist at GlaxoSmithKline's vaccines division in Siena, Italy. This meant that companies could gamble on starting large-scale testing and manufacturing of candidates that might not work out. "It was totally de-risking the entire development process," says Kampmann.

The vaccine science would not have produced such fast results without this funding, she says. "It didn't happen with Ebola, which was devastating

communities in Africa [in 2014–16]" — and Ebola vaccines accordingly took longer to develop. The money only materialized this time because all countries, including wealthy ones, faced economic devastation: suggesting that the development of future vaccines, including for existing diseases such as malaria, will not be as speedy. "Unless you put in the money, there's no way to accelerate," says Rappuoli.

Virologist Peter Hotez at Baylor College of Medicine in Houston, Texas, suggests that large pharmaceutical companies might have been motivated not just by the desire to stop the pandemic, but also by the opportunity for governments to fund their research and development. With public investment of around US$10 billion, the US Operation Warp Speed vaccine programme "represents the largest government stimulus package the pharma companies have ever seen", says Hotez.

The impetus didn't all come from the urgency of the COVID-19 pandemic itself. Previous infectious and lethal viruses have motivated the creation of national and global infrastructures that can promote faster vaccine development. The Ebola and Zika outbreaks saw the beginning of better global coordination in how to respond to an infectious-disease crisis, Graham says. "If SARS in 2002 had spread like this, we wouldn't have had the vaccine technology or the coordinated systems, and we'd have had a much more difficult time," he says.

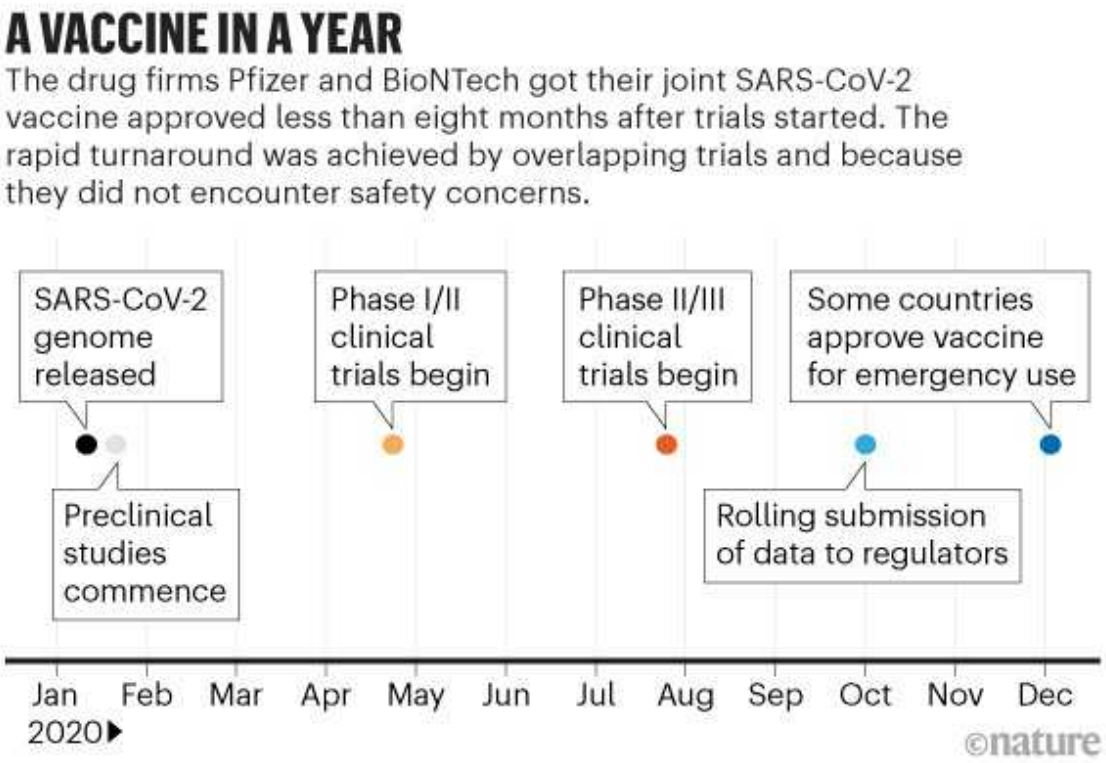

Sources: BioNTech/Pfizer; *Nature* analysis

In particular, the Coalition for Epidemic Preparedness Innovations (CEPI) was launched in 2017; its goal is to create the technological infrastructure needed for rapid and affordable development of vaccines against several of the viruses known to have epidemic potential, including MERS, Ebola and Zika. CEPI has partly funded work on SARS-CoV-2 vaccines, including that by Moderna and at Oxford.

In the final stages of trials, it helped that COVID-19 was everywhere because firms need infections to show that vaccines work. It's hard to run efficacy trials when the diseases themselves aren't prevalent — especially, says Dean, in cases such as MERS, for which outbreaks of disease were patchy, with peaks in some areas and low infection rates in others.

The COVID-19 experience might also prompt a regulatory rethink. Although there has been no relaxing of the stringent criteria for vaccine approval, the first candidates are mostly being approved under emergency-use regulations. These are faster but require companies to conduct follow-up

surveys to look for side effects and continuing efficacy. National regulators also swapped information on COVID-19 vaccine trials under the auspices of a global body called the International Coalition of Medicines Regulatory Authorities, set up in 2012. It has aimed to reach consensus on issues such as the best end-points for vaccine trials, and how to harmonize the monitoring of side effects as vaccines are rolled out (see also *Nature* 588, 195; 2020).

Benefits for other vaccines

The COVID-19 pandemic should see some permanent changes in vaccine development. For a start, it might establish the use of mRNA vaccines — which hadn't previously been approved for general use in people — as a speedy approach for other diseases. "This technology is revolutionizing vaccinology," says Kampmann. Candidate mRNA vaccines can be chemically synthesized in a few days, in contrast to the more complicated biotechnology involved in producing proteins in cells. "The technology lends itself to the nimble plug-and-play approach that will be required to respond to [future] pandemics," Kampmann says.

What's more, "RNA simplifies the manufacturing a lot," says Rappuoli. "You can use the same facility to make RNA for different diseases. That decreases the investment required." Companies should also be ramping up their manufacturing capacities because they still have to make vaccines for measles, polio and other diseases even as they produce COVID-19 immunizations. That could help to meet demand in future.

Moderna's mRNA COVID-19 vaccine will be made by the biotech firm Lonza at these facilities in Visp, Switzerland.Credit: Denis Balibouse/Reuters

The large clinical trials for COVID-19 vaccines, and others in development, should provide data that are more widely useful for understanding immune responses, says Hotez. "Given all the different technologies, and detailed information collected on clinical volunteer demographics, antibody and cellular responses, we might learn as much or more from human vaccine responses this year than in previous decades. Human vaccinology could make a quantum leap."

Still, other vaccines can probably only be developed at a comparable speed when infection levels are high — making it possible to run massive trials relatively quickly — and with huge amounts of funding. And other viruses might be harder to target than SARS-CoV-2 turned out to be.

That's why we need to know more about all families of viruses, say researchers. There are at least 24 other virus families that can infect humans, says Graham. Rather than waiting to sink resources into fighting the next

virus that pops up, money would be better spent now setting up systems to monitor all these viruses and to generate data on prototype infections in each of these families, he says.

In other words, no amount of money will help without a solid platform of basic science to build on. The extraordinary success of the COVID-19 vaccines "is a good example of what science can do very quickly", says Iwasaki, "but it didn't happen overnight."

Nature **589**, 16-18 (2021)

doi: https://doi.org/10.1038/d41586-020-03626-1

Jobs from Nature Careers

-
  -
    - All jobs
  -
    - **Aushilfe / Studentische Hilfskraft (m/w/d) im Abteilungssekretariat für 15 Std. / Woche**

      German Cancer Research Center in the Helmholtz Association (DKFZ)

      Heidelberg, Germany

      JOB POST

    - **Hochfrequenz Technikerin I Hochfrequenz Techniker (w/m/d)**

      Helmholtz-Zentrum Berlin for Materials and Energy (HZB)

      Berlin, Germany

      JOB POST

- **PhD position – Genetics of neuropathological changes in Alzheimer's disease**

  Flanders Institute for Biotechnology (VIB)

  Antwerp, Belgium

  JOB POST

- **53541: Physicist, Engineer or similar - Laser-spectroscopic methods for the protection of terrestrial infrastructures**

  German Aerospace Center (DLR)

  Köln, Germany

  JOB POST

This article was downloaded by **calibre** from https://www.nature.com/articles/d41586-020-03626-1

Opinion

- **Reburying World Heritage human remains would close window on Barkandji past** [05 January 2021]
  Correspondence •
- **Europe's 'green deal' and carbon dioxide removal** [05 January 2021]
  Correspondence •
- **Optimizing public services after COVID** [05 January 2021]
  Correspondence •
- **Africa's reforestation: European Union and United States should step up** [05 January 2021]
  Correspondence •

CORRESPONDENCE
05 January 2021

Reburying World Heritage human remains would close window on Barkandji past

Michael Westaway,

University of Queensland, Brisbane, Australia.
Contact

Search for this author in:

- Pub Med
- Nature.com
- Google Scholar

Warren Clark,

Barkandji man, Mildura, Australia.

Search for this author in:

- Pub Med
- Nature.com
- Google Scholar

Doug Williams &

Griffith University, Brisbane, Australia.

Search for this author in:

- Pub Med
- Nature.com
- Google Scholar

Gerald Quayle

Barkandji man, Broken Hill, Australia.

Search for this author in:

- Pub Med
- Nature.com
- Google Scholar

The largest collection outside Africa of modern human remains from the last glacial cycle was unearthed at the Willandra Lakes World Heritage Area in New South Wales (NSW), Australia, more than 30 years ago (J. M. Bowler *et al*. *Nature* **421**, 837–840; 2003). Held in a university collection, these fossil remains have barely been studied. They are now scheduled for reburial in 2021.

About 80 of the more than 100 individuals in the collection are from the northern Willandra Lakes, which overlaps with the Barkandji Native Title determination area. As members and affiliates of the Barkandji descendants, we call on NSW to delay reburial so we can discuss the fate of the fossils with other Aboriginal descendants and researchers.

Many Barkandji people do not want their ancestors reburied until more can be discovered about the age and complexity of their society. The Aboriginal Advisory Group for the Willandra site, composed of the Barkandji, Mutthi Mutthi and Ngyiampaa people, agreed with an unpublished 2019 report by the consulting group Extent Heritage in Sydney. This concluded that reburial should go ahead because it would not affect the region's world-heritage value. However, there was no consultation with either the

Barkandji Native Title Group Executive or the research community in reaching these conclusions.

Nature **589**, 19 (2021)

doi: https://doi.org/10.1038/d41586-020-03645-y

Jobs from Nature Careers

- All jobs

- **Aushilfe / Studentische Hilfskraft (m/w/d) im Abteilungssekretariat für 15 Std. / Woche**

  German Cancer Research Center in the Helmholtz Association (DKFZ)

  Heidelberg, Germany

  JOB POST

- **Hochfrequenz Technikerin I Hochfrequenz Techniker (w/m/d)**

  Helmholtz-Zentrum Berlin for Materials and Energy (HZB)

  Berlin, Germany

  JOB POST

- **PhD position – Genetics of neuropathological changes in Alzheimer's disease**

  Flanders Institute for Biotechnology (VIB)

Antwerp, Belgium

JOB POST

- **53541: Physicist, Engineer or similar - Laser-spectroscopic methods for the protection of terrestrial infrastructures**

  German Aerospace Center (DLR)

  Köln, Germany

  JOB POST

This article was downloaded by **calibre** from https://www.nature.com/articles/d41586-020-03645-y

CORRESPONDENCE
05 January 2021

Europe's 'green deal' and carbon dioxide removal

David M. Reiner,

University of Cambridge, UK.
Contact

Search for this author in:

- Pub Med
- Nature.com
- Google Scholar

Ilkka Hannula,

VTT Technical Research Centre, Finland.

Search for this author in:

- Pub Med
- Nature.com
- Google Scholar

Tiina Koljonen,

VTT Technical Research Centre, Finland.

Search for this author in:

- Pub Med
- Nature.com
- Google Scholar

Myles Allen,

University of Oxford, UK.

Search for this author in:

- Pub Med
- Nature.com
- Google Scholar

Wolfgang Lucht,

Potsdam Institute for Climate Impact Research, Germany.

Search for this author in:

- Pub Med
- Nature.com
- Google Scholar

Gonzalo Guillén-Gosálbez &

ETH, Zurich, Switzerland.

Search for this author in:

- Pub Med
- Nature.com
- Google Scholar

Niall Mac Dowell

Imperial College London, UK.

Search for this author in:

- Pub Med
- Nature.com
- Google Scholar

The European Union is debating whether to include carbon dioxide removal (CDR) as part of its 2030 targets on the road to climate neutrality by 2050. In our view, creating sustainable CDR could allow delivery of negative emissions at scale after 2030.

In October 2020, the European Parliament supported a 60% target for emissions reduction by 2030 without CDR. Last month, the European Council agreed to a 55% target that includes CDR. It will therefore be necessary to reconcile the two approaches.

A singular comprehensive target that includes CDR could offer more flexibility for EU policymaking (V. Scott and O. Geden *Nature Energy* 3, 350–352; 2018). But hitting net zero in 2050 through a complex cocktail of emissions and removals is insufficient if storing the removed CO_2 is not durable. A separate 2030 CDR-policy regime would provide clarity to project developers and ensure that high environmental and sustainability standards are upheld.

An independent scientific body will need to assess whether EU climate policy is consistent with the targets and whether near-term targets are suitable for achieving longer-term goals. It must incorporate social science into its assessments because techno-economic feasibility might not be the main constraint for many CDR options. The coming decade should herald a public conversation about the acceptability of the different possibilities.

Nature **589**, 19 (2021)

doi: https://doi.org/10.1038/d41586-020-03643-0

Jobs from Nature Careers

-
  -
    - All jobs
  -
    - **Aushilfe / Studentische Hilfskraft (m/w/d) im Abteilungssekretariat für 15 Std. / Woche**

      German Cancer Research Center in the Helmholtz Association (DKFZ)

      Heidelberg, Germany

      JOB POST

    - **Hochfrequenz Technikerin I Hochfrequenz Techniker (w/m/d)**

      Helmholtz-Zentrum Berlin for Materials and Energy (HZB)

      Berlin, Germany

      JOB POST

    - **PhD position – Genetics of neuropathological changes in Alzheimer's disease**

      Flanders Institute for Biotechnology (VIB)

      Antwerp, Belgium

      JOB POST

    -

53541: Physicist, Engineer or similar - Laser-spectroscopic methods for the protection of terrestrial infrastructures

German Aerospace Center (DLR)

Köln, Germany

JOB POST

This article was downloaded by **calibre** from https://www.nature.com/articles/d41586-020-03643-0

CORRESPONDENCE
05 January 2021

Optimizing public services after COVID

Jonathan Shepherd

Cardiff University, UK.
Contact

Search for this author in:

- Pub Med
- Nature.com
- Google Scholar

The devastating economic effects of the COVID-19 pandemic underscore the need to make public services as effective as possible in future. However, the evidence on how best to achieve this is copious, complex and unstandardized. The confusion is compounded by the existence of a great deal of guidance that does not adhere to quality standards. And because there is currently no accreditation system for guidance producers, it is hard for users to determine which guidance is authoritative.

Evidence for efficacy and cost benefit needs to be generated, synthesized, translated into advice and guidance, and then applied in policymaking and practice (see go.nature.com/37yrrde).

Evidence generation, systematic reviews of evidence, and practice and policy guidelines — such as the updated Appraisal of Guidelines for Research and Evaluation (AGREE) Instrument, AGREE II — need to conform to international standards. Quality marks, which should be

displayed prominently, would indicate this conformity. Published guidance, evidence syntheses and trials that do not comply should carry warnings.

Proportionate regulation to ensure standardization is fully justified, given the massive amount spent on public services around the world. What's at stake here is the public good, which scientific evaluation continues to allow us the opportunity to deliver in education, policing, health care, local government and much else.

Nature **589**, 19 (2021)

doi: https://doi.org/10.1038/d41586-020-03644-z

Jobs from Nature Careers

-
  -
    - All jobs
  -
    - **Aushilfe / Studentische Hilfskraft (m/w/d) im Abteilungssekretariat für 15 Std. / Woche**

      German Cancer Research Center in the Helmholtz Association (DKFZ)

      Heidelberg, Germany

      JOB POST

    - **Hochfrequenz Technikerin I Hochfrequenz Techniker (w/m/d)**

      Helmholtz-Zentrum Berlin for Materials and Energy (HZB)

      Berlin, Germany

JOB POST

- **PhD position – Genetics of neuropathological changes in Alzheimer's disease**

  Flanders Institute for Biotechnology (VIB)

  Antwerp, Belgium

  JOB POST

- **53541: Physicist, Engineer or similar - Laser-spectroscopic methods for the protection of terrestrial infrastructures**

  German Aerospace Center (DLR)

  Köln, Germany

  JOB POST

This article was downloaded by **calibre** from https://www.nature.com/articles/d41586-020-03644-z

CORRESPONDENCE
05 January 2021

Africa's reforestation: European Union and United States should step up

David Gurwitz

Tel Aviv University, Israel.
Contact

Search for this author in:

- Pub Med
- Nature.com
- Google Scholar

Africa's Great Green Wall, a 100-million-hectare reforestation project, will help to combat drought and desertification of the continent's drylands and mitigate global warming — at an estimated cost of US$43 billion over the next decade (*Nature* 587, **8**; 2020). I call on the European Union and the United States to commit generous funding towards this crucial project, which is far beyond the capacity of the African Union nations to fund by themselves.

European countries (in particular the United Kingdom, France, Belgium, Spain, Portugal and Italy) have exploited Africa's natural and human wealth during a large part of the second half of the last millennium (see, for example, go.nature.com/3gnbvy4). And much of the wealth of the United States has been built on the slavery of African people and their descendants (see, for instance, go.nature.com/3mokan4).

It would be a laudable reparation for historic injustices if Europe and the United States were to team up and provide funding for this extremely important cause. In addition to being a symbolic compensation for their past exploitation of Africa and its people — probably amounting to much more than the estimated $43 billion at current rates — such commitment will contribute to the well-being of future generations everywhere.

Nature **589**, 19 (2021)

doi: https://doi.org/10.1038/d41586-020-03642-1

Jobs from Nature Careers

-
  -
    - All jobs
  -
    - **Aushilfe / Studentische Hilfskraft (m/w/d) im Abteilungssekretariat für 15 Std. / Woche**

      German Cancer Research Center in the Helmholtz Association (DKFZ)

      Heidelberg, Germany

      JOB POST

    - **Hochfrequenz Technikerin I Hochfrequenz Techniker (w/m/d)**

      Helmholtz-Zentrum Berlin for Materials and Energy (HZB)

      Berlin, Germany

      JOB POST

- **PhD position – Genetics of neuropathological changes in Alzheimer's disease**

  Flanders Institute for Biotechnology (VIB)

  Antwerp, Belgium

  JOB POST

- **53541: Physicist, Engineer or similar - Laser-spectroscopic methods for the protection of terrestrial infrastructures**

  German Aerospace Center (DLR)

  Köln, Germany

  JOB POST

This article was downloaded by **calibre** from https://www.nature.com/articles/d41586-020-03642-1

Work

- **Rethinking travel in a post-pandemic world** [05 January 2021]
  Career Feature • Climate scientists recommend ways to boost the value of virtual conferences and reduce carbon footprints even when travel curbs ease.
- **What's your risk of catching COVID? These tools help you to find out** [21 December 2020]
  Technology Feature • A look at apps that predict the chance of infection and illness depending on what you're doing and where you are.
- **Travails of an intrepid platypus counter** [05 January 2021]
  Where I Work • For more than a decade, Josh Griffiths has been trapping the elusive venomous mammals to survey the status of their population.

CAREER FEATURE
05 January 2021

Rethinking travel in a post-pandemic world

Climate scientists recommend ways to boost the value of virtual conferences and reduce carbon footprints even when travel curbs ease.

Josie Glausiusz

Josie Glausiusz is a science journalist in Israel. Twitter: @josiegz

Search for this author in:

- Pub Med
- Nature.com
- Google Scholar

Find a new job

Train travel generates vastly fewer emissions than do flights.Credit: Leon Neal/Getty

In 2018, social scientist Roger Tyers pledged to stop flying for work and leisure. Soon afterwards, he won a research fellowship that included fieldwork in China. So he decided to take the train from Southampton to Shanghai, a journey of almost two weeks.

“I used to fly a lot,” says Tyers, now at the University of Nottingham, UK. His perspective changed when he read a 2018 report by the Intergovernmental Panel on Climate Change warning that unprecedented societal changes would be needed if humanity wanted to achieve the aims of the Paris climate agreement and keep global warming to 1.5 °C above pre-industrial levels. “That really brought home to me the urgency of climate change and how we need to make big changes in our behaviour,” he says, “including flying less.”

Tyers’s trip took him seven weeks, including fieldwork and train travel there and back. He calculates that it generated just 10% of the emissions that the equivalent flights would, which pleases him, even though his train tickets

came close to three times the price of the equivalent flights. “I don’t expect everybody to be taking the train to China to do fieldwork,” he says. “But I think that as academics we can do a little bit better.”

Tyers is one of many climate scientists who are advocating for less air travel and following their own advice. Today, as the coronavirus continues to ravage much of the world, Tyers’s concerns have receded — at least temporarily — because nearly all conferences and meetings have pivoted to virtual models. Researchers throughout the world have learnt to embrace technology-based solutions for connecting.

But the carbon-footprint issue will remain in the long term. Once the pandemic is brought to heel, scientists will again grapple with how to reconcile the need to fly to meetings and fieldwork sites with their desire to limit — if not eliminate — air travel. A study in October showed that climate scientists tend to fly more often for work compared with their peers (L. Whitmarsh *et al. Glob. Environ. Change* **65**, 102184; 2020), because of their remote fieldwork locations and their travel to international conferences, including those addressing climate-change mitigation.

Many feel strongly that virtual networking cannot adequately replace actual face-to-face time, and that opportunities to meet in person with peers and senior colleagues in their speciality are essential for career advancement.

Yet they point out that climate change is already having devastating effects. The past 12 months have brought record-high temperatures and vast wildfires on the US west coast, as well as increases in the frequency and ferocity of typhoons in Asia, a brutal drought in southern Africa, record flooding in Sudan, numerous back-to-back tropical storms and a record-breaking number of hurricanes in the Atlantic Ocean.

So what do climate scientists advise? There are multiple ways, they say, to connect with colleagues, collaborators, peers and others without boarding an aeroplane. Some are encouraging conference organizers to continue to offer virtual versions of all sessions, noting that attendance numbers rose dramatically for many conferences that went online-only last year. Virtual conferences also assist the participation of researchers who might lack the

funds or visas to fly to international meetings, and they can be more accessible for people with disabilities.

Others are calling for a regular series of webinars to help people connect virtually. Many researchers were already using video platforms such as Google Meet, Zoom and Skype for meetings, as well as text and messaging platforms such as Slack and Twitter for networking and posting updates and articles.

Pack it in

Perhaps counter-intuitively, climate scientist Katharine Hayhoe says that she needs to fly to spread the message about climate change. But to keep her carbon footprint to a minimum and maximize the efficiency of her travel, she packs as many events as she can into one region. In a trip to Alaska in September 2019, she spoke at 29 events and meetings in the space of six days.

Hayhoe, a co-director of the Texas Tech University Climate Center in Lubbock, advises early-career researchers to fill their trips with as many networking opportunities as possible. “At the beginning of your career, meeting people face-to-face is really important,” she says. “If you go to a scientific conference, make the most of it: don’t present your poster or paper and leave. Look up ahead of time who’s going to be there, schedule coffees and lunches and breakfasts. Use every minute of your travel to maximize effectiveness.”

To bring down her carbon footprint, Hayhoe purchases carbon offsets from a programme that invests in local environmental projects in countries such as Kenya, Ghana and Mexico. Stephen Flood, who researches climate at University College Cork in Ireland, has a similar strategy. He prefers to “sail and rail” when feasible. But when flying is unavoidable, he buys carbon offsets.

Climate researcher Stephen Flood at University College Cork in Ireland prefers to travel by boat and train.Credit: Stephen Flood

Kim Cobb, who researches climate-change solutions at the Georgia Institute of Technology in Atlanta, agrees that in-person time is imperative for junior researchers. Cobb, who has also pledged to go flight-free, wants conferences to adopt a hub model, in which one large conference is replaced by several smaller meetings held simultaneously on different continents. Scientists would then travel by train to their nearest meeting, and the hubs would be connected to each other virtually. To account for differing time zones, she suggests that scientists exchange content and discuss it virtually at pre-arranged times. Alternatively, she says, small groups of scientists who are in compatible time zones could meet virtually. “I can convene with 50 of the world’s experts on my sub-discipline,” she says, “but there is equal and different value in convening with 50 climate scientists in one area and exploring ways to collaborate and share findings.”

Another advocate of the virtual approach is Milan Klöwer, who studies climate models at the University of Oxford, UK. He calculated the travel-related carbon footprint of the American Geophysical Union meeting in San Francisco, California, in December 2019, and found that 28,000 scientists travelled a total of 285 million kilometres, emitting the equivalent of 80,000 tonnes of carbon dioxide. He estimates that moving the meeting to the more central location of Chicago, Illinois, would reduce emissions by 12%. And holding the conference there biennially, rather than annually, and encouraging the 36% who would have to travel farthest to participate virtually, would reduce the travel footprint by 90% (M. Klöwer *et al. Nature* **583**, 356–359; 2020). Furthermore, he noted that attendance for the May 2020 annual meeting of the European Geosciences Union ballooned to 26,000 after it became online-only, up from a typical attendance of 16,000.

Climate scientist Milan Klöwer takes a train through the Alps.Credit: L Picot

Klöwer, who flies only when it is unavoidable, says that his own networking efforts accelerated when he began to attend more virtual meetings. “Have an

active presence on Twitter," he advises. "Engage with people, write them e-mails, ask for virtual seminars." He also recommends organizing a monthly seminar series in which speakers are connected by software such as Zoom and the video chat is live-streamed through YouTube.

Social platforms

Slack groups are another way to connect virtually, says Divya Persaud, a planetary scientist at University College London. She is in a Slack group for people from minority ethnic backgrounds who study science, technology, engineering or mathematics. "We share opportunities, tips and events, and seek advice from other people, and that's been really great for networking," she says. Persaud also co-organized an experimental virtual conference called Space Science in Context in May 2020. Speakers recorded their talks in advance so that attendees could watch them and then ask questions at scheduled Zoom sessions. "It was a warm, inviting space," Persaud says. "We had a lot of concurrent conversations happening in the chats during the live panels, and some really excellent discussions during the poster sessions, which can be lacking at in-person conferences, particularly for women and minority scholars."

Ibukun Jacob Adewumi, director of international partnerships for the African Marine Environment and Sustainability Initiative in Paris, recommends organizing small meetings of two or three people in a laboratory, and then connecting virtually with other small groups on different continents. Participants can also optimize their use of Zoom with breakout rooms or virtual after-parties, Adewumi says. He urges early-career researchers to lobby governments to channel saved travel costs into research and development. Social-media platforms, he says, can amplify voices for this purpose.

Webinars promote inclusiveness

Sören Thomsen, who studies ocean and climate science at the Laboratory of Oceanography and Climate in Paris, launched a series of webinars in 2018 that brings together researchers from Africa, South America and Asia to exchange knowledge about coastal ecosystems. Thomsen designed the

programme with scientists from around the world, including Senegalese and Indian researchers who had never met in person. The participants use low-bandwidth video-conferencing software called eyeson and live-stream the video chat on YouTube. They then use a platform called Slido to allow audience members to ask questions. Many of the participants have never been to an international conference, he notes, adding that the programme is their only way to connect to the global scientific community.

Thomsen adds that virtual conferences offer the significant benefit of boosting diversity. He says that half of those who join his webinars come from nations in the global south, including Peru, Chile, Senegal, Namibia and South Africa. Adewumi says that online events also help to improve social justice by improving attendance by scientists who cannot afford to fly to faraway conferences or who might not be able to secure the necessary visa.

Thomsen and Adewumi were among the co-organizers of last December's #VirtualBlueCOP25, a multi-part free series of live virtual events at the United Nations Climate Change Conference featuring experts and climate negotiators. They brought together experts from Africa, southeast Asia and the Caribbean to participate in webinars about ocean-ecosystem management and climate change. On 'Ocean Day' (7–8 December), scientists, activists and artists shared their work virtually from their home countries. "We had people who sang, who read poems," says Adewumi. "It was fresh — we wanted to do something that is not conventional."

Participants at the Virtual Blue COP25 conference in Madrid in December 2019.Credit: VirtualBlueCOP25

Thomsen warns that when the pandemic ends, there is likely to be a rebound effect as scientists begin to fly to meet researchers with whom they have collaborated online. To keep emissions under control, he says, labs should calculate their carbon footprint with the aid of initiatives such as Labos 1point5, then set clear reduction targets that are in line with the Paris climate agreement. Each lab can then decide how to use its carbon budget for the year's travel or other activities, he suggests.

Adewumi, whose work includes making use of ocean resources in central African nations sustainable, says that he cannot completely eliminate work-related air travel, but had committed to cutting his number of round-trip flights to 5 a year, from 15–20. (He notes that he is not travelling anywhere right now because of COVID-19.) To do so, he prioritizes conferences by importance, and delegates some to colleagues who are closer to the venue. He also makes it possible for some early-career professionals in Nigeria to attend by transferring some of his frequent-flyer miles to them. Meeting at conferences, he says, can be an excellent way to exchange ideas, widen horizons and foster collaboration between researchers in vastly different economies.

Saleemul Huq, director of the International Centre for Climate Change and Development in Dhaka, agrees, noting that many scientists in the global south are isolated. Each January in Dhaka, Huq organizes Gobeshona, a conference on adaptation to climate change, to which he invites scientists from the Least Developed Countries Universities Consortium on Climate Change, among others.

Pre-pandemic curbs

Huq, who had already limited his air travel before pandemic-related lockdowns, says that PhD students and other early-career researchers should be judicious in making their own plans. “I’m not into making ‘not-flying’ a fetish,” he says. “If they have to fly for a good reason, they should fly. If they can avoid flying, and travel by train or road, that’s obviously preferable, if the distance isn’t too great.”

Junior researchers might not be in the best position to avoid all conference travel, says Flood, who adds that they have a greater need for in-person meeting events than do scientists in later career stages. “Face-to-face is still important and necessary,” he says. “It’s more difficult to build interpersonal relationships or a scientific community when it’s all online.” Tyers, too, admits that he misses in-person interactions: “I am an extrovert, and this much time working at home is not good for me.” In person, he says, small, non-verbal signals help people to build rapport. “You’re getting direct eye contact; you can always tell if someone is really engaged with what you are saying; you can tell if someone’s excitement is real or fake,” he says. “There are little nuances of communication that get lost through a screen.”

Even so, the pandemic has forced people to learn skills in virtual communication that they should have acquired long ago, he says. Cobb agrees. Early-career researchers, she adds, should be encouraged by the nimble nature of the scientific enterprise. “I’m sorry that it took this level of disruption to start these conversations at the highest level across every organization,” she says. “But it really goes to show that change is possible.”

Virtual conferences: the good, the bad, the improvable

Participation in virtual medical conferences increased drastically in 2020 — with the number of attendees doubling at some meetings compared with in-person events held the previous year.

That's a key conclusion of a study funded and carried out by Airfinity, a science information and analytics company in London. On the downside, posters — which are easy for participants to see when wandering through a physical space — were viewed by a tiny proportion of attendees at virtual conferences.

The Airfinity team collected data from four medical groups that held virtual conferences in 2020: the American College of Cardiology (ACC); the American Diabetes Association (ADA); the European Society of Cardiology (ESC); and the European Association for the Study of Diabetes (EASD).

"In a virtual congress, you have a much wider reach and much higher participation," says Airfinity report analyst Maia Morgan. But whereas late-breaking, 'hot' science tends to capture the audience, posters are often ignored. "In a virtual congress, you have to actively seek out the poster and look at it," she says.

Airfinity's other key conclusions were:

• Because travel is no longer necessary, virtual conferences have become more accessible, drawing larger audiences from a wider range of countries. Both the ADA and the ESC conferences were free, which probably drove a doubling in attendance.

• New science continues to have a high impact, but posters struggle for viewership online or on social media. Ninety-nine per cent of posters at the ESC meeting received fewer than 100 views. At the EASD congress, 2% of posters had no views at all.

• Few presenters have a Twitter account and even fewer use Twitter accounts to share their science. At ESC 2020, only 21% of authors had a Twitter account and only 11% of those with an account tweeted or re-tweeted during the meeting.

• Live sessions (in which the speaker addresses the audience in a video-conference format) had very high engagement at the ACC meeting, as shown by tweets and re-tweets.

• None of the virtual conferences offered dedicated networking sessions.

The move to virtual conferencing in 2020 is probably the largest shift in decades in how scientific knowledge is disseminated, says Airfinity chief executive Rasmus Bech Hansen. Even so, social media has to have a larger role if virtual meetings are to remain successful. He offers these recommendations for scientists and conference organizers.

• Conferences with large Twitter followings should post findings from emerging researchers on their main account and tag the authors, or appoint a moderator to run the account and live-tweet new findings, generating traffic.

• Researchers should make posters more interactive, perhaps including small videos, to widen viewership. The inclusion of a carousel on a website (a sliding gallery of content in a single coveted space) can also make it easier for attendees to find posters.

• For online networking sessions, match-making technologies such as Brella, Grip and SwapCard can help scientists to connect with those who have similar interests and to set up meetings in advance.

• Virtual-reality ‘plazas’ could allow attendees to use an avatar to ‘walk’ through immersive poster sessions.

Nature **589**, 155-157 (2021)

doi: https://doi.org/10.1038/d41586-020-03649-8

Jobs from Nature Careers

-
  -
    - All jobs
  -

- **Aushilfe / Studentische Hilfskraft (m/w/d) im Abteilungssekretariat für 15 Std. / Woche**

  German Cancer Research Center in the Helmholtz Association (DKFZ)

  Heidelberg, Germany

  JOB POST

- **Hochfrequenz Technikerin I Hochfrequenz Techniker (w/m/d)**

  Helmholtz-Zentrum Berlin for Materials and Energy (HZB)

  Berlin, Germany

  JOB POST

- **PhD position – Genetics of neuropathological changes in Alzheimer's disease**

  Flanders Institute for Biotechnology (VIB)

  Antwerp, Belgium

  JOB POST

- **53541: Physicist, Engineer or similar - Laser-spectroscopic methods for the protection of terrestrial infrastructures**

  German Aerospace Center (DLR)

  Köln, Germany

  JOB POST

This article was downloaded by **calibre** from https://www.nature.com/articles/d41586-020-03649-8

TECHNOLOGY FEATURE
21 December 2020

What's your risk of catching COVID? These tools help you to find out

A look at apps that predict the chance of infection and illness depending on what you're doing and where you are.

Michael Eisenstein

Michael Eisenstein is a freelance writer in Philadelphia, Pennsylvania.

Search for this author in:

- Pub Med
- Nature.com
- Google Scholar

People standing apart and wearing face masks look at their phones while waiting to cross the road in Tokyo

People wearing masks in Tokyo maintain physical distancing as they wait at a pedestrian crossing. Credit: Carl Court/Getty

As an emergency physician, Megan Ranney is used to dealing with hard questions about injury and illness. But during the COVID-19 pandemic, she has found herself scrambling for answers. "I kept getting asked by people whether it was safe to do certain activities," says Ranney. "'Is it safe to go to the beach, or to an outdoor party or a restaurant?'"

Millions have struggled with the same questions throughout 2020. Scientists and clinicians are still learning about the epidemiology and pathology of the coronavirus SARS-CoV-2 and, for the public, it can be difficult to understand how to maintain some semblance of normality while minimizing the risk of infection.

As co-director of the Brown-Lifespan Center for Digital Health in Providence, Rhode Island, Ranney saw an opportunity to use her expertise in developing online tools for public health. Working with her Brown-Lifespan colleague Elizabeth Goldberg, she developed MyCOVIDRisk, a simple, questionnaire-based web app that gives users a sense of their infection risk on the basis of their planned activity in a specific place or situation.

Filling the gaps

Launched in October, MyCOVIDRisk is just one of several apps developed to communicate the risks of COVID-19 to the public (see 'COVID risk calculators'). These tools are filling important gaps in public-health messaging, particularly in the United States, where an uneven response to the pandemic has exacerbated its severity. "This type of app is something that could have been developed very early in the pandemic by the [US] Centers for Disease Control and Prevention or another national entity," says Ranney. "But unfortunately, that wasn't done."

COVID risk calculators

Tool	Data it collects from the user	What it returns

Tool	Data it collects from the user	What it returns
19 and Me	Location, health status, safety precautions being taken and exposure to non-household members.	Numerical score reflecting risk of contracting COVID-19, or of developing severe disease.
MyCOVIDRisk	Location, the nature of the activity being done, the number of people involved and mask usage.	Relative risk of exposure and infection, on a scale from very low to very high.
COVID-19 Event Risk Assessment Planning Tool	Location and size of gathering.	The likelihood of coming into contact with someone who has COVID-19.
COVID-19 Mortality Risk Calculator	Information on demographic, pre-existing conditions and lifestyle.	Risk of dying from COVID-19 relative to the general population.

Individual research teams have approached risk assessment from different angles. Perhaps the most straightforward approach is the web-based COVID-19 Event Risk Assessment Planning Tool developed by scientists at the Georgia Institute of Technology in Atlanta. The site estimates the probability (as a percentage) that a person will encounter someone with COVID-19 at a gathering, on the basis of the size of the group and where the event takes place. For example, as of 14 December, the tool predicted that at a gathering of 10 people in Boston, Massachusetts, there would be a 30% chance of at least one attendee having the virus.

The 19 and Me calculator, developed by Mathematica, a policy-research company in Princeton, New Jersey, draws on demographic and health information as well as user behaviours such as hand washing and mask use to determine relative risk of exposure, infection and serious illness. And in December, a team led by biostatistician Nilanjan Chatterjee at Johns Hopkins University in Baltimore, Maryland, released the COVID-19 Mortality Risk Calculator, which estimates an individual's relative risk of death from COVID-19 on the basis of their location, pre-existing conditions and general health status.

MyCOVIDRisk takes a more situational approach, estimating the risks associated with specific errands or recreational activities. The estimate is based on the location and duration of a gathering, and the number of masked or unmasked people attending. This can help users to avoid activities that are likely to be high risk in a pandemic hotspot, such as spending an hour in an indoor gym, in favour of safer alternatives — a masked meet-up in the park, for instance.

Why emergency COVID-vaccine approvals pose a dilemma for

scientists

To make predictions, these tools require the latest data and models that accurately capture the current levels of infection and the likelihood of transmission in various scenarios. *The New York Times* runs a coronavirus database that has become a popular resource, and both MyCOVIDRisk and the Georgia Tech tool use it to assess local disease activity. These calculators are currently focused on the United States, although the Georgia Tech team has extended its tool to cover ten European countries.

Researchers are still teasing out the factors that predispose some individuals to infection and severe disease, and they continue to study how distance, ventilation and masks mitigate the spread of virus-laden droplets. For 19 and Me, Xindi Hu — the data scientist at Mathematica who led the tool's development — and her colleagues regularly comb through the latest peer-reviewed literature to refine their infection models, relying heavily on reports from the US Centers for Disease Control and Prevention (CDC). For MyCOVIDRisk, the team turned to an aerosol-transmission estimation model developed by atmospheric chemist Jose-Luis Jimenez and his colleagues at the University of Colorado Boulder, which simulates how far viral particles are likely to travel in various indoor and outdoor scenarios.

The researchers then have to come up with ways to wrangle this information into a format that is easy for non-experts to understand, without it being intrusive or frustrating. To build a simple and engaging app that balances depth with usability, the Brown-Lifespan team relied on user testing and guidance from behavioural scientists. "In an ideal world, you'd ask how big of a room are you in and what's the rate of ventilation," says Ranney, "But if you asked me, I wouldn't even know the answer."

The UK has approved a COVID vaccine — here's what scientists now want to know

This need for simplicity also motivated the Georgia Tech team. Its tool solicits only two pieces of information: a user's location and the size of the expected crowd. Initially, this ranged from 10 to 10,000 people. "Those upper bounds were useful when political rallies were occurring over the summer," says Andris. But as the holidays drew closer, the team decreased the upper bound to 5,000 people and increased the tool's level of detail at the lower end of the scale to deliver estimates for relatively modest gatherings of 10, 15 or 20 people.

To convey risk, MyCOVIDRisk opts for a simple, 5-tier continuum scale of green to red, whereas the 19 and Me team devised an abstract numerical readout ranging from 0 to 100, which Hu likens to a credit score. "That is a compromise we've made to keep the rigour of the calculation while making it into a number that is easily understood by the general public," she says. "And we couple it with a text explanation and an interactive risk gauge." This explanation summarizes the potential for exposure and infection, along

with the likelihood of serious health consequences and hospitalization if infection occurs.

However, developers caution that the apps provide estimates intended to assist in decision-making, and are not definitive indicators of the likelihood of contracting disease.

Casting a wider net

Quantifying and mapping COVID-19 risk has been challenging from the start, because scientists and physicians have struggled to understand the complex range of symptoms associated with the disease. This has been exacerbated by national and regional policies that have limited people's access to testing on the basis of symptoms that might not fully reflect the prevalence of infection. Online surveys are now helping researchers to get a better handle on the clinical manifestations of the disease.

As part of the Coronavirus Pandemic Epidemiology (COPE) consortium, Andrew Chan, an epidemiologist at Massachusetts General Hospital in Boston, and his US and UK colleagues launched the COVID Symptom Study. This effort initially recruited hundreds of thousands of volunteers in the United States and United Kingdom who were already participating in clinical studies; it has subsequently been opened up to the public in those two countries. In parallel, a team led by computational biologist Eran Segal at the Weizmann Institute of Science in Rehovot, Israel, has deployed its own online symptom questionnaire in that country. "We built an algorithm that basically allows self-assessment testing that integrates all the symptoms you report, and tells you the likelihood of testing COVID-positive," says Segal.

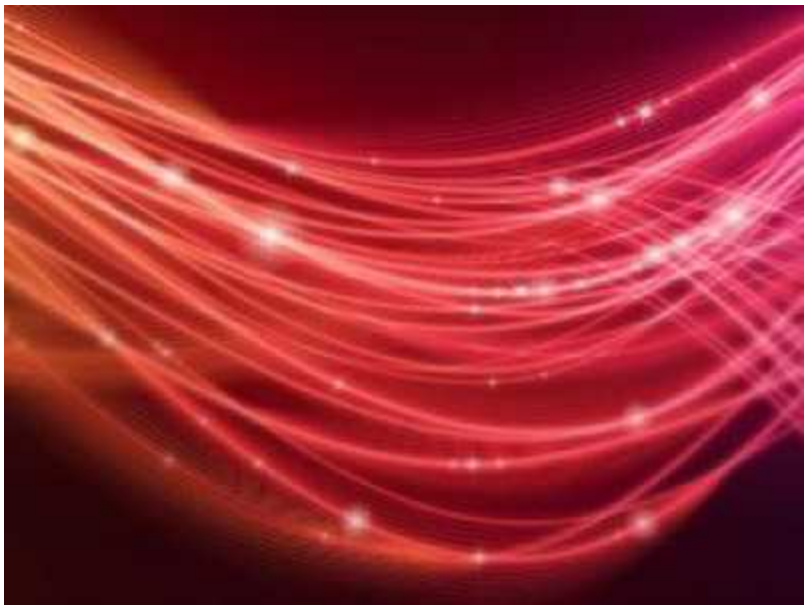

NatureTech hub

Such surveys are constrained by their dependence on willing users, and by access to the Internet. To bolster participation, Segal's team used a phone survey in the Israeli cities that were hit hardest by COVID-19. The data have revealed valuable insights that can distinguish the disease from colds and other common maladies. "These surveys contributed a lot to identifying loss of taste and smell as a symptom that is the most distinctive for COVID-19," says Segal, noting that Israel has now changed its testing practices to recognize the diagnostic importance of this symptom.

Symptom surveys are also informing maps of the pandemic. Segal says that initial data from his questionnaire suggested there were two to three times as many active COVID-19 cases in Israel as were represented in official clinical reports at the time. Signals generated from these surveys could, therefore, offer a real-time red flag for emerging hotspots where testing and personal protective equipment are needed, giving public-health authorities a valuable head start in responding.

In the United Kingdom, the National Health Service is supporting further development of the COVID Symptom Study app, which has now also been deployed in Sweden. Chan is enthusiastic about additional data in the

United States, as well. “We have been interested in aligning what we’ve been finding on the app with publicly available information on testing results or hospitalization rates,” he says.

But equally enthusiastic, if not more so, is the public. Ranney says that MyCOVIDRisk has been used more than one million times since it launched, and the Georgia Tech team says that its tool had delivered more than 40 million risk estimates as of late November, with a particular surge around the US Thanksgiving holiday. And despite several vaccines entering the clinic, the public is likely to remain hungry for these data well into 2021. “There are going to remain some very high-risk activities for months or even a year to come,” says Ranney. “So I think this kind of informational and behavioural change-motivating programme will unfortunately remain relevant.”

Nature **589**, 158-159 (2021)

doi: https://doi.org/10.1038/d41586-020-03637-y

Jobs from Nature Careers

-
  -
    - All jobs
  -
    - **Aushilfe / Studentische Hilfskraft (m/w/d) im Abteilungssekretariat für 15 Std. / Woche**

      German Cancer Research Center in the Helmholtz Association (DKFZ)

      Heidelberg, Germany

      JOB POST
    -

Hochfrequenz Technikerin I Hochfrequenz Techniker (w/m/d)

Helmholtz-Zentrum Berlin for Materials and Energy (HZB)

Berlin, Germany

JOB POST

- **PhD position – Genetics of neuropathological changes in Alzheimer's disease**

  Flanders Institute for Biotechnology (VIB)

  Antwerp, Belgium

  JOB POST

- **53541: Physicist, Engineer or similar - Laser-spectroscopic methods for the protection of terrestrial infrastructures**

  German Aerospace Center (DLR)

  Köln, Germany

  JOB POST

This article was downloaded by **calibre** from https://www.nature.com/articles/d41586-020-03637-y

WHERE I WORK
05 January 2021

Travails of an intrepid platypus counter

For more than a decade, Josh Griffiths has been trapping the elusive venomous mammals to survey the status of their population.

Virginia Gewin

Virginia Gewin is a freelance writer in Portland, Oregon.

Search for this author in:

- Pub Med
- Nature.com
- Google Scholar

Josh Griffiths photographed at night wearing a head torch crouching in a stream holding a platypus by the tail

Josh Griffiths is a wildlife ecologist for Cesar Australia in Parkville, Australia. Credit: Doug Gimesy/Nature Picture Library

As a wildlife ecologist, I study many species, but the platypus (*Ornithorhynchus anatinus*) is my speciality. I've worked with these duck-billed monotremes, which are indigenous to eastern Australia, for 13 years. So much remains unknown about them — as solitary animals, they are very hard to capture. The males have a venomous spur on each of their hind feet, so I always hold them by the tail. Luckily, I've never been spurred.

At the environmental consultancy firm Cesar Australia, we've focused on whether platypuses' numbers are rising or falling. Their aquatic habitat has shrunk by 25% in the past 30 years — partly owing to reduced rainfall from climate change and partly to residential and industrial development, leaving less water, which is of poorer quality.

To monitor the population's size and health, we do overnight trapping surveys — typically during the spring breeding season and in the autumn, when the babies emerge. For each survey, we set up nets along 5–10 kilometres of waterway and then drive round checking them through the night. It's a long, sleepless process that usually yields just one or two catches. In the 15 minutes or so for which each animal is out of the water, we weigh and measure it. If it's carrying an identification chip, we know we've caught it before. If not, we implant one in the animal. In this picture, I am releasing a platypus back into a stream outside Melbourne.

In the past five years, we've also been sampling environmental DNA for signatures of platypuses' presence. It's been a game-changer in terms of mapping their distribution. We can take a water sample, extract all the DNA and confidently identify whether platypus DNA is present. We've surveyed more than 2,000 sites spanning 500,000 square kilometres, enabling us to measure at scales never before possible.

We've also developed a citizen-science platform through which people can submit platypus sightings. This helps us still further.

Nature **589**, 162 (2021)

doi: https://doi.org/10.1038/d41586-020-03650-1

Jobs from Nature Careers

-
  -
    - All jobs
  -
    -

Aushilfe / Studentische Hilfskraft (m/w/d) im Abteilungssekretariat für 15 Std. / Woche

German Cancer Research Center in the Helmholtz Association (DKFZ)

Heidelberg, Germany

JOB POST

- **Hochfrequenz Technikerin I Hochfrequenz Techniker (w/m/d)**

  Helmholtz-Zentrum Berlin for Materials and Energy (HZB)

  Berlin, Germany

  JOB POST

- **PhD position – Genetics of neuropathological changes in Alzheimer's disease**

  Flanders Institute for Biotechnology (VIB)

  Antwerp, Belgium

  JOB POST

- **53541: Physicist, Engineer or similar - Laser-spectroscopic methods for the protection of terrestrial infrastructures**

  German Aerospace Center (DLR)

  Köln, Germany

  JOB POST

This article was downloaded by **calibre** from https://www.nature.com/articles/d41586-020-03650-1

Research

- **Hit movie reveals how a tuberculosis drug halts ATP synthesis** [09 December 2020]
  News & Views • Structural data revealing how an anti-tuberculosis drug works could aid efforts to improve therapeutic options for the disease. The findings also uncover aspects of how the drug's target, the ATP synthase enzyme, operates.
- **Machine learning reveals the complexity of dense amorphous silicon** [06 January 2021]
  News & Views • Transitions between amorphous forms of solids and liquids are difficult to study. Machine learning has now provided fresh insight into pressure-induced transformations of amorphous silicon, opening the way to studies of other systems.
- **A screen of brain organoids to study neurodevelopmental disease** [23 December 2020]
  News & Views • A high-throughput technique has been developed to screen genes implicated in neurodevelopmental diseases in 3D cell cultures. It reveals a mechanism that might be involved in a rare disorder called microcephaly.
- **Artificial intelligence accelerated by light** [06 January 2021]
  News & Views • The explosive growth of artificial intelligence calls for rapidly increasing computing power. Two reported photonic processors could meet these power requirements and revolutionize artificial-intelligence hardware.
- **Big data and simple models used to track the spread of COVID-19 in cities** [10 November 2020]
  News & Views • Understanding the dynamics of SARS-CoV-2 infections could help to limit viral spread. Analysing mobile-phone data to track human contacts at different city venues offers a way to model infection risks and explain infection disparities.
- **Core-collapse supernova explosion theory** [06 January 2021]
  Review Article • The factors affecting how and why supernovae occur are discussed, and the current status of core-collapse supernova explosion theory is reviewed.
- **Competing magnetic orders in a bilayer Hubbard model with ultracold atoms** [06 January 2021]
  Article • A bilayer Fermi–Hubbard model is realized in two coupled two-dimensional layers of fermionic ultracold atoms by tuning the interlayer coupling strength to create a crossover between magnetic orderings.

- **11 TOPS photonic convolutional accelerator for optical neural networks** [06 January 2021]
  Article • An optical vector convolutional accelerator operating at more than ten trillion operations per second is used to create an optical convolutional neural network that can successfully recognize handwritten digit images with 88 per cent accuracy.
- **Parallel convolutional processing using an integrated photonic tensor core** [06 January 2021]
  Article • An integrated photonic processor, based on phase-change-material memory arrays and chip-based optical frequency combs, which can operate at speeds of trillions of multiply-accumulate (MAC) operations per second, is demonstrated.
- **Origins of structural and electronic transitions in disordered silicon** [06 January 2021]
  Article • Machine learning models enable atomistic simulations of phase transitions in amorphous silicon, predict electronic fingerprints, and show that the pressure-induced crystallization occurs over three distinct stages.
- **Single-defect phonons imaged by electron microscopy** [06 January 2021]
  Article • State-of-the-art electron energy-loss spectroscopy in a transmission electron microscope maps the detailed phonon spectra of single defects in silicon carbide
- **Poleward and weakened westerlies during Pliocene warmth** [06 January 2021]
  Article • Analysis of dust from marine sediments in the North Pacific shows that warm periods during the Pliocene witnessed weaker and more poleward westerlies than during subsequent glacial periods.
- **Drivers and dynamics of a massive adaptive radiation in cichlid fishes** [18 November 2020]
  Article • Analyses of molecular, anatomical, pigmentation and ecological characteristics of nearly all of the approximately 240 species of cichlid fishes in Lake Tanganyika show that the massive adaptive radiation occurred within the confines of the lake through trait-specific pulses of accelerated evolution.
- **Mobility network models of COVID-19 explain inequities and inform reopening** [10 November 2020]
  Article • An epidemiological model that integrates fine-grained mobility networks illuminates mobility-related mechanisms that contribute to higher infection rates among disadvantaged socioeconomic and racial groups, and finds that restricting maximum occupancy at locations is especially effective for curbing infections.

- **Neuronal diversity and convergence in a visual system developmental atlas** [04 November 2020]
  Article • The neuronal diversity of the Drosophila optic lobe is described throughout pupal development by single-cell sequencing, leading to the discovery of transient extrinsic neurons and a dorsoventral asymmetry of the visual circuits.
- **Coupling of hippocampal theta and ripples with pontogeniculooccipital waves** [18 November 2020]
  Article • Studies using multi-structure recordings in macaque monkeys show that distinct phasic pontogeniculooccipital waves modulate hippocampal network events similar to those that underlie the learning and formation of memories during sleep.
- **TRF2-independent chromosome end protection during pluripotency** [25 November 2020]
  Article • Experiments in mouse pluripotent embryonic and epiblast stem cells show that TRF2 is dispensable for telomere protection specifically specifically in the pluripotent cells that form during early embryonic development, when cells form T-loops independently of this protein.
- **TRF2-mediated telomere protection is dispensable in pluripotent stem cells** [25 November 2020]
  Article • Depletion of TRF2—an essential mediator of telomere protection in most mammalian cells—in mouse embryonic stem cells activates a compensatory transcriptional program that renders TRF2 dispensable for their survival and proliferation.
- **A network of transcriptional repressors modulates auxin responses** [18 November 2020]
  Article • Genes encoding the class A auxin-response factor group of plant transcriptional activators reside in constitutively open chromatin, enabling their continual regulation by transcriptional repressors to modulate auxin signalling throughout development.
- **Prokaryotic viperins produce diverse antiviral molecules** [16 September 2020]
  Article • Eukaryotic viperins originated from a clade of bacterial and archaeal proteins that catalyse the production of antiviral molecules.
- **The coding capacity of SARS-CoV-2** [09 September 2020]
  Article • A high-resolution map of coding regions in the SARS-CoV-2 genome enables the identification of 23 unannotated open reading frames and quantification of the expression of canonical viral open reading frames.
- **Commensal-driven immune zonation of the liver promotes host defence** [25 November 2020]
  Article • The authors show that zonation extends to hepatic immune cells and that this spatial patterning is mediated by microbiome sensing by liver sinusoidal endothelial cells, and

provide evidence that immune zonation is required to protect the host from the dissemination of blood-borne pathogens.

- **RNA nucleation by MSL2 induces selective X chromosome compartmentalization** [18 November 2020]
  Article • Dosage compensation in Drosophila involves nucleation of the dosage compensation complex at the X chromosome by MSL2 and the non-coding RNA roX.
- **Structure of mycobacterial ATP synthase bound to the tuberculosis drug bedaquiline** [09 December 2020]
  Article • Structures of Mycobacterium smegmatis ATP synthase provide insights into how the enzyme conserves energy by autoinhibition of ATP hydrolysis and the mechanism of action of bedaquiline, a drug used in treatment of multidrug-resistant tuberculosis.
- **Structure of the class D GPCR Ste2 dimer coupled to two G proteins** [02 December 2020]
  Article • A cryo-electron microscopy structure of the yeast pheromone receptor Ste2, a class D G-protein-coupled receptor, in its active state reveals that Ste2 is a homodimer that couples to two G proteins.

NEWS AND VIEWS
09 December 2020

Hit movie reveals how a tuberculosis drug halts ATP synthesis

Structural data revealing how an anti-tuberculosis drug works could aid efforts to improve therapeutic options for the disease. The findings also uncover aspects of how the drug's target, the ATP synthase enzyme, operates.

Valerie Mizrahi &

Valerie Mizrahi is in the Molecular Mycobacteriology Research Unit and Wellcome Centre for Infectious Diseases Research in Africa, Institute of Infectious Disease and Molecular Medicine, University of Cape Town, Rondebosch 7701, South Africa.
Contact

Search for this author in:

- Pub Med
- Nature.com
- Google Scholar

Clifton E. Barry III

Clifton E. Barry III is in the Tuberculosis Research Section, National Institute of Allergy and Infectious Diseases, Bethesda, Maryland 20892, USA.
Contact

Search for this author in:

- Pub Med
- Nature.com
- Google Scholar

The 2017 Nobel Prize in Chemistry was awarded for the development of an imaging method called cryo-electron microscopy. On bestowing the prize, the Royal Swedish Academy of Sciences stated that this technique has "moved biochemistry into a new era". Writing in *Nature*, Guo *et al.*[1] provide a compelling glimpse into this new age.

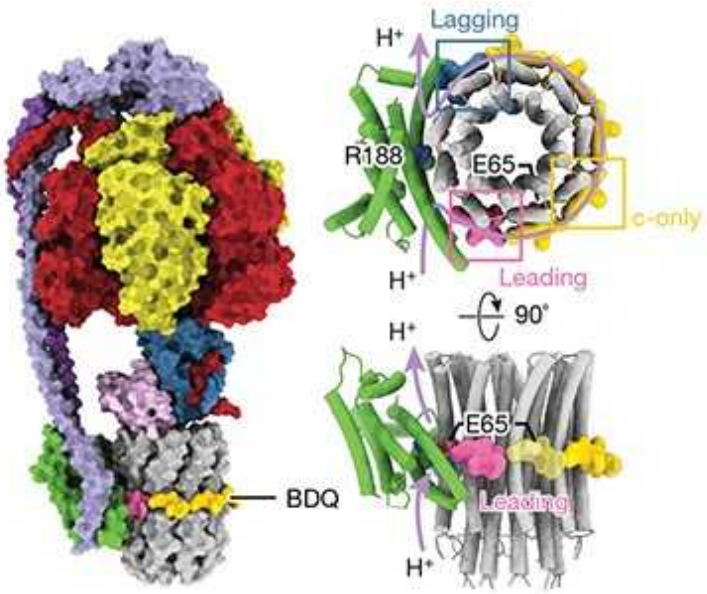

Read the paper: Structure of mycobacterial ATP synthase bound to the tuberculosis drug bedaquiline

The authors' work reveals how a drug called bedaquiline, which has revolutionized the treatment of drug-resistant tuberculosis[2,3], interacts with its target. The drug binds to the ATP synthase enzyme of the microorganism *Mycobacterium tuberculosis* that causes tuberculosis[4]. Adding to a rapidly

growing body of work elucidating the structure of ATP synthases by cryo-electron microscopy[5,6], the details presented by Guo and colleagues — and particularly the videos (see Supplementary Videos 1 and 2 of ref. 1) generated from their structural data — are breathtaking in their ability to reveal how this macromolecular machine works. Moreover, the authors show how the drug binds to the enzyme and disrupts its synthesis of the molecule ATP, providing crucial information that had eluded detection through other, more conventional structural and biochemical investigative techniques.

ATP synthases are found in every domain of life, and their basic structure is evolutionarily conserved. These amazing protein complexes harness a gradient of protons (positively charged hydrogen ions) established across the cellular membrane, and couple the protons' movement across the membrane to the synthesis of ATP, the main currency of cellular energy[5,6]. These macromolecular assemblies have a common architecture comprising an F_1 head region (Fig. 1) — which can either produce or break down (hydrolyse) ATP — lodged above a membrane-embedded 'wheel', the rotating F_0 rotor. The F_1 head and F_0 rotor are connected by a central stalk (the enzyme's γ-subunit) in the centre of the wheel and by a peripheral stalk that is in contact with F_0 in the lipid membrane. Driven by proton movement, the peripheral stalk rotates around the wheel so that individual active sites of the enzyme in the F_1 head are energized and drive ATP synthesis; if the direction of rotation is reversed, ATP is hydrolysed instead.

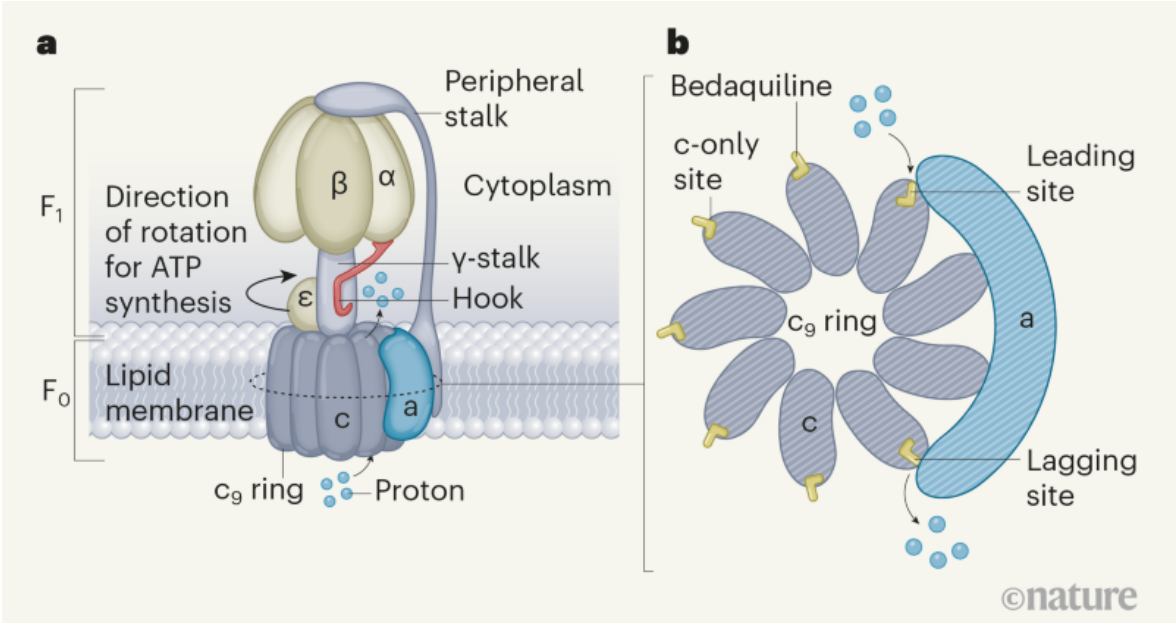

Figure 1 | The ATP synthase enzyme of the bacterium *Mycobacterium tuberculosis*. Guo *et al.*[1] report structural data obtained using cryo-electron microscopy. **a**, The molecule ATP (not shown) can be generated as the enzyme rotates when transporting protons (hydrogen ions) across the lipid membrane into the cytoplasm. The F_1 region of ATP synthase consists of a peripheral stalk, a γ-stalk and α-, β- and ε-subunits. The F_0 region includes a ring of nine c-subunits and an a-subunit. The authors discovered a 'hook' structure on the α-subunit that could bind to the γ-stalk and prevent rotation in the reverse direction that would cause the breakdown (hydrolysis), rather than the synthesis, of ATP. **b**, The authors determined how the anti-tuberculosis drug bedaquiline binds to the enzyme, as shown in this top-down view of the horizontal section of the F_0 region indicated by the dotted line in **a**. Guo and colleagues report that the drug binds better to the c-subunits in the complex where protons normally enter or exit (leading and lagging drug-binding sites, respectively) than to the other c-subunits (c-only drug-binding sites).

The ATP synthase of *M. tuberculosis* consists of nine types of subunit (α, β, γ, δ, ε, a, b, b' and c), from which the F_0 rotor (comprising one a-, one b-, one b'- and nine c-subunits) and F_1 head (three α, three β, one γ, one δ and one ε) are assembled. Unlike other bacterial ATP synthases, this version of the enzyme lacks ATP-hydrolysis activity[7,8]. However, the molecular basis

of this distinctive feature, which is thought to enable these mycobacteria to conserve energy[9], has remained elusive[10].

Guo and colleagues now provide an answer to this puzzle with their discovery that the enzyme uses a 'hook and ratchet' mechanism to prevent ATP hydrolysis. The hook is formed from an extension of an α-subunit of the F_1 head, and this can catch a region of the γ-subunit at a central part of the F_0 rotor (Fig. 1). The binding of the hook to this ratchet prevents F_0 from rotating in the reverse direction that drives ATP hydrolysis. If, instead, F_0 rotates in the opposite direction, which leads to ATP synthesis, this releases the hook.

However, the more-crucial advance made by this study is the insight it provides into exactly how bedaquiline interferes with enzyme function. Genetic analysis[4,11] had already shown that the c-subunit, which forms the ring at the heart of the F_0 rotor, is bedaquiline's target. Biochemical analysis[11] indicated that the drug has only low (millimolar) affinity for purified c-subunits studied *in vitro*, whereas bedaquiline's affinity is a million times higher (in the nanomolar range) when tested in *M. tuberculosis* cells[4]. A previous structural study[12] of the c-ring, using X-ray crystallography, suggested that one bedaquiline molecule binds to each of the nine c-subunits, and identified key features of the binding interaction that the drug makes with the c-ring's proton-binding sites.

Tuberculosis vaccine finds an improved route

By contrast, Guo and colleagues revealed (Fig. 1) seven bedaquiline molecules bound to seven of the nine c-subunits; the other two potential c-subunit binding sites were obstructed by the adjacent a-subunit. Five of the bedaquiline molecules were bound to c-subunits (at 'c-only' sites) in the same type of binding as previously revealed by X-ray analysis[12], whereas the other two sites in c-subunits that bound to bedaquiline had further interactions with subunit a. Designated as leading and lagging sites, respectively, these two sites are located in c-subunits that, in the absence of a drug to hinder enzyme function, would have either just picked up a proton in the proton-entry channel of the c-ring (the leading site) or just deposited a proton in the proton-exit channel of the c-ring (the lagging site).

When the authors washed the complex to remove the drug, bedaquiline disappeared from the images of the five C-only sites but remained clearly visible in the leading site, with some also remaining in the lagging site. The reason for this became clear when the authors looked at where the drug interacted with the protein: the leading site was created by large movements of specific amino-acid residues in the c- and a-subunits that formed a deeper and more extensive binding pocket for the drug compared with that of the c-only binding site. This difference provides a probable explanation for the striking difference between the drug's potency *in vitro* and *in vivo*. By binding particularly tightly to the leading and lagging sites that are created as the c-ring rotates, bedaquiline jams the rotation of the ring, thereby blocking proton transport and halting ATP synthesis.

It is unsurprising that a binding site's location with regard to the peripheral stalk should affect the possible conformations at that site, but it is nonetheless beautiful to actually observe the difference it makes to drug binding. The structural details of the leading-site pocket offer information for researchers wanting to develop an improved version of bedaquiline. But most of us will be riveted by the movies made possible by cryo-electron microscopy, showing ATP synthase at work. It highlights exactly how

complex this machine — the basis of almost all life — actually is, while simultaneously revealing a vulnerability that bedaquiline exploits. The 2017 Nobel committee recognized how crucial it is to be able to visualize biochemical processes in three dimensions; we hope they are proudly watching the movies in this paper.

Nature **589**, 21-22 (2021)

doi: https://doi.org/10.1038/d41586-020-03406-x

References

1. 1.

   Guo, H. *et al. Nature* **589**, 143–147 (2021).

2. 2.

   Schnippel, K. *et al. Lancet Respir. Med.* **6**, 699–706 (2018).

3. 3.

   Conradie, F. *et al. N. Engl. J. Med.* **382**, 893–902 (2020).

4. 4.

   Andries, K. *et al. Science* **307**, 223–227 (2005).

5. 5.

   Kühlbrandt, W. *Annu. Rev. Biochem.* **88**, 515–549 (2019).

6. 6.

   Roh, S.-H. *et al. Sci. Adv.* **6**, eabb9605 (2020).

7. 7.

Haagsma, A. C., Driessen, N. N., Hahn, M.-M., Lill, H. & Bald, D. *FEMS Microbiol. Lett.* **313**, 68–74 (2010).

8. 8.

   Zhang, A. T., Montgomery, M. G., Leslie, A. G. W., Cook, G. M. & Walker, J. E. *Proc. Natl Acad. Sci. USA* **116**, 4206–4211 (2019).

9. 9.

   Lu, P., Lill, H. & Bald, D. *Biochim. Biophys. Acta* **1837**, 1208–1218 (2014).

10. 10.

    Ragunathan, P. *et al. J. Biol. Chem.* **292**, 11262–11279 (2017).

11. 11.

    Koul, A. *et al. Nature Chem. Biol.* **3**, 323–324 (2007).

12. 12.

    Preiss, L. *et al. Sci. Adv.* **1**, e1500106 (2015).

Jobs from Nature Careers

-
  -
    - All jobs
  -
    - **Aushilfe / Studentische Hilfskraft (m/w/d) im Abteilungssekretariat für 15 Std. / Woche**

      German Cancer Research Center in the Helmholtz Association (DKFZ)

Heidelberg, Germany

JOB POST

- **Hochfrequenz Technikerin I Hochfrequenz Techniker (w/m/d)**

  Helmholtz-Zentrum Berlin for Materials and Energy (HZB)

  Berlin, Germany

  JOB POST

- **PhD position – Genetics of neuropathological changes in Alzheimer's disease**

  Flanders Institute for Biotechnology (VIB)

  Antwerp, Belgium

  JOB POST

- **53541: Physicist, Engineer or similar - Laser-spectroscopic methods for the protection of terrestrial infrastructures**

  German Aerospace Center (DLR)

  Köln, Germany

  JOB POST

This article was downloaded by **calibre** from https://www.nature.com/articles/d41586-020-03406-x

NEWS AND VIEWS
06 January 2021

Machine learning reveals the complexity of dense amorphous silicon

Transitions between amorphous forms of solids and liquids are difficult to study. Machine learning has now provided fresh insight into pressure-induced transformations of amorphous silicon, opening the way to studies of other systems.

Paul F. McMillan

Paul F. McMillan is in the Department of Chemistry, University College London, London WC1H 0AJ, UK.
Contact

Search for this author in:

- Pub Med
- Nature.com
- Google Scholar

Machine-learning approaches are being developed to produce accurate simulations of the structure and chemical bonding of disordered solids and liquids, modelling a sufficient number of atoms to enable direct comparison with experimental data. Writing in *Nature*, Deringer *et al.*[1] report their use of this approach to probe the structure of amorphous silicon under compression, as the element transforms from semiconducting to metallic states. Their work demonstrates that the structural transformations of amorphous forms of materials can take place much more gradually than

those between crystalline phases, and can involve the formation of nanostructured domains and localized atomic arrangements that are not found in any of the crystalline states.

Silicon is one of a small class of elements whose density increases on melting[2]. This unusual behaviour is shared with crystalline ice, which floats on top of liquid water. Such unexpected reversal of solid and liquid densities has been linked to a phenomenon called polyamorphism — the ability of a substance to exist as different amorphous phases that have distinct structures and properties.

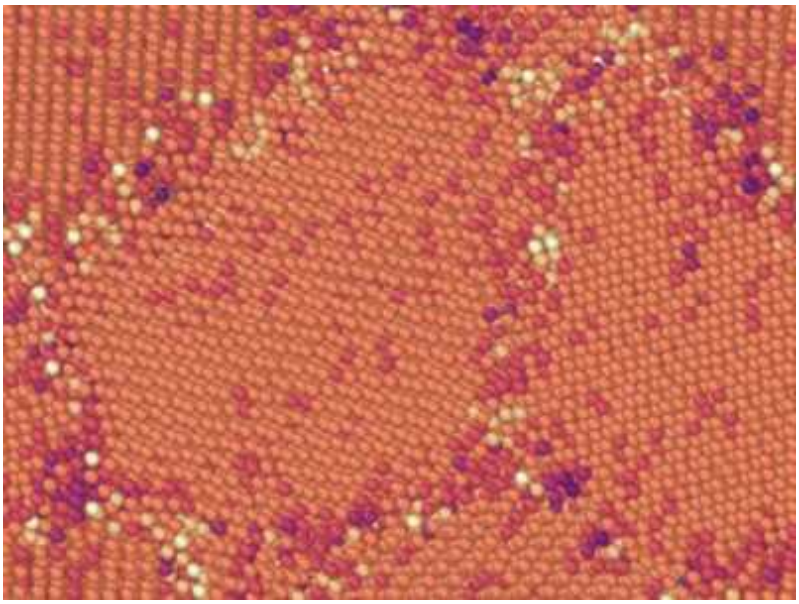

Read the paper: Origins of structural and electronic transitions in disordered silicon

Liquid silicon is a metallic electrical conductor, whereas solid silicon is a semiconductor in ambient conditions, a fact that underpins its use in technologies ranging from computer chips to solar panels. The solid can adopt either a crystalline or a structurally disordered amorphous form at room temperature and pressure; in both cases, each atom bonds to four

others in a tetrahedral arrangement. However, both the crystalline and amorphous solids transform into denser structures under compression, a process that is accompanied by a transition to metallic conducting behaviour.

In the 1970s, calorimetric experiments were carried out to study the energy changes that accompany the transformations between amorphous and crystalline forms of silicon during heating and cooling[3]. Analysis of the results suggested that two amorphous forms of silicon exist, with a phase transition between them. Simulations have since suggested that silicon transforms from a low-density amorphous (LDA) phase, in which the coordination number — the number of neighbouring atoms around each silicon atom — is four, to a high-density amorphous (HDA) phase whose structure is similar to that of metallic liquid silicon[3,4]. The LDA–HDA transition has been observed both during rapid heating of the amorphous solid and on compression of amorphous silicon at ambient temperature[5–7].

Structural transformations between crystalline phases of silicon are readily observed using diffraction methods[8], but those involving the amorphous state are more difficult to study because they occur less abruptly as density increases. This is where computational simulations come into play: they can visualize the arrangements of atoms in different phases, and predict and explain the resulting properties. The main challenge is always to model enough atoms to enable the comparison of simulation results with macroscopic data for real samples, while maintaining sufficient accuracy to describe the arrangements and bonding of the atoms.

Computational simulations are also limited by their characteristic timescales when studying phase transitions. Currently available computational resources often restrict simulations based on accurate quantum-mechanical calculations to systems that incorporate a few tens to hundreds of atoms, which are typically examined over timescales of up to several femto-seconds (1 femtosecond is 10^{-15} s). Simulations that use less computationally demanding modelling strategies can be extended to several hundreds or a few thousands of atoms. However, the accuracy of the predictions of the structural and physical properties of the material being investigated is sacrificed as the system size increases, or as the simulation time is extended.

Deringer *et al.* now describe a machine-learning approach that gives unprecedented levels of information about the structure and bonding energetics for a system of 100,000 silicon atoms as it is cooled from the liquid state and compressed to pressures up to 200,000 atmospheres (20 gigapascals). This represents a great increase in the number of atoms that can be modelled (see Extended Data Fig. 1 of the paper[1]). The accuracy of the method approaches those of the best simulations carried out from first principles using quantum-mechanical calculations.

Crucially, the modelled system was large enough to reveal the metastable aggregation of amorphous clusters of atoms. The simulations also uncovered crystallization phenomena that could not be observed using simulations with smaller numbers of atoms, or by using less-accurate models to describe the atomic interactions. The findings closely reproduce the temperatures and pressures observed experimentally for the macroscopic melting of silicon, for the other phase transitions, and for the onset of metallic behaviour.

The simulations show that the structural changes that occur on compression are more complex than was previously realized (Fig. 1). The atoms do not transform simultaneously between an arrangement with a coordination number of four to a phase that has a higher coordination number, as occurs in transitions between crystalline phases of silicon[8]. Instead, the amorphous structure evolves more gradually to produce high-density nanoscale domains of high coordination number, which develop within the original tetrahedral LDA structure. Linkages form between the HDA domains as the density increases, producing a material that exhibits bulk metallic conduction. It might be possible to modify this metallic conductivity in the real world by applying directionally oriented stresses to compressed silicon.

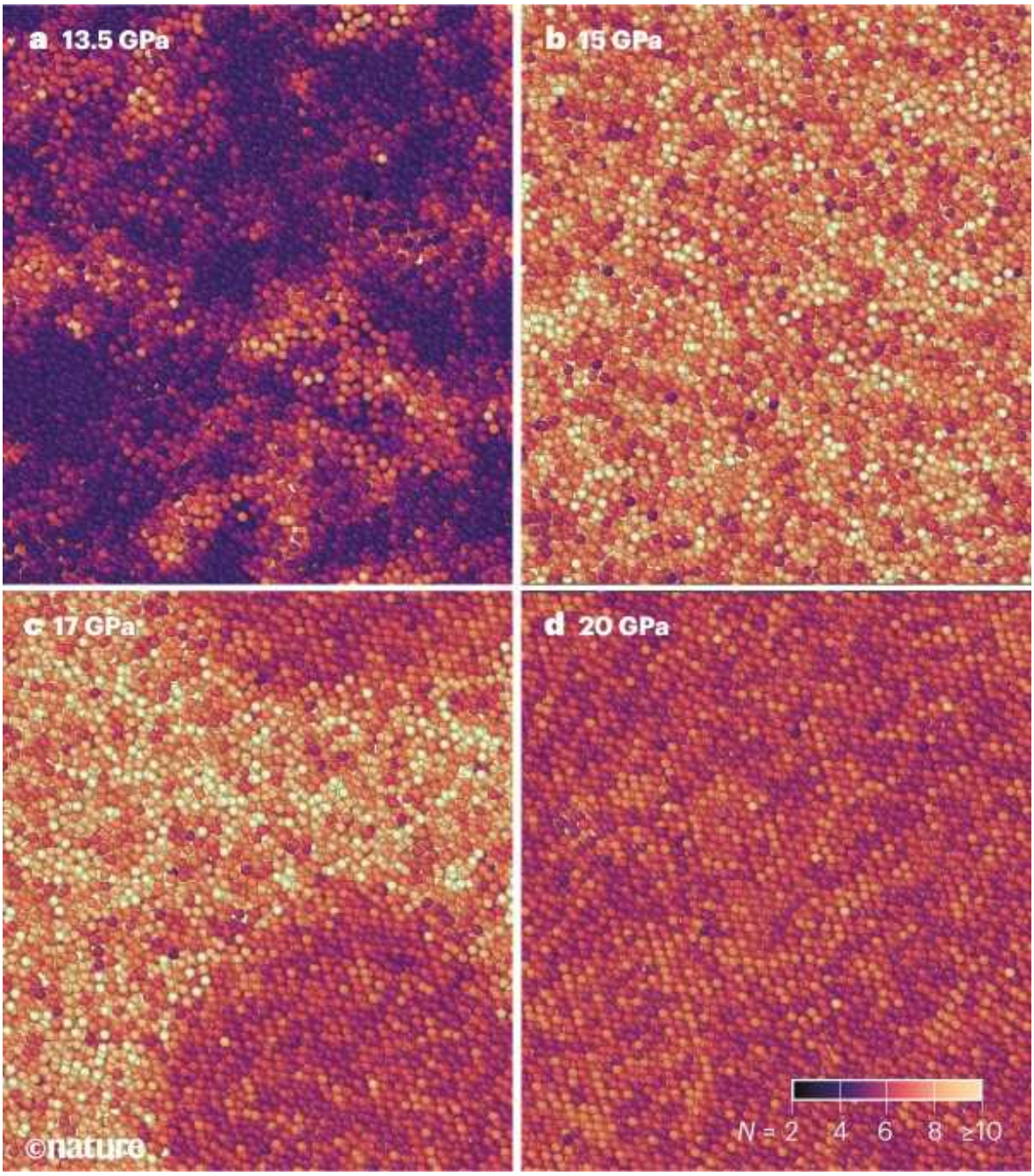

Figure 1 | Large-scale simulations of amorphous silicon. Deringer *et al.*[1] used machine learning to simulate a system of 100,000 silicon atoms at increasing pressures and at 500 kelvin, to predict the resulting changes in structure and properties of the element. The colour of each atom indicates the number of other atoms bonded to it (the coordination number, *N*). The coordination number is four at ambient pressure. **a**, At 13.5 gigapascals, most atoms still have a coordination number of four, corresponding to a low-

density semiconducting phase of silicon, but high-density regions of atoms with higher coordination numbers and metal-like conductivity have appeared. **b**, At 15 GPa, these regions predominate, and have coalesced to form a high-density metallic phase. **c**, At 17 GPa, domains of a new, very-high-density amorphous phase have started to form within the material. **d**, At 20 GPa, the amorphous structure has rapidly equilibrated to produce a crystalline metallic phase that has a simple hexagonal structure. (Images from Extended Data Fig. 4 of ref. 1.)

The authors' simulations also show that, as the system is compressed further, it quickly collapses by about 25% of its volume, thus producing a very-high-density metallic state. This crystallizes rapidly on the nanosecond time-scale of the simulations, to form nanodomains of a metallic phase of silicon.

The results have implications for our understanding of how polyamorphic transitions might emerge between different liquid phases and glassy structures more generally[9]. Deringer and colleagues' machine-learning approach has allowed them to accurately simulate amorphous silicon structures on a picosecond timescale (1 picosecond is 10^{-12} s), and over temperature and pressure ranges that are relevant to transitions between liquids and crystal phases, between liquids and glasses, and between two amorphous phases. Their findings therefore offer the chance to study transitions of a wide array of amorphous materials that have previously been difficult to probe.

The authors' approach could also now be used to explore the possibilities of transforming amorphous silicon, or 'doped' materials in which silicon contains small amounts of other elements, to produce nanostructures that contain metallic and semiconducting domains. Such nanostructures could open up many opportunities for developing new technology, such as in electronic communication, data processing and energy harvesting.

Nature **589**, 22-23 (2021)

doi: https://doi.org/10.1038/d41586-020-03574-w

References

1. 1.

Deringer, V. L. *et al. Nature* **589**, 59–64 (2021).

2. 2.

McMillan, P. F. *J. Mater. Chem.* **14**, 1506–1512 (2004).

3. 3.

Sastry, S. & Angell, C. A. *Nature Mater.* **2**, 739–743 (2003).

4. 4.

Durandurdu, M. & Drabold, D. A. *Phys. Rev. B* **64**, 014101 (2001).

5. 5.

Aptekar, L. I. *Sov. Phys. Dokl.* **24**, 993–995 (1979).

6. 6.

Ponyatovsky, E. G. & Barkalov, O. I. *Mater. Sci. Rep.* **8**, 147–191 (1992).

7. 7.

McMillan, P. F., Wilson, M., Daisenberger, D. & Machon, D. *Nature Mater*. **4**, 680–684 (2005).

8. 8.

McMahon, M. I. & Nelmes, R. J. *Chem. Soc. Rev.* **35**, 943–963 (2006).

9. 9.

Machon, D., Meersman, F. Wilding, M. C., Wilson, M. & McMillan, P. F. *Progr. Mater. Sci.* **61**, 216–282 (2014).

Jobs from Nature Careers

-
  -
    - All jobs
  -
    - **Aushilfe / Studentische Hilfskraft (m/w/d) im Abteilungssekretariat für 15 Std. / Woche**

      German Cancer Research Center in the Helmholtz Association (DKFZ)

      Heidelberg, Germany

      JOB POST

    - **Hochfrequenz Technikerin I Hochfrequenz Techniker (w/m/d)**

      Helmholtz-Zentrum Berlin for Materials and Energy (HZB)

      Berlin, Germany

      JOB POST

    - **PhD position – Genetics of neuropathological changes in Alzheimer's disease**

      Flanders Institute for Biotechnology (VIB)

      Antwerp, Belgium

      JOB POST

    - **53541: Physicist, Engineer or similar - Laser-spectroscopic methods for the protection of**

terrestrial infrastructures

German Aerospace Center (DLR)

Köln, Germany

JOB POST

This article was downloaded by **calibre** from https://www.nature.com/articles/d41586-020-03574-w

NEWS AND VIEWS
23 December 2020

A screen of brain organoids to study neurodevelopmental disease

A high-throughput technique has been developed to screen genes implicated in neurodevelopmental diseases in 3D cell cultures. It reveals a mechanism that might be involved in a rare disorder called microcephaly.

Adriana Cherskov &

Adriana Cherskov is in the Department of Neuroscience, Yale School of Medicine, New Haven, Connecticut 06510, USA.
Contact

Search for this author in:

- Pub Med
- Nature.com
- Google Scholar

Nenad Sestan

Nenad Sestan is in the Department of Neuroscience, Yale School of Medicine, New Haven, Connecticut 06510, USA.
Contact

Search for this author in:

- Pub Med
- Nature.com
- Google Scholar

Thousands of genetic variants increase the risk that a person will be affected by a major disorder of the nervous system, such as improper brain growth[1–3]. Understanding the effects of these variants could reveal disease mechanisms and point to possible drug targets. But studying each variant individually is a slow and arduous process. Moreover, the complexity of the human brain makes such studies difficult. Writing in *Science*, Esk *et al.*[4] outline a high-throughput *in vitro* screening approach that can overcome these obstacles. The authors then use their screen to analyse genes associated with a rare developmental condition called microcephaly.

In microcephaly, the brain — in particular, its outer part, known as the cerebral cortex — is significantly smaller than usual[1–3]. The condition is the result of decreased proliferation of neural stem cells or increased cell death in the developing brain. Microcephaly has been associated with a range of genes and genetic syndromes[1–3]. Determining whether each of these genes is really involved in microcephaly requires high-throughput technologies, but existing screens have limitations. For instance, those that use animals can be problematic because equivalent mutations in different animal models often have different effects[5], and because genes associated with neurodevelopmental disorders can be expressed differently in different species. And 2D cell-culture systems cannot fully capture processes such as interactions between the various types of neuron and glial cell found in 3D tissues, which are crucial for normal cell proliferation.

Read the paper: A human tissue screen identifies a regulator of ER secretion as a brain-size determinant

But 3D cell-culture systems called organoids, in which stem cells can produce brain-like structures, provide a powerful way to overcome the

problems of using animal models and 2D cultures[6]. Organoids form brain-like tissues and can recapitulate key cellular and gene-expression features of human cortical development from early to mid-gestation[6,7]. However, mimicking complex tissues in 3D is a double-edged sword for high-throughput screens. Variability in growth rates in a diverse population of cells makes it difficult to determine whether differences in cell survival or proliferation are due to the nature of the experiment or to the inherent variability of the organoids.

Esk *et al.* set out to overcome this issue by combining brain organoids with a new method based on the gene-editing technique CRISPR–Cas9. In CRISPR–Cas9, a guide RNA (gRNA) is designed to bind to the DNA sequence that is to be edited. The Cas9 enzyme then binds to the gRNA and makes a break in the DNA. Often, this DNA break is incorrectly repaired by the cell, which can result in gene 'knockout', meaning that the gene of interest is no longer translated into a functioning protein. Esk and colleagues designed gRNAs to target 173 genes that are implicated in microcephaly, and tagged every gRNA with a unique DNA sequence called a lineage barcode. They then infected stem cells with these barcoded gRNAs. Each cell that receives a given gRNA, and all its descendants, carry the same barcode, making it easy to identify cell lineages. The stem cells were cultured in 3D for up to 40 days, to form a brain organoid, and the DNA from all the cells in the organoid was then extracted and pooled.

The aim of the screen was to count the number of lineage barcodes present for each gene of interest, and to compare them with the number of lineage barcodes from a control gRNA that did not mutate any gene. Depletion of lineage barcodes for a candidate gene compared with the control would indicate that this gene is necessary for proper cell proliferation. However, it is difficult to detect small numbers of lineage barcodes (that is, those from small lineages) during analysis. Greater resolution is required to be sure of detecting cases of the moderate cell loss that is typical of microcephaly. Moreover, in a 3D brain organoid, baseline lineage sizes vary widely, as discussed above.

To overcome these problems, Esk *et al.* added a second barcode to each cell during DNA processing, thereby labelling the DNA of each cell in a lineage individually (Fig. 1). Barcoding cells individually allowed the researchers to

track exactly how many cells are in each lineage. Together, the dual barcodes account for the variability in organoid-cell growth (multiple gRNAs are used for each gene, enabling trends to be reliably detected), and barcoding each cell makes it possible to detect changes in proliferation for small lineages, so it is easier to identify cases where gene deletions cause moderate cell loss. The group named their technique CRISPR-lineage tracing at cellular resolution in heterogeneous tissue (CRISPR-LICHT).

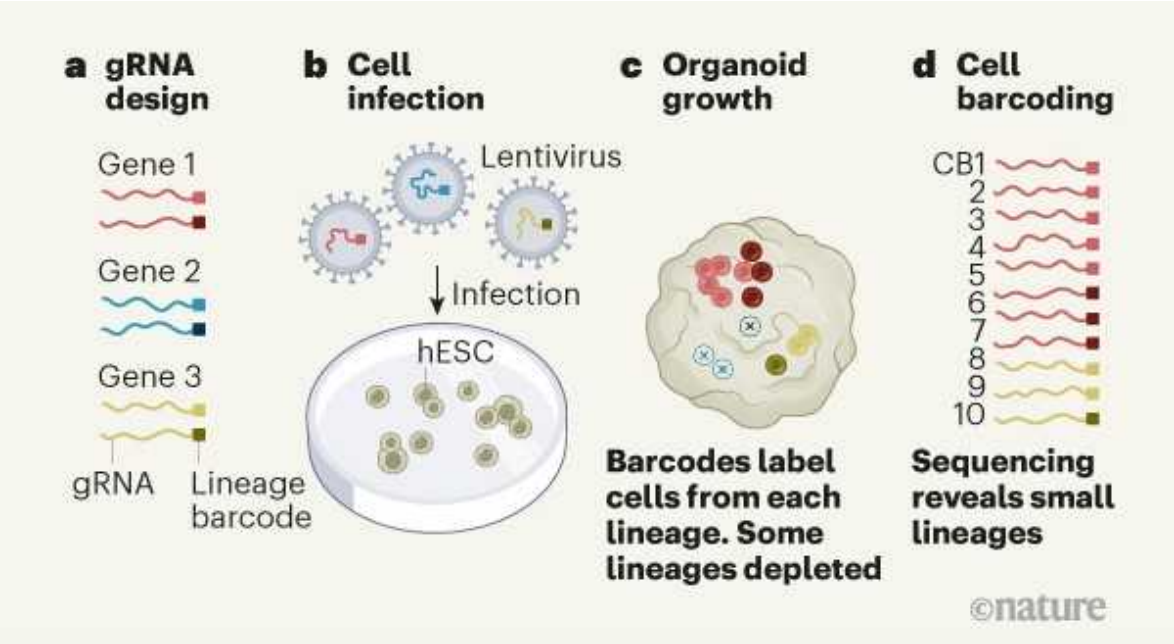

Figure 1 | A gene-editing and lineage-tracing approach called CRISPR-LICHT. Esk *et al.*[4] used their CRISPR-LICHT approach to analyse how genetic mutations can alter cell numbers in the brain. **a**, The authors designed guide RNA (gRNA) molecules that each bind to one of 173 genes of interest. They labelled each gRNA molecule with a unique DNA sequence called a lineage barcode (LB). **b**, Each gRNA was then packaged into a lentivirus (only three are shown here, for simplicity), and the lentivirus pool was used to infect human embryonic stem cells (hESCs). **c**, The cells were placed in 3D culture and the enzyme Cas9 induced (this enzyme targets the gRNAs, causing them to delete genes in each infected cell; not shown). The cells were cultured for up to 40 days to produce complex 3D brain organoids. Some lineages grew rapidly, whereas others were depleted (crosses). **d**, The organoids were collected and the cells containing Cas9 selected (not shown). The DNA from these cells was amplified, and a second unique DNA barcode (a cell barcode, CB) was

added. The DNA was then sequenced for gRNAs and barcodes. The LBs allow accurate measurements of the size of each lineage, and the CBs increase the ability to pick out small lineages. If lineages containing gRNAs for one gene are consistently small (here, genes 2 and 3), the gene is likely to have a role in cell proliferation in the brain.

The researchers ranked the lineage-barcode depletion of the 173 genes thought to pose a risk of microcephaly, and examined the top 32 genes in further detail. They investigated the role of these genes in regulating cell proliferation by using a mixing strategy, in which they grew organoids from a combination of control cells and cells that had been genetically edited to lack the gene, and analysed the ratio of control to edited cells in the fully grown organoids. Finding significantly reduced numbers of edited cells suggests that deletion of the gene causes reduced proliferation. Of the 32 genes studied, 25 were found to be implicated in cell proliferation.

Finally, Esk *et al.* focused on one particular gene of the set, which encodes immediate early response 3 interacting protein 1 (IER3IP1). When cells were engineered to lack this gene, the resulting organoids were smaller than the controls. Analysis of organoids lacking this gene revealed that it seems to regulate the unfolded protein response — a cellular response to stress in an intracellular organelle called the endoplasmic reticulum that leads to reduced protein synthesis. Treatment of cells with a small molecule called the integrated stress response inhibitor, which restores protein synthesis, led to normal size and organization of neural progenitors in the organoids. These findings are particularly interesting because they tie the stress-induced unfolded protein response, which has previously been associated with Zika virus-related microcephaly[8], to a genetic cause of the disorder. The experiments highlight the enormous potential of CRISPR-LICHT to investigate the mechanisms that underlie neurodevelopmental disorders.

Although Esk and colleagues focused specifically on genes associated with microcephaly, their cost-effective and time-saving method will be widely applicable to other neurodevelopmental disorders. The Developmental Brain Disorder Gene Database (go.nature.com/3mezn8d) lists about 600 genes whose deletion is associated with neurodevelopmental disorders such as autism, schizophrenia and epilepsy. These genes can now be screened by CRISPR-LICHT.

The approach could also be used to study genes that are under- or overexpressed in neurodevelopmental disorders, by adapting it to modify, rather than eliminate, gene expression. Furthermore, the dual-barcoding techniques of CRISPR-LICHT could be used to create and track genetically distinct populations of cells, to model the effects of genetic variations among cells in the developing brain[9]. Finally, the approach could be used to analyse genes associated with cancer.

There are some limitations, however. CRISPR-LICHT is most suited to studies of early development or cell proliferation. The cerebral organoids in the current study were grown for 40 days, corresponding to development of the human brain early in the first trimester, so neurons and glia that develop and mature later were not considered. Using longer differentiation times would increase the turnaround time. Furthermore, current protocols for organoid growth might activate cellular stress pathways, impairing cell-type specification and fidelity[10]. Finally, not all of the cortex is the same, with different regions having cell types and connections that serve different functions. More-precise protocols would be required to model this complexity and regionalization.

Beyond clinical studies, the CRISPR-LICHT platform could be applied to study the genetic changes and mechanisms underlying the evolution of the healthy human brain. Evidence indicates that the expansion and folding of the human cortex depend on human-specific properties of early neuronal development[11–13]. Using brain organoids to screen genes and other DNA elements that are unique to humans, or that exhibit a distinct pattern of activity in humans[14], could be a powerful way of connecting genes to traits in the context of human neural development.

Nature **589**, 24-25 (2021)

doi: https://doi.org/10.1038/d41586-020-03636-z

References

1. 1.

Woods, C. G. *Curr. Opin. Neurobiol.* **14**, 112–117 (2004).

2. 2.

Dixon-Salazar, T. J. & Gleeson, J. G. *Ann. NY Acad. Sci.* **1214**, 156–167 (2010).

3. 3.

Jayaraman, D., Bae, B.-I. & Walsh, C. A. *Annu. Rev. Genom. Hum. Genet.* **19**, 177–200 (2018).

4. 4.

Esk C. *et al. Science* **370**, 935–941 (2020).

5. 5.

Liao, B.-Y. & Zhang, J. *Proc. Natl Acad. Sci. USA* **105**, 6987–6992 (2008).

6. 6.

Eiraku, M. *et al. Cell Stem Cell* **3**, 519–532 (2008).

7. 7.

Mariani, J. *et al. Proc. Natl Acad. Sci. USA* **109**, 12770–12775 (2012).

8. 8.

Gladwyn-Ng, I. *et al. Nature Neurosci.* **21**, 63–71 (2018).

9. 9.

McConnell, M. J. *et al. Science* **356**, eaal1641 (2017).

10. 10.

Bhaduri, A. *et al. Nature* **578**, 142–148 (2020).

11. 11.

    Heide, M. *et al. Science* **369**, 546–550 (2020).

12. 12.

    Fiddes, I. T. *et al. Cell* **173**, 1356–1369 (2018).

13. 13.

    Suzuki, I. K. *et al. Cell* **173**, 1370–1384 (2018).

14. 14.

    Sousa, A. M. M., Meyer, K. A., Santpere, G., Gulden, F. O. & Sestan, N. *Cell* **170**, 226–247 (2017).

Jobs from Nature Careers

-
  -
    - All jobs
  -
    - **Aushilfe / Studentische Hilfskraft (m/w/d) im Abteilungssekretariat für 15 Std. / Woche**

      German Cancer Research Center in the Helmholtz Association (DKFZ)

      Heidelberg, Germany

      JOB POST

    - **Hochfrequenz Technikerin I Hochfrequenz Techniker (w/m/d)**

      Helmholtz-Zentrum Berlin for Materials and Energy (HZB)

Berlin, Germany

JOB POST

- **PhD position – Genetics of neuropathological changes in Alzheimer's disease**

  Flanders Institute for Biotechnology (VIB)

  Antwerp, Belgium

  JOB POST

- **53541: Physicist, Engineer or similar - Laser-spectroscopic methods for the protection of terrestrial infrastructures**

  German Aerospace Center (DLR)

  Köln, Germany

  JOB POST

This article was downloaded by **calibre** from https://www.nature.com/articles/d41586-020-03636-z

NEWS AND VIEWS
06 January 2021

Artificial intelligence accelerated by light

The explosive growth of artificial intelligence calls for rapidly increasing computing power. Two reported photonic processors could meet these power requirements and revolutionize artificial-intelligence hardware.

Huaqiang Wu &

Huaqiang Wu is at the Institute of Microelectronics, Tsinghua University, Beijing 100084, China.
Contact

Search for this author in:

- Pub Med
- Nature.com
- Google Scholar

Qionghai Dai

Qionghai Dai is in the Department of Automation, Tsinghua University, Beijing 100084, China.
Contact

Search for this author in:

- Pub Med
- Nature.com

- Google Scholar

Artificial intelligence (AI) is transforming various fields, such as clinical diagnosis, autonomous driving and speech translation. However, the quickly increasing volume of data in modern society poses great challenges for the electronic computing hardware used in AI, in terms of both computing speed and power consumption. Such issues have become a major bottleneck for AI. Writing in *Nature*, Xu *et al.*[1] and Feldmann *et al.*[2] report photonic processors that accelerate AI processing by harnessing the distinctive properties of light. These demonstrations could inspire a renaissance of optical computing.

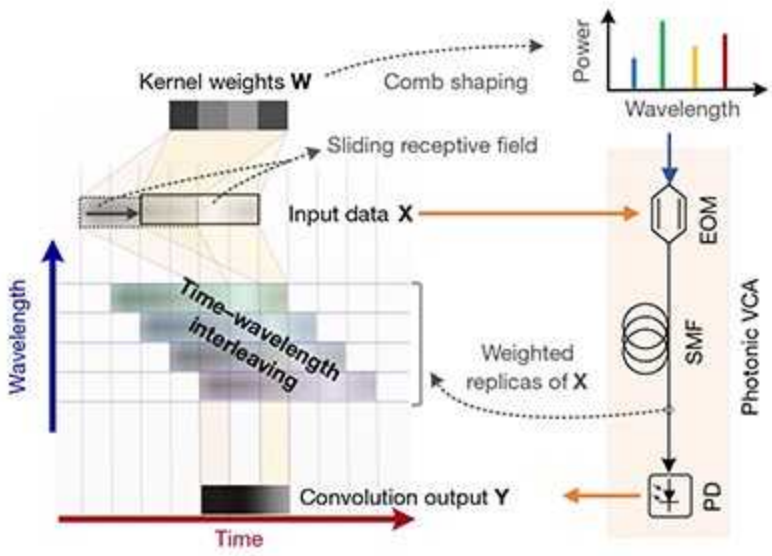

Read the paper: 11 TOPS photonic convolutional accelerator for optical neural networks

With the rise of AI, conventional electronic computing approaches are gradually reaching their performance limits and lagging behind the rapid growth of data available for processing. Among the various types of AI, artificial neural networks are widely used for AI tasks because of their

excellent performance. These networks perform complex mathematical operations using many layers of interconnected artificial neurons[3]. The fundamental operation that uses most of the computational resources is called matrix–vector multiplication.

Various efforts have been made to design and implement specific electronic computing systems to accelerate processing in artificial neural networks. In particular, considerable success has been achieved using custom chips known as application-specific integrated circuits[4], brain-inspired computing[5] and in-memory computing[6], whereby processing is performed *in situ* with an array of memory devices called memristors.

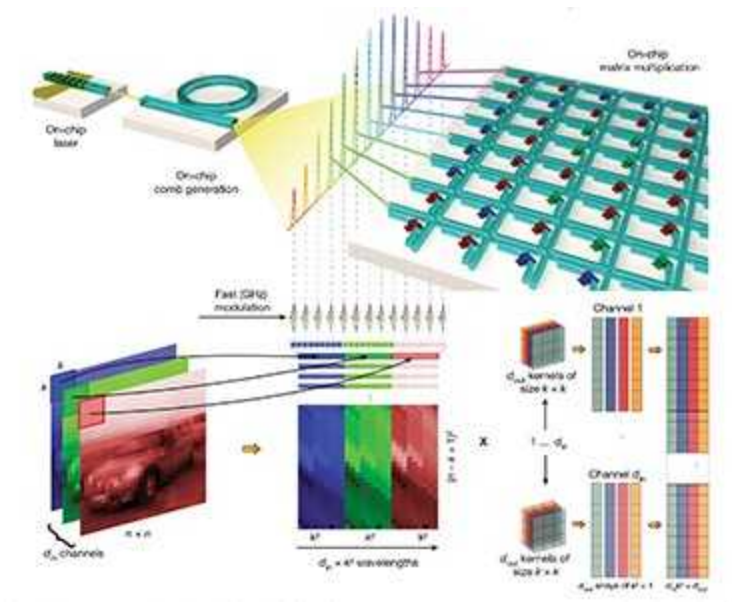

[Read the paper: Parallel convolutional processing using an integrated photonic tensor core]

Electrons are the carriers of information in electronic computing, but photons have long been considered an alternative option. Because the spectrum of light covers a wide range of wavelengths, photons of many

different wavelengths can be multiplexed (transmitted in parallel) and modulated (altered in such a way that they can carry information) simultaneously without the optical signals interfering with each other. This propagation of information at the speed of light results in minimal time delays. Moreover, passive transmission (in which no input power is required) aids ultralow power consumption[7], and phase modulation (whereby the quantum-mechanical phases of light waves are varied) enables light to be easily modulated and detected at frequencies greater than 40 gigahertz (ref. 8)[8].

In the past few decades, great success has been attained in optical-fibre communication. However, it remains challenging to use photons for computing, especially at a scale and performance level comparable to those of state-of-the-art electronic processors. This difficulty arises from a lack of suitable parallel-computing mechanisms, materials that permit high-speed nonlinear (complex) responses of artificial neurons and scalable photonic devices for integration into computing hardware.

Fortunately, developments over the past few years in devices called optical frequency combs[9] brought new opportunities for integrated photonic processors. Optical frequency combs are sets of light sources with emission spectra that consist of thousands or millions of sharp spectral lines that are uniformly and closely spaced in frequency. These devices have achieved substantial success in various fields, such as spectroscopy, optical-clock metrology and telecommunication, and were recognized with the 2005 Nobel Prize in Physics. Optical frequency combs can be integrated into a computer chip[9] and used as power-efficient energy sources for optical computing. This system is well suited for data parallelization by wavelength multiplexing.

Xu and colleagues used such a set-up to produce a versatile integrated photonic processor. This device performs a type of matrix–vector multiplication known as a convolution for image-processing applications. The authors implemented an ingenious method to carry out the convolution. They first used chromatic dispersion — whereby the speed of transmitted light depends on its wavelength — to produce different time delays for

wavelength-multiplexed optical signals. They then combined these signals along the dimension associated with the wavelength of the light.

By fully exploiting the wide range of photon wavelengths, Xu *et al.* achieved intrinsically parallel computing for different convolution operations. The optical-computing speed was beyond ten trillion operations per second using a single processing core and was limited only by the data throughput. Another welcome feature of this work is that the authors identify the entry point of their photonic convolution processor in practical applications. In particular, they suggest that the processor could be used in a hybrid optical–electronic framework, such as for *in situ* computations during optical-fibre communications.

Feldmann and colleagues independently made an integrated photonic processor that performs a convolution involving optical signals that span two dimensions. The device uses optical frequency combs in an 'in-memory' computing architecture that is based on a phase-change material (a material that can switch between an amorphous phase and a crystalline phase). The authors fully parallelized the input data through wavelength multiplexing and conducted analogue matrix–vector multiplication using an array of integrated cells of the phase-change material.

Such a highly parallelized framework can potentially process an entire image in a single step and at high speed. Moreover, in principle, the system can be substantially scaled up using commercial manufacturing procedures and aid *in situ* machine learning in the near future. Because the convolution process involves passive transmission, the calculations of the photonic processing core can, in theory, be performed at the speed of light and with low power consumption. This ability would be extremely valuable for energy-intensive applications, such as cloud computing.

Given the challenges facing conventional electronic computing approaches, it is exciting to see the emergence of integrated photonics as a potential successor to achieve unprecedented performance for future computing architectures. However, building a practical optical computer will require extensive interdisciplinary efforts and collaborations between researchers in materials science, photonics, electronics and so on. Although the reported photonic processors have high computing power per unit area and potential

scalability, the all-optical computing scale (the number of optical artificial neurons) remains small. Moreover, the energy efficiency is limited by the presence of computing elements that inherently absorb light and because electrical and optical signals frequently need to be interconverted.

Another avenue of research is the development of advanced nonlinear integrated photonic computing architectures, rather than one- or two-dimensional linear convolutions. By integrating electronic circuits and thousands or millions of photonic processors into a suitable architecture, a hybrid optical–electronic framework that takes advantage of both photonic and electronic processors could revolutionize AI hardware in the near future. Such hardware would have important applications in areas such as communication, data-centre operation and cloud computing.

Nature **589**, 25-26 (2021)

doi: https://doi.org/10.1038/d41586-020-03572-y

References

1. 1.

   Xu, X. *et al. Nature* **589**, 44–51 (2021).

2. 2.

   Feldmann, J. *et al. Nature* **589**, 52–58 (2021).

3. 3.

   LeCun, Y., Bengio, Y. & Hinton, G. *Nature* **521**, 436–444 (2015).

4. 4.

   Silver, D. *et al. Nature* **550**, 354–359 (2017).

5. 5.

Merolla, P. A. *et al. Science* **345**, 668–673 (2014).

6. 6.

Sebastian, A., Le Gallo, M., Khaddam-Aljameh, R. & Eleftheriou, E. *Nature Nanotechnol.* **15**, 529–544 (2020).

7. 7.

Lin, X. *et al. Science* **361**, 1004–1008 (2018).

8. 8.

Shen, Y. *et al. Nature Photon.* **11**, 441–446 (2017).

9. 9.

Stern, B., Ji, X., Okawachi, Y., Gaeta, A. L. & Lipson, M. *Nature* **562**, 401–405 (2018).

Jobs from Nature Careers

-
  -
    - All jobs
  -
    - **Aushilfe / Studentische Hilfskraft (m/w/d) im Abteilungssekretariat für 15 Std. / Woche**

      German Cancer Research Center in the Helmholtz Association (DKFZ)

      Heidelberg, Germany

      JOB POST
    -

Hochfrequenz Technikerin I Hochfrequenz Techniker (w/m/d)

Helmholtz-Zentrum Berlin for Materials and Energy (HZB)

Berlin, Germany

JOB POST

- **PhD position – Genetics of neuropathological changes in Alzheimer's disease**

  Flanders Institute for Biotechnology (VIB)

  Antwerp, Belgium

  JOB POST

- **53541: Physicist, Engineer or similar - Laser-spectroscopic methods for the protection of terrestrial infrastructures**

  German Aerospace Center (DLR)

  Köln, Germany

  JOB POST

This article was downloaded by **calibre** from https://www.nature.com/articles/d41586-020-03572-y

NEWS AND VIEWS
10 November 2020

Big data and simple models used to track the spread of COVID-19 in cities

Understanding the dynamics of SARS-CoV-2 infections could help to limit viral spread. Analysing mobile-phone data to track human contacts at different city venues offers a way to model infection risks and explain infection disparities.

Kevin C. Ma &

Kevin C. Ma is in the Department of Immunology and Infectious Diseases, Harvard T. H. Chan School of Public Health, Boston, Massachusetts 02115, USA.
Contact

Search for this author in:

- Pub Med
- Nature.com
- Google Scholar

Marc Lipsitch

Marc Lipsitch is in the Department of Immunology and Infectious Diseases, Harvard T. H. Chan School of Public Health, Boston, Massachusetts 02115, USA, and in the Department of Epidemiology, Center for Communicable Disease Dynamics, Harvard T. H. Chan School of Public Health.
Contact

Search for this author in:

- Pub Med
- Nature.com
- Google Scholar

Behind the highly politicized disagreements over COVID-19 control measures lies a widely shared desire to return economic and social life to sustainable levels as soon and for as long as possible, while preserving health-care systems and minimizing severe illness and death. The main arguments are about the extent to which these goals are mutually reinforcing, and whether there is a trade-off between greater viral transmission and increased social and economic activity. The difficulty in identifying control measures that are both effective and minimally disruptive motivates the search for new approaches to modelling transmission. Given the limited data available from epidemiological studies on how interventions can curb infection, such models can provide an initial framework for evaluating hypothetical control measures and help to guide policy decisions.

Writing in *Nature*, Chang *et al.*[1] present an innovative method that combines simple infectious-disease models with human-mobility data obtained from mobile-phone records. This data-rich model has enabled them to generate and, to some extent, test hypotheses on where the virus is transmitted, how racial and socio-economic disparities in COVID-19 infections arise, and how effective different types of control measure might be.

Read the paper: Mobility network models of COVID-19 explain inequities and inform reopening

Chang and colleagues analysed a data set of mobile-phone records for 98 million people in the United States, providing anonymized location information from 1 March to 1 May 2020 and comprising more than 5

billion time points. The authors looked at broad patterns of human interaction at non-residential locations of interest, for example in venues such as shops (Fig. 1), restaurants and places of worship, and used these data as parameters in their model to predict the numbers of new cases detected in entire cities each day. The authors also ‘ fitted’ the model (estimated a few additional unknown parameters) to the data indicating the number of cases. After fitting, the model estimates not only the total rate of infection, but also infection rates in different individual venues or types of venue. This method complements more-conventional epidemiological and surveillance approaches that try to estimate the risks individually for different sorts of activity[2,3].

Figure 1 | A grocery store in Chicago, Illinois. Image taken in April 2020.Credit: Kamil Krzaczynski/AFP/Getty

In principle, studies of outbreak clusters or contact-tracing data offer a way to identify the types of activity and location at which viral transmission does

or doesn't happen as a result of interventions, and the shared features of such findings could be used to infer which activities could be continued and which are key targets for control. For example, case studies of clusters of infections in locations such as those for indoor choir practice, on ships and in nursing homes demonstrate the high risks of poorly ventilated, crowded spaces. By contrast, case studies, such as those providing examples of test results indicating the lack of transmission from infected hair-salon workers to clients while all were wearing face coverings[4], have provided some support for the reopening of such establishments, given adequate mask policies.

These case-study approaches are essential but have substantial limitations. They often have small sample sizes[5], and frequently test only some of the people who have come into contact with a person confirmed to have a SARS-CoV-2 infection, making it difficult to identify the factors that determine whether or not an outbreak occurs. Furthermore, in many places, clusters and infections identified by contact tracing account for only a modest proportion of all transmissions, so inferences drawn from such examples might be of limited use for generalization. Randomized experiments to evaluate interventions (in which the introduction of an intervention is staggered over time in different populations)[6] are an alternative, but they are hard to do[7], and such studies have been rare for COVID-19.

Given the limited data available from these epidemiological and experimental studies, mathematical modelling presents an enticing approach for evaluating interventions. However, without data from epidemiological studies, modelling studies can, at best, assume only a possible range of effectiveness for particular interventions. A strength of Chang and colleagues' approach is that the estimates of effects of interventions are based on the modelled rate of transmission in a particular place. This is, in turn, based on mobile-phone data on people's locations, which provides information such as the number of people who come into close contact with each other at a particular venue, and is combined with strong but transparent assumptions about the factors underlying transmission at different types of venue.

For a given venue, the data used by Chang and colleagues provide detailed estimates of how many people visit per hour, how long they stay on average, and which neighbourhoods they are visiting from. The transmission model is designed to group people in each neighbourhood by their disease status — whether they are susceptible (not previously infected), exposed, infected or removed (having either recovered or died), corresponding to what is described as an SEIR model — and the model allows people to move sequentially through these compartments.

The key assumption made by Chang *et al.* is that the rate at which people in the population are likely to become infected (which in this context refers to their moving from the 'susceptible' to the 'exposed' compartment) depends on which venues they visit and how that changes over time. In this model, venues at which people stay for longer and that are more densely occupied carry a higher risk than do settings in which people stay for less time and that are less packed. This underlying model is exceptionally simple, but the texture of population behavioural changes over time is provided by the detailed mobility data.

One of the strengths of this data-rich modelling approach is that the number of other unknown parameters that need to be fitted to the model is low, reducing the risk that the model is 'overfitted' in a way that forces the model's structure to account for key features of the data. After fitting parameters to publicly available data for the daily number of infections, Chang *et al.* find that their model can better predict epidemic trajectories observed for multiple cities, when compared with the results of models that lack such detailed mobility data. This indicates that the addition of the mobility data improved the accuracy of their model. Although the goal of this mechanistic modelling was not to provide a forecast[8], confirming that the model has reasonable predictive power is often a necessary first step in trying to draw any conclusions about mechanisms that might underlie the observed patterns.

In addition to trying alternative fitting approaches, the authors analysed how sensitive particular outcomes were to the parameters of the model, finding that model outputs are consistent over a range of plausible parameter values. These give confidence that, although simple, the assumptions underlying this model generate predictions that match the data better than do equally

plausible alternatives, which increases the persuasiveness of the hypotheses generated about interventions. An important extension of this work will be to check whether the model continues to match the data for case numbers in more recent months, including the case surges observed during the summer in some cities.

Chang and colleagues' model predicts that infections in venues such as restaurants, gyms and religious establishments have a disproportionately large role in driving up infection rates, corroborating findings from epidemiological studies[5,9]. Locations missing from Chang and colleagues' analysis demonstrate some of the limitations of working with such mobility data. Children, elderly people and those in prison are under-represented in the data sets, so it was not possible to make inferences about the role of schools, nursing homes and prisons in community transmission of viral infection. Models that incorporate both mobility data and typical epidemiological data sources, such as social-contact surveys, might help to address this gap[10].

Nevertheless, the fine-level detail in the mobility data for the venues analysed enabled the authors to evaluate nuanced versions of reopening strategies beyond just simply modelling an overall reduction of activity across a city trying to cope with the pandemic. Chang *et al.* found that capping the maximum occupancy of venues — a strategy that implicitly reduces the number of person-hours spent in risky, high-occupancy settings — is predicted to result in a decreased number of new infections compared with a strategy of less-targeted, overall activity reduction. The authors' approach can be extended to evaluate other types of reopening strategy. For example, time-limited visits to places such as gyms and museums could be modelled by decreasing the average visit length.

Chang and colleagues' work also deepens our understanding of possible causes of the observed disparities in COVID-19 cases by income level, which are incompletely understood. By combining their mobility model with demographic census data, the authors identified two possible main contributors. The first is that lower-income neighbourhoods, which tend to have higher numbers of front-line workers, had less overall reduction in mobility during lockdowns than did higher-income neighbourhoods, a conclusion shared by other studies[11,12]. The second possible contributor is

that, across many types of setting, the venues visited by people from lower-income neighbourhoods tend to be more crowded than are the venues visited by those from higher-income areas. This type of observation is possible only because of the high level of detail on venue size and occupancy in the data analysed by Chang and colleagues.

The authors present clear hypotheses, whose plausibility is enhanced by their fit in the model to the observed infection data, the model's parsimony (which reduces concerns about overfitting), and their ability to provide explanations for observations that were not part of the data, such as disparities associated with income. Further model testing is needed, but given the challenges in gathering and interpreting other relevant data types, these findings could have a valuable role in guiding policy decisions on how to reopen society safely and minimize the harm caused by movement restrictions. Chang and colleagues' work underscores the value of integrating mobility data into epidemiological surveillance systems[13], an increasingly popular approach that should become routine as we rebuild such surveillance systems to incorporate the lessons of this pandemic.

Nature **589**, 26-28 (2021)

doi: https://doi.org/10.1038/d41586-020-02964-4

References

1. 1.

   Chang, S. *et al. Nature* **589**, 82–87 (2021).

2. 2.

   Lipsitch, M., Swerdlow, D. L. & Finelli, L. *N. Engl. J. Med.* **382**, 1194–1196 (2020).

3. 3.

   Lipsitch, M. *et al. Biosecur. Bioterror.* **9**, 89–115 (2011).

4. 4.

Hendrix, M. J., Walde, C., Findley, K. & Trotman, R. *Morbid. Mortal. Wkly Rep.* **69**, 930–932 (2020).

5. 5.

Fisher, K. A. *et al. Morbid. Mortal. Wkly Rep.* **69**, 1258–1264 (2020).

6. 6.

Haushofer, J. & Metcalf, C. J. E. *Science* **368**, 1063–1065 (2020).

7. 7.

Kennedy-Shaffer, L. & Lipsitch, M. *Am. J. Epidemiol.* **189**, 1324–1332 (2020).

8. 8.

Holmdahl, I. & Buckee, C. *N. Engl. J. Med.* **383**, 303–305 (2020).

9. 9.

Leclerc, Q. J. *et al. Wellcome Open Res.* **5**, 83 (2020).

10. 10.

Chamie, G. *et al. Clin. Infect. Dis*. https://doi.org/10.1093/cid/ciaa1234 (2020).

11. 11.

Zelner, J. *et al.* Preprint at medRxiv https://doi.org/10.1101/2020.09.10.20192369 (2020).

12. 12.

Kissler, S. M. *et al. Nature Commun.* **11**, 4674 (2020).

13. 13.

Grantz, K. H. *et al. Nature Commun.* **11**, 4961 (2020).

Competing Financial Interests

M.L. discloses honoraria/consulting payment from Merck, Affinivax, Sanofi-Pasteur, Bristol Myers Squibb and Antigen Discovery and research funding (institutional) from Pfizer. M.L. has provided unpaid scientific advice related to this topic to Janssen, Astra-Zeneca, One Day Sooner and Covaxx (United Biomedical).

Jobs from Nature Careers

- All jobs

- **Aushilfe / Studentische Hilfskraft (m/w/d) im Abteilungssekretariat für 15 Std. / Woche**

  German Cancer Research Center in the Helmholtz Association (DKFZ)

  Heidelberg, Germany

  JOB POST

- **Hochfrequenz Technikerin I Hochfrequenz Techniker (w/m/d)**

  Helmholtz-Zentrum Berlin for Materials and Energy (HZB)

  Berlin, Germany

  JOB POST

- **PhD position – Genetics of neuropathological changes in Alzheimer's disease**

  Flanders Institute for Biotechnology (VIB)

  Antwerp, Belgium

  JOB POST

- **53541: Physicist, Engineer or similar - Laser-spectroscopic methods for the protection of terrestrial infrastructures**

  German Aerospace Center (DLR)

  Köln, Germany

  JOB POST

This article was downloaded by **calibre** from https://www.nature.com/articles/d41586-020-02964-4

- Review
- Published: 06 January 2021

Core-collapse supernova explosion theory

- A. Burrows ORCID: orcid.org/0000-0002-3099-5024[1] &
- D. Vartanyan ORCID: orcid.org/0000-0003-1938-9282[2]

Nature **volume 589**, pages29–39(2021)Cite this article

- 832 Accesses
- 3 Altmetric
- Metrics details

Subjects

- Stars
- Stellar evolution

Abstract

Most supernova explosions accompany the death of a massive star. These explosions give birth to neutron stars and black holes, and eject solar masses of heavy elements. However, determining the mechanism of explosion has been a half-century journey of great numerical and physical complexity. Here we present the status of this theoretical quest and the physics and astrophysics upon which its resolution seems to depend. The delayed neutrino-heating mechanism is emerging as the key driver of

supernova explosions, but there remain many issues to address, such as the chaos of the involved dynamics.

Access through your institution
Change institution
Buy or subscribe

Access options

Subscribe to Journal

Get full journal access for 1 year

$199.00

only $3.90 per issue

Subscribe

All prices are NET prices.
VAT will be added later in the checkout.

Rent or Buy article

Get time limited or full article access on ReadCube.

from$8.99

Rent or Buy

All prices are NET prices.

Additional access options:

- Log in
- Access through your institution
- Learn about institutional subscriptions

Fig. 1: Progenitor mass density profiles.

Fig. 2: Turbulence in the belly of the beast.

Fig. 3: Early 3D explosion of the core of a 16$M_\odot$ star using Fornax.

Fig. 4: Mean shock radii of 2D models.

Fig. 5: Explosion energy and residual neutron star baryon mass.

Fig. 6: Comparison of theoretical and empirical explosion energy versus ejecta mass.

Fig. 7: 3D explosion structure of a representative massive-star progenitor model.

References

1. 1.

   Chandrasekhar, S. *An Introduction to the Study of Stellar Structure* (Dover Publications, 1939).

2. 2.

O'Connor, E. et al. Global comparison of core-collapse supernova simulations in spherical symmetry. *J. Phys. G* **45**, 104001 (2018). **One of the few group-to-group and code-to-code comparison papers in supernova theory**.

ADS Google Scholar

3. 3.

Radice, D., Burrows, A., Vartanyan, D., Skinner, M. A. & Dolence, J. C. Electron-capture and low-mass iron-core-collapse supernovae: new neutrino-radiation-hydrodynamics simulations. *Astrophys. J.* **850**, 43 (2017).

ADS Google Scholar

4. 4.

Burrows, A., Vartanyan, D., Dolence, J. C., Skinner, M. A. & Radice, D. Crucial physical dependencies of the core-collapse supernova mechanism. *Space Sci. Rev*. **214**, 33 (2018).

ADS Google Scholar

5. 5.

Vartanyan, D., Burrows, A., Radice, D., Skinner, M. A. & Dolence, J. Revival of the fittest: exploding core-collapse supernovae from 12 to 25 $M_\odot$. *Mon. Not. R. Astron. Soc*. **477**, 3091–3108 (2018).

ADS CAS Google Scholar

6. 6.

Vartanyan, D., Burrows, A., Radice, D., Skinner, M. A. & Dolence, J. A successful 3D core-collapse supernova explosion model. *Mon. Not. R. Astron. Soc*. **482**, 351–369 (2019).

ADS CAS Google Scholar

7. 7.

Burrows, A., Radice, D. & Vartanyan, D. Three-dimensional supernova explosion simulations of 9-, 10-, 11-, 12-, and 13-$M_\odot$ stars. *Mon. Not. R. Astron. Soc*. **485**, 3153–3168 (2019).

ADS CAS Google Scholar

8. 8.

Nagakura, H., Burrows, A., Radice, D. & Vartanyan, D. Towards an understanding of the resolution dependence of core-collapse supernova simulations. *Mon. Not. R. Astron. Soc*. **490**, 4622–4637 (2019).

ADS CAS Google Scholar

9. 9.

Burrows, A. et al. The overarching framework of core-collapse supernova explosions as revealed by 3D FORNAX simulations. *Mon. Not. R. Astron. Soc*. **491**, 2715–2735 (2020). **The largest collection of full-physics 3D simulations published so far, describing the witnessed systematics with progenitor mass and initial core density structure**.

ADS CAS Google Scholar

10. 10.

Nagakura, H., Burrows, A., Radice, D. & Vartanyan, D. A systematic study of proto-neutron star convection in three-dimensional core-collapse supernova simulations. *Mon. Not. R. Astron. Soc*. **492**, 5764–5779 (2020).

ADS CAS Google Scholar

11. 11.

Skinner, M. A., Dolence, J. C., Burrows, A., Radice, D. & Vartanyan, D. FORNAX: a flexible code for multiphysics astrophysical simulations. *Astrophys. J. Suppl. Ser*. **241**, 7 (2019).

ADS CAS Google Scholar

12. 12.

Lentz, E. J. et al. Three-dimensional core-collapse supernova simulated using a 15 $M_{\odot}$ progenitor. *Astrophys. J. Lett*. **807**, L31 (2015). **A comprehensive study of the hydrodynamics of a 3D core-collapse simulation**.

ADS Google Scholar

13. 13.

Melson, T. et al. Neutrino-driven explosion of a 20 solar-mass star in three dimensions enabled by strange-quark contributions to neutrino–nucleon scattering. *Astrophys. J. Lett*. **808**, L42 (2015).

ADS Google Scholar

14. 14.

Melson, T., Janka, H.-T. & Marek, A. Neutrino-driven supernova of a low-mass iron-core progenitor boosted by three-dimensional turbulent convection. *Astrophys. J*. **801**, L24 (2015).

ADS Google Scholar

15. 15.

Janka, H.-T., Melson, T. & Summa, A. Physics of core-collapse supernovae in three dimensions: a sneak preview. *Annu. Rev. Nucl. Part. Sci*. **66**, 341–375 (2016). **A useful review of core-collapse systematics, with some insights into the possible effects of rapid rotation**.

ADS CAS Google Scholar

16. 16.

Takiwaki, T., Kotake, K. & Suwa, Y. Three-dimensional simulations of rapidly rotating core-collapse supernovae: finding a neutrino-powered explosion aided by non-axisymmetric flows. *Mon. Not. R. Astron. Soc*. **461**, L112–L116 (2016).

ADS CAS Google Scholar

17. 17.

Müller, B., Melson, T., Heger, A. & Janka, H.-T. Supernova simulations from a 3D progenitor model – impact of perturbations and evolution of explosion properties. *Mon. Not. R. Astron. Soc*. **472**, 491–513 (2017). **An important paper on the potential effects of initial perturbations on supernova explosions**.

ADS Google Scholar

18. 18.

O'Connor, E. P. & Couch, S. M. Exploring fundamentally three-dimensional phenomena in high-fidelity simulations of core-collapse supernovae. *Astrophys. J*. **865**, 81 (2018).

ADS Google Scholar

19. 19.

Kuroda, T., Kotake, K., Takiwaki, T. & Thielemann, F.-K. A full general relativistic neutrino radiation-hydrodynamics simulation of a collapsing very massive star and the formation of a black hole. *Mon. Not. R. Astron. Soc*. **477**, L80–L84 (2018). **An important study using a fully general-relativistic hydrodynamic and transport approach**.

ADS CAS Google Scholar

20. 20.

Glas, R., Just, O., Janka, H. T. & Obergaulinger, M. Three-dimensional core-collapse supernova simulations with multidimensional neutrino transport compared to the ray-by-ray-plus approximation. *Astrophys. J.* **873**, 45 (2019).

ADS CAS Google Scholar

21. 21.

Kuroda, T., Arcones, A., Takiwaki, T. & Kotake, K. Magnetorotational explosion of a massive star supported by neutrino heating in general relativistic three-dimensional simulations. *Astrophys. J.* **896**, 102 (2020).

ADS CAS Google Scholar

22. 22.

Jones, S. et al. Do electron-capture supernovae make neutron stars? First multidimensional hydrodynamic simulations of the oxygen deflagration. *Astron. Astrophys*. **593**, A72 (2016).

Google Scholar

23. 23.

Kirsebom, O. S. et al. Discovery of an exceptionally strong β-decay transition of ^{20}F and implications for the fate of intermediate-mass stars. *Phys. Rev. Lett*. **123**, 262701 (2019).

ADS CAS PubMed PubMed Central Google Scholar

24. 24.

Jones, S. et al. Remnants and ejecta of thermonuclear electron-capture supernovae. Constraining oxygen-neon deflagrations in high-density white dwarfs. *Astron. Astrophys*. **622**, A74 (2019).

CAS Google Scholar

25. 25.

Zha, S., Leung, S.-C., Suzuki, T. & Nomoto, K. Evolution of ONeMg core in super-AGB stars toward electron-capture supernovae: effects of updated electron-capture rate. *Astrophys. J.* **886**, 22 (2019).

ADS CAS Google Scholar

26. 26.

Burrows, A., Dessart, L., Livne, E., Ott, C. D. & Murphy, J. Simulations of magnetically driven supernova and hypernova explosions in the context of rapid rotation. *Astrophys. J.* **664**, 416–434 (2007). **A magneto-radiation-hydrodynamic study of magnetic jet-driven explosions for rapidly rotating cores**.

ADS CAS Google Scholar

27. 27.

Mösta, P. et al. A large-scale dynamo and magnetoturbulence in rapidly rotating core-collapse supernovae. *Nature* **528**, 376–379 (2015).

ADS PubMed PubMed Central Google Scholar

28. 28.

Bethe, H. A. Supernova mechanisms. *Rev. Mod. Phys.* **62**, 801–866 (1990). **An early qualitative discussion of the salient aspects of the delayed neutrino-driven explosion mechanism**.

ADS CAS Google Scholar

29. 29.

Woosley, S. & Janka, T. The physics of core-collapse supernovae. *Nat. Phys*. **1**, 147–154 (2005).

CAS Google Scholar

30. 30.

Janka, H.-T. Explosion mechanisms of core-collapse supernovae. *Annu. Rev. Nucl. Part. Sci*. **62**, 407–451 (2012). **An important review of general core-collapse supernova physics**.

ADS CAS Google Scholar

31. 31.

Burrows, A. Perspectives on core-collapse supernova theory. *Rev. Mod. Phys*. **85**, 245–261 (2013).

ADS CAS Google Scholar

32. 32.

Nomoto, K. Evolution of 8–10 solar mass stars toward electron capture supernovae. I – Formation of electron-degenerate O + Ne + Mg cores. *Astrophys. J*. **277**, 791–805 (1984).

ADS CAS Google Scholar

33. 33.

Kitaura, F. S., Janka, H.-T. & Hillebrandt, W. Explosions of O-Ne-Mg cores, the Crab supernova, and subluminous type II-P supernovae. *Astron. Astrophys*. **450**, 345–350 (2006).

ADS CAS Google Scholar

34. 34.

Burrows, A., Hayes, J. & Fryxell, B. A. On the nature of core-collapse supernova explosions. *Astrophys. J.* **450**, 830 (1995). **One of the early papers detailing the role of convection and turbulence in the supernova explosion mechanism**.

ADS CAS Google Scholar

35. 35.

Foglizzo, T., Scheck, L. & Janka, H. T. Neutrino-driven convection versus advection in core-collapse supernovae. *Astrophys. J.* **652**, 1436–1450 (2006).

ADS Google Scholar

36. 36.

Chatzopoulos, E., Graziani, C. & Couch, S. M. Characterizing the convective velocity fields in massive stars. *Astrophys. J.* **795**, 92 (2014).

ADS Google Scholar

37. 37.

Couch, S. M. & Ott, C. D. The role of turbulence in neutrino-driven core-collapse supernova explosions. *Astrophys. J.* **799**, 5 (2015).

ADS Google Scholar

38. 38.

Müller, B. & Janka, H.-T. Non-radial instabilities and progenitor asphericities in core-collapse supernovae. *Mon. Not. R. Astron. Soc.* **448**, 2141–2174 (2015).

ADS Google Scholar

39. 39.

Murphy, J. W. & Burrows, A. Criteria for core-collapse supernova explosions by the neutrino mechanism. *Astrophys. J.* **688**, 1159–1175 (2008).

ADS Google Scholar

40. 40.

Müller, B. & Varma, V. A 3D simulation of a neutrino-driven supernova explosion aided by convection and magnetic fields. *Mon. Not. R. Astron. Soc*. **498**, L109–L113 (2020).

ADS Google Scholar

41. 41.

Burrows, A. & Sawyer, R. F. Effects of correlations on neutrino opacities in nuclear matter. *Phys. Rev. C* **58**, 554–571 (1998).

ADS CAS Google Scholar

42. 42.

Burrows, A. & Sawyer, R. F. Many-body corrections to charged-current neutrino absorption rates in nuclear matter. *Phys. Rev. C* **59**, 510–514 (1999).

ADS CAS Google Scholar

43. 43.

Reddy, S., Prakash, M., Lattimer, J. M. & Pons, J. A. Effects of strong and electromagnetic correlations on neutrino interactions in dense matter. *Phys. Rev. C* **59**, 2888–2918 (1999).

ADS CAS Google Scholar

44. 44.

Burrows, A., Reddy, S. & Thompson, T. A. Neutrino opacities in nuclear matter. *Nucl. Phys. A* **777**, 356–394 (2006).

ADS Google Scholar

45. 45.

Roberts, L. F., Reddy, S. & Shen, G. Medium modification of the charged-current neutrino opacity and its implications. *Phys. Rev. C* **86**, 065803 (2012).

ADS Google Scholar

46. 46.

Fischer, T. et al. Neutrino signal from proto-neutron star evolution: effects of opacities from charged-current–neutrino interactions and inverse neutron decay. *Phys. Rev. C* **101**, 025804 (2020).

ADS CAS Google Scholar

47. 47.

Roberts, L. F. & Reddy, S. Charged current neutrino interactions in hot and dense matter. *Phys. Rev. C* **95**, 045807 (2017).

ADS Google Scholar

48. 48.

Horowitz, C. J., Caballero, O. L., Lin, Z., O'Connor, E. & Schwenk, A. Neutrino–nucleon scattering in supernova matter from the virial expansion. *Phys. Rev. C* **95**, 025801 (2017).

ADS Google Scholar

49. 49.

Langanke, K. et al. Electron capture rates on nuclei and implications for stellar core collapse. *Phys. Rev. Lett*. **90**, 241102 (2003).

ADS CAS PubMed PubMed Central Google Scholar

50. 50.

Juodagalvis, A., Langanke, K., Hix, W. R., Martínez-Pinedo, G. & Sampaio, J. M. Improved estimate of electron capture rates on nuclei during stellar core collapse. *Nucl. Phys. A* **848**, 454–478 (2010).

ADS Google Scholar

51. 51.

Lentz, E. J., Mezzacappa, A., Messer, O. E. B., Hix, W. R. & Bruenn, S. W. Interplay of neutrino opacities in core-collapse supernova simulations. *Astrophys. J*. **760**, 94 (2012).

ADS Google Scholar

52. 52.

Mezzacappa, A. & Bruenn, S. W. Stellar core collapse: a Boltzmann treatment of neutrino–electron scattering. *Astrophys. J*. **410**, 740 (1993).

ADS CAS Google Scholar

53. 53.

Bruenn, S. W. et al. CHIMERA: a massively parallel code for core-collapse supernova simulations. *Astrophys. J. Suppl. Ser*. **248**, 11 (2020).

ADS Google Scholar

54. 54.

Dolence, J. C., Burrows, A., Murphy, J. W. & Nordhaus, J. Dimensional dependence of the hydrodynamics of core-collapse supernovae. *Astrophys. J.* **765**, 110 (2013).

ADS Google Scholar

55. 55.

Vartanyan, D., Burrows, A. & Radice, D. Temporal and angular variations of 3D core-collapse supernova emissions and their physical correlations. *Mon. Not. R. Astron. Soc*. **489**, 2227–2246 (2019).

ADS CAS Google Scholar

56. 56.

Couch, S. M., Chatzopoulos, E., Arnett, W. D. & Timmes, F. X. The three-dimensional evolution to core collapse of a massive star. *Astrophys. J.* **808**, L21 (2015). **A benchmark study of 3D stellar evolution just prior to core collapse**.

ADS Google Scholar

57. 57.

Chatzopoulos, E., Couch, S. M., Arnett, W. D. & Timmes, F. X. Convective properties of rotating two-dimensional core-collapse supernova progenitors. *Astrophys. J.* **822**, 61 (2016).

ADS Google Scholar

58. 58.

Müller, B. et al. Three-dimensional simulations of neutrino-driven core-collapse supernovae from low-mass single and binary star progenitors. *Mon. Not. R. Astron. Soc*. **484**, 3307–3324 (2019).

ADS Google Scholar

59. 59.

Keil, W., Janka, H.-T. & Mueller, E. Ledoux convection in protoneutron stars—a clue to supernova nucleosynthesis? *Astrophys. J.* **473**, L111 (1996).

ADS CAS Google Scholar

60. 60.

Dessart, L., Burrows, A., Livne, E. & Ott, C. D. Multidimensional radiation/hydrodynamic simulations of proto-neutron star convection. *Astrophys. J.* **645**, 534–550 (2006).

ADS Google Scholar

61. 61.

Sukhbold, T., Woosley, S. E. & Heger, A. A high-resolution study of presupernova core structure. *Astrophys. J.* **860**, 93 (2018). **An important source of 1D massive star progenitor models using a state-of-the-art stellar evolution code**.

ADS Google Scholar

62. 62.

O'Connor, E. & Ott, C. D. Black hole formation in failing core-collapse supernovae. *Astrophys. J.* **730**, 70 (2011).

ADS Google Scholar

63. 63.

Ebinger, K. et al. PUSHing core-collapse supernovae to explosions in spherical symmetry. IV. Explodability, remnant properties, and nucleosynthesis yields of low-metallicity stars. *Astrophys. J.* **888**, 91 (2020).

ADS CAS Google Scholar

64. 64.

Müller, B. The dynamics of neutrino-driven supernova explosions after shock revival in 2D and 3D. *Mon. Not. R. Astron. Soc*. **453**, 287–310 (2015).

ADS Google Scholar

65. 65.

Hanke, F., Marek, A., Müller, B. & Janka, H.-T. Is strong SASI activity the key to successful neutrino-driven supernova explosions? *Astrophys. J*. **755**, 138 (2012).

ADS Google Scholar

66. 66.

Hanke, F., Müller, B., Wongwathanarat, A., Marek, A. & Janka, H.-T. SASI activity in three-dimensional neutrino-hydrodynamics simulations of supernova cores. *Astrophys. J*. **770**, 66 (2013).

ADS Google Scholar

67. 67.

Couch, S. M. On the impact of three dimensions in simulations of neutrino-driven core-collapse supernova explosions. *Astrophys. J*. **775**, 35 (2013).

ADS Google Scholar

68. 68.

Summa, A. et al. Progenitor-dependent explosion dynamics in self-consistent, axisymmetric simulations of neutrino-driven core-collapse supernovae. *Astrophys. J*. **825**, 6 (2016).

ADS Google Scholar

69. 69.

Summa, A., Janka, H.-T., Melson, T. & Marek, A. Rotation-supported neutrino-driven supernova explosions in three dimensions and the critical luminosity condition. *Astrophys. J.* **852**, 28 (2018).

ADS Google Scholar

70. 70.

Sukhbold, T., Ertl, T., Woosley, S. E., Brown, J. M. & Janka, H.-T. Core-collapse supernovae from 9 to 120 solar masses based on neutrino-powered explosions. *Astrophys. J.* **821**, 38 (2016).

ADS Google Scholar

71. 71.

Ertl, T., Woosley, S. E., Sukhbold, T. & Janka, H. T. The explosion of helium stars evolved with mass loss. *Astrophys. J.* **890**, 51 (2020).

ADS CAS Google Scholar

72. 72.

Özel, F., Psaltis, D., Narayan, R. & Santos Villarreal, A. On the mass distribution and birth masses of neutron stars. *Astrophys. J.* **757**, 55 (2012).

ADS Google Scholar

73. 73.

Pruet, J., Hoffman, R. D., Woosley, S. E., Janka, H. T. & Buras, R. Nucleosynthesis in early supernova winds. II. The role of neutrinos. *Astrophys. J.* **644**, 1028–1039 (2006).

ADS CAS Google Scholar

74. 74.

Fröhlich, C. et al. Neutrino-induced nucleosynthesis of $A > 64$ nuclei: the *νp* process. *Phys. Rev. Lett*. **96**, 142502 (2006).

ADS PubMed PubMed Central Google Scholar

75. 75.

Fischer, T., Whitehouse, S. C., Mezzacappa, A., Thielemann, F.-K. & Liebendörfer, M. Protoneutron star evolution and the neutrino-driven wind in general relativistic neutrino radiation hydrodynamics simulations. *Astron. Astrophys*. **517**, A80 (2010).

MATH Google Scholar

76. 76.

Thielemann, F.-K., Hashimoto, M.-A. & Nomoto, K. Explosive nucleosynthesis in SN 1987A. II. Composition, radioactivities, and the neutron star mass. *Astrophys. J*. **349**, 222 (1990).

ADS CAS Google Scholar

77. 77.

Tamborra, I. et al. Self-sustained asymmetry of lepton-number emission: a new phenomenon during the supernova shock-accretion phase in three dimensions. *Astrophys. J*. **792**, 96 (2014).

ADS Google Scholar

78. 78.

Glas, R., Janka, H. T., Melson, T., Stockinger, G. & Just, O. Effects of LESA in three-dimensional supernova simulations with

multidimensional and ray-by-ray-plus neutrino transport. *Astrophys. J.* **881**, 36 (2019).

ADS CAS Google Scholar

79. 79.

Arzoumanian, Z., Chernoff, D. F. & Cordes, J. M. The velocity distribution of isolated radio pulsars. *Astrophys. J.* **568**, 289–301 (2002).

ADS Google Scholar

80. 80.

Faucher-Giguère, C.-A. & Kaspi, V. M. Birth and evolution of isolated radio pulsars. *Astrophys. J.* **643**, 332–355 (2006).

ADS Google Scholar

81. 81.

Cordes, J. M., Romani, R. W. & Lundgren, S. C. The Guitar nebula: a bow shock from a slow-spin, high-velocity neutron star. *Nature* **362**, 133–135 (1993).

ADS Google Scholar

82. 82.

Burrows, A. & Hayes, J. Pulsar recoil and gravitational radiation due to asymmetrical stellar collapse and explosion. *Phys. Rev. Lett.* **76**, 352–355 (1996).

ADS CAS Google Scholar

83. 83.

Scheck, L., Plewa, T., Janka, H. T., Kifonidis, K. & Müller, E. Pulsar recoil by large-scale anisotropies in supernova explosions. *Phys. Rev. Lett*. **92**, 011103 (2004). **A summary of general theory and results concerning the recoil mechanism of pulsar kick speeds**.

ADS CAS Google Scholar

84. 84.

Scheck, L., Kifonidis, K., Janka, H. T. & Müller, E. Multidimensional supernova simulations with approximative neutrino transport. I. Neutron star kicks and the anisotropy of neutrino-driven explosions in two spatial dimensions. *Astron. Astrophys*. **457**, 963–986 (2006).

ADS Google Scholar

85. 85.

Wongwathanarat, A., Janka, H.-T. & Müller, E. Hydrodynamical neutron star kicks in three dimensions. *Astrophys. J*. **725**, L106–L110 (2010).

ADS Google Scholar

86. 86.

Nordhaus, J., Brandt, T. D., Burrows, A. & Almgren, A. The hydrodynamic origin of neutron star kicks. *Mon. Not. R. Astron. Soc*. **423**, 1805–1812 (2012).

ADS Google Scholar

87. 87.

Wongwathanarat, A., Janka, H. T. & Müller, E. Three-dimensional neutrino-driven supernovae: neutron star kicks, spins, and asymmetric ejection of nucleosynthesis products. *Astron. Astrophys*. **552**, A126 (2013).

ADS Google Scholar

88. 88.

Nakamura, K., Takiwaki, T. & Kotake, K. Long-term simulations of multi-dimensional core-collapse supernovae: implications for neutron star kicks. *Publ. Astron. Soc. Jpn*. **71**, 98 (2019).

ADS Google Scholar

89. 89.

Burrows, A., Livne, E., Dessart, L., Ott, C. D. & Murphy, J. Features of the acoustic mechanism of core-collapse supernova explosions. *Astrophys. J*. **655**, 416–433 (2007).

ADS CAS Google Scholar

90. 90.

Burrows, A. The birth of neutron stars and black holes. *Phys. Today* **40**, 28–37 (1987).

CAS Google Scholar

91. 91.

Timmes, F. X., Woosley, S. E. & Weaver, T. A. The neutron star and black hole initial mass function. *Astrophys. J*. **457**, 834 (1996).

ADS CAS Google Scholar

92. 92.

Chan, C., Müller, B., Heger, A., Pakmor, R. & Springel, V. Black hole formation and fallback during the supernova explosion of a 40 $M_{\odot}$ star. *Astrophys. J. Lett*. **852**, 19 (2018).

ADS Google Scholar

93. 93.

Woosley, S., Sukhbold, T. & Janka, H. T. The birth function for black holes and neutron stars in close binaries. *Astrophys. J.* **896**, 56 (2020).

ADS CAS Google Scholar

94. 94.

Farr, W. M. et al. The mass distribution of stellar-mass black holes. *Astrophys. J.* **741**, 103 (2011).

ADS Google Scholar

95. 95.

Seadrow, S., Burrows, A., Vartanyan, D., Radice, D. & Skinner, M. A. Neutrino signals of core-collapse supernovae in underground detectors. *Mon. Not. R. Astron. Soc.* **480**, 4710–4731 (2018).

ADS CAS Google Scholar

96. 96.

Cerdá-Durán, P., DeBrye, N., Aloy, M. A., Font, J. A. & Obergaulinger, M. Gravitational wave signatures in black hole forming core collapse. *Astrophys. J.* **779**, L18 (2013).

ADS Google Scholar

97. 97.

Burrows, A. Speculations on the fizzled collapse of a massive star. *Astrophys. J.* **300**, 488 (1986).

ADS CAS Google Scholar

98. 98.

Nadyozhin, D. K. Some secondary indications of gravitational collapse. *Astrophys. Space Sci*. **69**, 115–125 (1980).

ADS Google Scholar

99. 99.

Lovegrove, E. & Woosley, S. E. Very low energy supernovae from neutrino mass loss. *Astrophys. J*. **769**, 109 (2013).

ADS Google Scholar

100. 100.

Blondin, J. M. & Mezzacappa, A. Pulsar spins from an instability in the accretion shock of supernovae. *Nature* **445**, 58–60 (2007).

ADS CAS PubMed PubMed Central Google Scholar

101. 101.

Rantsiou, E., Burrows, A., Nordhaus, J. & Almgren, A. Induced rotation in three-dimensional simulations of core-collapse supernovae: implications for pulsar spins. *Astrophys. J*. **732**, 57 (2011).

ADS Google Scholar

102. 102.

Stockinger, G. et al. Three-dimensional models of core-collapse supernovae from low-mass progenitors with implications for Crab. *Mon. Not. R. Astron. Soc*. **496**, 2039–2084 (2020).

ADS Google Scholar

103. 103.

Morozova, V., Piro, A. L. & Valenti, S. Measuring the progenitor masses and dense circumstellar material of Type II supernovae.

Astrophys. J. **858**, 15 (2018).

ADS Google Scholar

104. 104.

Martinez, L. & Bersten, M. C. Mass discrepancy analysis for a select sample of Type II-plateau supernovae. *Astron. Astrophys*. **629**, A124 (2019).

ADS CAS Google Scholar

105. 105.

Pumo, M. L. & Zampieri, L. Radiation-hydrodynamical modeling of core-collapse supernovae: light curves and the evolution of photospheric velocity and temperature. *Astrophys. J.* **741**, 41 (2011).

ADS Google Scholar

106. 106.

Pumo, M. L. et al. Radiation-hydrodynamical modelling of underluminous Type II plateau supernovae. *Mon. Not. R. Astron. Soc*. **464**, 3013–3020 (2017).

ADS CAS Google Scholar

107. 107.

Utrobin, V. P. Nonthermal ionization and excitation in Type IIb supernova 1993J. *Astron. Astrophys*. **306**, 219 (1996).

ADS CAS Google Scholar

108. 108.

Utrobin, V. P. & Chugai, N. N. Type IIP supernova 2008in: the explosion of a normal red supergiant. *Astron. Astrophys*. **555**, A145

(2013).

ADS Google Scholar

109. 109.

Utrobin, V. P. & Chugai, N. N. Luminous Type IIP SN 2013ej with high-velocity ^{56}Ni ejecta. *Mon. Not. R. Astron. Soc*. **472**, 5004–5010 (2017).

ADS CAS Google Scholar

110. 110.

Utrobin, V. P. & Chugai, N. N. Resolving the puzzle of type IIP SN 2016X. *Mon. Not. R. Astron. Soc*. **490**, 2042–2049 (2019).

ADS CAS Google Scholar

Download references

Acknowledgements

We thank J. Insley and S. Rizzi of the Argonne National Laboratory and the Argonne Leadership Computing Facility (ALCF) for considerable support with the 3D graphics. We also acknowledge ongoing collaborations with H. Nagakura, D. Radice, J. Dolence, A. Skinner and M. Coleman. We acknowledge E. O'Connor regarding the equation of state, G. Martínez-Pinedo concerning electron capture on heavy nuclei, T. Sukhbold and S. Woosley for providing details concerning the initial models, and T. Thompson and T. Wang regarding inelastic scattering. Funding was provided by the US Department of Energy (DOE) Office of Science and the Office of Advanced Scientific Computing Research via the Scientific Discovery through Advanced Computing (SciDAC4) programme and Grant DE-SC0018297 (subaward 00009650) and by the US NSF under grants AST-1714267 and PHY-1804048 (the latter via the Max-Planck/Princeton Center (MPPC) for Plasma Physics). Awards of computer time were provided by the INCITE programme using resources of the ALCF, which is

a DOE Office of Science User Facility supported under Contract DE-AC02-06CH11357, under a Blue Waters sustained-petascale computing project, supported by the National Science Foundation (awards OCI-0725070 and ACI-1238993) and the state of Illinois, under a PRAC allocation from the National Science Foundation (#OAC-1809073), and under award #TG-AST170045 to the resource Stampede2 in the Extreme Science and Engineering Discovery Environment (XSEDE, ACI-1548562). Finally, we employed computational resources provided by the TIGRESS high-performance computer centre at Princeton University, which is jointly supported by the Princeton Institute for Computational Science and Engineering (PICSciE) and the Princeton University Office of Information Technology, and acknowledge their continuing allocation at the National Energy Research Scientific Computing Center (NERSC), supported by the DOE Office of Science under contract DE-AC03-76SF00098.

Author information

Affiliations

1. Department of Astrophysical Sciences, Princeton University, Princeton, NJ, USA

   A. Burrows

2. Department of Astronomy, University of California, Berkeley, CA, USA

   D. Vartanyan

Authors

1. A. Burrows
   View author publications

   You can also search for this author in PubMed Google Scholar

2. D. Vartanyan

View author publications

You can also search for this author in PubMed Google Scholar

Contributions

A.B. organized the paper and wrote most of it. D.V. conducted the 2D calculations. Otherwise, the authors contributed equally to the document.

Corresponding author

Correspondence to A. Burrows.

Ethics declarations

Competing interests

The authors declare no competing interests.

Additional information

Peer review information *Nature* thanks Friedrich-Karl Thielemann and Stan Woosley for their contribution to the peer review of this work.

Publisher's note Springer Nature remains neutral with regard to jurisdictional claims in published maps and institutional affiliations.

Rights and permissions

Reprints and Permissions

About this article

Check for updates

Cite this article

Burrows, A., Vartanyan, D. Core-collapse supernova explosion theory. *Nature* **589,** 29–39 (2021). https://doi.org/10.1038/s41586-020-03059-w

Download citation

- Received: 20 July 2020
- Accepted: 29 September 2020
- Published: 06 January 2021
- Issue Date: 07 January 2021
- DOI: https://doi.org/10.1038/s41586-020-03059-w

Comments

By submitting a comment you agree to abide by our Terms and Community Guidelines. If you find something abusive or that does not comply with our terms or guidelines please flag it as inappropriate.

Access through your institution
Change institution
Buy or subscribe

This article was downloaded by **calibre** from https://www.nature.com/articles/s41586-020-03059-w

| Section menu | Main menu |

- Article
- Published: 06 January 2021

Competing magnetic orders in a bilayer Hubbard model with ultracold atoms

- Marcell Gall[1] [na1],
- Nicola Wurz[1] [na1],
- Jens Samland[1],
- Chun Fai Chan[1] &
- Michael Köhl ORCID: orcid.org/0000-0003-4055-713X[1]

Nature **volume 589**, pages40–43(2021)Cite this article

- 1140 Accesses
- 122 Altmetric
- Metrics details

Subjects

- Quantum simulation
- Ultracold gases

Abstract

Fermionic atoms in optical lattices have served as a useful model system in which to study and emulate the physics of strongly correlated matter. Driven by the advances of high-resolution microscopy, the current research

focus is on two-dimensional systems[1,2,3], in which several quantum phases —such as antiferromagnetic Mott insulators for repulsive interactions[4,5,6,7] and charge-density waves for attractive interactions[8]—have been observed. However, the lattice structure of real materials, such as bilayer graphene, is composed of coupled layers and is therefore not strictly two-dimensional, which must be taken into account in simulations. Here we realize a bilayer Fermi–Hubbard model using ultracold atoms in an optical lattice, and demonstrate that the interlayer coupling controls a crossover between a planar antiferromagnetically ordered Mott insulator and a band insulator of spin-singlets along the bonds between the layers. We probe the competition of the magnetic ordering by measuring spin–spin correlations both within and between the two-dimensional layers. Our work will enable the exploration of further properties of coupled-layer Hubbard models, such as theoretically predicted superconducting pairing mechanisms[9,10].

Access through your institution
Change institution
Buy or subscribe

Access options

Subscribe to Journal

Get full journal access for 1 year

$199.00

only $3.90 per issue

Subscribe

All prices are NET prices.
VAT will be added later in the checkout.

Rent or Buy article

Get time limited or full article access on ReadCube.

from$8.99

Rent or Buy

All prices are NET prices.

Additional access options:

- Log in
- Access through your institution
- Learn about institutional subscriptions

Fig. 1: Illustration of the bilayer Hubbard model.

Fig. 2: Detection of intralayer correlations.

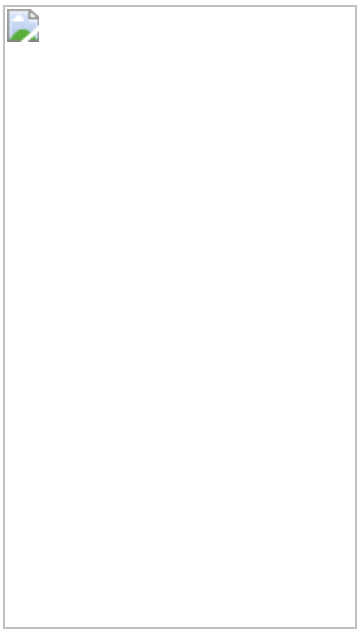

Fig. 3: Magnetic correlations between the layers.

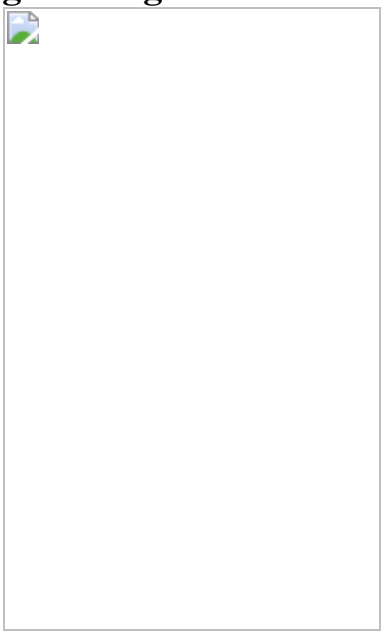

Fig. 4: Crossover from the antiferromagnetic Mott insulator to a band insulator of singlets.

Data availability

The data presented in the figures are available at https://osf.io/u9wj6. More detailed data and information of this study are available from the corresponding author upon request.

Code availability

The DQMC theory simulations were performed using the QUEST Fortran 90/95 package, version 1.44, from https://code.google.com/archive/p/quest-qmc/.

References

1. 1.

   Greif, D. et al. Site-resolved imaging of a fermionic Mott insulator. *Science* **351**, 953–957 (2016).

   ADS CAS Article Google Scholar

2. 2.

Cheuk, L. W. et al. Observation of 2D fermionic Mott insulators of ^{40}K with single-site resolution. *Phys. Rev. Lett*. **116**, 235301 (2016).

ADS Article Google Scholar

3. 3.

Cocchi, E. et al. Equation of state of the two-dimensional Hubbard model. *Phys. Rev. Lett*. **116**, 175301 (2016).

ADS Article Google Scholar

4. 4.

Cheuk, L. W. et al. Observation of spatial charge and spin correlations in the 2D Fermi–Hubbard model. *Science* **353**, 1260–1264 (2016).

ADS MathSciNet CAS Article Google Scholar

5. 5.

Parsons, M. F. et al. Site-resolved measurement of the spin-correlation function in the Fermi–Hubbard model. *Science* **353**, 1253–1256 (2016).

ADS MathSciNet CAS Article Google Scholar

6. 6.

Drewes, J. H. et al. Antiferromagnetic correlations in two-dimensional fermionic Mott-insulating and metallic phases. *Phys. Rev. Lett*. **118**, 170401 (2017).

ADS CAS Article Google Scholar

7. 7.

Mazurenko, A. et al. A cold-atom Fermi–Hubbard antiferromagnet. *Nature* **545**, 462–466 (2017).

ADS CAS Article Google Scholar

8. 8.

Mitra, D. et al. Quantum gas microscopy of an attractive Fermi–Hubbard system. *Nat. Phys*. **14**, 173–177 (2018).

CAS Article Google Scholar

9. 9.

Scalettar, R. T., Cannon, J. W., Scalapino, D. J. & Sugar, R. L. Magnetic and pairing correlations in coupled Hubbard planes. *Phys. Rev. B* **50**, 13419–13427 (1994).

ADS CAS Article Google Scholar

10. 10.

Maier, T. A. & Scalapino, D. Pair structure and the pairing interaction in a bilayer Hubbard model for unconventional superconductivity. *Phys. Rev. B* **84**, 180513 (2011).

ADS Article Google Scholar

11. 11.

Kancharla, S. S. & Okamoto, S. Band insulator to Mott insulator transition in a bilayer Hubbard model. *Phys. Rev. B* **75**, 193103 (2007).

ADS Article Google Scholar

12. 12.

Golor, M., Reckling, T., Classen, L., Scherer, M. M. & Wessel, S. Ground-state phase diagram of the half-filled bilayer Hubbard model.

Phys. Rev. B **90**, 195131 (2014).

ADS Article Google Scholar

13. 13.

dos Santos, R. R. Magnetism and pairing in Hubbard bilayers. *Phys. Rev. B* **51**, 15540–15546 (1995).

ADS Article Google Scholar

14. 14.

Rüger, R., Tocchio, L. F., Valentí, R. & Gros, C. The phase diagram of the square lattice bilayer Hubbard model: a variational Monte Carlo study. *New J. Phys*. **16**, 033010 (2014).

ADS Article Google Scholar

15. 15.

Sandvik, A. & Scalapino, D. Order–disorder transition in a two-layer quantum antiferromagnet. *Phys. Rev. Lett*. **72**, 2777–2780 (1994).

ADS CAS Article Google Scholar

16. 16.

Hafermann, H., Katsnelson, M. & Lichtenstein, A. Metal–insulator transition by suppression of spin fluctuations. *Europhys. Lett*. **85**, 37006 (2009).

ADS Article Google Scholar

17. 17.

Koepsell, J. et al. Robust bilayer charge-pumping for spin-and density-resolved quantum gas microscopy. *Phys. Rev. Lett*. **125**, 010403 (2020).

ADS CAS Article Google Scholar

18. 18.

Hartke, T., Oreg, B., Jia, N. & Zwierlein, M. Doublon–hole correlations and fluctuation thermometry in a Fermi–Hubbard gas. *Phys. Rev. Lett*. **125**, 113601 (2020).

ADS CAS Article Google Scholar

19. 19.

Wurz, N. et al. Coherent manipulation of spin correlations in the Hubbard model. *Phys. Rev. A* **97**, 051602 (2018).

ADS CAS Article Google Scholar

20. 20.

Scalettar, R. T. Magnetism and spin liquid behavior in a two layer Hubbard model. *J. Low Temp. Phys*. **99**, 499–504 (1995).

ADS CAS Article Google Scholar

21. 21.

Greif, D., Uehlinger, T., Jotzu, G., Tarruell, L. & Esslinger, T. Short-range quantum magnetism of ultracold fermions in an optical lattice. *Science* **340**, 1307–1310 (2013).

ADS CAS Article Google Scholar

22. 22.

Bouadim, K., Batrouni, G. G., Hébert, F. & Scalettar, R. Magnetic and transport properties of a coupled hubbard bilayer with electron and hole doping. *Phys. Rev. B* **77**, 144527 (2008).

ADS Article Google Scholar

23. 23.

Varney, C. N. et al. Quantum Monte Carlo study of the two-dimensional fermion Hubbard model. *Phys. Rev. B* **80**, 075116 (2009).

ADS Article Google Scholar

Download references

Acknowledgements

This work has been supported by BCGS, the Alexander-von-Humboldt Stiftung, DFG (SFB/TR 185 project B4), Cluster of Excellence Matter and Light for Quantum Computing (ML4Q) EXC 2004/1 - 390534769 and Stiftung der deutschen Wirtschaft.

Author information

Author notes

1. These authors contributed equally: Marcell Gall, Nicola Wurz

Affiliations

1. Physikalisches Institut, University of Bonn, Bonn, Germany

   Marcell Gall, Nicola Wurz, Jens Samland, Chun Fai Chan & Michael Köhl

Authors

1. Marcell Gall
   View author publications

   You can also search for this author in PubMed Google Scholar

2. Nicola Wurz

View author publications

You can also search for this author in PubMed Google Scholar

3. Jens Samland
   View author publications

   You can also search for this author in PubMed Google Scholar

4. Chun Fai Chan
   View author publications

   You can also search for this author in PubMed Google Scholar

5. Michael Köhl
   View author publications

   You can also search for this author in PubMed Google Scholar

Contributions

The idea for the experiment was conceived by M.G., N.W., C.F.C. and M.K. Data taking was performed by M.G., N.W. and C.F.C. with contributions by J.S. Data analysis was primarily performed by M.G. and N.W. Numerical simulations were performed by C.F.C. and N.W. The results were discussed and interpreted by all coauthors, and the manuscript was written by M.K. with contributions from all coauthors.

Corresponding author

Correspondence to Michael Köhl.

Ethics declarations

Competing interests

The authors declare no competing interests.

Additional information

Peer review information *Nature* thanks the anonymous reviewer(s) for their contribution to the peer review of this work.

Publisher's note Springer Nature remains neutral with regard to jurisdictional claims in published maps and institutional affiliations.

Rights and permissions

Reprints and Permissions

About this article

Check for updates

Cite this article

Gall, M., Wurz, N., Samland, J. *et al.* Competing magnetic orders in a bilayer Hubbard model with ultracold atoms. *Nature* **589,** 40–43 (2021). https://doi.org/10.1038/s41586-020-03058-x

Download citation

- Received: 25 April 2020
- Accepted: 02 October 2020
- Published: 06 January 2021
- Issue Date: 07 January 2021
- DOI: https://doi.org/10.1038/s41586-020-03058-x

Comments

By submitting a comment you agree to abide by our Terms and Community Guidelines. If you find something abusive or that does not comply with our terms or guidelines please flag it as inappropriate.

Access through your institution
Change institution
Buy or subscribe

This article was downloaded by **calibre** from https://www.nature.com/articles/s41586-020-03058-x

- Article
- Published: 06 January 2021

11 TOPS photonic convolutional accelerator for optical neural networks

- Xingyuan Xu ORCID: orcid.org/0000-0002-8190-4700[1] [nAff9],
- Mengxi Tan[1],
- Bill Corcoran ORCID: orcid.org/0000-0001-8653-3999[2],
- Jiayang Wu[1],
- Andreas Boes ORCID: orcid.org/0000-0001-8443-3396[3],
- Thach G. Nguyen[3],
- Sai T. Chu ORCID: orcid.org/0000-0001-8263-8507[4],
- Brent E. Little[5],
- Damien G. Hicks ORCID: orcid.org/0000-0001-8322-9983[1,6],
- Roberto Morandotti ORCID: orcid.org/0000-0001-7717-1519[7,8],
- Arnan Mitchell ORCID: orcid.org/0000-0002-2463-2956[3] &
- David J. Moss ORCID: orcid.org/0000-0001-5195-1744[1]

Nature **volume 589**, pages44–51(2021)Cite this article

- 2250 Accesses
- 234 Altmetric
- Metrics details

Subjects

- Electrical and electronic engineering

- Frequency combs

Abstract

Convolutional neural networks, inspired by biological visual cortex systems, are a powerful category of artificial neural networks that can extract the hierarchical features of raw data to provide greatly reduced parametric complexity and to enhance the accuracy of prediction. They are of great interest for machine learning tasks such as computer vision, speech recognition, playing board games and medical diagnosis[1,2,3,4,5,6,7]. Optical neural networks offer the promise of dramatically accelerating computing speed using the broad optical bandwidths available. Here we demonstrate a universal optical vector convolutional accelerator operating at more than ten TOPS (trillions (10^{12}) of operations per second, or tera-ops per second), generating convolutions of images with 250,000 pixels—sufficiently large for facial image recognition. We use the same hardware to sequentially form an optical convolutional neural network with ten output neurons, achieving successful recognition of handwritten digit images at 88 per cent accuracy. Our results are based on simultaneously interleaving temporal, wavelength and spatial dimensions enabled by an integrated microcomb source. This approach is scalable and trainable to much more complex networks for demanding applications such as autonomous vehicles and real-time video recognition.

Access through your institution
Change institution
Buy or subscribe

Access options

Subscribe to Journal

Get full journal access for 1 year

$199.00

only $3.90 per issue

Subscribe

All prices are NET prices.
VAT will be added later in the checkout.

Rent or Buy article

Get time limited or full article access on ReadCube.

from$8.99

Rent or Buy

All prices are NET prices.

Additional access options:

- Log in
- Access through your institution
- Learn about institutional subscriptions

Fig. 1: Operation principle of the TOPS photonic CA.

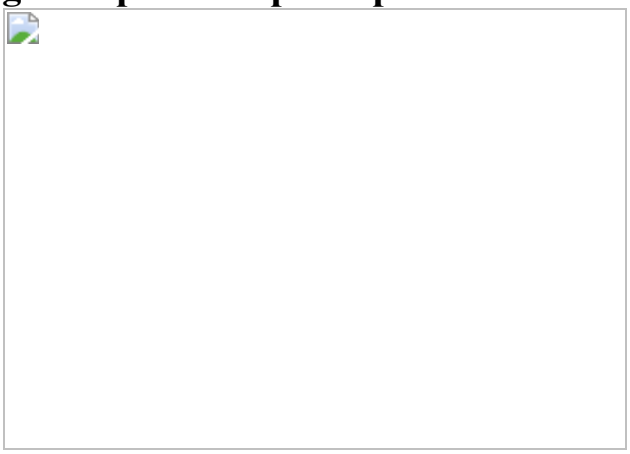

Fig. 2: Image processing.

Fig. 3: Experimental results of the image processing.

Fig. 4: Experimental schematic of the optical CNN.

Fig. 5: Convolutional layer.

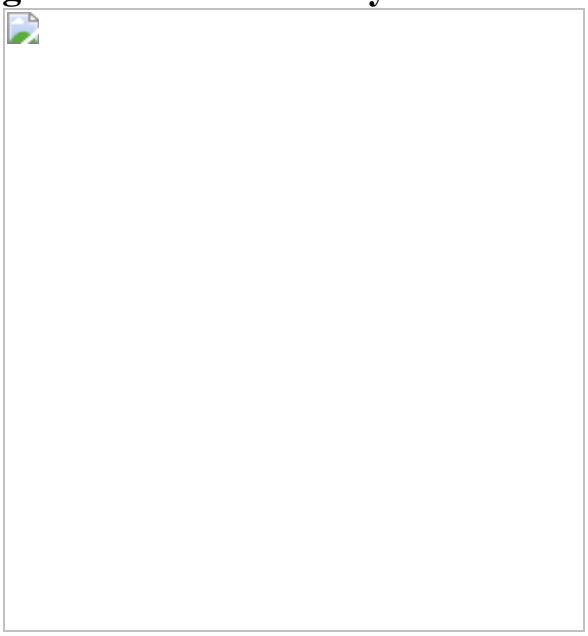

Fig. 6: Experimental and theoretically calculated results for image recognition.

Data availability

The authors declare that the data supporting the findings of this study are available within the paper and its supplementary information files.

Code availability

The authors declare that the algorithm of the demonstrated neural network supporting the findings of this study is available within the paper and its supplementary information files.

References

1. 1.

   LeCun, Y., Bengio, Y. & Hinton, G. Deep learning. *Nature* **521**, 436–444 (2015).

   ADS CAS Article Google Scholar

2. 2.

   Schalkoff, R. J. Pattern recognition. In *Wiley Encyclopedia of Computer Science and Engineering* (ed. Wah, B. W.) https://doi.org/10.1002/9780470050118.ecse302 (Wiley, 2007).

3. 3.

   Mnih, V. et al. Human-level control through deep reinforcement learning. *Nature* **518**, 529–533 (2015).

   ADS CAS Article Google Scholar

4. 4.

   Silver, D. et al. Mastering the game of Go without human knowledge. *Nature* **550**, 354–359 (2017).

   ADS CAS Article Google Scholar

5. 5.

   Krizhevsky, A., Sutskever, I. & Hinton, G. E. ImageNet classification with deep convolutional neural networks. *Commun. ACM* **60**, 84–90 (2017).

   Article Google Scholar

6. 6.

Yao, P. et al. Fully hardware-implemented memristor convolutional neural network. *Nature* **577**, 641–646 (2020).

ADS CAS Article Google Scholar

7. 7.

Lawrence, S., Giles, C. L., Tsoi, A. C. & Back, A. D. Face recognition: a convolutional neural-network approach. *IEEE Trans. Neural Netw*. **8**, 98–113 (1997).

CAS Article Google Scholar

8. 8.

Shen, Y. et al. Deep learning with coherent nanophotonic circuits. *Nat. Photon*. **11**, 441–446 (2017).

ADS CAS Article Google Scholar

9. 9.

Larger, L. et al. High-speed photonic reservoir computing using a time-delay-based architecture: Million words per second classification. *Phys. Rev. X* **7**, 011015 (2017).

Google Scholar

10. 10.

Peng, H.-T., Nahmias, M. A., de Lima, T. F., Tait, A. N. & Shastri, B. J. Neuromorphic photonic integrated circuits. *IEEE J. Sel. Top. Quantum Electron*. **24**, 6101715 (2018).

Google Scholar

11. 11.

Lin, X. et al. All-optical machine learning using diffractive deep neural networks. *Science* **361**, 1004–1008 (2018).

ADS MathSciNet CAS Article Google Scholar

12. 12.

Feldmann, J., Youngblood, N., Wright, C. D., Bhaskaran, H. & Pernice, W. H. P. All-optical spiking neurosynaptic networks with self-learning capabilities. *Nature* **569**, 208–214 (2019).

ADS CAS Article Google Scholar

13. 13.

Ambrogio, S. et al. Equivalent-accuracy accelerated neural-network training using analogue memory. *Nature* **558**, 60–67 (2018).

ADS CAS Article Google Scholar

14. 14.

Esser, S. K. et al. Convolutional networks for fast, energy-efficient neuromorphic computing. *Proc. Natl Acad. Sci. USA* **113**, 11441–11446 (2016).

CAS Article Google Scholar

15. 15.

Graves, A. et al. Hybrid computing using a neural network with dynamic external memory. *Nature* **538**, 471–476 (2016).

ADS Article Google Scholar

16. 16.

Miller, D. A. B. Attojoule optoelectronics for low-energy information processing and communications. *J. Lightwave Technol*. **35**, 346–396

(2017).

ADS CAS Article Google Scholar

17. 17.

Appeltant, L. et al. Information processing using a single dynamical node as complex system. *Nat. Commun*. **2**, 468 (2011).

ADS CAS Article Google Scholar

18. 18.

Chang, J., Sitzmann, V., Dun, X., Heidrich, W. & Wetzstein, G. Hybrid optical-electronic convolutional neural networks with optimized diffractive optics for image classification. *Sci. Rep*. **8**, 12324 (2018).

ADS Article Google Scholar

19. 19.

Vandoorne, K. et al. Experimental demonstration of reservoir computing on a silicon photonics chip. *Nat. Commun*. **5**, 3541 (2014).

ADS Article Google Scholar

20. 20.

Brunner, D., Soriano, M. C., Mirasso, C. R. & Fischer, I. Parallel photonic information processing at gigabyte per second data rates using transient states. *Nat. Commun*. **4**, 1364 (2013).

ADS Article Google Scholar

21. 21.

Tait, A. N., Chang, J., Shastri, B. J., Nahmias, M. A. & Prucnal, P. R. Demonstration of WDM weighted addition for principal component analysis. *Opt. Express* **23**, 12758–12765 (2015).

ADS Article Google Scholar

22. 22.

Xu, X. et al. Photonic perceptron based on a Kerr microcomb for high-speed, scalable, optical neural networks. *Laser Photon. Rev.* **14**, https://doi.org/10.1002/lpor.202000070 (2020).

23. 23.

Pasquazi, A. et al. Micro-combs: a novel generation of optical sources. *Phys. Rep.* **729**, 1–81 (2018).

ADS MathSciNet CAS Article Google Scholar

24. 24.

Moss, D. J., Morandotti, R., Gaeta, A. L. & Lipson, M. New CMOS-compatible platforms based on silicon nitride and Hydex for nonlinear optics. *Nat. Photon.* **7**, 597–607 (2013).

ADS CAS Article Google Scholar

25. 25.

Kippenberg, T. J., Gaeta, A. L., Lipson, M. & Gorodetsky, M. L. Dissipative Kerr solitons in optical microresonators. *Science* **361**, eaan8083 (2018).

Article Google Scholar

26. 26.

Savchenkov, A. A. et al. Tunable optical frequency comb with a crystalline whispering gallery mode resonator. *Phys. Rev. Lett.* **101**, 093902 (2008).

ADS Article Google Scholar

27. 27.

Spencer, D. T. et al. An optical-frequency synthesizer using integrated photonics. *Nature* **557**, 81–85 (2018).

ADS CAS Article Google Scholar

28. 28.

Marin-Palomo, P. et al. Microresonator-based solitons for massively parallel coherent optical communications. *Nature* **546**, 274–279 (2017).

ADS CAS Article Google Scholar

29. 29.

Kues, M. et al. Quantum optical microcombs. *Nat. Photon*. **13**, 170–179 (2019).

ADS CAS Article Google Scholar

30. 30.

Cole, D. C., Lamb, E. S., Del'Haye, P., Diddams, S. A. & Papp, S. B. Soliton crystals in Kerr resonators. *Nat. Photon*. **11**, 671–676 (2017).

ADS CAS Article Google Scholar

31. 31.

Stern, B., Ji, X., Okawachi, Y., Gaeta, A. L. & Lipson, M. Battery-operated integrated frequency comb generator. *Nature* **562**, 401–405 (2018).

ADS CAS Article Google Scholar

32. 32.

Wu, J. et al. RF photonics: an optical microcombs' perspective. *IEEE J. Sel. Top. Quant. Electron*. **24**, 6101020 (2018).

ADS Google Scholar

33. 33.

LeCun, Y., Cortes, C. & Borges, C. J. C. The MNIST database of handwritten digits. http://yann.lecun.com/exdb/mnist/

34. 34.

Metcalf, A. J. et al. Integrated line-by-line optical pulse shaper for high-fidelity and rapidly reconfigurable RF-filtering. *Opt. Express* **24**, 23925–23940 (2016).

ADS CAS Article Google Scholar

35. 35.

NVIDIA Corporation. *Comparison of Convolution Methods for GPUs*. http://ska-sdp.org/publications/released-sdp-memos-2 (2018).

36. 36.

Sahin, E., Ooi, K., Png, C. & Tan, D. Large, scalable dispersion engineering using cladding-modulated Bragg gratings on a silicon chip. *Appl. Phys. Lett*. **110**, 161113 (2017).

ADS Article Google Scholar

37. 37.

Roeloffzen, C. G. H. et al. Low-loss Si_3N_4 TriPleX optical waveguides: technology and applications overview. *IEEE J. Sel. Top. Quantum Electron*. **24**, 4400321 (2018).

Article Google Scholar

38. 38.

Wang, C. et al. Integrated lithium niobate electro-optic modulators operating at CMOS-compatible voltages. *Nature* **562**, 101–104 (2018).

ADS CAS Article Google Scholar

39. 39.

Esteva, A. et al. Dermatologist-level classification of skin cancer with deep neural networks. *Nature* **542**, 115–118 (2017).

ADS CAS Article Google Scholar

40. 40.

Capper, D. et al. DNA methylation-based classification of central nervous system tumours. *Nature* **555**, 469–474 (2018).

ADS CAS Article Google Scholar

Download references

Acknowledgements

This work was supported by the Australian Research Council Discovery Projects Program (grant numbers DP150104327, DP190102773 and DP190101576). R.M. acknowledges support by the Natural Sciences and Engineering Research Council of Canada (NSERC) through the Strategic, Discovery and Acceleration Grants Schemes, by the MESI PSR-SIIRI Initiative in Quebec, and by the Canada Research Chair Program. B.E.L. was supported by the Strategic Priority Research Program of the Chinese Academy of Sciences (grant number XDB24030000). D.G.H. was supported in part by the Australian Research Council (grant number FT104101104). R.M. is affiliated with the Institute of Fundamental and Frontier Sciences (China) as an adjoint faculty member.

Author information

Author notes

1. Xingyuan Xu

   Present address: Electro-Photonics Laboratory, Department of Electrical and Computer Systems Engineering, Monash University, Clayton, Victoria, Australia

Affiliations

1. Optical Sciences Centre, Swinburne University of Technology, Hawthorn, Victoria, Australia

   Xingyuan Xu, Mengxi Tan, Jiayang Wu, Damien G. Hicks & David J. Moss

2. Department of Electrical and Computer Systems Engineering, Monash University, Clayton, Victoria, Australia

   Bill Corcoran

3. School of Engineering, RMIT University, Melbourne, Victoria, Australia

   Andreas Boes, Thach G. Nguyen & Arnan Mitchell

4. Department of Physics, City University of Hong Kong, Tat Chee Avenue, Hong Kong, China

   Sai T. Chu

5. Xi'an Institute of Optics and Precision Mechanics, Chinese Academy of Sciences, Xi'an, China

   Brent E. Little

6. Bioinformatics Division, Walter & Eliza Hall Institute of Medical Research, Parkville, Victoria, Australia

   Damien G. Hicks

7. INRS-Énergie, Matériaux et Télécommunications, Varennes, Québec, Canada

   Roberto Morandotti

8. Institute of Fundamental and Frontier Sciences, University of Electronic Science and Technology of China, Chengdu, China

   Roberto Morandotti

Authors

1. Xingyuan Xu
   View author publications

   You can also search for this author in PubMed Google Scholar

2. Mengxi Tan
   View author publications

   You can also search for this author in PubMed Google Scholar

3. Bill Corcoran
   View author publications

   You can also search for this author in PubMed Google Scholar

4. Jiayang Wu
   View author publications

   You can also search for this author in PubMed Google Scholar

5. Andreas Boes
   View author publications

You can also search for this author in PubMed Google Scholar

6. Thach G. Nguyen
   View author publications

   You can also search for this author in PubMed Google Scholar

7. Sai T. Chu
   View author publications

   You can also search for this author in PubMed Google Scholar

8. Brent E. Little
   View author publications

   You can also search for this author in PubMed Google Scholar

9. Damien G. Hicks
   View author publications

   You can also search for this author in PubMed Google Scholar

10. Roberto Morandotti
    View author publications

    You can also search for this author in PubMed Google Scholar

11. Arnan Mitchell
    View author publications

    You can also search for this author in PubMed Google Scholar

12. David J. Moss
    View author publications

    You can also search for this author in PubMed Google Scholar

Contributions

X.X. conceived the idea and designed the project. X.X. and M.T. performed the experiments. X.X. analysed the data, and performed the numerical simulations and the offline training. S.T.C. and B.E.L. designed and fabricated the integrated devices. B.C., J.W., A.B., T.G.N., R.M. and A.M. contributed to the development of the experiment and to the data analysis. X.X. and D.J.M. wrote the manuscript. D.J.M. supervised the research.

Corresponding author

Correspondence to David J. Moss.

Ethics declarations

Competing interests

The authors declare no competing interests.

Additional information

Peer review information *Nature* thanks Sylvain Gigan and the other, anonymous, reviewer(s) for their contribution to the peer review of this work.

Publisher's note Springer Nature remains neutral with regard to jurisdictional claims in published maps and institutional affiliations.

Extended data figures and tables

Extended Data Fig. 1 VCA, for processing one-dimensional data.

It consists of the experimental setup (right panel), the optical and electronic control and signal flow (left panel). ADC, analogue-to-digital converter. 1D, one-dimensional.

Extended Data Fig. 2 Generation of soliton crystal microcombs.

a, Schematic diagram of the soliton crystal microcomb, generated by pumping an on-chip high-Q (quality factor >1 million) nonlinear micro-ring resonator with a continuous-wave laser. **b**, Image of the MRR (upper inset) and a scanning electron microscope image of the MRR's waveguide cross-section (lower inset). **c**, Measured dispersion D_{int} of the MRR showing the mode crossing at about 1,552 nm. **d**, Measured soliton crystal step of the intra-cavity power. **e**, Optical spectrum of the microcomb when sweeping the pump wavelength. **f**, Optical spectrum of the generated coherent microcomb at different pump detunings at a fixed power. FSR, free spectral range.

Extended Data Fig. 3 The architecture of the optical CNN.

The architecture includes a convolutional layer, a pooling layer and a fully connected layer.

Extended Data Fig. 4 Fully connected layers.

Architecture and experimental results. The left panel depicts the experimental setup, similar to the convolutional layer. The right panel shows the experimental results for one output neuron, including the shaped comb spectrum (top); the pooled feature maps of the digit 3 and the corresponding input electrical waveform (the grey and red lines illustrate the ideal and experimentally generated waveforms, respectively; middle); and the output waveform of the neuron and sampled intensities (bottom). Conv layer, convolutional layer. CW pump, continuous-wave pump laser.

Supplementary information

Supplementary Information

Information on the operation principle of the photonic convolution accelerator, matrix flattening, network training and digital processing, additional experimental results, a performance comparison with other

results in the literature, scaling the networks in performance and speed, and a theoretical evaluation of a scaled network, including Supplementary Figures S1–S30, Tables S1 to S2, and Supplementary References.

Supplementary Information

A Supplementary Presentation. Digital neuromorphic processors typically process one dimensional data streams and so to process matrices, the matrix must first be converted to a vector – effectively "flattened". How this is done will be determined by the size of the kernel being used to process the data, and this in turn will result in a reduction of the matrix processing speed relative to the vector processing speed – effectively a speed "overhead". This is a fundamental and generic issue that applies to any processor. This presentation graphically illustrates this issue and includes a presentation of methods designed to eliminate this overhead.

Rights and permissions

Reprints and Permissions

About this article

Check for updates

Cite this article

Xu, X., Tan, M., Corcoran, B. *et al.* 11 TOPS photonic convolutional accelerator for optical neural networks. *Nature* **589,** 44–51 (2021). https://doi.org/10.1038/s41586-020-03063-0

Download citation

- Received: 15 April 2020

- Accepted: 20 October 2020
- Published: 06 January 2021
- Issue Date: 07 January 2021
- DOI: https://doi.org/10.1038/s41586-020-03063-0

Comments

By submitting a comment you agree to abide by our Terms and Community Guidelines. If you find something abusive or that does not comply with our terms or guidelines please flag it as inappropriate.

Access through your institution
Change institution
Buy or subscribe

Associated Content

Nature | News & Views

Artificial intelligence accelerated by light

- Huaqiang Wu
- & Qionghai Dai

This article was downloaded by **calibre** from https://www.nature.com/articles/s41586-020-03063-0

- Article
- Published: 06 January 2021

Parallel convolutional processing using an integrated photonic tensor core

- J. Feldmann[1] na1,
- N. Youngblood ORCID: orcid.org/0000-0003-2552-9376[2] na1 nAff7,
- M. Karpov ORCID: orcid.org/0000-0002-9304-3936[3] na1,
- H. Gehring[1],
- X. Li[2],
- M. Stappers ORCID: orcid.org/0000-0002-3742-1592[1],
- M. Le Gallo ORCID: orcid.org/0000-0003-1600-6151[4],
- X. Fu[3],
- A. Lukashchuk[3],
- A. S. Raja[3],
- J. Liu ORCID: orcid.org/0000-0003-2405-6028[3],
- C. D. Wright ORCID: orcid.org/0000-0003-4087-7467[5],
- A. Sebastian ORCID: orcid.org/0000-0001-5603-5243[4],
- T. J. Kippenberg ORCID: orcid.org/0000-0002-3408-886X[3],
- W. H. P. Pernice ORCID: orcid.org/0000-0003-4569-4213[1,6] &
- H. Bhaskaran ORCID: orcid.org/0000-0003-0774-8110[2]

Nature **volume 589**, pages52–58(2021)Cite this article

- 1796 Accesses
- 208 Altmetric
- Metrics details

Subjects

- Frequency combs
- Information technology
- Nanophotonics and plasmonics

Abstract

With the proliferation of ultrahigh-speed mobile networks and internet-connected devices, along with the rise of artificial intelligence (AI)[1], the world is generating exponentially increasing amounts of data that need to be processed in a fast and efficient way. Highly parallelized, fast and scalable hardware is therefore becoming progressively more important[2]. Here we demonstrate a computationally specific integrated photonic hardware accelerator (tensor core) that is capable of operating at speeds of trillions of multiply-accumulate operations per second (10^{12} MAC operations per second or tera-MACs per second). The tensor core can be considered as the optical analogue of an application-specific integrated circuit (ASIC). It achieves parallelized photonic in-memory computing using phase-change-material memory arrays and photonic chip-based optical frequency combs (soliton microcombs[3]). The computation is reduced to measuring the optical transmission of reconfigurable and non-resonant passive components and can operate at a bandwidth exceeding 14 gigahertz, limited only by the speed of the modulators and photodetectors. Given recent advances in hybrid integration of soliton microcombs at microwave line rates[3,4,5], ultralow-loss silicon nitride waveguides[6,7], and high-speed on-chip detectors and modulators, our approach provides a path towards full complementary metal–oxide–semiconductor (CMOS) wafer-scale integration of the photonic tensor core. Although we focus on convolutional processing, more generally our results indicate the potential of integrated photonics for parallel, fast, and efficient computational hardware in data-heavy AI applications such as autonomous driving, live video processing, and next-generation cloud computing services.

Access through your institution
Change institution

Buy or subscribe

Access options

Subscribe to Journal

Get full journal access for 1 year

$199.00

only $3.90 per issue

Subscribe

All prices are NET prices.
VAT will be added later in the checkout.

Rent or Buy article

Get time limited or full article access on ReadCube.

from$8.99

Rent or Buy

All prices are NET prices.

Additional access options:

- Log in
- Access through your institution
- Learn about institutional subscriptions

Fig. 1: Photonic in-memory computing using a photonic-chip-based microcomb and PCMs.

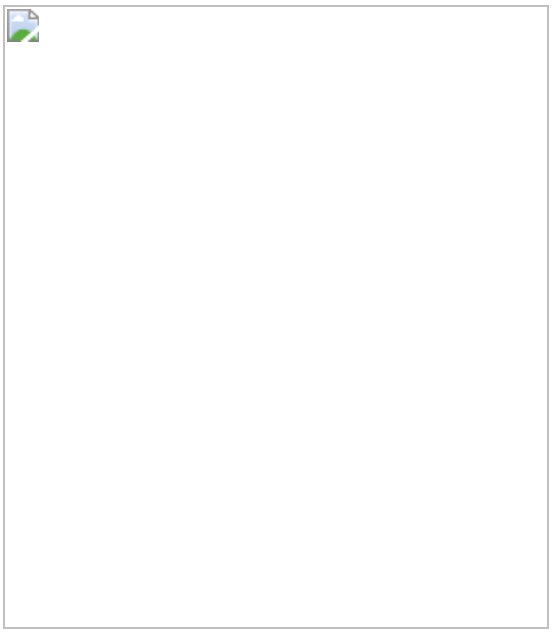

Fig. 2: Concept of photonic tensor cores for convolution operations.

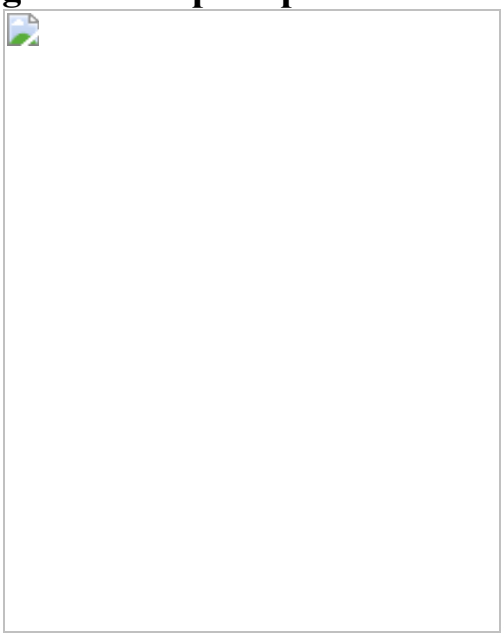

Fig. 3: Convolution using sequential MVM operations.

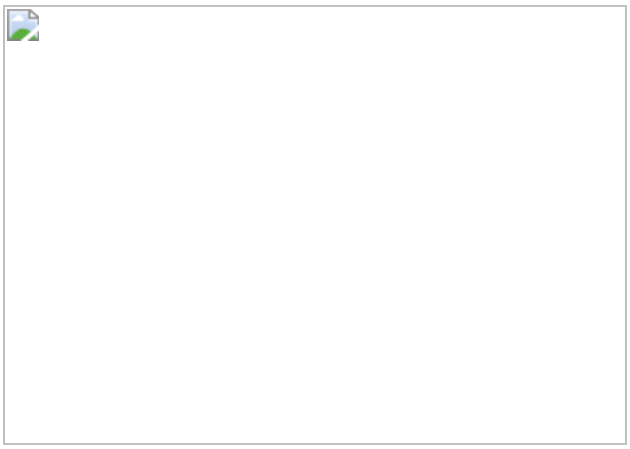

Fig. 4: Convolution using parallel MVM operations.

Fig. 5: Digit recognition with a CNN and scalability.

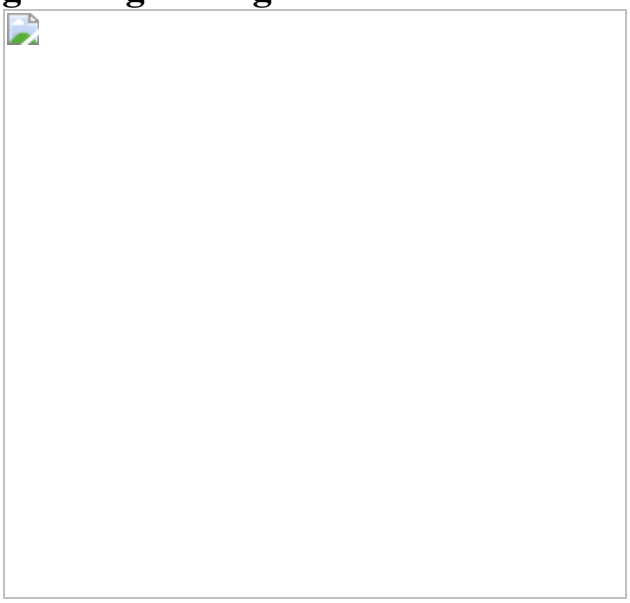

Data availability

All data used in this study are available from the corresponding author upon reasonable request.

References

1. 1.

Batra, G., Jacobson, Z., Madhav, S., Queirolo, A. & Santhanam, N. Artificial-intelligence hardware: new opportunities for semiconductor companies. https://www.mckinsey.com/industries/semiconductors/our-insights/artificial-intelligence-hardware-new-opportunities-for-semiconductor-companies (McKinsey & Company, 2019).

2. 2.

Ben-Nun, T. & Hoefler, T. Demystifying parallel and distributed deep learning: an in-depth concurrency analysis. *ACM Comput. Surv*. **52**, https://doi.org/10.1145/3320060 (2019).

3. 3.

Herr, T. et al. Temporal solitons in optical microresonators. *Nat. Photon*. **8**, 145–152 (2014).

ADS CAS Google Scholar

4. 4.

Herr, T., Gorodetsky, M. L. & Kippenberg, T. J. Dissipative Kerr solitons in optical microresonators. In *Nonlinear Optical Cavity Dynamics From Microresonators to Fiber Lasers* (ed. Grelu, P.) Vol. 8083, Ch. 6, 129–162 (Wiley, 2015).

5. 5.

Raja, A. S. et al. Electrically pumped photonic integrated soliton microcomb. *Nat. Commun*. **10**, 680 (2019).

ADS CAS PubMed PubMed Central Google Scholar

6. 6.

Pfeiffer, M. H. P. et al. Photonic damascene process for integrated high-*Q* microresonator based nonlinear photonics. *Optica* **3**, 20–25

(2016).

ADS CAS Google Scholar

7. 7.

Liu, J. et al. Ultralow-power chip-based soliton microcombs for photonic integration. *Optica* **5**, 1347–1353 (2019).

ADS Google Scholar

8. 8.

Machine Learning on AWS https://aws.amazon.com/machine-learning/ (accessed 12 October 2020).

9. 9.

Google Cloud *AI And Machine Learning Products* https://cloud.google.com/products/machine-learning/ (accessed 12 October 2020).

10. 10.

Zhang, C. et al. Optimizing FPGA-based Accelerator Design for Deep Convolutional Neural Networks. In *ACM/SIGDA Int. Symp. Field-Programmable Gate Arrays (FPGA' 15)* https://doi.org/10.1145/2684746.2689060 (2015).

11. 11.

Jouppi, N. P. et al. In-datacenter performance analysis of a tensor processing unit. *Proc. ISCA' 17* https://doi.org/10.1145/3079856.3080246 (2017).

12. 12.

Wang, P. S., Liu, Y., Guo, Y. X., Sun, C. Y. & Tong, X. O-CNN: octree-based convolutional neural networks for 3D shape analysis.

ACM Trans. Graph. **36**, https://doi.org/10.1145/3072959.3073608 (2017).

13. 13.

Miller, D. A. B. Attojoule optoelectronics for low-energy information processing and communications. *J. Lightwave Technol*. **35**, 346–396 (2017).

ADS CAS Google Scholar

14. 14.

Agrawal, S. R. et al. A many-core architecture for in-memory data processing. In *Proc. 50th Annu. IEEE/ACM Int. Symp. Microarchitecture (MICRO-50' 17)* 245–258, https://doi.org/10.1145/3123939.3123985 (IEEE/ACM, 2017).

15. 15.

Miller, D. A. B. Are optical transistors the logical next step? *Nat. Photon*. **4**, 3–5 (2010).

ADS CAS Google Scholar

16. 16.

Ielmini, D. & Wong, H. S. P. In-memory computing with resistive switching devices. *Nat. Electron*. **1**, 333–343 (2018).

Google Scholar

17. 17.

Le Gallo, M. et al. Mixed-precision in-memory computing. *Nat. Electron*. **1**, 246–253 (2018).

Google Scholar

18. 18.

Boybat, I. et al. Neuromorphic computing with multi-memristive synapses. *Nat. Commun*. **9**, 2514 (2018).

ADS PubMed PubMed Central Google Scholar

19. 19.

Sebastian, A., Le Gallo, M., Khaddam-Aljameh, R. & Eleftheriou, E. Memory devices and applications for in-memory computing. *Nat. Nanotechnol*. **15**, 529–544 (2020).

ADS CAS PubMed PubMed Central Google Scholar

20. 20.

Hu, M. et al. Dot-product engine for neuromorphic computing: programming 1T1M crossbar to accelerate matrix-vector multiplication. In *Proc. 53rd Annu. Design Automation Conf. (DAC ' 16)* https://doi.org/10.1145/2897937.2898010 (ACM Digital Library, 2016).

21. 21.

Gong, N. et al. Signal and noise extraction from analog memory elements for neuromorphic computing. *Nat. Commun*. **9**, 2102 (2018).

ADS CAS PubMed PubMed Central Google Scholar

22. 22.

Joshi, V. et al. Accurate deep neural network inference using computational phase-change memory. *Nat. Commun*. **11**, 2473 (2020).

ADS CAS PubMed PubMed Central Google Scholar

23. 23.

Yang, T. Y., Park, I. M., Kim, B. J. & Joo, Y. C. Atomic migration in molten and crystalline $Ge_2Sb_2Te_5$ under high electric field. *Appl. Phys. Lett*. **95**, 032104 (2009).

ADS Google Scholar

24. 24.

Koelmans, W. W. et al. Projected phase-change memory devices. *Nat. Commun*. **6**, 8181 (2015).

ADS PubMed PubMed Central Google Scholar

25. 25.

Kim, S. et al. A phase change memory cell with metallic surfactant layer as a resistance drift stabilizer. In *2013 IEEE Int. Electron Devices Meeting* https://doi.org/10.1109/IEDM.2013.6724727 (IEEE, 2013).

26. 26.

Bell, T. E. Optical computing: a field in flux: a worldwide race is on to develop machines that compute with photons instead of electrons but what is the best approach? *IEEE Spectr*. **23**, 34–38 (1986).

ADS Google Scholar

27. 27.

Hamerly, R., Bernstein, L., Sludds, A., Soljačić, M. & Englund, D. Large-scale optical neural networks based on photoelectric multiplication. *Phys. Rev. X* **9**, 021032 (2018).

Google Scholar

28. 28.

Silva, A. et al. Performing mathematical operations with metamaterials. *Science* **343**, 160–163 (2014).

ADS MathSciNet CAS PubMed PubMed Central MATH Google Scholar

29. 29.

Lin, X. et al. All-optical machine learning using diffractive deep neural networks. *Science* **361**, 1004–1008 (2018).

ADS MathSciNet CAS MATH Google Scholar

30. 30.

Colburn, S., Chu, Y., Shilzerman, E. & Majumdar, A. Optical frontend for a convolutional neural network. *Appl. Opt*. **58**, 3179–3186 (2019).

ADS Google Scholar

31. 31.

Shen, Y. et al. Deep learning with coherent nanophotonic circuits. *Nat. Photon*. **11**, 441–446 (2017).

ADS CAS Google Scholar

32. 32.

Tait, A. N. et al. Silicon photonic modulator neuron. *Phys. Rev. Appl*. **11**, 064043 (2019).

ADS CAS Google Scholar

33. 33.

Pérez, D. et al. Multipurpose silicon photonics signal processor core. *Nat. Commun*. **8**, 636 (2017).

ADS PubMed PubMed Central Google Scholar

34. 34.

Galal, S. & Horowitz, M. Energy-efficient floating-point unit design. *IEEE Trans. Comput*. **60**, 913–922 (2011).

MathSciNet MATH Google Scholar

35. 35.

Bangari, V. et al. Digital electronics and analog photonics for convolutional neural networks (DEAP-CNNs). *IEEE J. Sel. Top. Quantum Electron*. **26**, https://doi.org/10.1109/JSTQE.2019.2945540 (2020).

36. 36.

LeCun, Y., Cortes, C. & Borges, C. J. C. The MNIST database of handwritten digits. http://yann.lecun.com/exdb/mnist.

37. 37.

Stern, B., Ji, X., Okawachi, Y., Gaeta, A. L. & Lipson, M. Battery-operated integrated frequency comb generator. *Nature* **562**, 401–405 (2018).

ADS CAS Google Scholar

38. 38.

Jones, R. et al. Heterogeneously integrated InP/silicon photonics: fabricating fully functional transceivers. *IEEE Nanotechnol. Mag*. **13**, 17–26 (2019).

Google Scholar

39. 39.

Marin-Palomo, P. et al. Microresonator-based solitons for massively parallel coherent optical communications. *Nature* **546**, 274–279 (2017).

ADS CAS Google Scholar

40. 40.

Spencer, D. T. et al. An optical-frequency synthesizer using integrated photonics. *Nature* **557**, 81–85 (2018).

ADS CAS Google Scholar

41. 41.

Riemensberger, J. et al. Massively parallel coherent laser ranging using soliton microcombs. *Nature* **581**, 164–170 (2019).

ADS Google Scholar

42. 42.

Moss, D. J., Morandotti, R., Gaeta, A. L. & Lipson, M. New CMOS-compatible platforms based on silicon nitride and Hydex for nonlinear optics. *Nat. Photon*. **7**, 597–607 (2013).

ADS CAS Google Scholar

43. 43.

He, K., Zhang, X., Ren, S. & Sun, J. Deep residual learning for image recognition. In *2016 Proc. IEEE Conf. Computer Vision and Pattern Recognition (CVPR)* https://doi.org/10.1109/CVPR.2016.90 (IEEE, 2016).

44. 44.

Simonyan, K. & Zisserman, A. Very deep convolutional networks for large-scale image recognition. In *3rd Int. Conf. Learning Representations (ICLR 2015)* (eds Bengio, Y. & LeCun, Y.) 4 (2015); https://arxiv.org/abs/1409.1556.

45. 45.

Al-Ashrafy, M., Salem, A. & Anis, W. An efficient implementation of floating point multiplier. In *2011 Saudi Int. Electronics, Communications and Photonics Conf. (SIECPC)* https://doi.org/10.1109/SIECPC.2011.5876905 (2011).

46. 46.

Gao, L., Chen, P. Y. & Yu, S. Demonstration of convolution kernel operation on resistive cross-point array. *IEEE Electron Device Lett*. **37**, 870–873 (2016).

ADS Google Scholar

47. 47.

Shafiee, A. et al. ISAAC: a convolutional neural network accelerator with in-situ analog arithmetic in crossbars. In *Proc. 2016 43rd Int. Symp. Computer Architecture (ISCA 2016)* https://doi.org/10.1109/ISCA.2016.12 (2016).

48. 48.

Li, X. et al. Fast and reliable storage using a 5 bit, nonvolatile photonic memory cell. *Optica* **6**, 1–6 (2019).

ADS Google Scholar

49. 49.

Ríos, C. et al. Integrated all-photonic non-volatile multi-level memory. *Nat. Photon*. **9**, 725–732 (2015).

ADS Google Scholar

50. 50.

Feldmann, J. et al. Calculating with light using a chip-scale all-optical abacus. *Nat. Commun*. **8**, 1256 (2017).

ADS CAS PubMed PubMed Central Google Scholar

51. 51.

Gehring, H. et al. Low-loss fiber-to-chip couplers with ultrawide optical bandwidth. *APL Photon*. **4**, 010801 (2019).

ADS Google Scholar

52. 52.

Gehring, H., Eich, A., Schuck, C. & Pernice, W. H. P. Broadband out-of-plane coupling at visible wavelengths. *Opt. Lett*. **44**, 5089 (2019).

ADS CAS Google Scholar

53. 53.

Nahmias, M. A. et al. Photonic multiply-accumulate operations for neural networks. *IEEE J. Sel. Top. Quantum Electron*. https://doi.org/10.1109/jstqe.2019.2941485 (2019).

Article Google Scholar

54. 54.

Gehring, H., Blaicher, M., Hartmann, W. & Pernice, W. H. P. Python based open source design framework for integrated nanophotonic and superconducting circuitry with 2D-3D-hybrid integration. *OSA Continuum* **2**, 3091–3101 (2019).

CAS Google Scholar

55. 55.

Guo, H. et al. Universal dynamics and deterministic switching of dissipative Kerr solitons in optical microresonators. *Nat. Phys*. **13**, 94–102 (2017).

CAS Google Scholar

56. 56.

Karpov, M. et al. Dynamics of soliton crystals in optical microresonators. *Nat. Phys*. **15**, 1071–1077 (2019).

CAS Google Scholar

57. 57.

Fialka, O. & Čadík, M. FFT and convolution performance in image filtering on GPU. In *Proc. 10th Int. Conf. Information Visualisation (IV' 06)* https://doi.org/10.1109/IV.2006.53 (IEEE, 2006).

58. 58.

Krizhevsky, A., Sutskever, I. & Hinton, G. E. ImageNet classification with deep convolutional neural networks. *Commun. ACM* **60**, https://doi.org/10.1145/3065386 (2017).

59. 59.

Szegedy, C. et al. Going deeper with convolutions. In *Proc. IEEE Conf. Computer Vision and Pattern Recognition (CVPR)* https://doi.org/10.1109/CVPR.2015.7298594 (IEEE, 2015).

60. 60.

Ríos, C. et al. In-memory computing on a photonic platform. *Sci. Adv*. **5**, eaau5759 (2019).

ADS PubMed PubMed Central Google Scholar

61. 61.

Gaeta, A. L., Lipson, M. & Kippenberg, T. J. Photonic-chip-based frequency combs. *Nat. Photon*. **13**, 158–169 (2019).

ADS CAS Google Scholar

62. 62.

Ma, Y. et al. Ultralow loss single layer submicron silicon waveguide crossing for SOI optical interconnect. *Opt. Express* **21**, 29374–29382 (2013).

ADS PubMed PubMed Central Google Scholar

63. 63.

Lu, Z. et al. Broadband silicon photonic directional coupler using asymmetric-waveguide based phase control. *Opt. Express* **23**, 3795–3808 (2015).

ADS CAS PubMed PubMed Central Google Scholar

64. 64.

Farmakidis, N. et al. Plasmonic nanogap enhanced phase change devices with dual electrical-optical functionality. *Sci. Adv*. **5**, eaaw2687 (2019).

ADS CAS PubMed PubMed Central Google Scholar

65. 65.

Zhang, H. et al. Miniature multilevel optical memristive switch using phase change material. *ACS Photon*. **6**, 2205–2212 (2019).

CAS Google Scholar

66. 66.

Atabaki, A. H. et al. Integrating photonics with silicon nanoelectronics for the next generation of systems on a chip. *Nature* **556**, 349–354 (2018).

ADS CAS PubMed PubMed Central Google Scholar

67. 67.

Wang, X. & Liu, J. Emerging technologies in Si active photonics. *J. Semicond*. **39**, 061001 (2018).

ADS Google Scholar

68. 68.

Sun, J., Timurdogan, E., Yaacobi, A., Hosseini, E. S. & Watts, M. R. Large-scale nanophotonic phased array. *Nature* **493**, 195–199 (2013).

ADS CAS PubMed PubMed Central Google Scholar

Download references

Acknowledgements

This research was supported by EPSRC via grants EP/J018694/1, EP/M015173/1 and EP/M015130/1 in the UK and Deutsche Forschungsgemeinschaft (DFG) grant PE 1832/5-1 in Germany. This material is based upon work supported by the Air Force Office of Scientific Research under award number FA9550-19-1-0250. W.H.P.P. gratefully acknowledges support by the European Research Council through grant 724707. We further acknowledge funding for this work from the European Union's Horizon 2020 Research and Innovation Programme (Fun-COMP project number 780848). A.S. acknowledges support by the European Research Council though grant 682675. H.G. thanks the Studienstiftung des deutschen Volkes for financial support. We thank F. Brückerhoff-Plückelmann, S. Agarwal and W. Zhou for help with sample fabrication and discussions of the experimental results.

Author information

Author notes

1. N. Youngblood

   Present address: Department of Electrical and Computer Engineering, University of Pittsburgh, Pittsburgh, PA, USA

2. These authors contributed equally: J. Feldmann, N. Youngblood, M. Karpov

Affiliations

1. Institute of Physics, University of Münster, Münster, Germany

   J. Feldmann, H. Gehring, M. Stappers & W. H. P. Pernice

2. Department of Materials, University of Oxford, Oxford, UK

   N. Youngblood, X. Li & H. Bhaskaran

3. Laboratory of Photonics and Quantum Measurements, Swiss Federal Institute of Technology Lausanne (EPFL), Lausanne, Switzerland

   M. Karpov, X. Fu, A. Lukashchuk, A. S. Raja, J. Liu & T. J. Kippenberg

4. IBM Research Europe, Rüschlikon, Switzerland

   M. Le Gallo & A. Sebastian

5. Department of Engineering, University of Exeter, Exeter, UK

   C. D. Wright

6. Center for Soft Nanoscience, University of Münster, Münster, Germany

   W. H. P. Pernice

Authors

1. J. Feldmann
   View author publications

   You can also search for this author in PubMed Google Scholar

2. N. Youngblood
   View author publications

   You can also search for this author in PubMed Google Scholar

3. M. Karpov
   View author publications

   You can also search for this author in PubMed Google Scholar

4. H. Gehring
   View author publications

   You can also search for this author in PubMed Google Scholar

5. X. Li
   View author publications

   You can also search for this author in PubMed Google Scholar

6. M. Stappers
   View author publications

   You can also search for this author in PubMed Google Scholar

7. M. Le Gallo
   View author publications

   You can also search for this author in PubMed Google Scholar

8. X. Fu
   View author publications

   You can also search for this author in PubMed Google Scholar

9. A. Lukashchuk
View author publications

You can also search for this author in PubMed Google Scholar

10. A. S. Raja
View author publications

You can also search for this author in PubMed Google Scholar

11. J. Liu
View author publications

You can also search for this author in PubMed Google Scholar

12. C. D. Wright
View author publications

You can also search for this author in PubMed Google Scholar

13. A. Sebastian
View author publications

You can also search for this author in PubMed Google Scholar

14. T. J. Kippenberg
View author publications

You can also search for this author in PubMed Google Scholar

15. W. H. P. Pernice
View author publications

You can also search for this author in PubMed Google Scholar

16. H. Bhaskaran
View author publications

You can also search for this author in PubMed Google Scholar

Contributions

W.H.P.P., H.B., A.S., T.J.K. and C.D.W. conceived the experiment. J.F. fabricated the devices with assistance from N.Y., H.G. and X.L. N.Y. performed the deposition of the $Ge_2Sb_2Te_5$ material, together with X.L. J.F. implemented the measurement setup and carried out the measurements with help from N.Y., M.K., M.S. and H.G. M.K., X.F., A.L., A.S.R. and J.L. implemented the frequency comb source. All authors discussed the data and wrote the manuscript together.

Corresponding authors

Correspondence to A. Sebastian or T. J. Kippenberg or W. H. P. Pernice or H. Bhaskaran.

Ethics declarations

Competing interests

The authors declare no competing interests.

Additional information

Peer review information *Nature* thanks Huaqiang Wu and the other, anonymous, reviewer(s) for their contribution to the peer review of this work. Peer reviewer reports are available.

Publisher's note Springer Nature remains neutral with regard to jurisdictional claims in published maps and institutional affiliations.

Supplementary information

Supplementary Information

Supplementary methods and notes. The file contains Supplementary Tables 1–2, Supplementary Figures 1–22 and Supplementary References. It gives further methodological information on the experimental setups and provides additional data to validate and illustrate the main results of the manuscript.

Peer Review File

Rights and permissions

Reprints and Permissions

About this article

Check for updates

Cite this article

Feldmann, J., Youngblood, N., Karpov, M. *et al.* Parallel convolutional processing using an integrated photonic tensor core. *Nature* **589,** 52–58 (2021). https://doi.org/10.1038/s41586-020-03070-1

Download citation

- Received: 01 February 2020
- Accepted: 02 November 2020
- Published: 06 January 2021
- Issue Date: 07 January 2021
- DOI: https://doi.org/10.1038/s41586-020-03070-1

Comments

By submitting a comment you agree to abide by our Terms and Community Guidelines. If you find something abusive or that does not comply with our terms or guidelines please flag it as inappropriate.

Access through your institution
Change institution
Buy or subscribe

Associated Content

Nature | News & Views

Artificial intelligence accelerated by light

- Huaqiang Wu
- & Qionghai Dai

This article was downloaded by **calibre** from https://www.nature.com/articles/s41586-020-03070-1

- Article
- Published: 06 January 2021

Origins of structural and electronic transitions in disordered silicon

- Volker L. Deringer ORCID: orcid.org/0000-0001-6873-0278[1],
- Noam Bernstein ORCID: orcid.org/0000-0002-6532-1337[2],
- Gábor Csányi ORCID: orcid.org/0000-0002-8180-2034[3],
- Chiheb Ben Mahmoud ORCID: orcid.org/0000-0002-6695-1402[4,5],
- Michele Ceriotti ORCID: orcid.org/0000-0003-2571-2832[4,5],
- Mark Wilson ORCID: orcid.org/0000-0003-4599-7943[6],
- David A. Drabold ORCID: orcid.org/0000-0001-5344-5837[7] &
- Stephen R. Elliott[8] nAff9

Nature **volume 589**, pages59–64(2021)Cite this article

- 2358 Accesses
- 129 Altmetric
- Metrics details

Subjects

- Atomistic models
- Molecular dynamics
- Phase transitions and critical phenomena
- Structure of solids and liquids

Abstract

Structurally disordered materials pose fundamental questions[1,2,3,4], including how different disordered phases (‘polyamorphs’) can coexist and transform from one phase to another[5,6,7,8,9]. Amorphous silicon has been extensively studied; it forms a fourfold-coordinated, covalent network at ambient conditions and much-higher-coordinated, metallic phases under pressure[10,11,12]. However, a detailed mechanistic understanding of the structural transitions in disordered silicon has been lacking, owing to the intrinsic limitations of even the most advanced experimental and computational techniques, for example, in terms of the system sizes accessible via simulation. Here we show how atomistic machine learning models trained on accurate quantum mechanical computations can help to describe liquid–amorphous and amorphous–amorphous transitions for a system of 100,000 atoms (ten-nanometre length scale), predicting structure, stability and electronic properties. Our simulations reveal a three-step transformation sequence for amorphous silicon under increasing external pressure. First, polyamorphic low- and high-density amorphous regions are found to coexist, rather than appearing sequentially. Then, we observe a structural collapse into a distinct very-high-density amorphous (VHDA) phase. Finally, our simulations indicate the transient nature of this VHDA phase: it rapidly nucleates crystallites, ultimately leading to the formation of a polycrystalline structure, consistent with experiments[13,14,15] but not seen in earlier simulations[11,16,17,18]. A machine learning model for the electronic density of states confirms the onset of metallicity during VHDA formation and the subsequent crystallization. These results shed light on the liquid and amorphous states of silicon, and, in a wider context, they exemplify a machine learning-driven approach to predictive materials modelling.

Access through your institution
Change institution
Buy or subscribe

Access options

Subscribe to Journal

Get full journal access for 1 year

$199.00

only $3.90 per issue

Subscribe

All prices are NET prices.
VAT will be added later in the checkout.

Rent or Buy article

Get time limited or full article access on ReadCube.

from$8.99

Rent or Buy

All prices are NET prices.

Additional access options:

- Log in
- Access through your institution
- Learn about institutional subscriptions

Fig. 1: Vitrification of supercooled liquid silicon.

Fig. 2: a-Si at high and very-high pressure.

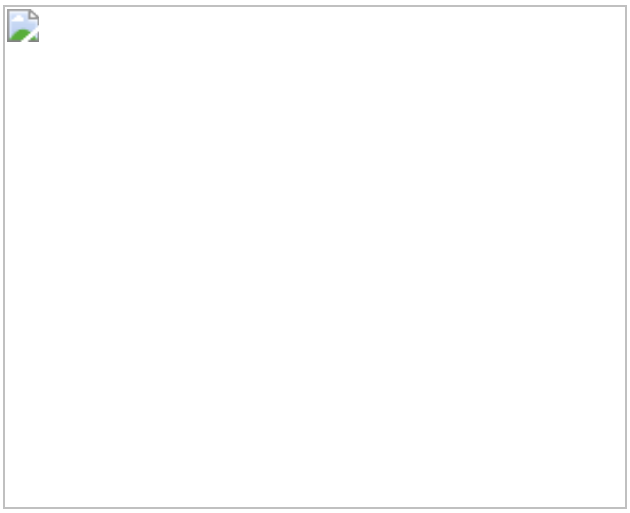

Fig. 3: Electronic fingerprints of structural transitions.

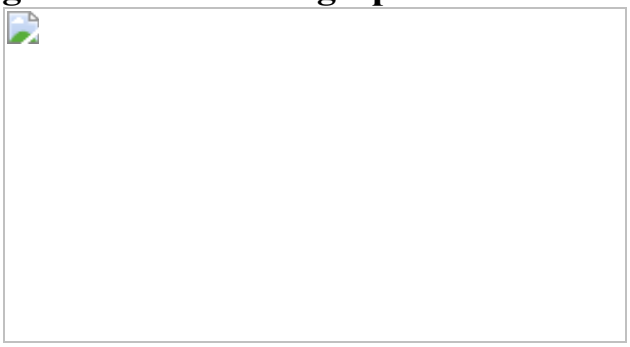

Data availability

Original data supporting this work, including coordinates for all reported structural models, are openly available in the Zenodo repository (https://doi.org/10.5281/zenodo.4174139).

Code availability

The QUIP code, which provides the interface for carrying out GAP-driven simulations with LAMMPS, is publicly available at https://github.com/libAtoms/QUIP; additional information may be found there. The GAP code is available freely for non-commercial research at http://www.libatoms.org/gap/gap_download.html.

References

1. 1.

Elliott, S. R. Medium-range structural order in covalent amorphous solids. *Nature* **354**, 445–452 (1991).

ADS CAS Google Scholar

2. 2.

Sheng, H. W., Luo, W. K., Alamgir, F. M., Bai, J. M. & Ma, E. Atomic packing and short-to-medium-range order in metallic glasses. *Nature* **439**, 419–425 (2006).

ADS CAS Google Scholar

3. 3.

Xie, R. et al. Hyperuniformity in amorphous silicon based on the measurement of the infinite-wavelength limit of the structure factor. *Proc. Natl Acad. Sci. USA* **110**, 13250–13254 (2013).

ADS CAS Google Scholar

4. 4.

Keen, D. A. & Goodwin, A. L. The crystallography of correlated disorder. *Nature* **521**, 303–309 (2015).

ADS CAS Google Scholar

5. 5.

Hedler, A., Klaumünzer, S. L. & Wesch, W. Amorphous silicon exhibits a glass transition. *Nat. Mater*. **3**, 804–809 (2004).

ADS CAS Google Scholar

6. 6.

Wilding, M. C., Wilson, M. & McMillan, P. F. Structural studies and polymorphism in amorphous solids and liquids at high pressure. *Chem. Soc. Rev*. **35**, 964–986 (2006).

CAS Google Scholar

7. 7.

Sheng, H. W. et al. Polyamorphism in a metallic glass. *Nat. Mater*. **6**, 192–197 (2007).

ADS CAS Google Scholar

8. 8.

Debenedetti, P. G., Sciortino, F. & Zerze, G. H. Second critical point in two realistic models of water. *Science* **369**, 289–292 (2020).

ADS CAS Google Scholar

9. 9.

Cheng, B., Mazzola, G., Pickard, C. J. & Ceriotti, M. Evidence for supercritical behaviour of high-pressure liquid hydrogen. *Nature* **585**, 217–220 (2020).

CAS Google Scholar

10. 10.

Deb, S. K., Wilding, M., Somayazulu, M. & McMillan, P. F. Pressure-induced amorphization and an amorphous–amorphous transition in densified porous silicon. *Nature* **414**, 528–530 (2001).

ADS CAS Google Scholar

11. 11.

McMillan, P. F., Wilson, M., Daisenberger, D. & Machon, D. A density-driven phase transition between semiconducting and metallic polyamorphs of silicon. *Nat. Mater*. **4**, 680–684 (2005).

ADS CAS Google Scholar

12. 12.

Daisenberger, D. et al. Polyamorphic amorphous silicon at high pressure: Raman and spatially resolved X-ray scattering and molecular dynamics studies. *J. Phys. Chem. B* **115**, 14246–14255 (2011).

CAS Google Scholar

13. 13.

Pandey, K. K., Garg, N., Shanavas, K. V., Sharma, S. M. & Sikka, S. K. Pressure induced crystallization in amorphous silicon. *J. Appl. Phys*. **109**, 113511 (2011).

ADS Google Scholar

14. 14.

Garg, N., Pandey, K. K., Shanavas, K. V., Betty, C. A. & Sharma, S. M. Memory effect in low-density amorphous silicon under pressure. *Phys. Rev. B* **83**, 115202 (2011).

ADS Google Scholar

15. 15.

Haberl, B., Guthrie, M., Sprouster, D. J., Williams, J. S. & Bradby, J. E. New insight into pressure-induced phase transitions of amorphous silicon: the role of impurities. *J. Appl. Cryst*. **46**, 758–768 (2013).

CAS Google Scholar

16. 16.

Durandurdu, M. & Drabold, D. A. Ab initio simulation of first-order amorphous-to-amorphous phase transition of silicon. *Phys. Rev. B* **64**, 014101 (2001).

ADS Google Scholar

17. 17.

Morishita, T. High density amorphous form and polyamorphic transformations of silicon. *Phys. Rev. Lett*. **93**, 055503 (2004).

ADS Google Scholar

18. 18.

Daisenberger, D. et al. High-pressure X-ray scattering and computer simulation studies of density-induced polyamorphism in silicon. *Phys. Rev. B* **75**, 224118 (2007).

ADS Google Scholar

19. 19.

Behler, J. First principles neural network potentials for reactive simulations of large molecular and condensed systems. *Angew. Chem. Int. Ed*. **56**, 12828–12840 (2017).

CAS Google Scholar

20. 20.

Butler, K. T., Davies, D. W., Cartwright, H., Isayev, O. & Walsh, A. Machine learning for molecular and materials science. *Nature* **559**, 547–555 (2018).

ADS CAS Google Scholar

21. 21.

Deringer, V. L., Caro, M. A. & Csányi, G. Machine learning interatomic potentials as emerging tools for materials science. *Adv. Mater*. **31**, 1902765 (2019).

CAS Google Scholar

22. 22.

Behler, J., Martoňák, R., Donadio, D. & Parrinello, M. Metadynamics simulations of the high-pressure phases of silicon employing a high-dimensional neural network potential. *Phys. Rev. Lett*. **100**, 185501 (2008).

ADS Google Scholar

23. 23.

Bonati, L. & Parrinello, M. Silicon liquid structure and crystal nucleation from ab initio deep metadynamics. *Phys. Rev. Lett*. **121**, 265701 (2018).

ADS CAS Google Scholar

24. 24.

Bartók, A. P., Payne, M. C., Kondor, R. & Csányi, G. Gaussian approximation potentials: the accuracy of quantum mechanics, without the electrons. *Phys. Rev. Lett*. **104**, 136403 (2010).

ADS Google Scholar

25. 25.

Bartók, A. P., Kermode, J., Bernstein, N. & Csányi, G. Machine learning a general-purpose interatomic potential for silicon. *Phys. Rev. X* **8**, 041048 (2018).

Google Scholar

26. 26.

Deringer, V. L. et al. Realistic atomistic structure of amorphous silicon from machine-learning-driven molecular dynamics. *J. Phys. Chem. Lett*. **9**, 2879–2885 (2018).

CAS Google Scholar

27. 27.

Bernstein, N. et al. Quantifying chemical structure and machine-learned atomic energies in amorphous and liquid silicon. *Angew. Chem. Int. Ed*. **58**, 7057–7061 (2019).

CAS Google Scholar

28. 28.

Hejna, M., Steinhardt, P. J. & Torquato, S. Nearly hyperuniform network models of amorphous silicon. *Phys. Rev. B* **87**, 245204 (2013).

ADS Google Scholar

29. 29.

Dahal, D., Atta-Fynn, R., Elliott, S. R. & Biswas, P. Hyperuniformity and static structure factor of amorphous silicon in the infinite-wavelength limit. *J. Phys. Conf. Ser*. **1252**, 012003 (2019).

CAS Google Scholar

30. 30.

Jia, W. et al. Pushing the limit of molecular dynamics with ab initio accuracy to 100 million atoms with machine learning. In *SC' 20: Proc. Int. Conf. High Performance Computing, Networking, Storage and Analysis* (ed. Cuicchi, C.) 5 (2020).

31. 31.

Khaliullin, R. Z., Eshet, H., Kühne, T. D., Behler, J. & Parrinello, M. Nucleation mechanism for the direct graphite-to-diamond phase transition. *Nat. Mater*. **10**, 693–697 (2011).

ADS CAS PubMed PubMed Central Google Scholar

32. 32.

Bartók, A. P., Kondor, R. & Csányi, G. On representing chemical environments. *Phys. Rev. B* **87**, 184115 (2013).

ADS Google Scholar

33. 33.

De, S., Bartók, A. P., Csányi, G. & Ceriotti, M. Comparing molecules and solids across structural and alchemical space. *Phys. Chem. Chem. Phys*. **18**, 13754–13769 (2016).

CAS Google Scholar

34. 34.

Imai, M., Mitamura, T., Yaoita, K. & Tsuji, K. Pressure-induced phase transition of crystalline and amorphous silicon and germanium at low temperatures. *High Press. Res*. **15**, 167–189 (1996).

ADS Google Scholar

35. 35.

Moras, G. et al. Shear melting of silicon and diamond and the disappearance of the polyamorphic transition under shear. *Phys. Rev. Mater*. **2**, 083601 (2018).

CAS Google Scholar

36. 36.

Hu, J. Z. & Spain, I. L. Phases of silicon at high pressure. *Solid State Commun*. **51**, 263–266 (1984).

ADS CAS Google Scholar

37. 37.

Shanavas, K. V., Pandey, K. K., Garg, N. & Sharma, S. M. Computer simulations of crystallization kinetics in amorphous silicon under pressure. *J. Appl. Phys*. **111**, 063509 (2012).

ADS Google Scholar

38. 38.

Xu, M. et al. Pressure-induced crystallization of amorphous $Ge_2Sb_2Te_5$. *J. Appl. Phys*. **108**, 083519 (2010).

ADS Google Scholar

39. 39.

Wu, M., Tse, J. S., Wang, S. Y., Wang, C. Z. & Jiang, J. Z. Origin of pressure-induced crystallization of $Ce_{75}Al_{25}$ metallic glass. *Nat. Commun*. **6**, 6493 (2015).

ADS CAS Google Scholar

40. 40.

Sun, J., Ruzsinszky, A. & Perdew, J. P. Strongly constrained and appropriately normed semilocal density functional. *Phys. Rev. Lett*. **115**, 036402 (2015).

ADS Google Scholar

41. 41.

Stillinger, F. H. & Weber, T. A. Computer simulation of local order in condensed phases of silicon. *Phys. Rev. B* **31**, 5262–5271 (1985).

ADS CAS Google Scholar

42. 42.

Ben Mahmoud, C., Anelli, A., Csányi, G. & Ceriotti, M. Learning the electronic density of states in condensed matter. *Phys. Rev. B* (in the press).

43. 43.

Mott, N. F. & Davis, E. A. *Electronic Processes in Non-crystalline Materials* (Oxford Univ, Press, 2012).

44. 44.

Beye, M., Sorgenfrei, F., Schlotter, W. F., Wurth, W. & Fohlisch, A. The liquid–liquid phase transition in silicon revealed by snapshots of valence electrons. *Proc. Natl Acad. Sci. USA* **107**, 16772–16776 (2010).

ADS CAS Google Scholar

45. 45.

Barkalov, O. I. et al. Pressure-induced transformations and superconductivity of amorphous germanium. *Phys. Rev. B* **82**, 020507 (2010).

ADS Google Scholar

46. 46.

Mignot, J. M., Chouteau, G. & Martinez, G. High pressure superconductivity of silicon. *Physica B+C* **135**, 235–238 (1985).

ADS CAS Google Scholar

47. 47.

Helfrecht, B., Cersonsky, R. K., Fraux, G. & Ceriotti, M. Structure-property maps with Kernel principal covariates regression. *Mach. Learn. Sci. Technol*. **1**, 045021 (2020).

Google Scholar

48. 48.

Stukowski, A. Visualization and analysis of atomistic simulation data with OVITO–the Open Visualization Tool. *Model. Simul. Mater. Sci. Eng*. **18**, 015012 (2010).

ADS Google Scholar

49. 49.

Deringer, V. L. & Csányi, G. Machine learning based interatomic potential for amorphous carbon. *Phys. Rev. B* **95**, 094203 (2017).

ADS Google Scholar

50. 50.

Caro, M. A., Csányi, G., Laurila, T. & Deringer, V. L. Machine learning driven simulated deposition of carbon films: from low-density to diamondlike amorphous carbon. *Phys. Rev. B* **102**, 174201 (2020).

ADS CAS Google Scholar

51. 51.

Blöchl, P. E. Projector augmented-wave method. *Phys. Rev. B* **50**, 17953–17979 (1994).

ADS Google Scholar

52. 52.

Kresse, G. & Furthmüller, J. Efficient iterative schemes for ab initio total-energy calculations using a plane-wave basis set. *Phys. Rev. B* **54**, 11169–11186 (1996).

ADS CAS Google Scholar

53. 53.

Kresse, G. & Joubert, D. From ultrasoft pseudopotentials to the projector augmented-wave method. *Phys. Rev. B* **59**, 1758–1775 (1999).

ADS CAS Google Scholar

54. 54.

Deringer, V. L., Pickard, C. J. & Csányi, G. Data-driven learning of total and local energies in elemental boron. *Phys. Rev. Lett*. **120**, 156001 (2018).

ADS CAS Google Scholar

55. 55.

Harl, J. & Kresse, G. Accurate bulk properties from approximate many-body techniques. *Phys. Rev. Lett*. **103**, 056401 (2009).

ADS Google Scholar

56. 56.

Harl, J., Schimka, L. & Kresse, G. Assessing the quality of the random phase approximation for lattice constants and atomization energies of solids. *Phys. Rev. B* **81**, 115126 (2010).

ADS Google Scholar

57. 57.

Schimka, L. et al. Accurate surface and adsorption energies from many-body perturbation theory. *Nat. Mater*. **9**, 741–744 (2010).

ADS CAS Google Scholar

58. 58.

Bartók, A. P. et al. Machine-learning approach for one- and two-body corrections to density functional theory: applications to molecular and condensed water. *Phys. Rev. B* **88**, 054104 (2020).

ADS Google Scholar

59. 59.

Ramakrishnan, R. et al. Big data meets quantum chemistry approximations: the Δ-machine learning approach. *J. Chem. Theory Comput*. **11**, 2087–2096 (2015).

CAS Google Scholar

60. 60.

Bernstein, N., Csányi, G. & Deringer, V. L. De novo exploration and self-guided learning of potential-energy surfaces. *npj Comput. Mater*. **5**, 99 (2019).

ADS Google Scholar

61. 61.

Pickard, C. J. & Needs, R. J. High-pressure phases of silane. *Phys. Rev. Lett*. **97**, 045504 (2006).

ADS Google Scholar

62. 62.

Pickard, C. J. & Needs, R. J. Ab initio random structure searching. *J. Phys. Condens. Matter* **23**, 053201 (2011).

ADS Google Scholar

63. 63.

Perdew, J. P., Burke, K. & Ernzerhof, M. Generalized gradient approximation made simple. *Phys. Rev. Lett*. **77**, 3865–3868 (1996).

ADS CAS Google Scholar

64. 64.

Plimpton, S. Fast parallel algorithms for short-range molecular dynamics. *J. Comput. Phys*. **117**, 1–19 (1995).

ADS CAS MATH Google Scholar

65. 65.

Parrinello, M. & Rahman, A. Polymorphic transitions in single crystals: a new molecular dynamics method. *J. Appl. Phys*. **52**, 7182–7190 (1981).

ADS CAS Google Scholar

66. 66.

Martyna, G. J., Tobias, D. J. & Klein, M. L. Constant pressure molecular dynamics algorithms. *J. Chem. Phys*. **101**, 4177–4189 (1994).

ADS CAS Google Scholar

67. 67.

Shinoda, W., Shiga, M. & Mikami, M. Rapid estimation of elastic constants by molecular dynamics simulation under constant stress.

Phys. Rev. B **69**, 134103 (2004).

ADS Google Scholar

68. 68.

Bringuier, S. dump2VDOS.py. Python code http://www.u.arizona.edu/~stefanb/Codes/dump2VDOS.py (2014).

69. 69.

Drabold, D. A. & Sankey, O. F. Maximum entropy approach for linear scaling in the electronic structure problem. *Phys. Rev. Lett*. **70**, 3631–3634 (1993).

ADS CAS Google Scholar

70. 70.

Kwon, I., Biswas, R., Wang, C. Z., Ho, K. M. & Soukoulis, C. M. Transferable tight-binding models for silicon. *Phys. Rev. B* **49**, 7242–7250 (1994).

ADS CAS Google Scholar

71. 71.

Drabold, D. A., Li, Y., Cai, B. & Zhang, M. Urbach tails of amorphous silicon. *Phys. Rev. B* **83**, 045201 (2011).

ADS Google Scholar

72. 72.

Skilling, J. The eigenvalues of mega-dimensional matrices. In *Maximum Entropy and Bayesian Methods* (ed. Skilling, J.) 455–466 (Kluwer, 1989).

73. 73.

Jaynes, E. T. *Probability Theory: The Logic of Science* (Cambridge Univ. Press, 2003).

74. 74.

Mead, L. R. & Papanicolaou, N. Maximum entropy in the problem of moments. *J. Math. Phys*. **25**, 2404–2417 (1984).

ADS MathSciNet Google Scholar

75. 75.

Bandyopadhyay, K., Bhattacharya, A. K., Biswas, P. & Drabold, D. A. Maximum entropy and the problem of moments: a stable algorithm. *Phys. Rev. E* **71**, 057701 (2005).

ADS CAS Google Scholar

76. 76.

Weiße, A., Wellein, G., Alvermann, A. & Fehske, H. The kernel polynomial method. *Rev. Mod. Phys*. **78**, 275–306 (2006).

ADS MathSciNet MATH Google Scholar

77. 77.

Drabold, D. A., Ordejón, P., Dong, J. & Martin, R. M. Spectral properties of large fullerenes: from cluster to crystal. *Solid State Commun*. **96**, 833–838 (1995).

ADS CAS Google Scholar

78. 78.

Willatt, M. J., Musil, F. & Ceriotti, M. Feature optimization for atomistic machine learning yields a data-driven construction of the periodic table of the elements. *Phys. Chem. Chem. Phys*. **20**, 29661–29668 (2018).

CAS Google Scholar

79. 79.

Imbalzano, G. et al. Automatic selection of atomic fingerprints and reference configurations for machine-learning potentials. *J. Chem. Phys*. **148**, 241730 (2018).

ADS Google Scholar

80. 80.

Blum, V. et al. Ab initio molecular simulations with numeric atom-centered orbitals. *Comput. Phys. Commun*. **180**, 2175–2196 (2009).

ADS CAS MATH Google Scholar

81. 81.

Heyd, J., Scuseria, G. E. & Ernzerhof, M. Hybrid functionals based on a screened Coulomb potential. *J. Chem. Phys*. **118**, 8207–8215 (2003).

ADS CAS Google Scholar

82. 82.

Krukau, A. V., Vydrov, O. A., Izmaylov, A. F. & Scuseria, G. E. Influence of the exchange screening parameter on the performance of screened hybrid functionals. *J. Chem. Phys*. **125**, 224106 (2006).

ADS Google Scholar

83. 83.

Borlido, P. et al. Large-scale benchmark of exchange–correlation functionals for the determination of electronic band gaps of solids. *J. Chem. Theory Comput*. **15**, 5069–5079 (2019).

CAS PubMed PubMed Central Google Scholar

84. 84.

Musil, F., Willatt, M. J., Langovoy, M. A. & Ceriotti, M. Fast and accurate uncertainty estimation in chemical machine learning. *J. Chem. Theory Comput*. **15**, 906–915 (2019).

Google Scholar

85. 85.

Bundy, F. P. Phase diagrams of silicon and germanium to 200 kbar, 1000 °C. *J. Chem. Phys*. **41**, 3809–3814 (1964).

ADS CAS Google Scholar

86. 86.

Funamori, N. & Tsuji, K. Pressure-induced structural change of liquid silicon. *Phys. Rev. Lett*. **88**, 255508 (2002).

ADS Google Scholar

87. 87.

Dharma-wardana, M. W. C., Klug, D. D. & Remsing, R. C. Liquid-liquid phase transitions in silicon. *Phys. Rev. Lett*. **125**, 075702 (2020).

ADS CAS Google Scholar

88. 88.

Desgranges, C. & Delhommelle, J. Unraveling liquid polymorphism in silicon driven out-of-equilibrium. *J. Chem. Phys*. **153**, 054502 (2020).

CAS Google Scholar

89. 89.

Needs, R. J. & Martin, R. M. Transition from β-tin to simple hexagonal silicon under pressure. *Phys. Rev. B* **30**, 5390–5392 (1984).

ADS CAS Google Scholar

90. 90.

Laaziri, K. et al. High-energy X-ray diffraction study of pure amorphous silicon. *Phys. Rev. B* **60**, 13520–13533 (1999).

ADS CAS Google Scholar

Download references

Acknowledgements

V.L.D. acknowledges a Leverhulme Early Career Fellowship and support from the Isaac Newton Trust. Parts of the simulations reported here were carried out during his previous affiliation with the University of Cambridge (until August 2019). N.B. acknowledges support from the Office of Naval Research through the US Naval Research Laboratory's core basic research programme, and computer time through the US DOD HPCMPO at the AFRL DSRC. D.A.D. acknowledges support from the US NSF under award DMR 1506836. M.C. and C.B.M. acknowledge support by the Swiss National Science Foundation (project no. 200021-182057), and by the NCCR MARVEL, funded by the Swiss National Science Foundation. This work used the ARCHER UK National Supercomputing Service via a Resource Allocation Panel award (project e599) and the UKCP consortium (EPSRC grant EP/P022596/1). All structural drawings were created using OVITO[48]. We thank A. P. Bartók for technical help.

Author information

Author notes

1. Stephen R. Elliott

Present address: Trinity College, Cambridge, UK

Affiliations

1. Department of Chemistry, Inorganic Chemistry Laboratory, University of Oxford, Oxford, UK

   Volker L. Deringer

2. Center for Materials Physics and Technology, US Naval Research Laboratory, Washington, DC, USA

   Noam Bernstein

3. Engineering Laboratory, University of Cambridge, Cambridge, UK

   Gábor Csányi

4. Laboratory of Computational Science and Modeling, IMX, École Polytechnique Fédérale de Lausanne, Lausanne, Switzerland

   Chiheb Ben Mahmoud & Michele Ceriotti

5. National Centre for Computational Design and Discovery of Novel Materials (MARVEL), École Polytechnique Fédérale de Lausanne, Lausanne, Switzerland

   Chiheb Ben Mahmoud & Michele Ceriotti

6. Department of Chemistry, Physical and Theoretical Chemistry Laboratory, University of Oxford, Oxford, UK

   Mark Wilson

7. Department of Physics and Astronomy, Ohio University, Athens, OH, USA

   David A. Drabold

8. Department of Chemistry, University of Cambridge, Cambridge, UK

Stephen R. Elliott

Authors

1. Volker L. Deringer
View author publications

You can also search for this author in PubMed Google Scholar

2. Noam Bernstein
View author publications

You can also search for this author in PubMed Google Scholar

3. Gábor Csányi
View author publications

You can also search for this author in PubMed Google Scholar

4. Chiheb Ben Mahmoud
View author publications

You can also search for this author in PubMed Google Scholar

5. Michele Ceriotti
View author publications

You can also search for this author in PubMed Google Scholar

6. Mark Wilson
View author publications

You can also search for this author in PubMed Google Scholar

7. David A. Drabold
View author publications

You can also search for this author in PubMed Google Scholar

8. Stephen R. Elliott
View author publications

You can also search for this author in PubMed Google Scholar

Contributions

V.L.D., G.C. and S.R.E. initiated the project. V.L.D. and N.B. performed the ambient-pressure simulations; V.L.D. performed the high-pressure simulations; V.L.D., N.B. and G.C. carried out further validation with other machine learning potentials. D.A.D. performed the tight-binding electronic-structure computations. C.B.M. and M.C. performed the electronic DOS machine learning predictions and the KPCovR analysis. V.L.D., M.W., D.A.D. and S.R.E. analysed the data and developed the main conclusions regarding high-pressure phases. All authors contributed to discussions. V.L.D. drafted the paper, and all authors contributed to its final version.

Corresponding author

Correspondence to Volker L. Deringer.

Ethics declarations

Competing interests

G.C. is listed as an inventor on a patent filed by Cambridge Enterprise Ltd related to SOAP and GAP (US patent 8843509, filed on 5 June 2009 and published on 23 September 2014). The other authors declare no competing interests.

Additional information

Peer review information *Nature* thanks Davide Donadio, Paul McMillan and the other, anonymous, reviewer(s) for their contribution to the peer

review of this work.

Publisher's note Springer Nature remains neutral with regard to jurisdictional claims in published maps and institutional affiliations.

Extended data figures and tables

Extended Data Fig. 1 Machine learning-driven modelling beyond the nanometric length scale.

The fully relaxed a-Si structure with 100,000 atoms is shown. The smaller boxes on the left show the size of a 512-atom system from a recent study[26], marking the limit of current DFT methods for simulations over several nanoseconds, and that of a 4,096-atom system in our pilot GAP-MD studies[26]. All boxes are drawn to scale.

Extended Data Fig. 2 Compression of liquid silicon.

a, Overview of the transition pathways investigated in the present work. The quench (vitrification) and compression runs are discussed in the text. We focus here on additional data that we have collected for validation: namely, the description of the high-temperature liquid. We melted a structure at 1,800 K, above the melting point of diamond-type silicon, and then compressed it by simultaneously adapting the thermostat and barostat settings so as to trace the estimated phase coexistence lines given by Bundy[85], in analogy to ref. [86]. The temperature was reduced by 41 K GPa^{-1} to follow the diamond melting line, up to the estimated triple point at 15 GPa, after which the slope was inverted and followed the metallic silicon melting line (+14 K GPa^{-1})[85]. The compression rate was 0.5 GPa ps^{-1}. **b**, Structure factors of liquid silicon during this compression run. Computed values from our simulations (red) are overlaid on experimental reference data by Funamori and Tsuji[86] (black) for which the estimated temperatures are at about 50 K above the melting line[86], closely mirrored by our computations. In the original experimental work[86], arrows indicate the location of the maxima (labelled there as Q_1 and Q_2) and a shoulder in the

first peak (Q_h). The height of Q_h gradually diminishes at higher pressure, and all these features are correctly described by our simulations. In the context of liquid–liquid transitions, we mention in passing very recent density-functional[87] and empirical force-field based studies[88]; such research questions may become worthwhile targets for future GAP-driven studies as well. Reprinted figure with permission from ref. [86], copyright 2002 by the American Physical Society. Expt., experimental.

Extended Data Fig. 3 Vibrational densities of states (VDOS).

We obtained these by Fourier transformation of the velocity–velocity autocorrelation function, as described in Methods. Two characteristic features associated with the amorphous–amorphous transition under high pressure, observed in previous Raman spectroscopy experiments[10,11,12], are reproduced by these simulations. First, the peak at large wavenumbers persists throughout the LDA/HDA coexistence but then disappears entirely. Second, the VHDA formation is associated with the formation of another peak at intermediate wavenumbers. It is noted that this feature appears in both the simulated VHDA and the polycrystalline sh system. The predictions here might be tested, in the future, by combined in situ X-ray diffraction and Raman spectroscopy; the former technique will easily be able to distinguish VHDA silicon from crystalline phases.

Extended Data Fig. 4 Reproducibility of VHDA formation with a separate machine learning potential.

a, Snapshots from a compression simulation using the same starting structure and protocol as for the main result (Fig. 2a–e), but now using a newly fitted GAP machine learning model based on SCAN meta-GGA input data (Methods). This simulation confirms the structural collapse at high pressure, seen in the third panel, and the subsequent crystallization. The SCAN-level machine learning potential initially nucleated β-Sn-like crystallites ($N = 6$; red colour on the atoms), which is explained in the following. **b**, Energy–volume curves for relevant crystalline allotropes of silicon, computed using the GAP-18 model (based on PW91 data; top) and the new SCAN-based model (bottom). In both cases, the sequence of dia →

β-Sn-type → sh with increasing pressure (decreasing cell volume) is correctly reproduced, consistent with early DFT studies[89]. With SCAN, the β-Sn-like phase is favoured over a wider range of pressures; the crossover between the two $E(V)$ curves is indicated by arrows in both panels. Note that the absolute energies for both allotropes are very similar, leading to a delicate balance between both. **c**, Oblique view of the simulation cell from the SCAN simulation after reaching 20 GPa. Initially, β-tin-like crystallites had formed ($N = 6$; red); then, an sh grain emerged ($N = 8$; orange). Note that the absolute pressure values at which the subsequent transitions occur are slightly different between the GAP-18 (Fig. 2a–e) and SCAN (Extended Data Fig. 4a) simulations, but the VHDA phases and subsequent formation of polycrystalline phases are clearly observed in both. The same is not the case with an established, empirically fitted interatomic potential, as shown in Extended Data Fig. 6b.

Extended Data Fig. 5 Beyond-DFT modelling with a Δ-GAP machine learning fit.

a, Schematic illustration of the approach, as discussed in Methods. The key ideas are that: (i) the RPA potential-energy surface (PES) can only be sampled at selected points, because of the computational cost, and that: (ii) the difference Δ(RPA–DFT), indicated by red shading, varies more smoothly than the full PES and is therefore more easily amenable to a machine learning fit. **b**, Example structural snapshots from a GAP-RSS search[60]. We use such very-small simulation cells to represent large structural diversity in machine learning potential fitting where computational cost is at a premium. **c**, Quality-of-fit for the difference model, shown in the form of a scatter plot for the training data (blue) and a separate test set (green) of the machine learning prediction (vertical axis) against the 'ground truth' to be learned (horizontal axis). The distribution of the target values, σ, is given at the top left, alongside the root mean square error (RMSE) measures for training and testing set. **d**, Snapshots from a compression simulation using the same starting structure and protocol as for the GAP-18 (Fig. 2a–e) and SCAN (Extended Data Fig. 4) results, but now using the GAP-18 + Δ-GAP(RPA–DFT) difference machine learning potential. The collapse into VHDA is clearly reproduced, as is the

subsequent nucleation of crystallites; the result at 20 GPa is a poly-crystalline β-Sn-like phase (compare with Extended Data Fig. 4a).

Extended Data Fig. 6 Describing VHDA formation and crystallization requires quantum-accurate simulations.

a, The results of our machine learning-driven simulation, with the collapse to VHDA between 12 and 13 GPa, and the crystallization between 15 and 20 GPa (presented in Fig. 2 and shown here for comparison). **b**, As in **a**, now using the empirical Stillinger–Weber (SW) potential[41], which had been the state of the art for 100,000-atom simulations of silicon so far. Here, neither VHDA formation nor the subsequent crystallization are observed.

Extended Data Fig. 7 The enthalpy landscape of metastable disordered forms of silicon.

a, Computed enthalpy of 100,000-atom systems, ΔH, given relative to the respective most stable crystalline form at any given pressure (diamond-type → β-Sn-type → sh); see Methods. The red line shows the result for snapshots along the 500 K compression trajectory. Square symbols indicate results for snapshots, which have been frozen-in by rapid molecular-dynamics quenching (over 1 ps) and subsequently relaxed with a conjugate-gradient algorithm, all at the given external pressure (relevant structures are visualized below). The shaded area is a guide to the eye and corresponds to the enthalpy difference between the 500 K and fully relaxed a-Si structures at 0 GPa. Relevant structures are shown: note the near-perfect ordering of layers in the polycrystalline ('pc') sample. est., estimated; at^{-1}, per atom. **b**, Enthalpy changes associated with the structural changes during compression. Copies of the 10 GPa structure (LDA/HDA polyamorph) were relaxed with increased external pressure (open symbols); this direct relaxation fixes the structure in place and does not allow it to transform to VHDA. A direct comparison between two competing phases at 13 GPa is therefore possible (labelled as ΔH_1) and indicates the preference for VHDA formation. The enthalpy is lowered much further upon crystallization (ΔH_2). **c**, Relaxation of copies of the pc-sh structure with decreased external pressure, mirroring decompression of a sample in experiment. The relative

enthalpic stability over a relatively wide pressure range is qualitatively consistent with the observation of a hysteresis upon decompression: for example, in a previous work[10], the LDA phase was fully recovered only after decompression to about 4 GPa. A dashed vertical line in **b** and **c** emphasizes the change in the crystalline reference, from diamond-type (dia) to β-Sn-type silicon.

Extended Data Fig. 8 Computed structure factors.

a, The static structure factor, $S(q)$, as a probe for medium-range structural order, has been evaluated for the fully relaxed amorphous system. The computed result, including the height of the first sharp diffraction peak (FSDP), is in excellent agreement with previous experimental data[90]. The inset shows a radial distribution function, $g(r)$, for the same structure, indicating long-range correlations beyond the first nanometre, which our machine learning-driven simulations can access. A dashed line at approximately 11 Å illustrates the limit of DFT modelling (half the cell length of the smallest system sketched in Extended Data Fig. 1). Expt., experimental. **b**, Computed structure factors during quenching. Left, the evolution of simulated structure factors through the relevant part of the liquid-quenching trajectory in the vicinity of the glass transition, plotted in 1-K temperature increments. The emergence of the FSDP (between 1.5 and 2.0 $Å^{-1}$), as well as the structuring of the third peak (between 5 and 6 $Å^{-1}$), are clearly visible. Right, detail view for $1.0\ Å^{-1} \leq q \leq 4.0\ Å^{-1}$ of the evolution of the FSDP with decreasing temperature, using the same colour scale as on the left-hand side.

Extended Data Fig. 9 Tight-binding DOS for an ultralarge system.

Supplementing the tight-binding electronic-structure computations in Fig. 3a–d, this figure shows the electronic DOS computed with the same approach but for a diamond-type crystalline silicon supercell at atmospheric pressure, containing >2 million atoms (see details in Methods). The energy scale is set by ref. [70].

Rights and permissions

Reprints and Permissions

About this article

Check for updates

Cite this article

Deringer, V.L., Bernstein, N., Csányi, G. *et al.* Origins of structural and electronic transitions in disordered silicon. *Nature* **589,** 59–64 (2021). https://doi.org/10.1038/s41586-020-03072-z

Download citation

- Received: 14 December 2019
- Accepted: 12 November 2020
- Published: 06 January 2021
- Issue Date: 07 January 2021
- DOI: https://doi.org/10.1038/s41586-020-03072-z

Comments

By submitting a comment you agree to abide by our Terms and Community Guidelines. If you find something abusive or that does not comply with our terms or guidelines please flag it as inappropriate.

Access through your institution
Change institution

Buy or subscribe

Associated Content

Nature | News & Views

Machine learning reveals the complexity of dense amorphous silicon

- Paul F. McMillan

This article was downloaded by **calibre** from https://www.nature.com/articles/s41586-020-03072-z

- Article
- Published: 06 January 2021

Single-defect phonons imaged by electron microscopy

- Xingxu Yan ORCID: orcid.org/0000-0001-7991-4849[1,2],
- Chengyan Liu[3,4],
- Chaitanya A. Gadre[3],
- Lei Gu[3],
- Toshihiro Aoki ORCID: orcid.org/0000-0001-6620-9390[2],
- Tracy C. Lovejoy[5],
- Niklas Dellby[5],
- Ondrej L. Krivanek[5],
- Darrell G. Schlom ORCID: orcid.org/0000-0003-2493-6113[6,7,8],
- Ruqian Wu ORCID: orcid.org/0000-0002-6156-7874[3] &
- Xiaoqing Pan ORCID: orcid.org/0000-0002-0965-8568[1,2,3]

Nature **volume 589**, pages65–69(2021)Cite this article

- 1811 Accesses
- 14 Altmetric
- Metrics details

Subjects

- Characterization and analytical techniques
- Condensed-matter physics
- Transmission electron microscopy

Abstract

Crystal defects affect the thermal and heat-transport properties of materials by scattering phonons and modifying phonon spectra[1,2,3,4,5,6,7,8]. To appreciate how imperfections in solids influence thermal conductivity and diffusivity, it is thus essential to understand phonon–defect interactions. Sophisticated theories are available to explore such interactions, but experimental validation is limited because most phonon-detecting spectroscopic methods do not reach the high spatial resolution needed to resolve local vibrational spectra near individual defects. Here we demonstrate that space- and angle-resolved vibrational spectroscopy in a transmission electron microscope makes it possible to map the vibrational spectra of individual crystal defects. We detect a red shift of several millielectronvolts in the energy of acoustic vibration modes near a single stacking fault in cubic silicon carbide, together with substantial changes in their intensity, and find that these changes are confined to within a few nanometres of the stacking fault. These observations illustrate that the capabilities of a state-of-the-art transmission electron microscope open the door to the direct mapping of phonon propagation around defects, which is expected to provide useful guidance for engineering the thermal properties of materials.

Access through your institution
Change institution
Buy or subscribe

Access options

Subscribe to Journal

Get full journal access for 1 year

$199.00

only $3.90 per issue

Subscribe

All prices are NET prices.
VAT will be added later in the checkout.

Rent or Buy article

Get time limited or full article access on ReadCube.

from$8.99

Rent or Buy

All prices are NET prices.

Additional access options:

- Log in
- Access through your institution
- Learn about institutional subscriptions

Fig. 1: Experimental setup of high-spatial-resolution imaging and optimal-momentum-resolution vibrational spectroscopy of a single stacking fault in 3C-phase SiC.

Fig. 2: Vibrational spectra of SiC with and without a stacking fault and taken with wide and narrow momentum ranges.

Fig. 3: High-spatial-resolution mapping of acoustic phonon enhancement.

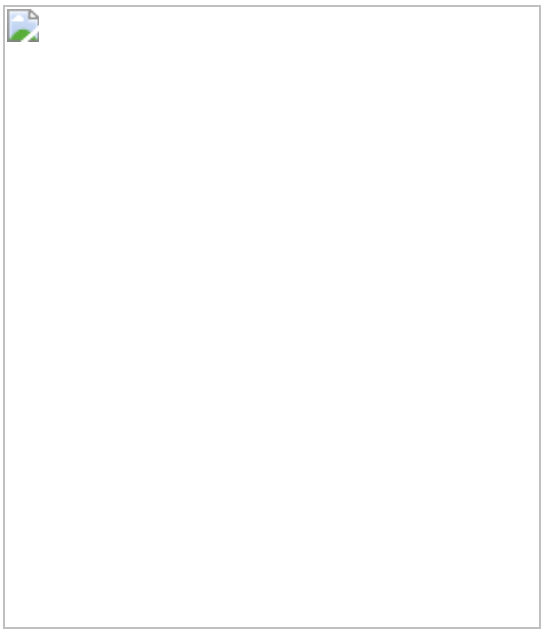

Fig. 4: Spatial distribution of individual phonon modes and the red energy shift of local phonon resonances under the angle-resolved condition.

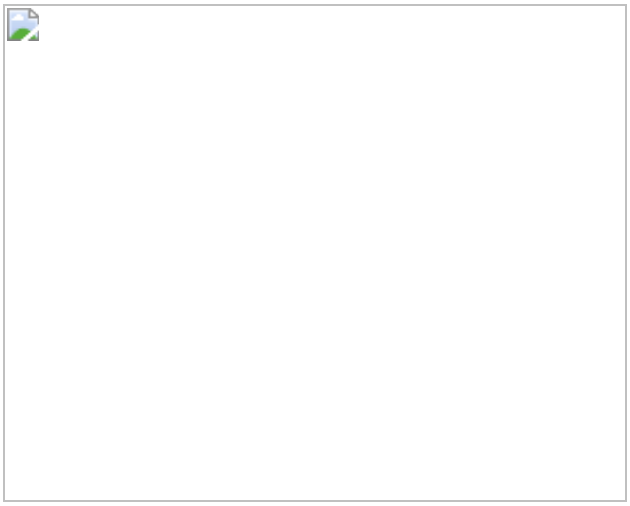

Data availability

The datasets generated during and/or analysed during the current study are available from the corresponding authors on reasonable request.

References

1. 1.

Krumhansl, J. A. Lattice vibrations in solids. *J. Appl. Phys*. **33**, 307–319 (1962).

ADS CAS MATH Google Scholar

2. 2.

Li, M. D. et al. Nonperturbative quantum nature of the dislocation phonon interaction. *Nano Lett*. **17**, 1587–1594 (2017).

ADS CAS Google Scholar

3. 3.

Walker, C. T. & Pohl, R. O. Phonon scattering by point defects. *Phys. Rev*. **131**, 1433–1442 (1963).

ADS CAS Google Scholar

4. 4.

Katcho, N. A., Carrete, J., Li, W. & Mingo, N. Effect of nitrogen and vacancy defects on the thermal conductivity of diamond: an ab initio Green's function approach. *Phys. Rev. B* **90**, 094117 (2014).

ADS Google Scholar

5. 5.

Klemens, P. G. The scattering of low-frequency lattice waves by static imperfections. *Proc. Phys. Soc. A* **68**, 1113–1128 (1955).

ADS MATH Google Scholar

6. 6.

Katre, A., Carrete, J., Dongre, B., Madsen, G. K. H. & Mingo, N. Exceptionally strong phonon scattering by B substitution in cubic SiC. *Phys. Rev. Lett*. **119**, 075902 (2017).

ADS Google Scholar

7. 7.

Singh, B. K., Menon, V. J. & Sood, K. C. Phonon conductivity of plastically deformed crystals: role of stacking faults and dislocations. *Phys. Rev. B* **74**, 184302 (2006).

ADS Google Scholar

8. 8.

Ohashi, K. & Ohashi, Y. Mean-square displacement of a vibrating dislocation. *Phil. Mag. A* **38**, 187–204 (1978).

ADS CAS Google Scholar

9. 9.

Pernot, G. et al. Precise control of thermal conductivity at the nanoscale through individual phonon-scattering barriers. *Nat. Mater*. **9**, 491–495 (2010).

ADS CAS Google Scholar

10. 10.

Huberman, S. et al. Observation of second sound in graphite at temperatures above 100 K. *Science* **364**, 375–379 (2019).

ADS CAS Google Scholar

11. 11.

Lindsay, L., Katre, A., Cepellotti, A. & Mingo, N. Perspective on ab initio phonon thermal transport. *J. Appl. Phys*. **126**, 050902 (2019).

ADS Google Scholar

12. 12.

Arrigoni, M., Carrete, J., Mingo, N. & Madsen, G. K. H. First-principles quantitative prediction of the lattice thermal conductivity in random semiconductor alloys: the role of force-constant disorder. *Phys. Rev. B* **98**, 115205 (2018).

ADS CAS Google Scholar

13. 13.

Carrete, J. et al. Phonon transport across crystal-phase interfaces and twin boundaries in semiconducting nanowires. *Nanoscale* **11**, 16007–16016 (2019).

CAS Google Scholar

14. 14.

Sheng, P. *Introduction to Wave Scattering, Localization and Mesoscopic Phenomena* (Springer Series in Materials Science Vol. 88, Springer, 2006).

15. 15.

McCreery, R. L. *Raman Spectroscopy for Chemical Analysis* (Chemical Analysis: a Series of Monographs on Analytical Chemistry and its Applications Vol. 157, Wiley, 2000).

16. 16.

Bechelany, M., Brioude, A., Cornu, D., Ferro, G. & Miele, P. A Raman spectroscopy study of individual SiC nanowires. *Adv. Funct. Mater*. **17**, 939–943 (2007).

CAS Google Scholar

17. 17.

Stuart, B. *Infrared Spectroscopy: Fundamentals and Applications* (Wiley, 2004).

18. 18.

Chan, K. L. A. & Kazarian, S. G. New opportunities in micro- and macro-attenuated total reflection infrared spectroscopic imaging: spatial resolution and sampling versatility. *Appl. Spectrosc*. **57**, 381–389 (2003).

ADS CAS Google Scholar

19. 19.

Maciel, I. O. et al. Electron and phonon renormalization near charged defects in carbon nanotubes. *Nat. Mater*. **7**, 878–883 (2008).

ADS CAS Google Scholar

20. 20.

Burkel, E. Phonon spectroscopy by inelastic x-ray scattering. *Rep. Prog. Phys*. **63**, 171–232 (2000).

ADS CAS Google Scholar

21. 21.

Mitchell, P. C. H. *Vibrational Spectroscopy with Neutrons: with Applications in Chemistry, Biology, Materials Science and Catalysis* Vol. 3 (World Scientific, 2005).

22. 22.

Stipe, B. C., Rezaei, M. A. & Ho, W. Single-molecule vibrational spectroscopy and microscopy. *Science* **280**, 1732–1735 (1998).

ADS CAS Google Scholar

23. 23.

Altfeder, I. et al. Scanning tunneling microscopy observation of phonon condensate. *Sci. Rep*. **7**, 43214 (2017).

ADS CAS PubMed PubMed Central Google Scholar

24. 24.

Krivanek, O. L. et al. Vibrational spectroscopy in the electron microscope. *Nature* **514**, 209–212 (2014).

ADS CAS Google Scholar

25. 25.

Hachtel, J. A. et al. Identification of site-specific isotopic labels by vibrational spectroscopy in the electron microscope. *Science* **363**, 525–528 (2019).

ADS CAS Google Scholar

26. 26.

Hage, F., Kepaptsoglou, D., Ramasse, Q. & Allen, L. Phonon spectroscopy at atomic resolution. *Phys. Rev. Lett*. **122**, 016103 (2019).

ADS CAS Google Scholar

27. 27.

Lagos, M. J., Trügler, A., Hohenester, U. & Batson, P. E. Mapping vibrational surface and bulk modes in a single nanocube. *Nature* **543**, 529–532 (2017).

ADS CAS Google Scholar

28. 28.

Govyadinov, A. A. et al. Probing low-energy hyperbolic polaritons in van der Waals crystals with an electron microscope. *Nat. Commun*. **8**, 95 (2017).

ADS PubMed PubMed Central Google Scholar

29. 29.

Venkatraman, K., Rez, P., March, K. & Crozier, P. A. The influence of surfaces and interfaces on high spatial resolution vibrational EELS from SiO_2. *Microscopy* **67**, i14–i23 (2018).

CAS Google Scholar

30. 30.

Hage, F. S. et al. Nanoscale momentum-resolved vibrational spectroscopy. *Sci. Adv*. **4**, eaar7495 (2018).

ADS PubMed PubMed Central Google Scholar

31. 31.

Rez, P. et al. Damage-free vibrational spectroscopy of biological materials in the electron microscope. *Nat. Commun*. **7**, 10945 (2016); erratum **7**, 11592 (2016).

ADS CAS PubMed PubMed Central Google Scholar

32. 32.

Dwyer, C. et al. Electron-beam mapping of vibrational modes with nanometer spatial resolution. *Phys. Rev. Lett*. **117**, 256101 (2016).

ADS CAS Google Scholar

33. 33.

Lindefelt, U., Iwata, H., Öberg, S. & Briddon, P. R. Stacking faults in 3C-, 4H-, and 6H-SiC polytypes investigated by an ab initio supercell method. *Phys. Rev. B* **67**, 155204 (2003).

ADS Google Scholar

34. 34.

Goela, J. S., Brese, N. E., Burns, L. E. & Pickering, M. A. in *High Thermal Conductivity Materials* (eds Shindé, S. L. & Goela, J. S.) 167–198 (Springer, 2006).

35. 35.

Yamasaki, J., Inamoto, S., Nomura, Y., Tamaki, H. & Tanaka, N. Atomic structure analysis of stacking faults and misfit dislocations at 3C-SiC/Si(001) interfaces by aberration-corrected transmission electron microscopy. *J. Phys. D* **45**, 494002 (2012).

Google Scholar

36. 36.

Stevens, R. Defects in silicon carbide. *J. Mater. Sci*. **7**, 517–521 (1972).

ADS CAS Google Scholar

37. 37.

Williams, D. B. & Carter, C. B. *Transmission Electron Microscopy: a Textbook for Materials Science* Vol. 2 (Springer Science & Business Media, 2009).

38. 38.

Nienhaus, H., Kampen, T. U. & Mönch, W. Phonons in 3C-SiC, 4H-SiC, and 6H-SiC. *Surf. Sci*. **324**, L328–L332 (1995).

ADS CAS Google Scholar

39. 39.

Serrano, J. et al. Determination of the phonon dispersion of zinc blende (3C) silicon carbide by inelastic X-ray scattering. *Appl. Phys. Lett*. **80**, 4360–4362 (2002).

ADS CAS Google Scholar

40. 40.

Strauch, D. et al. Phonons in SiC from INS, IXS, and ab-initio calculations. *Mater. Sci. Forum* **527–529**, 689–694 (2006).

Google Scholar

41. 41.

Yan, X. et al. Unexpected strong thermally induced phonon energy shift for mapping local temperature. *Nano Lett*. **19**, 7494–7502 (2019).

ADS CAS Google Scholar

42. 42.

Lourenço-Martins, H. & Kociak, M. Vibrational surface electron-energy-loss spectroscopy probes confined surface-phonon modes. *Phys. Rev. X* **7**, 041059 (2017).

Google Scholar

43. 43.

Venkatraman, K., Levin, B. D. A., March, K., Rez, P. & Crozier, P. A. Vibrational spectroscopy at atomic resolution with electron impact scattering. *Nat. Phys*. **15**, 1237–1241 (2019).

CAS Google Scholar

44. 44.

Senga, R. et al. Position and momentum mapping of vibrations in graphene nanostructures. *Nature* **573**, 247–250 (2019).

ADS CAS Google Scholar

45. 45.

Koch, C. T. *Determination of Core Structure Periodicity and Point Defect Density along Dislocations*. DPhil thesis, Arizona State University (2002).

46. 46.

Kresse, G. & Hafner, J. Ab initio molecular dynamics for liquid metals. *Phys. Rev. B* **47**, 558–561 (1993).

ADS CAS Google Scholar

47. 47.

Kresse, G. & Hafner, J. Ab initio molecular-dynamics simulation of the liquid-metal amorphous-semiconductor transition in germanium. *Phys. Rev. B* **49**, 14251–14269 (1994).

ADS CAS Google Scholar

48. 48.

Kresse, G. & Joubert, D. From ultrasoft pseudopotentials to the projector augmented-wave method. *Phys. Rev. B* **59**, 1758–1775 (1999).

ADS CAS Google Scholar

49. 49.

Monkhorst, H. J. & Pack, J. D. Special points for Brillouin-zone integrations. *Phys. Rev. B* **13**, 5188–5192 (1976).

ADS MathSciNet Google Scholar

50. 50.

Togo, A., Oba, F. & Tanaka, I. First-principles calculations of the ferroelastic transition between rutile-type and $CaCl_2$-type SiO_2 at high pressures. *Phys. Rev. B* **78**, 134106 (2008).

ADS Google Scholar

51. 51.

Gonze, X. & Lee, C. Dynamical matrices, Born effective charges, dielectric permittivity tensors, and interatomic force constants from density-functional perturbation theory. *Phys. Rev. B* **55**, 10355–10368 (1997).

ADS CAS Google Scholar

52. 52.

Giannozzi, P., de Gironcoli, S., Pavone, P. & Baroni, S. Ab initio calculation of phonon dispersions in semiconductors. *Phys. Rev. B* **43**, 7231–7242 (1991).

ADS CAS Google Scholar

53. 53.

Henry, C. H. & Hopfield, J. J. Raman scattering by polaritons. *Phys. Rev. Lett*. **15**, 964–966 (1965).

ADS CAS Google Scholar

54. 54.

García de Abajo, F. L. Optical excitations in electron microscopy. *Rev. Mod. Phys*. **82**, 209–275 (2010).

ADS Google Scholar

55. 55.

Wang, T., Carrete, J., van Roekeghem, A., Mingo, N. & Madsen, G. K. H. Ab initio phonon scattering by dislocations. *Phys. Rev. B* **95**, 245304 (2017).

ADS Google Scholar

Download references

Acknowledgements

The experimental work was supported by the Department of Energy (DOE), Office of Basic Energy Sciences, Division of Materials Sciences and Engineering under grant DESC0014430. DFT studies were supported by the US Department of Energy (grant no. DE-FG02-05ER46237) and the National Energy Research Scientific Computing Center (NERSC). This research was partially supported by the NSF through the University of California-Irvine Materials Research Science and Engineering Center (grant no. DMR-2011967). We thank Z. Cheng and S. Graham (Georgia Institute of Technology) and Q. Ramasse (SuperSTEM Laboratory) for their constructive suggestions. TEM experiments were conducted using the facilities in the Irvine Materials Research Institute (IMRI) at the University of California, Irvine.

Author information

Affiliations

1. Department of Materials Science and Engineering, University of California, Irvine, Irvine, CA, USA

Xingxu Yan & Xiaoqing Pan

2. Irvine Materials Research Institute, University of California, Irvine, Irvine, CA, USA

   Xingxu Yan, Toshihiro Aoki & Xiaoqing Pan

3. Department of Physics and Astronomy, University of California, Irvine, Irvine, CA, USA

   Chengyan Liu, Chaitanya A. Gadre, Lei Gu, Ruqian Wu & Xiaoqing Pan

4. Key Laboratory for Special Functional Materials of Ministry of Education, School of Materials Science and Engineering, Henan University, Kaifeng, China

   Chengyan Liu

5. Nion R&D, Kirkland, WA, USA

   Tracy C. Lovejoy, Niklas Dellby & Ondrej L. Krivanek

6. Department of Materials Science and Engineering, Cornell University, Ithaca, NY, USA

   Darrell G. Schlom

7. Kavli Institute at Cornell for Nanoscale Science, Ithaca, NY, USA

   Darrell G. Schlom

8. Leibniz-Institut für Kristallzüchtung, Berlin, Germany

   Darrell G. Schlom

Authors

1. Xingxu Yan

View author publications

You can also search for this author in PubMed Google Scholar

2. Chengyan Liu
   View author publications

   You can also search for this author in PubMed Google Scholar

3. Chaitanya A. Gadre
   View author publications

   You can also search for this author in PubMed Google Scholar

4. Lei Gu
   View author publications

   You can also search for this author in PubMed Google Scholar

5. Toshihiro Aoki
   View author publications

   You can also search for this author in PubMed Google Scholar

6. Tracy C. Lovejoy
   View author publications

   You can also search for this author in PubMed Google Scholar

7. Niklas Dellby
   View author publications

   You can also search for this author in PubMed Google Scholar

8. Ondrej L. Krivanek
   View author publications

   You can also search for this author in PubMed Google Scholar

9. Darrell G. Schlom
View author publications

You can also search for this author in PubMed Google Scholar

10. Ruqian Wu
View author publications

You can also search for this author in PubMed Google Scholar

11. Xiaoqing Pan
View author publications

You can also search for this author in PubMed Google Scholar

Contributions

X.Y., R.W. and X.P. conceived this project and designed the studies. X.Y. performed STEM-EELS experiments. X.Y. and C.A.G. analysed EELS data. C.L., L.G. and R.W. designed and performed the theoretical simulations. T.A., T.C.L., N.D. and O.L.K. set up the angular resolved condition with high-energy-resolution EELS. The SiC films were provided by D.G.S. All authors discussed and commented on the results. The manuscript was prepared by X.Y., C.L., C.A.G., O.L.K., R.W. and X.P., with contributions from all other co-authors.

Corresponding authors

Correspondence to Ruqian Wu or Xiaoqing Pan.

Ethics declarations

Competing interests

T.C.L., N.D. and O.L.K. declare a financial interest in Nion Company.

Additional information

Peer review information *Nature* thanks Kazu Suenaga and the other, anonymous, reviewer(s) for their contribution to the peer review of this work.

Publisher's note Springer Nature remains neutral with regard to jurisdictional claims in published maps and institutional affiliations.

Extended data figures and tables

Extended Data Fig. 1 STEM observations of 3C-phase SiC showing stacking faults.

The SiC was grown on a Si(001) wafer. **a**, **b**, High-angle (**a**) and medium-angle (**b**) ADF-STEM of SiC along [01\(\bar{ 1} \)]. The medium-angle condition is more sensitive to the defect structure, owing to the contribution of diffraction contrast, and hence the stacking faults and other defects have a stronger contrast in **b**. The SiC film was epitaxially grown on an (001) plane of the Si wafer. The stacking faults form along the <111> direction with angles of 54.7° with respect to the interface between SiC and Si. **c**, Atomic-resolution high-angle ADF-STEM image of the SiC–Si interface along [01\(\bar{ 1} \)]. Owing to the large lattice mismatch of 24.5% between film and substrate (a_{SiC} = 0.543 nm and a_{Si} = 0.436 nm), many structural defects, including multiple stacking faults (arrowed), are generated from the interface. **d**, Low-magnification medium-angle ADF-STEM image with marked electron beam locations for acquiring the aloof, SiC and SiC-SF vibrational spectra shown in main-text Fig. 2a. **e**, HAADF STEM image of one stacking fault with a large field of view acquired with a convergence semi-angle of 33 mrad and an ADF detector collection semi-angle of 70–210 mrad. **f**, Vertically integrated intensity profile along the blue box in **e**. The grey dots are average intensity and used in the line profile of the ADF intensity in main-text Fig. 3b. The average intensities of the atomic columns are uniform except the region near the stacking fault.

Extended Data Fig. 2 Relationship of the diffraction pattern and the FBZ in defect-free SiC and in a region containing a stacking fault.

a, **b**, Convergent beam diffraction patterns of defect-free SiC (**a**) and a stacking-fault region (**b**) taken with a 3 mrad convergence semi-angle. The additional diffuse scattering signal marked by the blue arrow in **b** is correlated with the stacking-fault structure and local symmetry breaking. **c**, **d**, Reciprocal space diagrams, including the diffraction pattern and the location of the FBZ (blue contours), corresponding to **a** and **b**, respectively. For the stacking fault, a 2H phase is used to simulate the phonon dispersion relations in **d**. Although the X point in 3C phase is outside the FBZ of 2H phase, an equivalent path to Γ–X is indicated by the red lines along Γ–P–X′, in which X′ is at the edge of the FBZ of the 2H-SiC structure and has coordinates of (1/2, 0, 2/3) in fractions of reciprocal lattice vectors ($\mathbf{g_1}$, $\mathbf{g_2}$, $\mathbf{g_3}$) of 2H phase. $\mathbf{g_1}$ and $\mathbf{g_3}$ are in-plane reciprocal lattice vectors and indicated as two arrows, while $\mathbf{g_2}$ is out-of-plane and not indicated here.

Extended Data Fig. 3 Interaction between the energy–momentum relation for fast electrons and the phonon dispersion curves of SiC.

a, The energy–momentum (E–q) relation for fast electrons (red line) along with the calculated phonon dispersion curves of 3C-phase SiC (black lines), which are duplicated from main-text Fig. 2b. The E–q relation for fast electrons follows $E = \hbar v q$ in the long-wavelength range, where ħ is the reduced Planck constant and $v = 1.34 \times 10^8$ m s^{-1} is the velocity of fast electrons for an accelerating voltage of 60 kV. Because the red line is near-vertical, we show in **b** and **c** enlarged sections of **a** for clarity. **b**, Enlarged plot to show intersections between the E–q relation for fast electrons and the optical branches. [00q] denotes the direction towards the X point and parallel to [001] with a momentum of q. **c**, Enlarged plot of the corner of the Γ point with very small energy and momentum. To further clarify the E–q relation for fast electrons at this small momentum, the energy is divided by 1,000 as indicated by the red dashed line. The polariton mode occurs

when the E–q relation of the fast electrons intersects the phonon dispersion curves[53,54]. Owing to the high speed of fast electrons, their E–q relation is very close to the vertical line at the Γ point, and intersects with LO and TO branches (shown in **b**), but does not have any non-zero intersections with either LA or TA branches (as shown in **c**) because of their slow velocities (9.5×10^3 m s^{-1} and 4.1×10^3 m s^{-1} for LA and TA in 3C-phase SiC, respectively).

Extended Data Fig. 4 Vibrational spectra of defect-free SiC and of a region containing a stacking fault obtained using a convergence semi-angle (α) of 10 mrad.

a, Diffraction pattern of defect-free SiC along the [01\(\bar{ 1} \)] direction with α = 10 mrad. The blue contour is the FBZ. 200, 111 and 1\(\bar{ 1} \bar{ 1} \) diffraction spots are marked by orange circles with a radius of 10 mrad. The small red circle indicates the location of the EELS entrance aperture with a collection semi-angle of 2.5 mrad, which is at the X point to avoid the polariton mode. **b**, Vibrational spectra of defect-free SiC (black curve) and a stacking-fault-containing region (SiC-SF, red curve) with α = 10 mrad. Background-subtracted vibrational spectra in **b** are almost identical to the data obtained using 33 mrad in Fig. 2a. The TA signal (at 30–50 meV) in the spectrum of stacking-fault region is slightly stronger than that in the spectrum of the defect-free region, which is also consistent with the observed discrepancy using 33 mrad in Fig. 2a.

Extended Data Fig. 5 Spatially resolved simulation of projected PDOS across a stacking fault.

a, Eleven-layer atomic structure for the simulation, comprising 3C-phase SiC with a two-layer stacking fault (purple) in the middle. The number of each layer is given on the left-hand side. **b**, Projected PDOS plots corresponding to individual layers in the atomic structure. The two simulated spectra in main-text Fig. 2c are from the stacking fault (purple curve) and from the defect-free region (green curve). These results even reproduced the 4-meV red shift of the TA mode centre in the stacking fault. **c**, Reciprocal space diagram illustrating the location of the FBZ of the 11-

layer defect structure in **a** (orange contour) along with FBZs of the 3C-phase structure (light blue contour) and the 2H-phase structure (blue contour). The X″ point is equivalent to the X point of the 3C structure and positioned at the edge of the new FBZ with coordinates (1/2, 0, 1/6) in fractions of reciprocal lattice vectors ($\mathbf{g_1}$, $\mathbf{g_2}$, $\mathbf{g_3}'$) of the 11-layer defect structure. $\mathbf{g_1}$ and $\mathbf{g_3}'$ are in-plane reciprocal lattice vectors as indicated by two arrows, while $\mathbf{g_2}$ is out-of-plane and not indicated here. The X″ point was further used to calculate the angle-resolved vibrational spectra. **d**, Integrated signal of the TA mode in the projected PDOS spectra in the energy range 30–40 meV.

Extended Data Fig. 6 Angle-resolved vibrational spectra along X→Γ′ and phonon dispersions of all phonon branches in the defect-free SiC as well as aloof spectra of SiC film using a convergence semi-angle of 3 mrad.

a, Diffraction pattern of SiC with annotations including the FBZ (solid blue contour) and selected momentum positions of the EELS entrance aperture (red circles) along X→Γ′, where Γ′ is the centre of the adjacent BZ (dashed blue contour). **b**, Angle-resolved vibrational spectra along X→Γ′. The TA (red), LA (blue), TO (green) and LO (orange) modes are separated after multi-Gaussian peak fitting. Four dashed lines are guides to the eye to show the shift of corresponding modes at different momentum positions. The value of momentum q is the reciprocal distance from the selected position to Γ′. **c**, Experimental phonon dispersion relation of the phonon energy (red points) from **b**, superimposed with the simulated phonon dispersion curves (black curves). In order to exclude the surface phonon polariton signal, the angle-resolved line-scan was acquired along X→Γ′ in the adjacent BZ rather than the FBZ. On the basis of the equivalence of each BZ, the angle-resolved phonon information along X→Γ′ should be identical to that along X→Γ. At the Γ′ point ($q = 0$ Å^{-1}), the LO and TO modes can be distinguished in the raw spectrum without the presence of the polariton signal, which is due to the long wavelength dipole scattering. TA and LA modes can also be detected at most momentum positions as shown in **b**, but were not easily separable at $q = 0.36$ Å^{-1} because of their energy difference being smaller than the energy resolution. The experimental peak locations

of all four branches are consistent with theoretical phonon dispersion curves as shown in **c**. The discrepancy between experiment and theory is much reduced compared to previous work[30], thanks to the improved energy resolution. **d**, Aloof spectra of SiC film with different momentum exchanges by angle-resolved vibrational spectroscopy. The convergence semi-angle was 3 mrad and spectra were obtained at the Γ point (centre of FBZ, red curve) and the X point (black curve) of the SiC film. Spectra were acquired when the electron beam was 20 nm from the surface of the SiC sample. The intensity of the X point spectrum is multiplied by 1,000. The polariton mode only appears in the aloof spectrum of the Γ point, which is consistent with the aloof spectrum acquired at large convergence semi-angle in main-text Fig. 2a.

Extended Data Fig. 7 Contribution of local atomic vibrations at a stacking fault along three orthogonal directions.

a, Atomic structure of an 11-layer defect structure, showing **x**, **y** and **z** directions. The electron beam (e-beam) direction is parallel to the **x** direction in our experimental setup. **b**–**e**, Bubble plots of phonon dispersion of the structure shown in **a** along the Γ to X″ direction with the contribution of local atomic vibrations at the stacking fault (inside purple box) in all directions (**b**, black dots), and along **x** (**c**, red dots), **y** (**d**, blue dots) and **z** (**e**, green dots) directions. The X″ point is the same as shown in Extended Data Fig. 5c. The size of each dot (the 'bubble') represents the local vibrational density of states at the stacking-fault region. The density of states was calculated by summing the square of an eigenvector's amplitude for selected phonon modes and directions. In **b**–**e**, the calculated phonon dispersion curves are added as dashed curves. Vibrations along the electron beam direction (the **x** direction in **a** and **c**) cannot be detected in our experimental setup[44]. As a result, the vibrational spectrum at the stacking fault should comprise vibrations moving along both **y** and **z** directions in **d** and **e**.

Extended Data Fig. 8 Atomic structure of simulated models and corresponding phonon dispersion curves.

a, 4 × 4 × 4 supercell of 3C SiC. **b**, 3 × 3 × 3 supercell of 2H SiC. **c**, Simulated phonon dispersion curves of 2H SiC (red) superimposed with those of 3C phase (black) in the Γ–X direction. The 2H phase was used to mimic the stacking-fault structure, and the Γ–P–X′ path in the 2H phase is identical to the Γ–X path in 3C phase, as mentioned in Extended Data Fig. 2. **d**, Energy positions of simulated phonon modes of the stacking fault (SiC-SF) and defect-free 3C-phase SiC in **c** at the X point. **e**, Vibrational spectra of defect-free SiC (black) and the stacking-fault region (red) with a convergence semi-angle of 3 mrad at the Δ point, which is the midpoint of the Γ–X line. The location of the Δ point is marked by a violet bar in **c**.

Extended Data Fig. 9 Spatial distribution of local phonon resonances.

a, Top panel, the TA (red dots) and LA (blue dots) signals were integrated in the respective energy ranges 45–50 meV and 70–75 meV using the spectrum image data in main-text Fig. 4b, and overlaid with Gaussian-type fitting curves. 'Nor.' means normalized with respect to the height of the ZLP in each spectrum. Bottom panel, ADF intensity of the STEM image in main-text Fig. 4a. **b**, Fitting of the signal intensity of TA as a function of the distance to the stacking fault. Red dots are duplicated from the positive *x*-axis data of the integrated intensity in the energy range 45–50 meV in **a**. The fitting function is indicated near the red dashed fitting curve, where *y* is the signal intensity, and *x* is the distance to the stacking fault. We estimated the decay length of the defect phonon mode near the stacking fault according to the one-dimensional Schrödinger equation for the quasiparticle (the defect phonon at the X point). The wavefunction (ψ) of the defect mode should decay exponentially outside the fault, following $\psi(x) = A\exp(-x/\xi)$, where *x* is the distance away from the stacking fault and *A* is a coefficient. The localization length, ξ, depends on the energy difference between the defect mode and corresponding TA mode in the defect-free region, ΔE_{Ph} (3.8 meV in this case), and can be estimated from \(1/\xi =\sqrt{ 2{ m} ^{ * } \Delta { E} _{ { \rm{ Ph} } } } /\hbar \), where m^* is the effective mass of the defect mode and $\hbar$ is the reduced Planck constant. Taking the effective mass from the phonon dispersion curve of 3C-phase SiC at the X point ($m^* \approx 2.03 \times 10^{-28}$ kg, only absolute values in the square root), ξ is about 2.7 nm. This is close to the experimental observation,

4.6 nm, obtained through a fitting as shown in **b**. It appears that the relationship $1/\xi =\sqrt{ 2{ m} ^{ * } \Delta { E} _{ { \rm{ Ph} } } } /\hbar$ holds well for estimating the decay length of local phonon modes.

Extended Data Fig. 10 Local PDOS of the defect structure calculated by the real-space Green's function approach.

a, Projected PDOS plots corresponding to individual layers in a 42-layer structure at the X point. This structure was constructed by inserting a 2-layer stacking-fault structure into a periodic 3C-bulk SiC of 40 layers (each layer was designed as in Extended Data Fig. 5a, and the thickness of the 42-layer structure is about 10.5 nm). The stacking-fault structure was inserted at layers L21 and L22, marked on the right-hand side. Then, the retarded Green's function was calculated at the specific momentum, and simulation details followed the procedure in the literature[55]. The simulated results were broadened with a Gaussian peak of 8 meV FWHM, resulting in all curves as shown. **b**, Peak centre of the 40–50 meV TA mode as a function of distance to the stacking fault. This result predicted a 4-meV red shift of TA modes at 40–50 meV in **a**. Also, the variation extended to a distance of 1.125 nm around the stacking fault and affects a region 2.25 nm wide in total, which is much broader than the size of the stacking fault (0.25 nm). This broadening is closer to our experimental observation than the DFT results in Extended Data Fig. 5b.

Rights and permissions

Reprints and Permissions

About this article

Check for updates

Cite this article

Yan, X., Liu, C., Gadre, C.A. *et al.* Single-defect phonons imaged by electron microscopy. *Nature* **589,** 65–69 (2021). https://doi.org/10.1038/s41586-020-03049-y

Download citation

- Received: 27 October 2019
- Accepted: 07 October 2020
- Published: 06 January 2021
- Issue Date: 07 January 2021
- DOI: https://doi.org/10.1038/s41586-020-03049-y

Comments

By submitting a comment you agree to abide by our Terms and Community Guidelines. If you find something abusive or that does not comply with our terms or guidelines please flag it as inappropriate.

Access through your institution
Change institution
Buy or subscribe

This article was downloaded by **calibre** from https://www.nature.com/articles/s41586-020-03049-y

- Article
- Published: 06 January 2021

Poleward and weakened westerlies during Pliocene warmth

- Jordan T. Abell ORCID: orcid.org/0000-0002-2458-8844[1,2],
- Gisela Winckler ORCID: orcid.org/0000-0001-8718-2684[1,2],
- Robert F. Anderson ORCID: orcid.org/0000-0002-8472-2494[1,2] &
- Timothy D. Herbert ORCID: orcid.org/0000-0003-1556-4290[3]

Nature **volume 589**, pages70–75(2021)Cite this article

- 831 Accesses
- 162 Altmetric
- Metrics details

Subjects

- Palaeoceanography
- Palaeoclimate

Abstract

The prevailing mid-latitude westerly winds, known as the westerlies, are a fundamental component of the climate system because they have a crucial role in driving surface ocean circulation[1] and modulating air–sea heat, momentum and carbon exchange[1,2,3]. Recent work suggests that westerly wind belts are migrating polewards in response to anthropogenic forcing[4,5]. Reconstructing the westerlies during past warm periods such as the

Pliocene epoch, in which atmospheric carbon dioxide (CO_2) was about 350 to 450 parts per million[6] and temperatures were about 2 to 4 degrees Celsius higher than today[7], can improve our understanding of changes in the position and strength of these wind systems as the climate continues to warm. Here we show that the westerlies were weaker and more poleward during the warm Pliocene than during glacial periods after the intensification of Northern Hemisphere glaciation (iNHG), which occurred around 2.73 million years ago[8]. Our results, which are based on dust and export productivity reconstructions, indicate that major ice sheet development during the iNHG was accompanied by substantial increases in dust fluxes in the mid-latitude North Pacific Ocean, especially compared to those in the subarctic North Pacific. Following this shift, changes in dust and productivity largely track the glacial–interglacial cycles of the late Pliocene and early Pleistocene epochs. On the basis of this pattern, we infer that shifts in the westerlies were primarily driven by variations in Plio-Pleistocene thermal gradients and ice volume. By combining this relationship with other dust records[9,10,11] and climate modelling results[12], we find that the proposed changes in the westerlies were globally synchronous. If the Pliocene is predictive of future warming, we posit that continued poleward movement and weakening of the present-day westerlies in both hemispheres can be expected.

Access through your institution
Change institution
Buy or subscribe

Access options

Subscribe to Journal

Get full journal access for 1 year

$199.00

only $3.90 per issue

Subscribe

All prices are NET prices.
VAT will be added later in the checkout.

Rent or Buy article

Get time limited or full article access on ReadCube.

from$8.99

Rent or Buy

All prices are NET prices.

Additional access options:

- Log in
- Access through your institution
- Learn about institutional subscriptions

Fig. 1: Dust flux reconstructions from the Pliocene North Pacific indicate shifts in the westerlies after the iNHG.

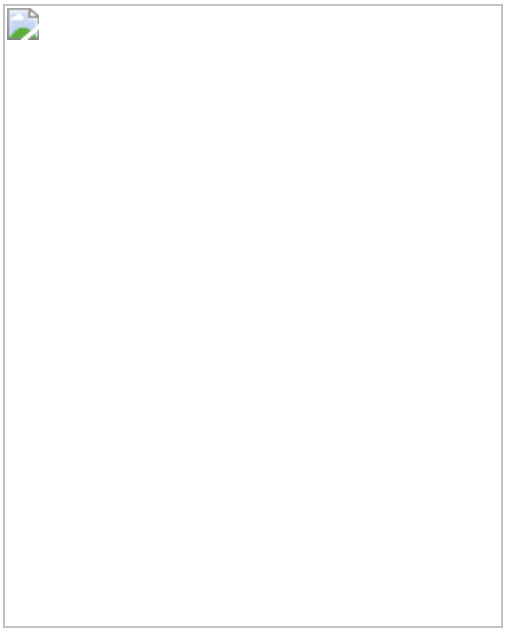

Fig. 2: ODP 1208 SST and export productivity records support westerly wind shifts.

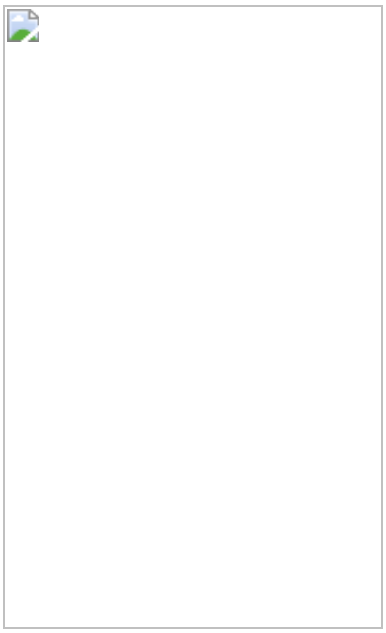

Fig. 3: North Pacific, Atlantic and Loess Plateau Plio-Pleistocene dust proxy fluxes display coherent increases at the iNHG.

Data availability

All data produced for this study are available at https://doi.org/10.6084/m9.figshare.12472646.v6. Source data are provided with this paper.

Code availability

The code used in this study to produce all figures is available at https://doi.org/10.6084/m9.figshare.12472676.v5.

References

1. 1.

   Russell, J. L., Dixon, K. W., Gnanadesikan, A., Stouffer, R. J. & Toggweiler, J. The Southern Hemisphere westerlies in a warming world: propping open the door to the deep ocean. *J. Clim*. **19**, 6382–6390 (2006).

   ADS Google Scholar

2. 2.

   Toggweiler, J. R., Russell, J. L. & Carson, S. R. Midlatitude westerlies, atmospheric CO_2, and climate change during the ice ages. *Paleoceanography* **21**, PA2005 (2006).

   ADS Google Scholar

3. 3.

   Anderson, R. et al. Wind-driven upwelling in the Southern Ocean and the deglacial rise in atmospheric CO_2. *Science* **323**, 1443–1448 (2009).

   ADS CAS PubMed PubMed Central Google Scholar

4. 4.

   Chen, G. & Held, I. M. Phase speed spectra and the recent poleward shift of Southern Hemisphere surface westerlies. *Geophys. Res. Lett*. **34**, L21805 (2007).

   ADS Google Scholar

5. 5.

   Yang, H. et al. Poleward shift of the major ocean gyres detected in a warming climate. *Geophys. Res. Lett*. **47**, e2019GL085868 (2020).

ADS Google Scholar

6. 6.

Martínez-Botí, M. et al. Plio-Pleistocene climate sensitivity evaluated using high-resolution CO_2 records. *Nature* **518**, 49–54 (2015); addendum **526**, 458 (2015).

ADS PubMed PubMed Central Google Scholar

7. 7.

Haywood, A. M. et al. A return to large-scale features of Pliocene climate: the Pliocene Model Intercomparison Project Phase 2. *Clim. Past* **16**, 2095–2123 (2020).

Google Scholar

8. 8.

Haug, G. H., Sigman, D. M., Tiedemann, R., Pedersen, T. F. & Sarnthein, M. Onset of permanent stratification in the subarctic Pacific Ocean. *Nature* **401**, 779–782 (1999).

ADS CAS Google Scholar

9. 9.

Sun, Y. & An, Z. Late Pliocene-Pleistocene changes in mass accumulation rates of eolian deposits on the central Chinese Loess Plateau. *J. Geophys. Res. D* **110**, D23101 (2005).

ADS Google Scholar

10. 10.

Naafs, B. D. A. et al. Strengthening of North American dust sources during the late Pliocene (2.7 Ma). *Earth Planet. Sci. Lett*. **317–318**, 8–19 (2012).

ADS Google Scholar

11. 11.

Martínez-Garcia, A. et al. Southern Ocean dust–climate coupling over the past four million years. *Nature* **476**, 312–315 (2011).

ADS PubMed PubMed Central Google Scholar

12. 12.

Li, X. et al. Mid-Pliocene westerlies from PlioMIP simulations. *Adv. Atmos. Sci*. **32**, 909–923 (2015).

CAS Google Scholar

13. 13.

Gillett, N. P. & Thompson, D. W. Simulation of recent Southern Hemisphere climate change. *Science* **302**, 273–275 (2003).

ADS CAS Google Scholar

14. 14.

Shindell, D. T., Miller, R. L., Schmidt, G. A. & Pandolfo, L. Simulation of recent northern winter climate trends by greenhouse-gas forcing. *Nature* **399**, 452–455 (1999).

ADS CAS Google Scholar

15. 15.

Chavaillaz, Y., Codron, F. & Kageyama, M. Southern westerlies in LGM and future (RCP4. 5) climates. *Clim. Past Discuss*. **8**, 3693–3717 (2012).

ADS Google Scholar

16. 16.

Gray, W. R. et al. Wind-driven evolution of the North Pacific subpolar gyre over the last deglaciation. *Geophys. Res. Lett*. **47**, e2019GL086328 (2020).

ADS Google Scholar

17. 17.

Nagashima, K. et al. Orbital-and millennial-scale variations in Asian dust transport path to the Japan Sea. *Palaeogeogr. Palaeoclimatol. Palaeoecol*. **247**, 144–161 (2007).

Google Scholar

18. 18.

Sime, L. C. et al. Southern Hemisphere westerly wind changes during the Last Glacial Maximum: model–data comparison. *Quat. Sci. Rev*. **64**, 104–120 (2013).

ADS Google Scholar

19. 19.

Lora, J. M., Mitchell, J. L., Risi, C. & Tripati, A. E. North Pacific atmospheric rivers and their influence on western North America at the Last Glacial Maximum. *Geophys. Res. Lett*. **44**, 1051–1059 (2017).

ADS Google Scholar

20. 20.

Burke, K. et al. Pliocene and Eocene provide best analogs for near-future climates. *Proc. Natl Acad. Sci. USA* **115**, 13288–13293 (2018).

ADS CAS Google Scholar

21. 21.

Lisiecki, L. E. & Raymo, M. E. A Pliocene-Pleistocene stack of 57 globally distributed benthic δ18O records. *Paleoceanography* **20**, PA1003 (2005).

ADS Google Scholar

22. 22.

Raymo, M. E. The initiation of Northern Hemisphere glaciation. *Annu. Rev. Earth Planet. Sci*. **22**, 353–383 (1994).

ADS Google Scholar

23. 23.

Lawrence, K. T. et al. Time-transgressive North Atlantic productivity changes upon Northern Hemisphere glaciation. *Paleoceanography* **28**, 740–751 (2013).

ADS Google Scholar

24. 24.

Tanaka, T. Y. & Chiba, M. A numerical study of the contributions of dust source regions to the global dust budget. *Glob. Planet. Change* **52**, 88–104 (2006).

ADS Google Scholar

25. 25.

Heermance, R. V. et al. Erg deposition and development of the ancestral Taklimakan Desert (western China) between 12.2 and 7.0 Ma. *Geology* **46**, 919–922 (2018).

ADS Google Scholar

26. 26.

Lang, D. C. et al. The transition on North America from the warm humid Pliocene to the glaciated Quaternary traced by eolian dust deposition at a benchmark North Atlantic Ocean drill site. *Quat. Sci. Rev*. **93**, 125–141 (2014).

ADS Google Scholar

27. 27.

Janecek, T. R. & Rea, D. K. Eolian deposition in the northeast Pacific Ocean: Cenozoic history of atmospheric circulation. *Geol. Soc. Am. Bull*. **94**, 730–738 (1983).

ADS Google Scholar

28. 28.

Rea, D. K., Snoeckx, H. & Joseph, L. H. Late Cenozoic eolian deposition in the North Pacific: Asian drying, Tibetan uplift, and cooling of the northern hemisphere. *Paleoceanography* **13**, 215–224 (1998).

ADS Google Scholar

29. 29.

Zhang, W., Chen, J., Ji, J. & Li, G. Evolving flux of Asian dust in the North Pacific Ocean since the late Oligocene. *Aeolian Res*. **23**, 11–20 (2016).

ADS Google Scholar

30. 30.

McGee, D. & Mukhopadhyay, S. in *The Noble Gases as Geochemical Tracers* 155–176 (Springer, 2013).

31. 31.

Dickens, G., Snoeckx, H., Arnold, E., Morley, J. & Owen, R. Composite depth scale and stratigraphy for Sites 885/886. In *Proc. ODP Sci. Res.* Vol. 145, 205–217 (Ocean Drilling Program, 1995).

32. 32.

McGee, D., Broecker, W. S. & Winckler, G. Gustiness: the driver of glacial dustiness? *Quat. Sci. Rev*. **29**, 2340–2350 (2010).

ADS Google Scholar

33. 33.

Mahowald, N. M. et al. Change in atmospheric mineral aerosols in response to climate: Last glacial period, preindustrial, modern, and doubled carbon dioxide climates. *J. Geophys. Res. D* **111**, D10202 (2006).

ADS Google Scholar

34. 34.

Albani, S. et al. Improved dust representation in the Community Atmosphere Model. *J. Adv. Model. Earth Syst*. **6**, 541–570 (2014).

ADS Google Scholar

35. 35.

Uno, I. et al. Asian dust transported one full circuit around the globe. *Nat. Geosci*. **2**, 557–560 (2009).

ADS CAS Google Scholar

36. 36.

Jia, Y. et al. Cenozoic aridification in Northwest China evidenced by paleovegetation evolution. *Palaeogeogr. Palaeoclimatol. Palaeoecol*. **557**, 109907 (2020).

Google Scholar

37. 37.

Herbert, T. D., Peterson, L. C., Lawrence, K. T. & Liu, Z. Tropical ocean temperatures over the past 3.5 million years. *Science* **328**, 1530–1534 (2010).

ADS CAS Google Scholar

38. 38.

Bauer, E. & Ganopolski, A. Aeolian dust modeling over the past four glacial cycles with CLIMBER-2. *Global Planet. Change* **74**, 49–60 (2010).

ADS Google Scholar

39. 39.

Li, X., Liu, X. & Zhou, H. Joint influence of surface erosion and high-latitude ice-sheet extent on Asian dust cycle during the last glacial maximum. *Geol. Mag*. **157**, 777–789 (2020).

ADS Google Scholar

40. 40.

Lorenz, S., Grieger, B., Helbig, P. & Herterich, K. Investigating the sensitivity of the atmospheric general circulation model ECHAM 3 to paleoclimatic boundary conditions. *Geol. Rundsch*. **85**, 513–524 (1996).

ADS Google Scholar

41. 41.

Kienast, S. S., Winckler, G., Lippold, J., Albani, S. & Mahowald, N. M. Tracing dust input to the global ocean using thorium isotopes in marine sediments: ThoroMap. *Glob. Biogeochem. Cycles* **30**, 1526–1541 (2016).

ADS CAS Google Scholar

42. 42.

Serno, S. et al. Eolian dust input to the Subarctic North Pacific. *Earth Planet. Sci. Lett*. **387**, 252–263 (2014).

ADS CAS Google Scholar

43. 43.

Costa, K. M. *Geochemical Fingerprints of Paleoceanographic Variability in the Subarctic Pacific over the Last 500,000 Years*. PhD thesis, Columbia Univ. (2006).

44. 44.

Maeda, L., Kawahata, H. & Nohara, M. Fluctuation of biogenic and abiogenic sedimentation on the Shatsky Rise in the western North Pacific during the late Quaternary. *Mar. Geol*. **189**, 197–214 (2002).

ADS CAS Google Scholar

45. 45.

Venti, N. L., Billups, K. & Herbert, T. D. Increased sensitivity of the Plio-Pleistocene northwest Pacific to obliquity forcing. *Earth Planet. Sci. Lett*. **384**, 121–131 (2013).

ADS CAS Google Scholar

46. 46.

Venti, N. L., Billups, K. & Herbert, T. D. Paleoproductivity in the northwestern Pacific Ocean during the Pliocene-Pleistocene climate transition (3.0–1.8 Ma). *Paleoceanography* **32**, 92–103 (2017).

ADS Google Scholar

47. 47.

Brierley, C. M. et al. Greatly expanded tropical warm pool and weakened Hadley circulation in the early Pliocene. *Science* **323**, 1714–1718 (2009).

ADS CAS PubMed PubMed Central Google Scholar

48. 48.

Benxing, Z. & Rutter, N. On the problem of Quaternary glaciations, and the extent and patterns of Pleistocene ice cover in the Qinghai-Xizang (Tibet) Plateau. *Quat. Int*. **45–46**, 109–122 (1998).

Google Scholar

49. 49.

Bolton, C. T., Lawrence, K. T., Gibbs, S. J., Wilson, P. A. & Herbert, T. D. Biotic and geochemical evidence for a global latitudinal shift in ocean biogeochemistry and export productivity during the late Pliocene. *Earth Planet. Sci. Lett*. **308**, 200–210 (2011).

ADS CAS Google Scholar

50. 50.

Venti, N. L. & Billups, K. Stable-isotope stratigraphy of the Pliocene–Pleistocene climate transition in the northwestern subtropical Pacific. *Palaeogeogr. Palaeoclimatol. Palaeoecol*. **326–328**, 54–65 (2012).

Google Scholar

51. 51.

Shipboard Scientific Party. Site 1208. In *Proc. ODP Init. Rep.* Vol. 198 (eds Bralower, T. J. et al.) 1–93 (Ocean Drilling Program, 2002).

52. 52.

Shipboard Scientific Party. Sites 885/886. In *Proc. ODP Init. Rep.* Vol. 145 (eds Rea, D. K. et al.) 303–334 (Ocean Drilling Program, 1993).

53. 53.

Evans, H. F. *Magnetic Stratigraphy and Environmental Magnetism of Oceanic Sediments*. PhD thesis, Univ. of Florida (2006).

54. 54.

Gradstein, F. M., Ogg, J. G., Schmitz, M. B. & Ogg, G. M. *The Geologic Time Scale 2012* (Elsevier, 2012).

55. 55.

Winckler, G., Anderson, R. F. & Schlosser, P. Equatorial Pacific productivity and dust flux during the mid-Pleistocene climate transition. *Paleoceanography* **20**, PA4025 (2005).

ADS Google Scholar

56. 56.

Clarke, W. B., Jenkins, W. & Top, Z. Determination of tritium by mass spectrometric measurement of 3He. *Int. J. Appl. Radiat. Isot*. **27**, 515–522 (1976).

CAS Google Scholar

57. 57.

Welhan, J. A. *Carbon and Hydrogen Gases in Hydrothermal Systems: the Search for a Mantle Source*. PhD thesis, Univ. of California, San Diego (1981).

58. 58.

Mamyrin, B. A. & Tolstikhin, I. N. *Helium Isotopes in Nature* (Elsevier, 1984).

59. 59.

McGee, D. et al. Tracking eolian dust with helium and thorium: impacts of grain size and provenance. *Geochim. Cosmochim. Acta* **175**, 47–67 (2016).

ADS CAS Google Scholar

60. 60.

Patterson, D. B., Farley, K. & Norman, M. ^{4}He as a tracer of continental dust: a 1.9 million year record of aeolian flux to the west equatorial Pacific Ocean. *Geochim. Cosmochim. Acta* **63**, 615–625 (1999).

ADS CAS Google Scholar

61. 61.

Mukhopadhyay, S., Farley, K. & Montanari, A. A. 35 Myr record of helium in pelagic limestones from Italy: implications for interplanetary dust accretion from the early Maastrichtian to the middle Eocene. *Geochim. Cosmochim. Acta* **65**, 653–669 (2001).

ADS CAS Google Scholar

62. 62.

Farley, K. A. Cenozoic variations in the flux of interplanetary dust recorded by ^{3}He in a deep-sea sediment. *Nature* **376**, 153–156 (1995).

ADS CAS Google Scholar

63. 63.

Farley, K., Love, S. & Patterson, D. B. Atmospheric entry heating and helium retentivity of interplanetary dust particles. *Geochim. Cosmochim. Acta* **61**, 2309–2316 (1997).

ADS CAS Google Scholar

64. 64.

Farley, K. & Mukhopadhyay, S. An extraterrestrial impact at the Permian-Triassic boundary? *Science* **293**, 2343 (2001).

CAS PubMed PubMed Central Google Scholar

65. 65.

Nier, A. & Schlutter, D. Extraction of helium from individual interplanetary dust particles by step-heating. *Meteoritics* **27**, 166–173 (1992).

ADS CAS Google Scholar

66. 66.

Ozima, M. & Podosek, F. A. *Noble Gas Geochemistry* (Cambridge Univ. Press, 1983).

67. 67.

Farley, K. & Patterson, D. A 100-kyr periodicity in the flux of extraterrestrial 3 He to the sea floor. *Nature* **378**, 600–603 (1995).

ADS Google Scholar

68. 68.

Marcantonio, F. et al. A comparative study of accumulation rates derived by He and Th isotope analysis of marine sediments. *Earth Planet. Sci. Lett*. **133**, 549–555 (1995).

ADS CAS Google Scholar

69. 69.

Patterson, D. B. & Farley, K. Extraterrestrial ^{3}He in seafloor sediments: evidence for correlated 100 kyr periodicity in the accretion rate of interplanetary dust, orbital parameters, and Quaternary climate. *Geochim. Cosmochim. Acta* **62**, 3669–3682 (1998).

ADS CAS Google Scholar

70. 70.

Middleton, J. L., Langmuir, C. H., Mukhopadhyay, S., McManus, J. F. & Mitrovica, J. X. Hydrothermal iron flux variability following rapid sea level changes. *Geophys. Res. Lett*. **43**, 3848–3856 (2016).

ADS CAS Google Scholar

71. 71.

Middleton, J. L., Mukhopadhyay, S., Langmuir, C. H., McManus, J. F. & Huybers, P. J. Millennial-scale variations in dustiness recorded in Mid-Atlantic sediments from 0 to 70 ka. *Earth Planet. Sci. Lett*. **482**, 12–22 (2018).

ADS CAS Google Scholar

72. 72.

Costa, K. M. et al. ^{230}Th normalization: New insights on an essential tool for quantifying sedimentary fluxes in the modern and Quaternary ocean. *Paleoceanogr. Paleoclimatol*. **35**, e2019PA003820 (2020).

Google Scholar

73. 73.

Burls, N. J. et al. Active Pacific meridional overturning circulation (PMOC) during the warm Pliocene. *Sci. Adv*. **3**, e1700156 (2017).

ADS PubMed PubMed Central Google Scholar

74. 74.

Fleisher, M. & Anderson, R. Assessing the collection efficiency of Ross Sea sediment traps using ^{230}Th and ^{231}Pa. *Deep Sea Res. Part II* **50**, 693–712 (2003).

ADS CAS Google Scholar

75. 75.

Taylor, S. R. & McLennan, S. M. The geochemical evolution of the continental crust. *Rev. Geophys*. **33**, 241–265 (1995).

ADS Google Scholar

76. 76.

Mortlock, R. A. & Froelich, P. N. A simple method for the rapid determination of biogenic opal in pelagic marine sediments. *Deep-Sea Res. A* **36**, 1415–1426 (1989).

ADS CAS Google Scholar

77. 77.

Müller, P. J., Kirst, G., Ruhland, G., Von Storch, I. & Rosell-Melé, A. Calibration of the alkenone paleotemperature index $U_{37}^{K'}$ based on core-tops from the eastern South Atlantic and the global ocean (60°N-60°S). *Geochim. Cosmochim. Acta* **62**, 1757–1772 (1998).

ADS Google Scholar

78. 78.

Haug, G., Maslin, M., Sarnthein, M., Stax, R. & Tiedemann, R. Evolution of northwest Pacific sedimentation patterns since 6 Ma (Site 882). In *Proc. ODP Sci. Res.* Vol. 293 (Ocean Drilling Program, 1995).

79. 79.

Zhang, Q. et al. Mechanism for enhanced eolian dust flux recorded in North Pacific Ocean sediments since 4.0 Ma: aridity or humidity at dust source areas in the Asian interior? *Geology* **48**, 77–81 (2020).

ADS Google Scholar

80. 80.

Bailey, I. et al. Iron fertilisation and biogeochemical cycles in the sub-Arctic northwest Pacific during the late Pliocene intensification of northern hemisphere glaciation. *Earth Planet. Sci. Lett*. **307**, 253–265 (2011).

ADS CAS Google Scholar

81. 81.

Andrews, J. T. Icebergs and iceberg rafted detritus (IRD) in the North Atlantic: facts and assumptions. *Oceanography* **13**, 100–108 (2000).

Google Scholar

82. 82.

Weber, E. T. et al. Quantitative resolution of eolian continental crustal material and volcanic detritus in North Pacific surface sediment. *Paleoceanography* **11**, 115–127 (1996).

ADS Google Scholar

83. 83.

Lam, P. J. & Bishop, J. K. The continental margin is a key source of iron to the HNLC North Pacific Ocean. *Geophys. Res. Lett*. **35**, L07608 (2008).

ADS Google Scholar

84. 84.

Bigg, G., Clark, C. & Hughes, A. A last glacial ice sheet on the Pacific Russian coast and catastrophic change arising from coupled ice–volcanic interaction. *Earth Planet. Sci. Lett*. **265**, 559–570 (2008).

ADS CAS Google Scholar

85. 85.

Caves, J. K., Sjostrom, D. J., Mix, H. T., Winnick, M. J. & Chamberlain, C. P. Aridification of Central Asia and uplift of the Altai and Hangay Mountains, Mongolia: stable isotope evidence. *Am. J. Sci*. **314**, 1171–1201 (2014).

ADS CAS Google Scholar

86. 86.

Caves, J. K. et al. Late Miocene uplift of the Tian Shan and Altai and reorganization of Central Asia climate. *GSA Today* **27**, 20–26 (2017).

Google Scholar

87. 87.

Guo, Z. et al. Onset of Asian desertification by 22 Myr ago inferred from loess deposits in China. *Nature* **416**, 159–163 (2002).

ADS CAS PubMed PubMed Central Google Scholar

88. 88.

Zan, J., Fang, X., Zhang, W., Yan, M. & Zhang, D. A new record of late Pliocene-early Pleistocene aeolian loess–red clay deposits from the western Chinese Loess Plateau and its palaeoenvironmental implications. *Quat. Sci. Rev*. **186**, 17–26 (2018).

ADS Google Scholar

89. 89.

Che, X. & Li, G. Binary sources of loess on the Chinese Loess Plateau revealed by U–Pb ages of zircon. *Quat. Res*. **80**, 545–551 (2013).

CAS Google Scholar

90. 90.

Bird, A. et al. Quaternary dust source variation across the Chinese Loess Plateau. *Palaeogeogr. Palaeoclimatol. Palaeoecol*. **435**, 254–264 (2015).

Google Scholar

91. 91.

Nie, J. et al. Loess plateau storage of northeastern Tibetan plateau-derived Yellow River sediment. *Nat. Commun*. **6**, 8511 (2015); corrigendum **7**, 10831 (2016).

ADS CAS PubMed PubMed Central Google Scholar

92. 92.

Qian, W., Quan, L. & Shi, S. Variations of the dust storm in China and its climatic control. *J. Clim*. **15**, 1216–1229 (2002).

ADS Google Scholar

93. 93.

Prospero, J. M., Ginoux, P., Torres, O., Nicholson, S. E. & Gill, T. E. Environmental characterization of global sources of atmospheric soil dust identified with the Nimbus 7 Total Ozone Mapping Spectrometer (TOMS) absorbing aerosol product. *Rev. Geophys*. **40**, 1002 (2002).

ADS Google Scholar

94. 94.

Bory, A. J., Biscaye, P. E. & Grousset, F. E. Two distinct seasonal Asian source regions for mineral dust deposited in Greenland (NorthGRIP). *Geophys. Res. Lett*. **30**, 1167 (2003).

ADS Google Scholar

95. 95.

Sun, Y. et al. Tracing the provenance of fine-grained dust deposited on the central Chinese Loess Plateau. *Geophys. Res. Lett*. **35**, L01804 (2008).

ADS Google Scholar

96. 96.

Kapp, P. et al. Wind erosion in the Qaidam basin, central Asia: implications for tectonics, paleoclimate, and the source of the Loess Plateau. *GSA Today* **21**, 4–10 (2011).

Google Scholar

97. 97.

Pullen, A. et al. Qaidam Basin and northern Tibetan Plateau as dust sources for the Chinese Loess Plateau and paleoclimatic implications. *Geology* **39**, 1031–1034 (2011).

ADS CAS Google Scholar

98. 98.

Licht, A., Pullen, A., Kapp, P., Abell, J. & Giesler, N. Eolian cannibalism: reworked loess and fluvial sediment as the main sources of the Chinese Loess Plateau. *Geol. Soc. Am. Bull*. **128**, 944–956 (2016).

ADS CAS Google Scholar

99. 99.

Sun, J., Zhang, Z. & Zhang, L. New evidence on the age of the Taklimakan Desert. *Geology* **37**, 159–162 (2009).

ADS Google Scholar

100. 100.

Zheng, H. et al. Late oligocene–early miocene birth of the Taklimakan Desert. *Proc. Natl Acad. Sci. USA* **112**, 7662–7667 (2015).

ADS CAS Google Scholar

101. 101.

Heermance, R. V. et al. Climatic and tectonic controls on sedimentation and erosion during the Pliocene–Quaternary in the Qaidam Basin (China). *Geol. Soc. Am. Bull*. **125**, 833–856 (2013).

ADS Google Scholar

102. 102.

Luo, Z. et al. Orbital forcing of Plio-Pleistocene climate variation in a Qaidam Basin lake based on paleomagnetic and evaporite mineralogic analysis. *Palaeogeogr. Palaeoclimatol. Palaeoecol*. **510**, 31–39 (2018).

Google Scholar

103. 103.

Jijun, L. et al. Geomorphological and environmental evolution in the upper reaches of the Yellow River during the late Cenozoic. *Sci. China Ser. D* **39**, 380–390 (1996).

Google Scholar

104. 104.

Teng, Z. & Li, L. Loess stratum and an analysis on the environment of Pleistocene in south bank of the Yellow River between Zhengzhou and Luoyang. *J. Northw. Univ*. **28**, 153–156 (1997).

Google Scholar

105. 105.

Yue, L. P., Lei, X. Y. & Qu, H. J. The age of terrace development in the middle reaches of the Yellow River. *Geol. Rev.* **43**, 186–192 (1997).

Google Scholar

106. 106.

Craddock, W. H. et al. Rapid fluvial incision along the Yellow River during headward basin integration. *Nat. Geosci*. **3**, 209–213 (2010).

ADS CAS Google Scholar

107. 107.

Molnar, P., England, P. & Martinod, J. Mantle dynamics, uplift of the Tibetan Plateau, and the Indian monsoon. *Rev. Geophys*. **31**, 357–396 (1993).

ADS Google Scholar

108. 108.

Bird, A. et al. A constant Chinese Loess Plateau dust source since the late Miocene. *Quat. Sci. Rev*. **227**, 106042 (2020).

Google Scholar

109. 109.

Li, Z. et al. Chronology studies of a drill core in the central Tengger Desert of China and its implication for Asian desertification. *Quat. Sci. Rev*. **85**, 85–98 (2014).

ADS Google Scholar

110. 110.

Wang, F. et al. Formation and evolution of the Badain Jaran Desert, North China, as revealed by a drill core from the desert centre and by geological survey. *Palaeogeogr. Palaeoclimatol. Palaeoecol*. **426**, 139–158 (2015).

Google Scholar

111. 111.

Rea, D. K. The paleoclimatic record provided by eolian deposition in the deep sea: the geologic history of wind. *Rev. Geophys*. **32**, 159–195 (1994).

ADS Google Scholar

112. 112.

Wu, F. et al. Plio–Quaternary stepwise drying of Asia: evidence from a 3-Ma pollen record from the Chinese Loess Plateau. *Earth Planet. Sci. Lett*. **257**, 160–169 (2007).

ADS CAS Google Scholar

Download references

Acknowledgements

We thank F. Pavia, J. Middleton, M. Ting, M. Raymo, J. Schaefer, S. Rahimi, T. Weiss and J. Bridges for discussions that greatly improved the research and manuscript. Support at the Lamont-Doherty Earth Observatory laboratories was provided by R. Schwartz, M. Fleisher, L. Bolge, L. Baker, J. Hansen and C. Chang. ODP 1208 and ODP 885/886 core samples were provided by the Integrated Ocean Drilling Program (IODP). IODP is sponsored by the US National Science Foundation (NSF) and participating countries under the management of Joint Oceanographic Institutions, Inc. We acknowledge the NSF-PIRE project (PIRE: DUST) that supported the work through funding to G.W., R.F.A. and T.D.H., and a Climate Center Grant from Lamont-Doherty Earth Observatory.

Author information

Affiliations

1. Lamont-Doherty Earth Observatory, Columbia University, Palisades, NY, USA

   Jordan T. Abell, Gisela Winckler & Robert F. Anderson

2. Department of Earth and Environmental Sciences, Columbia University, New York, NY, USA

   Jordan T. Abell, Gisela Winckler & Robert F. Anderson

3. Department of Earth, Environmental and Planetary Sciences, Brown University, Providence, RI, USA

   Timothy D. Herbert

Authors

1. Jordan T. Abell
   View author publications

You can also search for this author in PubMed Google Scholar

2. Gisela Winckler
   View author publications

   You can also search for this author in PubMed Google Scholar

3. Robert F. Anderson
   View author publications

   You can also search for this author in PubMed Google Scholar

4. Timothy D. Herbert
   View author publications

   You can also search for this author in PubMed Google Scholar

Contributions

J.T.A. and G.W. designed the project and developed the conceptual framework. J.T.A. collected all isotope, major and trace element, and opal data; T.D.H. collected alkenone data. J.T.A. and G.W. analysed data. J.T.A. and G.W. wrote the manuscript, and all authors provided comments and revisions.

Corresponding author

Correspondence to Jordan T. Abell.

Ethics declarations

Competing interests

The authors declare no competing interests.

Additional information

Peer review information *Nature* thanks the anonymous reviewer(s) for their contribution to the peer review of this work. Peer reviewer reports are available.

Publisher's note Springer Nature remains neutral with regard to jurisdictional claims in published maps and institutional affiliations.

Extended data figures and tables

Extended Data Fig. 1 Modelled dust flux ratios show little zonal dust variability between the LGM and today.

Contours represent the ratio of annual average LGM and modern dust deposition rates to the North Pacific. The model output is from the C4fn and C4fn-lgm simulations of ref. [34].

Extended Data Fig. 2 SST, dust and export productivity records from ODP 1208 for the period ~2.5–4.5 Ma.

a, Benthic oxygen isotope stack from ref. [21] and ODP 1208 from ref. [50]. **b**, Alkenone-derived SSTs. The record is a combination of data produced in this study and those from ref. [45]. **c**, Dust fluxes determined from Th concentrations and $^{3}He_{ET}$ -derived sediment fluxes. Blue filled circles indicate samples with measured $^{3}He_{ET}$. **d**, $C_{37total}$ fluxes. The record is a combination of data produced in this study and those from ref. [46]. **e**, Ba_{xs} fluxes. Purple filled circles indicate samples with measured $^{3}He_{ET}$. **f**, Opal fluxes. Light blue filled circles indicate samples with measured $^{3}He_{ET}$. All error bars or 'clouds' for dust and export production proxies represent propagated analytical errors on concentrations, as well as analytical and statistical uncertainties for the $^{3}He_{ET}$ -derived MARs (1σ).

Extended Data Fig. 3 Fractional differences for helium isotope replicates.

a, Frequency of ODP 1208 fractional differences between replicate samples for $^{3}He_{ET}$ (blue, top) and $^{4}He_{terr}$ (red, bottom). **b**, Same as **a**, except for ODP 885/886. **c**, Combined data for both cores. Fractional differences are calculated by dividing the absolute value of the maximum difference between replicates samples (if more than one replicate is run) by the average.

Extended Data Fig. 4 Comparison of $^{3}He_{ET}$ sediment fluxes and age-model-derived MARs/LSRs.

a, ODP 1208. **b**, ODP 885/886. Both CFP records use the Quaternary constant flux of $^{3}He_{ET}$ (0.8 pcc cm^{-2} kyr^{-1}). Error bars represent propagated uncertainties on analytical and statistical uncertainties for the $^{3}He_{ET}$-derived MARs (1σ). The LSRs/MARs for ODP 1208 are based on the age models of refs. [50,53] and dry bulk densities. The higher-resolution MARs between astronomically tuned reversal tie-points for the period of ~3.7–4.5 Ma at site 1208 are calculated using samples for which densities are provided from shipboard measurements. In the later portion of the ODP 1208 record, for which oxygen isotope stratigraphy is available (~2.5–3.7 Ma), densities are interpolated to samples with oxygen isotope data for determination of MARs. LSRs/MARs for ODP 885/886 are based on the age model of ref. [31] and dry bulk densities. The higher-resolution MARs between magnetic reversal stratigraphy tie-points at site 885/886 are calculated using the provided shipboard measurements of density interpolated to sample depths used in this study, which have higher resolution.

Extended Data Fig. 5 Comparison of dust proxy concentrations for ODP 1208 and 885/886.

a–**d**, $^{4}He_{terr}$ (**a**), Al (**b**), Fe (**c**) and Ti (**d**) are plotted against Th for ODP 1208. **e**–**h**, Same as **a**–**d**, but for ODP 885/886. Black lines denote the UCC relationships of the elements[59,75] (see Methods). All error bars denote analytical uncertainties on measured concentrations (1σ), except for $^{4}He_{terr}$, where the error bars incorporate the additional statistical uncertainty associated with replicates (1σ) (see Methods).

Extended Data Fig. 6 ODP 1208 and 885/886 dust fluxes derived from all five dust proxies used in this study.

a, $^{4}He_{terr}$-derived dust fluxes for ODP 1208. **b**, Th-derived dust fluxes for ODP 1208. **c**, Al-derived dust fluxes for ODP 1208. **d**, Fe-derived dust

fluxes for ODP 1208. **e**, Ti-derived dust fluxes for ODP 1208. **f–j**, Same as **a–e**, but for ODP 885/886. Error bars include propagated analytical uncertainties on concentrations as well as analytical and statistical uncertainties for the $^{3}He_{ET}$-derived MARs (1σ). The much lower $^{4}He_{terr}$-derived dust fluxes are probably a result of the large uncertainty in the terrestrial endmember[59].

Extended Data Fig. 7 Compilation of dust flux reconstructions from the open-ocean Pliocene North Pacific.

a, LR04 benthic oxygen isotope stack[21]. **b**, Th- and $^{3}He_{ET}$-derived dust fluxes from ODP 1208. **c**, Siliciclastic (>2 μm) fluxes from ODP 882[78]. **d**, Th- and $^{3}He_{ET}$-derived dust flux data from ODP 885/886. **e**, Aeolian flux from ODP 885/886[28]. **f**, Flux of relative Hm+Gt from ODP 885/886[79]. Error bars for records in this study represent propagated analytical uncertainties on concentrations, as well as analytical and statistical uncertainties for the $^{3}He_{ET}$-derived MARs (1σ).

Extended Data Fig. 8 ODP 885/886 dust concentrations and fluxes derived from various methods.

a, Aeolian percentages (grey curve) from ref. [28] are determined using a sequential leaching procedure to removed opal and Fe-Mn (oxy)hydroxides. Dust concentrations from this study are calculated using Th concentrations. Error bars represent analytical uncertainties on element concentration measurements (1σ). **b**, Aeolian fluxes (black curve) from ref. [28] are based on aeolian percentages and age-model-derived MARs. Dust fluxes from this study are calculated using Th concentrations and $^{3}He_{ET}$-derived MARs. Error bars represent propagated analytical uncertainties on concentrations, as well as analytical and statistical uncertainties for the $^{3}He_{ET}$-derived MARs (1σ).

Supplementary information

Peer Review File

Source data

Source Data Fig. 1

Source Data Fig. 2

Source Data Fig. 3

Rights and permissions

Reprints and Permissions

About this article

Check for updates

Cite this article

Abell, J.T., Winckler, G., Anderson, R.F. *et al.* Poleward and weakened westerlies during Pliocene warmth. *Nature* **589,** 70–75 (2021). https://doi.org/10.1038/s41586-020-03062-1

Download citation

- Received: 26 June 2020
- Accepted: 19 October 2020
- Published: 06 January 2021
- Issue Date: 07 January 2021

- DOI: https://doi.org/10.1038/s41586-020-03062-1

Comments

By submitting a comment you agree to abide by our Terms and Community Guidelines. If you find something abusive or that does not comply with our terms or guidelines please flag it as inappropriate.

Access through your institution
Change institution
Buy or subscribe

This article was downloaded by **calibre** from https://www.nature.com/articles/s41586-020-03062-1

| Section menu | Main menu |

- Article
- Published: 18 November 2020

Drivers and dynamics of a massive adaptive radiation in cichlid fishes

- Fabrizia Ronco ORCID: orcid.org/0000-0003-1583-8108[1],
- Michael Matschiner ORCID: orcid.org/0000-0003-4741-3884[1,2,3],
- Astrid Böhne ORCID: orcid.org/0000-0002-1284-3115[1,4],
- Anna Boila[1],
- Heinz H. Büscher[1],
- Athimed El Taher[1],
- Adrian Indermaur[1],
- Milan Malinsky ORCID: orcid.org/0000-0002-1462-6317[1],
- Virginie Ricci ORCID: orcid.org/0000-0001-6466-1930[1],
- Ansgar Kahmen[5],
- Sissel Jentoft ORCID: orcid.org/0000-0001-8707-531X[3] &
- Walter Salzburger ORCID: orcid.org/0000-0002-9988-1674[1,3]

Nature **volume 589**, pages76–81(2021)Cite this article

- 5169 Accesses
- 1 Citations
- 288 Altmetric
- Metrics details

Subjects

- Evolution

- Zoology

Abstract

Adaptive radiation is the likely source of much of the ecological and morphological diversity of life[1,2,3,4]. How adaptive radiations proceed and what determines their extent remains unclear in most cases[1,4]. Here we report the in-depth examination of the spectacular adaptive radiation of cichlid fishes in Lake Tanganyika. On the basis of whole-genome phylogenetic analyses, multivariate morphological measurements of three ecologically relevant trait complexes (body shape, upper oral jaw morphology and lower pharyngeal jaw shape), scoring of pigmentation patterns and approximations of the ecology of nearly all of the approximately 240 cichlid species endemic to Lake Tanganyika, we show that the radiation occurred within the confines of the lake and that morphological diversification proceeded in consecutive trait-specific pulses of rapid morphospace expansion. We provide empirical support for two theoretical predictions of how adaptive radiations proceed, the 'early-burst' scenario[1,5] (for body shape) and the stages model[1,6,7] (for all traits investigated). Through the analysis of two genomes per species and by taking advantage of the uneven distribution of species in subclades of the radiation, we further show that species richness scales positively with per-individual heterozygosity, but is not correlated with transposable element content, number of gene duplications or genome-wide levels of selection in coding sequences.

Access through your institution
Change institution
Buy or subscribe

Access options

Subscribe to Journal

Get full journal access for 1 year

$199.00

only $3.90 per issue

Subscribe

All prices are NET prices.
VAT will be added later in the checkout.

Rent or Buy article

Get time limited or full article access on ReadCube.

from$8.99

Rent or Buy

All prices are NET prices.

Additional access options:

- Log in
- Access through your institution
- Learn about institutional subscriptions

Fig. 1: Time-calibrated species tree of the cichlid fishes of African Lake Tanganyika.

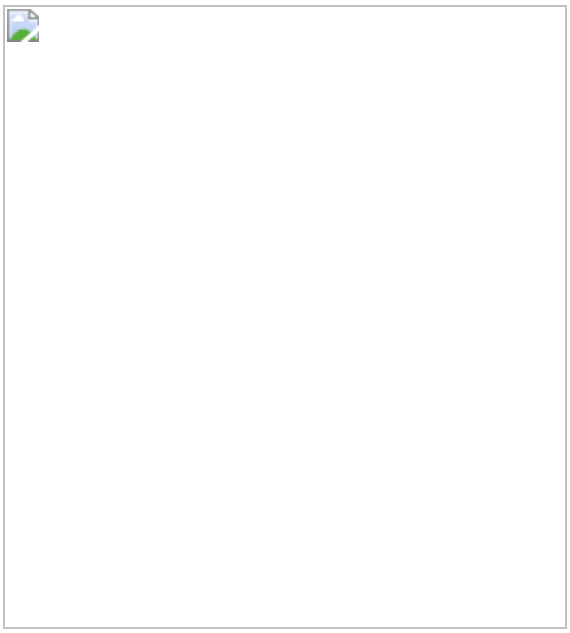

Fig. 2: Morphospace and ecospace occupation of the cichlid fishes of Lake Tanganyika.

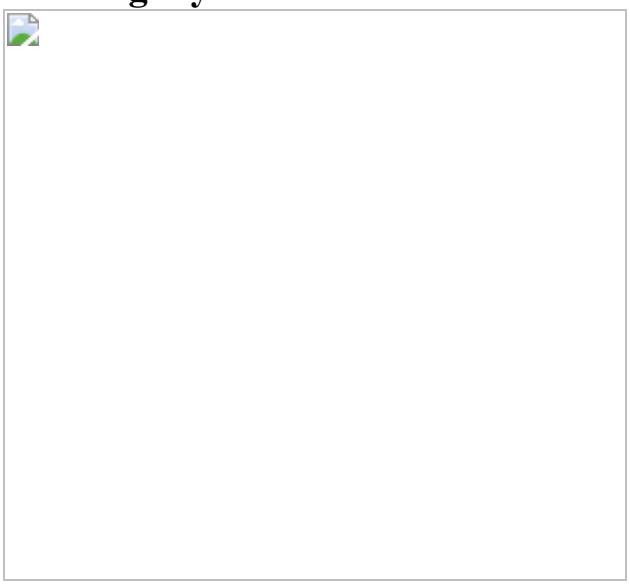

Fig. 3: Temporal dynamics of morphological diversification in the adaptive radiation of cichlid fishes in Lake Tanganyika.

Fig. 4: Association between genomic features and species richness across the cichlid tribes in Lake Tanganyika.

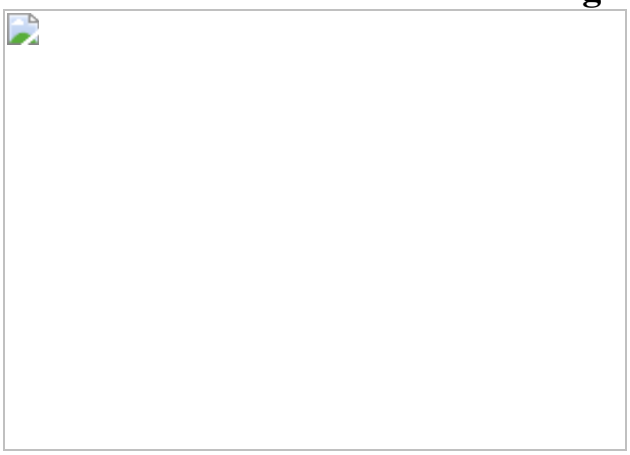

Data availability

All newly sequenced genomes for this study and their raw reads are available from NCBI under the BioProject accession number PRJNA550295 (https://www.ncbi.nlm.nih.gov/bioproject/). The VCF file, tree files, summary statistics of the assembled genomes and phenotypic datasets generated and analysed during this study are available as downloadable files on Dryad (https://doi.org/10.5061/dryad.9w0vt4bbf). The Nile tilapia reference genome used is available under RefSeq accession GCF_001858045.1. All X-ray data are available on MorphoSource under the project number P1093. Source data are provided with this paper.

Code availability

Code used to analyse the data is available on GitHub (https://github.com/cichlidx/ronco_et_al), except for analyses where single commands from publicly available software were used and where all settings are fully reported in the Methods and/or Supplementary Methods.

References

1. 1.

   Gavrilets, S. & Losos, J. B. Adaptive radiation: contrasting theory with data. *Science* **323**, 732–737 (2009).

   ADS CAS PubMed Article PubMed Central Google Scholar

2. 2.

   Schluter, D. *The Ecology of Adaptive Radiation* (Oxford Univ. Press, 2000).

3. 3.

   Simpson, G. G. *The Major Features of Evolution* (Columbia Univ. Press, 1953).

4. 4.

   Glor, R. E. Phylogenetic insights on adaptive radiation. *Annu. Rev. Ecol. Evol. Syst*. **41**, 251–270 (2010).

   Article Google Scholar

5. 5.

   Foote, M. The evolution of morphological diversity. *Annu. Rev. Ecol. Syst*. **28**, 129–152 (1997).

Article Google Scholar

6. 6.

Danley, P. D. & Kocher, T. D. Speciation in rapidly diverging systems: lessons from Lake Malawi. *Mol. Ecol*. **10**, 1075–1086 (2001).

CAS PubMed Article PubMed Central Google Scholar

7. 7.

Streelman, J. T. & Danley, P. D. The stages of vertebrate evolutionary radiation. *Trends Ecol. Evol*. **18**, 126–131 (2003).

Article Google Scholar

8. 8.

Benton, M. J. Diversification and extinction in the history of life. *Science* **268**, 52–58 (1995).

ADS CAS PubMed Article PubMed Central Google Scholar

9. 9.

Sepkoski, J. J., Jr. Rates of speciation in the fossil record. *Phil. Trans. R. Soc. Lond. B* **353**, 315–326 (1998).

Article Google Scholar

10. 10.

Berner, D. & Salzburger, W. The genomics of organismal diversification illuminated by adaptive radiations. *Trends Genet*. **31**, 491–499 (2015).

CAS PubMed Article PubMed Central Google Scholar

11. 11.

Wagner, C. E., Harmon, L. J. & Seehausen, O. Ecological opportunity and sexual selection together predict adaptive radiation. *Nature* **487**, 366–369 (2012).

ADS CAS PubMed Article PubMed Central Google Scholar

12. 12.

Salzburger, W. Understanding explosive diversification through cichlid fish genomics. *Nat. Rev. Genet*. **19**, 705–717 (2018).

CAS PubMed Article PubMed Central Google Scholar

13. 13.

Brawand, D. et al. The genomic substrate for adaptive radiation in African cichlid fish. *Nature* **513**, 375–381 (2014).

ADS CAS PubMed PubMed Central Article Google Scholar

14. 14.

Fryer, G. & Iles, T. D. *The Cichlid Fishes of the Great Lakes of Africa* (T.F.H. Publications, 1972).

15. 15.

Ronco, F., Büscher, H. H., Indermaur, A. & Salzburger, W. The taxonomic diversity of the cichlid fish fauna of ancient Lake Tanganyika, East Africa. *J. Gt. Lakes Res*. **46**, 1067–1078 (2020).

Article Google Scholar

16. 16.

Muschick, M., Indermaur, A. & Salzburger, W. Convergent evolution within an adaptive radiation of cichlid fishes. *Curr. Biol*. **22**, 2362–2368 (2012).

CAS PubMed Article PubMed Central Google Scholar

17. 17.

Salzburger, W., Van Bocxlaer, B. & Cohen, A. S. Ecology and evolution of the African Great Lakes and their faunas. *Annu. Rev. Ecol. Evol. Syst*. **45**, 519–545 (2014).

Article Google Scholar

18. 18.

Matschiner, M., Böhne, A., Ronco, F. & Salzburger, W. The genomic timeline of cichlid diversification across continents. *Nat. Commun*. https://doi.org/10.1038/s41467-020-17827-9 (2020).

19. 19.

Koch, M. et al. Evolutionary history of the endemic Lake Tanganyika cichlid fish *Tylochromis polylepis*: A recent intruder to a mature adaptive radiation. *J. Zool. Syst. Evol. Res*. **45**, 64–71 (2007).

Article Google Scholar

20. 20.

Salzburger, W., Meyer, A., Baric, S., Verheyen, E. & Sturmbauer, C. Phylogeny of the Lake Tanganyika cichlid species flock and its relationship to the Central and East African haplochromine cichlid fish faunas. *Syst. Biol*. **51**, 113–135 (2002).

PubMed Article PubMed Central Google Scholar

21. 21.

Schedel, F. D. B., Musilova, Z. & Schliewen, U. K. East African cichlid lineages (Teleostei: Cichlidae) might be older than their ancient host lakes: new divergence estimates for the east African cichlid radiation. *BMC Evol. Biol*. **19**, 94 (2019).

PubMed PubMed Central Article Google Scholar

22. 22.

Irisarri, I. et al. Phylogenomics uncovers early hybridization and adaptive loci shaping the radiation of Lake Tanganyika cichlid fishes. *Nat. Commun*. **9**, 3159 (2018).

ADS PubMed PubMed Central Article CAS Google Scholar

23. 23.

Cohen, A. S., Soreghan, M. J. & Scholz, C. A. Estimating the age of formation of lakes: an example from Lake Tanganyika, East African Rift system. *Geology* **21**, 511–514 (1993).

ADS CAS Article Google Scholar

24. 24.

Post, D. M. Using stable isotopes to estimate trophic position: models, methods, and assumptions. *Ecology* **83**, 703–718 (2002).

Article Google Scholar

25. 25.

Liem, K. F. Evolutionary strategies and morphological innovations: cichlid pharyngeal jaws. *Syst. Zool*. **22**, 425–441 (1973).

Article Google Scholar

26. 26.

Salzburger, W. The interaction of sexually and naturally selected traits in the adaptive radiations of cichlid fishes. *Mol. Ecol*. **18**, 169–185 (2009).

PubMed Article PubMed Central Google Scholar

27. 27.

Venditti, C., Meade, A. & Pagel, M. Multiple routes to mammalian diversity. *Nature* **479**, 393–396 (2011).

ADS CAS PubMed Article PubMed Central Google Scholar

28. 28.

Cooney, C. R. et al. Mega-evolutionary dynamics of the adaptive radiation of birds. *Nature* **542**, 344–347 (2017).

ADS CAS PubMed PubMed Central Article Google Scholar

29. 29.

Ellegren, H. & Galtier, N. Determinants of genetic diversity. *Nat. Rev. Genet*. **17**, 422–433 (2016).

CAS PubMed Article PubMed Central Google Scholar

30. 30.

Schluter, D. & Pennell, M. W. Speciation gradients and the distribution of biodiversity. *Nature* **546**, 48–55 (2017).

ADS CAS PubMed Article PubMed Central Google Scholar

31. 31.

Grant, P. R. & Grant, B. R. *40 Years of Evolution: Darwin's Finches on Daphne Major Island* (Princeton Univ. Press, 2014).

32. 32.

Meier, J. I. et al. Ancient hybridization fuels rapid cichlid fish adaptive radiations. *Nat. Commun*. **8**, 14363 (2017).

ADS CAS PubMed PubMed Central Article Google Scholar

33. 33.

Malinsky, M. et al. Whole-genome sequences of Malawi cichlids reveal multiple radiations interconnected by gene flow. *Nat. Ecol. Evol*. **2**, 1940–1955 (2018).

PubMed PubMed Central Article Google Scholar

34. 34.

Patterson, N. et al. Ancient admixture in human history. *Genetics* **192**, 1065–1093 (2012).

PubMed PubMed Central Article Google Scholar

35. 35.

Bolger, A. M., Lohse, M. & Usadel, B. Trimmomatic: a flexible trimmer for Illumina sequence data. *Bioinformatics* **30**, 2114–2120 (2014).

CAS PubMed PubMed Central Article Google Scholar

36. 36.

Conte, M. A., Gammerdinger, W. J., Bartie, K. L., Penman, D. J. & Kocher, T. D. A high quality assembly of the Nile Tilapia (*Oreochromis niloticus*) genome reveals the structure of two sex determination regions. *BMC Genomics* **18**, 341 (2017).

PubMed PubMed Central Article CAS Google Scholar

37. 37.

Li, H. & Durbin, R. Fast and accurate short read alignment with Burrows–Wheeler transform. *Bioinformatics* **25**, 1754–1760 (2009).

CAS PubMed PubMed Central Article Google Scholar

38. 38.

McKenna, A. et al. The Genome Analysis Toolkit: a MapReduce framework for analyzing next-generation DNA sequencing data. *Genome Res*. **20**, 1297–1303 (2010).

CAS PubMed PubMed Central Article Google Scholar

39. 39.

Li, H. A statistical framework for SNP calling, mutation discovery, association mapping and population genetical parameter estimation from sequencing data. *Bioinformatics* **27**, 2987–2993 (2011).

CAS PubMed PubMed Central Article Google Scholar

40. 40.

Danecek, P. et al. The variant call format and VCFtools. *Bioinformatics* **27**, 2156–2158 (2011).

CAS PubMed PubMed Central Article Google Scholar

41. 41.

Browning, S. R. & Browning, B. L. Rapid and accurate haplotype phasing and missing-data inference for whole-genome association studies by use of localized haplotype clustering. *Am. J. Hum. Genet*. **81**, 1084–1097 (2007).

CAS PubMed PubMed Central Article Google Scholar

42. 42.

Böhne, A. et al. Repeated evolution versus common ancestry: Sex chromosome evolution in the haplochromine *Pseudocrenilabrus philander*. *Genome Biol. Evol*. **11**, 439–458 (2019).

PubMed PubMed Central Article CAS Google Scholar

43. 43.

Malmstrøm, M., Matschiner, M., Tørresen, O. K., Jakobsen, K. S. & Jentoft, S. Data descriptor: Whole genome sequencing data and de novo draft assemblies for 66 teleost species. *Sci. Data* **4**, 1–13 (2017).

Article CAS Google Scholar

44. 44.

Myers, E. W. et al. A whole-genome assembly of *Drosophila*. *Science* **287**, 2196–2204 (2000).

ADS CAS PubMed Article Google Scholar

45. 45.

Magoč, T. & Salzberg, S. L. FLASH: fast length adjustment of short reads to improve genome assemblies. *Bioinformatics* **27**, 2957–2963 (2011).

PubMed PubMed Central Article CAS Google Scholar

46. 46.

Gurevich, A., Saveliev, V., Vyahhi, N. & Tesler, G. QUAST: quality assessment tool for genome assemblies. *Bioinformatics* **29**, 1072–1075 (2013).

CAS PubMed PubMed Central Article Google Scholar

47. 47.

Simão, F. A., Waterhouse, R. M., Ioannidis, P., Kriventseva, E. V. & Zdobnov, E. M. BUSCO: assessing genome assembly and annotation completeness with single-copy orthologs. *Bioinformatics* **31**, 3210–3212 (2015).

PubMed Article CAS PubMed Central Google Scholar

48. 48.

Ewels, P., Magnusson, M., Lundin, S., Käller, M. & Multi, Q. C. MultiQC: summarize analysis results for multiple tools and samples in a single report. *Bioinformatics* **32**, 3047–3048 (2016).

CAS PubMed PubMed Central Article Google Scholar

49. 49.

Zhang, C., Rabiee, M., Sayyari, E. & Mirarab, S. ASTRAL-III: polynomial time species tree reconstruction from partially resolved gene trees. *BMC Bioinformatics* **19** (Suppl 6), 153 (2018).

PubMed PubMed Central Article Google Scholar

50. 50.

Bouckaert, R. et al. BEAST 2.5: An advanced software platform for Bayesian evolutionary analysis. *PLOS Comput. Biol*. **15**, e1006650 (2019).

CAS PubMed PubMed Central Article Google Scholar

51. 51.

Ogilvie, H. A., Bouckaert, R. R. & Drummond, A. J. StarBEAST2 brings faster species tree inference and accurate estimates of substitution rates. *Mol. Biol. Evol*. **34**, 2101–2114 (2017).

CAS PubMed PubMed Central Article Google Scholar

52. 52.

Stamatakis, A. RAxML version 8: a tool for phylogenetic analysis and post-analysis of large phylogenies. *Bioinformatics* **30**, 1312–1313 (2014).

CAS PubMed PubMed Central Article Google Scholar

53. 53.

Nguyen, L.-T., Schmidt, H. A., von Haeseler, A. & Minh, B. Q. IQ-TREE: a fast and effective stochastic algorithm for estimating maximum-likelihood phylogenies. *Mol. Biol. Evol*. **32**, 268–274 (2015).

CAS Article PubMed Google Scholar

54. 54.

Bryant, D., Bouckaert, R., Felsenstein, J., Rosenberg, N. A. & RoyChoudhury, A. Inferring species trees directly from biallelic genetic markers: bypassing gene trees in a full coalescent analysis. *Mol. Biol. Evol*. **29**, 1917–1932 (2012).

CAS PubMed PubMed Central Article Google Scholar

55. 55.

Schindelin, J. et al. Fiji: an open-source platform for biological-image analysis. *Nat. Methods* **9**, 676–682 (2012).

CAS PubMed Article Google Scholar

56. 56.

Schunke, A. C., Bromiley, P. A., Tautz, D. & Thacker, N. A. TINA manual landmarking tool: software for the precise digitization of 3D landmarks. *Front. Zool*. **9**, 6 (2012).

PubMed PubMed Central Article Google Scholar

57. 57.

Paradis, E., Claude, J. & Strimmer, K. APE: Analyses of phylogenetics and evolution in R language. *Bioinformatics* **20**, 289–290 (2004).

CAS PubMed Article PubMed Central Google Scholar

58. 58.

Kembel, S. W. et al. Picante: R tools for integrating phylogenies and ecology. *Bioinformatics* **26**, 1463–1464 (2010).

CAS PubMed Article PubMed Central Google Scholar

59. 59.

R Development Core Team. R: A language and environment for statistical computing. *R Foundation for Statistical Computing* (2018).

60. 60.

Adams, D. C. & Otárola-Castillo, E. Geomorph: An R package for the collection and analysis of geometric morphometric shape data. *Methods Ecol. Evol*. **4**, 393–399 (2013).

Article Google Scholar

61. 61.

Schlager, S. in *Statistical Shape and Deformation Analysis* (eds Zheng, G., Li, S. & Szekely, G.) 217–256 (Academic Press, 2017).

62. 62.

Ronco, F., Roesti, M. & Salzburger, W. A functional trade-off between trophic adaptation and parental care predicts sexual dimorphism in cichlid fish. *Proc. R. Soc. Lond. B* **286**, 20191050 (2019).

Google Scholar

63. 63.

Orme, D. *The Caper Package: Comparative Analysis of Phylogenetics and Evolution in R* https://cran.r-project.org/web/packages/caper/vignettes/caper.pdf (2018).

64. 64.

Seehausen, O., Mayhew, P. J. & Van Alphen, J. J. M. Evolution of colour patterns in East African cichlid fish. *J. Evol. Biol*. **12**, 514–534 (1999).

Article Google Scholar

65. 65.

Landgraf, A. J. & Lee, Y. Dimensionality reduction for binary data through the projection of natural parameters. *J. Multivar. Anal*. 104668 (2020).

66. 66.

Revell, L. J. phytools: An R package for phylogenetic comparative biology (and other things). *Methods Ecol. Evol*. **3**, 217–223 (2012).

Article Google Scholar

67. 67.

Harmon, L. J., Weir, J. T., Brock, C. D., Glor, R. E. & Challenger, W. GEIGER: investigating evolutionary radiations. *Bioinformatics* **24**, 129–131 (2008).

CAS PubMed Article PubMed Central Google Scholar

68. 68.

Plummer, M., Best, N., Cowles, K. & Vines, K. CODA: convergence diagnosis and output analysis for MCMC. *R News* **6**, 7–11 (2005).

Google Scholar

69. 69.

Ciampaglio, C. N., Kemp, M. & McShea, D. W. Detecting changes in morphospace occupation patterns in the fossil record: characterization and analysis of measures of disparity. *Paleobiology* **27**, 695–715 (2001).

Article Google Scholar

70. 70.

Layer, R. M., Chiang, C., Quinlan, A. R. & Hall, I. M. LUMPY: a probabilistic framework for structural variant discovery. *Genome Biol*. **15**, R84 (2014).

PubMed PubMed Central Article Google Scholar

71. 71.

Chiang, C. et al. SpeedSeq: ultra-fast personal genome analysis and interpretation. *Nat. Methods* **12**, 966–968 (2015).

CAS PubMed PubMed Central Article Google Scholar

72. 72.

Knaus, B. J. & Grünwald, N. J. vcfr: a package to manipulate and visualize variant call format data in R. *Mol. Ecol. Resour*. **17**, 44–53 (2017).

CAS PubMed Article Google Scholar

73. 73.

Stanke, M., Schöffmann, O., Morgenstern, B. & Waack, S. Gene prediction in eukaryotes with a generalized hidden Markov model that uses hints from external sources. *BMC Bioinformatics* **7**, 62 (2006).

PubMed PubMed Central Article CAS Google Scholar

74. 74.

Wu, T. D. & Watanabe, C. K. GMAP: a genomic mapping and alignment program for mRNA and EST sequences. *Bioinformatics* **21**, 1859–1875 (2005).

CAS PubMed Article PubMed Central Google Scholar

75. 75.

Ranwez, V., Douzery, E. J. P., Cambon, C., Chantret, N. & Delsuc, F. MACSE v2: Toolkit for the alignment of coding sequences accounting for frameshifts and stop codons. *Mol. Biol. Evol*. **35**, 2582–2584 (2018).

CAS PubMed PubMed Central Article Google Scholar

76. 76.

Yang, Z. PAML 4: phylogenetic analysis by maximum likelihood. *Mol. Biol. Evol*. **24**, 1586–1591 (2007).

CAS PubMed PubMed Central Article Google Scholar

77. 77.

Malinsky, M., Matschiner, M. & Svardal, H. Dsuite–fast *D*-statistics and related admixture evidence from VCF files. *Methods Ecol. Evol*. https://doi.org/10.1111/1755-0998.13265 (2020).

78. 78.

Kelleher, J., Etheridge, A. M. & McVean, G. Efficient coalescent simulation and genealogical analysis for large sample sizes. *PLOS Comput. Biol*. **12**, e1004842 (2016).

ADS PubMed PubMed Central Article CAS Google Scholar

79. 79.

Malinsky, M. et al. Genomic islands of speciation separate cichlid ecomorphs in an East African crater lake. *Science* **350**, 1493–1498 (2015).

ADS CAS PubMed PubMed Central Article Google Scholar

Download references

Acknowledgements

We thank the University of Burundi, the Ministère de l'Eau, de l'Environnement, de l'Amenagement du Territoire et de l'Urbanisme, Republic of Burundi, the Centre de Recherche en Hydrobiologie (CRH), Uvira, DR Congo, the Tanzania Commission for Science and Technology (COSTECH), the Tanzania Fisheries Research Institute (TAFIRI), the Tanzania National Parks Authority (TANAPA), the Tanzania Wildlife Research Institute (TAWIRI), the Lake Tanganyika Research Unit, Department of Fisheries, Republic of Zambia, and the Zambian Department for Immigration for research permits; G. Banyankimbona, H. Mwima, G. Hakizimana, N. Muderhwa, P. Masilya, I. Kimirei, M. Mukuli Wa-Teba, G. Moshi, A. Mwakatobe, C. Katongo, T. Banda and L. Makasa for assistance with obtaining research permits; the boat crews of the *Chomba* (D. Mwanakulya, J. Sichilima, H. D. Sichilima Jr and G. Katai) and the *Maji Makubwa II* (G. Kazumbe and family) for navigation, guidance and company; the boat drivers M. Katumba and T. Musisha; the car drivers A. Irakoze and J. Leonard; M. Schreyen-Brichard, M. Mukuli Wa-Teba, G. Kazumbe, I. Kimirei, D. Schlatter, R. Schlatter, M. K. Dominico, H. Sichilima Sr, C. Zytkow, P. Lassen and V. Huwiler for logistic support; G. Banyankimbona, N. Boileau, B. Egger, Y. Fermon, G. Kazumbe, G. Katai, R. Lusoma, K. Smailus, L. Widmer and numerous fishermen at Lake Tanganyika for help during sampling; V. Huwiler, Charity, O. Mangwangwa and the Zytkow family for lodging; people of innumerable villages on the shores of Lake Tanganyika for providing workspace, shelter for night-camps and access to village infrastructure; M. Barluenga, H. Gante, Z. Musilová, F. Schedel, J. Snoeks, M. Stiassny, H. Tanaka, G. Turner and M. Van Steenberge for providing additional samples and/or specimens; M. Sánchez, A. Schweizer and A. Wegmann for assistance with the

μCT scanning of large specimens; C. Moes for help with radiographs; V. Evrard for help with stable isotopes; I. Nissen and E. Burcklen for assistance with DNA shearing; M. Conte and T. D. Kocher for sharing the RepeatMasker annotations for Nile tilapia; C. Klingenberg and M. Sánchez for discussions on the morphometric approach; A. Tooming-Klunderud and team at the Norwegian Sequencing Centre and C. Beisel and team at the Genomics Facility Basel at the ETH Zurich Department of Biosystems Science and Engineering (D-BSSE), Basel, for assistance with next-generation sequencing; M. Jacquot, E. Pujades and T. Sengstag for the setup and assistance with the collection database system (LabKey); and J. Johnson and A. Viertler for fish illustrations in Fig. 1 and Extended Data Fig. 5, respectively. Calculations were performed at sciCORE (http://scicore.unibas.ch/) scientific computing centre at University of Basel (with support by the SIB/Swiss Institute of Bioinformatics) and the Abel computer cluster, University of Oslo. This work was funded by the European Research Council (ERC, Consolidator Grant Nr. 617585 'CICHLID~X' jointly hosted by the University of Basel and the University of Oslo) and the Swiss National Science Foundation (SNSF, grants 156405 and 176039) to W.S. A. Böhne was supported by the SNSF (Ambizione grant 161462).

Author information

Affiliations

1. Zoological Institute, Department of Environmental Sciences, University of Basel, Basel, Switzerland

   Fabrizia Ronco, Michael Matschiner, Astrid Böhne, Anna Boila, Heinz H. Büscher, Athimed El Taher, Adrian Indermaur, Milan Malinsky, Virginie Ricci & Walter Salzburger

2. Palaeontological Institute and Museum, University of Zurich, Zurich, Switzerland

   Michael Matschiner

3. Centre for Ecological and Evolutionary Synthesis (CEES), Department of Biosciences, University of Oslo, Oslo, Norway

   Michael Matschiner, Sissel Jentoft & Walter Salzburger

4. Centre for Molecular Biodiversity Research (ZMB), Zoological Research Museum Alexander Koenig, Bonn, Germany

   Astrid Böhne

5. Botany, Department of Environmental Sciences, University of Basel, Basel, Switzerland

   Ansgar Kahmen

Authors

1. Fabrizia Ronco
   View author publications

   You can also search for this author in PubMed Google Scholar

2. Michael Matschiner
   View author publications

   You can also search for this author in PubMed Google Scholar

3. Astrid Böhne
   View author publications

   You can also search for this author in PubMed Google Scholar

4. Anna Boila
   View author publications

   You can also search for this author in PubMed Google Scholar

5. Heinz H. Büscher
   View author publications

You can also search for this author in PubMed Google Scholar

6. Athimed El Taher
   View author publications

   You can also search for this author in PubMed Google Scholar

7. Adrian Indermaur
   View author publications

   You can also search for this author in PubMed Google Scholar

8. Milan Malinsky
   View author publications

   You can also search for this author in PubMed Google Scholar

9. Virginie Ricci
   View author publications

   You can also search for this author in PubMed Google Scholar

10. Ansgar Kahmen
    View author publications

    You can also search for this author in PubMed Google Scholar

11. Sissel Jentoft
    View author publications

    You can also search for this author in PubMed Google Scholar

12. Walter Salzburger
    View author publications

    You can also search for this author in PubMed Google Scholar

Contributions

F.R., A.I. and W.S. designed this study (with input from H.H.B., A.K. and S.J.). F.R., A.I., H.H.B. and W.S. collected the specimens in the field. F.R. and A. Böhne extracted DNA and prepared the libraries for sequencing. S.J. coordinated sequencing. M. Matschiner performed the mapping, variant calling, phylogenetic analyses and coalescent simulations. M. Malinsky contributed to the variant calling pipelines and performed the f_4-ratio statistics. A. Böhne assembled the genomes and quantified gene duplications, A.E.T. conducted the d*N*/d*S* analyses and V.R. analysed transposable elements. A. Boila assessed stable-isotope compositions, H.H.B. radiographed the specimens and W.S. scored pigmentation patterns. F.R. curated the samples and performed μCT scanning, geometric morphometric analyses, and all analyses incorporating morphological and ecological data as well as correlations with species richness. F.R. and W.S. wrote the manuscript with contributions and/or feedback from all authors. All authors read and approved the final version of the manuscript.

Corresponding authors

Correspondence to Fabrizia Ronco or Walter Salzburger.

Ethics declarations

Competing interests

The authors declare no competing interests.

Additional information

Peer review information *Nature* thanks the anonymous reviewer(s) for their contribution to the peer review of this work.

Publisher's note Springer Nature remains neutral with regard to jurisdictional claims in published maps and institutional affiliations.

Extended data figures and tables

Extended Data Fig. 1 Age of the adaptive radiation of cichlid fishes in African Lake Tanganyika.

Time-calibrated species tree of species representing divergent tribes and subfamilies within cichlids as well as closely-related non-cichlid outgroups, generated with the multi-species coalescent model in StarBEAST2. Nodes marked with a black dot were constrained according to species-tree analyses with ASTRAL. Node bars indicate 95% highest-posterior density age intervals. Outgroup divergence times are not drawn to scale. Insets visualize the prior distribution applied for the age of African cichlids according to Matschiner et al.[18], as well as posterior age estimates for Oreochromini and the cichlid adaptive radiation in Lake Tanganyika (LT).

Extended Data Fig. 2 Time-calibrated species tree of the cichlid adaptive radiation in Lake Tanganyika.

The species tree is based on the maximum-likelihood topology estimated with RAxML (Fig. 1) and was time-calibrated using a relaxed-clock model in BEAST2, applied to a selected set of alignments.

Extended Data Fig. 3 Alternative time-calibrated species tree of the cichlid adaptive radiation in Lake Tanganyika.

The species tree is based on the topology estimated with ASTRAL and was time-calibrated using a relaxed-clock model in BEAST2, applied to a selected set of alignments.

Extended Data Fig. 4 Alternative time-calibrated species tree of the cichlid adaptive radiation in Lake Tanganyika.

The species tree is based on the topology estimated with SNAPP and was time-calibrated using a relaxed-clock model in BEAST2, applied to a selected set of alignments.

Extended Data Fig. 5 Phenotyping of the specimens.

a, Two-dimensional landmarks placed on X-ray images of the specimens. To quantify overall body shape we excluded landmark 16 (to minimise the effect of the orientation of the oral jaw). To analyse upper oral jaw morphology we used landmarks 1, 2, 16 and 21. **b**, Three-dimensional landmarks used to analyse lower pharyngeal jaw shape on µCT scans of the heads. True landmarks are indicated in red, sliding semi-landmarks are indicated in blue. **c**, Body regions scored for presence/absence of pigmentation patterns.

Extended Data Fig. 6 Ecospace and morphospace occupation of the cichlid adaptive radiation in Lake Tanganyika.

Scatter plots for each focal tribe (indicated with colours, see Fig. 1 for colour key) against the total eco-and morphospace (grey). Species ranges are indicated with convex hulls. **a**, Stable N and C isotope compositions ($\delta^{15}N$ and $\delta^{13}C$ values). The additional plot shows $\delta^{15}N$ and $\delta^{13}C$ values of a baseline dataset which confirms the interpretability of the stable N and C isotope composition in Lake Tanganyika (see Supplementary Methods and Discussion). **b**, PC1 and PC2 of body shape (for shape changes associated with the PC axes see Fig. 2). The last plot for each trait shows the size of the traitspace per tribe in relation to species numbers (stable isotopes: Pearson's $r = 0.88$, d.f. = 9, $P = 0.0004$; body shape: Pearson's $r = 0.91$, d.f. = 9, $P = 0.0001$). Traitspace size was calculated as the square root of the convex hull area spanned by species means.

Extended Data Fig. 7 Morphospace occupation of the cichlid adaptive radiation in Lake Tanganyika.

a, **b**, Scatter plots of PC1 and PC2 for upper oral jaw morphology (**a**) and lower pharyngeal jaw shape per tribe (**b**) (indicated with colours, see Fig. 1 for colour key) against the total morphospace (grey). Species ranges are indicated with convex hulls. For shape changes associated with the respective PC-axis see Fig. 2. The last plot for each trait shows the size of the morphospace per tribe in relation to species numbers (upper oral jaw morphology: Pearson's $r = 0.88$, d.f. = 9, $P = 0.0003$; lower pharyngeal jaw shape: Pearson's $r = 0.83$, d.f. = 9, $P = 0.0017$). Morphospace size was

calculated as the square root of the convex hull area spanned by species means.

Extended Data Fig. 8 PLS fit for each multivariate trait against the stable N and C isotope compositions ($\delta^{15}N$ and $\delta^{13}C$ values) and models of trait evolution.

a–**c**, PLS fits for body shape (**a**), upper oral jaw morphology (**b**) and lower pharyngeal jaw shape (**c**). Associated shape changes and loadings of the respective stable isotope projection are indicated next to the axes. Data points represent species means and are coloured according to tribe. **d**, Comparison of model fits for different models of trait evolution and phylogenetic signal for each trait complex using three time-calibrated species trees with alternative topologies. **e**, Overview of the model fits and phylogenetic signal inferred using 100 trees sampled from the posterior distributions of the time calibrations for each of the three alternative tree topologies.

Extended Data Fig. 9 Genome-wide statistical analyses.

a, Proportion of the different classes of transposable elements (TE) among all TE for each tribe (one genome per species, $n = 245$). **b**, Species means of dN (left) and dS (right) values over alignment length for each tribe ($n = 243$ taxa, 471 genomes). The boxes' centre lines show median, box limits show first and third quartiles, and whiskers show the 1.5 × interquartile ranges. **c**, f_4-ratio statistics among species within each tribe in simulated data (tribe means are based on the mean across 20 simulations of each species triplet). Data points are coloured according to tribes; large points are tribe means shown with 95% confidence intervals, small points represent species means and are only shown for group sizes <40 species. To test for a correlation with species richness per tribe (log-transformed), we calculated phylogenetic independent contrasts for each variable and inferred Pearson's r through the origin.

Extended Data Fig. 10 Signals of introgression among Lake Tanganyika cichlid species.

Upper matrix: maximum values of the f_4-ratio statistics between all pairs of species, derived from calculations across all combinations of species trios with *T. sparrmanii* fixed as the outgroup. The f_4-ratio estimates the proportion of the genome affected by gene flow, all presented values are statistically significant (one-sided block-jackknife tests: $P < 5 \times 10^{-5}$ after Benjamini–Hochberg correction for multiple testing). Lower matrix: D_{tree}-statistics (hue) with corresponding P-value (two-tailed binomial test, not adjusted for multiple testing; log-transformed; saturation) based on a phylogenetic approach testing for asymmetry in the relationships of species trios in 1,272 local maximum-likelihood trees (see Supplementary Methods). The two different approaches uncovered little gene flow among the tribes (see Supplementary Discussion).

Supplementary information

Supplementary Information

This file contains Supplementary Methods with a detailed description of methods used to collect and analyse the data presented in the manuscript, and a Supplementary Discussion, and Supplementary Figures 1 and 2.

Reporting Summary

Supplementary Tables

This file contains Supplementary Tables 1 and 2 with sample size information per species for each data set, read depth of the genomes, and information on each of the specimens used in the study, including taxonomic information and sampling locations. The title and caption of each Supplementary Table can be found in the Supplementary Information file.

Source data

Source Data Fig. 1

Source Data Fig. 2

Source Data Fig. 3

Source Data Fig. 4

Rights and permissions

Reprints and Permissions

About this article

Check for updates

Cite this article

Ronco, F., Matschiner, M., Böhne, A. *et al.* Drivers and dynamics of a massive adaptive radiation in cichlid fishes. *Nature* **589,** 76–81 (2021). https://doi.org/10.1038/s41586-020-2930-4

Download citation

- Received: 04 February 2020
- Accepted: 20 August 2020
- Published: 18 November 2020
- Issue Date: 07 January 2021
- DOI: https://doi.org/10.1038/s41586-020-2930-4

Further reading

- **Gene expression dynamics during rapid organismal diversification in African cichlid fishes**

  - Athimed El Taher
  - , Astrid Böhne
  - , Nicolas Boileau
  - , Fabrizia Ronco
  - , Adrian Indermaur
  - , Lukas Widmer
  - & Walter Salzburger

Nature Ecology & Evolution (2020)

Comments

By submitting a comment you agree to abide by our Terms and Community Guidelines. If you find something abusive or that does not comply with our terms or guidelines please flag it as inappropriate.

Access through your institution
Change institution
Buy or subscribe

This article was downloaded by **calibre** from https://www.nature.com/articles/s41586-020-2930-4

Mobility network models of COVID-19 explain inequities and inform reopening
Download PDF

- Article
- Published: 10 November 2020

Mobility network models of COVID-19 explain inequities and inform reopening

- Serina Chang ORCID: orcid.org/0000-0002-4253-1016[1 na1],
- Emma Pierson[1,2 na1],
- Pang Wei Koh[1 na1],
- Jaline Gerardin ORCID: orcid.org/0000-0001-8071-9928[3],
- Beth Redbird[4,5],
- David Grusky[6,7] &
- Jure Leskovec ORCID: orcid.org/0000-0002-5411-923X[1,8]

Nature **volume 589**, pages82–87(2021)Cite this article

- 438k Accesses
- 7 Citations
- 8659 Altmetric
- Metrics details

Subjects

- Computational science
- Epidemiology
- SARS-CoV-2
- Society

Abstract

The coronavirus disease 2019 (COVID-19) pandemic markedly changed human mobility patterns, necessitating epidemiological models that can capture the effects of

these changes in mobility on the spread of severe acute respiratory syndrome coronavirus 2 (SARS-CoV-2)[1]. Here we introduce a metapopulation susceptible–exposed–infectious–removed (SEIR) model that integrates fine-grained, dynamic mobility networks to simulate the spread of SARS-CoV-2 in ten of the largest US metropolitan areas. Our mobility networks are derived from mobile phone data and map the hourly movements of 98 million people from neighbourhoods (or census block groups) to points of interest such as restaurants and religious establishments, connecting 56,945 census block groups to 552,758 points of interest with 5.4 billion hourly edges. We show that by integrating these networks, a relatively simple SEIR model can accurately fit the real case trajectory, despite substantial changes in the behaviour of the population over time. Our model predicts that a small minority of 'superspreader' points of interest account for a large majority of the infections, and that restricting the maximum occupancy at each point of interest is more effective than uniformly reducing mobility. Our model also correctly predicts higher infection rates among disadvantaged racial and socioeconomic groups[2,3,4,5,6,7,8] solely as the result of differences in mobility: we find that disadvantaged groups have not been able to reduce their mobility as sharply, and that the points of interest that they visit are more crowded and are therefore associated with higher risk. By capturing who is infected at which locations, our model supports detailed analyses that can inform more-effective and equitable policy responses to COVID-19.

Download PDF

Main

In response to the COVID-19 crisis, stay-at-home orders were enacted in many countries to reduce contact between individuals and slow the spread of the SARS-CoV-2[9]. Since then, public officials have continued to deliberate over when to reopen, which places are safe to return to and how much activity to allow[10]. Answering these questions requires epidemiological models that can capture the effects of changes in mobility on virus spread. In particular, findings of COVID-19 superspreader events[11,12,13,14] motivate models that can reflect the heterogeneous risks of visiting different locations, whereas well-reported disparities in infection rates among different racial and socioeconomic groups[2,3,4,5,6,7,8] require models that can explain the disproportionate effect of the virus on disadvantaged groups.

To address these needs, we construct fine-grained dynamic mobility networks from mobile-phone geolocation data, and use these networks to model the spread of SARS-CoV-2 within 10 of the largest metropolitan statistical areas (hereafter referred to as metro areas) in the USA. These networks map the hourly movements of 98 million people from census block groups (CBGs), which are geographical units that typically

contain 600–3,000 people, to specific points of interest (POIs). As shown in Supplementary Table 1, POIs are non-residential locations that people visit such as restaurants, grocery stores and religious establishments. On top of each network, we overlay a metapopulation SEIR model that tracks the infection trajectories of each CBG as well as the POIs at which these infections are likely to have occurred. This builds on prior research that models disease spread using aggregate[15,16,17,18,19], historical[20,21,22] or synthetic mobility data[23,24,25]; separately, other studies have analysed mobility data in the context of COVID-19, but without an underlying model of disease spread[26,27,28,29,30].

Combining our epidemiological model with these mobility networks allows us to not only accurately fit observed case counts, but also to conduct detailed analyses that can inform more-effective and equitable policy responses to COVID-19. By capturing information about individual POIs (for example, the hourly number of visitors and median visit duration), our model can estimate the effects of specific reopening strategies, such as only reopening certain POI categories or restricting the maximum occupancy at each POI. By modelling movement from CBGs, our model can identify at-risk populations and correctly predict, solely from mobility patterns, that disadvantaged racial and socioeconomic groups face higher rates of infection. Our model thus enables the analysis of urgent health disparities; we use it to highlight two mobility-related mechanisms that drive these disparities and to evaluate the disparate effect of reopening on disadvantaged groups.

Mobility network model

We use data from SafeGraph, a company that aggregates anonymized location data from mobile applications, to study mobility patterns from 1 March to 2 May 2020. For each metro area, we represent the movement of individuals between CBGs and POIs as a bipartite network with time-varying edges, in which the weight of an edge between a CBG and POI represents the number of visitors from that CBG to that POI during a given hour (Fig. 1a). SafeGraph also provides the area in square feet of each POI, as well as its category in the North American industry classification system (for example, fitness centre or full-service restaurant) and median visit duration in minutes. We validated the SafeGraph mobility data by comparing the dataset to Google mobility data (Supplementary Fig. 1 and Supplementary Tables 2, 3) and used iterative proportional fitting[31] to derive POI–CBG networks from the raw SafeGraph data. Overall, these networks comprise 5.4 billion hourly edges between 56,945 CBGs and 552,758 POIs (Extended Data Table 1).

Fig. 1: Model description and fit.

figure1

a, The mobility network captures hourly visits from each CBG to each POI. The vertical lines indicate that most visits are between nearby POIs and CBGs. Visits dropped markedly from March to April, as indicated by the lower density of grey lines. Mobility networks in the Chicago metro area are shown for 13:00 on two Mondays, 2 March 2020 (top) and 6 April 2020 (bottom). **b**, We overlaid a disease-spread model on the mobility network, with each CBG having its own set of SEIR compartments. New infections occur at both POIs and CBGs, with the mobility network governing how subpopulations from different CBGs interact as they visit POIs. **c**, Left, to test the out-of-sample prediction, we calibrated the model on data before 15 April 2020 (vertical black line). Even though its parameters remain fixed over time, the model accurately predicts the case trajectory in the Chicago metro area after 15 April using the mobility data (r.m.s.e. on daily cases = 406 for dates ranging from 15 April to 9 May). Right, model fit was further improved when we calibrated the model on the full range of data (r.m.s.e. on daily cases = 387 for the dates ranging from 15 April to 9 May). **d**, We fitted separate models to 10 of the largest US metro areas, modelling a total population of 98 million people; here, we show full model fits, as in **c** (right). In **c** and **d**, the blue line represents the model predictions and the grey

crosses represent the number of daily reported cases; as the numbers of reported cases tend to have great variability, we also show the smoothed weekly average (orange line). Shaded regions denote the 2.5th and 97.5th percentiles across parameter sets and stochastic realizations. Across metro areas, we sample 97 parameter sets, with 30 stochastic realizations each (n = 2,910); see Supplementary Table 6 for the number of sets per metro area.

Full size image

We overlay a SEIR model on each mobility network[15,20], in which each CBG maintains its own susceptible (S), exposed (E), infectious (I) and removed (R) states (Fig. 1b). New infections occur at both POIs and CBGs, with the mobility network governing how subpopulations from different CBGs interact as they visit POIs. We use the area, median visit duration and time-varying density of infectious individuals for each POI to determine the hourly infection rate of that POI. The model has only three free parameters that scale: (1) transmission rates at POIs, (2) transmission rates at CBGs and (3) the initial proportion of exposed individuals (Extended Data Table 2); all three parameters remain constant over time. We calibrate a separate model for each metro area using the confirmed case counts from *The New York Times* by minimizing the root mean square error (r.m.s.e.) to daily incident cases[32]. Our model accurately fits observed daily case counts in all 10 metro areas from 8 March to 9 May 2020 (Fig. 1c, d). In addition, when calibrated on only the case counts up to 14 April, the model predicts case counts reasonably well on the held-out time period of 15 April–9 May 2020 (Fig. 1c and Extended Data Fig. 1a). Our key technical finding is that the dynamic mobility network allows even our relatively simple SEIR model with just three static parameters to accurately fit observed cases, despite changing policies and behaviours during that period.

Mobility reduction and reopening plans

We can estimate the impact of mobility-related policies by constructing a hypothetical mobility network that reflects the expected effects of each policy, and running our SEIR model forward with this hypothetical network. Using this approach, we assess a wide range of mobility reduction and reopening strategies.

The magnitude of mobility reduction is at least as important as its timing

Mobility in the USA dropped sharply in March 2020: for example, overall POI visits in the Chicago metro area fell by 54.7% between the first week of March and the first week of April 2020. We constructed counterfactual mobility networks by scaling the magnitude of mobility reduction down and by shifting the timeline earlier and later,

and applied our model to the counterfactual networks to simulate the resulting infection trajectories. Across metro areas, we found that the magnitude of mobility reduction was at least as important as its timing (Fig. 2a and Supplementary Tables 4, 5): for example, if the mobility reduction in the Chicago metro area had been only a quarter of the size, the predicted number of infections would have increased by 3.3× (95% confidence interval, 2.8–3.8×), compared with a 1.5× (95% confidence interval, 1.4–1.6×) increase had people begun reducing their mobility one full week later. Furthermore, if no mobility reduction had occurred at all, the predicted number of infections in the Chicago metro area would have increased by 6.2× (95% confidence interval, 5.2–7.1×). Our results are in accordance with previous findings that mobility reductions can markedly reduce infections[18,19,33,34].

Fig. 2: Assessing mobility reduction and reopening.

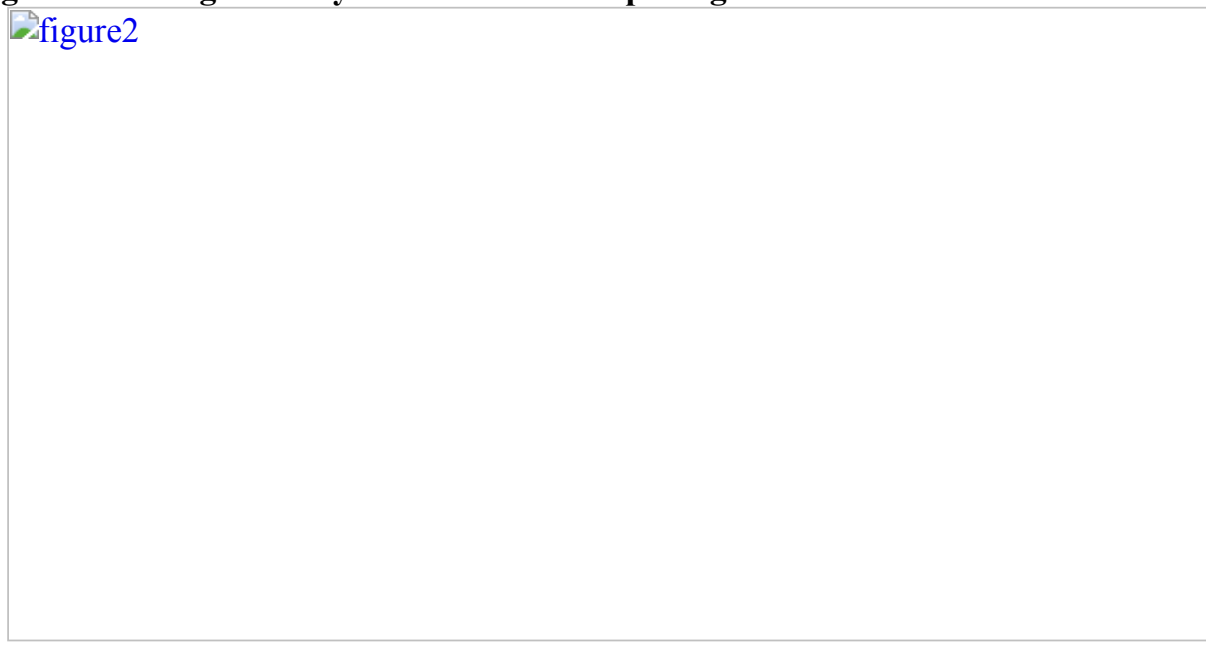

The Chicago metro area is used as an example; results for all metro areas are included in Extended Data Figs. 3, 4, Supplementary Figs. 10, 15–24 and Supplementary Tables 4, 5, as indicated. **a**, Counterfactual simulations (left) of past reductions in mobility illustrate that the magnitude of the reduction (middle) was at least as important as its timing (right) (Supplementary Tables 4, 5). **b**, The model predicts that most infections at POIs occur at a small fraction of superspreader POIs (Supplementary Fig. 10). **c**, Left, the cumulative number of predicted infections after one month of reopening is plotted against the fraction of visits lost by partial instead of full reopening (Extended Data Fig. 3); the annotations within the plot show the fraction of maximum occupancy that is used as the cap and the horizontal red line indicates the cumulative number of predicted infections at the point of reopening (on 1 May 2020). Compared to full reopening, capping at 20% of the maximum occupancy in Chicago reduces the number of new infections by more than 80%, while only losing 42% of overall visits. Right,

compared to uniformly reducing visits, the reduced maximum occupancy strategy always results in a smaller predicted increase in infections for the same number of visits (Extended Data Fig. 4). The horizontal grey line at 0% indicates when the two strategies result in an equal number of infections, and we observe that the curve falls well below this baseline. The *y* axis plots the relative difference between the predicted number of new infections under the reduced occupancy strategy compared to a uniform reduction. **d**, Reopening full-service restaurants has the largest predicted impact on infections, due to the large number of restaurants as well as their high visit densities and long dwell times (Supplementary Figs. 15–24). Colours are used to distinguish the different POI categories, but do not have any additional meaning. All results in this figure are aggregated across 4 parameter sets and 30 stochastic realizations ($n = 120$). Shaded regions in **a**–**c** denote the 2.5th to 97.5th percentiles; boxes in **d** denote the interquartile range and data points outside this range are shown as individual dots.

Full size image

A minority of POIs account for the majority of the predicted infections

We next investigated whether it matters how we reduce mobility—that is, to which POIs. We computed the number of infections that occurred at each POI in our simulations from 1 March to 2 May 2020, and found that the majority of the predicted infections occurred at a small fraction of superspreader POIs; for example, in the Chicago metro area, 10% of POIs accounted for 85% (95% confidence interval, 83–87%) of the predicted infections at the POIs (Fig. 2b and Supplementary Fig. 10). Certain categories of POIs also contributed far more to infections (for example, full-service restaurants and hotels), although our model predicted time-dependent variation in how much each category contributed (Extended Data Fig. 2). For example, restaurants and fitness centres contributed less to the predicted number of infections over time, probably because of lockdown orders to close these POIs, whereas grocery stores remained steady or even grew in their contribution, which is in agreement with their status as essential businesses.

Reopening with a reduced maximum occupancy

If a minority of POIs produce the majority of infections, then reopening strategies that specifically target high-risk POIs should be especially effective. To test one such strategy, we simulated reopening on 1 May, and modelled the effects of reducing the maximum occupancy in which the numbers of hourly visits to each POI returned to their 'normal' levels from the first week of March but were capped if they exceeded a fraction of the maximum occupancy of that POI[35]. Full reopening without reducing the maximum occupancy produced a spike in the predicted number of infections: in the

Chicago metro area, our models projected that an additional 32% (95% confidence interval, 25–35%) of the population would be infected by the end of May (Fig. 2c). However, reducing the maximum occupancy substantially reduced the risk without sharply reducing overall mobility: capping at 20% of the maximum occupancy in the Chicago metro area reduced the predicted number of new infections by more than 80% but only lost 42% of overall visits, and we observed similar trends across other metro areas (Extended Data Fig. 3). This result highlights the nonlinearity of the predicted number of infections as a function of the number of visits: one can achieve a disproportionately large reduction in infections with a small reduction in visits. Furthermore, in comparison to a different reopening strategy, in which the number of visits to each POI was uniformly reduced from their levels in early March, reducing the maximum occupancy always resulted in fewer predicted infections for the same number of total visits (Fig. 2c and Extended Data Fig. 4). This is because reducing the maximum occupancies takes advantage of the time-varying visit density within each POI, disproportionately reducing visits to the POI during the high-density periods with the highest risk, but leaving visit counts unchanged during periods with lower risks. These results support previous findings that precise interventions, such as reducing the maximum occupancy, may be more effective than less targeted measures, while incurring substantially lower economic costs[36].

Relative risk of reopening different categories of POIs

Because we found that certain POI categories contributed far more to predicted infections in March (Extended Data Fig. 2), we also expected that reopening some POI categories would be riskier than reopening others. To assess this, we simulated reopening each category in turn on 1 May 2020 (by returning its mobility patterns to early March levels, as above), while keeping all other POIs at their reduced mobility levels from the end of April. We found large variation in predicted reopening risks: on average across metro areas, full-service restaurants, gyms, hotels, cafes, religious organizations and limited-service restaurants produced the largest predicted increases in infections when reopened (Extended Data Fig. 5d). Reopening full-service restaurants was associated with a particularly high risk: in the Chicago metro area, we predicted an additional 595,805 (95% confidence interval, 433,735–685,959) infections by the end of May, more than triple that of the POI category with the next highest risk (Fig. 2d). These risks are summed over all POIs in the category, but the relative risks after normalizing by the number of POIs were broadly similar (Extended Data Fig. 5c). These categories were predicted to be have a higher risk because, in the mobility data, their POIs tended to have higher visit densities and/or visitors stayed there longer (Supplementary Figs. 15–24).

Demographic disparities in infections

We characterize the differential spread of SARS-CoV-2 along demographic lines by using US census data to annotate each CBG with its racial composition and median income, then tracking predicted infection rates in CBGs with different demographic compositions: for example, within each metro area, comparing CBGs in the top and bottom deciles for income. We use this approach to study the mobility mechanisms behind disparities and to quantify how different reopening strategies affect disadvantaged groups.

Predicting disparities from mobility data

Despite having access to only mobility data and no demographic information, our models correctly predicted higher risks of infection among disadvantaged racial and socioeconomic groups[2,3,4,5,6,7,8]. Across all metro areas, individuals from CBGs in the bottom decile for income had a substantially higher likelihood of being infected by the end of the simulation, even though all individuals began with equal likelihoods of infection (Fig. 3a). This predicted disparity was driven primarily by a few POI categories (for example, full-service restaurants); far greater proportions of individuals from lower-income CBGs than higher-income CBGs became infected in these POIs (Fig. 3c and Supplementary Fig. 2). We similarly found that CBGs with fewer white residents had higher predicted risks of infection, although results were more variable across metro areas (Fig. 3b). In the Supplementary Discussion, we confirm that the magnitude of the disparities that our model predicts is generally consistent with real-world disparities and further explore the large predicted disparities in Philadelphia, that stem from substantial differences in the POIs that are frequented by higher- versus lower-income CBGs. In the analysis below, we discuss two mechanisms that lead higher predicted infection rates among lower-income CBGs, and we show in Extended Data Fig. 6 and Extended Data Table 4 that similar results hold for racial disparities as well.

Fig. 3: Mobility patterns give rise to infection disparities.

figure3

a, In every metro area, our model predicts that people in lower-income CBGs are likelier to be infected. **b**, People in non-white CBGs area are also likelier to be infected, although results are more variable across metro areas. For **c**–**f**, the Chicago metro area is used as an example, but references to results for all metro areas are provided for each panel. **c**, The overall predicted disparity is driven by a few POI categories such as full-service restaurants (Supplementary Fig. 2). **d**, One reason for the predicted disparities is that higher-income CBGs were able to reduce their mobility levels below those of lower-income CBGs (Extended Data Fig. 6). **e**, Within each POI category, people from lower-income CBGs tend to visit POIs that have higher predicted transmission rates (Extended Data Table 3). The size of each dot represents the average number of visits per capita made to the category. The top 10 out of 20 categories with the most visits are labelled, covering 0.48–2.88 visits per capita (hardware stores–full-service restaurants). **f**, Reopening (at different levels of reduced maximum occupancy) leads to more predicted infections in lower-income CBGs than in the overall population (Extended Data Fig. 3). In **c**–**f**, purple denotes lower-income CBGs, yellow denotes higher-income CBGs and blue represents the overall population. Aside from **d** and **e**, which were directly extracted from mobility data, all results in this figure represent predictions aggregated over model realizations. Across metro areas, we sample 97 parameter sets, with 30 stochastic realizations each (n = 2,910); see Supplementary Table 6 for the number of sets per metro area. Shaded regions in **c** and **f** denote the 2.5th–97.5th percentiles; boxes in (**a**, **b**) denote the interquartile range; data points outside the range are shown as individual dots.

Full size image

Lower-income CBGs saw smaller reductions in mobility

A first mechanism producing disparities was that, across all metro areas, lower-income CBGs did not reduce their mobility as sharply in the first few weeks of March 2020, and these groups showed higher mobility than higher-income CBGs for most of March–May (Fig. 3d and Extended Data Fig. 6). For example, in April, individuals from lower-income CBGs in the Chicago metro area had 27% more POI visits per capita than those from higher-income CBGs. Category-level differences in visit patterns partially explained the infection disparities within each category: for example, individuals from lower-income CBGs made substantially more visits per capita to grocery stores than did those from higher-income CBGs (Supplementary Fig. 3) and consequently experienced more predicted infections for that category (Supplementary Fig. 2).

POIs visited by lower-income CBGs have higher transmission rates

Differences in visits per capita do not fully explain the infection disparities: for example, cafes and snack bars were visited more frequently by higher-income CBGs in every metro area (Supplementary Fig. 3), but our model predicted that a larger proportion of individuals from lower-income CBGs were infected at cafes and snack bars in the majority of metro areas (Supplementary Fig. 2). We found that even within a POI category, the predicted transmission rates at POIs frequented by individuals fom lower-income CBGs tended to be higher than the corresponding rates for those from higher-income CBGs (Fig. 3e and Extended Data Table 3), because POIs frequented by individuals from lower-income CBGs tended to be smaller and more crowded in the mobility data. As a case study, we examined grocery stores in further detail. In eight of the ten metro areas, visitors from lower-income CBGs encountered higher predicted transmission rates at grocery stores than visitors from higher-income CBGs (median transmission rate ratio of 2.19) (Extended Data Table 3). We investigated why one visit to the grocery store was predicted to be twice as dangerous for an individual from a lower-income CBG: the mobility data showed that the average grocery store visited by individuals from lower-income CBGs had 59% more hourly visitors per square foot, and their visitors stayed 17% longer on average (medians across metro areas). These findings highlight how fine-grained differences in mobility patterns—how often people go out and which POIs that they go to—can ultimately contribute to marked disparities in predicted infection outcomes.

Reopening plans must account for disparate effects

Because disadvantaged groups suffer a larger burden of infection, it is critical to not only consider the overall impact of reopening plans but also their disparate effects on disadvantaged groups specifically. For example, our model predicted that full

reopening in the Chicago metro area would result in an additional 39% (95% confidence interval, 31–42%) of the population of CBGs in the bottom income decile being infected within a month, compared to 32% (95% confidence interval, 25–35%) of the overall population (Fig. 3f; results for all metro areas are shown in Extended Data Fig. 3). Similarly, Supplementary Fig. 4 illustrates that reopening individual POI categories tends to have a larger predicted effect on lower-income CBGs. More stringent reopening plans produce smaller absolute disparities in predicted infections —for example, we predict that reopening at 20% of the maximum occupancy in Chicago would result in additional infections for 6% (95% confidence interval, 4–8%) of the overall population and 10% (95% confidence interval, 7–13%) of the population in CBGs in the bottom income decile (Fig. 3f)—although the relative disparity remains.

Discussion

The mobility dataset that we use has limitations: it does not cover all populations, does not contain all POIs and cannot capture sub-CBG heterogeneity. Our model itself is also parsimonious, and does not include all real-world features that are relevant to disease transmission. We discuss these limitations in more detail in the Supplementary Discussion. However, the predictive accuracy of our model suggests that it broadly captures the relationship between mobility and transmission, and we thus expect our broad conclusions—for example, that people from lower-income CBGs have higher infection rates in part because they tend to visit denser POIs and because they have not reduced mobility by as much (probably because they cannot work from home as easily[4])—to hold robustly. Our fine-grained network modelling approach naturally extends to other mobility datasets and models that capture more aspects of real-world transmission, and these represent interesting directions for future work.

Our results can guide policy-makers that seek to assess competing approaches to reopening. Despite growing concern about racial and socioeconomic disparities in infections and deaths, it has been difficult for policy-makers to act on those concerns; they are currently operating without much evidence on the disparate effects of reopening policies, prompting calls for research that both identifies the causes of observed disparities and suggests policy approaches to mitigate them[5,8,37,38]. Our fine-grained mobility modelling addresses both these needs. Our results suggest that infection disparities are not the unavoidable consequence of factors that are difficult to address in the short term, such as differences in preexisting conditions; on the contrary, short-term policy decisions can substantially affect infection outcomes by altering the overall amount of mobility allowed and the types of POIs reopened. Considering the disparate effects of reopening plans may lead policy-makers to adopt policies that can drive down infection densities in disadvantaged neighbourhoods by supporting, for example, more stringent caps on POI occupancies, emergency food distribution

centres to reduce densities in high-risk stores, free and widely available testing in neighbourhoods predicted to be high risk (especially given known disparities in access to tests[2]), improved paid leave policy or income support that enables essential workers to curtail mobility when sick, and improved workplace infection prevention for essential workers, such as high-quality personal protective equipment, good ventilation and physical distancing when possible. As reopening policies continue to be debated, it is critical to build tools that can assess the effectiveness and equity of different approaches. We hope that our model, by capturing heterogeneity across POIs, demographic groups and cities, helps to address this need.

Methods

The Methods is structured as follows. We describe the datasets that we used in the 'Datasets' section and the mobility network that we derived from these datasets in the 'Mobility network' section. In the 'Model dynamics' section, we discuss the SEIR model that we overlaid on the mobility network; in the 'Model calibration' section, we describe how we calibrated this model and quantified uncertainty in its predictions. Finally, in the 'Analysis details' section, we provide details on the experimental procedures used for our analyses of mobility reduction, reopening plans and demographic disparities.

Datasets

SafeGraph

We use data provided by SafeGraph, a company that aggregates anonymized location data from numerous mobile applications. SafeGraph data captures the movement of people between CBGs, which are geographical units that typically contain a population of between 600 and 3,000 people, and POIs such as restaurants, grocery stores or religious establishments. Specifically, we use the following SafeGraph datasets.

First, we used the Places Patterns[39] and Weekly Patterns (v1)[40] datasets. These datasets contain, for each POI, hourly counts of the number of visitors, estimates of median visit duration in minutes (the 'dwell time') and aggregated weekly and monthly estimates of the home CBGs of visitors. We use visitor home CBG data from the Places Patterns dataset: for privacy reasons, SafeGraph excludes a home CBG from this dataset if fewer than five devices were recorded at the POI from that CBG over the course of the month. For each POI, SafeGraph also provides their North American industry classification system category, as well as estimates of its physical area in square feet. The area is computed using the footprint polygon SafeGraph that

assigns to the POI[41,42]. We analyse Places Patterns data from 1 January 2019 to 29 February 2020 and Weekly Patterns data from 1 March 2020 to 2 May 2020.

Second, we used the Social Distancing Metrics dataset[43], which contains daily estimates of the proportion of people staying home in each CBG. We analyse Social Distancing Metrics data from 1 March 2020 to 2 May 2020.

We focus on 10 of the largest metro areas in the United States (Extended Data Table 1). We chose these metro areas by taking a random subset of the SafeGraph Patterns data and selecting the 10 metro areas with the most POIs in the data. The application of the methods described in this paper to the other metro areas in the original SafeGraph data should be straightforward. For each metro area, we include all POIs that meet all of the following requirements: (1) the POI is located in the metro area ; (2) SafeGraph has visit data for this POI for every hour that we model, from 00:00 on 1 March 2020 to 23:00 on 2 May 2020; (3) SafeGraph has recorded the home CBGs of visitors to this POI for at least one month from January 2019 to February 2020; (4) the POI is not a 'parent' POI. Parent POIs comprise a small fraction of POIs in the dataset that overlap and include the visits from their 'child' POIs: for example, many malls in the dataset are parent POIs, which include the visits from stores that are their child POIs. To avoid double-counting visits, we remove all parent POIs from the dataset. After applying these POI filters, we include all CBGs that have at least one recorded visit to at least ten of the remaining POIs; this means that CBGs from outside the metro area may be included if they visit this metro area frequently enough. Summary statistics of the post-processed data are shown in Extended Data Table 1. Overall, we analyse 56,945 CBGs from the 10 metro areas, and more than 310 million visits from these CBGs to 552,758 POIs.

SafeGraph data have been used to study consumer preferences[44] and political polarization[45]. More recently, it has been used as one of the primary sources of mobility data in the USA for tracking the effects of the COVID-19 pandemic[26,28,46,47,48]. In Supplementary Methods section 1, we show that aggregate trends in SafeGraph mobility data match the aggregate trends in Google mobility data in the USA[49], before and after the imposition of stay-at-home measures. Previous analyses of SafeGraph data have shown that it is geographically representative—for example, it does not systematically overrepresent individuals from CBGs in different counties or with different racial compositions, income levels or educational levels[50,51].

US census

Our data on the demographics of the CBGs comes from the American Community Survey (ACS) of the US Census Bureau[52]. We use the 5-year ACS data (2013–2017) to extract the median household income, the proportion of white residents and the

proportion of Black residents of each CBG. For the total population of each CBG, we use the most-recent one-year estimates (2018); one-year estimates are noisier but we wanted to minimize systematic downward bias in our total population counts (due to population growth) by making them as recent as possible.

The New York Times dataset

We calibrated our models using the COVID-19 dataset published by the *The New York Times*[32]. Their dataset consists of cumulative counts of cases and deaths in the USA over time, at the state and county level. For each metro area that we modelled, we sum over the county-level counts to produce overall counts for the entire metro area. We convert the cumulative case and death counts to daily counts for the purposes of model calibration, as described in the 'Model calibration' section.

Data ethics

The dataset from *The New York Times* consists of aggregated COVID-19-confirmed case and death counts collected by journalists from public news conferences and public data releases. For the mobility data, consent was obtained by the third-party sources that collected the data. SafeGraph aggregates data from mobile applications that obtain opt-in consent from their users to collect anonymous location data. Google's mobility data consists of aggregated, anonymized sets of data from users who have chosen to turn on the location history setting. Additionally, we obtained IRB exemption for SafeGraph data from the Northwestern University IRB office.

Mobility network

Definition

We consider a complete undirected bipartite graph $\mathscr{G}=(\mathscr{V},\mathcal{E})$ with time-varying edges. The vertices $\mathscr{V}$ are partitioned into two disjoint sets $\mathscr{C}=\{c_1,\ldots,c_m\}$, representing m CBGs, and $\mathscr{P}=\{p_1,\ldots,p_n\}$, representing n POIs. From US census data, each CBG c_i is labelled with its population N_{c_i}, income distribution, and racial and age demographics. From SafeGraph data, each POI p_j is similarly labelled with its category (for example, restaurant, grocery store or religious organization), its physical size in square feet a_{p_j}, and the median dwell time d_{p_j} of visitors to p_j. The weight $w_{ij}^{(t)}$ on an edge (c_i, p_j) at time t represents our estimate of the number of individuals from CBG c_i visiting POI p_j at the tth hour of simulation. We

record the number of edges (with non-zero weights) in each metro area and for all hours from 1 March 2020 to 2 May 2020 in Extended Data Table 1. Across all 10 metro areas, we study 5.4 billion edges between 56,945 CBGs and 552,758 POIs.

Overview of the network estimation

The central technical challenge in constructing this network is estimating the network weights $\{ W\} ^{ (t)} \,=\,\{ \{ w\} _{ ij} ^{ (t)} \} \)$ from SafeGraph data, as this visit matrix is not directly available from the data. Our general methodology for network estimation is as follows.

First, from SafeGraph data, we derived a time-independent estimate $\(\bar{ W} \)$ of the visit matrix that captures the aggregate distribution of visits from CBGs to POIs from January 2019 to February 2020.

Second, because visit patterns differ substantially from hour to hour (for example, day versus night) and day to day (for example, before versus after lockdown), we used current SafeGraph data to capture these hourly variations and to estimate the CBG marginals $U^{(t)}$, that is, the number of people in each CBG who are out visiting POIs at hour t, as well as the POI marginals $V^{(t)}$, that is, the total number of visitors present at each POI p_j at hour t.

Finally, we applied the iterative proportional fitting procedure (IPFP) to estimate an hourly visit matrix $W^{(t)}$ that is consistent with the hourly marginals $U^{(t)}$ and $V^{(t)}$ but otherwise 'as similar as possible' to the distribution of visits in the aggregate visit matrix $\(\bar{ W} \)$, in terms of Kullback–Leibler divergence.

IPFP is a classic statistical method[31] for adjusting joint distributions to match prespecified marginal distributions, and it is also known in the literature as biproportional fitting, the RAS algorithm or raking[53]. In the social sciences, it has been widely used to infer the characteristics of local subpopulations (for example, within each CBG) from aggregate data[54,55,56]. IPFP estimates the joint distribution of visits from CBGs to POIs by alternating between scaling each row to match the hourly row (CBG) marginals $U^{(t)}$ and scaling each column to match the hourly column (POI) marginals $V^{(t)}$. Further details about the estimation procedure are provided in Supplementary Methods section 3.

Model dynamics

To model the spread of SARS-CoV-2, we overlay a metapopulation disease transmission model on the mobility network defined in the 'Mobility Network'

section. The transmission model structure follows previous work[15,20] on epidemiological models of SARS-CoV-2 but incorporates a fine-grained mobility network into the calculations of the transmission rate. We construct separate mobility networks and models for each metropolitan statistical area.

We use a SEIR model with susceptible (*S*), exposed (*E*), infectious (*I*) and removed (*R*) compartments. Susceptible individuals have never been infected, but can acquire the virus through contact with infectious individuals, which may happen at POIs or in their home CBG. They then enter the exposed state, during which they have been infected but are not infectious yet. Individuals transition from exposed to infectious at a rate inversely proportional to the mean latency period. Finally, they transition into the removed state at a rate inversely proportional to the mean infectious period. The removed state represents individuals who can no longer be infected or infect others, for example, because they have recovered, self-isolated or died.

Each CBG c_i maintains its own SEIR instantiation, with $S_{c_i}^{(t)}$, $E_{c_i}^{(t)}$, $I_{c_i}^{(t)}$ and $R_{c_i}^{(t)}$ representing how many individuals in CBG c_i are in each disease state at hour *t*, and $N_{c_i}=S_{c_i}^{(t)}+E_{c_i}^{(t)}+I_{c_i}^{(t)}+R_{c_i}^{(t)}$. At each hour *t*, we sample the transitions between states as follows:

$$N_{S_{c_i}\to E_{c_i}}^{(t)} \sim \mathrm{Pois}\left(\frac{S_{c_i}^{(t)}}{N_{c_i}}\mathop{\sum}\limits_{j=1}^{n}\lambda_{p_j}^{(t)}w_{ij}^{(t)}\right)+\mathrm{Binom}(S_{c_i}^{(t)},\lambda_{c_i}^{(t)})$$
(1)
$$N_{E_{c_i}\to I_{c_i}}^{(t)} \sim \mathrm{Binom}(E_{c_i}^{(t)},1/\delta_E)$$
(2)
$$N_{I_{c_i}\to R_{c_i}}^{(t)} \sim \mathrm{Binom}(I_{c_i}^{(t)},1/\delta_I),$$
(3)

where $\lambda_{p_j}^{(t)}$ is the rate of infection at POI p_j at time *t*; $w_{ij}^{(t)}$, the *ij*th entry of the visit matrix from the mobility network (see 'Mobility network'), is the number of visitors from CBG c_i to POI p_j at time *t*; $\lambda_{c_i}^{(t)}$ is the base rate of infection that is independent of visiting POIs; δ_E is the mean latency period; and δ_I is the mean infectious period.

We then update each state to reflect these transitions. Let $\Delta S_{c_i}^{(t)}=S_{c_i}^{(t+1)}-S_{c_i}^{(t)}$ and likewise for

$\Delta E_{c_i}^{(t)}$, $\Delta I_{c_i}^{(t)}$ and $\Delta R_{c_i}^{(t)}$. Then, we make the following updates:

$$\Delta S_{c_i}^{(t)} = -N_{S_{c_i} \to E_{c_i}}^{(t)} \tag{4}$$

$$\Delta E_{c_i}^{(t)} = N_{S_{c_i} \to E_{c_i}}^{(t)} - N_{E_{c_i} \to I_{c_i}}^{(t)} \tag{5}$$

$$\Delta I_{c_i}^{(t)} = N_{E_{c_i} \to I_{c_i}}^{(t)} - N_{I_{c_i} \to R_{c_i}}^{(t)} \tag{6}$$

$$\Delta R_{c_i}^{(t)} = N_{I_{c_i} \to R_{c_i}}^{(t)} . \tag{7}$$

The number of new exposures

We separate the number of new exposures $N_{S_{c_i} \to E_{c_i}}^{(t)}$ in CBG c_i at time t into two parts: cases from visiting POIs, which are sampled from $\mathrm{Pois}\left(\frac{S_{c_i}^{(t)}}{N_{c_i}} \sum_{j=1}^{n} \lambda_{p_j}^{(t)} w_{ij}^{(t)}\right)$, and other cases not captured by visiting POIs, which are sampled from $\mathrm{Binomial}\left(S_{c_i}^{(t)}, \lambda_{c_i}^{(t)}\right)$.

First, we calculate the number of new exposures from visiting POIs. We assume that any susceptible visitor to POI p_j at time t has the same independent probability $\lambda_{p_j}^{(t)}$ of being infected and transitioning from the susceptible (S) to the exposed (E) state. As there are $w_{ij}^{(t)}$ visitors from CBG c_i to POI p_j at time t, and we assume that a $S_{c_i}^{(t)}/N_{c_i}$ fraction of them are susceptible, the number of new exposures among these visitors is distributed as $\mathrm{Binomial}\left(w_{ij}^{(t)} \frac{S_{c_i}^{(t)}}{N_{c_i}}, \lambda_{p_j}^{(t)}\right) \approx \mathrm{Poisson}\left(\lambda_{p_j}^{(t)} w_{ij}^{(t)} \frac{S_{c_i}^{(t)}}{N_{c_i}}\right)$. The number of new exposures among all outgoing visitors from CBG c_i is therefore distributed as the sum of the above expression over all POIs, $\mathrm{Pois}\left(\frac{S_{c_i}^{(t)}}{N_{c_i}} \sum_{j=1}^{n} \lambda_{p_j}^{(t)} w_{ij}^{(t)}\right)$.

We model the infection rate at POI p_j at time t, $\lambda_{p_j}^{(t)} = \beta_{p_j}^{(t)} \left(\frac{I_{p_j}^{(t)}}{V_{p_j}^{(t)}}\right)$, as the product of its transmission rate $\beta_{p_j}^{(t)}$ and proportion of infectious individuals $I_{p_j}^{(t)}/V_{p_j}^{(t)}$, where $V_{p_j}^{(t)} = \sum$

} _{ i=1} ^{ m} { w} _{ ij} ^{ (t)} \) is the total number of visitors to p_j at time t. We model the transmission rate at POI p_j at time t as

$${ \beta } _{ { p} _{ j} } ^{ (t)} =\psi { d} _{ { p} _{ j} } ^{ 2} \frac{ { V} _{ { p} _{ j} } ^{ (t)} } { { a} _{ { p} _{ j} } } ,$$
(8)

where \({ a} _{ { p} _{ j} } \) is the physical area of p_j, and ψ is a transmission constant (shared across all POIs) that we fit to data. The inverse scaling of transmission rate with area \({ a} _{ { p} _{ j} } \) is a standard simplifying assumption[57]. The dwell time fraction \({ d} _{ { p} _{ j} } \in [0,1]\) is what fraction of an hour an average visitor to p_j at any hour will spend there (Supplementary Methods section 3); it has a quadratic effect on the POI transmission rate \({ \beta } _{ { p} _{ j} } ^{ (t)} \) because it reduces both the time that a susceptible visitor spends at p_j and the density of visitors at p_j. With this expression for the transmission rate \({ \beta } _{ { p} _{ j} } ^{ (t)} \), we can calculate the infection rate at POI p_j at time t as

$${ \lambda } _{ { p} _{ j} } ^{ (t)} ={ \beta } _{ { p} _{ j} } ^{ (t)} \frac{ { I} _{ { p} _{ j} } ^{ (t)} } { { V} _{ { p} _{ j} } ^{ (t)} } =\psi { d} _{ { p} _{ j} } ^{ 2} \frac{ { I} _{ { p} _{ j} } ^{ (t)} } { { a} _{ { p} _{ j} } } .$$
(9)

For sufficiently large values of ψ and a sufficiently large proportion of infected individuals, the expression above can sometimes exceed 1. To address this, we simply clip the infection rate to 1. However, this occurs very rarely for the parameter settings and simulation duration that we use.

Finally, to compute the number of infectious individuals at p_j at time t, \({ I} _{ { p} _{ j} } ^{ (t)} \), we assume that the proportion of infectious individuals among the \({ w} _{ kj} ^{ (t)} \) visitors to p_j from a CBG c_k mirrors the overall density of infections \({ I} _{ { c} _{ k} } ^{ (t)} / { N} _{ { c} _{ k} } \) in that CBG, although we note that the scaling factor ψ can account for differences in the ratio of infectious individuals who visit POIs. This gives

$${ I} _{ { p} _{ j} } ^{ (t)} =\mathop{ \sum } \limits_{ k=1} ^{ m} \frac{ { I} _{ { c} _{ k} } ^{ (t)} } { { N} _{ { c} _{ k} } } { w} _{ kj} ^{ (t)} .$$
(10)

In addition to the new exposures from infections at POIs, we model a CBG-specific base rate of new exposures that is independent of POI visit activity. This captures other sources of infections, for example, household infections or infections at POIs that are absent from the SafeGraph data. We assume that at each hour, every

susceptible individual in CBG c_i has a base probability $\lambda_{c_i}^{(t)}$ of becoming infected and transitioning to the exposed state, where

$$\lambda_{c_i}^{(t)} = \beta_{\rm base} \frac{I_{c_i}^{(t)}}{N_{c_i}} \tag{11}$$

is the product of the base transmission rate $\beta_{\rm base}$ and the proportion of infectious individuals in CBG c_i. $\beta_{\rm base}$ is a constant (shared across all CBGs) that we fit to data.

By adding all of the above together, the expression for the distribution of the overall number of new exposures in CBG c_i at time t becomes

$$\begin{array}{c} N_{S_{c_i} \to E_{c_i}}^{(t)} \sim {\rm Pois}\left(\frac{S_{c_i}^{(t)}}{N_{c_i}} \mathop{\sum}\limits_{j=1}^{n} \lambda_{p_j}^{(t)} w_{ij}^{(t)}\right) + {\rm Binom}(S_{c_i}^{(t)}, \lambda_{c_i}^{(t)}) \\ = \mathop{\underbrace{{\rm Pois}\left(\psi \frac{S_{c_i}^{(t)}}{N_{c_i}} \mathop{\sum}\limits_{j=1}^{n} \frac{d_{p_j}^{2}}{a_{p_j}} \left(\mathop{\sum}\limits_{k=1}^{m} \frac{I_{c_k}^{(t)}}{N_{c_k}} w_{kj}^{(t)}\right) w_{ij}^{(t)}\right)}}\limits_{\rm New\,infections\,from\,visiting\,POIs} + \mathop{\underbrace{{\rm Binom}\left(S_{c_i}^{(t)}, \beta_{\rm base} \frac{I_{c_i}^{(t)}}{N_{c_i}}\right)}}\limits_{\rm Base\,rate\,of\,new\,CBG\,infections}. \end{array}$$ (12)

The number of new infectious and removed cases

We model exposed individuals as becoming infectious at a rate that is inversely proportional to the mean latency period δ_E. At each time step t, we assume that each exposed individual has a constant, time-independent probability of becoming infectious, with

$$N_{E_{c_i} \to I_{c_i}}^{(t)} \sim {\rm Binom}(E_{c_i}^{(t)}, 1/\delta_E). \tag{13}$$

Similarly, we model infectious individuals as transitioning to the removed state at a rate that is inversely proportional to the mean infectious period δ_I, with

$$N_{I_{c_i}} \to R_{c_i}^{(t)} \sim \mathrm{Binom}(I_{c_i}^{(t)}, 1/\delta_I), \tag{14}$$

We estimate $\delta_E = 96$ h (refs. [20,58]) and $\delta_I = 84$ h (ref. [20]) based on previous studies.

Model initialization

In our experiments, $t = 0$ is the first hour of 1 March 2020. We approximate the infectious I and removed R compartments at $t = 0$ as initially empty, with all infected individuals in the exposed E compartment. We further assume that the same expected initial prevalence p_0 occurs in every CBG c_i. At $t = 0$, every individual in the metro area has the same independent probability p_0 of being exposed E instead of susceptible S. We thus initialize the model state by setting

$$S_{c_i}^{(0)} = N_{c_i} - E_{c_i}^{(0)} \tag{15}$$
$$E_{c_i}^{(0)} \sim \mathrm{Binom}(N_{c_i}, p_0) \tag{16}$$
$$I_{c_i}^{(0)} = 0 \tag{17}$$
$$R_{c_i}^{(0)} = 0. \tag{18}$$

Aggregate mobility and no-mobility baseline models

To test whether the detailed mobility network is necessary, or whether our model is simply making use of aggregate mobility patterns, we tested an alternative SEIR model that uses the aggregate number of visits made to any POI in the metro area in each hour, but not the breakdown of visits between specific CBGs to specific POIs. Like our model, the aggregate mobility model also captures new cases from visiting POIs and a base rate of infection that is independent of POI visit activity; thus, the two models have the same three free parameters (ψ, scaling transmission rates at POIs; β_{base}, the base transmission rate ; and p_0, the initial fraction of infected individuals). However, instead of having POI-specific rates of infection, the aggregate mobility model captures only a single probability that a susceptible person from any CBG will become infected due to a visit to any POI at time t; we make this simplification because the aggregate mobility model no longer has access to the breakdown of visits between CBGs and POIs. This probability $\lambda_{\mathrm{POI}}^{(t)}$ is defined as

$$\lambda_{\rm POI}^{(t)}=\psi \mathop{\underbrace{\frac{\sum_{i=1}^{m}\sum_{j=1}^{n}w_{ij}^{(t)}}{nm}}\limits_{\rm Average}\,\rm mobility\,\rm at\,\rm time\,t}\frac{I^{(t)}}{N},$$
(19)

where m is the number of CBGs, n is the number of POIs, $I^{(t)}$ is the total number of infectious individuals at time t, and N is the total population size of the metro area. For the base rate of infections in CBGs, we assume the same process as in our network model: the probability $\lambda_{c_i}^{(t)}$ that a susceptible person in CBG c_i will become infected in their CBG at time t is equal to $\beta_{\rm base}$ times the current infectious fraction of c_i (equation (11)). Putting it together, the aggregate mobility model defines the number of new exposures in CBG c_i at time t as

$$N_{S_{c_i}}\to E_{c_i}^{(t)}\sim \mathop{\underbrace{\rm Binom}(S_{c_i}^{(t)},\lambda_{\rm POI}^{(t)})}\limits_{\rm New\,infections\,from\,visiting\,POIs}+\mathop{\underbrace{\rm Binom}(S_{c_i}^{(t)},\lambda_{c_i}^{(t)})}\limits_{\rm Base\,rateof\,new\,CBG\,infections}.$$
(20)

All other dynamics remain the same between the aggregate mobility model and our network model, and we calibrated the models in the same way, which we describe in the 'Model calibration' section. We found that our network model substantially outperformed the aggregate mobility model in predictions of out-of-sample cases: on average across metro areas, the out-of-sample r.m.s.e. of our best-fit network model was only 58% that of the best-fit aggregate mobility model (Extended Data Fig. 1). This demonstrates that it is not only general mobility patterns, but specifically the mobility network that allows our model to accurately fit observed cases.

Next, to determine the extent to which mobility data could aid in modelling the case trajectory, we compared our model to a baseline SEIR model that does not use mobility data and simply assumes that all individuals within an metro area mix uniformly. In this no-mobility baseline, an individual's risk of being infected and transitioning to the exposed state at time t is

$$\lambda^{(t)}=\beta_{\rm base}\frac{I^{(t)}}{N},$$
(21)

where $I^{(t)}$ is the total number of infectious individuals at time t, and N is the total population size of the metro area. As above, the other model dynamics are identical, and for model calibration we performed a similar grid search over $\beta_{\rm base}$ and p_0. As

expected, we found both the network and aggregate mobility models outperformed the no-mobility model on out-of-sample case predictions (Extended Data Fig. 1).

Model calibration and validation

Most of our model parameters can either be estimated from SafeGraph and US census data, or taken from previous studies (see Extended Data Table 2 for a summary). This leaves three model parameters that do not have direct analogues in the literature, and that we therefore need to calibrate with data: (1) the transmission constant in POIs, ψ (equation (9)); (2) the base transmission rate, β_{base} (equation (11)); and (3) the initial proportion of exposed individuals at time $t = 0$, p_0 (equation (16)).

In this section, we describe how we fitted these parameters to published numbers of confirmed cases, as reported by *The New York Times*. We fitted models for each metro area separately.

Selecting parameter ranges for ψ, β_{base} and p_0

We select parameter ranges for the transmission rate factors ψ and β_{base} by checking whether the model outputs match plausible ranges of the basic reproduction number R_0 before lockdown, as R_0 has been the study of substantial previous work on SARS-CoV-2[59]. Under our model, we can decompose $R_0 = R_{\text{base}} + R_{\text{POI}}$, where R_{POI} describes transmission due to POIs and R_{base} describes the remaining transmission (as in equation (12)). We first establish plausible ranges for R_{base} and R_{POI} before translating these into plausible ranges for β_{base} and ψ.

We assume that R_{base} ranges from 0.1 to 2. R_{base} models transmission that is not correlated with activity at POIs in the SafeGraph dataset, including within-household transmission and transmission at POI categories that are not well-captured in the SafeGraph dataset. We chose the lower limit of 0.1 because beyond that point, base transmission would only contribute minimally to overall R, whereas previous studies have suggested that within-household transmission is a substantial contributor to overall transmission[60,61,62]. Household transmission alone is not estimated to be sufficient to tip the overall R_0 above 1; for example, a single infected individual has been estimated to cause an average of 0.32 (0.22–0.42) secondary within-household infections[60]. However, because R_{base} may also capture transmission at POIs that are not captured in the SafeGraph dataset, to be conservative, we chose an upper limit of $R_{\text{base}} = 2$; as we describe below, the best-fit models for all 10 metro areas have $R_{\text{base}} < 2$, and 9 out of 10 have $R_{\text{base}} < 1$. We allow R_{POI} to range from 1 to 3, which

corresponds to allowing $R_0 = R_{\mathrm{POI}} + R_{\mathrm{base}}$ to range from 1.1 to 5. This is a conservatively wide range, as a previous study[59] estimated a pre-lockdown R_0 of 2–3.

To determine the values of R_{base} and R_{POI} that a given pair of β_{base} and ψ imply, we seeded a fraction of index cases and then ran the model on looped mobility data from the first week of March to capture pre-lockdown conditions. We initialized the model by setting p_0, the initial proportion of exposed individuals at time $t = 0$, to $p_0 = 10^{-4}$, and then sampling in accordance with equation (16). Let N_0 be the number of initial exposed individuals sampled. We computed the number of individuals that these N_0 index cases went on to infect through base transmission, N_{base}, and POI transmission, N_{POI}, which gives

$$R_{\mathrm{POI}} = \frac{N_{\mathrm{POI}}}{N_0} \tag{22}$$

$$R_{\mathrm{base}} = \frac{N_{\mathrm{base}}}{N_0}. \tag{23}$$

We averaged these quantities over stochastic realizations for each metro area. Supplementary Figure 6 shows that, as expected, R_{base} is linear in β_{base} and R_{POI} is linear in ψ. R_{base} lies in the plausible range when β_{base} ranges from 0.0012 to 0.024, and R_{POI} lies in the plausible range (for at least one metro area) when ψ ranges from 515 to 4,886; we therefore consider these parameter ranges when fitting the model.

The extent to which SARS-CoV-2 infections had spread in the USA by the start of our simulation (1 March 2020) is currently unclear[63]. To account for this uncertainty, we allow p_0 to vary across a large range between 10^{-5} and 10^{-2}. As described in the next section, we verified that case count data for all metro areas can be fit using parameter settings for β_{base}, ψ and p_0 within this range.

Fitting to the number of confirmed cases

Using the parameter ranges described above, we grid-searched over ψ, β_{base} and p_0 to find the models that best fit the number of confirmed cases reported by *The New York Times*[32]. For each metro area, we tested 1,500 different combinations of ψ, β_{base} and p_0 in the parameter ranges specified above, with parameters linearly spaced for ψ and β_{base} and logarithmically spread for p_0.

In the 'Model dynamics' section, we directly model the number of infections but not the number of confirmed cases. To estimate the number of confirmed cases, we

assume that an $r_c = 0.1$ proportion[20,58,64,65,66] of infections will be confirmed, and moreover that they will confirmed exactly $\delta_c = 168$ h (7 days)[20,66] after becoming infectious. From these assumptions, we can calculate the predicted number of newly confirmed cases across all CBGs in the metro area on day d,

$$N_{\rm cases}^{(\rm day)}\,d) = r_c \mathop{\sum}\limits_{i=1}^{m} \mathop{\sum}\limits_{\tau=24(d-1)+1-\delta_c}^{24d-\delta_c} N_{E_c^i \to I_c^i}^{(\tau)},$$
(24)

where m indicates the total number of CBGs in the metro area and for convenience we define $N_{E_c^i \to I_c^i}^{(\tau)}$, the number of newly infectious people at hour τ, to be 0 when $\tau < 1$.

From the dataset of *The New York Times*, we have the reported number of new cases $\hat{N}_{\rm cases}^{(\rm day)}\,d)$ for each day d, summed over each county in the metro area. We compare the reported number of cases and the number of cases that our model predicts by computing the r.m.s.e. between each of the $D = \lfloor T/24 \rfloor$ days of our simulations,

$$\rm r_{.m.s.e.} = \sqrt{\frac{1}{D} \mathop{\sum}\limits_{d=1}^{D} \left(N_{\rm cases}^{(\rm day)}\,d) - \hat{N}_{\rm cases}^{(\rm day)}\,d) \right)^2}.$$
(25)

For each combination of model parameters and for each metro area, we quantify the model fit with the data from *The New York Times* by running 30 stochastic realizations and averaging their r.m.s.e. Note that we measure model fit based on the daily number of new reported cases (as opposed to the cumulative number of reported cases)[67].

Our simulation spans 1 March to 2 May 2020, and we use mobility data from that period. However, because we assume that cases will be confirmed $\delta_c = 7$ days after individuals become infectious, we predict the number of cases with a 7-day offset, from 8 March to 9 May 2020.

Parameter selection and uncertainty quantification

Throughout this paper, we report aggregate predictions from different parameter sets of ψ, $\beta_{\rm base}$ and p_0, and multiple stochastic realizations. For each metro area, we: (1) find the best-fit parameter set, that is, with the lowest average r.m.s.e. on daily incident cases over stochastic realizations; (2) select all parameter sets that achieve an r.m.s.e. (averaged over stochastic realizations) within 20% of the r.m.s.e. of the best-fit

parameter set; and (3) pool together all predictions across those parameter sets and all of their stochastic realizations, and report their mean and 2.5–97.5th percentiles.

On average, each metro area has 9.7 parameter sets that achieve an r.m.s.e. within 20% of the best-fitting parameter set (Supplementary Table 6). For each parameter set, we have results for 30 stochastic realizations.

This procedure corresponds to rejection sampling in an approximate Bayesian computation framework[15], for which we assume an error model that is Gaussian with constant variance; we pick an acceptance threshold based on what the best-fit model achieves; and we use a uniform parameter grid instead of sampling from a uniform prior. It quantifies uncertainty from two sources. First, the multiple realizations capture stochastic variability between model runs with the same parameters. Second, simulating with all parameter sets that are within 20% of the r.m.s.e. of the best fit captures uncertainty in the model parameters ψ, β_{base} and p_0. This procedure is equivalent to assuming that the posterior probability over the true parameters is uniformly spread among all parameter sets within the 20% threshold.

Model validation on out-of-sample cases

We validate our models by showing that they predict the number of confirmed cases on out-of-sample data when we have access to corresponding mobility data. For each metro area, we split the available dataset from the *The New York Times* into a training set (spanning from 8 March 2020 to 14 April 2020) and a test set (spanning from 15 April 2020 to 9 May 2020). We fit the model parameters ψ, β_{base} and p_0, as described in the 'Mobility network' section, but using only the training set. We then evaluate the predictive accuracy of the resulting model on the test set. When running our models on the test set, we still use mobility data from the test period. Thus, this is an evaluation of whether the models can accurately predict the number of cases, given mobility data, in a time period that was not used for model calibration. Extended Data Figure 1 shows that our network model fits the out-of-sample case data fairly well, and that our model substantially outperforms alternative models that use aggregated mobility data (without a network) or do not use mobility data at all (see 'Aggregate mobility and no-mobility baseline models'). Note that we only use this train/test split to evaluate out-of-sample model accuracy. All other results are generated using parameter sets that best fit the entire dataset, as described above.

Analysis details

In this section, we include additional details about the experiments that underlie the figures in the paper. We do not include explanations for figures that are completely described in the main text.

Counterfactuals of mobility reduction

Associated with Fig. 2a and Supplementary Tables 4, 5. To simulate what would have happened if we changed the magnitude or timing of mobility reduction, we modified the real mobility networks from 1 March to 2 May 2020, and then ran our models on the hypothetical data. In Fig. 2a, we report the total number of people per 100,000 of the population ever infected (that is, in the exposed, infectious and removed states) by the end of the simulation.

To simulate a smaller magnitude of mobility reduction, we interpolate between the mobility network from the first week of simulation (1–7 March 2020), which we use to represent typical mobility levels, and the actual observed mobility network for each week. Let $W^{(t)}$ represent the observed visit matrix at the tth hour of simulation, and let $f(t) = t \bmod 168$ map t to its corresponding hour in the first week of simulation, since there are 168 h in a week. To represent the scenario in which people had committed to $\alpha \in [0, 1]$ times the actual observed reduction in mobility, we construct a visit matrix $\tilde{W}_{\alpha}^{(t)}$ that is an α-convex combination of $W^{(t)}$ and $W^{f(t)}$,

$$\tilde{W}_{\alpha}^{(t)}=\alpha W^{(t)}+(1-\alpha)W^{f(t)}.$$
(26)

If α is 1, then $\tilde{W}_{\alpha}^{(t)}=W^{(t)}$, and we use the actual observed mobility network for the simulation. On the other hand, if $\alpha = 0$, then $\tilde{W}_{\alpha}^{(t)}=W^{f(t)}$, and we assume that people did not reduce their mobility levels at all by looping the visit matrix for the first week of March throughout the simulation. Any other $\alpha \in [0, 1]$ interpolates between these two extremes.

To simulate changing the timing of mobility reduction, we shift the mobility network by $d \in [-7, 7]$ days. Let T represent the last hour in our simulation (2 May 2020, 23:00), let $f(t) = t \bmod 168$ map t to its corresponding hour in the first week of simulation as above, and similarly let $g(t)$ map t to its corresponding hour in the last week of simulation (27 April–2 May 2020). We construct the time-shifted visit matrix $\tilde{W}_{d}^{(t)}$

$$\tilde{W}_{d}^{(t)}=\begin{array}{ll} W^{(t-24d)} & \text{if}\,0\le t-24d\le T,\\ W^{f(t-24d)} & \text{if}\,t-24d < 0,\\ W^{g(t-24d)} & \text{otherwise}.\end{array}$$
(27)

If d is positive, this corresponds to starting mobility reduction d days later; if we imagine time on a horizontal line, this shifts the time series to the right by $24d$ hours. However, doing so leaves the first $24d$ hours without visit data, so we fill it in by

reusing visit data from the first week of simulation. Likewise, if d is negative, this corresponds to starting mobility reduction d days earlier, and we fill in the last $24d$ hours with visit data from the last week of simulation.

Distribution of predicted infections across POIs

Associated with Fig. 2b, Extended Data Fig. 2 and Supplementary Fig. 10. We run our models on the observed mobility data from 1 March–2 May 2020 and record the number of predicted infections that occur at each POI. Specifically, for each hour t, we compute the number of expected infections that occur at each POI p_j by taking the number of susceptible people who visit p_j in that hour multiplied by the POI infection rate $\lambda_{p_j}^{(t)}$ (equation (9)). In Fig. 2b and Supplementary Fig. 10, we sort the POIs by their total predicted number of infections (summed over hours) and plot the cumulative distribution of infections over this ordering of POIs. In Extended Data Fig. 2, we select the POI categories that contribute the most to predicted infections and plot the daily proportion of POI infections each category accounted for (summed over POIs within the category) over time.

Reducing mobility by capping maximum occupancy

Associated with Figs. 2c and Extended Data Fig. 3. We implemented two partial reopening strategies: one that uniformly reduced visits at POIs to a fraction of full activity, and the other that 'capped' the number of hourly visits at each POI to a fraction of the maximum occupancy of that the POI. For each reopening strategy, we started the simulation on 1 March 2020 and ran it until 30 May 2020, using the observed mobility network from 1 March to 30 April 2020, and then using a hypothetical post-reopening mobility network from 1 May to 30 May 2020, corresponding to the projected impact of that reopening strategy. Because we only have observed mobility data from 1 March to 2 May 2020, we impute the missing mobility data up to 30 May 2020 by looping mobility data from the first week of March, as in the above analysis on the effect of past reductions in mobility. Let T represent the last hour for which we have observed mobility data (2 May 2020, 23:00). To simplify the notation, we define

$$h(t)=\begin{array}{ll} t & \text{if}\,t < T,\\ f(t) & \text{otherwise},\end{array}$$

(28)

where, as above, $f(t) = t \bmod 168$. This function leaves t unchanged if there is observed mobility data at time t, and otherwise maps t to the corresponding hour in the first week of our simulation.

To simulate a reopening strategy that uniformly reduced visits to an γ fraction of their original level, where $\gamma \in [0, 1]$, we constructed the visit matrix

$$\tilde{W}_{\gamma}^{(t)} = \begin{array}{ll} W^{h(t)} & \text{if } t < \tau, \\ \gamma W^{h(t)} & \text{otherwise}, \end{array}$$
(29)

where τ represents the first hour of reopening (1 May 2020, 00:00). In other words, we use the actual observed mobility network up until hour τ, and then subsequently simulate an γ fraction of full mobility levels.

To simulate the reduced occupancy strategy, we first estimated the maximum occupancy M_{pj} of each POI p_j as the maximum number of visits that it ever had in one hour, across all of 1 March–2 May 2020. As in previous sections, let $w_{ij}^{(t)}$ represent the ijth entry in the observed visit matrix $W^{(t)}$, that is, the number of people from CBG c_i who visited p_j in hour t, and let $V_{p_j}^{(t)}$ represent the total number of visitors to p_j in that hour, that is, $\sum_i w_{ij}^{(t)}$. We simulated capping at a β fraction of maximum occupancy, where $\beta \in [0, 1]$, by constructing the visit matrix $\tilde{W}_{\beta}^{(t)}$ for which the ijth entry is

$$\tilde{w}_{ij\beta}^{(t)} = \begin{array}{ll} w_{ij}^{h(t)} & \text{if } t < \tau \text{ or } V_{p_j}^{(t)} \le \beta M_{p_j}, \\ \frac{\beta M_{p_j}}{V_{p_j}^{(t)}} w_{ij}^{h(t)} & \text{otherwise}. \end{array}$$
(30)

This corresponds to the following procedure: for each POI p_j and time t, we first check whether $t < \tau$ (reopening has not started) or whether $V_{p_j}^{(t)} \le \beta M_{p_j}$ (the total number of visits to p_j at time t is below the allowed maximum βM_{p_j}). If so, we leave $w_{ij}^{h(t)}$ unchanged. Otherwise, we compute the scaling factor $\frac{\beta M_{p_j}}{V_{p_j}^{(t)}}$ that would reduce the total visits to p_j at time t down to the allowed maximum βM_{p_j}, and then scale down all visits from each CBG c_i to p_j proportionately. For both reopening strategies, we calculate the predicted increase in cumulative incidence at the end of the reopening period (30 May 2020) compared to the start of the reopening period (1 May 2020).

Relative risk of reopening different categories of POIs

Associated with Fig. 2d, Extended Data Fig. 5 and Supplementary Figs. 11, 15–24. We study separately the reopening of the 20 POI categories with the most visits in SafeGraph data. In this analysis, we follow previous studies[28] and do not study four categories: 'child day-care services' and 'elementary and secondary schools' (because children under 13 are not well-tracked by SafeGraph); 'drinking places (alcoholic beverages)' (because SafeGraph seems to undercount these locations[28]) and 'nature parks and other similar institutions' (because boundaries and therefore areas are not well-defined by SafeGraph). We also exclude 'general medical and surgical hospitals' and 'other airport operations' (because hospitals and air travel both involve many additional risk factors that our model is not designed to capture). We do not filter out these POIs during model fitting (that is, we assume that people visit these POIs, and that transmissions occur there) because including them still increases the proportion of overall mobility that our dataset captures; we simply do not analyse these categories, because we wish to be conservative and only focus on categories for which we are most confident that we are capturing transmission faithfully.

This reopening analysis is similar to the previous experiments on reducing maximum occupancy versus uniform reopening (see 'Reducing mobility by capping maximum occupancy'). As above, we set the reopening time τ to 1 May 2020, 00:00. To simulate reopening a POI category, we take the set

of POIs in that category, $\mathscr{V}$, and set their activity levels after reopening to that of the first week of March. For POIs not in the category $\mathscr{V}$, we keep their activity levels after reopening the same, that is, we simply repeat the activity levels of the last week of our data (27 April–2 May 2020): This gives us the visit matrix $\tilde{W}^{(t)}$ with entries

$$\tilde{w}_{ij}^{(t)}=\begin{array}{ll} w_{ij}^{(t)} & \rm{if}\,t<\tau, \\ w_{ij}^{f(t)} & \rm{if}\,t\ge\tau, p_j\in\mathscr{V} \\ w_{ij}^{g(t)} & \rm{if}\,t\ge\tau, p_j\notin\mathscr{V}. \end{array}$$
(31)

As in the above reopening analysis, $f(t)$ maps t to the corresponding hour in the first week of March, and $g(t)$ maps t to the corresponding hour in the last week of our data. For each category, we calculate the predicted difference between (1) the cumulative fraction of people who have been infected by the end of the reopening period (30 May 2020) and (2) the cumulative fraction of people infected by 30 May 2020 had we not reopened the POI category (that is, if we simply repeated the activity levels of the last week of our data). This seeks to model the increase in cumulative incidence by the end of May from reopening the POI category. In Extended Data Fig. 5 and Supplementary Figs. 15–24, the bottom right panel shows the predicted increase for the category as a whole, and the bottom left panel shows the predicted increase per POI (that is, the total increase divided by the number of POIs in the category).

Per-capita mobility

Associated with Fig. 3d, Extended Data Fig. 6 and Supplementary Fig. 3. Each group of CBGs (for example, the bottom income decile) comprises a set $\mathscr{U}$ of CBGs that fit the corresponding criteria. In Fig. 3d and Extended Data Fig. 6, we show the daily per-capita mobilities of different pairs of groups (broken down by income and by race). To measure the per-capita mobility of a group on day d, we take the total number of visits made from those CBGs to any POI, $\sum_{c_i\in\mathscr{U}}\sum_{p_j\in\mathscr{P}}\sum$

$_{t=24d}^{24d+23} w_{ij}^{(t)}$), and divide it by the total population of the CBGs in the group, $\sum_{c_i \in \mathscr{U}} N_{c_i}$. In Supplementary Fig. 3, we show the total number of visits made by each group to each POI category, accumulated over the entire data period (1 March–2 May 2020) and then divided by the total population of the group.

Average predicted transmission rate of a POI category

Associated with Fig. 3e and Extended Data Tables 3, 4. We compute the predicted average hourly transmission rate experienced by a group of CBGs $\mathscr{U}$ at a POI category $\mathscr{V}$ as

$$\bar{\beta}_{\mathscr{U}\mathscr{V}} = \frac{\sum_{c_i \in \mathscr{U}} \sum_{p_j \in \mathscr{V}} \sum_{t=1}^{T} w_{ij}^{(t)} \beta_{p_j}^{(t)}}{\sum_{c_i \in \mathscr{U}} \sum_{p_j \in \mathscr{V}} \sum_{t=1}^{T} w_{ij}^{(t)}},$$
(32)

where, as above, $\beta_{p_j}^{(t)}$ is the transmission rate at POI p_j in hour t (equation (8)), $w_{ij}^{(t)}$ is the number of visitors from CBG c_i at POI p_j in hour t, and T is the last hour in our simulation. This represents the expected transmission rate encountered during a visit by someone from a CBG in group $\mathscr{U}$ to a POI in category $\mathscr{V}$.

Reporting summary

Further information on research design is available in the Nature Research Reporting Summary linked to this paper.

Data availability

Inferred hourly mobility networks as well as the estimated models are available at the project website (http://covid-mobility.stanford.edu). Raw

census data (https://www.census.gov/programs-surveys/acs), case and death counts from *The New York Times* (https://github.com/nytimes/covid-19-data) and Google mobility data (https://www.google.com/covid19/mobility/) are also publicly available. Mobile phone mobility data are freely available to researchers, non-profit organizations and governments through the SafeGraph COVID-19 Data Consortium (https://www.safegraph.com/covid-19-data-consortium).

Code availability

Code is publicly available at the project website (http://covid-mobility.stanford.edu).

References

1. 1.

   Buckee, C. O. et al. Aggregated mobility data could help fight COVID-19. *Science* **368**, 145–146 (2020).

   ADS PubMed Google Scholar

2. 2.

   Wilson, C. These graphs show how COVID-19 is ravaging New York City's low-income neighborhoods. *Time* (15 April 2020).

3. 3.

   Garg, S. et al. Hospitalization rates and characteristics of patients hospitalized with laboratory-confirmed coronavirus disease 2019 — COVID-NET, 14 states, March 1—30, 2020. *MMWR Morb. Mortal. Wkly Rep*. **69**, 458–464 (2020).

   CAS Article Google Scholar

4. 4.

Reeves, R. V. & Rothwell, J. *Class and COVID: How the Less Affluent face Double Risks*. https://www.brookings.edu/blog/up-front/2020/03/27/class-and-covid-how-the-less-affluent-face-double-risks/ (The Brookings Institution, 2020).

5. 5.

Pareek, M. et al. Ethnicity and COVID-19: an urgent public health research priority. *Lancet* **395**, 1421–1422 (2020).

CAS Article Google Scholar

6. 6.

Dorn, A. V., Cooney, R. E. & Sabin, M. L. COVID-19 exacerbating inequalities in the US. *Lancet* **395**, 1243–1244 (2020).

CAS Article Google Scholar

7. 7.

Yancy, C. W. COVID-19 and African Americans. *J. Am. Med. Assoc*. **323**, 1891–1892 (2020).

CAS Article Google Scholar

8. 8.

Chowkwanyun, M. & Reed, A. L. Jr. Racial Health Disparities and Covid-19 — caution and context. *N. Engl. J. Med*. **383**, 201–203 (2020).

CAS Article Google Scholar

9. 9.

Flaxman, S. et al. Estimating the effects of non-pharmaceutical interventions on COVID-19 in Europe. *Nature* **584**, 257–261 (2020).

CAS Article Google Scholar

10. 10.

Rojas, R. & Delkic, M. As states reopen, governors balance existing risks with new ones. *The New York Times* (17 May 2020).

11. 11.

Endo, A., Abbott, S., Kucharski, A. J. & Funk, S. Estimating the overdispersion in COVID-19 transmission using outbreak sizes outside China. *Wellcome Open Res*. **5**, 67 (2020).

Article Google Scholar

12. 12.

Adam, D. C. et al. Clustering and superspreading potential of SARS-CoV-2 infections in Hong Kong. *Nat. Med*. https://doi.org/10.1038/s41591-020-1092-0 (2020).

13. 13.

Park, S. Y. et al. Coronavirus disease outbreak in call center, South Korea. *Emerg. Infect. Dis*. **26**, 1666–1670 (2020).

CAS Article Google Scholar

14. 14.

Bi, Q. et al. Epidemiology and transmission of COVID-19 in 391 cases and 1286 of their close contacts in Shenzhen, China: a retrospective cohort study. *Lancet Infect. Dis*. **20**, 911–919 (2020).

CAS Article Google Scholar

15. 15.

Chinazzi, M. et al. The effect of travel restrictions on the spread of the 2019 novel coronavirus (COVID-19) outbreak. *Science* **368**, 395–400 (2020).

ADS CAS Article Google Scholar

16. 16.

Jia, J. S. et al. Population flow drives spatio-temporal distribution of COVID-19 in China. *Nature* **582**, 389–394 (2020).

ADS CAS Article Google Scholar

17. 17.

Pei, S., Kandula, S. & Shaman, J. Differential effects of intervention timing on COVID-19 spread in the United States. Preprint at https://doi.org/10.1101/2020.05.15.20103655 (2020).

18. 18.

Lai, S. et al. Effect of non-pharmaceutical interventions to contain COVID-19 in China. *Nature* **585**, 410–413 (2020).

CAS Article Google Scholar

19. 19.

Badr, H. S. et al. Association between mobility patterns and COVID-19 transmission in the USA: a mathematical modelling study. *Lancet Infect. Dis*. **20**, 1247–1254 (2020).

CAS Article Google Scholar

20. 20.

Li, R. et al. Substantial undocumented infection facilitates the rapid dissemination of novel coronavirus (SARS-CoV-2). *Science* **368**, 489–493 (2020).

ADS CAS Article Google Scholar

21. 21.

Pei, S. & Shaman, J. Initial simulation of SARS-CoV2 spread and intervention effects in the continental US. Preprint at https://doi.org/10.1101/2020.03.21.20040303 (2020).

22. 22.

Aleta, A. et al. Modelling the impact of testing, contact tracing and household quarantine on second waves of COVID-19. *Nat. Hum. Behav*. **4**, 964–971 (2020).

Article Google Scholar

23. 23.

Duque, D. et al. Timing social distancing to avert unmanageable COVID-19 hospital surges. *Proc. Natl Acad. Sci. USA* **177**, 19873–19878 (2020).

Article Google Scholar

24. 24.

Block, P. et al. Social network-based distancing strategies to flatten the COVID-19 curve in a post-lockdown world. *Nat. Hum. Behav*. **4**, 588–596 (2020).

Article Google Scholar

25. 25.

Karin, O. et al. Adaptive cyclic exit strategies from lockdown to suppress COVID-19 and allow economic activity. Preprint at https://doi.org/10.1101/2020.04.04.20053579 (2020).

26. 26.

Gao, S. et al. Mapping county-level mobility pattern changes in the United States in response to COVID-19. *SIGSPATIAL Special* **12**, 16–26 (2020).

Article Google Scholar

27. 27.

Klein, B. et al. *Assessing Changes in Commuting and Individual Mobility in Major Metropolitan Areas in the United States during the COVID-19 Outbreak*. https://www.networkscienceinstitute.org/publications/assessing-changes-in-commuting-and-individual-mobility-in-major-metropolitan-areas-in-the-united-states-during-the-covid-19-outbreak (2020).

28. 28.

Benzell, S. G., Collis, A. & Nicolaides, C. Rationing social contact during the COVID-19 pandemic: transmission risk and social benefits of US locations. *Proc. Natl Acad. Sci. USA* **117**, 14642–14644 (2020).

Article Google Scholar

29. 29.

Baicker, K. et al. Is it safer to visit a coffee shop or a gym? *The New York Times* (6 May 2020).

30. 30.

Hsiang, S. et al. The effect of large-scale anti-contagion policies on the COVID-19 pandemic. *Nature* **584**, 262–267 (2020).

ADS CAS Article Google Scholar

31. 31.

Deming, W. E. & Stephan, F. F. On a least squares adjustment of a sampled frequency table when the expected marginal totals are known. *Ann. Math. Stat*. **11**, 427–444 (1940).

MathSciNet Article Google Scholar

32. 32.

The New York Times. *Coronavirus (COVID-19) Data in the United States*. https://github.com/nytimes/covid-19-data (2020).

33. 33.

Tian, H. et al. An investigation of transmission control measures during the first 50 days of the COVID-19 epidemic in China. *Science* **368**, 638–642 (2020).

ADS CAS Article Google Scholar

34. 34.

Watts, D. J., Muhamad, R., Medina, D. C. & Dodds, P. S. Multiscale, resurgent epidemics in a hierarchical metapopulation model. *Proc. Natl Acad. Sci. USA* **102**, 11157–11162 (2005).

ADS CAS Article Google Scholar

35. 35.

California Department of Public Health. *COVID-19 Industry Guidance: Retail*. https://covid19.ca.gov/pdf/guidance-retail.pdf (2020).

36. 36.

Birge, J., Candogan, O. & Feng, Y. Controlling epidemic spread: reducing economic losses with targeted closures. *BFI Working Paper No. 2020-57* (8 May 2020).

37. 37.

Webb Hooper, M., Nápoles, A. M. & Pérez-Stable, E. J. COVID-19 and racial/ethnic disparities. *J. Am. Med. Assoc*. **323**, 2466–2467 (2020).

Article Google Scholar

38. 38.

Laurencin, C. T. & McClinton, A. The COVID-19 pandemic: a call to action to identify and address racial and ethnic disparities. *J. Racial Ethn. Health Disparities* **7**, 398–402 (2020).

Article Google Scholar

39. 39.

SafeGraph. *Places Schema*. https://docs.safegraph.com/docs/places-schema (2020).

40. 40.

SafeGraph. *Weekly Patterns*. https://docs.safegraph.com/docs/weekly-patterns (2020).

41. 41.

SafeGraph. *Using SafeGraph Polygons to Estimate Point-Of-Interest Square Footage*. https://www.safegraph.com/blog/using-safegraph-polygons-to-estimate-point-of-interest-square-footage (2019).

42. 42.

SafeGraph. *Guide to Points-of-Interest Data: POI Data FAQ*. https://www.safegraph.com/points-of-interest-poi-data-guide (2020).

43. 43.

SafeGraph. *Social Distancing Metrics*. https://docs.safegraph.com/docs/social-distancing-metrics (2020).

44. 44.

Athey, S. et al. Estimating heterogeneous consumer preferences for restaurants and travel time using mobile location data. In *AEA Papers and Proceedings* Vol. 108, 64–67 (2018).

45. 45.

Chen, M. K. & Rohla, R. The effect of partisanship and political advertising on close family ties. *Science* **360**, 1020–1024 (2018).

ADS CAS Article Google Scholar

46. 46.

Farboodi, M., Jarosch, G. & Shimer, R. Internal and external effects of social distancing in a pandemic. *NBER Working Paper 27059* https://doi.org/10.3386/w27059 (National Bureau Of Economic Research, 2020).

47. 47.

Killeen, B. D. et al. A county-level dataset for informing the United States' response to COVID-19. Preprint at https://arxiv.org/abs/2004.00756 (2020).

48. 48.

Allcott, H. et al. Polarization and public health: partisan differences in social distancing during the coronavirus pandemic. *NBER Working Paper 26946* https://doi.org/10.3386/w26946 (National Bureau Of Economic Research, 2020).

49. 49.

Google. *COVID-19 Community Mobility Reports*. https://google.com/covid19/mobility/ (2020).

50. 50.

Athey, S. et al. Experienced Segregation. *Working Paper 3785* https://gsb.stanford.edu/faculty-research/working-papers/experienced-segregation (2019).

51. 51.

Squire, R. F. *What about Bias in the SafeGraph Dataset?* https://safegraph.com/blog/what-about-bias-in-the-safegraph-dataset (2019).

52. 52.

US Census Bureau. *American Community Survey (ACS)* https://census.gov/programs-surveys/acs (published 30 January 2020).

53. 53.

Bishop, Y. M., Fienberg, S. E. & Holland, P. W. *Discrete Multivariate Analysis: Theory and Practice* (MIT Press, 1975).

54. 54.

Birkin, M. & Clarke, M. Synthesis—a synthetic spatial information system for urban and regional analysis: methods and examples. *Environ. Plann. A* **20**, 1645–1671 (1988).

Article Google Scholar

55. 55.

Wong, D. W. The reliability of using the iterative proportional fitting procedure. *Prof. Geogr*. **44**, 340–348 (1992).

Article Google Scholar

56. 56.

Simpson, L. & Tranmer, M. Combining sample and census data in small area estimates: iterative proportional fitting with standard software. *Prof. Geogr*. **57**, 222–234 (2005).

Article Google Scholar

57. 57.

Hu, H., Nigmatulina, K. & Eckhoff, P. The scaling of contact rates with population density for the infectious disease models. *Math. Biosci*. **244**, 125–134 (2013).

MathSciNet Article Google Scholar

58. 58.

Kucharski, A. J. et al. Early dynamics of transmission and control of COVID-19: a mathematical modelling study. *Lancet Infect. Dis*. **20**, 553–558 (2020).

CAS Article Google Scholar

59. 59.

Park, M., Cook, A. R., Lim, J. T., Sun, Y. & Dickens, B. L. A systematic review of COVID-19 epidemiology based on current evidence. *J. Clin. Med*. **9**, 967 (2020).

CAS Article Google Scholar

60. 60.

Curmei, M. et al. Estimating household transmission of SARS-CoV-2. Preprint at https://doi.org/10.1101/2020.05.23.20111559 (2020).

61. 61.

Li, W. et al. The characteristics of household transmission of COVID-19. *Clin. Infect. Dis*. **71**, 1943–1946 (2020).

62. 62.

Gudbjartsson, D. F. et al. Spread of SARS-CoV-2 in the Icelandic population. *N. Engl. J. Med*. **382**, 2302–2315 (2020).

CAS Article Google Scholar

63. 63.

Carey, B. & Glanz, J. Hidden outbreaks spread through U.S. cities far earlier than Americans knew, estimates say. *The New York Times* (23 April 2020).

64. 64.

Bommer, C. & Vollmer, S. *Average Detection Rate of SARS-CoV-2 Infections is Estimated Around Nine Percent*. https://www.uni-goettingen.de/en/606540.html (2020).

65. 65.

Javan, E., Fox, S. J. & Meyers, L. A. The unseen and pervasive threat of COVID-19 throughout the US. Preprint at https://doi.org/10.1101/2020.04.06.20053561 (2020).

66. 66.

Perkins, T. A. et al. Estimating unobserved SARS-CoV-2 infections in the United States. *Proc. Natl Acad. Sci. USA* **117**, 22597–22602 (2020).

CAS Article Google Scholar

67. 67.

King, A. A., Domenech de Cellès, M., Magpantay, F. M. & Rohani, P. Avoidable errors in the modelling of outbreaks of emerging pathogens, with special reference to Ebola. *Proc. R. Soc. Lond. B* **282**, 20150347 (2015).

Google Scholar

Download references

Acknowledgements

We thank Y.-Y. Ahn, R. Appel, C. Chen, J. Feng, N. Fishman, S. Fullerton, T. Hashimoto, M. Kraemer, P. Liang, M. Lipsitch, K. Loh, D. Ouyang, R. Rosenfeld, S. Sagawa, J. Steinhardt, R. Tibshirani, J. Ugander, D. Vrabac, seminar participants and Stanford's Computer Science and Civil Society for support and comments; and N. Singh, R. F. Squire, J. Williams-Holt, J. Wolf, R. Yang and others at SafeGraph for mobile phone mobility data and feedback. This research was supported by US National Science Foundation under OAC-1835598 (CINES), OAC-1934578 (HDR), CCF-1918940 (Expeditions), IIS-2030477 (RAPID), Stanford Data Science Initiative, Wu Tsai Neurosciences Institute and Chan Zuckerberg Biohub. S.C. was supported by an NSF Fellowship. E.P. was supported by a Hertz Fellowship. P.W.K. was supported by the Facebook Fellowship Program. J.L. is a Chan Zuckerberg Biohub investigator.

Author information

Author notes

1. These authors contributed equally: Serina Chang, Emma Pierson, Pang Wei Koh

Affiliations

1. Department of Computer Science, Stanford University, Stanford, CA, USA

Serina Chang, Emma Pierson, Pang Wei Koh & Jure Leskovec

2. Microsoft Research, Cambridge, MA, USA

   Emma Pierson

3. Department of Preventive Medicine, Northwestern University, Chicago, IL, USA

   Jaline Gerardin

4. Department of Sociology, Northwestern University, Evanston, IL, USA

   Beth Redbird

5. Institute for Policy Research, Northwestern University, Evanston, IL, USA

   Beth Redbird

6. Department of Sociology, Stanford University, Stanford, CA, USA

   David Grusky

7. Center on Poverty and Inequality, Stanford University, Stanford, CA, USA

   David Grusky

8. Chan Zuckerberg Biohub, San Francisco, CA, USA

   Jure Leskovec

Authors

1. Serina Chang
   View author publications

You can also search for this author in PubMed Google Scholar

2. Emma Pierson
   View author publications

   You can also search for this author in PubMed Google Scholar

3. Pang Wei Koh
   View author publications

   You can also search for this author in PubMed Google Scholar

4. Jaline Gerardin
   View author publications

   You can also search for this author in PubMed Google Scholar

5. Beth Redbird
   View author publications

   You can also search for this author in PubMed Google Scholar

6. David Grusky
   View author publications

   You can also search for this author in PubMed Google Scholar

7. Jure Leskovec
   View author publications

   You can also search for this author in PubMed Google Scholar

Contributions

S.C., E.P. and P.W.K. performed computational analysis. All authors jointly analysed the results and wrote the paper.

Corresponding author

Correspondence to Jure Leskovec.

Ethics declarations

Competing interests

The authors declare no competing interests.

Additional information

Peer review information *Nature* thanks Moritz Kraemer, Marc Lipsitch and the other, anonymous, reviewer(s) for their contribution to the peer review of this work. Peer reviewer reports are available.

Publisher's note Springer Nature remains neutral with regard to jurisdictional claims in published maps and institutional affiliations.

Extended data figures and tables

Extended Data Fig. 1 Mobility-based epidemiological model and its predictions.

a–**c**, Predicted (blue) and true (orange) daily case counts for our model (**a**), which uses hourly mobility networks, an SEIR model (**b**) that uses hourly aggregated mobility data and a baseline SEIR model (**c**) that does not use mobility data (see Methods, 'Aggregate mobility and no-mobility baseline models' for details). Incorporating mobility information improves out-of-sample fit and using a mobility network, instead of an aggregate measure of mobility, further improves fit: on average across metro areas, the out-of-sample error (r.m.s.e.) of our best-fit network model was only 58% that of the best-fit aggregate mobility model. All three models are calibrated on observed case counts before 15 April 2020 (vertical black line). The grey crosses represent the daily reported cases; as they tend to have great variability, we also show the smoothed weekly average (orange line).

Shaded regions denote the 2.5th and 97.5th percentiles across sampled parameters and stochastic realizations.

Extended Data Fig. 2 Distribution of POI infections over time.

We selected the POI categories that our models predicted to contribute the most to infections, and plotted the predicted proportion of POI infections that each category accounted for over time. Our model predicts time-dependent variation of where transmissions may have occurred. For example, full-service restaurants (blue) and fitness centres (brown) contributed less to predicted infections over time, probably due to lockdown orders closing these POIs, whereas grocery stores remained steady or even grew in their predicted contribution, probably because they remained open as essential businesses. Hotels and motels (yellow) also feature in these plots; most notably, the model predicts a peak in their contributed infections in Miami around mid-March, which aligns with college spring break, as Miami is a popular vacation spot for students. The proportions are stacked in these plots, and the *y* axes are truncated at 0.7 because every plot would only show 'other' from 0.7 to 1.0.

Extended Data Fig. 3 Trade-off between new infections and visits lost from reopening.

We simulate reduced maximum occupancy reopening starting on 1 May 2020 and run the simulation until the end of the month. Each dot represents the level of occupancy reduction: for example, capping visits at 50% of the maximum occupancy. The *y* coordinate represents the predicted number of new infections incurred after reopening (per 100,000 population) and the *x* coordinate represents the fraction of visits lost from partial reopening compared to full reopening. Shaded regions denote the 2.5th and 97.5th percentiles across parameter sets and stochastic realizations. In four metro areas, the predicted cost of new infections from reopening is roughly similar for lower-income CBGs and the overall population, but in five metro areas, the lower-income CBGs incur more predicted infections from reopening. Notably, New York City (NYC) is the only metro area in which this trend is reversed; this is because the model predicts that such a high fraction—65% (95% confidence interval, 62–68%)—of lower-income

CBGs in NYC had been infected before reopening that after reopening, only a minority of the lower-income population is still susceptible (in comparison, the second highest fraction infected before reopening was 31% (95% confidence interval, 28–35%) for Philadelphia, and the rest ranged from 1 to 14%).

Extended Data Fig. 4 Reduced maximum occupancy versus uniform reduction reopening.

In comparison to partially reopening by uniformly reducing visits, the reduced maximum occupancy strategy—which disproportionately targets POIs during their most risky high-density periods—always results in a smaller predicted increase in infections for the same number of visits. The *y* axis plots the relative difference between the predicted increase in cumulative infections (from 1 May to 30 May 2020) under the reduced occupancy strategy compared to the uniform reduction strategy. The shaded regions denote the 2.5th and 97.5th percentiles across the sampled parameters and stochastic realizations.

Extended Data Fig. 5 POI attributes in all 10 metro areas combined.

a, **b**, The POIs from all metro areas are pooled and the quantities from the mobility data are shown. **a**, The distribution of dwell time. **b**, The average number of hourly visitors divided by the area of the POI in square feet. Each point represents one POI; boxes depict the interquartile range across POIs; data points outside the range are shown as individual dots. **c**, **d**, The data are pooled across model realizations from all metro areas and model predictions are shown for the increase in infections (per 100,000 population) because of reopening a POI category. **c**, Data per POI. **d**, Data for the category as a whole. Each point represents a model realization; boxes depict the interquartile range across realizations; data points outside the range are shown as individual dots. Across MSAs, we model 552,758 POIs in total, and we sample 97 parameters and 30 stochastic realizations (n = 2,910); see Supplementary Table 6 for the number of sets per metro

area. Colours are used to distinguish the different POI categories, but do not have any additional meaning.

Extended Data Fig. 6 Daily per-capita mobility over time.

a, **b**, We compare mobility in the lowest and highest deciles of CBGs based on median household income (**a**) and the percentage of white residents (**b**). See Methods, ‘Analysis details’ for details.

Extended Data Table 1 Dataset summary statistics from 1 March to 2 May 2020
Full size table
Extended Data Table 2 Model parameters
Full size table
Extended Data Table 3 Predicted transmission rate disparities at each POI category between income groups
Full size table
Extended Data Table 4 Predicted transmission rate disparities at each POI category between racial groups
Full size table

Supplementary information

Supplementary Information

The Supplementary Information contains four sections: Supplementary Methods, Supplementary Discussion, Supplementary Tables, and Supplementary Figures. The Supplementary Methods section describes (1) our comparison of SafeGraph mobility data to Google mobility data, where we find high correlation; (2) sensitivity analyses of the model (e.g., modifying CBG and POI transmission rates, fitting to deaths instead of cases) and tests of model identifiability, (3) a detailed description of how we estimated dynamic mobility networks from raw SafeGraph data using iterative proportional fitting. The Supplementary Discussion section covers (1) further discussion of the racial and socioeconomic disparities predicted by our model; (2) limitations of the model and mobility dataset. There are 6

Supplementary Tables, which provide more details about the SafeGraph data, the comparison to Google mobility data, and additional model results. There are 24 Supplementary Figures, which include additional results about predicted disparities, results from all sensitivity analyses and identifiability checks, and POI attributes and predicted reopening risks for every POI category and metro area.

Reporting Summary

Peer Review File

Rights and permissions

Reprints and Permissions

About this article

Check for updates

Cite this article

Chang, S., Pierson, E., Koh, P.W. *et al.* Mobility network models of COVID-19 explain inequities and inform reopening. *Nature* **589,** 82–87 (2021). https://doi.org/10.1038/s41586-020-2923-3

Download citation

- Received: 15 June 2020
- Accepted: 21 October 2020
- Published: 10 November 2020
- Issue Date: 07 January 2021

- DOI: https://doi.org/10.1038/s41586-020-2923-3

Further reading

- **Big data and simple models used to track the spread of COVID-19 in cities**

  - Kevin C. Ma
  - & Marc Lipsitch

  Nature (2021)

- **Mobility Behaviour in View of the Impact of the COVID-19 Pandemic—Public Transport Users in Gdansk Case Study**

  - Adam Przybylowski
  - , Sandra Stelmak
  - & Michal Suchanek

  Sustainability (2021)

- **Coronavirus Infections and Deaths by Poverty Status: Time Trends and Patterns**

  - Juergen Jung
  - , James Manley
  - & Vinish Shrestha

  SSRN Electronic Journal (2020)

- **The spread of COVID-19 shows the importance of policy coordination**

  - Joshua Graff Zivin
  - & Nicholas Sanders

Proceedings of the National Academy of Sciences (2020)

- **Controlling Epidemic Spread: Reducing Economic Losses with Targeted Closures**

  - John R. Birge
  - , Ozan Candogan
  - & Yiding Feng

  SSRN Electronic Journal (2020)

Comments

By submitting a comment you agree to abide by our Terms and Community Guidelines. If you find something abusive or that does not comply with our terms or guidelines please flag it as inappropriate.

Download PDF

This article was downloaded by **calibre** from https://www.nature.com/articles/s41586-020-2923-3

- Article
- Published: 04 November 2020

Neuronal diversity and convergence in a visual system developmental atlas

- Mehmet Neset Özel ORCID: orcid.org/0000-0002-0185-5866[1 na1],
- Félix Simon[1 na1],
- Shadi Jafari[1,2],
- Isabel Holguera ORCID: orcid.org/0000-0003-2796-6596[1],
- Yen-Chung Chen ORCID: orcid.org/0000-0002-8529-1251[1],
- Najate Benhra[3],
- Rana Naja El-Danaf[3],
- Katarina Kapuralin[3],
- Jennifer Amy Malin[1],
- Nikolaos Konstantinides ORCID: orcid.org/0000-0002-9525-2838[1] &
- Claude Desplan ORCID: orcid.org/0000-0002-6914-1413[1,3]

Nature **volume 589**, pages88–95(2021)Cite this article

- 6720 Accesses
- 192 Altmetric
- Metrics details

Subjects

- Bioinformatics

- Cell death in the nervous system
- Cell type diversity
- Genome-wide analysis of gene expression
- Neuronal development

Abstract

Deciphering how neuronal diversity is established and maintained requires a detailed knowledge of neuronal gene expression throughout development. In contrast to mammalian brains[1,2], the large neuronal diversity of the *Drosophila* optic lobe[3] and its connectome[4,5,6] are almost completely characterized. However, a molecular characterization of this neuronal diversity, particularly during development, has been lacking. Here we present insights into brain development through a nearly complete description of the transcriptomic diversity of the optic lobes of *Drosophila*. We acquired the transcriptome of 275,000 single cells at adult and at five pupal stages, and built a machine-learning framework to assign them to almost 200 cell types at all time points during development. We discovered two large neuronal populations that wrap neuropils during development but die just before adulthood, as well as neuronal subtypes that partition dorsal and ventral visual circuits by differential Wnt signalling throughout development. Moreover, we show that the transcriptomes of neurons that are of the same type but are produced days apart become synchronized shortly after their production. During synaptogenesis we also resolved neuronal subtypes that, although differing greatly in morphology and connectivity, converge to indistinguishable transcriptomic profiles in adults. Our datasets almost completely account for the known neuronal diversity of the *Drosophila* optic lobes, and serve as a paradigm to understand brain development across species.

Access through your institution
Change institution
Buy or subscribe

Access options

Subscribe to Journal

Get full journal access for 1 year

$199.00

only $3.90 per issue

Subscribe

All prices are NET prices.
VAT will be added later in the checkout.

Rent or Buy article

Get time limited or full article access on ReadCube.

from$8.99

Rent or Buy

All prices are NET prices.

Additional access options:

- Log in
- Access through your institution
- Learn about institutional subscriptions

Fig. 1: High-resolution transcriptomic atlases of the optic lobe across development.

Fig. 2: TE neurons demarcate the optic lobe neuropils and undergo apoptosis during late pupal development.

Fig. 3: Transcriptomic synchronization of optic lobe neurons.

Fig. 4: Increased transcriptomic diversity during synaptogenesis.

Fig. 5: Dorsal and ventral visual circuits are partitioned by differential Wnt signalling.

Data availability

All raw and processed data referenced were uploaded to the GEO with accession number GSE142789. The following publicly accessible datasets were also used: GSE103771, GSE103772 and GSE116969.

References

1. 1.

   Lodato, S. & Arlotta, P. Generating neuronal diversity in the mammalian cerebral cortex. *Annu. Rev. Cell Dev. Biol*. **31**, 699–720 (2015).

   CAS PubMed PubMed Central Article Google Scholar

2. 2.

   Cembrowski, M. S. & Spruston, N. Heterogeneity within classical cell types is the rule: lessons from hippocampal pyramidal neurons. *Nat. Rev. Neurosci*. **20**, 193–204 (2019).

CAS PubMed Article PubMed Central Google Scholar

3. 3.

Fischbach, K. F. & Dittrich, A. P. M. The optic lobe of *Drosophila melanogaster*. I. A Golgi analysis of wild-type structure. *Cell Tissue Res*. **258**, 441–475 (1989).

Article Google Scholar

4. 4.

Takemura, S. Y. et al. Synaptic circuits and their variations within different columns in the visual system of *Drosophila*. *Proc. Natl Acad. Sci. USA* **112**, 13711–13716 (2015).

ADS CAS PubMed Article PubMed Central Google Scholar

5. 5.

Rivera-Alba, M. et al. Wiring economy and volume exclusion determine neuronal placement in the *Drosophila* brain. *Curr. Biol*. **21**, 2000–2005 (2011).

CAS PubMed PubMed Central Article Google Scholar

6. 6.

Shinomiya, K. et al. Comparisons between the ON- and OFF-edge motion pathways in the *Drosophila* brain. *eLife* **8**, e40025 (2019).

PubMed PubMed Central Article Google Scholar

7. 7.

Nern, A., Pfeiffer, B. D. & Rubin, G. M. Optimized tools for multicolor stochastic labeling reveal diverse stereotyped cell arrangements in the fly visual system. *Proc. Natl Acad. Sci. USA* **112**, E2967–E2976 (2015).

ADS CAS PubMed Article PubMed Central Google Scholar

8. 8.

Otsuna, H. & Ito, K. Systematic analysis of the visual projection neurons of *Drosophila melanogaster*. I. Lobula-specific pathways. *J. Comp. Neurol*. **497**, 928–958 (2006).

PubMed Article PubMed Central Google Scholar

9. 9.

Panser, K. et al. Automatic segmentation of *Drosophila* neural compartments using GAL4 expression data reveals novel visual pathways. *Curr. Biol*. **26**, 1943–1954 (2016).

CAS PubMed PubMed Central Article Google Scholar

10. 10.

Raghu, S. V. & Borst, A. Candidate glutamatergic neurons in the visual system of *Drosophila*. *PLoS ONE* **6**, e19472 (2011).

ADS CAS PubMed PubMed Central Article Google Scholar

11. 11.

Varija Raghu, S., Reiff, D. F. & Borst, A. Neurons with cholinergic phenotype in the visual system of *Drosophila*. *J. Comp. Neurol*. **519**, 162–176 (2011).

PubMed Article CAS PubMed Central Google Scholar

12. 12.

Wu, M. et al. Visual projection neurons in the *Drosophila* lobula link feature detection to distinct behavioral programs. *eLife* **5**, e21022 (2016).

PubMed PubMed Central Article Google Scholar

13. 13.

Erclik, T. et al. Integration of temporal and spatial patterning generates neural diversity. *Nature* **541**, 365–370 (2017).

ADS CAS PubMed PubMed Central Article Google Scholar

14. 14.

Ngo, K. T., Andrade, I. & Hartenstein, V. Spatio-temporal pattern of neuronal differentiation in the *Drosophila* visual system: A user's guide to the dynamic morphology of the developing optic lobe. *Dev. Biol*. **428**, 1–24 (2017).

CAS PubMed PubMed Central Article Google Scholar

15. 15.

Özel, M. N. et al. Serial synapse formation through filopodial competition for synaptic seeding factors. *Dev. Cell* **50**, 447–461.e8 (2019).

PubMed PubMed Central Article CAS Google Scholar

16. 16.

Hiesinger, P. R. et al. Activity-independent prespecification of synaptic partners in the visual map of *Drosophila*. *Curr. Biol*. **16**, 1835–1843 (2006).

CAS PubMed PubMed Central Article Google Scholar

17. 17.

Holguera, I. & Desplan, C. Neuronal specification in space and time. *Science* **362**, 176–180 (2018).

ADS CAS PubMed PubMed Central Article Google Scholar

18. 18.

Konstantinides, N. et al. Phenotypic convergence: distinct transcription factors regulate common terminal features. *Cell* **174**, 622–635.e13 (2018).

CAS PubMed PubMed Central Article Google Scholar

19. 19.

Davie, K. et al. A single-cell transcriptome atlas of the aging *Drosophila* brain. *Cell* **174**, 982–998.e20 (2018).

CAS PubMed PubMed Central Article Google Scholar

20. 20.

Davis, F. P. et al. A genetic, genomic, and computational resource for exploring neural circuit function. *eLife* **9**, e50901 (2020).

CAS PubMed PubMed Central Article Google Scholar

21. 21.

Stuart, T. et al. Comprehensive integration of single-cell data. *Cell* **177**, 1888–1902.e21 (2019).

CAS PubMed PubMed Central Article Google Scholar

22. 22.

Butler, A., Hoffman, P., Smibert, P., Papalexi, E. & Satija, R. Integrating single-cell transcriptomic data across different conditions, technologies, and species. *Nat. Biotechnol*. **36**, 411–420 (2018).

CAS PubMed PubMed Central Article Google Scholar

23. 23.

Hewes, R. S., Gu, T., Brewster, J. A., Qu, C. & Zhao, T. Regulation of secretory protein expression in mature cells by DIMM, a basic helix–loop–helix neuroendocrine differentiation factor. *J. Neurosci*. **26**, 7860–7869 (2006).

CAS PubMed PubMed Central Article Google Scholar

24. 24.

Bertet, C. et al. Temporal patterning of neuroblasts controls Notch-mediated cell survival through regulation of Hid or Reaper. *Cell* **158**, 1173–1186 (2014).

CAS PubMed PubMed Central Article Google Scholar

25. 25.

Hay, B. A., Wolff, T. & Rubin, G. M. Expression of baculovirus P35 prevents cell death in *Drosophila*. *Development* **120**, 2121–2129 (1994).

CAS PubMed PubMed Central Google Scholar

26. 26.

Lin, H. V., Rogulja, A. & Cadigan, K. M. Wingless eliminates ommatidia from the edge of the developing eye through activation of apoptosis. *Development* **131**, 2409–2418 (2004).

CAS PubMed Article PubMed Central Google Scholar

27. 27.

Pentek, J., Parker, L., Wu, A. & Arora, K. Follistatin preferentially antagonizes activin rather than BMP signaling in *Drosophila*. *Genesis* **47**, 261–273 (2009).

CAS PubMed Article PubMed Central Google Scholar

28. 28.

Ting, C. Y. et al. Photoreceptor-derived activin promotes dendritic termination and restricts the receptive fields of first-order interneurons in *Drosophila*. *Neuron* **81**, 830–846 (2014).

CAS PubMed PubMed Central Article Google Scholar

29. 29.

Hasegawa, E. et al. Concentric zones, cell migration and neuronal circuits in the *Drosophila* visual center. *Development* **138**, 983–993 (2011).

CAS PubMed Article PubMed Central Google Scholar

30. 30.

Soriano, E. & Del Río, J. A. The cells of Cajal–Retzius: still a mystery one century after. *Neuron* **46**, 389–394 (2005).

CAS PubMed Article PubMed Central Google Scholar

31. 31.

Yu, F., Kuo, C. T. & Jan, Y. N. *Drosophila* neuroblast asymmetric cell division: recent advances and implications for stem cell biology. *Neuron* **51**, 13–20 (2006).

CAS PubMed Article PubMed Central Google Scholar

32. 32.

Hofbauer, A. & Campos-Ortega, J. A. Proliferation pattern and early differentiation of the optic lobes in *Drosophila melanogaster*. *Rouxs Arch. Dev. Biol*. **198**, 264–274 (1990).

PubMed Article PubMed Central Google Scholar

33. 33.

Apitz, H. & Salecker, I. A region-specific neurogenesis mode requires migratory progenitors in the *Drosophila* visual system. *Nat. Neurosci*. **18**, 46–55 (2015).

CAS PubMed Article PubMed Central Google Scholar

34. 34.

Selleck, S. B. & Steller, H. The influence of retinal innervation on neurogenesis in the first optic ganglion of *Drosophila*. *Neuron* **6**, 83–99 (1991).

CAS PubMed Article PubMed Central Google Scholar

35. 35.

Monastirioti, M. et al. *Drosophila* Hey is a target of Notch in asymmetric divisions during embryonic and larval neurogenesis. *Development* **137**, 191–201 (2010).

CAS PubMed PubMed Central Article Google Scholar

36. 36.

Xu, J. et al. Prevention of medulla neuron dedifferentiation by Nerfin-1 requires inhibition of Notch activity. *Development* **144**, 1510–1517 (2017).

CAS PubMed Article PubMed Central Google Scholar

37. 37.

Nien, C.-Y. et al. Temporal coordination of gene networks by Zelda in the early *Drosophila* embryo. *PLoS Genet*. **7**, e1002339 (2011).

CAS PubMed PubMed Central Article Google Scholar

38. 38.

Cao, J. et al. The single-cell transcriptional landscape of mammalian organogenesis. *Nature* **566**, 496–502 (2019).

ADS CAS PubMed PubMed Central Article Google Scholar

39. 39.

Langen, M. et al. The developmental rules of neural superposition in *Drosophila*. *Cell* **162**, 120–133 (2015).

CAS PubMed PubMed Central Article Google Scholar

40. 40.

Özel, M. N., Langen, M., Hassan, B. A. & Hiesinger, P. R. Filopodial dynamics and growth cone stabilization in *Drosophila* visual circuit development. *eLife* **4**, e10721 (2015).

PubMed PubMed Central Article Google Scholar

41. 41.

Maisak, M. S. et al. A directional tuning map of *Drosophila* elementary motion detectors. *Nature* **500**, 212–216 (2013).

ADS CAS PubMed Article PubMed Central Google Scholar

42. 42.

Pinto-Teixeira, F. et al. Development of concurrent retinotopic maps in the fly motion detection circuit. *Cell* **173**, 485–498.e11 (2018).

CAS PubMed PubMed Central Article Google Scholar

43. 43.

Apitz, H. & Salecker, I. Spatio-temporal relays control layer identity of direction-selective neuron subtypes in *Drosophila*. *Nat. Commun*. **9**, 2295 (2018).

ADS PubMed PubMed Central Article CAS Google Scholar

44. 44.

Li, H. et al. Classifying *Drosophila* olfactory projection neuron subtypes by single-cell RNA sequencing. *Cell* **171**, 1206–1220.e22 (2017).

CAS PubMed PubMed Central Article Google Scholar

45. 45.

Wernet, M. F., Perry, M. W. & Desplan, C. The evolutionary diversity of insect retinal mosaics: common design principles and emerging molecular logic. *Trends Genet*. **31**, 316–328 (2015).

CAS PubMed PubMed Central Article Google Scholar

46. 46.

Kurmangaliyev, Y. Z., Yoo, J., Valdes-Aleman, J., Sanfilippo, P. & Zipursky, S.L. Transcriptional programs of circuit assembly in the *Drosophila* visual system. *Neuron* https://doi.org/10.1016/j.neuron.2020.10.006 (2020).

47. 47.

Lancichinetti, A. & Fortunato, S. Limits of modularity maximization in community detection. *Phys. Rev. E* **84**, 066122 (2011).

ADS Article CAS Google Scholar

48. 48.

Stoeckius, M. et al. Cell hashing with barcoded antibodies enables multiplexing and doublet detection for single cell genomics. *Genome Biol*. **19**, 224 (2018).

CAS PubMed PubMed Central Article Google Scholar

49. 49.

Ilicic, T. et al. Classification of low quality cells from single-cell RNA-seq data. *Genome Biol*. **17**, 29 (2016).

PubMed PubMed Central Article CAS Google Scholar

50. 50.

Srivastava, N., Hinton, G., Krizhevsky, A., Sutskever, I. & Salakhutdinov, R. Dropout: a simple way to prevent neural networks from overfitting. *J. Mach. Learn. Res*. **15**, 1929–1958 (2014).

MathSciNet MATH Google Scholar

51. 51.

Yarin, G. & Zoubin, G. Dropout as a Bayesian approximation: representing model uncertainty in deep learning. In *Proc. 33rd International Conference on Machine Learning* Vol. 48 (eds Balcan, M. F. and Weinberger, K. Q.) 1050–1059 (MLResearch Press, 2016).

52. 52.

Kurmangaliyev, Y. Z., Yoo, J., LoCascio, S. A. & Zipursky, S. L. Modular transcriptional programs separately define axon and dendrite connectivity. *eLife* **8**, e50822 (2019).

CAS PubMed PubMed Central Article Google Scholar

53. 53.

Supek, F., Bošnjak, M., Škunca, N. & Šmuc, T. REVIGO summarizes and visualizes long lists of gene ontology terms. *PLoS ONE* **6**, e21800 (2011).

ADS CAS PubMed PubMed Central Article Google Scholar

54. 54.

Kuznetsova, I., Lugmayr, A., Siira, S. J., Rackham, O. & Filipovska, A. CirGO: an alternative circular way of visualising gene ontology terms. *BMC Bioinformatics* **20**, 84 (2019).

PubMed PubMed Central Article Google Scholar

55. 55.

Karuppudurai, T. et al. A hard-wired glutamatergic circuit pools and relays UV signals to mediate spectral preference in *Drosophila*. *Neuron* **81**, 603–615 (2014).

CAS PubMed PubMed Central Article Google Scholar

56. 56.

Johnston, R. J., Jr et al. Interlocked feedforward loops control cell-type-specific rhodopsin expression in the *Drosophila* eye. *Cell* **145**, 956–968 (2011).

CAS PubMed PubMed Central Article Google Scholar

Download references

Acknowledgements

We thank all members of the Desplan laboratory, S.-y. Takemura and F. P. Davis for discussions; L. Luo, C. Doe, F. Pinto Teixeira, J. Slabbaert and S. Cordoba for critical reading of the manuscript; and I. Salecker and R. Hiesinger for reagents. The C.D. laboratory is supported by NYSTEM

(DOH01-C32604GG), the National Eye Institute (R01 EY017916) and by ADHPG-CGSB1 to the CGSB of the NYU Abu Dhabi Research Institute. M.N.O. is a Leon Levy Neuroscience Fellow. F.S. and Y.-C.C. are supported by New York University (MacCracken Fellowship). S.J. is supported by the Swedish Research Council (Vetenskapsrådet VR grant 2016- 06726). I.H. is supported by a Human Frontier Science Program postdoctoral fellowship (LT000757/2017). J.A.M is supported by the National Eye Institute (F32 F32EY028012). N.K. is supported by the National Eye Institute (K99 EY029356-01).

Author information

Author notes

1. These authors contributed equally: Mehmet Neset Özel, Félix Simon

Affiliations

1. Department of Biology, New York University, New York, NY, USA

   Mehmet Neset Özel, Félix Simon, Shadi Jafari, Isabel Holguera, Yen-Chung Chen, Jennifer Amy Malin, Nikolaos Konstantinides & Claude Desplan

2. Department of Molecular Biology, Umeå University, Umeå, Sweden

   Shadi Jafari

3. New York University Abu Dhabi, Abu Dhabi, United Arab Emirates

   Najate Benhra, Rana Naja El-Danaf, Katarina Kapuralin & Claude Desplan

Authors

1. Mehmet Neset Özel
   View author publications

You can also search for this author in PubMed Google Scholar

2. Félix Simon
   View author publications

   You can also search for this author in PubMed Google Scholar

3. Shadi Jafari
   View author publications

   You can also search for this author in PubMed Google Scholar

4. Isabel Holguera
   View author publications

   You can also search for this author in PubMed Google Scholar

5. Yen-Chung Chen
   View author publications

   You can also search for this author in PubMed Google Scholar

6. Najate Benhra
   View author publications

   You can also search for this author in PubMed Google Scholar

7. Rana Naja El-Danaf
   View author publications

   You can also search for this author in PubMed Google Scholar

8. Katarina Kapuralin
   View author publications

   You can also search for this author in PubMed Google Scholar

9. Jennifer Amy Malin
   View author publications

You can also search for this author in PubMed Google Scholar

10. Nikolaos Konstantinides
View author publications

You can also search for this author in PubMed Google Scholar

11. Claude Desplan
View author publications

You can also search for this author in PubMed Google Scholar

Contributions

M.N.O., F.S., N.K. and C.D. designed the project. M.N.O., F.S., S.J., I.H., N.B., R.N.E.-D., K.K. and J.A.M. performed the experiments. M.N.O., F.S., S.J., I.H., Y.-C.C., N.B., R.N.E.-D. and K.K. analysed the data. M.N.O., F.S. and S.J. acquired the scRNA-seq data. M.N.O. and F.S. performed all scRNA-seq data analysis and M.N.O., F.S. and C.D. wrote the manuscript. All authors edited the manuscript.

Corresponding authors

Correspondence to Nikolaos Konstantinides or Claude Desplan.

Ethics declarations

Competing interests

The authors declare no competing interests.

Additional information

Peer review information *Nature* thanks Stein Aerts and the other, anonymous, reviewer(s) for their contribution to the peer review of this work.

Publisher's note Springer Nature remains neutral with regard to jurisdictional claims in published maps and institutional affiliations.

Extended data figures and tables

Extended Data Fig. 1 Batch effect removal and biological relevance of the adult clusters.

a. The proportions of UMIs from mitochondrial genes per cell (*n* = number of cells in each library, indicated on the right) and the total number of cells passing filters in each of the 15 libraries comprising the adult dataset. Names indicated correspond to the names in the Seurat object provided (Adult.rds, GSE142787). Boxplots display the first, second and third quartiles. Whiskers extend from the box to the highest or lowest values in the 1.5 interquartile range, and outlying data points are represented by a dot. **b**, Origin of the cells in the final adult clusters, coloured as in **a**. Green arrows represent clusters for which the unique library distribution can be explained by variable contamination from surrounding tissues (cluster 3 is photoreceptors, 112 is probably Kenyon cells from the central brain) or the number of lamina neuropils dissociated (clusters 107, 108, 109 are lamina neurons). Red arrows indicate clusters that are probably enriched in low quality transcriptomes, as they are enriched in cells from libraries with high number of mitochondrial genes (38, 120, 192) or high number of cells sequenced (102, probably corresponding to multiplets). Brackets indicate glial clusters, some of them enriched in libraries with high number of mitochondrial genes as ambient RNA is more similar to RNA from glial versus neuronal cells (Extended Data Fig. 2). **c**, Number of clusters obtained with different pairs of clustering parameters. The red rectangle indicates the pair of parameters used. **d**, Left, Pearson correlation between the average gene expression of the adult dataset clusters (*x* axis) and the transcriptome of isolated Lawf1 and L1 neurons (Methods). Right, number of isolated neuronal type transcriptomes matching to 1–5 of our adult clusters, for each pair of parameters in **c**, which we used as a measure of the biological relevance of our clusters. Matching was defined by the presence of a correlation gap greater than 0.05 (Methods). We took into account any correlation gap between the six best-correlated clusters, because similar cell

types or overclustering can affect the size of the first correlation gap as illustrated on the left graphs. The red rectangle indicates the pair of parameters used. **e**, *t*-SNE visualization of the adult optic lobe single-cell transcriptomes, using 120 principal components calculated on the log-normalized integrated gene expression. Cell colours indicate the cluster they belonged to before we merged artificially split clusters (red circles; Methods). **f**, Heat map showing scaled log-normalized non-integrated expression of the top20 cluster markers between the merged clusters. Merged clusters had almost indistinguishable gene expression patterns, but often differed by their proportions of UMIs from mitochondrial genes per cell or the expression levels of the genes highlighted in red, which are enriched in the 'ambient RNA cluster' 192 (see also Extended Data Fig. 3).

Extended Data Fig. 2 Identification of neuronal and glial clusters.

a, Pearson correlation between the average log-normalized non-integrated expression of the top10 cluster markers of the adult dataset clusters (*x* axis) and the transcriptome of isolated Repo$^+$ (glial marker) or Elav$^+$ (neuronal marker) populations. LQ, clusters containing a proportion of cells with features of lower-quality transcriptomes; PR, photoreceptor. **b**, Violin plots of features tending to be higher (proportions of UMIs from mitochondrial genes) or lower (number of UMIs or genes per cell) in low-quality cells[48,49]. **c**, Heat map showing the scaled log-normalized non-integrated expression of the top5 cluster markers of the adult dataset. The first 5 neuronal adult clusters (1 to 6, cluster 1 and 2 having been merged) are plotted for reference as they clearly have specific gene expression patterns. Clusters 38, 85, 102 and 120 present much less defined gene expression patterns and probably contain low-quality neuronal transcriptomes (see also Extended Data Fig. 1). Clusters 188 and 189 could be further separated in two groups with different gene expression patterns, as illustrated by the dashed line in the insert. Cluster 191 expresses several markers that are found in no other clusters and probably correspond to neither glia nor optic-lobe neurons. Cluster 192 expresses mainly low levels of glia-specific genes, without specific markers. It probably corresponds to ambient RNA, which would be enriched in RNA from burst glial cells.

Extended Data Fig. 3 Identification of the adult neuronal clusters.

a, Pearson correlation between the average log-normalized non-integrated expression of the top10 cluster markers of the adult dataset clusters (*x* axis) and the transcriptome of isolated neurons[18,20]. We represented Dm3, Tm9, T4 and T5 before their split into Dm3a/Dm3b, Tm9v/Tm9d, T4/T5ab and T4/T5cd. When two transcriptomes were published for a given neuronal type, the one presenting the highest correlation gap is displayed in this figure. R1–8, average gene expression of all photoreceptors[20]. KC, Kenyon cells; cluster 112 therefore probably corresponds to contamination from the central brain. **b**, Legend as in **a** but for LC cells. We indicated several matching clusters to highlight the high similarity between the transcriptomes of LC cells, which explains the lower correlation gaps observed for these neurons. **c**, Left, legend as in **a** but for Pm3 cells. Right, mixture modelling of Pm3 markers[19] (*y* axis). Clusters are spread on the *x* axis, with the probability of expression of the markers figured by the size of the black dots.

Extended Data Fig. 4 Marker gene expressions in TmY4, TmY8, TmY14, LC12 and LC17 neurons.

a, Expression pattern of *TmY4-LexA* (green) in the adult optic lobe ($n = 7$ brains) with anti-Ncad immunostaining (white). The LexA line shows weak or no expression in the most anterior medulla region. **b**–**d**, Expression pattern of *TmY4-LexA* (green) in the adult optic lobe with anti-Dichaete (D) (**b**), anti-Vvl (**c**) and anti-Toy (**d**) immunostainings (magenta), $n = 15$ neurons for each. TmY4 cell bodies express Dichaete but not Vvl or Toy. **e**, Sparse labelling of cell types (anti-Flag, green) expressing *CG42548* in the adult optic lobe using MCFO and immunostained with anti-Brp (white) and anti-Vvl (magenta). A TmY8 neuron ($n = 4$ neurons) is labelled (arborized layers shown by arrows) and expresses Vvl. Adult flies were heat-shocked for 5 min and dissected after 6 days. **f**–**h**, Expression pattern of *R24F10-Gal4* (green) in late L3 optic lobes with anti-Ncad (white, **f**), anti-Dac (magenta, **f**), anti-Dichaete (magenta, **g**) and anti-Toy (magenta, **h**) immunostainings, $n = 15$ neurons for each. *R24F10-Gal4* is expressed in

TmY14 neurons during larval stage (unpublished data). TmY14 neurons express Toy (**h**) but not Dac or D (**f**, **g**). **i**, Expression pattern of *LC12-Gal4* (green) in the adult optic lobe (*n* = 7 brains) with anti-Ncad immunostaining (magenta) showing processes in lobula layers 2–4, and a projection to an optic glomerulus in the posterior ventrolateral protocerebrum (PVLP) of the central brain (white outline). The cell bodies of LC12 are located in the lateral cell body rind, the region separating the optic lobe and central brain. **j**, Expression pattern of *beat-Ic* (green) in the adult optic lobe (*n* = 6 brains) with anti-Ncad immunostaining (magenta) showing a strong expression profile in the optic glomerulus corresponding to LC12 in the PVLP (white outline). **k**–**m**, Expression pattern of *LC12-Gal4* (green) in the adult optic lobes with anti-Cut (**k**, magenta-top panel, grey-bottom panel), anti-Acj6 (**l**, magenta, top panel; grey, bottom panel), and anti-Toy (**m**, magenta, top panel; grey, bottom panel) immunostainings, *n* = 77 neurons. All LC12 cells bodies are cut^+, $Acj6^+$ and toy^+. Red line delineates LC12 cell body location. **n**, Expression pattern of *LC17-Gal4* (green) in the adult optic lobe (*n* = 5 brains) with anti-Ncad immunostaining (magenta) showing processes in lobula layers 2–5. LC17 project to the PVLP optic glomerulus (white outline) adjacent to that of LC12 (asterisk, see also **i**). **o**, Expression pattern of *Kn-Gal4* (green) in the adult optic lobe (*n* = 3 brains) with anti-Ncad immunostaining (magenta) showing a strong expression profile in the optic glomerulus corresponding to LC17 in the PVLP (white outline). Note its absence from LC12 neurons (asterisk). **p**, **q**, Expression pattern of *LC17-Gal4* (green) in the adult optic lobes with anti-Acj6 (**p**, magenta, top panel; grey, bottom panel) and anti-Toy (**q**, magenta, top panel; grey, bottom panel) immunostainings, *n* = 62 neurons. All LC17 cells bodies are $Acj6^+$ and toy^+. Red line delineates LC17 cell body location (**p**, **q**). Me, medulla; Lo, lobula; LoP, lobula plate. Scale bars: 25 µm (**a**–**j**, **n**, **o**), 15 µm (**k**–**m**, **p**, **q**).

Extended Data Fig. 5 Overview of the final adult clusters.

a, Hierarchical clustering tree of our adult clusters, based on the average log-normalized non-integrated expression of the 2,000 most variable genes of the dataset (the genes used to define the unsupervised clusters, Methods). Indicated in blue are the glial clusters. **b**, Number of cells in our identified neuronal clusters, excluding the T4–T5 cluster that contains 10,780 cells,

with unicolumnar neurons in blue and multicolumnar neurons in orange. Importantly, photoreceptors (PR) and lamina neurons L1–L5 clusters contain fewer cells, as these neuronal types were not included in equal proportions in all libraries. Because the number of cells per optic lobe for a given neuronal type is rarely formally counted, unicolumnar versus multicolumnar character is based both on general knowledge and the following references[7,8,12,55].

Extended Data Fig. 6 Benchmarking of the neural network classifier.

a, **b**, *t*-SNE visualization of the P70 optic lobe single-cell transcriptomes, using 120 principal components calculated on the log-normalized integrated gene expression. Cells colours indicate the clusters they belonged to according to unsupervised clustering (**a**), or the adult clusters they were classified as by the neural network (**b**, same as in Fig. 1e). Black circles indicate high granularity regions, where less frequent cell types were grouped together by unsupervised clustering but could be resolved accurately by the neural network. **c**, Same as in **a**, **b** but cells are named and coloured by the adult cluster they were classified as by Seurat label transfer (Methods). **d**, *t*-SNE visualization (same as **c**) including only the cells that were assigned inconsistent identities by Seurat and the neural network. Highest rates of inconsistencies were observed in the centre (LQ cells), in L1 and L2 clusters (red ellipses), in most glia clusters (green ellipses), the TE neurons and a glia-like cluster (identity 214, Supplementary Table 1) with no adult correspondence (blue ellipses). **e**, **f**, *t*-SNE visualizations of 56,902 cells sequenced from whole fly brains[19], using 120 principal components calculated on the log-normalized gene expression. **e**, Cells are named and coloured by the clusters they were classified as by our neural network. **f**, Cells are named by the cluster identities from the original study and coloured by the confidence score they received from our neural network. Black circles mark the following central brain clusters (from left to right): Poxn, OPN, clock neurons and dopaminergic neurons, that all received low scores from the neural network. Kenyon cells (red circles) were assigned with high confidence as our adult dataset was contaminated by them (cluster 112).

Extended Data Fig. 7 High-resolution transcriptomic atlases of the optic lobe across development.

a–**f**, *t*-SNE visualizations of all optic lobe single-cell transcriptomes acquired for this study, using 120 principal components calculated on the log-normalized integrated gene expression. The cells are named and coloured consistently at all stages by the neural network classifications with manual adjustments as detailed in Methods. Blue ellipses highlight Dm3 and Tm9 neuronal subtypes, which could only be resolved at P50 and earlier.

Extended Data Fig. 8 Transient extrinsic neurons.

a, **b**, *t*-SNE visualization of the P70 optic lobe single-cell transcriptomes, using 120 principal components calculated on the log-normalized integrated gene expression. Cells are named by the unsupervised cluster they were assigned to and coloured by the confidence score they received from the neural network (NN) (**a**) or by the log-normalized non-integrated expression of *Fs* (green), *dimm* (blue), and *skl* (red) (**b**), which are co-expressed in TE neurons (red ellipses). **c**, Violin plot of log-normalized non-integrated *prt* expression in all clusters at P50. TE neuron clusters are indicated by the circle. **d**, *R10D10-Gal4* co-expression with anti-Prt staining in a P50 optic lobe (n = 15 neurons). Scale bar, 10 µm. **e**, FLEXAMP memory cassette labelling of *R10D10-Gal4* in an adult optic lobe (n = 28 brains) with anti-Ncad staining. Scale bar, 30 µm. **f**, *R10D10-Gal4* expression pattern in L3 optic lobe (n = 15 brains), with anti-Ncad, anti-Bsh and anti-Hth staining. Arrow indicates $Bsh^{+}Hth^{-}$ neurons labelled by *R10D10-Gal4*. Scale bar, 30 µm. **g**, **h**, *R10D10-Gal4* sparse expression at P30 (n = 40 neurons), with anti-Ncad, anti-Bsh and anti-Hth staining. Scale bars, 5 µm (**g**) and 15 µm (**h**). dMe, distal Medulla; pMe, proximal Medulla; Lo, Lobula; Lp, Lobula plate. **i**, Co-labelling of *R10D10-LexA* expression and *bsh-Gal4* FLEXAMP memory cassette with anti-Ncad staining in a P50 optic lobe (n = 13 brains). Dashed ellipses highlight TE neurons. Scale bar, 20 µm.

Extended Data Fig. 9 Early differentiation and transcriptomic synchronization of optic lobe neurons and summary of the main findings.

a, **b**, *t*-SNE visualization of the P15 optic lobe single-cell transcriptomes, using 120 principal components calculated on the log-normalized integrated gene expression. Cells are named by the unsupervised cluster they were assigned to and coloured by the confidence score they received from the neural network (**a**) or by the log-normalized non-integrated expression of *dpn* (green), *ase* (blue), and *grim* (red) (**b**). Circles match those of Fig. 3a. **c**, UMAP visualization of the P15 optic lobe single-cell transcriptomes, using 120 principal components calculated on the log-normalized integrated gene expression. Cells are coloured by the log-normalized non-integrated expression of *nerfin-1* (green), *Hey* (blue), and *vfl* (red). **d**, UMAP visualization of Tm3 and T1 cells (above and below the dashed line, respectively) from all stages sequenced in this study, using 25 principal components calculated on the log-normalized non-integrated gene expression. Cells are coloured by their developmental stage. **e**, Ventral and dorsal transient extrinsic (TE) neurons as well as transient photoreceptors (PRs) line the edges of all optic lobe neuropils and express *Follistatin* (*Fs*). Moreover, TE and at least three other neuronal types express *Wnt4* in the ventral medulla/lobula but express *Wnt10* in the dorsal part of these neuropils. **f**, The transcriptome of neurons from the same neuronal type but produced days apart converge towards a similar transcriptomic state, which they reach by P30. Moreover, the inter-neuronal type transcriptomic diversity is highest during P40–P70.

Extended Data Fig. 10 Increased transcriptomic diversity during synaptogenesis.

a, Log-normalized and scaled (to the max of 1 for each gene across all time points) expression of top10 (by logFC, calculated at P50) subcluster markers between T4 and T5 subtypes at all stages. TF, transcription factor; CSM, cell-surface molecule. **b**, **c**, GO enrichment analysis of all (269) differentially expressed genes between the T4–T5 subclusters at P50. All Biological Process (**b**) and Molecular Function (**c**) terms with greater than

twofold enrichment were summarized by REVIGO to eliminate redundant terms and group related ones together. Inner rings in the CirGO plots indicate the summarized terms (names in bold). Some individual terms (outer ring) relevant to neuronal function and development are also labelled. Areas within the graphs are determined by the *P* values of the terms. **d**, Average normalized number of presynaptic sites from Dm3 neurons with orthogonally oriented dendritic arbors (because we could not assign the anatomical directions from the EM data, we plotted them as Dm3x and Dm3y) to indicated neuronal types (Methods). Only the outputs showing differences between the subtypes are plotted. Error bars denote s.e.m. $P = 0.004$ (Dm3x), 0.006 (Dm3y), 0.04 (Tm28), unpaired parametric two-tailed *t*-tests ($n = 5$ and 7 Dm3 cells per type). **e**, Number of genes differentially expressed between the indicated subtypes with a $P < 0.01$ (two-sided Wilcoxon rank-sum test), calculated after downsampling the number of cells in each group to 150 for consistency.

Extended Data Fig. 11 GO enrichment analysis of the cluster and stage markers.

a, **b**, GO terms were determined from the most differentially expressed genes between neuronal clusters (ranked top20 by logFC for at least one cluster) at all stages separately (**a**) or all genes differentially expressed between stages (Methods) in all neurons (aggregated) (**b**). All terms with greater than twofold enrichment were summarized by REVIGO to eliminate redundant terms and group related ones together. Inner rings (labelled within the graphs or in bold) indicate the summarized terms. Some individual terms (outer ring, not bold), if non-redundant with the summary terms, are also labelled. Areas within the graphs are determined by the *P* values of the terms.

Extended Data Fig. 12 Dorsal and ventral visual circuits are partitioned by differential Wnt signalling.

a, *Tm9-Gal4* sparse labelling in the ventral and dorsal part of the same adult optic lobe ($n = 4$ neurons) with anti-Ncad immunostaining (grey). **b**, Expression pattern of *Wnt4-Gal4* (green) with anti-Chaoptin

immunostaining (magenta) in the adult optic lobe (n = 8 brains). **c**, Expression pattern of *Wnt4-Gal4* (green) with anti-Chaoptin (magenta) and anti-Dve (cyan) immunostainings, in the ventral retina at P30 (n = 6 eye discs). Chaoptin marks all photoreceptors, and Dve is expressed in the photoreceptors R1-6 and a subset of R7 (yellow R7), but not in R8 and the rest of R7[56]. **d**, Expression pattern of *Tm4-Gal4* (green) with anti-Aop immunostaining (magenta) at P50 (n = 3 brains), showing that almost all Aop^+ neurons are co-labelled by *Tm4-Gal4*. Arrowheads show Aop^+ neurons that are not co-labelled by *Tm4-Gal4*. **e**, *Wnt4*-Gal4 expression pattern with anti-Aop staining (Tm4 marker, see **d**) at P50 (n = 6 brains). Aop^+ neurons co-express *Wnt4-Gal4* in the ventral (white arrows) but not dorsal (white arrowheads) optic lobe. **f**, *fz2*, *mamo* or *CG9896* differential expression between either Tm9v and Tm9d cells, TEv and TEd cells, $Wnt4^+Wnt10^-$ and $Wnt4^-Wnt10^+$ Tm4 cells or $Wnt4^+Wnt10^-$ and $Wnt4^-Wnt10^+$ cluster 62 cells (log-normalized non-integrated expression). Two-sided Wilcoxon rank-sum test, P values are indicated on the figure, NS, not significant. Scale bars, 10 μm (**a**, **c**) or 30 μm (**b**, **d**, **e**).

Supplementary information

Supplementary Information

This file contains the Supplementary Discussion and Supplementary References.

Reporting Summary

FACS Gating Strategy

Supplementary Figure 1 . This figure contains plots exemplifying the gating strategies used for sorting specific cell types for the bulk sequencing experiments.

Details on the annotation of the adult and pupal datasets

Supplementary Table 1 . This table indicates how the annotation of our adult clusters was determined, gives details about how these annotations were transferred to pupal clusters (i.e. if cells were discarded in the process, if new identities were created, etc.), and list general observations we made about the clusters but did not list in main text (i.e. if a cluster could include low quality transcriptomes, potential identifications for some clusters based with their proximity with other cell types, etc.).

Unique transcription factor combinations in the neuronal clusters

Supplementary Table 2 . Please refer to the Methods subsection named "Stable transcription factor markers in neuronal clusters" for details.

Origins of fly strains and antibodies used

Supplementary Table 3 .

Appendix 1

Supplementary Data . This zipped file includes the instructions, Python/R code and example datasets to locally run the neural network classifier.

Rights and permissions

Reprints and Permissions

About this article

Check for updates

Cite this article

Özel, M.N., Simon, F., Jafari, S. *et al.* Neuronal diversity and convergence in a visual system developmental atlas. *Nature* **589,** 88–95 (2021). https://doi.org/10.1038/s41586-020-2879-3

Download citation

- Received: 23 January 2020
- Accepted: 27 August 2020
- Published: 04 November 2020
- Issue Date: 07 January 2021
- DOI: https://doi.org/10.1038/s41586-020-2879-3

Comments

By submitting a comment you agree to abide by our Terms and Community Guidelines. If you find something abusive or that does not comply with our terms or guidelines please flag it as inappropriate.

Access through your institution
Change institution
Buy or subscribe

This article was downloaded by **calibre** from https://www.nature.com/articles/s41586-020-2879-3

- Article
- Published: 18 November 2020

Coupling of hippocampal theta and ripples with pontogeniculooccipital waves

- Juan F. Ramirez-Villegas[1,2] nAff8,
- Michel Besserve ORCID: orcid.org/0000-0003-0025-2323[1,3],
- Yusuke Murayama[1,4],
- Henry C. Evrard[1,4,5,6],
- Axel Oeltermann[1] &
- Nikos K. Logothetis ORCID: orcid.org/0000-0001-7728-4118[1,4,7]

Nature **volume 589**, pages96–102(2021)Cite this article

- 4058 Accesses
- 56 Altmetric
- Metrics details

Subjects

- Anatomy
- Cognitive neuroscience
- Neuroscience

An Author Correction to this article was published on 09 December 2020

This article has been updated

Abstract

The hippocampus has a major role in encoding and consolidating long-term memories, and undergoes plastic changes during sleep[1]. These changes require precise homeostatic control by subcortical neuromodulatory structures[2]. The underlying mechanisms of this phenomenon, however, remain unknown. Here, using multi-structure recordings in macaque monkeys, we show that the brainstem transiently modulates hippocampal network events through phasic pontine waves known as pontogeniculooccipital waves (PGO waves). Two physiologically distinct types of PGO wave appear to occur sequentially, selectively influencing high-frequency ripples and low-frequency theta events, respectively. The two types of PGO wave are associated with opposite hippocampal spike-field coupling, prompting periods of high neural synchrony of neural populations during periods of ripple and theta instances. The coupling between PGO waves and ripples, classically associated with distinct sleep stages, supports the notion that a global coordination mechanism of hippocampal sleep dynamics by cholinergic pontine transients may promote systems and synaptic memory consolidation as well as synaptic homeostasis.

Access through your institution
Change institution
Buy or subscribe

Access options

Subscribe to Journal

Get full journal access for 1 year

$199.00

only $3.90 per issue

Subscribe

All prices are NET prices.
VAT will be added later in the checkout.

Rent or Buy article

Get time limited or full article access on ReadCube.

from$8.99

Rent or Buy

All prices are NET prices.

Additional access options:

- Log in
- Access through your institution
- Learn about institutional subscriptions

Fig. 1: Electrode position in pontine–LGN–HC recordings.

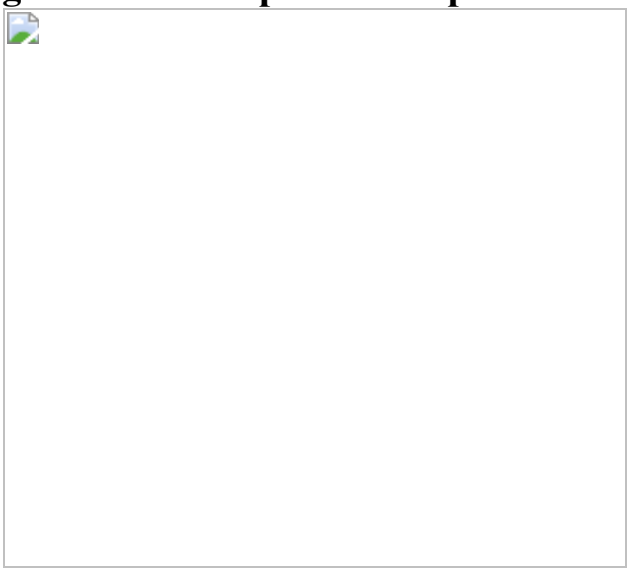

Fig. 2: Phasic waves in the PBn, LGN and HC.

Fig. 3: Type I and type II PGO waves are brain-state specific.

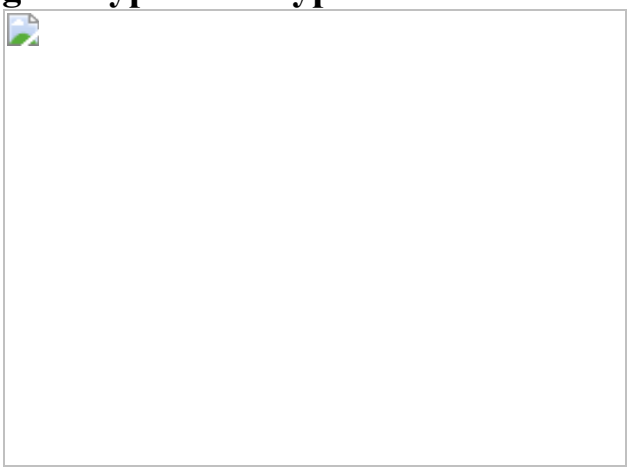

Fig. 4: Modulation of hippocampal activity at the time of PGO-wave occurrence.

Data availability

All data are available from the corresponding author upon reasonable request.

Code availability

All analyses reported in this work were made with custom code written in MATLAB (The MathWorks), and will be available from the corresponding author upon reasonable request.

Change history

- **09 December 2020**

  A Correction to this paper has been published: https://doi.org/10.1038/s41586-020-03068-9.

References

1. 1.

   Stickgold, R. & Walker, M. P. Memory consolidation and reconsolidation: what is the role of sleep? *Trends Neurosci*. **28**, 408–415 (2005).

   CAS PubMed Article PubMed Central Google Scholar

2. 2.

   Pace-Schott, E. F. & Hobson, J. A. The neurobiology of sleep: genetics, cellular physiology and subcortical networks. *Nat. Rev. Neurosci*. **3**, 591–605 (2002).

   CAS PubMed Article PubMed Central Google Scholar

3. 3.

   Buzsáki, G. Hippocampal sharp wave-ripple: a cognitive biomarker for episodic memory and planning. *Hippocampus* **25**, 1073–1188 (2015).

   PubMed PubMed Central Article Google Scholar

4. 4.

Grosmark, A. D., Mizuseki, K., Pastalkova, E., Diba, K. & Buzsáki, G. REM sleep reorganizes hippocampal excitability. *Neuron* **75**, 1001–1007 (2012).

CAS PubMed PubMed Central Article Google Scholar

5. 5.

Vertes, R. P. Brain stem generation of the hippocampal EEG. *Prog. Neurobiol*. **19**, 159–186 (1982).

CAS PubMed Article PubMed Central Google Scholar

6. 6.

Girardeau, G., Benchenane, K., Wiener, S. I., Buzsáki, G. & Zugaro, M. B. Selective suppression of hippocampal ripples impairs spatial memory. *Nat. Neurosci*. **12**, 1222–1223 (2009).

CAS PubMed Article PubMed Central Google Scholar

7. 7.

Green, J. D. & Arduini, A. A. Hippocampal electrical activity in arousal. *J. Neurophysiol*. **17**, 533–557 (1954).

CAS PubMed Article PubMed Central Google Scholar

8. 8.

Montgomery, S. M., Sirota, A. & Buzsáki, G. Theta and gamma coordination of hippocampal networks during waking and rapid eye movement sleep. *J. Neurosci*. **28**, 6731–6741 (2008).

CAS PubMed PubMed Central Article Google Scholar

9. 9.

Tononi, G. & Cirelli, C. Sleep and the price of plasticity: from synaptic and cellular homeostasis to memory consolidation and integration. *Neuron* **81**, 12–34 (2014).

CAS PubMed PubMed Central Article Google Scholar

10. 10.

Logothetis, N. K. et al. Hippocampal–cortical interaction during periods of subcortical silence. *Nature* **491**, 547–553 (2012).

ADS CAS PubMed Article Google Scholar

11. 11.

Datta, S. Cellular basis of pontine ponto–geniculo–occipital wave generation and modulation. *Cell. Mol. Neurobiol*. **17**, 341–365 (1997).

CAS PubMed Article Google Scholar

12. 12.

Jouvet, M. Recherches sur les structures nerveuses et les mecanismes responsables des differentes phases du sommeil physiologique (Research on the neural structures and responsible mechanisms in different phases of physiological sleep). *Arch. Ital. Biol*. **100**, 125–206 (1962).

CAS PubMed Google Scholar

13. 13.

Fernández-Mendoza, J. et al. Evidence of subthalamic PGO-like waves during REM sleep in humans: a deep brain polysomnographic study. *Sleep* **32**, 1117–1126 (2009).

PubMed PubMed Central Article Google Scholar

14. 14.

Vuillon-Cacciuttolo, G. & Seri, B. Effets de la section des nerfs optiques chez le babouin sur l'activite a type de pointes genouillees et corticales au cours des divers etats de vigilance (Effects of optic nerve section in baboons on the geniculate and cortical spike activity during various states of vigilance). *Electroencephalogr. Clin. Neurophysiol*. **44**, 754–768 (1978).

CAS PubMed Article Google Scholar

15. 15.

Mavanji, V. & Datta, S. Activation of the phasic pontine-wave generator enhances improvement of learning performance: a mechanism for sleep-dependent plasticity. *Eur. J. Neurosci*. **17**, 359–370 (2003).

PubMed Article Google Scholar

16. 16.

Datta, S. & O'Malley, M. W. Fear extinction memory consolidation requires potentiation of pontine-wave activity during REM sleep. *J. Neurosci*. **33**, 4561–4569 (2013).

CAS PubMed PubMed Central Article Google Scholar

17. 17.

Mavanji, V., Ulloor, J., Saha, S. & Datta, S. Neurotoxic lesions of phasic pontine-wave generator cells impair retention of 2-way active avoidance memory. *Sleep* **27**, 1282–1292 (2004).

PubMed Article Google Scholar

18. 18.

Hobson, J. A. REM sleep and dreaming: towards a theory of protoconsciousness. *Nat. Rev. Neurosci*. **10**, 803–813 (2009).

CAS PubMed Article Google Scholar

19. 19.

Boyce, R., Glasgow, S. D., Williams, S. & Adamantidis, A. Causal evidence for the role of REM sleep theta rhythm in contextual memory consolidation. *Science* **352**, 812–816 (2016).

ADS CAS Article Google Scholar

20. 20.

Buzsáki, G. Theta oscillations in the hippocampus. *Neuron* **33**, 325–340 (2002).

PubMed Article Google Scholar

21. 21.

Karashima, A., Nakao, M., Katayama, N. & Honda, K. Instantaneous acceleration and amplification of hippocampal theta wave coincident with phasic pontine activities during REM sleep. *Brain Res*. **1051**, 50–56 (2005).

CAS PubMed Article Google Scholar

22. 22.

Jutras, M. J., Fries, P. & Buffalo, E. A. Oscillatory activity in the monkey hippocampus during visual exploration and memory formation. *Proc. Natl Acad. Sci. USA* **110**, 13144–13149 (2013).

ADS CAS PubMed Article Google Scholar

23. 23.

Bohbot, V. D., Copara, M. S., Gotman, J. & Ekstrom, A. D. Low-frequency theta oscillations in the human hippocampus during real-world and virtual navigation. *Nat. Commun*. **8**, 14415 (2017).

ADS CAS PubMed PubMed Central Article Google Scholar

24. 24.

Ramirez-Villegas, J. F., Logothetis, N. K. & Besserve, M. Diversity of sharp-wave-ripple LFP signatures reveals differentiated brain-wide dynamical events. *Proc. Natl Acad. Sci. USA* **112**, E6379–E6387 (2015).

ADS CAS PubMed Article Google Scholar

25. 25.

Carr, M. F., Karlsson, M. P. & Frank, L. M. Transient slow gamma synchrony underlies hippocampal memory replay. *Neuron* **75**, 700–713 (2012).

CAS PubMed PubMed Central Article Google Scholar

26. 26.

Calvo, J. M. & Fernández-Guardiola, A. Phasic activity of the basolateral amygdala, cingulate gyrus, and hippocampus during REM sleep in the cat. *Sleep* **7**, 202–210 (1984).

CAS PubMed Article Google Scholar

27. 27.

Amzica, F. & Steriade, M. Progressive cortical synchronization of ponto–geniculo–occipital potentials during rapid eye movement sleep. *Neuroscience* **72**, 309–314 (1996).

CAS PubMed Article Google Scholar

28. 28.

Bowker, R. M. Variability in the characteristics of pontogeniculooccipital spikes during paradoxical sleep. *Exp. Neurol*.

87, 212–224 (1985).

CAS PubMed Article Google Scholar

29. 29.

Datta, S., Calvo, J. M., Quattrochi, J. & Hobson, J. A. Cholinergic microstimulation of the peribrachial nucleus in the cat. I. Immediate and prolonged increases in ponto–geniculo–occipital waves. *Arch. Ital. Biol*. **130**, 263–284 (1992).

CAS PubMed Google Scholar

30. 30.

Morrison, A. R. & Pompeiano, O. Vestibular influences during sleep. IV. Functional relations between vestibular nuclei and lateral geniculate nucleus during desynchronized sleep. *Arch. Ital. Biol*. **104**, 425–458 (1966).

CAS PubMed PubMed Central Google Scholar

31. 31.

Datta, S. Activation of phasic pontine-wave generator: a mechanism for sleep-dependent memory processing. *Sleep Biol. Rhythms* **4**, 16–26 (2006).

Article Google Scholar

32. 32.

Logothetis, N. K. What we can do and what we cannot do with fMRI. *Nature* **453**, 869–878 (2008).

ADS CAS PubMed Article PubMed Central Google Scholar

33. 33.

Shajarisales, N., Janzing, D., Schoelkopf, B. & Besserve, M. Telling cause from effect in deterministic linear dynamical systems. In *Proc. 32nd International Conference on Machine Learning* Vol. 37 (eds F. Bach & D. Blei) 285–294 (Proceedings of Machine Learning Research, 2015).

34. 34.

Hsieh, K.-C., Robinson, E. L. & Fuller, C. A. Sleep architecture in unrestrained rhesus monkeys (*Macaca mulatta*) synchronized to 24-hour light-dark cycles. *Sleep* **31**, 1239–1250 (2008).

PubMed PubMed Central Google Scholar

35. 35.

Fernández-Ruiz, A. et al. Long-duration hippocampal sharp wave ripples improve memory. *Science* **364**, 1082–1086 (2019).

ADS PubMed PubMed Central Article CAS Google Scholar

36. 36.

Griffin, A. L., Asaka, Y., Darling, R. D. & Berry, S. D. Theta-contingent trial presentation accelerates learning rate and enhances hippocampal plasticity during trace eyeblink conditioning. *Behav. Neurosci*. **118**, 403–411 (2004).

PubMed Article PubMed Central Google Scholar

37. 37.

Huerta, P. T. & Lisman, J. E. Bidirectional synaptic plasticity induced by a single burst during cholinergic theta oscillation in CA1 in vitro. *Neuron* **15**, 1053–1063 (1995).

CAS PubMed Article PubMed Central Google Scholar

38. 38.

Poe, G. R., Nitz, D. A., McNaughton, B. L. & Barnes, C. A. Experience-dependent phase-reversal of hippocampal neuron firing during REM sleep. *Brain Res*. **855**, 176–180 (2000).

CAS PubMed Article PubMed Central Google Scholar

39. 39.

Datta, S., Siwek, D. F., Patterson, E. H. & Cipolloni, P. B. Localization of pontine PGO wave generation sites and their anatomical projections in the rat. *Synapse* **30**, 409–423 (1998).

CAS PubMed Article Google Scholar

40. 40.

Steriade, M., Datta, S., Paré, D., Oakson, G. & Curró Dossi, R. C. Neuronal activities in brain-stem cholinergic nuclei related to tonic activation processes in thalamocortical systems. *J. Neurosci*. **10**, 2541–2559 (1990).

CAS PubMed PubMed Central Article Google Scholar

41. 41.

Moriizumi, T., Nakamura, Y., Tokuno, H., Kudo, M. & Kitao, Y. Synaptic organization of the pedunculopontine tegmental nucleus of the cat. *Brain Res*. **478**, 315–325 (1989).

CAS PubMed Article Google Scholar

42. 42.

Datta, S. Cellular and chemical neuroscience of mammalian sleep. *Sleep Med*. **11**, 431–440 (2010).

PubMed PubMed Central Article Google Scholar

43. 43.

Soltani, S. et al. Sleep–wake cycle in young and older mice. *Front. Syst. Neurosci*. **13**, 51 (2019).

CAS PubMed PubMed Central Article Google Scholar

44. 44.

Ulloor, J. & Datta, S. Spatio-temporal activation of cyclic AMP response element-binding protein, activity-regulated cytoskeletal-associated protein and brain-derived nerve growth factor: a mechanism for pontine-wave generator activation-dependent two-way active-avoidance memory processing in the rat. *J. Neurochem*. **95**, 418–428 (2005).

CAS PubMed Article PubMed Central Google Scholar

45. 45.

Paxinos, G., Petrides, M., Huang, X. F. & Toga, A. W. *The Rhesus Monkey Brain in Stereotaxic Coordinates* (Elsevier Science, 2008).

46. 46.

Ramirez-Villegas, J. F., Willeke, K. F., Logothetis, N. K. & Besserve, M. Dissecting the synapse- and frequency-dependent network mechanisms of in vivo hippocampal sharp wave-ripples. *Neuron* **100**, 1224–1240 (2018).

CAS PubMed Article PubMed Central Google Scholar

47. 47.

Leonard, T. K., Mikkila, J. M., Eskandar, E. N., Gerrard, J. L., Kaping, D., Patel, S. R., Womelsdorf, T., & Hoffman, K. L. Sharp wave ripples during visual exploration in the primate hippocampus. *J. Neurosci*. **35**, 14771–14782 (2015).

CAS PubMed PubMed Central Article Google Scholar

48. 48.

Leppä, M. et al. Acute opioid effects on human brain as revealed by functional magnetic resonance imaging. *Neuroimage* **31**, 661–669 (2006).

PubMed Article PubMed Central Google Scholar

49. 49.

Talbot, J. D. et al. Multiple representations of pain in human cerebral cortex. *Science* **251**, 1355–1358 (1991).

ADS CAS PubMed Article PubMed Central Google Scholar

50. 50.

Jones, A. K. et al. In vivo distribution of opioid receptors in man in relation to the cortical projections of the medial and lateral pain systems measured with positron emission tomography. *Neurosci. Lett*. **126**, 25–28 (1991).

CAS PubMed Article Google Scholar

51. 51.

Grønlykke, L. et al. Remifentanil-induced spike activity as a diagnostic tool in epilepsy surgery. *Acta Neurol. Scand*. **117**, 90–93 (2008).

PubMed Google Scholar

52. 52.

Iannetti, G. D. et al. Pharmacological modulation of pain-related brain activity during normal and central sensitization states in humans. *Proc. Natl Acad. Sci. USA* **102**, 18195–18200 (2005).

ADS CAS PubMed Article Google Scholar

53. 53.

Wise, R. G. et al. Combining fMRI with a pharmacokinetic model to determine which brain areas activated by painful stimulation are specifically modulated by remifentanil. *Neuroimage* **16**, 999–1014 (2002).

PubMed Article Google Scholar

54. 54.

Goense, J. B. M. & Logothetis, N. K. Neurophysiology of the BOLD fMRI signal in awake monkeys. *Curr. Biol*. **18**, 631–640 (2008).

CAS PubMed Article Google Scholar

55. 55.

Logothetis, N. K., Pauls, J., Augath, M., Trinath, T. & Oeltermann, A. Neurophysiological investigation of the basis of the fMRI signal. *Nature* **412**, 150–157 (2001).

ADS CAS PubMed Article Google Scholar

56. 56.

Mortazavi, S., Thompson, J., Baghdoyan, H. A. & Lydic, R. Fentanyl and morphine, but not remifentanil, inhibit acetylcholine release in pontine regions modulating arousal. *Anesthesiology* **90**, 1070–1077 (1999).

CAS PubMed Article Google Scholar

57. 57.

Lozito, R. J., La Marca, S., Dunn, R. W. & Jerussi, T. P. Single versus multiple infusions of fentanyl analogues in a rat EEG model. *Life Sciences* **55**, 1337–1342 (1994).

CAS PubMed Article Google Scholar

58. 58.

Egan, T. D., Minto, C. F., Hermann, D. J., Barr, J., Muir, K. T. & Shafer, S. L. Remifentanil versus alfentanil: comparative pharmacokinetics and pharmacodynamics in healthy adult male volunteers. *Anesthesiology* **84**, 821–833 (1996).

CAS PubMed Article Google Scholar

59. 59.

Bonafide, C. P., Aucutt-Walter, N., Divittore, N., King, T., Bixler, E. O. & Cronin, A. J. Remifentanil inhibits rapid eye movement sleep but not the nocturnal melatonin surge in humans. *Anesthesiology* **108**, 627–633 (2008).

CAS PubMed Article Google Scholar

60. 60.

Besserve, M., Lowe, S. C., Logothetis, N. K., Schölkopf, B. & Panzeri, S. Shifts of gamma phase across primary visual cortical sites reflect dynamic stimulus-modulated information transfer. *PLoS Biol*. **13**, e1002257 (2015).

PubMed PubMed Central Article CAS Google Scholar

61. 61.

Brillinger, D. R. Estimation of 2nd-order intensities of a bivariate stationary point process. *J. R. Stat. Soc. B* **38**, 60–66 (1976).

MATH Google Scholar

62. 62.

Saleem, K. S. & Logothetis, N. K. *A Combined MRI and Histology Atlas of the Rhesus Monkey Brain* (Academic, 2006).

63. 63.

Blair, R. C., & Karniski, W. An alternative method for significance testing of waveform difference potentials. *Psychophysiology* **30**, 518–524 (1993).

CAS PubMed PubMed Central Article Google Scholar

Download references

Acknowledgements

We thank O. Eschenko and M. Constantinou for providing feedback on earlier versions of this work, and J. Werner and M. Schnabel for technical support during the development of this study. This research was supported by the Max Planck Society.

Author information

Author notes

1. Juan F. Ramirez-Villegas

   Present address: IST Austria (Institute of Science and Technology Austria), Klosterneuburg, Austria

Affiliations

1. Department of Physiology of Cognitive Processes, Max Planck Institute for Biological Cybernetics, Tübingen, Germany

   Juan F. Ramirez-Villegas, Michel Besserve, Yusuke Murayama, Henry C. Evrard, Axel Oeltermann & Nikos K. Logothetis

2. Graduate School of Neural and Behavioral Sciences, International Max Planck Research School, Eberhard-Karls University of Tübingen, Tübingen, Germany

   Juan F. Ramirez-Villegas

3. Department of Empirical Inference, Max Planck Institute for Intelligent Systems, Tübingen, Germany

   Michel Besserve

4. International Center for Primate Brain Research, Songjiang, Shanghai, China

   Yusuke Murayama, Henry C. Evrard & Nikos K. Logothetis

5. Werner-Reichardt Centre for Integrative Neuroscience, Tübingen, Germany

   Henry C. Evrard

6. Nathan Kline Institute for Psychiatric Research, Orangeburg, NY, USA

   Henry C. Evrard

7. Centre for Imaging Sciences, Biomedical Imaging Institute, The University of Manchester, Manchester, UK

   Nikos K. Logothetis

Authors

1. Juan F. Ramirez-Villegas
   View author publications

   You can also search for this author in PubMed Google Scholar

2. Michel Besserve
   View author publications

You can also search for this author in PubMed Google Scholar

3. Yusuke Murayama
   View author publications

   You can also search for this author in PubMed Google Scholar

4. Henry C. Evrard
   View author publications

   You can also search for this author in PubMed Google Scholar

5. Axel Oeltermann
   View author publications

   You can also search for this author in PubMed Google Scholar

6. Nikos K. Logothetis
   View author publications

   You can also search for this author in PubMed Google Scholar

Contributions

N.K.L. conceived and designed the research. J.F.R.-V., Y.M., M.B. and N.K.L. performed the research. M.B. and N.K.L. supervised the research. J.F.R.-V., M.B., H.C.E., A.O. and N.K.L. contributed new reagents and analytical tools. J.F.R.-V. and N.K.L. analysed the data. J.F.R.-V., M.B. and N.K.L. wrote the manuscript.

Corresponding author

Correspondence to Nikos K. Logothetis.

Ethics declarations

Competing interests

The authors declare no competing interests.

Additional information

Peer review information *Nature* thanks the anonymous reviewers for their contribution to the peer review of this work.

Publisher's note Springer Nature remains neutral with regard to jurisdictional claims in published maps and institutional affiliations.

Extended data figures and tables

Extended Data Fig. 1 Ripple-triggered functional MRI responses in the macaque brain.

a, SWR-Triggered Peri-Event time courses. Typically cortical and subcortical brain regions are up and down modulated respectively, at the time of ripple-occurrence. **b**, Observed was a consistent (in every single experimental session) and robust down-modulation of Pons, LGN-Pulvinar (Pul) and the foveal and perifoveal regions of the primary visual cortex (V1). **c**, Average time courses of every brain regions of interest (ROI) in the peri-ripple epochs. **d**, Mean ripple-triggered fMRI responses in Pons, LGN-Pul and striate cortex, calculated based on the multiple regression (General Linear Model, that is, GLM) method selecting voxels by fitting a linear combination of two response models of different start points by 4 s. Trials with positive or negative BOLD responses (PBR or NBR) were selected with GLM only by for pons (Pontine Region and Parabrachial Nucleus). The selected PBR- and NBR trials were used to plot the responses in LGN and Striate Cortex. Left most plot shows the overall response in pons, that is, the average of all trials, just as it is shown in **c**. Middle and right most plots show the average response of the three structures for PBR- and NBR-Trials respectively. Shaded areas indicate SEM. Abbreviations: LGN Lateral Geniculate Nucleus, HP Hippocampus, PontReg Pontine Region Including Parabrachial Nucleus, fV1 – pfV1 Foveal, parafoveal and perifoveal striate cortex (V1).

Extended Data Fig. 2 Detailed description of the collected data.

The collected data (total of over 100 h of recordings) comprised a total of 630 10-min Data-Acquisition-Epochs, grouped in 66 groups, recorded during 42 experimental sessions (note that one session corresponds to one recording day). Experimental sessions consisted of concurrent functional MRI and electrophysiology recordings of spontaneous activity in 2 structures (24 sessions for PBn-HC, 6 sessions for PBn-LGN, 4 sessions for HC-LGN; animals A13, F12, K13, CM029, and E10), one session with the three structures (PBn-HC-LGN; animal K13) and 7 additional sessions with 3 structures including the LGN, VCX and hippocampus (LGN-HC-VCX; animals I09 and A13). A collation of the LFP recording sites for the PBn (25 exemplary experimental sessions; animals K13, CM029 and F12) and HC (26 exemplary experimental sessions; animals A13, E10, F12, I09 and K13) is reported here and in Extended Data Fig. 3. Electrode locations were derived from high-resolution anatomical scans, overlaid onto the corresponding coronal slices of the Paxinos rhesus monkey brain atlas or the Saleem–Logothetis combined histology-MRI of the rhesus monkey brain atlas. The remaining experimental sessions shared similar electrode positions to the ones reported here and in Extended Data Fig. 3, in consensus with the anatomical scans and the electrical profiles of the recorded signals.

Extended Data Fig. 3 Collation of the LFP recording sites in or around the parabrachial nucleus, from 25 exemplary recording sessions made in three monkeys (k13: 19 sessions; cm029: 4 sessions; f12: 3 sessions).

The location of the recording sites was derived from high-resolution anatomical scans and transposed onto the corresponding location on drawing of coronal slices of the rhesus macaque monkey brain. With the exception of k13m1, all recording sites were located inside the parabrachial nucleus. Relevant abbreviations: KF: Kolliker-Fuse; LPB, lateral parabrachial; LPBC, lateral parabrachial central; LPBD, lateral parabrachial dorsal; LPBE, lateral parabrachial external; LPBV, lateral parabrachial ventral; MPB, medial parabrachial; MPBE, medial parabrachial external;

scp, superior cerebellar peduncle. The values in mm indicate the interaural distance of the atlas. All anatomical images have been adapted with permission from the Paxinos et al. rhesus monkey brain atlas[45].

Extended Data Fig. 4 Collation of the LFP recording sites in the hippocampal formation.

The images display a total of 26 recording sessions made in 5 monkeys (A13, 3 sessions; E10, 1 session; F12, 3 sessions; I09, 1 session; K13, 18 sessions). The location of the recording sites was derived from high-resolution anatomical scans and transposed onto the corresponding location on drawing of coronal slices of the Saleem–Logothetis rhesus monkey brain atlas[62,63] (adapted with permission). All recording sites were located inside the hippocampal formation, with 12 sessions made in CA1, 9 in both CA1 and CA2, and 5 in CA3 or CA4. Relevant abbreviations: CA1-4, Ammon's Horn 1-4; DG, dentate gyrus. Optic Tract at +18 LGN starts (clear in MRI) = +10 session AP(mm) Possible HP regions.

Extended Data Fig. 5 Time and frequency profiles of reported hTheta oscillations and PGOw.

a, Exemplary traces of hTheta episodes (left) and their associated spectra (right) reported in various macaque studies[7,22,47]. **b**, Same as **a**, but for the pontine and geniculate components of PGO events in independent feline and non-human primate studies[14,40]. Spectra are based on autoregressive power spectral density estimate, using the Yule-Walker method with order 6, using MATLAB's function pyulear).

Extended Data Fig. 6 Pontine events characteristics in the ponto-geniculo-hippocampal recordings.

a, Pontine peri-event LFP activity for p-waves (uncoupled, black trace), ripple-coupled (red trace) and theta-coupled (blue trace) PGO waves: averaged time courses (top) and spectrogram averages (bottom). Shaded areas indicate SEM. **b**, Analogous to panel **a**, but for LGN activity. **c**, Peri-event BLP signals averages in the 4–10 Hz LFP range in PBn, LGN and

hippocampus. Whereas PGO waves occur in all structures, P-waves display significant power increases only in the pons ($P < 0.01$, permutation t-test for PBn responses; $P > 0.05$, permutation t-test for LGN and hippocampal responses). Shaded areas indicate SEM. **d**, Consistency score for the detection of pontine waves (P-waves and PGO waves) using the recording pairs PBn-LGN and PBn-HC (Methods). Statistics are computed across experiments of the three-structure experimental session. **e**, Exemplary LFP traces of ongoing LGN, neocortical, that is, primary VCX and HC activity. The dashed line encloses a PGO event. **f**, Expanded version of the event highlighted in **e**. **g**, Statistics of the phase shift (left) and time lag (right) between LGN and visual cortex during PGO events across experimental sessions. Individual dots (right subpanel) correspond to each of the 7 experimental sessions where the triad LGN-VCX-HC were recorded, animals A13, D11 and i09. **h**, Putative causal interaction between LGN and VCX assessed using transfer entropy (TE) ($P > 0.2890$ sign test; $N = 7$ experimental sessions, animals A13, D11 and i09). **i**, Point-process conditional intensity functions between these events and detected PGO waves in LGN-VCX-HC sessions (asterisks indicate significant coupling, $P < 0.01$ permutation test against an H_0 distribution of random point proceses of the same rate; 7 experimental sessions; animals A13, D11 and i09). For the visual cortex data, we detected candidate PGO waves as peaks of low-frequency (2–15 Hz) LFP power exceeding an event-related threshold proportional to the standard deviation of the signal (z-scores) in LGN. Theta (2-15 Hz), gamma (25-75 Hz) and ripples (90-190 Hz) were detected independently from the hippocampal LFP traces ($N = 7$ experimental sessions; animals A13, D11 and I09). Point-process cross-correlation analysis revealed that PGO-associated potentials in LGN significantly co-occur with hippocampal theta and SWR, but not gamma episodes (Panel **i**). Analogous to our analysis of PBn-LGN PGO waves, albeit more variable, we found a phase lag of visual cortex activity with respect to LGN activity in the PGO frequency band (2-15 Hz) (Panel **g**). This phase lag was consistent across all sessions and animals where LGN and visual cortex activities were recorded (mean phase lag with 95% circular confidence interval 8.76 ± 8.44 degrees; $P < 10^{-2}$ circular test for the significance of the median; $N = 7$ experimental sessions, animals A13, D11 and I09). The corresponding time delay between LGN and VCX found in this analysis is consistent with previous studies in cats[26]. We found

difficult to detect a putative causal influence of the phase of LGN on the phase of visual cortex during peri-PGO potentials, as hinted by the non-significant differences in the LGN-to-VCX interaction direction as compared to the opposite VCX-to-LGN direction (Panel **h**; $P = 0.2890$, sign test for the comparison between TE values associated with the LGN-to-VCX direction and the VCX-to-LGN direction; $N = 7$ experimental sessions, animals A13, D11 and I09). The results of this causal inference analysis for PBn-LGN and LGN-VCX experimental sessions, were found consistent with the spectral independence-based causal inference analysis introduced in the next subsection of the manuscript in the context of PBn-hippocampus PGO event-related interactions (Supplementary Methods). These results indicated that causal inference might be difficult to detect in LGN-VCX recording pairs due to the highly recurrent connectivity of the macaque visual cortex. In addition, our results indicate that the detected phasic events in our recordings are indeed potentials that co-occur in the brainstem, thalamic nuclei, and neocortex, thus corresponding to PGO waves[11].

Extended Data Fig. 7 Hippocampal event features in PBn-HC recordings of macaque monkeys.

a, Detected SWR (red arrows) and theta-like events in an exemplary hippocampal raw LFP trace (0.5-190 Hz) and its filtered version in the ripple frequency band (90-190 Hz). SWR are clearly marked by the occurrence of high-frequency oscillations as shown in the top insets. **b**, Theta- (left panel), gamma- (middle panel) and ripple-triggered (right panel) complex Morlet-wavelet power spectrograms. **c**, Averaged zero-lag spectral profiles in correspondence with each hippocampal event type. Shaded areas indicate SEM. **d**, Bivariate distribution of FWHM versus frequency peak (after Logothetis et al., 2012) (left panel). **e**, **f**, Frequency peak (**e**) and FWHM (**f**) box plots are also shown separately. Colours indicate the hippocampal event type shown in B. On each box, the top and bottom are the 25th and 75th percentiles of the samples, respectively; the middle dot of each box is the sample median; the dashed lines extending below and above each box are drawn to the extreme points; black crosses in the diagrams are the outliers of the samples. **g**, Theta- (top), gamma- (middle) and SWR-triggered (bottom) BLP signals population grand

averages in and beyond the LFP frequency range: delta (1–4 Hz), theta (4–10 Hz), spindle (10–16 Hz), sigma (16–30 Hz), slow and high gamma (30–70 Hz; 70–90 Hz, respectively), ripple (90–190 Hz) and high-frequency oscillations (190–320 Hz) and MUA (801–2500 Hz). BLP signals were *z*-scored and averaged across all recording tips. All responses were thresholded for a significant deviation from zero at a statistical significance level $P < 0.05$ (permutation test) and Bonferroni-corrected across frequency bands. **h**, Time course population averages of BLP modulations in hippocampus over MUA (801–2500 Hz) for SWR (top), gamma (middle) and theta (bottom) episodes. Note the prevalent negative modulation associated with theta events, as opposed by a consistent increase of activity associated with ripple events. **i**, Point-process conditional intensities (cross-correlograms) accounting for the relationship between the occurrences of theta, gamma and SWR episodes. Conditional intensities were computed from pooled experiments across pons-hippocampus experimental sessions, at a resolution of 50 ms bins. Asterisks indicate a significant relationship ($P < 0.01$, Bonferroni-corrected) at and around the time of the occurrence of theta (left), gamma (middle) and SWR (right) events, according to an H_0 distribution derived from cross-correlograms of randomized point processes of the same rate. The reference event for computing the conditional intensity is indicated by the first event of each pair in the top part of each plot. For panels **b**–**i**, $N = 24$ experimental sessions contributed to the statistics; animals CM031, F12 and K13; virtually identical event profiles were obtained with sessions from animals A13, D11, i09 and e10).

Extended Data Fig. 8 PGO wave oscillation and discharge statistics across all experimental sessions and exemplary time courses.

a, Box plots illustrating the proportion of PGO-waves in each experimental session. The session marked in red (bottom subpanel) corresponds to the session in which PBn, LGN and hippocampus were recorded simultaneously ($N = 29$ experimental sessions; animals CM029, K13, F12, CM031; sessions with animals E10, A13, D11 and i09 produced virtually identical results). **b**, Box plots displaying the pooled statistic of the proportion of PGO waves (right) across all experimental sessions. About

30% of all pontine events are classified as PGO waves ($N = 29$ experimental sessions; animals CM029, K13, F12, CM031). **c**, Two-dimensional projection of type I and type II PGO waves (red and blue LFP traces, respectively) using Laplacian eigenmaps for one exemplary experimental session. The projection is computed using the peri-event MUA (801-2500 Hz). In this case, type I PGO waves are segregated to the left, whereas type II PGO waves are segregated to the right. **d**, Zoomed-in version of two patches enclosed by a dashed square in **c**. Type I PGO waves usually display one biphasic cycle, whereas type II PGO waves display more oscillatory behaviour. **e**, PGO-wave time course averages for the experimental session in **c** and **d**. **f**, Global (across-sessions) statistics of the number of oscillatory cycles displayed by PGO waves recorded in PBn ($N = 24$ experimental sessions, animals K13, F12 and CM031). The empirical distribution associated with type II PGO waves is consistently shifted to the right, indicating a larger number of oscillations. **g**, Analogous to **f**, but for SWR and theta events recorded in hippocampus. **h**, Peri-event time histogram of pontine multi-unit discharges (25-ms bins) during the occurrence of type I (left) and type II (centre) PGO waves, and P-waves (right). Shaded areas indicate SEM across experimental sessions. **i**, Multi-unit modulation associated with P-waves and PGO-wave subtypes. Note the stronger multi-unit modulation associated with type I and type II PGO waves. For panels **h**, **i**, $N = 24$ experimental sessions, K13, F12 and CM031.

Extended Data Fig. 9 PGOw in LGN.

a, Two-dimensional projection of type I and type II PGOw (red and blue LFP traces, respectively) using Laplacian eigenmaps for one exemplary PBn-LGN experimental session. Each trace corresponds to one event. Events are classified on the basis of their peri-event MUA (801–2500 Hz), also used to compute the projection. Note the segregation of type I PGOw and type II PGOw in this space. **b**, Zoomed-in version of two patches enclosed by a dashed square in **a**. Type I PGOw usually display one biphasic cycle, whereas type II PGOw display more oscillatory behaviour. **c**–**e**, PGO-wave LFP (**c**) spectrogram (**d**) and MUA (801–2,500 Hz) (**e**) averages are shown for the selected events of this experimental session exhibited in **a** and **b**. **f**, **g**, SDR results for putative PBn-LGN and LGN-VCX causal interactions during PGOw. Unlike that of neocortex, note the

significantly increased SDR in the PBn → LGN interaction direction, indicating a putative causal effect of PBn over LGN PGO wave activity. Here we asked whether the brainstem exerted a causal influence on LGN, and whether LGN exerted a similar influence on VCX activity during the occurrence of PGOw. SDR analysis confirmed that PGOw propagate from PBn to LGN ($P < 0.004$ sign test, $N = 7$ experimental sessions; Panel **f**). In addition, we did not find statistically significant evidence for the direction of causation for the case of LGN and VCX recording pairs ($P = 1$ sign test, $N = 7$ experimental sessions; Panel **g**).

Extended Data Fig. 10 Multiunit activity (MUA) and ripple- and theta-event density functions (EDF) for the sessions with recordings from two PGO-related structures.

The events included in this figure were selected as "propagating", namely as events in the first PGO-related structure, which induced a suprathreshold response in a second structure. The sign of the Phase-Locking Value (PLV) implying the that second structure is following the first did not change the profile of responses shown here. **a**, Pontine MUA and Hippocampal Event Density Functions (EDFs) for the single PBn-LGN-HC session (left group of plots), and for LGN-VCx-HC sessions, where LGN was the first and Cortex the second PGO-related anatomical structure (right group of plots). Experimental sessions and groups associated with each group of plots are indicated at the top. Type-I PGO events, as shown in main text figures, are strongly associated with occurrence of hippocampal ripples, while the Type-II PGO events are associated with theta-bouts. Shaded areas indicate SEM. **b**, Same as **a**, but in this case events were simply detected in the first PGO-associated structure and were subsequently clustered in an unsupervised fashion using the Growing Neural Gas-based clustering algorithm (Supplementary Methods). Grey areas correspond to SEM estimated from the data of all groups (spont & spont1) across experimental sessions. **c**, Percentage of propagating events (PGO waves) that were predicted by unsupervised clustering, assuming the detection of PGO waves using a second PGO-associated structure as the ground truth (left subpanel). For most sessions, the events are consistently predicted as PGO waves, corresponding to more than 80% of the ground-truth events. The percentage of each PGO wave type (right subpanel) shows that there are characteristic

differences and variability across sessions, probably reflecting the state of the animal during individual preparations. Sessions in which hippocampus and LGN were recorded (animal e10) yielded virtually identical results.

Extended Data Fig. 11 Pontine MUA and hippocampal EDF profiles for the largest session-groups used in the current report.

a, PBn MUA profiles for type I, type II PGO waves, that is, associated with hippocampal SWR and theta waves, and P-waves (uncoupled events). **b**, EDFs associated with hippocampal SWR. Note the increased SWR density, illustrating that SWR notably co-occur with type I PGO waves. **c**, Same as **b**, but for theta events. Recordings from PBn only did not permit the exact identification of propagating PGO-events. However, as mentioned in the previous figures, strongly increasing all thresholds used for clustering the responses yielded virtually the same results.

Extended Data Fig. 12 Brain state scoring on the basis hippocampal and neocortical recordings.

a, Exemplary broad-band (0.5-200 Hz) (top) LFP trace from the hippocampal CA1, and its filtered version in the ripple frequency band (90-190 Hz). NREM (red shades) and REM (blue shades) episodes have been scored on the basis of power-power correlations between two recording sites located close by (150 µm) in the same hippocampal subfield. Similar scoring can be done using neocortical recordings, on the basis of the LFP low-frequency power (<12 Hz, Supplementary Methods). Note the occurrence of SWR episodes (increases in high-frequency oscillations) during epochs classified as NREM-like states, and absence thereof during epochs classified as REM-like states. **b**, State-scoring consistency for experimental sessions in which hippocampus and neocortex were recorded (left), which was found to correlate with ripple signal-to-noise ratio (right; here measured in SD, computed from surrogate epochs were no ripples are observed) (statistics are derived from groups spont & spont1; $N = 7$ experimental sessions, animals A13, D11 and i09). **c**, Exemplary LFP traces displaying neocortical delta waves (1-4 Hz) oscillations, a well-known

landmark of desynchronized (NREM) sleep. **d**, State-associated LFP power across neocortical, LGN and hippocampal recording sites in the delta [1-4 Hz] and theta [5-12 Hz] ($P < 0.001$ Wilcoxon's ranksum test for the difference of LFP power across states, Bonferroni-corrected; $N = 7$ experimental sessions, animals A13, D11 and i09). **e**, Proportion of all SWR and theta episodes across sleep-like states, and across the two different state-scoring procedures ($P > 0.05$ pair-wise Wilcoxon's ranksum test, uncorrected; $N = 7$ experimental sessions, animals A13, D11 and i09). **f**, Same as **a**, for one experimental session in which no neocortical activities were recorded. The scoring strongly mirrors the one performed when neocortical recordings are available. The observed changes in event occurrence (coloured dots at the top of the panel) are mirrored by fluctuations the *z*-scored multi-unit activity (MUA) (801-2500 Hz) of the mEFP corresponding to the same recording site illustrated in **a**. NREM states are accompanied by strong up-down state-like modulations (bottom subpanel), and MUA episodes, essentially absent during REM states. **g**, Averaged power-power correlations between two recording sites located close by (150 μm) in the same hippocampal subfield for NREM (left) and REM (right) episodes, for: one exemplary LGN-CTX-HC experimental session (top); the only PBN-LGN-HC experimental session (middle); and across all 24 PBN-HC experimental sessions (bottom). Note the increased high-frequency (>100 Hz) coupling associated with SWR episodes during the NREM-like state, which is otherwise absent during the REM-like state (black and white arrows).

Extended Data Fig. 13 Hippocampus-PBn field coherency, and hippocampal multi-unit spiking activity, as modulated by brainstem PGO waves.

a, Coherency maps grand-averages of PGO-uncoupled (left) and PGO-coupled (right) hippocampal SWR (top) and theta episodes (bottom). **b**, Zero-lag profiles of the events in a. **c**, PBn-LFP-triggered modulation of hippocampal multi-unit discharges for PGO-uncoupled (left) and PGO-coupled (right) SWR (red) and theta (blue) events. Shaded areas indicate SEM. **d**, Depth of hippocampal multi-unit modulation with respect to PBn LFP during the occurrence of PGO-uncoupled (dashed boxes) and PGO-coupled (continuous boxes) SWR (red) and theta episodes (blue). Note the

significantly greater multi-unit modulation depth of PGO-coupled events as compared to that of PGO-uncoupled events ($P < 10^{-5}$ Wilcoxon's ranksum test, Bonferroni-corrected). **e**, Circular histograms of the PBn LFP (2–15 Hz) phase at maximal hippocampal multi-unit spike discharge for PGO-coupled SWR (red) and theta (blue) events. Panels **a**–**e** were derived from $N = 24$ experimental sessions; animals K13, F12 and CM31.

Extended Data Fig. 14 Posture of the animal during data collection.

a, Site-Localization. The chambers for deep brain recordings were designed to be positioned at an optimum angle to prevent possible injuries to large blood vessels. In more than 30 reversible experiments with electrodes under anaesthesia, the animals – with few exceptions – did not show any complications as a result of the electrode placement in the pons region. Figure: Example design of a pons chamber using MR angiography. The Brainsight system (Rogue Research, https://www.rogue-research.com/) was used for the precise implantation of electrophysiology chambers aimed to explore deep brain structures (for example, the lateral geniculate nucleus, and the parabrachial nucleus). Before the surgery, anatomical scans of the animal's head were produced with markers to obtain data on the skull shape and pertinent target structures for tailor-made implants. The brain-vasculature was reconstructed, and a path with lowest probability of hitting large vessels/arteries was chosen. During the surgery, the position of the implant was determined by the Brainsight computer programme, which can superimpose a virtual implant with its trajectory and targets on the reconstructed skull using the pointer tool. These techniques can prevent the undesirable misplacement of recording chambers, which could be the case when there is a small difference in shape between the skull and the implant (for example, an angle of 5 degrees causes a shift of about 2.6 mm under a 30-mm chamber. This shift would be sufficient to miss a smaller deep brain structure). At right of panel **a**, is an example of multisite/multilaminar electrode in two magnifications. **b**, Placement of the electrodes before the combined physiology-fMRI experiments. **c**, It shows the posture of the animal during the experiment. Due to the fact that all magnets were vertical for reducing any stress to the animal in alert monkey experiments, the anaesthetized monkeys were prepared with all measure for maintaining

normal blood pressure (foot-bandage), and temperature, as well as for measuring of physiological parameters. During the maintenance of aneesthesia, as well as data collection, the animal was always in a “sitting” position with closed eyes with all necessary items for the maintenance of anaesthesia and measurement of physiological parameters. **d**, The animal before shifting the chair into the magnet.

Supplementary information

Reporting Summary

Rights and permissions

Reprints and Permissions

About this article

Check for updates

Cite this article

Ramirez-Villegas, J.F., Besserve, M., Murayama, Y. *et al.* Coupling of hippocampal theta and ripples with pontogeniculooccipital waves. *Nature* **589,** 96–102 (2021). https://doi.org/10.1038/s41586-020-2914-4

Download citation

- Received: 07 October 2019
- Accepted: 01 September 2020
- Published: 18 November 2020

- Issue Date: 07 January 2021
- DOI: https://doi.org/10.1038/s41586-020-2914-4

Comments

By submitting a comment you agree to abide by our Terms and Community Guidelines. If you find something abusive or that does not comply with our terms or guidelines please flag it as inappropriate.

Access through your institution
Change institution
Buy or subscribe

This article was downloaded by **calibre** from https://www.nature.com/articles/s41586-020-2914-4

- Article
- Published: 25 November 2020

TRF2-independent chromosome end protection during pluripotency

- Phil Ruis[1],
- David Van Ly[2,3],
- Valerie Borel[1],
- Georgia R. Kafer[2],
- Afshan McCarthy[1],
- Steven Howell[1],
- Robert Blassberg ORCID: orcid.org/0000-0001-8577-3544[1],
- Ambrosius P. Snijders ORCID: orcid.org/0000-0002-5416-8592[1],
- James Briscoe ORCID: orcid.org/0000-0002-1020-5240[1],
- Kathy K. Niakan ORCID: orcid.org/0000-0003-1646-4734[1],
- Paulina Marzec ORCID: orcid.org/0000-0002-4081-7539[1],
- Anthony J. Cesare ORCID: orcid.org/0000-0002-0864-1254[2] &
- Simon J. Boulton ORCID: orcid.org/0000-0001-6936-6834[1]

Nature **volume 589**, pages103–109(2021)Cite this article

- 5520 Accesses
- 182 Altmetric
- Metrics details

Subjects

- Telomeres

Abstract

Mammalian telomeres protect chromosome ends from aberrant DNA repair[1]. TRF2, a component of the telomere-specific shelterin protein complex, facilitates end protection through sequestration of the terminal telomere repeat sequence within a lariat T-loop structure[2,3]. Deleting *TRF2* (also known as *TERF2*) in somatic cells abolishes T-loop formation, which coincides with telomere deprotection, chromosome end-to-end fusions and inviability[3,4,5,6,7,8,9]. Here we establish that, by contrast, TRF2 is largely dispensable for telomere protection in mouse pluripotent embryonic stem (ES) and epiblast stem cells. ES cell telomeres devoid of TRF2 instead activate an attenuated telomeric DNA damage response that lacks accompanying telomere fusions, and propagate for multiple generations. The induction of telomere dysfunction in ES cells, consistent with somatic deletion of *Trf2* (also known as *Terf2*), occurs only following the removal of the entire shelterin complex. Consistent with TRF2 being largely dispensable for telomere protection specifically during early embryonic development, cells exiting pluripotency rapidly switch to TRF2-dependent end protection. In addition, *Trf2*-null embryos arrest before implantation, with evidence of strong DNA damage response signalling and apoptosis specifically in the non-pluripotent compartment. Finally, we show that ES cells form T-loops independently of TRF2, which reveals why TRF2 is dispensable for end protection during pluripotency. Collectively, these data establish that telomere protection is solved by distinct mechanisms in pluripotent and somatic tissues.

Access through your institution
Change institution
Buy or subscribe

Access options

Subscribe to Journal

Get full journal access for 1 year

$199.00

only $3.90 per issue

Subscribe

All prices are NET prices.
VAT will be added later in the checkout.

Rent or Buy article

Get time limited or full article access on ReadCube.

from$8.99

Rent or Buy

All prices are NET prices.

Additional access options:

- Log in
- Access through your institution
- Learn about institutional subscriptions

Fig. 1: TRF2 is largely dispensable for telomere end protection and cell viability in ES cells.

Fig. 2: The shelterin complex is required for telomere protection in ES cells.

Fig. 3: TRF2-dependent chromosome end protection begins at the exit from pluripotency.

Fig. 4: TRF2-null embryos are compromised as expanding blastocysts.

Fig. 5: T-loop formation occurs independently of TRF2 in ES cells.

Data availability

The datasets generated during and/or analysed during the current study are included alongside the Article or are available from S.J.B and A.J.C on reasonable request. Data were searched against a recent copy of the UniProt *M. musculus* reference proteome UP000000589 (https://www.uniprot.org/proteomes/UP000000589). For gel source data, see Supplementary Fig. 1. All data are archived at the Francis Crick Institute or CMRI. Source data are provided with this paper.

References

1. 1.

   Palm, W. & de Lange, T. How shelterin protects mammalian telomeres. *Annu. Rev. Genet*. **42**, 301–334 (2008).

   CAS Article Google Scholar

2. 2.

Griffith, J. D. C. et al. Mammalian telomeres end in a large duplex loop. *Cell* **97**, 503–514 (1999).

CAS Article Google Scholar

3. 3.

Van Ly, D. et al. Telomere loop dynamics in chromosome end protection. *Mol. Cell* **71**, 510–525.e6 (2018).

Article Google Scholar

4. 4.

van Steensel, B., Smogorzewska, A. & de Lange, T. TRF2 protects human telomeres from end-to-end fusions. *Cell* **92**, 401–413 (1998).

Article Google Scholar

5. 5.

Karlseder, J., Broccoli, D., Dai, Y., Hardy, S. & de Lange, T. p53- and ATM-dependent apoptosis induced by telomeres lacking TRF2. *Science* **283**, 1321–1325 (1999).

CAS Article Google Scholar

6. 6.

Celli, G. B. & de Lange, T. DNA processing is not required for ATM-mediated telomere damage response after TRF2 deletion. *Nat. Cell Biol*. **7**, 712–718 (2005).

CAS Article Google Scholar

7. 7.

Denchi, E. L. & de Lange, T. Protection of telomeres through independent control of ATM and ATR by TRF2 and POT1. *Nature*

448, 1068–1071 (2007).

ADS CAS Article Google Scholar

8. 8.

Doksani, Y., Wu, J. Y., de Lange, T. & Zhuang, X. Super-resolution fluorescence imaging of telomeres reveals TRF2-dependent T-loop formation. *Cell* **155**, 345–356 (2013).

CAS Article Google Scholar

9. 9.

Sarek, G. et al. CDK phosphorylation of TRF2 controls t-loop dynamics during the cell cycle. *Nature* **575**, 523–527 (2019).

ADS CAS Article Google Scholar

10. 10.

Loh, Y. H. et al. The Oct4 and Nanog transcription network regulates pluripotency in mouse embryonic stem cells. *Nat. Genet*. **38**, 431–440 (2006).

CAS Article Google Scholar

11. 11.

Déjardin, J. & Kingston, R. E. Purification of proteins associated with specific genomic loci. *Cell* **136**, 175–186 (2009).

Article Google Scholar

12. 12.

Chapman, J. R. et al. RIF1 is essential for 53BP1-dependent nonhomologous end joining and suppression of DNA double-strand break resection. *Mol. Cell* **49**, 858–871 (2013).

CAS Article Google Scholar

13. 13.

Takai, K. K., Kibe, T., Donigian, J. R., Frescas, D. & de Lange, T. Telomere protection by TPP1/POT1 requires tethering to TIN2. *Mol. Cell* **44**, 647–659 (2011).

CAS Article Google Scholar

14. 14.

Sfeir, A. et al. Mammalian telomeres resemble fragile sites and require TRF1 for efficient replication. *Cell* **138**, 90–103 (2009).

CAS Article Google Scholar

15. 15.

Sfeir, A. & de Lange, T. Removal of shelterin reveals the telomere end-protection problem. *Science* **336**, 593–597 (2012).

ADS CAS Article Google Scholar

16. 16.

Takaoka, K. & Hamada, H. Cell fate decisions and axis determination in the early mouse embryo. *Development* **139**, 3–14 (2012).

CAS Article Google Scholar

17. 17.

Brons, I. G. et al. Derivation of pluripotent epiblast stem cells from mammalian embryos. *Nature* **448**, 191–195 (2007).

ADS CAS Article Google Scholar

18. 18.

Nichols, J. & Smith, A. Naive and primed pluripotent states. *Cell Stem Cell* **4**, 487–492 (2009).

CAS Article Google Scholar

19. 19.

Acampora, D., Di Giovannantonio, L. G. & Simeone, A. Otx2 is an intrinsic determinant of the embryonic stem cell state and is required for transition to a stable epiblast stem cell condition. *Development* **140**, 43–55 (2013).

CAS Article Google Scholar

20. 20.

Gouti, M. et al. In vitro generation of neuromesodermal progenitors reveals distinct roles for Wnt signalling in the specification of spinal cord and paraxial mesoderm identity. *PLoS Biol*. **12**, e1001937 (2014).

Article Google Scholar

21. 21.

Okamoto, K. et al. A two-step mechanism for TRF2-mediated chromosome-end protection. *Nature* **494**, 502–505 (2013).

ADS CAS Article Google Scholar

22. 22.

Ding, H. et al. Regulation of murine telomere length by *Rtel*: an essential gene encoding a helicase-like protein. *Cell* **117**, 873–886 (2004

CAS Article Google Scholar

23. 23.

Ran, F. A. et al. Genome engineering using the CRISPR–Cas9 system. *Nat. Protoc.* **8**, 2281–2308 (2013).

CAS Article Google Scholar

24. 24.

Tzelepis, K. et al. A CRISPR dropout screen identifies genetic vulnerabilities and therapeutic targets in acute myeloid leukemia. *Cell Rep*. **17**, 1193–1205 (2016).

CAS Article Google Scholar

25. 25.

Doench, J. G. et al. Optimized sgRNA design to maximize activity and minimize off-target effects of CRISPR–Cas9. *Nat. Biotechnol*. **34**, 184–191 (2016).

CAS Article Google Scholar

26. 26.

Zelensky, A. N., Schimmel, J., Kool, H., Kanaar, R. & Tijsterman, M. Inactivation of Pol θ and C-NHEJ eliminates off-target integration of exogenous DNA. *Nat. Commun*. **8**, 66 (2017).

ADS Article Google Scholar

27. 27.

Wamaitha, S. E. et al. Gata6 potently initiates reprograming of pluripotent and differentiated cells to extraembryonic endoderm stem cells. *Genes Dev*. **29**, 1239–1255 (2015).

CAS Article Google Scholar

28. 28.

Vannier, J. B., Pavicic-Kaltenbrunner, V., Petalcorin, M. I., Ding, H. & Boulton, S. J. RTEL1 dismantles T loops and counteracts telomeric G4-DNA to maintain telomere integrity. *Cell* **149**, 795–806 (2012).

CAS Article Google Scholar

29. 29.

Panier, S. et al. SLX4IP antagonizes promiscuous BLM activity during ALT maintenance. *Mol. Cell* **76**, 27–43 (2019).

CAS Article Google Scholar

30. 30.

Meltser, V., Ben-Yehoyada, M., Reuven, N. & Shaul, Y. c-Abl downregulates the slow phase of double-strand break repair. *Cell Death Dis*. **1**, e20 (2010).

CAS Article Google Scholar

31. 31.

Bellelli, R. et al. Polε instability drives replication stress, abnormal development, and tumorigenesis. *Mol. Cell* **70**, 707–721 (2018).

CAS Article Google Scholar

Download references

Acknowledgements

We thank members of the Boulton and Cesare laboratories for suggestions and discussions, and for critical reading of the manuscript; S. Page and the Australian Cancer Research Foundation Telomere Analysis Centre at the Children's Medical Research Institute (CMRI) for microscopy infrastructure; the Crick BRF and GEMs for support with animal experiments; and T. de Lange for advice on G-overhang analysis. Work in

the Boulton laboratory is supported by the Francis Crick Institute, which receives its core funding from Cancer Research UK (FC0010048), the UK Medical Research Council (FC0010048) and the Wellcome Trust (FC0010048); a European Research Council (ERC) Advanced Investigator Grant (TelMetab); and Wellcome Trust Senior Investigator and Collaborative Grants. The laboratory of A.J.C. is supported by grants from the Australian NHMRC (1162886 and 1185870) and philanthropy from the Neil and Norma Hill Foundation.

Author information

Affiliations

1. The Francis Crick Institute, London, UK

   Phil Ruis, Valerie Borel, Afshan McCarthy, Steven Howell, Robert Blassberg, Ambrosius P. Snijders, James Briscoe, Kathy K. Niakan, Paulina Marzec & Simon J. Boulton

2. Genome Integrity Unit, Children's Medical Research Institute, University of Sydney, Sydney, New South Wales, Australia

   David Van Ly, Georgia R. Kafer & Anthony J. Cesare

3. School of Medicine, The University of Notre Dame Australia, Sydney, New South Wales, Australia

   David Van Ly

Authors

1. Phil Ruis
   View author publications

   You can also search for this author in PubMed Google Scholar

2. David Van Ly
   View author publications

You can also search for this author in PubMed Google Scholar

3. Valerie Borel
   View author publications

   You can also search for this author in PubMed Google Scholar

4. Georgia R. Kafer
   View author publications

   You can also search for this author in PubMed Google Scholar

5. Afshan McCarthy
   View author publications

   You can also search for this author in PubMed Google Scholar

6. Steven Howell
   View author publications

   You can also search for this author in PubMed Google Scholar

7. Robert Blassberg
   View author publications

   You can also search for this author in PubMed Google Scholar

8. Ambrosius P. Snijders
   View author publications

   You can also search for this author in PubMed Google Scholar

9. James Briscoe
   View author publications

   You can also search for this author in PubMed Google Scholar

10. Kathy K. Niakan
    View author publications

You can also search for this author in PubMed Google Scholar

11. Paulina Marzec
View author publications

You can also search for this author in PubMed Google Scholar

12. Anthony J. Cesare
View author publications

You can also search for this author in PubMed Google Scholar

13. Simon J. Boulton
View author publications

You can also search for this author in PubMed Google Scholar

Contributions

P.R., P.M. and S.J.B. conceived the study; P.R. generated all cell lines and performed the large majority of experiments in this Article, including all those not listed below; V.B., A.M. and P.R. performed EmbryoScope and embryo IF–FISH experiments; G.R.K. adapted stem cell culture for T-loop visualization; D.V.L. performed all AiryScan imaging and analysis; R.B. provided protocols and reagents for directed differentiation of ES cells; and P.M., S.H. and A.P.S. performed PICh mass spectrometry analysis. P.R., D.V.L., V.B., G.R.K., A.M., S.H., P.M., A.J.C. and S.J.B. analysed data; P.R., A.J.C. and S.J.B. wrote the manuscript with editorial input from D.V.L., P.M., J.B. and K.K.N.

Corresponding authors

Correspondence to Paulina Marzec or Anthony J. Cesare or Simon J. Boulton.

Ethics declarations

Competing interests

The authors declare no competing interests.

Additional information

Peer review information *Nature* thanks Ylli Doksani and the other, anonymous, reviewer(s) for their contribution to the peer review of this work. Peer reviewer reports are available.

Publisher's note Springer Nature remains neutral with regard to jurisdictional claims in published maps and institutional affiliations.

Extended data figures and tables

Extended Data Fig. 1 TRF2-null ES cells do not undergo telomere fusions and show only a mild growth defect.

a, **b**, Growth curves of *Trf2*$^{f/f}$ ES cells and ear fibroblasts after treatment with OHT or EtOH. Cells were counted and re-seeded every 2 or 3 days (mean ± s.d., n = 3 biologically independent experiments). **c**, Bright-field images of the indicated cells 7 days after treatment with EtOH or OHT. **d**, Western blot of whole-cell extracts from *Trf2*$^{f/f}$ ES cells at the indicated times after treatment with EtOH or OHT. **e**, Flow cytometry determination of DNA content for the indicated cells 96 h after OHT or EtOH treatment (≥10,000 cells per condition, n = 3 independent experiments). **f**, Western blot of whole-cell extracts from indicated cells 96 h after treatment with EtOH or OHT. IR, 2 h post-treatment with 20 Gy ionizing radiation. **g**, Gating strategy for flow cytometry determination of DNA content. Example shown is *Trf2*$^{f/f}$ ear fibroblast EtOH sample from Fig. 1d. Similar strategies to gate live cells and singlets were applied for all flow cytometry experiments. **h**, Western blot of whole-cell extracts from three independently generated *Trf2*$^{f/f}$ ES cell clones 96 h after treatment with EtOH or OHT. **i**, Mitotic chromosome spreads from *Trf2*$^{f/f}$ ES cells 10 days after treatment with OHT or EtOH. The DNA is stained with DAPI (red)

and the telomeres by FISH (green), with the mean percentage of telomere fusions from **j** indicated. Scale bar, 5 μm, **j**, Quantification of the experiment shown in **i**. Mean ± s.d., ≥60 spreads per condition across 3 independent experiments, unpaired two-tailed *t*-test; ns, not significant. **k**. Western blot of whole-cell extracts from *Trf2*$^{f/f}$ ES cells 10 days after treatment with EtOH or OHT. Source data

Extended Data Fig. 2 The telomeric DDR is attenuated in ES cells lacking TRF2.

a, In-gel hybridization assay for single-stranded telomeric G-overhang DNA after *Trf2* deletion. Left, TelC signals under the native condition. Right, same gel re-hybridized after in situ denaturation of the DNA. Overhang signals (bottom) were normalized to the total telomeric signals (right) and compared to *Trf2*$^{f/f}$ ear fibroblasts treated with EtOH, which was given an arbitrary value of 1 in each of three independent experiments. The mean of these normalized values is shown for each condition (n = 3 biologically independent experiments, representative example shown). **b**–**d**, Quantification of telomere fragility (**b**), heterogeneity (**c**) and loss (**d**) from mitotic chromosome spreads shown in Fig. 1b. Mean ± s.d., ≥70 spreads per condition across 3 independent experiments, unpaired two-tailed *t*-tests. **e**, Representative examples of the phenotypes quantified in **b**–**d** with relevant abnormalities marked with arrows. The DNA is stained with DAPI (red) and the telomeres by FISH (green). **f**, IF–FISH analysis to detect endogenous TRF2 in *Trf2*$^{f/f}$ ES cells 96 h after treatment with OHT or EtOH. TRF2 was detected by immunofluorescence (green), telomeric DNA with FISH (red) and the DNA with DAPI (blue). **g**, IF–FISH analysis to detect exogenous MYC–TRF2 in *Trf2*$^{f/f}$ ES cells stably expressing MYC–TRF2 or a vector-only control 96 h after treatment with OHT. MYC–TRF2 was detected by immunofluorescence (green), telomeric DNA with FISH (red) and the DNA with DAPI (blue). **h**, IF–FISH analysis to detect TRF1 in *Trf1*$^{f/f}$ ES cells 48 h after treatment with OHT or EtOH. TRF1 was detected by immunofluorescence (green), telomeric DNA with FISH (red) and the DNA with DAPI (blue). **i**, Cartoon depicting the SILAC–PICh workflow used in **j**, **k**. **j**, **k**, Results of SILAC–PICh mass spectrometry of *Trf2*$^{f/f}$ ES cells (**j**) and *Trf2*$^{f/f}$ ear fibroblasts (**k**) 96 h after OHT or EtOH

treatment. Data are shown as the fold change of heavy/light ratio for each protein in duplicate experiments, for which opposite labelling with heavy/light isotopes was used. Shelterin subunits and select DNA repair factors are indicated in the plot. NA indicates protein was not detected in that experiment. **l**, Venn diagram showing overlap of the proteins identified by SILAC–PICh in wild-type *Trf2*$^{f/f}$ ES cells and *Trf2*$^{f/f}$ ear fibroblasts (EtOH conditions). **m**, IF–FISH analysis to detect γH2AX TIF in *Trf2*$^{f/f}$ ES cells and *Trf2*$^{f/f}$ ear fibroblasts 96 h after treatment with OHT or EtOH. γH2AX was detected by immunofluorescence (red), telomeric DNA with FISH (white) and the DNA with DAPI (blue). **n**, Quantification of the experiment shown in **m**. Mean ± s.d., ≥200 cells per condition across 3 independent experiments, one-way ANOVA. **o**, Quantification of the experiment shown in **m**. Each dot represents percentage of cells with >3 TIF in each of 3 independent experiments analysing around 100 cells per condition per experiment, bars represent mean ± s.d. of these values, one-way ANOVA. **p**, Quantification from experiment shown in Fig. 1g. Each dot represents percentage of cells with >3 TIF in each of 4 independent experiments analysing around 100 cells per condition per experiment, bars represent mean ± s.d. of these values, one-way ANOVA. **q**, Quantification of IF–FISH to detect 53BP1 TIF in the indicated cells, 96 h after treatment with EtOH or OHT. 53BP1 was detected by immunofluorescence (green), telomeric DNA with FISH (red) and DNA with DAPI (blue). c1, c2 and c3 indicate three independently derived clones. Mean ± s.d., ≥200 cells per condition across 3 independent experiments, one-way ANOVA. ns, not significant, ****$P \leq 0.0001$. Scale bars, 5 μm (**e**–**h**, **m**). Source data

Extended Data Fig. 3 The DDR and NHEJ are functional in ES cells.

a, Immunofluorescence to detect γH2AX (green) and 53BP1 (red) in untreated *Trf2*$^{f/f}$ ES cells and *Trf2*$^{f/f}$ ear fibroblasts or 1 h after treatment with 0.5 Gy ionizing radiation. DNA stained with DAPI (blue). **b**, Quantification from experiment shown in **a**. Each dot represents percentage of cells with >4 foci in each of 2 independent experiments analysing ≥100 cells per condition per experiment, bars represent mean ± s.d. of these values, one-way ANOVA. **c**, Flow cytometry determination of DNA content

for the indicated cells at the indicated times after ionizing radiation treatment, 96 h after treatment with EtOH or OHT. $n = 3$ independent experiments, ≥10,000 cells per condition in each experiment. **d**, DNA from *Trf2*$^{f/f}$ ES cells and *Trf2*$^{f/f}$ MEFs was collected, subjected to pulsed-field gel electrophoresis and stained with EtBr at the indicated times after irradiation with 20 Gy. The band of DNA resulting from double-strand breaks (DSBs) is indicated. **e**, Quantification of the experiment in **d**. The DNA band resulting from DNA double-strand breaks was quantified and normalized to the unbroken DNA. The level of DNA resulting from double-strand breaks was subsequently compared to the sample collected 10 min after ionizing radiation from that condition, which was normalized as 100% double-strand breaks remaining. Mean ± s.d. $n = 3$ biologically independent experiments for MEF samples, $n = 4$ independent experiments for ES cell samples. **f**, Survival of non-targeting control, *Ku70* knockout or *Lig4*-knockout *Trf1*$^{f/f}$ *Trf2*$^{f/f}$ ES cells after exposure to the indicated doses of ionizing radiation as measured using CellTiter-Glo, 4 days after ionizing radiation treatment. $n = 3$ (NTC and *Ku70* KO) or 2 (*Lig4* KO) biologically independent experiments, mean ± s.e.m. Individual clonal knockout lines are denoted c1 and c2. **g**, **h**, Western blot of whole-cell extracts from the cells used in **f**. Asterisk indicates a non-specific band. **i**, Ninety-six h after treatment with EtOH or OHT, *Trf2*$^{f/f}$ ES cells were grown asynchronously or treated for 16 h with mimosine to induce G1 arrest. DNA content from these cells was determined using flow cytometry at 0 h, 4 h and 9 h after release from mimosine. **j**, Mitotic chromosome spreads from asynchronous cells and cells released from mimosine block for 9 h as in **i**. The DNA was stained with DAPI (red) and the telomeric DNA with FISH (green). The mean percentage of fused chromosomes from **k** is indicated. **k**, Quantification from experiment shown in **i**, **j**. Mean ± s.d., ≥70 spreads per condition across 3 independent experiments, unpaired two-tailed *t*-test. **l**, Mitotic chromosome spreads from *Trf2*$^{f/f}$ ES cells 96 h after treatment with OHT and 24 h after mock treatment or treatment with 2 Gy ionizing radiation. Samples are stained as in **j** and the mean percentage of telomere fusions from **m** is indicated. **m**, Quantification of experiment shown in **l**. Mean ± s.d., ≥50 spreads per condition across 2 independent experiments, unpaired two-tailed *t*-test. ns, not significant, ****$P \leq 0.0001$. Scale bars, 5 μm;. Source data

Extended Data Fig. 4 TPP1 and TRF1 function are conserved in ES cell and somatic tissues.

a, Western blot of whole-cell extracts from indicated cells 96 h after EtOH or OHT treatment, and 72 h after siRNA transfection. **b**, TPP1 expression in the indicated cells analysed by RT–qPCR. Data were normalized to the ES cell *Trf2*$^{f/f}$ EtOH control siRNA (siCon) condition, which was arbitrarily assigned a value of 1. Mean ± s.d., $n = 3$ biologically independent experiments, one-way ANOVA. **c**, Quantification of 53BP1 TIF from cells shown in **d**. Mean ± s.d., ≥300 cells per condition across 3 independent experiments, one-way ANOVA, $^{**}P = 0.0013$. **d**, 53BP1 TIF in the indicated cells. 53BP1 was detected by immunofluorescence (green), telomeres by FISH (red) and DNA with DAPI (blue). **e**, Mitotic chromosome spreads from indicated cells 96 h after OHT or EtOH treatment, and 72 h after siRNA transfection. Telomeres stained with FISH (green) and the DNA with DAPI (red). The mean percentage of fused telomeres from **f** is shown. **f**, Quantification of telomere fusions from **e**. Mean ± s.d., 90 spreads per condition across 4 independent experiments, one-way ANOVA. **g**, Flow cytometry determination of DNA content for the indicated cells 96 h after OHT or EtOH treatment. $n = 3$, ≥10,000 cells per condition. **h**, Telomeric RPA-pSer33 foci in *Trf1*$^{f/f}$ ES cells 72 h after treatment with EtOH or OHT. RPA-pSer33 was detected by immunofluorescence (green), telomeres by FISH (red) and DNA with DAPI (blue). **i**, Quantification of the experiment in **h**. Mean ± s.d., ≥300 cells per condition across 3 independent experiments, unpaired two-tailed *t*-test. **j**, 53BP1 TIF in *Trf1*$^{f/f}$ ES cells 72 h after treatment with OHT or EtOH. Samples are stained as in **d**. **k**, Quantification of **j**. Mean ± s.d., ≥300 cells per condition across 3 independent experiments, unpaired two-tailed *t*-test. Scale bars, 5 μm; ns, not significant, $^{****}P \leq 0.0001$. Source data

Extended Data Fig. 5 ES cells require shelterin for chromosome end protection.

a, Equal numbers of the indicated cells were seeded and treated with EtOH or OHT. The cells were counted at 72 h and the number of cells in each condition normalized to the ES cell *Trf1*$^{+/+}$ *Trf2*$^{f/f}$ EtOH condition, which

was given an arbitrary value of 1. Mean ± s.d., $n = 3$ biologically independent experiments. **b**, Flow cytometry determination of DNA content for the indicated cells 48 or 72 h after OHT or EtOH treatment. $n = 3$, ≥10,000 cells per condition. **c**, 53BP1 TIF in the indicated cells 72 h after treatment with OHT or EtOH. 53BP1 was detected by immunofluorescence (green), the telomeres with FISH (red) and DNA with DAPI (blue). Scale bar, 5 µm. **d**, Quantification of the experiment shown in **c**. Mean ± s.d., roughly 300 cells per condition across 3 independent experiments, one-way ANOVA, ****$P \leq 0.0001$. **e**, Western blot of whole-cell extracts from *Trf2*$^{f/f}$ ES cells at indicated times after treatment with 2 Gy or 20 Gy ionizing radiation. Source data

Extended Data Fig. 6 Shelterin-free ES cells activate a full DDR equivalent to that in shelterin-free somatic cells.

a, Western blotting of whole-cell extracts from *Trf1*$^{f/f}$ *Trf2*$^{f/f}$ ES cells at indicated times after EtOH or OHT treatment. **b**, **c**, Quantification of telomere fusions (**b**) or γH2AX TIF (**c**) in *Trf1*$^{f/f}$ *Trf2*$^{f/f}$ ES cells at the indicated times after OHT or EtOH treatment. Mean ± s.d., ≥70 mitotic spreads per condition for **b** or ≥175 cells per condition for **c**, across 3 independent experiments ($n = 2$ for 12 h condition), one-way ANOVA. **d**, 53BP1 TIF in the indicated cells, 48 h after EtOH or OHT treatment or infection with AdGFP or AdCre. 53BP1 was detected by immunofluorescence (green), telomeres by FISH (red) and DNA with DAPI (blue). **e**, Quantification of the experiment shown in **d**. Mean ± s.d., ≥200 cells per condition across 2 independent experiments, one-way ANOVA. **f**, Quantification of γH2AX TIF in the indicated cells 48 after treatment with EtOH or OHT or infection with AdGFP or AdCre. Mean ± s.d., ≥180 cells per condition across 3 independent experiments, one-way ANOVA. **g**, Western blotting of whole-cell extracts from *Trf1*$^{f/f}$ *Trf2*$^{f/f}$ ES cells and *Trf1*$^{f/f}$ *Trf2*$^{f/f}$ MEFs at the indicated times after EtOH or OHT treatment or infection with AdGFP or AdCre. **h**, Quantification of telomere fragility from mitotic chromosome spreads shown in Fig. 2f, 72 h after EtOH or OHT treatment. Mean ± s.d., ≥70 spreads per condition examined over 3 experiments, one-way ANOVA. **i**, γH2AX TIF in the indicated cells 36 h after EtOH or OHT treatment. γH2AX was detected by

immunofluorescence (green) telomeric DNA with FISH (red) and the DNA with DAPI (blue). **j**, Quantification of the experiment shown in **i**. Mean ± s.d., ≥250 cells per condition across 3 independent experiments, one-way ANOVA. Scale bars, 5 μm; ns, not significant; ****$P \leq 0.0001$. Source data

Extended Data Fig. 7 Shelterin-free ES cell telomeres are substrates for both ATM and ATR kinases and fuse primarily via ATM signalling and NHEJ.

a, IF–FISH analysis to detect telomeric ATM-pSer1987 foci in CSK-extracted *Trf1*$^{f/f}$ *Trf2*$^{f/f}$ ES cells 36 h after treatment with OHT or EtOH. ATM-pSer1987 was detected by immunofluorescence (green), telomeres by FISH (red) and DNA with DAPI (blue). **b**, Quantification from experiment shown in **a**. Mean ± s.d., $n = 2$ independent experiments, ≥100 cells per condition per experiment, unpaired two-tailed *t*-test. **c**, IF–FISH analysis to detect telomeric RPA-pSer33 foci in CSK-extracted *Trf1*$^{f/f}$ *Trf2*$^{f/f}$ ES cells 36 h after treatment with OHT or EtOH. RPA-pSer33 (green) was detected by immunofluorescence, telomeres by FISH (red) and DNA with DAPI (blue). **d**, Quantification from experiment shown in **c**. Mean ± s.d., $n = 4$ independent experiments, ≥100 cells per condition per experiment, unpaired two-tailed *t*-test. **e**, IF–FISH analysis to detect telomeric ATM-pSer1987 foci in CSK-extracted *Trf1*$^{f/f}$ *Trf2*$^{f/f}$ MEFs 48 h after infection with AdGFP or AdCre. ATM-pSer1987 was detected by immunofluorescence (green), telomeres by FISH (red) and DNA with DAPI (blue). **f**, Quantification from experiment shown in **e**. Mean ± s.d., $n = 2$ independent experiments, ≥150 cells per condition per experiment, unpaired two-tailed *t*-test. **g**, IF–FISH analysis to detect telomeric RPA-pSer33 foci in CSK-extracted *Trf1*$^{f/f}$ *Trf2*$^{f/f}$ MEFs 48 h after infection with AdGFP or AdCre. RPA-pSer33 was detected by immunofluorescence (green), telomeres by FISH (red) and DNA with DAPI (blue). **h**, Quantification from experiment shown in **g**. Mean ± s.d., $n = 2$ independent experiments, ≥150 cells per condition per experiment, unpaired two-tailed *t*-test. **i**, Mitotic chromosome spreads from the indicated cells 72 h after treatment with OHT or EtOH, mock-treated or treated with an ATR inhibitor (ATRi). The DNA is stained with DAPI (red) and the telomeres by FISH (green). The mean percentage of fused

chromosome ends from Fig. 2k is noted. **j**, Western blotting of whole-cell lysates from the indicated cells, 72 h after infection with AdGFP or AdCre. Asterisk indicates a non-specific band. **k**, Quantification of telomere fusions in the indicated cells 72 h after infection with AdGFP or AdCre. Cells were either mock-treated or treated with an ATRi. $n \geq 48$ spreads per condition analysed over 2 biologically independent experiments, one-way ANOVA. ns, not significant; ****$P \leq 0.0001$. **l**, Western blotting of whole-cell lysates from *Ku70*-knockout or non-targeting control *Trf1*$^{f/f}$ *Trf2*$^{f/f}$ ES cells 72 h after treatment with EtOH or OHT. **m**, Mitotic chromosome spreads from the indicated cells 72 h after treatment with OHT or EtOH. Cells were stained as in **i** and the mean percentage of fused chromosome ends from Fig. 2l is shown. **n**, Western blotting of whole-cell lysates from *Lig4*-knockout or non-targeting control *Trf1*$^{f/f}$ *Trf2*$^{f/f}$ ES cells 72 h after treatment with EtOH or OHT. Asterisk indicates a non-specific band. **o**, Mitotic chromosome spreads from the indicated cells 72 h after treatment with OHT or EtOH. Cells were stained as in **i**. The mean percentage of chromosome ends fused from Fig. 2m is noted. Scale bars, 5 μm; ****$P \leq 0.0001$. For **b**, **d**, **f**, **g**, each dot represents the value from each independent experiment, bars represent mean ± s.d. of these values. Source data

Extended Data Fig. 8 TRF2 is required for telomere protection and viability upon loss of pluripotency.

a, Bright-field images of *Trf2*$^{f/f}$ epiblast stem cells 96 h after EtOH or OHT treatment. **b**–**f**, Gene expression in the indicated cells analysed by RT–qPCR 96 h after EtOH or OHT treatment. Data were normalized to expression in the ES cell *Trf2*$^{f/f}$ EtOH sample, which was arbitrarily assigned a value of 1 for each gene in each experiment. Mean ± s.d., $n = 2$ biologically independent experiments. **g**, **h**, γH2AX TIF images (**g**) and quantification (**h**), 96 h hours after EtOH or OHT treatment. Mean ± s.d. ≥300 cells across 4 independent experiments, unpaired two-tailed *t*-test, **** $P \leq 0.0001$. γH2AX was detected by immunofluorescence (green), telomeres by FISH (red) and DNA with DAPI (blue). **i**, 53BP1 TIF in *Trf2*$^{f/f}$ epiblast stem cells 96 h after OHT or EtOH treatment. 53BP1 was detected by immunofluorescence (green), telomeric DNA by FISH (red) and the DNA with DAPI. **j**–**n**, Gene expression in the indicated cells

analysed by RT–qPCR from 2–5 days after initiating differentiation. Data were normalized as described for **b**–**f**. 'Diff day x' refers to cells on day *x* of the differentiation protocol. Mean ± s.d., $n = 3$ biologically independent experiments. **o**–**r**, Gene expression in the indicated cells analysed by RT–qPCR. Data were normalized as described in **b**–**f**. Mean ± s.d., $n = 3$ biologically independent experiments. **s**, Western blots of whole-cell extracts from *Trf2*$^{f/f}$ ES cells differentiated as in Fig. 3e. **t**, **u**, *Nanog* and *Fgf5* gene expression in the indicated cells analysed by RT–qPCR 96 h after treatment with EtOH or OHT. Data were normalized as described for **b**–**f**. Mean ± s.d., $n = 3$. **v**, Western blot of whole-cell extracts from the indicated cells 96 h after treatment with EtOH or OHT. Asterisk indicates a non-specific band. Scale bar, 5 μm (**h**, **i**). Source data

Extended Data Fig. 9 TRF2 is required for blastocyst development before implantation.

a, Quantification of Nanog-positive and Nanog-negative cells in each of the embryos assessed in Fig. 5e, f. Mean ± s.d., one-way ANOVA, ns, not significant. **b**, Maximal projection of *z*-stacks from *Trf2*$^{-/-}$ embryos displaying pan-nuclear γH2AX-positive cells, which are highlighted with arrows. γH2AX (green) and Nanog (magenta) were detected by immunofluorescence, telomeres by FISH (red) and DNA with DAPI (blue). **c**, Quantification of percentage of cells within an embryo showing pan-nuclear γH2AX staining from experiment shown in **b**. Mean ± s.d., one-way ANOVA. Source data

Extended Data Fig. 10 TRF2 is not required for T-loop formation in ES cells.

a, IF–FISH analysis to detect telomeric ATM-pSer1987 foci in *Trf2*$^{f/f}$ ES cells 96 h after treatment with OHT or EtOH. ATM-pSer1987 was detected by immunofluorescence (green), telomeres by FISH (red) and DNA with DAPI (blue). **b**, Quantification from experiment shown in **a**. Mean ± s.d., ≥300 cells across 3 independent experiments, unpaired two-tailed *t*-test. **c**, Schematic of TRF1 and the TRF2 variants used in this study[21]. **d**, Western blots of whole-cell extracts from *Trf2*$^{f/f}$ ES cells

expressing wild-type, mutant or hybrid *Trf2* alleles 96 h after treatment with EtOH or OHT. **e**, IF–FISH detection of γH2AX TIF in the indicated cells 96 h after treatment with OHT or EtOH. γH2AX was detected by immunofluorescence (green), telomeric DNA by FISH (red) and DNA with DAPI (blue). **f**, Quantification of the experiment shown in **e**. Mean ± s.d., ≥300 cells across at least 3 independent experiments, two-tailed *t*-test. **g**, Quantification (top) of the cross-linking efficiency test (bottom) in *Trf2*$^{f/f}$ ES cells 96 h after treatment with EtOH or OHT. Mean ± s.e.m., $n = 3$ biologically independent experiments, unpaired two-tailed *t*-test. **h**, Measurement of linear and T-loop molecules shown in Fig. 5f. Mean ± s.e.m., $n = 3$ biological replicates scoring ≥2,804 molecules per replicate. T-loop measurements are a sum of the loop and tail portions of the molecule. Scale bar, 5 μm (**a**, **e**). ns, not significant, ****$P \leq 0.0001$.
Source data

Supplementary information

Reporting Summary

Peer Review File

Source data

Source Data Fig. 1

Source Data Fig. 2

Source Data Fig. 3

Source Data Fig. 4

Source Data Fig. 5

Source Data Extended Data Fig. 1

Source Data Extended Data Fig. 2

Source Data Extended Data Fig. 3

Source Data Extended Data Fig. 4

Source Data Extended Data Fig. 5

Source Data Extended Data Fig. 6

Source Data Extended Data Fig. 7

Source Data Extended Data Fig. 8

Source Data Extended Data Fig. 9

Source Data Extended Data Fig. 10

Rights and permissions

Reprints and Permissions

About this article

Check for updates

Cite this article

Ruis, P., Van Ly, D., Borel, V. *et al.* TRF2-independent chromosome end protection during pluripotency. *Nature* **589,** 103–109 (2021). https://doi.org/10.1038/s41586-020-2960-y

Download citation

- Received: 04 February 2020
- Accepted: 14 September 2020
- Published: 25 November 2020
- Issue Date: 07 January 2021
- DOI: https://doi.org/10.1038/s41586-020-2960-y

Comments

By submitting a comment you agree to abide by our Terms and Community Guidelines. If you find something abusive or that does not comply with our terms or guidelines please flag it as inappropriate.

Access through your institution
Change institution
Buy or subscribe

This article was downloaded by **calibre** from https://www.nature.com/articles/s41586-020-2960-y

| Section menu | Main menu |

- Article
- Published: 25 November 2020

TRF2-mediated telomere protection is dispensable in pluripotent stem cells

- Marta Markiewicz-Potoczny ORCID: orcid.org/0000-0002-3586-6977[1],
- Anastasia Lobanova[2],
- Anisha M. Loeb[1],
- Oktay Kirak ORCID: orcid.org/0000-0002-6524-4685[3],
- Teresa Olbrich[1],
- Sergio Ruiz[1] &
- Eros Lazzerini Denchi ORCID: orcid.org/0000-0001-5378-4644[1]

Nature **volume 589**, pages110–115(2021)Cite this article

- 6361 Accesses
- 75 Altmetric
- Metrics details

Subjects

- DNA damage response
- Embryonic stem cells
- Telomeres

Abstract

In mammals, telomere protection is mediated by the essential protein TRF2, which binds chromosome ends and ensures genome integrity[1,2]. TRF2 depletion results in end-to-end chromosome fusions in all cell types that have been tested so far. Here we find that TRF2 is dispensable for the proliferation and survival of mouse embryonic stem (ES) cells. *Trf2*$^{-/-}$ (also known as *Terf2*) ES cells do not exhibit telomere fusions and can be expanded indefinitely. In response to the deletion of TRF2, ES cells exhibit a muted DNA damage response that is characterized by the recruitment of γH2AX—but not 53BP1—to telomeres. To define the mechanisms that control this unique DNA damage response in ES cells, we performed a CRISPR–Cas9-knockout screen. We found a strong dependency of TRF2-null ES cells on the telomere-associated protein POT1B and on the chromatin remodelling factor BRD2. Co-depletion of POT1B or BRD2 with TRF2 restores a canonical DNA damage response at telomeres, resulting in frequent telomere fusions. We found that TRF2 depletion in ES cells activates a totipotent-like two-cell-stage transcriptional program that includes high levels of ZSCAN4. We show that the upregulation of ZSCAN4 contributes to telomere protection in the absence of TRF2. Together, our results uncover a unique response to telomere deprotection during early development.

Access through your institution
Change institution
Buy or subscribe

Access options

Subscribe to Journal

Get full journal access for 1 year

$199.00

only $3.90 per issue

Subscribe

All prices are NET prices.
VAT will be added later in the checkout.

Rent or Buy article

Get time limited or full article access on ReadCube.

from$8.99

Rent or Buy

All prices are NET prices.

Additional access options:

- Log in
- Access through your institution
- Learn about institutional subscriptions

Fig. 1: *Trf2*$^{-/-}$ ES cells are viable and do not exhibit end-to-end chromosome fusions.

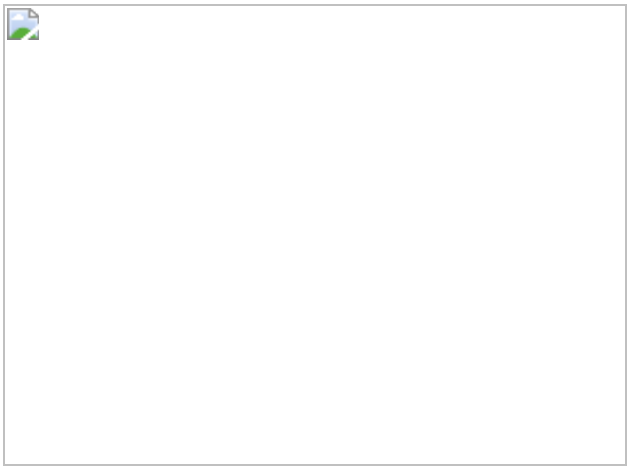

Fig. 2: A synthetic lethality CRISPR screen in TRF2-deficient ES cells.

Fig. 3: POT1B and BRD2 are required for telomere protection in the absence of TRF2.

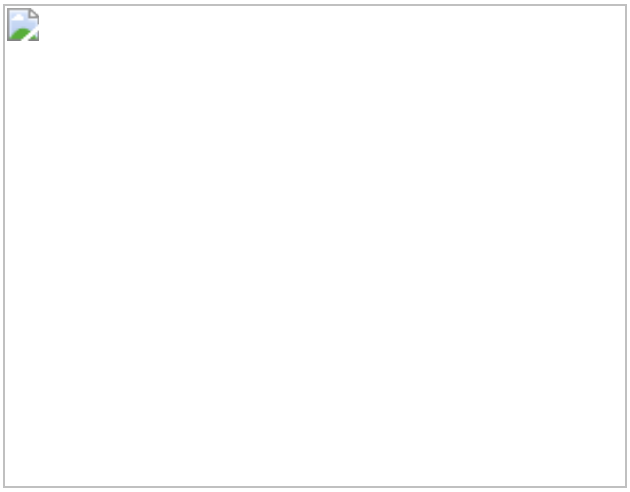

Fig. 4: Two-cell-signature genes are involved in telomere protection of ES cells.

Data availability

All raw sequencing reads for RNA-seq are available on NCBI Gene Expression Omnibus under accession number GSE156534. Source data are provided with this paper.

References

1. 1.

   Celli, G. B. & de Lange, T. DNA processing is not required for ATM-mediated telomere damage response after TRF2 deletion. *Nat. Cell Biol*. **7**, 712–718 (2005).

   CAS Article Google Scholar

2. 2.

   de Lange, T. Shelterin: the protein complex that shapes and safeguards human telomeres. *Genes Dev*. **19**, 2100–2110 (2005).

   Article Google Scholar

3. 3.

   Artandi, S. E. et al. Telomere dysfunction promotes non-reciprocal translocations and epithelial cancers in mice. *Nature* **406**, 641–645 (2000).

   ADS CAS Article Google Scholar

4. 4.

   Griffith, J. D. et al. Mammalian telomeres end in a large duplex loop. *Cell* **97**, 503–514 (1999).

   CAS Article Google Scholar

5. 5.

Doksani, Y., Wu, J. Y., de Lange, T. & Zhuang, X. Super-resolution fluorescence imaging of telomeres reveals TRF2-dependent T-loop formation. *Cell* **155**, 345–356 (2013).

CAS Article Google Scholar

6. 6.

Okamoto, K. et al. A two-step mechanism for TRF2-mediated chromosome-end protection. *Nature* **494**, 502–505 (2013).

ADS CAS Article Google Scholar

7. 7.

Martínez, P., Ferrara-Romeo, I., Flores, J. M. & Blasco, M. A. Essential role for the TRF2 telomere protein in adult skin homeostasis. *Aging Cell* **13**, 656–668 (2014).

Article Google Scholar

8. 8.

Lobanova, A. et al. Different requirements of functional telomeres in neural stem cells and terminally differentiated neurons. *Genes Dev*. **31**, 639–647 (2017).

CAS Article Google Scholar

9. 9.

White, D. E. et al. KAP1, a novel substrate for PIKK family members, colocalizes with numerous damage response factors at DNA lesions. *Cancer Res*. **66**, 11594–11599 (2006).

CAS Article Google Scholar

10. 10.

Dimitrova, N. & de Lange, T. Cell cycle-dependent role of MRN at dysfunctional telomeres: ATM signaling-dependent induction of nonhomologous end joining (NHEJ) in G1 and resection-mediated inhibition of NHEJ in G2. *Mol. Cell Biol*. **29**, 5552–5563 (2009).

CAS Article Google Scholar

11. 11.

Hockemeyer, D., Daniels, J. P., Takai, H. & de Lange, T. Recent expansion of the telomeric complex in rodents: two distinct POT1 proteins protect mouse telomeres. *Cell* **126**, 63–77 (2006).

CAS Article Google Scholar

12. 12.

Wu, L. et al. *Pot1* deficiency initiates DNA damage checkpoint activation and aberrant homologous recombination at telomeres. *Cell* **126**, 49–62 (2006).

CAS Article Google Scholar

13. 13.

Gyuris, A. et al. The chromatin-targeting protein Brd2 is required for neural tube closure and embryogenesis. *Biochim. Biophys. Acta* **1789**, 413–421 (2009).

CAS Article Google Scholar

14. 14.

Kim, J. J. et al. Systematic bromodomain protein screens identify homologous recombination and R-loop suppression pathways involved in genome integrity. *Genes Dev*. **33**, 1751–1774 (2019).

CAS Article Google Scholar

15. 15.

Kratz, K. & de Lange, T. Protection of telomeres 1 proteins POT1a and POT1b can repress ATR signaling by RPA exclusion, but binding to CST limits ATR repression by POT1b. *J. Biol. Chem*. **293**, 14384–14392 (2018).

CAS Article Google Scholar

16. 16.

Denchi, E. L. & de Lange, T. Protection of telomeres through independent control of ATM and ATR by TRF2 and POT1. *Nature* **448**, 1068–1071 (2007).

ADS CAS Article Google Scholar

17. 17.

Gursoy-Yuzugullu, O., Carman, C. & Price, B. D. Spatially restricted loading of BRD2 at DNA double-strand breaks protects H4 acetylation domains and promotes DNA repair. *Sci. Rep*. **7**, 12921 (2017).

ADS Article Google Scholar

18. 18.

Eckersley-Maslin, M. A. et al. MERVL/Zscan4 network activation results in transient genome-wide DNA demethylation of mESCs. *Cell Rep*. **17**, 179–192 (2016).

CAS Article Google Scholar

19. 19.

Zhang, W. et al. Zscan4c activates endogenous retrovirus MERVL and cleavage embryo genes. *Nucleic Acids Res*. **47**, 8485–8501 (2019).

CAS PubMed PubMed Central Google Scholar

20. 20.

Macfarlan, T. S. et al. Embryonic stem cell potency fluctuates with endogenous retrovirus activity. *Nature* **487**, 57–63 (2012).

ADS CAS PubMed PubMed Central Google Scholar

21. 21.

Falco, G. et al. *Zscan4*: a novel gene expressed exclusively in late 2-cell embryos and embryonic stem cells. *Dev. Biol*. **307**, 539–550 (2007).

CAS Article Google Scholar

22. 22.

Zalzman, M. et al. *Zscan4* regulates telomere elongation and genomic stability in ES cells. *Nature* **464**, 858–863 (2010).

ADS CAS Article Google Scholar

23. 23.

Dan, J. et al. Zscan4 inhibits maintenance DNA methylation to facilitate telomere elongation in mouse embryonic stem cells. *Cell Rep*. **20**, 1936–1949 (2017).

CAS Article Google Scholar

24. 24.

Pucci, F., Gardano, L. & Harrington, L. Short telomeres in ESCs lead to unstable differentiation. *Cell Stem Cell* **12**, 479–486 (2013).

CAS Article Google Scholar

25. 25.

Colla, S. et al. Telomere dysfunction drives aberrant hematopoietic differentiation and myelodysplastic syndrome. *Cancer Cell* **27**, 644–657 (2015).

CAS Article Google Scholar

26. 26.

Ferron, S. R. et al. Telomere shortening in neural stem cells disrupts neuronal differentiation and neuritogenesis. *J. Neurosci*. **29**, 14394–14407 (2009).

CAS Article Google Scholar

27. 27.

Vooijs, M., Jonkers, J. & Berns, A. A highly efficient ligand-regulated Cre recombinase mouse line shows that LoxP recombination is position dependent. *EMBO Rep*. **2**, 292–297 (2001).

CAS Article Google Scholar

28. 28.

Chavez, A., George, V., Agrawal, V. & Johnson, F. B. Sumoylation and the structural maintenance of chromosomes (Smc) 5/6 complex slow senescence through recombination intermediate resolution. *J. Biol. Chem*. **285**, 11922–11930 (2010).

CAS Article Google Scholar

29. 29.

Baerlocher, G. M., Vulto, I., de Jong, G. & Lansdorp, P. M. Flow cytometry and FISH to measure the average length of telomeres (flow FISH). *Nat. Protoc.* **1**, 2365–2376 (2006).

CAS Article Google Scholar

30. 30.

Li, W. et al. MAGeCK enables robust identification of essential genes from genome-scale CRISPR/Cas9 knockout screens. *Genome Biol*. **15**, 554 (2014).

Article Google Scholar

31. 31.

Tzelepis, K. et al. A CRISPR dropout screen identifies genetic vulnerabilities and therapeutic targets in acute myeloid leukemia. *Cell Rep*. **17**, 1193–1205 (2016).

CAS Article Google Scholar

32. 32.

Rucci, F. et al. Homozygous DNA ligase IV R278H mutation in mice leads to leaky SCID and represents a model for human LIG4 syndrome. *Proc. Natl Acad. Sci. USA* **107**, 3024–3029 (2010).

ADS CAS Article Google Scholar

Download references

Acknowledgements

We thank A. Nussenzweig, A. Sfeir, C. Attwooll and members of the Lazzerini Denchi laboratory for discussions and critical reading of the manuscript; F. Livak and the NCI Flow Cytometry Core Facility FACS for assistance with FACS analysis; and S. Shema and the CCR Genomics Core for assistance with next-generation sequencing experiments. M.M.-P. is a recipient of the William Guy Forbeck Research Foundation Award; T.O. is a recipient of the Helen Hay Whitney Postdoctoral Fellowship.

Author information

Affiliations

1. Laboratory of Genome Integrity, National Cancer Institute, NIH, Bethesda, MD, USA

   Marta Markiewicz-Potoczny, Anisha M. Loeb, Teresa Olbrich, Sergio Ruiz & Eros Lazzerini Denchi

2. The Scripps Research Institute, San Diego, CA, USA

   Anastasia Lobanova

3. Division of Pediatric Hematology and Oncology, Department of Pediatrics and Adolescent Medicine, Faculty of Medicine, Medical Center, University of Freiburg, Freiburg, Germany

   Oktay Kirak

Authors

1. Marta Markiewicz-Potoczny
   View author publications

   You can also search for this author in PubMed Google Scholar

2. Anastasia Lobanova
   View author publications

   You can also search for this author in PubMed Google Scholar

3. Anisha M. Loeb
   View author publications

   You can also search for this author in PubMed Google Scholar

4. Oktay Kirak
   View author publications

   You can also search for this author in PubMed Google Scholar

5. Teresa Olbrich
   View author publications

   You can also search for this author in PubMed Google Scholar

6. Sergio Ruiz
   View author publications

   You can also search for this author in PubMed Google Scholar

7. Eros Lazzerini Denchi
   View author publications

   You can also search for this author in PubMed Google Scholar

Contributions

E.L.D. and M.M.-P. conceived the study and designed the experiments; M.M.-P. and A.M.L. conducted experiments; E.L.D. and M.M.-P. analysed data; O.K. and A.L. generated TRF2 conditional-knockout ES cells. T.O. and S.R. provided critical reagents and assisted with the ES cell differentiation studies. E.L.D. and M.M.-P. wrote the manuscript with editorial help from A.M.L., T.O. and S.R.

Corresponding author

Correspondence to Eros Lazzerini Denchi.

Ethics declarations

Competing interests

The authors declare no competing interests.

Additional information

Peer review information *Nature* thanks Ylli Doksani and the other, anonymous, reviewer(s) for their contribution to the peer review of this work.

Publisher's note Springer Nature remains neutral with regard to jurisdictional claims in published maps and institutional affiliations.

Extended data figures and tables

Extended Data Fig. 1 *Trf2*$^{-/-}$ ES cells are not viable upon differentiation.

a, Schematic showing the hanging drops protocol used to generate embryoid bodies (EBs) and differentiated FLICs. **b**, Representative images of embryoid bodies derived from control and TRF2-depleted ES cells before adhesion (left) and 3 days after induction of differentiation (right). The experiment was performed three times with similar results. Scale bar, 400 µm. **c**, Growth properties of embryoid bodies derived from TRF2-proficient (control (cont.)) or TRF2-depleted ES cells (OHT) undergoing differentiation measured by confluence. Mean and s.d. are derived from the analysis of 47 images per condition. **d**, Immunofluorescence staining for the pluripotency marker OCT4 in ES cells and FLICs. The percentage of positive cells is shown. The experiment was performed three times with similar results. Scale bar, 10 µm. **e**, Schematics of the experimental approach used to derive single-cell isolates 3 weeks after OHT-mediated TRF2 deletion in ES cells and FLICs. The table summarizes the number of cells seeded, the number of colonies obtained and the TRF2 genotype of the isolated colonies. An example of a genotyping PCR performed on the resulting clones and the representation of the *Trf2*-floxed and *Trf2*-null alleles[1] is shown below. The unprocessed image is provided in the Source Data for Extended Data Fig. 1. **f**, Growth property measured by confluency of 4 heterozygous ES cells clones (*Trf2*$^{f/-}$) (dark blue) and 4 knockout clones (*Trf2*$^{-/-}$) (red) derived from the experiment described in **e**, and the parental ES cells (*Trf2*$^{f/f}$) (light blue). Mean and s.d. are derived from the analysis of 36 images per condition. Source data

Extended Data Fig. 2 Reduced activation of DDR in ES cells following telomere deprotection.

a, Representative immunofluorescence for KAP1 phosphorylated at S824 (p-KAP1) in ES cells and FLICs either before (cont.) or after Cre induction (OHT). Scale bar, 10 μm. Percentages of p-KAP1-positive cells are indicated in the figure as well as in **b**. The experiment was performed twice for ES cells with similar results and once for FLICs. **c**, Representative immunofluorescence staining for γH2AX (red), p-KAP1 (pink) and FISH staining for telomeric DNA (green) of TRF2-proficient (cont.) and TRF2-deficient (OHT) ES cells. Percentage of TIF-positive cells (third panel from left) and percentage of cells with TIF and positive for p-KAP1 (last panel from left) are shown. Scale bar, 4 μm. **d**, Percentage of ES cells and FLICs with more than 10 γH2AX TIF. Where indicated, TRF2-proficient (cont.) or TRF2-deficient (OHT) cells were treated with an ATM inhibitor. Data panels in the figure are representative of three experiments. ns, non-significant ($P \geq 0.05$), $*P < 0.05$, $**P < 0.01$, $***P < 0.001$, one-way ANOVA. **e**, 53BP1 (red) localization at telomeric DNA (green) in TRF2-proficient (cont.) and TRF2-deficient (OHT) ES cells and FLICs. Quantification of these data are reported in Fig. 1f. Scale bar, 4 μm. **f**, Western blotting analysis for p-KAP1, γH2AX and—as a loading control—tubulin. Protein lysates were isolated from ES cells or FLICs either mock-treated or gamma irradiated (2.5 Gy) 30 min before collection. **g**, Western blotting analysis for the expression of p-KAP1 or—as loading control—tubulin. Protein lysates were derived from ES cells that were either untreated or treated with the ATM inhibitor, as indicated. Where indicated, cells were treated with OHT to induce TRF2 depletion, with UV (1,200 J per m^2) or with gamma irradiation (2.5 Gy). **h**, Dissipation of 53BP1 DNA damage foci following IR-induced damage in FLICs (left) and ES cells (right). Cells were treated with gamma irradiation (2.5 Gy) and fixed at the indicated time points. 0, non-treated control samples. For each time point, at least 140 nuclei were scored and the percentage of cells with the indicated number of 53BP1 foci at any given time point is indicated; additional details can be found in Supplementary Table 2. Source data

Extended Data Fig. 3 Identification of synthetically lethal genes in TRF2-deficient ES cells.

a, Scatter plots from three independent CRISPR–Cas9 screens from Fig. 2b. Genes that are synthetically lethal with TRF2 knockout are labelled with dark blue dots. Genes that are essential for ES cells are labelled with magenta dots. **b**, Heat map displaying the essentiality score (β-score) of the 13 candidate synthetically lethal genes (dark blue), and for 8 genes that have previously been described as essential in ES cells[31] (purple), across 3 independent experiments. **c**, Schematic of the *Pot1b* and *Brd2* genomic loci showing genome organization, the predicted CRISPR–Cas9 cut site (scissors, red) and key domains required for protein function (blue). Sanger sequencing of *Pot1b*$^{-/-}$ (exon 2) and *Brd2*$^{-/-}$ (exon 4) for different clones isolated is shown. For *Pot1b*, a repair template cassette containing multiple STOP codons was used. gRNA sequences are highlighted in red.

Extended Data Fig. 4 Codepletion of TRF2 and POT1A or POT1B result in LIG4-dependent end-to-end fusions.

a, Immunofluorescence staining for the pluripotency marker OCT4 (green) in *Pot1b*$^{-/-}$ and *Brd2*$^{-/-}$ ES cells. The percentage of positive cells is shown. Scale bar, 10 µm. **b**, Schematic of the *Lig4* genomic locus, showing the predicted CRISPR–Cas9 cut site (scissors, red), and the sequence coding the essential R278 residue[32] (blue). Sanger sequencing results showing successful gene editing of the *Lig4* locus in four independent clones; the gRNA sequence is highlighted in red. **c**, Metaphases from ES cells of indicated genotypes. The percentage of telomeres engaging in telomere fusions are shown. In total, three independent experiments were performed. For a detailed summary of the data, see Supplementary Table 1 and Source Data for Extended Data Fig. 4.

Extended Data Fig. 5 *Pot1b*, *Pot1a* and *Brd2* depletion in TRF2-null cells induce the DDR pathway.

a, Representative IF–FISH for γH2AX (red) and telomeres (green) of control (cont.) and TRF2-depleted (OHT) ES cells with the indicated *Pot1b*

genotype. Quantifications are provided in Fig. 3e. Scale bar, 4 μm. **b**, Scatter plot representing the distribution of telomeric fusions in control (cont.) and TRF2-depleted (OHT) ES cells of the indicated *Pot1a* genotype. Each dot represents the percentage of telomeres fused in one metaphase spread. For detailed information, see Supplementary Table 1 and Source Data for Extended Data Fig. 5 (n = 3 independent experiments). **c**, Scatter plot representing the distribution of telomeric fusions in control (cont.) and TRF2-depleted (OHT) *Pot1a*$^{-/-}$ ES cells that were either left untreated or treated with the ATR inhibitor (ATRi). Each dot represents the percentage of telomeres fused in one metaphase spread. For detailed information, see Supplementary Table 1 and Source Data for Extended Data Fig. 5. **d**, Metaphases derived from TRF2-proficient (cont.) or TRF2-deficient (OHT) *Pot1b*$^{-/-}$ ES cells treated with ATMi (left) or ATRi (right). Percentage of telomere fusions were calculated from a total of >19 metaphases per genotype. **e**, Graph representing the percentage of telomeric fusions in FLICs of the indicated genotype and treatment. In total, >30 metaphases per genotype and treatment were analysed. **f**, Representative immunofluorescence for p-KAP1 (red) in ES cells of the indicated genotype in the presence (cont.) or absence of TRF2 (OHT). Scale bar, 10 μm. **g**, Percentage of p-KAP1-positive cells in response to TRF2 depletion (OHT) in ES cells of indicated genotype and in control cells. Additional information for **b**–**e** is provided in Supplementary Table 1 and Source Data for Extended Data Fig. 5. Source data

Extended Data Fig. 6 ZSCAN4 contributes to end protection in TRF2-depleted cells.

a, Differentially expressed genes in response to TRF2 depletion in ES cells (left) and differentiated cells (FLICs) (right). Volcano plots represent the $\log_2$-transformed fold change (FC) (x axis) and the $-\log_2$(P value) (y axis). Transcriptional profiling was performed three days after OHT-mediated TRF2 deletion. In the top panels, genes downregulated ($P < 0.005$ and FC < −2) upon OHT treatment are labelled with dark blue dots, and upregulated ($P < 0.005$ and FC >2) are labelled with red dots. Bottom panels, genes expressed in the 2-cell stage are labelled in purple, shelterin components are labelled in green. **b**, Quantifications of telomeric fusions detected in ES

cells following ZSCAN4C downregulation (relative to Fig. 4d). Scatter plot representing the distribution of telomeric fusions. Each dot represents the percentage of telomeres fused in one metaphase spread. For detailed analysis information, see Supplementary Table 1 and Source Data for Extended Data Fig. 6. **c**, ZSCAN4C downregulation does not induce ES cell differentiation. Representative immunofluorescence staining for the pluripotency marker OCT4 in control and OHT-treated ES cells following ZSCAN4C downregulation. The percentage of OCT4-positive cells is shown. Scale bar, 10 µm. **d**, Representative immunofluorescence staining for ZSCAN4 in FLICs with stable integration of a doxycycline-inducible ZSCAN4C expression construct (iZSCAN4). Cells were either left untreated (top) or treated with doxycycline to induce *Zscan4c* expression (bottom) for two days before collection. **e**, The FLICs described in **d** either induced with doxycycline (+) or not (−) were treated with OHT and collected 4 days later for western blot analysis. As a control (cont.), FLICs lacking the inducible cassette were used. **f**, Growth of *Trf2*$^{f/f}$ FLICs before (cont.) or after Cre induction (OHT), untreated (circle) or treated (inverted triangle) with doxycycline to induce *Zscan4c*. Mean and s.d. are derived from the analysis of 49 images per condition. **g**, Representative IF–FISH staining for 53BP1 (red) and telomeric DNA (green) in TRF2-proficient (cont.) or TRF2-deficient FLICs. Where indicated, cells were treated with doxycycline (Dox) 7 days before collection to induce expression of exogenous *Zscan4c*. Scale bar, 4 µm. **h**, Quantification of data shown in **g**, cells with more than 10 53BP1 foci at telomeres were scored as positive for TIF. Source data

Extended Data Fig. 7 TRF2-depleted cells show increased telomere length.

a, Representative FACS plots (*y* axes, cell count; *x* axes, PI staining) showing the cell-cycle profiles of TRF2-proficient (cont.) and TRF2-deficient (OHT) FLICs. Where indicated, cells were treated with doxycycline (Dox) for 7 days before collection to induce expression of exogenous *Zscan4c*. G1 phase of the cell cycle is marked in blue; S phase in yellow; G2 phase in green. The unmarked peak indicates presence of polyploid cells. **b**, Q-FISH histograms of telomere length distributions of chromosomes derived from TRF2-proficient (*Trf2*$^{f/-}$) and TRF2-deficient

(*Trf2*$^{-/-}$) ES cells clones, derived as described in Extended Data Fig. 1e. Telomere length was calculated on the basis of the florescence intensity of a telomeric FISH probe (PNA-TelC). **c**, Flow-FISH quantification of telomere length was performed on TRF2-proficient (*Trf2*$^{f/-}$) and TRF2-deficient (*Trf2*$^{-/-}$) ES cells clones. Top panels show the distribution of telomeric signal intensity (PNA-TelC) (*y* axis) and the DNA content (DAPI) (*x* axis). The bottom panels show the distribution of cells (*y* axis) on the basis of telomeric signal intensity (*x* axis). Cells were gated on the basis of DNA content into G1 (light blue) and S/G2 (orange). Note the shift in telomere length between the TRF2-proficient and TRF2-deficient cells. Source data

Extended Data Fig. 8 Model of the unique telomere protection mechanism in ES cells.

a, Overview of the DDR in response to TRF2 depletion in somatic cells. In response to uncapped telomeres, ATM kinase initiates DDR, leading to end-to-end fusions via the NHEJ pathway. **b**, POT1A, POT1B and BRD2ensure genomic stability in pluripotent mouse ES cells by inhibiting the activities of ATM and ATR kinases. As a result, mild DDR is not enough to cause end-to-end fusions. **c**, Increased expression of Zscan4—a cluster of two-cell-signature genes—might result in recombination-based telomere elongation. Alternatively, the ZSCAN4 -dependent inhibition of the ATM and ATR kinases at TRF2-depleted telomeres of ES cells ensures telomere stability.

Supplementary information

Reporting Summary

Supplementary Table 1

: List of number of chromosomes analyzed for each experiment performed in this study and relative number telomere fusions detected. In this table statistical analyzes was performed on the total number of chromosomes analyzed. The table contains data relative to Figures: 1b-c, 3a-b, 4d-f and

Extended Data Figures: 4c, 5b-e, 6b. Raw data used for graph generation are in Source Data File.

Supplementary Table

Supplementary Table 2: Number of cells examined for IF, IF-FISH and TIFs analysis. The table contains all data points of independent repeats for data shown for Figures: 1e-f, h-i, 3e-f, 4b and Extended Data Figures: 1d, 2b,d,h, 4a, 5g, 6c,g.

Supplementary Table

Supplementary Table 3 Essentiality score (β-score) across three independent experiments of the highest ranked genes identified in this study as synthetically lethal with TRF2 (synthetically lethal) and essential in ES cells regardless of the TRF2 status (essential in ES). β-scores were calculated using MAGeCK-MLE module. Essentiality scores for all the remaining genes can be found in the Source Data File.

Supplementary Table

Supplementary Table 4: List of genes detected as differentially expressed (DE) upon OHT-mediated TRF2 depletion in ESCs (DE_ESCs) and in FLICs (DE_FLICs). Fold change and p-values were calculated using DESeq2.

Source data

Source Data Fig. 1

Source Data Fig. 2

Source Data Fig. 3

Source Data Fig. 4

Source Data Extended Data Fig. 1

Source Data Extended Data Fig. 2

Source Data Extended Data Fig. 5

Source Data Extended Data Fig. 6

Source Data Extended Data Fig. 7

Rights and permissions

Reprints and Permissions

About this article

Check for updates

Cite this article

Markiewicz-Potoczny, M., Lobanova, A., Loeb, A.M. *et al.* TRF2-mediated telomere protection is dispensable in pluripotent stem cells. *Nature* **589,** 110–115 (2021). https://doi.org/10.1038/s41586-020-2959-4

Download citation

- Received: 07 February 2020
- Accepted: 14 September 2020
- Published: 25 November 2020
- Issue Date: 07 January 2021

- DOI: https://doi.org/10.1038/s41586-020-2959-4

Comments

By submitting a comment you agree to abide by our Terms and Community Guidelines. If you find something abusive or that does not comply with our terms or guidelines please flag it as inappropriate.

Access through your institution
Change institution
Buy or subscribe

This article was downloaded by **calibre** from https://www.nature.com/articles/s41586-020-2959-4

| Section menu | Main menu |

- Article
- Published: 18 November 2020

A network of transcriptional repressors modulates auxin responses

- Jekaterina Truskina[1,2],
- Jingyi Han[2 na1],
- Elina Chrysanthou ORCID: orcid.org/0000-0002-6298-9243[2 na1],
- Carlos S. Galvan-Ampudia[1],
- Stéphanie Lainé[1],
- Géraldine Brunoud[1],
- Julien Macé[1],
- Simon Bellows[3],
- Jonathan Legrand[1],
- Anne-Maarit Bågman ORCID: orcid.org/0000-0001-6051-866X[4,5],
- Margot E. Smit ORCID: orcid.org/0000-0001-8285-5130[4,5],
- Ondřej Smetana[6,7],
- Arnaud Stigliani ORCID: orcid.org/0000-0002-9436-2787[8],
- Silvana Porco[2],
- Malcolm J. Bennett ORCID: orcid.org/0000-0003-0475-390X[2],
- Ari Pekka Mähönen[6,7],
- François Parcy ORCID: orcid.org/0000-0003-2191-500X[8],
- Etienne Farcot ORCID: orcid.org/0000-0002-0742-3028[2,3],
- Francois Roudier[1],
- Siobhan M. Brady[4,5],
- Anthony Bishopp ORCID: orcid.org/0000-0003-2962-9542[2] &
- Teva Vernoux ORCID: orcid.org/0000-0002-8257-4088[1]

Nature **volume 589**, pages116–119(2021)Cite this article

- 6258 Accesses
- 101 Altmetric
- Metrics details

Subjects

- Auxin
- Developmental biology
- Plant development
- Plant molecular biology

A Publisher Correction to this article was published on 23 December 2020

This article has been updated

Abstract

The regulation of signalling capacity, combined with the spatiotemporal distribution of developmental signals themselves, is pivotal in setting developmental responses in both plants and animals[1]. The hormone auxin is a key signal for plant growth and development that acts through the AUXIN RESPONSE FACTOR (ARF) transcription factors[2,3,4]. A subset of these, the conserved class A ARFs[5], are transcriptional activators of auxin-responsive target genes that are essential for regulating auxin signalling throughout the plant lifecycle[2,3]. Although class A ARFs have tissue-specific expression patterns, how their expression is regulated is unknown. Here we show, by investigating chromatin modifications and accessibility, that loci encoding these proteins are constitutively open for transcription. Through yeast one-hybrid screening, we identify the transcriptional

regulators of the genes encoding class A ARFs from *Arabidopsis thaliana* and demonstrate that each gene is controlled by specific sets of transcriptional regulators. Transient transformation assays and expression analyses in mutants reveal that, in planta, the majority of these regulators repress the transcription of genes encoding class A ARFs. These observations support a scenario in which the default configuration of open chromatin enables a network of transcriptional repressors to regulate expression levels of class A ARF proteins and modulate auxin signalling output throughout development.

Access through your institution
Change institution
Buy or subscribe

Access options

Subscribe to Journal

Get full journal access for 1 year

$199.00

only $3.90 per issue

Subscribe

All prices are NET prices.
VAT will be added later in the checkout.

Rent or Buy article

Get time limited or full article access on ReadCube.

from$8.99

Rent or Buy

All prices are NET prices.

Additional access options:

- Log in
- Access through your institution
- Learn about institutional subscriptions

Fig. 1: Tissue-specific expression patterns and chromatin landscape of *Arabidopsis* class A *ARF* loci.

Fig. 2: Class A *ARF* transcription is regulated by repressors.

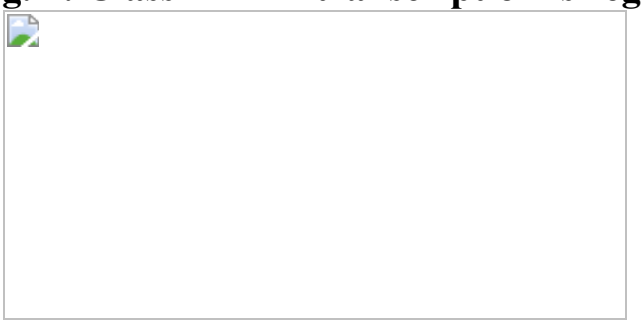

Fig. 3: Expression levels and patterns of class *ARF* genes are altered when upstream transcription factors are modulated.

Data availability

The data including the source data that supports the finding of this study are available within the paper, its supplementary information files or publicly available datasets. Publicly available position weight matrices were obtained from the Jaspar and CisBP databases. Publicly available chromatin

marking and accessibility datasets were acquired from the GEO and ArrayExpress databases with the following accession numbers: GSE24665, GSE24658, GSE7907, GSE24507, GSE50636, GSE24657, GSE24710, GSE19654, GSM2260231, GSM2260232, GSM2260235, GSM2260236, GSM2704255, GSM2704256, GSM2719200, GSM2719201, GSM2719202, GSM2719203, GSM2719204, GSM2719205, GSM1289362, GSM1289374, E-MTAB-4680, E-MTAB-4684 and GSM1289358.

Change history

- **23 December 2020**

  A Correction to this paper has been published: https://doi.org/10.1038/s41586-020-03066-x

References

1. 1.

   Sagner, A. & Briscoe, J. Morphogen interpretation: concentration, time, competence, and signaling dynamics. *Wiley Interdiscip. Rev. Dev. Biol*. **6**, e271 (2017).

   PubMed PubMed Central Google Scholar

2. 2.

   Leyser, O. Auxin signaling. *Plant Physiol*. **176**, 465–479 (2018).

   CAS Google Scholar

3. 3.

   Tiwari, S. B., Hagen, G. & Guilfoyle, T. The roles of auxin response factor domains in auxin-responsive transcription. *Plant Cell* **15**, 533–543 (2003).

CAS PubMed PubMed Central Google Scholar

4. 4.

Petrásek, J. & Friml, J. Auxin transport routes in plant development. *Development* **136**, 2675–2688 (2009).

Google Scholar

5. 5.

Finet, C., Berne-Dedieu, A., Scutt, C. P. & Marlétaz, F. Evolution of the ARF gene family in land plants: old domains, new tricks. *Mol. Biol. Evol*. **30**, 45–56 (2013).

CAS Google Scholar

6. 6.

Krogan, N. T., Marcos, D., Weiner, A. I. & Berleth, T. The auxin response factor MONOPTEROS controls meristem function and organogenesis in both the shoot and root through the direct regulation of PIN genes. *New Phytol*. **212**, 42–50 (2016).

CAS PubMed PubMed Central Google Scholar

7. 7.

Berleth, T. & Jurgens, G. The role of the monopteros gene in organising the basal body region of the *Arabidopsis* embryo. *Development* **118**, 575–587 (1993).

Google Scholar

8. 8.

Przemeck, G. K., Mattsson, J., Hardtke, C. S., Sung, Z. R. & Berleth, T. Studies on the role of the *Arabidopsis* gene MONOPTEROS in

vascular development and plant cell axialization. *Planta* **200**, 229–237 (1996).

CAS Google Scholar

9. 9.

Schlereth, A. et al. MONOPTEROS controls embryonic root initiation by regulating a mobile transcription factor. *Nature* **464**, 913–916 (2010).

ADS CAS Google Scholar

10. 10.

Nagpal, P. et al. Auxin response factors ARF6 and ARF8 promote jasmonic acid production and flower maturation. *Development* **132**, 4107–4118 (2005).

CAS PubMed Google Scholar

11. 11.

Gutierrez, L. et al. Phenotypic plasticity of adventitious rooting in *Arabidopsis* is controlled by complex regulation of AUXIN RESPONSE FACTOR transcripts and microRNA abundance. *Plant Cell* **21**, 3119–3132 (2009).

CAS PubMed PubMed Central Google Scholar

12. 12.

Okushima, Y. et al. Functional genomic analysis of the AUXIN RESPONSE FACTOR gene family members in *Arabidopsis thaliana*: unique and overlapping functions of ARF7 and ARF19. *Plant Cell* **17**, 444–463 (2005).

CAS PubMed PubMed Central Google Scholar

13. 13.

Harper, R. M. et al. The NPH4 locus encodes the auxin response factor ARF7, a conditional regulator of differential growth in aerial *Arabidopsis* tissue. *Plant Cell* **12**, 757–770 (2000).

CAS PubMed PubMed Central Google Scholar

14. 14.

Rademacher, E. H. et al. A cellular expression map of the *Arabidopsis* AUXIN RESPONSE FACTOR gene family. *Plant J*. **68**, 597–606 (2011).

CAS Google Scholar

15. 15.

Vernoux, T. et al. The auxin signalling network translates dynamic input into robust patterning at the shoot apex. *Mol. Syst. Biol*. **7**, 508 (2011).

PubMed PubMed Central Google Scholar

16. 16.

Hardtke, C. S. & Berleth, T. The *Arabidopsis* gene MONOPTEROS encodes a transcription factor mediating embryo axis formation and vascular development. *EMBO J*. **17**, 1405–1411 (1998).

CAS PubMed PubMed Central Google Scholar

17. 17.

Roudier, F. et al. Integrative epigenomic mapping defines four main chromatin states in *Arabidopsis*. *EMBO J*. **30**, 1928–1938 (2011).

CAS PubMed PubMed Central Google Scholar

18. 18.

Gifford, M. L., Dean, A., Gutierrez, R. A., Coruzzi, G. M. & Birnbaum, K. D. Cell-specific nitrogen responses mediate developmental plasticity. *Proc. Natl Acad. Sci. USA* **105**, 803–808 (2008).

ADS CAS Google Scholar

19. 19.

Jay, F. et al. Misregulation of AUXIN RESPONSE FACTOR 8 underlies the developmental abnormalities caused by three distinct viral silencing suppressors in *Arabidopsis*. *PLoS Pathog*. **7**, e1002035 (2011).

CAS PubMed PubMed Central Google Scholar

20. 20.

O'Malley, R. C. et al. Cistrome and epicistrome features shape the regulatory dna landscape. *Cell* **165**, 1280–1292 (2016).

PubMed PubMed Central Google Scholar

21. 21.

Ma, Y. et al. WUSCHEL acts as an auxin response rheostat to maintain apical stem cells in *Arabidopsis*. *Nat. Commun*. **10**, 5093 (2019).

ADS PubMed PubMed Central Google Scholar

22. 22.

Zhao, Z. et al. Hormonal control of the shoot stem-cell niche. *Nature* **465**, 1089–1092 (2010).

ADS CAS Google Scholar

23. 23.

Leibfried, A. et al. WUSCHEL controls meristem function by direct regulation of cytokinin-inducible response regulators. *Nature* **438**, 1172–1175 (2005).

ADS CAS Google Scholar

24. 24.

Dharmasiri, N. et al. Plant development is regulated by a family of auxin receptor F box proteins. *Dev. Cell* **9**, 109–119 (2005).

CAS Google Scholar

25. 25.

Kim, D.-H. & Sung, S. Polycomb-mediated gene silencing in *Arabidopsis thaliana*. *Mol. Cells* **37**, 841–850 (2014).

PubMed PubMed Central Google Scholar

26. 26.

Orosa-Puente, B. et al. Root branching toward water involves posttranslational modification of transcription factor ARF7. *Science* **362**, 1407–1410 (2018).

ADS CAS Google Scholar

27. 27.

Cho, H. et al. A secreted peptide acts on BIN2-mediated phosphorylation of ARFs to potentiate auxin response during lateral root development. *Nat. Cell Biol*. **16**, 66–76 (2014).

CAS Google Scholar

28. 28.

Ptashne, M. Repressors. *Curr. Biol*. **17**, R740–R741 (2007).

CAS Google Scholar

29. 29.

Jacob, F. & Monod, J. Genetic regulatory mechanisms in the synthesis of proteins. *J. Mol. Biol*. **3**, 318–356 (1961).

CAS Google Scholar

30. 30.

Clough, S. J. & Bent, A. F. Floral dip: a simplified method for Agrobacterium-mediated transformation of *Arabidopsis thaliana*. *Plant J*. **16**, 735–743 (1998).

CAS Google Scholar

31. 31.

Gaudinier, A. et al. Enhanced Y1H assays for Arabidopsis. *Nat. Methods* **8**, 1053–1055 (2011).

CAS Google Scholar

32. 32.

Kim, J. H. et al. High cleavage efficiency of a 2A peptide derived from porcine teschovirus-1 in human cell lines, zebrafish and mice. *PLoS ONE* **6**, e18556 (2011).

ADS CAS PubMed PubMed Central Google Scholar

33. 33.

Trichas, G., Begbie, J. & Srinivas, S. Use of the viral 2A peptide for bicistronic expression in transgenic mice. *BMC Biol*. **6**, 40 (2008).

PubMed PubMed Central Google Scholar

34. 34.

George, E. O. & Mudholkar, G. S. On the convolution of logistic random variables. *Metrika* **30**, 1–13 (1983).

MathSciNet MATH Google Scholar

35. 35.

Paponov, I. A. et al. Comprehensive transcriptome analysis of auxin responses in Arabidopsis. *Mol. Plant* **1**, 321–337 (2008).

CAS Google Scholar

36. 36.

Siligato, R. et al. MultiSite Gateway-compatible cell type-specific gene-inducible system for plants. *Plant Physiol*. **170**, 627–641 (2016).

CAS Google Scholar

37. 37.

Smetana, O. et al. High levels of auxin signalling define the stem-cell organizer of the vascular cambium. *Nature* **565**, 485–489 (2019).

ADS CAS Google Scholar

38. 38.

Brady, S. M. et al. A high-resolution root spatiotemporal map reveals dominant expression patterns. *Science* **318**, 801–806 (2007).

ADS CAS Google Scholar

39. 39.

Yadav, R. K., Girke, T., Pasala, S., Xie, M. & Reddy, G. V. Gene expression map of the Arabidopsis shoot apical meristem stem cell niche. *Proc. Natl Acad. Sci. USA* **106**, 4941–4946 (2009).

ADS CAS Google Scholar

40. 40.

Yadav, R. K., Tavakkoli, M., Xie, M., Girke, T. & Reddy, G. V. A high-resolution gene expression map of the Arabidopsis shoot meristem stem cell niche. *Development* **141**, 2735–2744 (2014).

CAS Google Scholar

41. 41.

Oh, S., Park, S. & van Nocker, S. Genic and global functions for Paf1C in chromatin modification and gene expression in Arabidopsis. *PLoS Genet*. **4**, e1000077 (2008).

PubMed PubMed Central Google Scholar

42. 42.

Willing, E.-M. et al. Genome expansion of *Arabis alpina* linked with retrotransposition and reduced symmetric DNA methylation. *Nat. Plants* **1**, 14023 (2015).

CAS Google Scholar

43. 43.

Deal, R. B. & Henikoff, S. A simple method for gene expression and chromatin profiling of individual cell types within a tissue. *Dev. Cell* **18**, 1030–1040 (2010).

CAS PubMed PubMed Central Google Scholar

44. 44.

You, Y. et al. Temporal dynamics of gene expression and histone marks at the Arabidopsis shoot meristem during flowering. *Nat. Commun*. **8**, 15120 (2017).

ADS CAS PubMed PubMed Central Google Scholar

45. 45.

Lafos, M. et al. Dynamic regulation of H3K27 trimethylation during Arabidopsis differentiation. *PLoS Genet*. **7**, e1002040 (2011).

CAS PubMed PubMed Central Google Scholar

46. 46.

Sullivan, A. M. et al. Mapping and dynamics of regulatory DNA and transcription factor networks in *A. thaliana*. *Cell Rep*. **8**, 2015–2030 (2014).

CAS Google Scholar

47. 47.

Lu, Z., Hofmeister, B. T., Vollmers, C., DuBois, R. M. & Schmitz, R. J. Combining ATAC-seq with nuclei sorting for discovery of cis-regulatory regions in plant genomes. *Nucleic Acids Res*. **45**, e41 (2017).

Google Scholar

48. 48.

Maher, K. A. et al. Profiling of accessible chromatin regions across multiple plant species and cell types reveals common gene regulatory principles and new control modules. *Plant Cell* **30**, 15–36 (2018).

CAS Google Scholar

49. 49.

Sijacic, P., Bajic, M., McKinney, E. C., Meagher, R. B. & Deal, R. B. Changes in chromatin accessibility between Arabidopsis stem cells and mesophyll cells illuminate cell type-specific transcription factor networks. *Plant J*. **94**, 215–231 (2018).

CAS PubMed PubMed Central Google Scholar

50. 50.

Thorvaldsdóttir, H., Robinson, J. T. & Mesirov, J. P. Integrative Genomics Viewer (IGV): high-performance genomics data visualization and exploration. *Brief. Bioinform*. **14**, 178–192 (2013).

Google Scholar

51. 51.

Robinson, J. T. et al. Integrative genomics viewer. *Nat. Biotechnol*. **29**, 24–26 (2011).

CAS PubMed PubMed Central Google Scholar

52. 52.

Khan, A. et al. JASPAR 2018: update of the open-access database of transcription factor binding profiles and its web framework. *Nucleic Acids Res*. **46** (D1), D260–D266 (2018).

CAS Google Scholar

53. 53.

Weirauch, M. T. et al. Determination and inference of eukaryotic transcription factor sequence specificity. *Cell* **158**, 1431–1443 (2014).

CAS PubMed PubMed Central Google Scholar

54. 54.

Berger, N., Dubreucq, B., Roudier, F., Dubos, C. & Lepiniec, L. Transcriptional regulation of Arabidopsis LEAFY COTYLEDON2 involves RLE, a cis-element that regulates trimethylation of histone H3 at lysine-27. *Plant Cell* **23**, 4065–4078 (2011).

CAS PubMed PubMed Central Google Scholar

55. 55.

Yu, C.-P., Lin, J.-J. & Li, W.-H. Positional distribution of transcription factor binding sites in *Arabidopsis thaliana*. *Sci. Rep*. **6**, 25164 (2016).

ADS CAS PubMed PubMed Central Google Scholar

56. 56.

Goda, H. et al. The AtGenExpress hormone and chemical treatment data set: experimental design, data evaluation, model data analysis and data access. *Plant J*. **55**, 526–542 (2008).

CAS Google Scholar

Download references

Acknowledgements

We thank F. Besnard, A. Larrieu and R. Azaïs for their help with data analysis and statistics; M. Herpola for RNA in situ hybridization analysis; G. Castiglione for help with root phenotyping; A. Mathelier for help with JASPAR; and D. Weijers for ARF transcriptional reporter lines. This work was supported by a joint INRA/University of Nottingham PhD grant to J.T.; ANR-2014-CE11-0018 grant and Human Frontier Science Program organization (HFSP) grant RPG0054-2013 to T.V.; a Royal Society University Research Fellowship and enhancement award (UF110249 and RGF\EA\180308) to A.B.; a starting grant from the Programme Avenir Lyon Saint Etienne (ANR-11-IDEX-0007) to F.R.; an HHMI Faculty Scholar fellowship to S.M.B.; ANR-10-LABX-49-01 and ANR-17-EURE-

0003 to F.P.; ANR-18-CE12-0014-02 to T.V., F.R. and F.P.; and Aux-ID CNRS PICS grant to T.V., A.B. and E.F.

Author information

Author notes

1. These authors contributed equally: Jingyi Han, Elina Chrysanthou

Affiliations

1. Laboratoire Reproduction et Développement des Plantes, Université de Lyon, ENS de Lyon, UCB Lyon 1, CNRS, INRAE, Lyon, France

   Jekaterina Truskina, Carlos S. Galvan-Ampudia, Stéphanie Lainé, Géraldine Brunoud, Julien Macé, Jonathan Legrand, Francois Roudier & Teva Vernoux

2. School of Biosciences, University of Nottingham, Loughborough, UK

   Jekaterina Truskina, Jingyi Han, Elina Chrysanthou, Silvana Porco, Malcolm J. Bennett, Etienne Farcot & Anthony Bishopp

3. School of Mathematical Sciences, University of Nottingham, Nottingham, UK

   Simon Bellows & Etienne Farcot

4. Department of Plant Biology, University of California Davis, Davis, CA, USA

   Anne-Maarit Bågman, Margot E. Smit & Siobhan M. Brady

5. Genome Center, University of California Davis, Davis, CA, USA

   Anne-Maarit Bågman, Margot E. Smit & Siobhan M. Brady

6. Institute of Biotechnology, HiLIFE, University of Helsinki, Helsinki, Finland

   Ondřej Smetana & Ari Pekka Mähönen

7. Organismal and Evolutionary Biology Research Programme, Faculty of Biological and Environmental Sciences, University of Helsinki, Helsinki, Finland

   Ondřej Smetana & Ari Pekka Mähönen

8. Université Grenoble Alpes, CNRS, CEA, INRAE, IRIG-DBSCI-LPCV, Grenoble, France

   Arnaud Stigliani & François Parcy

Authors

1. Jekaterina Truskina
   View author publications

   You can also search for this author in PubMed Google Scholar

2. Jingyi Han
   View author publications

   You can also search for this author in PubMed Google Scholar

3. Elina Chrysanthou
   View author publications

   You can also search for this author in PubMed Google Scholar

4. Carlos S. Galvan-Ampudia
   View author publications

   You can also search for this author in PubMed Google Scholar

5. Stéphanie Lainé

View author publications

You can also search for this author in PubMed Google Scholar

6. Géraldine Brunoud
   View author publications

   You can also search for this author in PubMed Google Scholar

7. Julien Macé
   View author publications

   You can also search for this author in PubMed Google Scholar

8. Simon Bellows
   View author publications

   You can also search for this author in PubMed Google Scholar

9. Jonathan Legrand
   View author publications

   You can also search for this author in PubMed Google Scholar

10. Anne-Maarit Bågman
    View author publications

    You can also search for this author in PubMed Google Scholar

11. Margot E. Smit
    View author publications

    You can also search for this author in PubMed Google Scholar

12. Ondřej Smetana
    View author publications

    You can also search for this author in PubMed Google Scholar

13. Arnaud Stigliani
View author publications

You can also search for this author in PubMed Google Scholar

14. Silvana Porco
View author publications

You can also search for this author in PubMed Google Scholar

15. Malcolm J. Bennett
View author publications

You can also search for this author in PubMed Google Scholar

16. Ari Pekka Mähönen
View author publications

You can also search for this author in PubMed Google Scholar

17. François Parcy
View author publications

You can also search for this author in PubMed Google Scholar

18. Etienne Farcot
View author publications

You can also search for this author in PubMed Google Scholar

19. Francois Roudier
View author publications

You can also search for this author in PubMed Google Scholar

20. Siobhan M. Brady
View author publications

You can also search for this author in PubMed Google Scholar

21. Anthony Bishopp
View author publications

You can also search for this author in PubMed Google Scholar

22. Teva Vernoux
View author publications

You can also search for this author in PubMed Google Scholar

Contributions

A.B. and T.V. designed the study and supervised the work; J.T., F.P., F.R., E.F., S.M.B., A.B. and T.V. designed the experiments; J.T., A-M.B. and M.E.S. performed the eY1H screen with the help of S.P. and M.B.; J.T., J.H., E.C., C.S.G.-A., S.L. and G.B. performed all experiments in relation to TF biological activity characterization; J.L. performed the statistical analysis of the protoplast experiment and participated in all statistical analysis; O.S. and A.P.M. performed the in situ hybridization experiments; A.S. and F.P. performed TF binding site analysis; S.B. and E.F. performed the modelling analysis; J.M. and F.R. performed the epigenetic data analysis; all authors were involved in data analysis; J.T., A.B. and T.V. wrote the manuscript with inputs from all authors.

Corresponding authors

Correspondence to Anthony Bishopp or Teva Vernoux.

Ethics declarations

Competing interests

The authors declare no competing interests.

Additional information

Peer review information *Nature* thanks the anonymous reviewer(s) for their contribution to the peer review of this work.

Publisher's note Springer Nature remains neutral with regard to jurisdictional claims in published maps and institutional affiliations.

Extended data figures and tables

Extended Data Fig. 1 Analysis of class A ARF expression in the RAM and the SAM using transcriptional reporter lines and in situ hybridization.

a–**j**, Confocal images showing expression of *ARF5* (**a**, **f**), *ARF6* (**b**, **g**), *ARF7* (**c**, **h**), *ARF8* (**d**, **i**) and *ARF19* (**e**, **j**) in the RAM and the SAM using promoters that lack sequences downstream of the start codon but contain the long upstream sequences (*pARF*$^{-\text{intron}}$*::mVenus*) (~3 kb for *ARF6* and *ARF7*; 5 kb for *ARF5*, *ARF8* and *ARF19*) (see Methods). For SAM images (**f**–**j**) an orthogonal projection is shown below to provide information about expression in different layers. **k**–**o**, For comparison, the expression of each class A *ARF* gene in the SAM using the previously published *pARF::GFP* lines with shorter (~2 kb) promoters containing sequences upstream of the start codon is shown in panels **k**–**o**[14]. *ARF5* (**k**), *ARF6* (**l**), *ARF7* (**m**), *ARF8* (**n**) and *ARF19* (**o**). (**p**–**r**) In situ hybridizations through the RAM for *ARF5* (**p**), *ARF6* (**q**) and *ARF8* (**r**). Note that expression patterns of the class A *ARF* reporters (**a**–**j**) differ from those with shorter (2 kb) promoters (**k**–**o**[14]) and recapitulate the patterns observed with RNA in situ hybridization (**p**–**r**; ref. [16]). This was particularly clear in the shoot for *ARF5* and *ARF6*. Shorter promoters drive GFP expression mostly in flower boundaries for *ARF5* and throughout the meristem for *ARF6*, in contrast with detection of both genes throughout the periphery of the meristem both with longer promoters (**k**–**o**; also Fig. 1f–j) or using in situ hybridization[15]. Experiments were done three (**a**–**e**) and two times (**f**–**r**). Scale bars: 50 μm.

Extended Data Fig. 2 Distribution of the repressive chromatin marker H3K27me3, the active chromatin marker H3K4me3

and chromatin accessibility at class A *ARF* loci.

a, Chromatin landscape of class A *ARF* and *LEC2* in whole seedlings illustrating the chromatin status of class A *ARF* loci. Repressive H3K27me3 marker (top row), active H3K4me3 marker (middle row) and FANS-ATAC chromatin accessibility (bottom row; see Supplementary Table 1). **b**, **c**, Chromatin landscape of class A *ARF* and *LEC2* loci showing distribution of the repressive chromatin marker H3K27me3 (**a**) and the active chromatin marker H3K4me3 (**b**) in various tissues. Seedling, whole seedlings[17]; leaf, rosette leaves[42]; root, whole roots[17]; seedling 2, whole seedlings[44]; SAM, shoot apical meristems after 0, 1, 2 or 3 d in long-day conditions[44]. Gene models are shown below with arrowheads indicating direction of transcription. **d**, The chromatin landscape of class A *ARF* and *LEC2* loci showing chromatin accessibility in various tissues. DNaseI-seq seedling: DNase I hypersensitive sites in whole seedling[46]; DNaseI-seq root: DNase I hypersensitive sites in root[46]; FANS-ATAC seedling: FANS-ATAC accessible regions in whole seedling[47]; FANS-ATAC roots: FANS-ATAC accessible regions in roots[47]; INTAC-ATAC root tip: INTACT-ATAC transposase hypersensitive sites in root tips[48]. The *LEC2* locus is included as a negative control for H3K4me3 marking and chromatin accessibility, and as a positive control for H3K27me3 marking[54]. The *y* axis scales (at right) show the minimum and maximum number of reads represented in each windows of the same row, except for the data set related to ref. [17], for which the data range corresponds to the IP/INPUT value of the ChIP-chip experiments. For the *x* axis the window size is fixed at 8.5 kb and centred on the gene of interest (gene model in blue below each column, 5′ sequences in green), with arrowheads by the gene name showing the direction of the locus.

Extended Data Fig. 3 Characterization of the TFs and TF binding sites that regulate class A *ARF* expression.

a, Yeast one-hybrid promoter–transcription factor interaction network for class A *ARF* genes. Green boxes correspond to the class A *ARF*; pink boxes are transcription factors binding to the *ARF* promoters. TF-associated functions and expression analysis are indicated in the upper and lower small

boxes and colour-coded as indicated in the key. Note that when two promoter fragments were used for the screen (see Methods), 35 out of 36 regulators bound to the more proximal fragment, supporting previous observations that the majority of transcription factor binding sites reside within a few kb of the transcriptional start site[55]. **b**, Frequency of TF gene families in the Y1H library collection (black) and in the Y1H network (white). Only families represented by at least two members in the Y1H network were analysed. The network is overrepresented with members of the WRKY and SPL TF families. Statistical analysis: hypergeometric test significant to 5% (*; P = 4e-05 for WRKY family and P = 0.044 for SPL family). Sample sizes for TFs in Y1H library in black/Y1H network in white: n = 29/8 TFs (WRKY); n = 68/6 (ZFP); n = 91/6 (AP2/ERF); n = 44/2 (NAC); n = 7/2 TFs (SPL); n = 52/2 TFs (homeobox); n = 61/2 TFs (bHLH). **c**, TF expression in the RAM[38] and the SAM[39,40]. 50% of the identified TFs are expressed in both shoots and roots, whereas 24% and 14% are expressed specifically in roots or shoots respectively. **d**, Known functions of the TFs in the Y1H network based on a literature search (see also Supplementary Table 2). **e**, Boxplot representation of the distribution of class A *ARF* promoter ranks. For TFs with established binding models, we ranked class A *ARF* promoters among all *Arabidopsis* promoters based on the score of the predicted TF binding sites. We repeated the same operation with a set of randomly chosen TFs from different families (see Methods). The comparison of rank distributions with those of a set of randomly chosen TFs from different families revealed significantly higher ranks for eY1H-identified TFs (see also Supplementary Table 3). Statistical analysis: one-sided t-test. Sample sizes: n = 29 for eY1H-selected TFs and n = 100 for randomly selected TFs. Data are represented as boxplots where the middle line is the median, the lower and upper hinges correspond to the first and third quartiles, the upper whisker extends from the hinge to the largest value no further than 1.5× interquartile range (IQR) from the hinge and the lower whisker extends from the hinge to the smallest value at most 1.5× IQR of the hinge. All the individual values are plotted. **f**, Summary of the DAP-seq analysis for the 17 TFs (see also Supplementary Table 3). **g**, Example of DAP-seq data, here a DAP-seq peak for WRKY33 in the promoter of *ARF8*. DAP-seq (**f**, **g**) thus confirms experimentally inferred bindings (**e**) for 4 of the 17 (24%) TFs for which DAP-seq data are available (see also Supplementary Table 3). Note also that chromatin

immunoprecipitation sequencing (ChIP-seq) confirms the binding of WUSCHEL to the *ARF8* promoter[21].

Extended Data Fig. 4 Methodology used for the transient protoplast assay.

a, Design of the standard reporter plasmid containing sequences upstream and downstream of the *ARF* promoter including the first intron (1), the alternative reporter plasmid containing only sequences upstream of the ARF promoter (2), the standard effector plasmid (3), and an alternative effector plasmid containing the VP16 domain fused to the TF coding sequence (4). **b**, Example of a nucleus of a transformed living protoplast imaged with confocal microscopy with channels for mVenus, TagBFP, mCherry and bright-field. The presence of TagBFP and mCherry specifically in the nucleus is used as a transformation control and as a test of viability of the protoplasts. Quantification: definition of the nucleus as a region of interest using ImageJ to quantify fluorescence (see also Methods). Measurements were conducted in at least 4 independent experiments for each TF (minimum of 2 experiments for TF alone and 2 experiments for TF fused to VP16 domain). Scale bars, 10 µm. **c**, **d**, Example of results using the *ARF5* reporter plasmid, with (**c**) and without (**d**) the VP16 activator domain fused to the TF coding sequence (left and right). Error bars, mean ± s.d.; statistical analysis, one-sided Mann–Whitney *U*-test with $P \leq 0.05$ (*); *N* of protoplasts (*P* values): (**c**) control, $n = 35$; DOF1.8, $n = 38$ (0.33); KNAT1, $n = 37$ (0.11), LBD3, $n = 38$ (6e-04); SMZ, $n = 43$ (3e-10); (**d**) control, $n = 43$ (1e-07); DOF1.8-VP16, $n = 46$; KNAT1-VP16, $n = 44$ (0.37); LBD3-VP16, $n = 32$ (1e-05); SMZ-VP16, $n = 39$ (0.015).

Extended Data Fig. 5 *ARF* transcriptional regulators mostly show complementary expression patterns to their target *ARF*s.

a, Plants carrying the *ARF* transcriptional reporters were transformed with transcriptional reporters for a subset of *ARF* regulators driving mCherry. For five out of seven constructs (see also Fig. 3), we saw complementary patterns of expression between transcriptional repressors and their ARFs in the root. **b**, To further quantify the complementarity of TF versus ARF

expression, we quantified the red versus green fluorescence levels in individual nuclei from different cell types (root cap, blue diamond; columella, green triangle; epidermis, red square; vascular cells, purple cross). These values were normalized so that the brightest nucleus of each channel in each line was set to 1, and values were plotted onto scatter plots. Any value falling outside the reference lines shows a >4× bias for expression of either TF or ARF ($n = 3$ for *pAT2G26940::mCherry* and *pAT2G44730::mCherry* in pARF8::mVenus; $n = 2$ for the remaining genotypes). In some cases there was clear complementarity in some cell types but not others. For example, *ZFP6* shows complementary expression patterns in the root cap, epidermis and columella but overlaps with *ARF8* in the vascular tissues. **c**, Analysis of *At2g26940* expression in the SAM, where it was found in organ primordia and weakly in the centre of the SAM; no clear expression was observed in roots. As previously observed with other developmental and hormonal regulators[22,23], co-localization of repressors and their target *ARF* occurs in some cells as in the case of *ZFP6/ARF8* in the root epidermis (**a**, **b**) and *At2g26940/ARF19* in shoot organ primordia (**c**), suggesting potential regulatory interactions to modulate transcription levels. Scale bars, 60 μm (**a**) and 40 μm (**c**). Experiments were done twice (**a**, **c**).

Extended Data Fig. 6 Expression of class A *ARF* in mutants for the regulatory transcription factors.

Expression of class A *ARF* in 24 mutants of the regulatory TFs measured with qRT–PCR, in whole root and whole shoot tissue of 7-d-old seedlings. Green boxes indicate statistically significant upregulation of the corresponding *ARF* in the mutant background compared to wild-type control, and blue boxes indicate statistically significant downregulation. Statistical analysis was performed using a one-sided Mann–Whitney test and a threshold at $P \leq 0.1$. For simplicity, only the interactions predicted by the Y1H are shown, with other combinations shaded with a grey box. The full data set is available in Supplementary Table 6.

Extended Data Fig. 7 Feedback regulations between the transcription factors and auxin signalling.

a, Expression of several TFs are regulated by auxin, which proves feedback regulation from auxin signalling output primarily on *ARF8* expression. Expression was measured after treatment with 1 μM IAA for 30 min, 1h or 3h[56]. Green boxes indicate upregulation, blue boxes indicate downregulation of gene expression compared with a mock treatment. **b**, Schematic representation of *ARF8* regulation with feedbacks. Feedback from auxin signalling on regulatory TFs is expected to induce complex nonlinear regulation of *ARF8* expression (see also Supplementary Note 2). **c**, Diagrammatic representation of the interactions taking place for different instances of model analysed in Supplementary Note 2. The two diagrams on the right (without feedback) are identical. However, for comparison with the models with feedback the parameters used for these differ (see Supplementary Note 2). **d**–**g**, left, bar chart displaying concentrations before and after knock out of transcription factor X, where Y is activated (**d**) or repressed (**f**) by ARF. Right, contour plot displaying ARF transcription rate before and after knock out of transcription factor X relative to Y and X populations, where Y is activated (**f**) or repressed (**g**) by ARF. Steady-state (SS) values corresponding to the bar plot are also reported. These results are discussed in Supplementary Note 2.

Extended Data Fig. 8 Modulating the levels of ARF transcriptional regulators regulates the expression of associated *ARFs*.

a–**f**, Comparison of *ARF* expression in wild-type versus mutants in roots. **g**, Comparison of *pARF7::VENUS* expression in wild-type versus *wrky38* shoot. For quantification (see **f**), fluorescence was measured in the central zone and primordia 2 (green circles). **h**, Quantification of fluorescence changes shown as relative changes in mean fluorescence level in mutant compared to wild type (single value). Quantifications are shown for **a**–**g** and for Fig. 3c,d. In roots, the total *pARF7/19*-driven fluorescent signal was quantified within a standardized zone covering the stele meristem zone and quantified relative to the wild-type controls. In the shoot, L1 and L2 correspond to quantification in the corresponding layers in the SAM of wild-type and *nf-yb13* (see also Fig. 3c, d). Quantification demonstrated a significant change in pattern in *wrky38* mutant SAMs (**g**), with an increase of *pARF7* activity in the centre and a loss of the differential expression

between the SAM centre and lateral organs. Statistical analysis: unpaired two-sided *t*-test with $P \leq 0.01$ (**). Number of samples observed and quantified: for mutant/wild type roots, 13/13 for *crf10*, 12/14 for *wrky38*, 9/9 for *nf-yb13*, 9/8 for *At2g26940*, 12/11 for *myb65*, 12/10 for *nlp5*; 7 shoots for *nf-yb13* and wild-type controls; 7 shoots for *wrky38* and 6 wild-type controls. *P* values from left to right: 0.003, 2e-05, 3e-08, 0.26, 0.57, 0.11, 0.84, 0.007, 0.009. Raw data are provided in Supplementary Table 11. **i**, Inducible constitutive overexpression of *CRF10:mCherry* and *AL3:mCherry* in the p*ARF7::VENUS* line. *pARF7::VENUS* is shown in yellow and the transcription factors fused to mCherry in red following a 24h induction with β-oestradiol. **j**, Both lines shown in **i** show a significant reduction in *pARF7::VENUS* expression. Unpaired two-sided *t*-test: P = 4e-10 (*CRF10*) and 2e-10 (*AL3*). Number of plants: wild-type control, n = 15; *CRF10*, n = 21; *AL3*, n = 20. Error bars: mean ± s.d.. Scale bars: 45 µm for root images; 50 µm for shoot images. For each analysis, the confocal settings were identical in the compared genetic backgrounds. All experiments were done two times.

Extended Data Fig. 9 Mutations in transcriptional regulators of class A *ARF* genes accelerate the root gravitropic response.

a–g, Kinetics of perturbed gravitropic responses of TF mutants (dashed line) compared to wild-type (solid line) over 12 h after application of the gravitational stimulus. Mutants with statistically significant difference in gravitropic response compared to the wild-type are shown: (**a**) *nlp5*, (**b**) *zfp6*, (**c**) *al3*, (**d**) *at2g44730*, (**e**) *wrky11*, (**f**) *myb65* and (**g**) *wrky38*. Statistical analyses: unpaired two-tailed *t*-test with $P \leq 0.05$ (*). *P* values from 1 h to 12 h (left to right): (**a**) 0.86, 0.19, 0.37, 0.004, 0.01, 0.0008, 0.0008, 0.001, 0.007, 0.004, 0.06, 0.07; (**b**) 0.01, 0.02, 0.05, 0.009, 0.002, 0.007, 0.01, 0.01, 0.14, 0.1, 0.01, 0.04; (**c**) 0.75, 0.25, 0.85, 0.12, 0.07, 0.16, 0.02, 0.1, 0.01, 0.02, 0.1, 0.06; (**d**) 0.40, 0.50, 0.71, 0.95, 0.86, 0.23, 0.07, 0.36, 0.12, 0.01, 0.009, 0.04; (**e**) 0.058, 0.97, 0.88, 0.27, 0.81, 0.16, 0.27, 0.04, 0.03, 0.01, 0.01, 0.01; (**f**) 0.31, 0.07, 0.09, 0.10, 0.45, 0.26, 0.08, 0.04, 0.01, 0.24, 0.02, 0.11. (**g**) 0.1, 0.26, 0.003, 0.003, 0.007, 0.0003, 0.0003, 0.0004, 8e-05, 0.0002, 0.001 and 0.001. Sample sizes (WT/mutant plants): (**a**) n = 29/29, (**b**) n = 32/32, (**c**) n = 28/30, (**d**) n = 28/26, (**e**) n = 30/29, (**f**)

n = 30/28, (**g**) 29/30. Raw data are provided in Supplementary Table 12. Error bars: mean ± s.d.

Extended Data Fig. 10 Transcriptional regulation of class A *ARF* genes regulates shoot development.

a, Phenotypic analysis of the shoot defects in TF mutants. Leaf nr, leaf number; rosette d., rosette diameter; C. branch nr, cauline branch number; A. branch nr, axillary branch number. Green boxes indicate statistically significant increases; blue boxes indicate statistically significant reductions in the indicated developmental parameter compared to Col-0. Statistical analyses: unpaired two-tailed t-test, $P \leq 0.05$ considered as statistically significant; number of plants n = 12 per genotype. **b**, Examples of shoot growth phenotypes: shoot growth during vegetative stage in the *at2g26940* mutant alongside the control after growth for 43 d in short-day conditions. **c**, The *dof1.8* mutant has a shorter inflorescence than control plants.

Supplementary information

Supplementary Information

Supplementary note 1**:** Raw data of the statistical analysis of the transcriptional activity of candidate transcription factors regulating ARF^{classA} in protoplasts.

Reporting Summary

Supplementary Information

Supplementary note 2**:** Modelling analysis of the non-linear feedback of ARF caused by the presence of multiple transcriptional regulators.

Supplementary Table

Supplementary table 1: Chromatin status of ARF^{classA} loci - Analysis of presence of H3K27me3 marks, H3K4me3 marks and of chromatin

accessibility in published datasets.

Supplementary Table

Supplementary table 2: Candidate TFs identified using eY1H and their biological function - List of candidate transcription factors identified using eY1H and bibliographic information on their biological functions.

Supplementary Table

Supplementary table 3: Position weight matrices (PWM) for TFs identified in the eYIH screen - Analysis of transcription factor binding sites (TF binding site analysis tab) and DAP-seq peaks presence in ARF^{classA} promoters (DAP-Seq analysis summary and DAP-Seq binding site list tabs).

Supplementary Table

Supplementary table 4: Analysis of transcriptional activity of candidate TF regulating ARF^{classA} – Results of statistical analysis and meta-analysis of the transcriptional activity of candidate transcription factors regulating ARF^{classA} in protoplasts.

Supplementary Table

Supplementary table 5: Characterization of mutants in genes encoding candidate TF regulating ARF^{classA} – Information (mutant information tab) and analysis of mutated gene expression (Gene expression in mutants tab) in T-DNA mutants for transcriptional regulators of ARF^{classA}.

Supplementary Table

Supplementary table 6: Analysis of ARF^{classA} expression in TF mutants using qRT-PCR – Determination of ARF^{classA} expression in T-DNA mutants for transcriptional regulators using qRT-PCR and statistical analysis.

Supplementary Table

Supplementary table 7: Root elongation of plants grown on 10 µM IAA at 15 days versus plants grown without IAA – Source data and statistical analysis.

Supplementary Table

Supplementary table 8: Expression of auxin-regulated genes in TF mutant background using qRT-PCR – Analysis of the expression of the *IAA13* and *19* auxin-regulated genes in T-DNA mutants for transcriptional regulators of ARF^{classA} using qRT-PCR.

Supplementary Table

Supplementary table 9: Shoot phenotyping of TF mutants – Analysis of different shoot phenotypes in T-DNA mutants for transcriptional regulators of ARF^{classA}. The five tabs corresponds to the 5 phenotypes analyzed: Number of leaves, Rosette diameter, Main shoot length, Number of cauline leaves, Number of axillary bracnhes.

Supplementary Table

Supplementary table 10: TF added to the collection used for the eY1H screen – List of transcription factors cloned to expand the collection of Gaudinier et al Nature Methods 2011 used in this study for eYIH screening.

Supplementary Table

Supplementary table 11: Expression of ARF reporters in mutants of regulatory TF measured in the root and the shoot apical meristems using fluorescent reporter lines – Source data and statistical analysis in roots (ARF expression root tab) and shoots (ARF expression shoot tab).

Supplementary Table

Supplementary table 12: Kinetics of gravitropic responses of TF mutants over 12h after application of the gravistimulus – Raw data and statistical analysis. Each tab contains the values for one mutant and the wild-type control.

Rights and permissions

Reprints and Permissions

About this article

Check for updates

Cite this article

Truskina, J., Han, J., Chrysanthou, E. *et al.* A network of transcriptional repressors modulates auxin responses. *Nature* **589,** 116–119 (2021). https://doi.org/10.1038/s41586-020-2940-2

Download citation

- Received: 09 October 2018
- Accepted: 04 September 2020
- Published: 18 November 2020
- Issue Date: 07 January 2021
- DOI: https://doi.org/10.1038/s41586-020-2940-2

Comments

By submitting a comment you agree to abide by our Terms and Community Guidelines. If you find something abusive or that does not comply with our terms or guidelines please flag it as inappropriate.

Access through your institution
Change institution
Buy or subscribe

This article was downloaded by **calibre** from https://www.nature.com/articles/s41586-020-2940-2

- Article
- Published: 16 September 2020

Prokaryotic viperins produce diverse antiviral molecules

- Aude Bernheim[1],
- Adi Millman ORCID: orcid.org/0000-0002-6844-7613[1],
- Gal Ofir ORCID: orcid.org/0000-0002-8307-9388[1],
- Gilad Meitav[1],
- Carmel Avraham[1],
- Helena Shomar ORCID: orcid.org/0000-0002-1090-2871[2],
- Masha M. Rosenberg[2],
- Nir Tal[2],
- Sarah Melamed[1],
- Gil Amitai[1] &
- Rotem Sorek ORCID: orcid.org/0000-0002-3872-4982[1]

Nature **volume 589**, pages120–124(2021)Cite this article

- 11k Accesses
- 2 Citations
- 494 Altmetric
- Metrics details

Subjects

- Bacteria
- Bacteriophages

Abstract

Viperin is an interferon-induced cellular protein that is conserved in animals[1]. It has previously been shown to inhibit the replication of multiple viruses by producing the ribonucleotide 3′-deoxy-3′,4′-didehydro (ddh)-cytidine triphosphate (ddhCTP), which acts as a chain terminator for viral RNA polymerase[2]. Here we show that eukaryotic viperin originated from a clade of bacterial and archaeal proteins that protect against phage infection. Prokaryotic viperins produce a set of modified ribonucleotides that include ddhCTP, ddh-guanosine triphosphate (ddhGTP) and ddh-uridine triphosphate (ddhUTP). We further show that prokaryotic viperins protect against T7 phage infection by inhibiting viral polymerase-dependent transcription, suggesting that it has an antiviral mechanism of action similar to that of animal viperin. Our results reveal a class of potential natural antiviral compounds produced by bacterial immune systems.

Access through your institution
Change institution
Buy or subscribe

Access options

Subscribe to Journal

Get full journal access for 1 year

$199.00

only $3.90 per issue

Subscribe

All prices are NET prices.
VAT will be added later in the checkout.

Rent or Buy article

Get time limited or full article access on ReadCube.

from$8.99

Rent or Buy

All prices are NET prices.

Additional access options:

- Log in
- Access through your institution
- Learn about institutional subscriptions

Fig. 1: pVips and human viperin exhibit antiviral activity in bacteria.

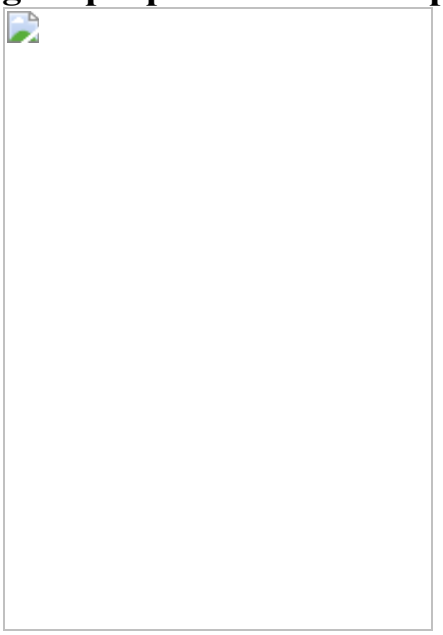

Fig. 2: Phylogenetic tree of the viperin family.

Fig. 3: pVips produce a variety of modified ribonucleotides.

Fig. 4: pVips inhibit T7 polymerase-dependent transcription.

Data availability

Data that support the findings of this study are available within the article and its Extended Data and Supplementary Tables. IMG accessions, protein sequences and nucleotide sequences when relevant to the pVips appear in the Methods and Supplementary Table 2. Mass spectrometry data are available on Metabolights under study number MTBLS1750.

References

1. 1.

   Rivera-Serrano, E. E. et al. Viperin reveals its true function. *Annu. Rev. Virol*. **7**, 1–26 (2020).

   Article Google Scholar

2. 2.

   Gizzi, A. S. et al. A naturally occurring antiviral ribonucleotide encoded by the human genome. *Nature* **558**, 610–614 (2018).

ADS CAS Article Google Scholar

3. 3.

Helbig, K. J. & Beard, M. R. The role of viperin in the innate antiviral response. *J. Mol. Biol*. **426**, 1210–1219 (2014).

CAS Article Google Scholar

4. 4.

Fenwick, M. K., Li, Y., Cresswell, P., Modis, Y. & Ealick, S. E. Structural studies of viperin, an antiviral radical SAM enzyme. *Proc. Natl Acad. Sci. USA* **114**, 6806–6811 (2017).

CAS PubMed Google Scholar

5. 5.

Fenwick, M. K., Su, D., Dong, M., Lin, H. & Ealick, S. E. Structural basis of the substrate selectivity of viperin. *Biochemistry* **59**, 652–662 (2020).

CAS Article Google Scholar

6. 6.

Honarmand Ebrahimi, K., Rowbotham, J. S., McCullagh, J. & James, W. S. Mechanism of diol dehydration by a promiscuous radical-SAM enzyme homologue of the antiviral enzyme viperin (RSAD2). *ChemBioChem* **21**, 1605–1612 (2020).

CAS Article Google Scholar

7. 7.

Makarova, K. S., Wolf, Y. I., Snir, S. & Koonin, E. V. Defense islands in bacterial and archaeal genomes and prediction of novel defense systems. *J. Bacteriol*. **193**, 6039–6056 (2011).

CAS Article Google Scholar

8. 8.

Doron, S. et al. Systematic discovery of antiphage defense systems in the microbial pangenome. *Science* **359**, eaar4120 (2018).

Article Google Scholar

9. 9.

Cohen, D. et al. Cyclic GMP–AMP signalling protects bacteria against viral infection. *Nature* **574**, 691–695 (2019).

ADS CAS Article Google Scholar

10. 10.

Kambara, H. et al. Negative regulation of the interferon response by an interferon-induced long non-coding RNA. *Nucleic Acids Res*. **42**, 10668–10680 (2014).

CAS Article Google Scholar

11. 11.

Thiem, J. & Stangier, P. Preparative-enzymatic formation of cytidine 5′-monophosphosialate by integrated cytidine 5′-triphosphate regeneration. *Liebigs Ann. Chem*.1101–1105 (1990).

12. 12.

Dukhovny, A., Shlomai, A. & Sklan, E. H. The antiviral protein Viperin suppresses T7 promoter dependent RNA synthesis—possible implications for its antiviral activity. *Sci. Rep*. **8**, 8100 (2018).

ADS Article Google Scholar

13. 13.

Makarova, K. S. et al. An updated evolutionary classification of CRISPR–cas systems. *Nat. Rev. Microbiol*. **13**, 722–736 (2015).

CAS Article Google Scholar

14. 14.

Tock, M. R. & Dryden, D. T. F. The biology of restriction and anti-restriction. *Curr. Opin. Microbiol*. **8**, 466–472 (2005).

CAS Article Google Scholar

15. 15.

Calendar, R. & Abedon, S. T. *The Bacteriophages* (Oxford Univ. Press, 2005).

16. 16.

Ebrahimi, K. H. et al. Viperin, through its radical-SAM activity, depletes cellular nucleotide pools and interferes with mitochondrial metabolism to inhibit viral replication. *FEBS Lett*. **594**, 1624–1630 (2020).

CAS Article Google Scholar

17. 17.

Kronheim, S. et al. A chemical defence against phage infection. *Nature* **564**, 283–286 (2018).

ADS CAS Article Google Scholar

18. 18.

De Clercq, E. & Neyts, J. *Antiviral Strategies* (eds H. –G. Kräusslich & R. Bartenschlager) 53–84 (2009).

19. 19.

Feld, J. J. et al. Sofosbuvir and velpatasvir for HCV genotype 1, 2, 4, 5, and 6 infection. *N. Engl. J. Med*. **373**, 2599–2607 (2015).

CAS Article Google Scholar

20. 20.

Chen, I. A. et al. IMG/M v.5.0: an integrated data management and comparative analysis system for microbial genomes and microbiomes. *Nucleic Acids Res*. **47**, D666–D677 (2019).

CAS Article Google Scholar

21. 21.

Nguyen, L. T., Schmidt, H. A., von Haeseler, A. & Minh, B. Q. IQ-TREE: a fast and effective stochastic algorithm for estimating maximum-likelihood phylogenies. *Mol. Biol. Evol*. **32**, 268–274 (2015).

CAS Article Google Scholar

22. 22.

Steinegger, M. & Söding, J. MMseqs2 enables sensitive protein sequence searching for the analysis of massive data sets. *Nat. Biotechnol*. **35**, 1026–1028 (2017).

CAS Article Google Scholar

23. 23.

Katoh, K., Misawa, K., Kuma, K. & Miyata, T. MAFFT: a novel method for rapid multiple sequence alignment based on fast Fourier transform. *Nucleic Acids Res*. **30**, 3059–3066 (2002).

CAS Article Google Scholar

24. 24.

Letunic, I. & Bork, P. Interactive tree of life (iTOL) v3: an online tool for the display and annotation of phylogenetic and other trees. *Nucleic Acids Res*. **44** (W1), W242–W245 (2016).

CAS Article Google Scholar

25. 25.

Eddy, S. R. Accelerated profile HMM searches. *PLOS Comput. Biol*. **7**, e1002195 (2011).

ADS MathSciNet CAS Article Google Scholar

26. 26.

Zimmermann, L. et al. A completely reimplemented MPI bioinformatics toolkit with a new HHpred server at its core. *J. Mol. Biol*. **430**, 2237–2243 (2018).

CAS Article Google Scholar

27. 27.

Baba, T. et al. Construction of *Escherichia coli* K-12 in-frame, single-gene knockout mutants: the Keio collection. *Mol. Syst. Biol*. **2**, 2006.0008 (2006).

Article Google Scholar

28. 28.

Roche, B. et al. Reprint of: Iron/sulfur proteins biogenesis in prokaryotes: formation, regulation and diversity. *Biochim. Biophys. Acta* **1827**, 923–937 (2013).

CAS Article Google Scholar

29. 29.

Schwartz, C. J. et al. IscR, an Fe-S cluster-containing transcription factor, represses expression of *Escherichia coli* genes encoding Fe–S cluster assembly proteins. *Proc. Natl Acad. Sci. USA* **98**, 14895–14900 (2001).

ADS CAS Article Google Scholar

30. 30.

Jiang, D. et al. Identification of three interferon-inducible cellular enzymes that inhibit the replication of hepatitis C virus. *J. Virol*. **82**, 1665–1678 (2008).

CAS Article Google Scholar

31. 31.

Fortier, L.-C. & Moineau, S. in *Bacteriophages: Methods and Protocols Volume 1: Isolation, Characterization, and Interactions* (eds Clokie, M. R. J. & Kropinski, A.) 203–219 (Springer, 2009).

32. 32.

Kropinski, A. M., Mazzocco, A., Waddell, T. E., Lingohr, E. & Johnson, R. P. in *Bacteriophages: Methods and Protocols, Volume 1: Isolation, Characterization, and Interactions* (eds Clokie, M. R. J. & Kropinski, A.) 69–76 (Springer, 2009).

33. 33.

Hsiao, J. J., Potter, O. G., Chu, T. W. & Yin, H. Improved LC/MS methods for the analysis of metal-sensitive analytes using medronic acid as a mobile phase additive. *Anal. Chem*. **90**, 9457–9464 (2018).

CAS Article Google Scholar

34. 34.

Dar, D. et al. Term-seq reveals abundant ribo-regulation of antibiotics resistance in bacteria. *Science* **352**, aad9822 (2016).

Article Google Scholar

Download references

Acknowledgements

We thank M. Danielsen and D. Malheiro from MS-omics for conducting the MS experiments and for the extensive help with the data analysis and the Sorek laboratory members for comments on earlier versions of this manuscript. A.B. is the recipient of a European Molecular Biology Organization Long-Term Fellowship (EMBO ALTF 186-2018). A.M. was supported by a fellowship from the Ariane de Rothschild Women Doctoral Program and, in part, by the Israeli Council for Higher Education via the Weizmann Data Science Research Center. G.O. was supported by the Weizmann Sustainability and Energy Research Initiative (SAERI) doctoral fellowship. R.S. was supported, in part, by the Israel Science Foundation (personal grant 1360/16), the European Research Council (grant ERC-CoG 681203), the Ernest and Bonnie Beutler Research Program of Excellence in Genomic Medicine, the Minerva Foundation with funding from the Federal German Ministry for Education and Research, the Ben B. and Joyce E. Eisenberg Foundation and the Knell Family Center for Microbiology.

Author information

Affiliations

1. Department of Molecular Genetics, Weizmann Institute of Science, Rehovot, Israel

   Aude Bernheim, Adi Millman, Gal Ofir, Gilad Meitav, Carmel Avraham, Sarah Melamed, Gil Amitai & Rotem Sorek

2. Pantheon Biosciences, Yavne, Israel

Helena Shomar, Masha M. Rosenberg & Nir Tal

Authors

1. Aude Bernheim
   View author publications

   You can also search for this author in PubMed Google Scholar

2. Adi Millman
   View author publications

   You can also search for this author in PubMed Google Scholar

3. Gal Ofir
   View author publications

   You can also search for this author in PubMed Google Scholar

4. Gilad Meitav
   View author publications

   You can also search for this author in PubMed Google Scholar

5. Carmel Avraham
   View author publications

   You can also search for this author in PubMed Google Scholar

6. Helena Shomar
   View author publications

   You can also search for this author in PubMed Google Scholar

7. Masha M. Rosenberg
   View author publications

   You can also search for this author in PubMed Google Scholar

8. Nir Tal
View author publications

You can also search for this author in PubMed Google Scholar

9. Sarah Melamed
View author publications

You can also search for this author in PubMed Google Scholar

10. Gil Amitai
View author publications

You can also search for this author in PubMed Google Scholar

11. Rotem Sorek
View author publications

You can also search for this author in PubMed Google Scholar

Contributions

A.B. and R.S. led the study and A.B. performed all experiments unless otherwise indicated. A.M. and A.B performed the computational analyses that appear in Figs. 1, 2, Extended Data Fig 9. H.S., M.M.R. and N.T. designed and performed purification of pVips and in vitro enzymatic assays that appear in Fig. 3, Extended Data Fig 6. G.M., C.A. and S.M. assisted with the plaque assays that appear in Extended Data Fig. 1. C.A. assisted in the preparation of cell lysates that appear in Fig. 3, Extended Data Figs 3–5. G.O. and G.A. assisted in the design and analysis of GFP-reporter studies presented in Fig 4, Extended Data Fig 7. R.S. supervised the study. R.S and A.B. wrote the paper together with the team.

Corresponding author

Correspondence to Rotem Sorek.

Ethics declarations

Competing interests

R.S. is a scientific cofounder and advisor of BiomX, Pantheon Bioscience and Ecophage. A.B., A.M. and R.S. are inventors on patent application PCT/IL2020/050377 licensed to Pantheon Bioscience. H.S., M.R. and N.T. are employed by Pantheon Bioscience. The other authors have no competing interests.

Additional information

Peer review information *Nature* thanks Pieter Dorrestein, Pei-Yong Shi and the other, anonymous, reviewer(s) for their contribution to the peer review of this work.

Extended data figures and tables

Extended Data Fig. 1 pVips protect against phage infection.

Bacteria expressing pVips, GFP or MoaA (negative controls), or the human viperin gene were grown on agar plates and tenfold serial dilutions of the phage lysate were dropped on the plates. **a**–**h**, Efficiency of plating (EOP) data, representing plaque-forming units per millilitre; each bar graph represents average of three replicates, with individual data points overlaid.

Extended Data Fig. 2 T7 infection in liquid culture in the presence of pVips.

a, For each pVip, growth curves of liquid cultures infected by phage T7 (MOI 0.001) are shown. Light and dark grey are uninfected and infected controls (strain expressing GFP), respectively. Light and dark red are uninfected and infected strains expressing pVips, respectively. Two technical replicates are presented as individual curves; representative of three biological replicates. The negative controls (GFP uninfected, GFP

infected) are the same for pVips 6, 7, 8, 10, 15, 27, 37, 39, 42, 50, 54, MoaA, and for pVip12, 19, 32, 44, 46, 47, 48, 57, 58, 60, 61, 62, 63. **b**, The catalytic activity of pVips is required for defence against T7 phage. For each pVip and its respective mutant (mutation of three cysteines in the active site), growth curves of liquid cultures infected by phage T7 (MOI 0.001) are presented. Light and dark grey are uninfected and infected controls (strain expressing MoaA), respectively. Light and dark red are uninfected and infected strains expressing viperins, respectively. Light and dark blue are uninfected and infected strains expressing catalytically inactive mutants. Two technical replicates are presented as individual curves; representative of three biological replicates.

Extended Data Fig. 3 Detection of ddhCTP and ddhCTP derivatives in cell lysates from an *E. coli* strain expressing the human viperin.

a, Extracted ion chromatogram of the ddhC standard. **b**–**d**, Extracted ion chromatogram for singly charged masses that are predicted to correspond to ddhC (m/z 226.0822, retention time (RT) of 2.2 min) (**b**), ddhCMP (m/z 306.0486, RT 9.7) (**c**) and ddhCTP (m/z 465.9812, RT 10.7) (**d**) in cell lysates from an *E. coli* strain expressing the human viperin. Representative of three replicates.

Extended Data Fig. 4 Detection of ddh-ribonucleotides in lysates of cells that express pVips.

a, Quantification of ddh-cytidine (ddhC) in lysates of cells expressing pVips. Detection and quantification of ddhC was performed using LC–MS with a synthesized chemical standard (Methods). For MoaA, the measurement was under the limit of detection (LOD 0.0003 uM). Bar graph represents average of three replicates, with individual data points overlaid. **b**–**h**, Relative abundance for singly charged masses that are predicted to correspond to ddhC (m/z 226.0822, retention time (RT) of 2.2 min) (**b**), ddhCMP (m/z 306.0486, RT 9.7) (**c**), ddhCTP (m/z 465.9812, RT 10.7) (**d**), ddhUMP (m/z 307.0326, RT 8.7) (**e**), ddhUTP (m/z 466.9652, RT 9.9) (**f**), ddhGMP (m/z 346.0547, RT 9.8) (**g**), and ddhGTP (m/z 505.9874, RT 10.7)

(**h**). Average relative abundance is presented as bar graph, with individual data points from three biological replicates overlaid. Limit of detection (LOD) is indicated by a dashed grey line. A compound was defined as present, in Fig. 3, if all three replicates were above the LOD.

Extended Data Fig. 5 MS/MS fragmentation spectra for predicted compounds.

a–**c**, MS/MS data were acquired in positive ionization mode for a synthesized chemical standard ddhC (**a**) as well as for masses from the human viperin cell lysate predicted to correspond to ddhC (**b**), and ddhCMP (**c**). **d**, **e**, Similar data were obtained for masses from the pVip21 cell lysate predicted to correspond to ddhGMP (**d**), and ddhGTP (**e**). **f**, **g**, MS/MS data were acquired, in negative ionization mode, from the pVip47 cell lysate for masses predicted to correspond to ddhUMP (**f**), and ddhUTP (**g**). In all panels, assignment of hypothetical structures is indicated for informative fragment ions. The ddhC molecule is annotated to level 1, and all other molecules are annotated to level 2b, per the Metabolomics Standards Initiative nomenclature.

Extended Data Fig. 6 MS/MS fragmentation spectra for predicted compounds from in vitro reactions with purified pVips.

a, **b**, MS/MS data were acquired in positive ionization mode for the product detected in reaction samples using purified pVip6 or purified pVip56 and CTP and GTP as nucleotide substrates respectively; the resulting products are predicted to correspond to ddhCTP (**a**) and ddhGTP (**b**). **c**, MS/MS data were acquired in negative ionization mode for product detected in reaction samples using purified pVip8 UTP as substrate; the resulting product is predicted to correspond to ddhUTP.

Extended Data Fig. 7 Transcription during induction of WT and mutant pVips.

a, The catalytic activity of pVips is required for defence against T7 phage and repression of viral transcription. Application of the reporter assay (same as presented in Fig. 4a) for strains expressing the human viperin, pVips and their cognate catalytically inactive mutants. Strains are first induced with arabinose for 45 min to express the pVip. At $t = 0$, IPTG is added to express the GFP. Fluorescence/OD over time curves are presented for each strain. Dark and light red correspond to induced and non-induced wild type viperins, respectively; Dark and light blue correspond to induced and non-induced mutant viperins, respectively. Grey curve corresponds to negative control (WT viperin, no addition of IPTG). Two technical replicates are presented as individual curves. Representative of two biological replicates. **b**, T7 RNAP expression as measured by RNA-seq. The expression (RPKM) of T7 RNAP in cells expressing viperins was compared to that in cells expressing the MoaA negative control. Bar graphs represent average of two replicates, with individual data points overlaid.

Extended Data Fig. 8 Heterologous expression of pVips is not toxic is *E. coli*.

Expression of pVips, human viperin or negative controls (GFP, MoaA) was induced at 45 min by addition of arabinose (final concentration 0.2%). Colony forming units (CFU) were measured right after dilution from overnight culture ($t = 0$), before induction ($t = 45$), and 45 and 90 min after induction ($t = 90$, $t = 135$). Bar graphs represent average of three replicates, with individual data points overlaid.

Extended Data Fig. 9 Putative multi-gene defence systems that include pVips.

Representative instances of pVips and their genomic neighbourhood. Genes predicted to be part of the pVip-containing defence system are highlighted. Genes known to be involved in defence are in yellow. Genes of mobile genetic elements are in dark grey. RM, restriction-modification; TA, toxin-antitoxin. The name of bacterial species, and the accession of the relevant genomic scaffold in the IMG database[20] are indicated on the left. **a**–**d**, Four

common configurations of putative pVip-containing systems found in bacterial and archaeal genomes.

Extended Data Fig. 10 Phylogenetic tree of pVips and putative eukaryotic viperins.

MoaA sequences were used as an outgroup (grey). pVips are depicted in red and putative eukaryotic viperins selected for the phylogenetic tree presented in Fig. 2 are depicted in blue.

Supplementary information

Reporting Summary

Supplementary Table 1

Clusters of genes retrieved by the homology-based search of human viperin in prokaryotic genomes. Genes used to calculate defense scores were those present on DNA scaffolds of sufficient size with at least ten genes from each side of the viperin homolog.

Supplementary Table 2

A list of pVips. Gene and genome accessions in the IMG database are indicated.

Supplementary Table 3

MoaA and eukaryotic viperin sequences. MoaA genes (outgroup) and eukaryotic viperin sequences used in the phylogenetic tree in Figure 2.

Supplementary Table 4

A list of primers used in this study.

Supplementary Table 5

A list of phages used in this study.

Rights and permissions

Reprints and Permissions

About this article

Check for updates

Cite this article

Bernheim, A., Millman, A., Ofir, G. *et al.* Prokaryotic viperins produce diverse antiviral molecules. *Nature* **589,** 120–124 (2021). https://doi.org/10.1038/s41586-020-2762-2

Download citation

- Received: 25 February 2020
- Accepted: 27 August 2020
- Published: 16 September 2020
- Issue Date: 07 January 2021
- DOI: https://doi.org/10.1038/s41586-020-2762-2

Further reading

- **A Path toward SARS-CoV-2 Attenuation: Metabolic Pressure on CTP Synthesis Rules the Virus Evolution**

  - Zhihua Ou
  - , Christos Ouzounis
  - , Daxi Wang
  - , Wanying Sun
  - , Junhua Li
  - , Weijun Chen
  - , Philippe Marlière
  - , Antoine Danchin
  - & Esther Angert

  Genome Biology and Evolution (2020)

- **Unearthing the Ancient Origins of Antiviral Immunity**

  - EmilyClare P. Baker
  - & Matthew F. Barber

  Cell Host & Microbe (2020)

Comments

By submitting a comment you agree to abide by our Terms and Community Guidelines. If you find something abusive or that does not comply with our terms or guidelines please flag it as inappropriate.

Access through your institution
Change institution
Buy or subscribe

This article was downloaded by **calibre** from https://www.nature.com/articles/s41586-020-2762-2

The coding capacity of SARS-CoV-2
Download PDF

- Article
- Published: 09 September 2020

The coding capacity of SARS-CoV-2

- Yaara Finkel ORCID: orcid.org/0000-0002-3843-2357[1 na1],
- Orel Mizrahi[1 na1],
- Aharon Nachshon[1],
- Shira Weingarten-Gabbay[2,3],
- David Morgenstern[4],
- Yfat Yahalom-Ronen[5],
- Hadas Tamir[5],
- Hagit Achdout[5],
- Dana Stein[6],
- Ofir Israeli[6],
- Adi Beth-Din[6],
- Sharon Melamed[5],
- Shay Weiss[5],
- Tomer Israely[5],
- Nir Paran[5],
- Michal Schwartz ORCID: orcid.org/0000-0001-5442-0201[1] &
- Noam Stern-Ginossar ORCID: orcid.org/0000-0003-3583-5932[1]

Nature **volume 589**, pages125–130(2021)Cite this article

- 38k Accesses
- 8 Citations
- 296 Altmetric
- Metrics details

Subjects

- Ribosome

- SARS-CoV-2

Abstract

Severe acute respiratory syndrome coronavirus 2 (SARS-CoV-2) is the cause of the ongoing coronavirus disease 2019 (COVID-19) pandemic[1]. To understand the pathogenicity and antigenic potential of SARS-CoV-2 and to develop therapeutic tools, it is essential to profile the full repertoire of its expressed proteins. The current map of SARS-CoV-2 coding capacity is based on computational predictions and relies on homology with other coronaviruses. As the protein complement varies among coronaviruses, especially in regard to the variety of accessory proteins, it is crucial to characterize the specific range of SARS-CoV-2 proteins in an unbiased and open-ended manner. Here, using a suite of ribosome-profiling techniques[2,3,4], we present a high-resolution map of coding regions in the SARS-CoV-2 genome, which enables us to accurately quantify the expression of canonical viral open reading frames (ORFs) and to identify 23 unannotated viral ORFs. These ORFs include upstream ORFs that are likely to have a regulatory role, several in-frame internal ORFs within existing ORFs, resulting in N-terminally truncated products, as well as internal out-of-frame ORFs, which generate novel polypeptides. We further show that viral mRNAs are not translated more efficiently than host mRNAs; instead, virus translation dominates host translation because of the high levels of viral transcripts. Our work provides a resource that will form the basis of future functional studies.

Download PDF

Main

SARS-CoV-2 is an enveloped virus consisting of a positive-sense, single-stranded RNA genome of around 30 kb. Two overlapping ORFs, ORF1a and ORF1b, are translated from the positive-strand genomic RNA and generate continuous polypeptides, which are cleaved into a total of 16 nonstructural proteins (NSPs). The translation of ORF1b is mediated by a −1 frameshift that allows translation to continue beyond the stop codon of ORF1a. Negative-strand RNA intermediates are produced from the viral genome and serve as templates for the synthesis of positive-strand genomic RNA and subgenomic RNAs[5]. The subgenomic RNAs contain a common 5′ leader fused to different segments from the 3′ end of the viral genome, a 5′-cap structure and a 3′ poly(A) tail[6,7]. These distinct fusions occur during negative-strand synthesis at 6–7 nucleotide (nt) core sequences called transcription-regulating sequences (TRSs), which are located at the 3′ end of the leader sequence as well as preceding each viral ORF. The different subgenomic RNAs encode four conserved structural proteins—spike (S), envelope (E), membrane (M) and nucleocapsid (N)—

and several accessory proteins. On the basis of sequence similarity to other betacoronaviruses, and specifically to SARS-CoV, the current annotation of SARS-CoV-2 includes predictions of six accessory proteins (3a, 6, 7a, 7b, 8 and 10, NC_045512.2), but not all have been experimentally confirmed[8,9].

To capture the full coding capacity of SARS-CoV-2, we applied a range of ribosome-profiling approaches to Vero E6 cells infected with SARS-CoV-2 for 5 or 24 h (Fig. 1a). At 24 h post-infection (hpi) the vast majority of cells were infected and cells were still intact (Extended Data Fig. 1). For each time point, we prepared three ribosome-profiling libraries (Ribo-seq), each one in two biological replicates. To facilitate mapping of translation initiation sites, we prepared two Ribo-seq libraries by treating cells with lactimidomycin (LTM) or harringtonine (Harr), two drugs with distinct mechanisms that prevent elongation at 80S ribosomes at translation initiation sites. These treatments lead to excessive accumulation of ribosomes precisely at the sites of translation initiation and depletion of ribosomes over the body of the ORF (Fig. 1a). The third Ribo-seq library was prepared from cells treated with the translation elongation inhibitor cycloheximide (CHX), and provides a snapshot of actively translating ribosomes across the body of the translated ORF (Fig. 1a). In parallel, RNA-sequencing (RNA-seq) was applied to map viral transcripts. Analysis of cellular genes from the different Ribo-seq libraries revealed the expected distinct profiles in both replicates. Ribosome footprints displayed a strong peak at the translation initiation site, which, as expected, is more pronounced in the Harr and LTM libraries; the CHX library also exhibited a distribution of ribosomes across the entire coding region, and the mapped ribosome footprints were enriched in fragments that align to the translated frame (Fig. 1b, Extended Data Fig. 2a). As expected, the RNA-seq reads were uniformly distributed across coding and non-coding regions (Fig. 1b). The footprint profiles of viral coding sequences at 5 hpi fit the expected profile of translated sequences (Fig. 1c, Extended Data Fig. 2b) and the footprint densities were highly reproducible between biological replicates, at single-nucleotide resolution (Extended Data Fig. 2c). Notably, the footprint profile over the viral genome at 24 hpi, did not fit the expected profile of translating ribosomes and was generally not affected by Harr or LTM treatments (Extended Data Fig. 2b). To further examine the characteristics of the footprints, we applied a fragment length organization similarity score (FLOSS) that measures the magnitude of disagreement between the footprint distribution on a given transcript and the footprint distribution on canonical coding sequences (CDSs)[10]. At 5 hpi, protected fragments from SARS-CoV-2 ORFs did not differ from highly expressed cellular transcripts (Fig. 1d). However, reads at 24 hpi could be clearly distinguished from cellular CDSs (Fig. 1e). We conclude that the footprint data from 5 hpi constitutes robust and reproducible ribosome footprint information but that viral protected fragments at 24 hpi may reflect additional interactions with viral RNA that occur at late time points in infection.

Fig. 1: Ribosome profiling of SARS-CoV-2 infected cells.

figure1

a, Vero E6 and Calu3 cells infected with SARS-CoV-2 were collected at 5, 24 (Vero E6) and 7 (Calu3) hpi for RNA-seq, and for Ribo-seq using LTM, Harr or CHX treatments. **b**, Metagene analysis of read densities relative to the maximal signal of

each gene around the start and stop codons of cellular CDSs at 5 hpi. The read densities are shown with different colours indicating the three frames (red, 0; black, +1; grey, +2). **c**, Metagene analysis around the start codon, as described in **b**, for viral ORFs at 5 hpi. **d**, **e**, FLOSS score for cellular and SARS-CoV-2 ORFs at 5 hpi (**d**) and 24 hpi (**e**).

Full size image

A global view of RNA and CHX-footprint reads mapping to the viral genome at 5 hpi demonstrates that RNA levels are constant across ORFs 1a and 1b, and steadily increase towards the 3′ end, reflecting the cumulative abundance of these sequences due to the nested transcription of subgenomic RNAs (Fig. 2a). Increased coverage is also seen at the 5′ untranslated region (UTR), reflecting the presence of the 5′ leader sequence in all subgenomic RNAs as well as the genomic RNA. Reduction in footprint density between ORF1a and ORF1b reflects the proportion of ribosomes that terminate at the ORF1a stop codon instead of frameshifting into ORF1b (Extended Data Fig. 3). By dividing the footprint density in ORF1b by the density in ORF1a we estimate a frameshift efficiency of 57% ± 12%. This value is similar to the frameshift efficiency measured by Ribo-seq of mouse hepatitis virus (MHV) (48–75%)[3]. Similar to observations in MHV and avian infectious bronchitis virus (IBV)[3,11], we did not observe noticeable ribosome pausing before or at the frameshift site, but we identified several potential pausing sites within ORF1a and ORF1b (Extended Data Fig. 3).

Fig. 2: Expression level of canonical viral ORFs.

figure2

a, RNA-seq (green) and Ribo-seq CHX (red) read densities (number of reads) at 5 hpi along the SARS-CoV-2 genome. SARS-CoV-2 canonical ORFs are labelled. **b**, Transcript abundance relative to ribosome densities of each SARS-CoV-2 canonical ORF at 5 hpi. **c**, Scatter plot of the abundance of reads that span canonical leader-dependent junctions (red), non-canonical leader-dependent junctions (green), non-canonical leader-independent junctions (purple) or genomic deletions (cyan) at 5 and 24 hpi.

Full size image

Besides ORF1a and ORF1b, all other canonical viral ORFs are translated from subgenomic RNAs. As raw RNA-seq densities represent the cumulative sum of genomic and subgenomic RNAs, we calculated transcript abundance using two approaches: deconvolution of RNA densities, in which RNA expression of each ORF is calculated by subtracting the RNA-read density of cumulative densities upstream of the ORF region; and relative abundances of RNA reads spanning leader–body junctions of each of the canonical subgenomic RNAs. For the majority of the ORFs, there was high correlation between these two approaches (Pearson's $R = 0.897$; Extended Data Fig. 4a), and in both approaches the N transcript was the most abundant transcript, in agreement with other studies[9,12]. We next compared footprint densities to RNA abundance. For the majority of viral ORFs, transcript abundance correlated almost perfectly with footprint densities (Fig. 2b), indicating that these viral ORFs are translated with similar efficiencies (probably owing to their almost identical 5′ UTRs); however, three ORFs were outliers. The translation efficiencies of ORF1a and ORF1b were considerably lower. This may stem from distinct features in their 5′ UTR (discussed below) or from under estimation of their true translation efficiency, as some of the full-length RNA molecules may serve as template for replication or packaging and are thus not part of the translated mRNA pool. The third outlier is ORF7b, for which we identified very few body–leader junctions; nevertheless, it exhibited relatively high translation, probably owing to ribosome leaky scanning of the ORF7a transcript, as was suggested for SARS-CoV[13].

Many transcripts derived from non-canonical junctions have been identified for SARS-CoV-2[9,12]. These junctions contain either the leader combined with 3′ fragments at unexpected sites in the middle of ORFs (leader-dependent noncanonical junction) or fusions between sequences that do not show similarity to the leader (leader-independent junction). We estimated the frequency of junction-spanning reads in our RNA libraries and obtained excellent agreement between our replicates (Extended Data Fig. 4b, c, Supplementary Table 1) and significant correlation with previous data from Vero E6 cells[12] (Pearson's $R = 0.81$; Extended Data Fig. 4d), illustrating that many of these junctions are reproducible between experimental systems. We also identified five abundant leader-independent junctions that, to our

knowledge, were unique to our data (Supplementary Table 2). We noted that three of these junctions represent short in-frame deletions in the spike protein that overlap deletions in the furin-like cleavage site that were recently described[9] (Extended Data Fig. 4e). The recurrence of the same genomic deletion supports the conclusion that this deletion is being selected for during passage in Vero E6 cells. To examine whether additional non-canonical junctions are derived from genomic deletions, we sequenced the genomic RNA of the virus we used in our infections. In addition to the deletions at the furin-like cleavage site, we identified an 8 amino acid (aa) deletion in ORF-E in 2.3% of the genomic RNA (Fig. 2c, Supplementary Table 2). When we compared the frequency of junctions between 5 h and 24 h time points, the leader-dependent junctions and the genomic deletions showed good correlation, but the leader-independent junctions were specifically increased at 24 hpi (Fig. 2c). These data show that a small number of the leader-independent junctions represent genomic deletions and a larger subset increases at late stages of infection when genome replication is dominant and therefore probably do not substantially affect viral transcripts and translated ORFs.

Examination of SARS-CoV-2 translation as reflected by the diverse Ribo-seq libraries, revealed unannotated translated ORFs. We detected in-frame internal ORFs (iORFs) within existing ORFs, resulting in N-terminally truncated products. These include relatively long truncated versions of canonical ORFs, such as the one found in ORF6 (Fig. 3a, Extended Data Fig. 5a), or very short truncated ORFs that may serve as an upstream ORF (uORF), such as truncated ORF7a, which might regulate ORF7b translation (Fig. 3b, Extended Data Fig. 5b). We also detected internal out-of-frame translations, which would yield novel polypeptides, such as ORFs within ORF3a (41 aa and 33 aa in size, respectively; Fig. 3c, Extended Data Fig. 5c) and within ORF-S (39 aa; Fig. 3d, Extended Data Fig. 5d) or short ORFs that probably serve as uORFs (Fig. 3e, Extended Data Fig. 5e). Additionally, we observed a 13-aa extended ORF-M, in addition to the canonical ORF-M, which is predicted to start at the near-cognate codon AUA (Fig. 3f, Extended Data Fig. 5f).

Fig. 3: Ribosome densities reveal novel viral coding regions.

figure3

a–**i**, Ribosome density profiles (number of reads) of CHX, Harr and LTM samples at 5 hpi. Densities are shown with different colours indicating the frame relative to the main ORF (red, 0; black, +1; grey, +2). Filled and open rectangles indicate the canonical and novel ORFs, respectively. ORFs starting in a near cognate codon are

labelled with stripes. **a**, **b**, In-frame iORFs within ORF6 (**a**) and within ORF7a (**b**). **c**–**e**, Out-of-frame internal initiations within ORF-3a, within ORF-S (**d**) and within ORF-M (**e**). **f**, An extended version of ORF-M. **g**, An uORF that overlaps ORF10 initiation and an in-frame internal initiation generating truncated ORF10. **h**, Two uORFs embedded in the ORF1a 5′ UTR. **i**, Non-canonical CUG initiation upstream of the TRS leader. Reads that were cut to fit the scale are indicated with horizontal lines.

Full size image

The presence of the annotated ORF10 was recently called into question, as almost no subgenomic reads were found for its corresponding transcript[12,14]. Although we also did not detect subgenomic RNA designated for ORF10 translation (Supplementary Table 1), the ribosome footprint densities indicate the presence of a translation initiation signal in ORF10 (Fig. 3g, Extended Data Fig. 5g). Of note, we additionally detected two putative ORFs in this region, an upstream out-of-frame ORF that overlaps ORF10 initiation and an in-frame internal initiation that leads to a truncated ORF10 product. Further research is needed to delineate how ORFs in this region are translated and whether they have any functional roles.

Finally, we detected four distinct initiation sites in the SARS-CoV-2 5′ UTR. Three of these encode for uORFs that are located just upstream of ORF1a; the first initiating at an AUG (uORF1) and the other two initiating at near-cognate codons (uORF2 and extended uORF2; Fig. 3h, Extended Data Fig. 5h). These uORFs are in line with findings in other coronaviruses[3,15]. The fourth site is the most prominent peak in the ribosome footprint densities on the SARS-CoV-2 genome and is located on a CUG codon at position 59, just 10 nucleotides upstream of the TRS leader (Fig. 3i, Extended Data Fig. 5i). The reads mapped to this site have the tight length-distribution characteristic of ribosome-protected fragments (Extended Data Fig. 6a). The occupancy at the CUG is higher than the downstream translation signal (Fig. 3i), implying that this peak might reflect ribosomal pausing. Notably, potenial ribosome pauses located just upstream of the TRS leader were also identified in MHV and IBV genomes[3,11]. Owing to its location upstream of the TRS leader, footprints mapping to this site could potentially derive from any of the subgenomic or genomic RNAs. Therefore, to view this initiation in its context, we aligned the footprints to the genomic RNA or to the most abundant subgenomic N transcript. On the genome and on ORF-N transcript, this initiation results in translation of uORFs, which, on the genome would generate an extension of uORF1 (Extended Data Fig. 6b, c). To assess the distribution of footprints at this initiation on the different viral transcripts, viral transcripts were divided into three groups on the basis of their sequence similarity downstream of the leader–junction site (to enable unique alignment) (Extended Data Fig. 6d). Of note, substantially more footprints were mapped to the group that includes the genomic RNA and the subgenomic E and M transcripts, than would be expected

from their relative RNA abundance (Extended Data Fig. 6e). When only footprints that allow unique mapping to genomic RNA or subgenomic M and E transcripts are used (sizes 31–33 base pairs (bp) to discriminate M from genome or E transcript, and sizes 32–33 bp to discriminate E from the genome) a strong enrichment of footprints that originate from the genome is observed (Extended Data Fig. 6f, g). This footprint enrichment on genomic RNA suggests that ribosome pausing might be more prominent on the genome or that ribosomes engage with genomic RNA differently than with subgenomic transcripts. The proximity of this pause to the leader TRS, which seems to be conserved in MHV and IBV[3,11], together with the relative enrichment on the viral genome, raises the possibility that a ribosome at this position might affect discontinuous transcription either by sterically blocking the TRS-L site or by affecting RNA secondary structure. In addition, ribosomes initiating at the CUG have the potential to generate uORFs or ORF extensions in the different subgenomic transcripts (Supplementary Table 3).

To systematically define the SARS-CoV-2 translated ORFs we used PRICE and ORF-RATER, two computational methods that rely on a combination of translation features to predict novel translated ORFs from ribosome-profiling measurements[16,17]. After application of a minimal expression cut-off and manual curation on the predictions, these classifiers identified 25 ORFs, these included 10 out of the 11 canonical translation initiations and 15 novel viral ORFs. In addition, ORF-RATER identified three putative ORFs that originate from the CUG initiation and extend to the subgenomic transcripts of S, M and ORF6 (Supplementary Table 3). The majority (85%) of the classifier-identified ORFs where independently identified in each of the biological replicates (Supplementary Table 4). Visual inspection of the ribosome-profiling data suggested eight additional putative novel ORFs, some of which are presented above (Fig. 3a, b, g, Supplementary Table 4). Overall, we identified 23 putative ORFs, in addition to the 12 canonical viral ORFs that are currently annotated in the NCBI database and 3 additional potential ORFs that stem from the CUG initiation upstream of the leader.

To confirm the robustness of these annotations, we extended these experiments to human cells. We first examined the infection efficiency of several human cell lines that were used to study SARS-CoV-2 infection: Calu3, A549 and Caco-2. Infection of Calu3 was most efficient and the presence of trypsin increased infection efficiency by at least twofold (Extended Data Fig. 7a). We infected Calu3 with a different SARS-CoV-2 isolate, which was sequenced to confirm its integrity. The same set of Ribo-seq techniques were applied to cells at 7 hpi, each in two biological replicates, in parallel with RNA-seq. The different Ribo-seq libraries showed the expected distinct profiles in both replicates, confirming the overall quality of these libraries (Extended Data Fig. 7b). We examined the translation of the new viral ORFs; all 23 novel ORFs we identified as being translated in Vero E6 cells also showed evidence of translation in

infected Calu3 cells and 16 were annotated by PRICE and ORF-RATER (Extended Data Fig. 8, Supplementary Table 4). ORF-RATER also identified the same three ORFs that originate from the CUG initiation upstream of the leader (Supplementary Table 3). LTM-induced ribosome accumulation at the canonical and predicted initiation sites was highly reproducible between biological replicates as well as between Calu3 and Vero E6 cells (Extended Data Fig. 9a–c). Furthermore, ribosome-protected footprints displayed a 3-nt periodicity that was in phase with the predicted start site in both Vero E6 and Calu3 cells, providing further evidence for the active translation of the predicted ORFs (Extended Data Fig. 9d). We conclude that 23 unannotated ORFs are reproducibly translated from SARS-CoV-2 independently of the host cell and the viral origin, and additional ORFs may be translated from the CUG initiation located upstream of the TRS leader.

Ribosome density also enables accurate quantification of viral protein production. We first quantified the relative expression levels of canonical viral ORFs on the basis of the non-overlapping regions. ORF-N shows the highest expression in Vero E6 and Calu3 cells, followed by the other viral ORFs, with some differences in the relative expression between the two cell types (Fig. 4a). To quantify the expression of out-of-frame iORFs, we computed the contribution of the iORF to the frame periodicity signal relative to the expected contribution of the main ORF. For in-frame iORF quantification, we subtracted the coverage of the main ORF in the non-overlapping region. We also used ORF-RATER, which uses a regression strategy to calculate relative expression of overlapping ORFs, resulting in largely similar estimates of translation levels (Extended Data Fig. 10a, b). These measurements show that many of the novel ORFs we annotated are expressed at similar levels to the canonical ORFs (Fig. 4b, Supplementary Table 5). Furthermore, the relative expression of viral proteins seems to be mostly independent of the host cell type (Fig. 4c).

Fig. 4: Translation of host and viral genes.

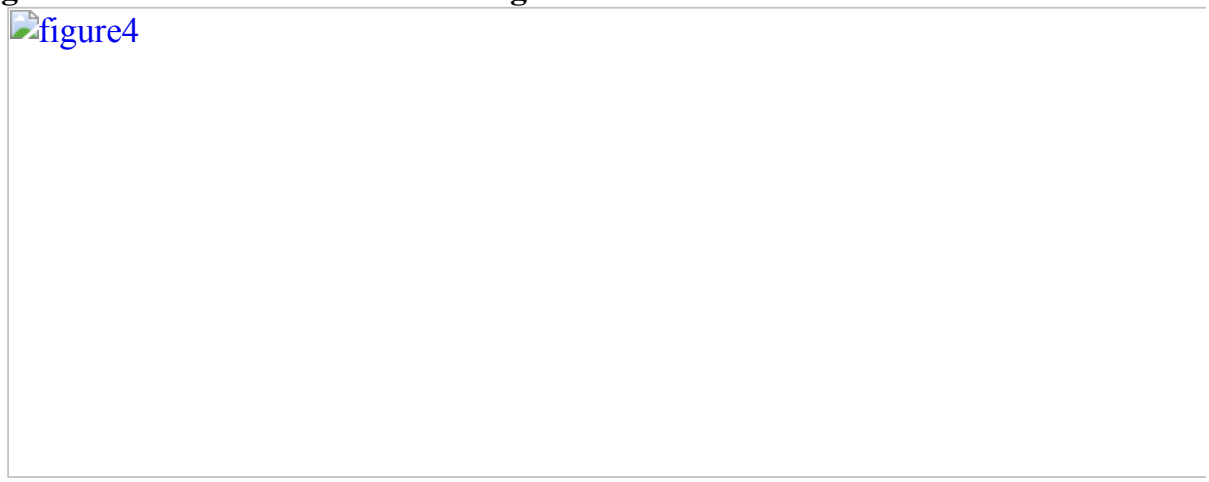

a, Translation levels of canonical viral ORFs in Vero E6 cells at 5 hpi and in Calu3 cells at 7 hpi. ORFs are ordered on the basis of their genomic location. **b**, Viral ORF translation levels, as calculated from ribosome densities for Vero E6 cells at 5 hpi. Solid fill represents canonical ORFs, and striped fill represents novel ORFs. **c**, Scatter plot of viral ORF expression in Vero E6 cells at 5 hpi and Calu3 cells at 7 hpi. Points representing canonical ORFs are outlined in black. **d**–**f**, Relative transcript abundance versus ribosome densities for each host and viral ORF at 5 hpi (**d**) and 24 hpi (**e**) in Vero E6 cells and at 7 hpi in Calu3 cells (**f**). Transcript abundance was estimated by counting the reads that span the corresponding junction and footprint densities were calculated from the CHX sample.

Full size image

Of the novel ORFs we identified, 14 are very short (up to 20 codons) or located in the 5′ UTR of the genomic RNA and therefore likely have a regulatory role, and three are extensions or truncations of canonical ORFs (M, 6 and 7a). We examined the properties of the six out-of-frame iORFs that are longer than 20 aa: one of these ORFs is ORF9b and its truncated version (size 97 aa and 90 aa; Extended Data Fig. 10c, d). ORF9b appears in UniProt annotations and was detected previously[8] in proteomic measurements. Together with our translation measurements this indicates that the product of ORF9b is a bona fide SARS-CoV-2 protein. In addition, we detected an iORF at the 5′ of ORF-S and its truncated version (39 aa and 31 aa; Fig. 3d), and two iORFs within ORF3a (41 aa and 33 aa; Fig. 3c). Mining proteomic measurements of SARS-CoV-2 infected cells[8,9] did not detect peptides that originate from these out-of-frame ORFs, probably owing to challenges in detecting trypsin-digested products from short coding regions[16]. Indeed, two canonical SARS-CoV-2 proteins, ORF7b (43 aa) and ORF-E (75 aa) were also not detected by mass-spectrometry[8,9], and our ribosome-profiling data are the first to show that these SARS-CoV-2 proteins are indeed expressed.

S.iORF1 and 3a.iORF1 are predicted to contain a transmembrane domain (Extended Data Fig. 10e, f) and 3a.iORF2 contains a predicted signal peptide (Extended Data Fig. 10g). Analysis of the conservation of these out-of-frame iORFs in SARS-CoV and in related viruses (sarbecoviruses) revealed that 3a.iORF1 is highly conserved (Supplementary Table 6). This ORF was also identified by three independent comparative genomic studies, which demonstrate that it has a purifying selection signature, implying that it is a functional polypeptide[18,19,20]. In combination, these findings indicate that 3a.iORF1 encodes a functional transmembrane protein, which is conserved throughout sarbecoviruses, and should thus be named ORF3c[19,20]. The second iORF overlapping ORF3a (3a.iORF2) and the iORF overlapping S (S.iORF1) are not conserved in most sarbecoviruses[19] (Supplementary Table 6). The expression level of 3a.iORF2 is much lower compared to those of ORF3a and ORF3c (Fig. 4b,

Extended Data Fig. 9d). A protein corresponding to an extended version of this ORF was pulled down[21] and shown to elicit an antibody response[22], but we found that translation of the truncated version predominated (Extended Data Fig. 10h, i). The internal S-ORF (S.iORF1) is situated just downstream of ORF-S AUG, suggesting that ribosomes might initiate translation via leaky scanning. This region in the S-protein shows extremely rapid evolution[20], but in the SARS-CoV-2 isolates that have been sequenced, its coding capacity is maintained[23]. Future work is needed to delineate whether this ORF, which is highly expressed (Fig. 4b), represents a functional transmembrane protein. Translated ORFs that do not act as functional polypeptides could still be an important part of the immunological repertoire of the virus, as MHC class I bound peptides are generated at higher efficiency from rapidly degraded polypeptides[24].

Finally, although we identified two internal out-of-frame ORFs within ORF3a, we did not detect translation of the SARS-CoV ORF3b homologue, which contains a premature stop codon in SARS-CoV-2 (Extended Data Fig. 10h, i). We also did not find evidence of translation of ORF14, which appears in some SARS-CoV-2 annotations[15] (Extended Data Fig. 10c, d).

Translation of viral proteins relies on the cellular translation machinery, and coronaviruses, like many other viruses, are known to cause host shut-off[25]. To quantitatively evaluate whether SARS-CoV-2 skews the translation machinery to preferentially translate viral transcripts, we compared the ratio of footprints to mRNAs for virus and host CDSs at 5 hpi and 24 hpi in Vero E6 cells and at 7 hpi in Calu3 cells. Because ribosome densities were masked by a contaminant signal at 24 hpi, for samples from this time point we used the footprints that were mapped to subgenomic RNA junctions (and therefore reflect bona fide transcripts) to estimate ribosome densities. In all samples, the virus translation efficiencies fall within the low range of most of the host genes (Fig. 4d–f), indicating that viral transcripts are not preferentially translated in infected cells. Instead, viral transcripts take over the mRNA pool, probably through massive transcription coupled to host-induced RNA degradation[26,27].

In summary, we have delineated the translation landscape of SARS-CoV-2. Comprehensive mapping of the expressed ORFs is a prerequisite for the functional investigation of viral proteins and for deciphering virus–host interactions. An in-depth analysis of the ribosome-profiling experiments demonstrated a highly complex landscape of translation products, including translation of 23 novel viral ORFs and revealed the relative production of canonical viral proteins. The ORFs that we have identified may serve as accessory proteins or as regulatory units controlling the balanced production of different viral proteins. Studies on the functional importance

and antigenic potential of these ORFs will increase our understanding of SARS-CoV-2 and coronaviruses in general.

Methods

No statistical methods were used to predetermine sample size. The experiments were not randomized. The investigators were not blinded to allocation during experiments and outcome assessment.

Cells and viruses

Vero C1008 (Vero E6) cells (ATCC CRL-1586) were cultured in T-75 flasks with DMEM supplemented with 10% fetal bovine serum (FBS), MEM non-essential amino acids, 2mM l-glutamine, 100 U ml^{-1} penicillin, 0.1 mg ml^{-1} streptomycin, 12.5 U ml^{-1} nystatin (Biological Industries). Calu3 cells (ATCC HTB-55) were cultured in 10-cm plates with DMEM supplemented with 10% FBS, MEM non-essential amino acids, 2 mM l-glutamine, 100 U ml^{-1} penicillin, 1% non-essential amino acid and 1% sodium pyruvate. Caco-2 cells (ATCC HTB-37) were cultured in 10-cm plates with DMEM supplemented with 20% BS, 1% GlutaMAX, 100 U ml^{-1} penicillin, 0.1 mg ml^{-1} streptomycin and 1% sodium pyruvate. A549 cells (ATCC CCL-185) were cultured in 10-cm plates with DMEM supplemented with 10% FBS, 100 U ml^{-1} penicillin, 0.1 mg ml^{-1} streptomycin and 2 mM l-glutamine. All cell lines were purchased from and authenticated by ATCC and tested negative for mycoplasma. Monolayers were washed once with DMEM (for Vero E6) or RPMI (for Calu3, A549 and Caco-2) without FBS and infected with SARS-CoV-2 virus, at a multiplicity of infection (MOI) of 0.2, For Calu3 infection, 20 μg ml^{-1} TPCK trypsin (Thermo scientific) was added unless otherwise stated. After 1 h of infection, cells were cultured in their respective medium supplemented with 2% FBS, MEM non-essential amino acids, l-glutamine and penicillin–streptomycin–nystatin at 37 °C with 5% CO_2. SARS-CoV-2 (GISAID accession no. EPI_ISL_406862), was provided by Bundeswehr Institute of Microbiology, Munich, Germany. It was propagated (4 passages) and titred on Vero E6 cells and then sequenced (details below) before it was used. SARS-CoV-2 BavPat1/2020 Ref-SKU: 026V-03883 was provided by C. Drosten, Charité–Universitätsmedizin Berlin, Germany. It was propagated (5 passages), titred on Vero E6 and then sequenced before use in experiments. Infected cells were collected at the indicated times as described below. Handling and work with SARS-CoV-2 virus was conducted in a Biosafety Level 3 facility in accordance with the biosafety guidelines of the Israel Institute for Biological Research. The Institutional Biosafety Committee of Weizmann Institute approved the protocol used in these studies.

Preparation of ribosome-profiling and RNA-seq samples

For RNA-seq, cells were washed with PBS and then collected with Tri-Reagent (Sigma-Aldrich), total RNA was extracted, and poly(A) selection was performed using Dynabeads mRNA DIRECT Purification Kit (Invitrogen). mRNA samples were subjected to DNaseI treatment and 3′ dephosphorylation using FastAP Thermosensitive Alkaline Phosphatase (Thermo Scientific) and T4 PNK (NEB) followed by 3′ adaptor ligation using T4 ligase (NEB). The ligated products were used for reverse transcription with SSIII (Invitrogen) for first-strand cDNA synthesis. The cDNA products were 3′ ligated with a second adaptor using T4 ligase and amplified with 8 cycles of PCR for final library products of 200–300 bp. For Ribo-seq libraries, cells were treated with 50 μM LTM for 30 min or 2 μg ml^{-1} Harr for 5 min for translation initiation libraries, or left untreated for the translation-elongation libraries (CHX library). All three samples were subsequently treated with 100 μg ml^{-1} CHX for 1 min. Cells were then placed on ice, washed twice with PBS containing 100 μg ml^{-1} CHX, scraped from the T-75 flasks (Vero E6 cells) or 10-cm plates (Calu3 cells), pelleted and lysed with lysis buffer (1% Triton X-100 in 20 mM Tris pH 7.5, 150 mM NaCl, 5 mM $MgCl_2$, 1 mM dithiothreitol supplemented with 10 U ml^{-1} Turbo DNase and 100 μg ml^{-1} CHX). After lysis, samples stood on ice for 2 h and subsequent Ribo-seq library generation was performed as previously described[4]. In brief, cell lysate was treated with RNaseI for 45 min at room temperature followed by SUPERase-In quenching. Sample was loaded on sucrose solution (34% sucrose, 20 mM Tris pH 7.5, 150 mM NaCl, 5 mM $MgCl_2$, 1 mM dithiothreitol and 100 μg ml^{-1} CHX) and spun for 1 h at 100,000 rpm in a TLA-110 rotor (Beckman) at 4 °C. Pellet was collected using TRI reagent and the RNA was collected using chloroform phase separation. For size selection, 15 μg total RNA was separated on a 15% TBE-urea gel for 65 min, and 28–34 footprints were excised using 28 and 34 flanking RNA oligos, followed by RNA extraction and Ribo-seq protocol[4].

Virus genomic sequencing

RNA from viruses (culture supernatant after removal of cell debris) was extracted using the viral RNA kit (Qiagen). The SMARTer Pico RNA V2 Kit (Clontech) was used for library preparation. Genome sequencing was conducted on the Illumina Miseq platform, in a single read mode 60 bp for BetaCoV/Germany/BavPat1/2020 EPI_ISL_406862 and in a paired-end mode 150 bp × 2 for BavPat1/2020 Ref-SKU: 026V-03883 producing 2,239,263 and 4,332,551 reads, respectively. Reads were aligned to the viral genome using STAR 2.5.3a aligner. Even coverage along the genome was assessed and the relative abundance junctions (which may reflect genomic deletion) were calculated. For EPI_ISL_406862 passage 4 (that was used for Vero E6 cells infection) the junctions that were found in more than 1% of genomes are

listed in Supplementary Table 2. For BavPat1/2020 Ref-SKU: 026V-03883 passage 5 (that was used for Calu3 infection) no junctions in abundance of more than 1% of the genomes were detected. All genomic sequencing data was recorded.

Sequence alignment, metagene analysis

Sequencing reads were aligned as previously described[28]. In brief, linker (CTGTAGGCACCATCAAT) and poly(A) sequences were removed and the remaining reads were aligned to the *Chlorocebus sabaeus* genome (ENSEMBL release 99) and to the SARS-Cov-2 genome (Genebank NC_045512.2 with 3 changes to match the used strain (BetaCoV/Germany/BavPat1/2020 EPI_ISL_406862): C241T, C3037T, A23403G) for infection of Vero E6 cells, or to the hg19 and NC_045512.2 sequence with the same sequence changes for infection of Calu3. Alignment was performed using Bowtie v.1.1.2[29] with a maximum of two mismatches per read. Reads that were not aligned to the genome were aligned to the transcriptome of *C. sabaeus* (ENSEMBL) and to SARS-CoV-2 junctions that were recently annotated[12]. The aligned position on the genome was determined as the 5′ position of RNA-seq reads, and for Ribo-seq reads, the P site of the ribosome was calculated according to reads length using the offset from the 5′ end of the reads that was calculated from canonical cellular ORFs. The offsets used are +12 for reads that were 28–29 bp and +13 for reads that were 30–33 bp. Reads that were different in length were discarded. In all figures presenting ribosome-density data, all footprint lengths (28–33 bp) are presented.

Novel junctions were mapped using STAR 2.5.3a aligner[30], with running flags as suggested[12] to overcome filtering of non-canonical junctions. Reads aligned to multiple locations were discarded. Junctions with 5′ break sites mapped to genomic location 55–85 were assigned as leader-dependent junctions. Matching of leader junctions to ORFs and categorization of junctions as canonical or non-canonical, was adapted from supplementary table 3 in ref. [12] or was assigned manually for strong novel junctions that appear only in our data.

For the metagene analysis only genes with more than 50 reads were used. For each gene, normalization was done to its maximum signal and each position was normalized to the number of genes contributing to the position. In the virus 24-h samples, normalization for each gene was done to its maximum signal within the presented region.

Quantification of gene expression

The deconvolution of RNA expression was done by subtracting the reads per kilobase of transcript, per million mapped reads (RPKM) of an ORF from the RPKM of the

ORF located just upstream of it in the genome. The junction counts were based on STAR alignment number of uniquely mapped reads crossing the junction. For comparing transcript and footprint expression level, RNA and footprint counts from bowtie alignments were normalized to units of RPKM to normalize for gene length and for sequencing depth. On the basis of the correlation between the deconvoluted RPKM and junction abundance of the subgenomic RNAs, the genomic RNA abundance was estimated and was used to estimate ORF1a and ORF1b RNA levels compared with footprint levels.

The estimation of the viral footprint densities from the 24 hpi samples was performed by calculating the ratio of the RPKM of ORF1a to the total number of leader canonical junctions at 5 hpi. This ratio was used as a factor to calculate a proxy for the 'true' viral footprint densities from the number of footprints that were mapped to leader canonical junctions at 24 hpi.

To quantify the translation levels of novel viral ORFs at 5 hpi and 7 hpi, many of which are overlapping, three types of calculations were used, based on ORF type. For ORFs that have a unique region, with no overlap to any other ORF, bowtie-aligned read density was calculated in that region. For out-of-frame iORFs, the read density of the iORF region was calculated by estimating the expected 3-bp periodicity distribution of footprints based on non-overlapping translated regions in the main ORF. Using linear regression, we calculated the relative contribution of the frames of the main and of the iORF to the reads covering the region of the iORF. The relative contribution of the iORF was then multiplied by the read density in that region to obtain the estimated translation level of the internal out-of-frame ORF. For in-frame iORFs the read density of the main overlapping ORF was calculated from a non-overlapping region and then subtracted from the read density in the overlapping iORF region to get an estimate of translation levels of the iORF. In cases where the unique region used to calculate read density contained the start codon of the ORF, the first 20% of the codons in the region were excluded from the calculation to avoid bias from initiation peaks, unless the region was very short and trimming it would harm the ability to estimate coverage (ORF 8 and extended ORF M). The exact regions that were used for calculation can be found in Supplementary Table 5. Finally, read density was normalized to the length of the region used for calculation and to the sum of length normalized reads in each sample to get transcripts per kilobase million (TPM) values. *P* values for the relative contribution levels of out-of-frame ORFs were calculated from both replicates using a mixed-effects linear model using the three-base periodicity distribution as the fixed effect and the replicates as random effect. In parallel, ORF-RATER was used to quantify the translation levels of the viral ORFs (using regression), giving largely similar values (Spearman's $R = 0.92$ and 0.87 in Vero E6 and Calu3 cells, respectively).

Prediction of translation initiation sites

Translation initiation sites were predicted using PRICE[16] and ORF-RATER[17]. To estimate the codons generating the sequencing reads with maximum likelihood, PRICE requires a predefined set of annotated coding sequences from the same experiment. Thus, it does not perform well on reference sequences with a small number of annotated ORFs such as SARS-CoV-2. As our experiment generated ribosome footprints from both SARS-CoV-2 and host mRNAs, which were exposed to the exact same conditions in the protocol, we used annotated CDSs from the host cells to evaluate the parameters of the experiment. For libraries of infected Vero E6 cells, sequencing reads were aligned using Bowtie to a fasta file containing chromosome 20 of *C. sabaeus* (1,240 annotated start codons, downloaded from ensembl: ftp://ftp.ensembl.org/pub/release99/fasta/chlorocebus_sabaeus/dna/) and the genomic sequence of SARS-CoV-2 (Refseq NC_045512.2). A gtf file with the annotations of *C. sabaeus* and SARS-CoV-2 genomes was constructed and provided as the annotations file when running PRICE. For technical reasons, the annotation of the first CDS of the two CDSs in the ORF1ab gene was deleted because having two CDSs encoded from a single gene was not permitted by PRICE. For libraries of infected Calu3 cells sequencing reads were mapped to a fasta file containing chromosome 1 of hg19 (2,843 annotated start codons) and the genomic sequence of SARS-CoV-2 (Refseq NC_045512.2). A gtf file with the annotations of hg19 and SARS-CoV-2 genomes was constructed and provided as the annotations file when running PRICE. For the data that were generated from infected Vero E6 cells at 5 hpi, training and ORF prediction by PRICE were done once using the CHX data from both replicates, and again using all Ribo-seq libraries from both replicates, and the resulting predictions were combined. To test reproducibility, the same predictions were performed on each replicate separately. For the data that were generated from infected Calu3 cells at 7 hpi training and ORF prediction by PRICE were done using all Ribo-seq libraries from both replicates. The predictions were further filtered to include only ORFs with at least 100 reads at the initiation site in the LTM samples of at least one replicate. ORFs were then defined by extending each initiating codon to the next in-frame stop codon.

ORF-RATER was used with the default values besides allowing all start codons with at most one mismatch to ATG. For each cell type, two runs of ORF-RATER were used: one in which ORF-RATER was trained on cellular annotations (chr 20 for the Vero E6 cells, and chr 1 for the Calu cells) and SARS-CoV-2 canonical ORFs (similar to the procedure that was used for running PRICE); and a second in which SARS-CoV-2 canonical ORFs were used for training. In both cases, ORF1b and ORF10 were omitted from the training set. BAM files from STAR alignment were used as input. The CHX data from both replicates was used in the first prune step to omit low-coverage ORFs. The calculations of the P-site offsets and the regression were performed for each type of Ribo-Seq library separately. The final score was calculated

on the basis of all three types of libraries. A score of 0.5 was used as cut-off for the final predictions; these were further manually curated. Additional ORFs that were not recognized by the trained models (probably owing to differences in the features of viral genome compared with cellular genomes) but presented reproducible translation profile in the two cell lines were added manually to the final ORF list (Supplementary Table 4). ORFs were manually identified as such if they had reproducible initiation peaks in the CHX libraries that were enhanced in the LTM and Harr libraries, and exhibited increased CHX signal in the correct reading frame along the coding region.

Mapping reads to CUG initiation upstream of the TRS leader

Reads from ribosome-profiling libraries were aligned using bowtie to a single reference that contained the transcripts and the genome allowing no mismatches or gaps. Reads with P-site mapped to position 59 of the viral genome were collected and divided to four groups according to the nucleotide in position +17 of the read (position 76 of the genome). The first group contains reads that are short (28 nucleotides) and do not have any nucleotide at position +17. The other three groups, referred to as T, A and G, correspond to combinations of genomic and subgenomic RNAs based on their sequence, as shown in Extended Data Fig. 6d. Group T is attributed to the genome or to ORF E and ORF M subgenomic RNAs, group A to the subgenomic RNAs of ORF S, ORF7a, ORF8 and ORF N, and group G to the subgenomic RNA of ORF 6. Reads that mapped uniquely to the subgenomic RNA of ORF3a were excluded from calculation, and the number of reads in each group was summed. Group T, containing genomic reads, was further divided on the basis of the nucleotide at position +18, where reads with A at that position can originate from the subgenomic RNA of ORF M and reads with T at that position can originate from the genome or from the subgenomic RNA of ORF E. Final division of the genomic group was done based on position +19 where T corresponds to genomic reads and A corresponds to ORF E subgenomic reads. RNA values as calculated from junction densities (as described in 'Quantification of gene expression') were summed for the subgenomic and genomic RNAs in each group. The analysis was performed for each ribosome-profiling library separately.

Mining of proteomics data and transmembrane predictions

Data from ref. [8] was searched using the Byonic search engine with 10 ppm tolerance for MS1 and 20 ppm tolerance for MS2, against the concatenated database containing our 26 novel ORFs as well as the human proteome DB (SwissProt, November 2019), and the SARS-CoV-2 proteome. Modifications allowed were fixed carbamidomethylation on C, fixed TMT6 on K and peptide N terminus, variable K8 and R10 SILAC labelling, variable M oxidation and Variable NQ deamidation. Data downloaded from ref. [9] was searched with the Byonic search engine using 10 ppm

tolerance for MS1 and 0.6 Da tolerance for MS2, against the concatenated database containing our 26 novel ORFs as well as the human proteome DB (SwissProt, November 2019), and the SARS-CoV-2 proteome. Modifications allowed were fixed carbamidomethylation on C, variable N-terminal protein acetylation, M oxidation and NQ deamidation. Transmembrane and signal peptide predictions were performed using Phobius[31].

Immunofluorescence

Cells were plated on Ibidi slides, fixed in 3% paraformaldehyde for 20 min, permeabilized with 0.5% Triton X-100 in PBS for 2 min, and then blocked with 2% FBS in PBS for 30 min. Immunostaining was performed with rabbit anti-SARS-CoV-2 serum[32] at a 1:200 dilution. Cells were washed and labelled with anti-rabbit FITC antibody and with DAPI at a 1:200 dilution. Imaging was performed on a Zeiss AxioObserver Z1 wide-field microscope using a ×40 objective and Axiocam 506 mono camera.

Reporting summary

Further information on research design is available in the Nature Research Reporting Summary linked to this paper.

Data availability

All next-generation sequencing data files were deposited in Gene Expression Omnibus under accession number GSE149973. All the RNA-seq and ribosome-profiling data generated in this study can be accessed through a UCSC browser session (http://genome.ucsc.edu/s/aharonn/CoV2%2DTranslation). The proteomics data analysed in this study are available from the PRIDE repository with the identifiers PXD017710[8] and PXD018241[9].

References

1. 1.

   Zhu, N. et al. A novel coronavirus from patients with pneumonia in China, 2019. *N. Engl. J. Med*. **382**, 727–733 (2020).

   CAS Article Google Scholar

2. 2.

Stern-Ginossar, N. et al. Decoding human cytomegalovirus. *Science* **338**, 1088–1093 (2012).

ADS CAS Article Google Scholar

3. 3.

Irigoyen, N. et al. High-resolution analysis of coronavirus gene expression by RNA sequencing and ribosome profiling. *PLoS Pathog*. **12**, e1005473 (2016).

Article Google Scholar

4. 4.

Finkel, Y. et al. Comprehensive annotations of human herpesvirus 6A and 6B genomes reveal novel and conserved genomic features. *eLife* **9**, e50960 (2020).

CAS Article Google Scholar

5. 5.

Sola, I., Almazán, F., Zúñiga, S. & Enjuanes, L. Continuous and discontinuous RNA synthesis in coronaviruses. *Annu. Rev. Virol*. **2**, 265–288 (2015).

CAS Article Google Scholar

6. 6.

Lai, M. M. & Stohlman, S. A. Comparative analysis of RNA genomes of mouse hepatitis viruses. *J. Virol*. **38**, 661–670 (1981).

CAS Article Google Scholar

7. 7.

Yogo, Y., Hirano, N., Hino, S., Shibuta, H. & Matumoto, M. Polyadenylate in the virion RNA of mouse hepatitis virus. *J. Biochem*. **82**, 1103–1108 (1977).

CAS Article Google Scholar

8. 8.

Bojkova, D. et al. Proteomics of SARS-CoV-2-infected host cells reveals therapy targets. *Nature* **583**, 469–472 (2020).

ADS CAS Article Google Scholar

9. 9.

Davidson, A. D. et al. Characterisation of the transcriptome and proteome of SARS-CoV-2 reveals a cell passage induced in-frame deletion of the furin-like cleavage site from the spike glycoprotein. *Genome Med*. **12**, 68 (2020).

CAS Article Google Scholar

10. 10.

Ingolia, N. T. et al. Ribosome profiling reveals pervasive translation outside of annotated protein-coding genes. *Cell Rep*. **8**, 1365–1379 (2014).

CAS Article Google Scholar

11. 11.

Dinan, A. M. et al. Comparative analysis of gene expression in virulent and attenuated strains of infectious bronchitis virus at subcodon resolution. *J. Virol*. **93**, 714–733 (2019).

Article Google Scholar

12. 12.

Kim, D. et al. The architecture of SARS-CoV-2 transcriptome. *Cell* **181**, 914–921 (2020).

CAS Article Google Scholar

13. 13.

Schaecher, S. R., Mackenzie, J. M. & Pekosz, A. The ORF7b protein of severe acute respiratory syndrome coronavirus (SARS-CoV) is expressed in virus-infected cells and incorporated into SARS-CoV particles. *J. Virol*. **81**, 718–731 (2007).

CAS Article Google Scholar

14. 14.

Davidson, A. D. et al. Characterisation of the transcriptome and proteome of SARS-CoV-2 reveals a cell passage induced in-frame deletion of the furin-like cleavage site from the spike glycoprotein. *Genome Med*. **12**, 68 (2020).

CAS Article Google Scholar

15. 15.

Wu, A. et al. Genome composition and divergence of the novel coronavirus (2019-nCoV) originating in China. *Cell Host Microbe* **27**, 325–328 (2020).

CAS Article Google Scholar

16. 16.

Erhard, F. et al. Improved Ribo-seq enables identification of cryptic translation events. *Nat. Methods* **15**, 363–366 (2018).

CAS Article Google Scholar

17. 17.

Fields, A. P. et al. A regression-based analysis of ribosome-profiling data reveals a conserved complexity to mammalian translation. *Mol. Cell* **60**, 816–827 (2015).

CAS Article Google Scholar

18. 18.

Cagliani, R., Forni, D., Clerici, M. & Sironi, M. Coding potential and sequence conservation of SARS-CoV-2 and related animal viruses. *Infect. Genet. Evol*. **83**, 104353 (2020).

CAS Article Google Scholar

19. 19.

Firth, A. E. A putative new SARS-CoV protein, 3c, encoded in an ORF overlapping ORF3a. *J. Gen. Virol*. https://doi.org/10.1099/jgv.0.001469 (2020).

20. 20.

Jungreis, I., Sealfon, R. & Kellis, M. SARS-CoV-2 gene content and COVID-19 mutation impact by comparing 44 Sarbecovirus genomes. Preprint at

https://doi.org/10.1101/2020.06.02.130955 (2020).

21. 21.

Gordon, D. E. et al. A SARS-CoV-2 protein interaction map reveals targets for drug repurposing. *Nature* **583**, 459–468 (2020).

ADS CAS Article Google Scholar

22. 22.

Hachim, A. et al. Beyond the spike: identification of viral targets of the antibody response to SARS-CoV-2 in COVID-19 patients. Preprint at https://doi.org/10.1101/2020.04.30.20085670 (2020).

23. 23.

Hadfield, J. et al. Nextstrain: real-time tracking of pathogen evolution. *Bioinformatics* **34**, 4121–4123 (2018).

CAS Article Google Scholar

24. 24.

Yewdell, J. W. DRiPs solidify: progress in understanding endogenous MHC class I antigen processing. *Trends Immunol*. **32**, 548–558 (2011).

CAS Article Google Scholar

25. 25.

Abernathy, E. & Glaunsinger, B. Emerging roles for RNA degradation in viral replication and antiviral defense. *Virology* **479-480**, 600–608 (2015).

CAS Article Google Scholar

26. 26.

Huang, C. et al. SARS coronavirus nsp1 protein induces template-dependent endonucleolytic cleavage of mRNAs: viral mRNAs are resistant to nsp1-induced RNA cleavage. *PLoS Pathog*. **7**, e1002433 (2011).

CAS Article Google Scholar

27. 27.

Kamitani, W., Huang, C., Narayanan, K., Lokugamage, K. G. & Makino, S. A two-pronged strategy to suppress host protein synthesis by SARS coronavirus Nsp1 protein. *Nat. Struct. Mol. Biol*. **16**, 1134–1140 (2009).

CAS Article Google Scholar

28. 28.

Tirosh, O. et al. The transcription and translation landscapes during human cytomegalovirus infection reveal novel host–pathogen interactions. *PLoS Pathog*. **11**, e1005288 (2015).

Article Google Scholar

29. 29.

Langmead, B., Trapnell, C., Pop, M. & Salzberg, S. L. Ultrafast and memory-efficient alignment of short DNA sequences to the human genome. *Genome Biol*. **10**, R25 (2009).

Article Google Scholar

30. 30.

Dobin, A. et al. STAR: ultrafast universal RNA-seq aligner. *Bioinformatics* **29**, 15–21 (2013).

CAS Article Google Scholar

31. 31.

Käll, L., Krogh, A. & Sonnhammer, E. L. L. A combined transmembrane topology and signal peptide prediction method. *J. Mol. Biol*. **338**, 1027–1036 (2004).

Article Google Scholar

32. 32.

Yahalom-Ronen, Y. *et al*. A single dose of recombinant VSV-ΔG-spike vaccine provides protection against SARS-CoV-2 challenge. Preprint at https://doi.org/10.1101/2020.06.18.160655 (2020).

Download references

Acknowledgements

We thank Stern-Ginossar laboratory members, I. Ulitsky and S. Schwartz for providing valuable feedback; E. Zehavi, M. Shnayder, I. Ulitsky and N. Gil for technical assistance; E. Wyler for the Calu3 cells; and I. Cohen-Gihon for sharing sequencing and bioinformatics data. This study was supported by the Ben B. and Joyce E. Eisenberg Foundation. Work in the Stern-Ginossar lab is supported by ERC-CoG-2019- 864012 and by the ISF grant no. 1526/18. S.W.-G. is the recipient of the HSFP fellowship, EMBO non-stipendiary Long-Term Fellowship, the Gruss-Lipper Postdoctoral Fellowship, the Zuckerman STEM Leadership Program and the Rothschild Postdoctoral Fellowship. N.S.-G. is an incumbent of the Skirball Career Development Chair in New Scientists and is a member of EMBO Young Investigator Program.

Author information

Author notes

1. These authors contributed equally: Yaara Finkel, Orel Mizrahi

Affiliations

1. Department of Molecular Genetics, Weizmann Institute of Science, Rehovot, Israel

   Yaara Finkel, Orel Mizrahi, Aharon Nachshon, Michal Schwartz & Noam Stern-Ginossar

2. Broad Institute of MIT and Harvard, Cambridge, MA, USA

   Shira Weingarten-Gabbay

3. Department of Organismal and Evolutionary Biology, Harvard University, Cambridge, MA, USA

   Shira Weingarten-Gabbay

4. de Botton Institute for Protein Profiling, The Nancy and Stephen Grand Israel National Center for Personalised Medicine, Weizmann Institute of Science, Rehovot, Israel

   David Morgenstern

5. Department of Infectious Diseases, Israel Institute for Biological Research, Ness Ziona, Israel

   Yfat Yahalom-Ronen, Hadas Tamir, Hagit Achdout, Sharon Melamed, Shay Weiss, Tomer Israely & Nir Paran

6. Department of Biochemistry and Molecular Genetics, Israel Institute for Biological Research, Ness Ziona, Israel

   Dana Stein, Ofir Israeli & Adi Beth-Din

Authors

1. Yaara Finkel
   View author publications

   You can also search for this author in PubMed Google Scholar

2. Orel Mizrahi
   View author publications

   You can also search for this author in PubMed Google Scholar

3. Aharon Nachshon
   View author publications

   You can also search for this author in PubMed Google Scholar

4. Shira Weingarten-Gabbay
   View author publications

   You can also search for this author in PubMed Google Scholar

5. David Morgenstern
   View author publications

   You can also search for this author in PubMed Google Scholar

6. Yfat Yahalom-Ronen
   View author publications

   You can also search for this author in PubMed Google Scholar

7. Hadas Tamir

View author publications

You can also search for this author in PubMed Google Scholar

8. Hagit Achdout
   View author publications

   You can also search for this author in PubMed Google Scholar

9. Dana Stein
   View author publications

   You can also search for this author in PubMed Google Scholar

10. Ofir Israeli
    View author publications

    You can also search for this author in PubMed Google Scholar

11. Adi Beth-Din
    View author publications

    You can also search for this author in PubMed Google Scholar

12. Sharon Melamed
    View author publications

    You can also search for this author in PubMed Google Scholar

13. Shay Weiss
    View author publications

    You can also search for this author in PubMed Google Scholar

14. Tomer Israely
    View author publications

    You can also search for this author in PubMed Google Scholar

15. Nir Paran
    View author publications

    You can also search for this author in PubMed Google Scholar

16. Michal Schwartz

View author publications

You can also search for this author in PubMed Google Scholar

17. Noam Stern-Ginossar
View author publications

You can also search for this author in PubMed Google Scholar

Contributions

Y.F., O.M., N.P and N.S.-G. conceptualized the study; O.M. performed experiments; Y.F., A.N. and S.W.-G. performed data analysis; Y.Y.-R., H.T., H.A., S.M., S.W., D.S., O.I., A.B.-D., T.I. and N.P. performed work with SARS-CoV-2. D.M. mined published proteomic data; Y.F., O.M., A.N., M.S. and N.S.-G. interpreted data; and M.S. and N.S.-G. wrote the manuscript with contributions from all other authors.

Corresponding author

Correspondence to Noam Stern-Ginossar.

Ethics declarations

Competing interests

The authors declare no competing interests.

Additional information

Peer review information *Nature* thanks Volker Thiel, Petra Van Damme and the other, anonymous, reviewer(s) for their contribution to the peer review of this work. Peer reviewer reports are available.

Publisher's note Springer Nature remains neutral with regard to jurisdictional claims in published maps and institutional affiliations.

Extended data figures and tables

Extended Data Fig. 1 24 h infection with SARS-CoV-2 of Vero E6 cells.

Vero E6 cells were infected with SARS-CoV-2 at an MOI = 0.2 and 24 hpi the cells were fixed and stained with antisera against SARS-CoV-2 (green) and D API (blue). The experiment was performed once and representative microscopy images are presented. Scale bars are 200µm.

Extended Data Fig. 2 Footprint and RNA-seq profiles of cellular and viral genes from SARS-CoV-2 infected Vero E6 cells.

a, **b**, Metagene analysis of read densities at the 5′ and the 3′ regions of cellular (**a**) and viral (**b**) protein coding genes as measured by the different Ribo-seq approaches and RNA-seq at 5 hpi and 24 hpi, from two biological replicates. The *x* axis shows the nucleotide position relative to the start or the stop codons. The read densities are shown with different colours indicating the three frames relative to the main ORF (red, frame 0; black, frame +1; grey, frame +2). NA reflect samples in which we did not obtain enough cellular genes that contain 50 reads at the 5′ or 3′ regions to generate metagene profile. **c**, Scatter plots depicting the number of reads in every position along the SARS-CoV-2 genome in two independent biological replicates, demonstrating reproducibility between our replicates at single nucleotide resolution. Pearson's *R* of log-transformed values is presented.

Extended Data Fig. 3 Footprint profiles reveal potential ribosome pausing sites within ORF1a and ORF1b.

Read densities are presented for ORF1a and ORF1b at 5 hpi from two biological replicates. The read densities are shown with different colours indicating the three frames relative to the translated frame of ORF1a (red, frame 0; black, frame +1; grey, frame +2). Black arrows mark potential ribosome pausing sites and their genomic positions.

Extended Data Fig. 4 The abundance of subgenomic RNAs.

a, Measurement of subgenomic RNA abundance using deconvolution of RNA densities versus using relative abundance of RNA reads spanning leader-body junctions, for seven canonical viral ORFs. ORF6, ORF7b and ORF10 obtained negative values in the RNA deconvolution, probably due to their short length and relative weaker expression. For ORF10 also no reads spanning leader-body junctions were detected. Spearman's *R* is presented. **b**, **c**, Scatter plots presenting the abundance of junction-spanning RNA-seq reads from two biological replicates from (**b**) 5 hpi and (**c**) 24 hpi. **d**, Scatter plots presenting the average abundance of junction-spanning RNA-seq reads from 24 hpi versus data from Kim et al.[12] Viral reads that span canonical leader-dependent junctions are marked in red, non-canonical leader-

dependent junctions are marked in green, non-canonical leader-independent junctions are marked in purple and non-canonical leader-dependent junctions originating from genomic deletions are marked in cyan. Pearson's *R* of log-transformed values is presented. **e**, Ribo-seq (CHX) and RNA densities over the 7 aa deletion in the S protein. Lower panels present the amino acid sequence in the region and the translation of the WT and of the 7-aa-deleted version of the S protein.

Extended Data Fig. 5 Footprint profiles reveal novel viral coding regions.

a–**i**, Read densities over SARS-CoV-2 unannotated translated ORFs as measured by the different Ribo-seq approaches from both replicates at 5 hpi. The read densities are shown with different colours indicating the three frames relative to the main ORF in each figure (red, frame 0; black, frame +1; grey, frame +2). Filled and open rectangles indicate the canonical and novel ORFs, respectively. ORFs starting in near cognate start codon are labelled with stripes. **a**, In frame internal initiation within ORF6 generating truncated product. **b**, In frame internal initiation within ORF7a. **c**, Out of frame internal initiations within ORF3a. **d**, Out of frame internal initiations within ORF-S. **e**, Out of frame internal initiation within ORF-M. **f**, An extended version of ORF-M. **g**, uORF that overlaps ORF10 initiation and in frame internal initiation generating truncated ORF10 product. **h**, Two uORFs embedded in ORF1ab 5′ UTR. **i**, Non-canonical CUG initiation upstream of the TRS leader.

Extended Data Fig. 6 The CUG initiation is enriched on the genomic RNA.

a, Comparison of the ribosome footprint read length distributions of reads that align to the CUG upstream of the TRS-L (red) and reads that align to ORF-N AUG (green). **b**, **c**, Read densities over the TRS-L CUG on the genomic RNA (**b**) or ORF-N transcript (**c**) as measured by the different Ribo-seq approaches at 5 hpi. The read densities are shown with different colours indicating the three frames relative to the CUG (red, frame 0; black, frame +1; grey, frame +2). Rectangles indicate adjacent ORFs and the striped rectangles indicate the ORFs initiating at the TRS-L CUG. **d**, The sequences of the genome and the most abundant subgenomic transcripts divided to three groups based on the base in position 76. The CUG position is labelled in grey and the location of the junction is labelled by a vertical line. **e**, The relative number of footprint reads that their P-site was mapped to the CUG (dark red) for each of the transcript groups (as defined in **c**) and the relative RNA abundance of these transcript groups (green). Data are presented for CHX, Harr and LTM libraries. **f**, The relative number of footprint reads that their P-site was mapped to the CUG (dark red) in ORF-M transcript or in ORF-E and the Genome RNA and the relative RNA abundance (green). Only footprint sizes 31–33 bp that allow unique alignment were used. Data

are presented for CHX, Harr and LTM libraries. **g**, The number of footprint reads that their P-site was mapped to the CUG in the genome or in ORF-E transcript out of all reads and the relative abundance of these RNAs. Only footprint sizes 32–33 bp that allow unique alignment were used. Read numbers is presented for CHX, Harr and LTM libraries and the relative RNA abundance is presented as percentage of total RNA included in the comparison.

Extended Data Fig. 7 SARS-CoV-2 infection of Calu3 cells.

a, Calu3 cells were either left uninfected, infected with SARS-CoV-2, or infected with SARS-CoV-2 in the presence of trypsin. 12 hpi the cells were fixed and stained with antisera against SARS-CoV-2 (green) and DAPI (blue). The experiment was performed once and representative microscopy images are presented. Scale bars are 200 µm. **b**, Metagene analysis of read densities at the 5′ and the 3′ regions of viral protein coding genes as measured by the different Ribo-seq approaches and RNA-seq at 7 hpi from two biological replicates. The *x* axis shows the nucleotide position relative to the start or the stop codons. The read densities are shown with different colours indicating the three frames relative to the main ORF (red, frame 0; black, frame +1; grey, frame +2).

Extended Data Fig. 8 Footprint profiles reveal novel viral coding regions are also translated in infected Calu3 cells.

a–**i**, Read densities over SARS-CoV-2 unannotated translated ORFs as measured by the different Ribo-seq approaches from both replicates at 7 hpi. The read densities are shown with different colours indicating the three frames relative to the main ORF in each figure (red, frame 0; black, frame +1; grey, frame +2). Filled and open rectangles indicate the canonical and novel ORFs, respectively. ORFs starting in near cognate start codon are labelled with stripes. **a**, In frame internal initiation within ORF6 generating truncated product. **b**, In frame internal initiation within ORF7a. **c**, Out of frame internal initiation within ORF3a. **d**, Out of frame internal initiation within ORF-S. **e**, Out of frame internal initiation within ORF-M. **f**, An extended version of ORF-M. **g**, uORF that overlap ORF10 initiation and in frame internal initiation generating truncated ORF10 product. **h**, Two uORFs embedded in ORF1ab 5′ UTR. **i**, Non-canonical CUG initiation upstream of the TRS-leader.

Extended Data Fig. 9 Reproduciblity of viral ORFs translation.

a–**c**, Scatter plot presenting the correlation of footprint densities at each initiation site relative to a 8bp window 3 nucleotides downstream of the initiation site in LTM treated samples between two biological replicates of infected Vero E6, 5 hpi (**a**), between two biological replicates of infected Calu3 cells, 7 hpi (**b**) and between

infected Vero E6 cells at 5 hpi and Calu3 cells at 7 hpi (**c**). Canonical ORFs are marked in dark green and newly identified ORFs are marked in light green. As a control, the relative occupancy of random positions was calculated in the same way (grey). Dashed lines mark the equal ratio of one. Spearman's *R* is presented. **d**, The position of ribosome footprints relative to the reading frame in all canonical ORFs and novel ORFs excluding in-frame iORFs are presented for our measurements of infected Vero E6 cells at 5 hpi (lower panels) and infected Calu3 cells (upper panels). Filled and open rectangles indicate the canonical and novel ORFs, respectively. ORFs starting in near cognate start codons are labelled with stripes. The frame of the footprints is summed on each of the indicated regions and is presented relative to the frame of the canonical ORF in each of these loci. In all non-overlapping regions, beside ORF10 in Vero E6 cells, clear enrichment to the translated frame is observed indicating active translation. For out-of-frame overlapping ORFs the bar of its frame is labelled by colour and the percentage of the footprints that originate from the overlapping frame as was calculated from linear regression is presented together with the corresponding *P* value for the contribution of the out-of-frame ORF to the frame distribution of the total reads in this region, using two degrees of freedom that reflect the two replicates. In two out-of-frame overlapping ORFs, ORF3.iORF2 and ORF8.iORF the expression relative to the main ORF was low and did not lead to a significant shift in the translation signal. In all other ORFs there is a significant signal in the alternative frame indicating active translation.

Extended Data Fig. 10 Characteristics of novel predicted ORFs.

a, **b**, Scatter plots presenting the correlation between translation levels as estimated by our curated quantification and as calculated by ORF-RATER for Vero (**a**) and Calu3 cells (**b**). Points representing canonical ORFs are outlined in black. Spearman's *R* is presented. **c**, **d**, Read densities over ORF-N as measured by the different Ribo-seq approaches in two replicates in Vero cells at 5 hpi (**c**) and Calu3 cells at 7 hpi (**d**). The read densities are shown with different colours indicating the three frames relative to the main ORF in each figure (red, frame 0; black, frame +1; grey, frame +2). Filled and open rectangles indicate the canonical and novel ORFs, respectively. ORF14 location is marked based on the homology to SARS-CoV. **e**, Transmembrane region predicted in S.iORF1 using Phobius. **f**, Transmembrane region predicted in ORF3c (3a.iORF1) using Phobius. **g**, Signal peptide prediction in 3a.iORF2 as predicted using Phobius. **h**, **i**, Read densities over ORF3a as measured by the different ribosome profiling approaches in two replicates in Vero cells at 5 hpi (**h**) and Calu3 cells at 7 hpi (**i**). The read densities are shown with different colours indicating the three frames relative to the main ORF in each figure (red, frame 0; black, frame +1; grey, frame +2). Filled and open rectangles indicate the canonical and novel ORFs, respectively. ORF3b and extended iORF2 are marked based on the homology to SARS-CoV.

Supplementary information

Reporting Summary

Supplementary Table 1.

Junctions sites detected from junction spanning reads This table lists junction sites that were identified by Kim et al. with more than 100 reads and were also detected in our RNA reads.

Supplementary Table 2.

Junctions sites uniquely detected in our samples This table lists junction sites that were identified in our RNA samples with more than 50 reads but were low or unidentified by Kim et al.

Supplementary Table 3.

Potential junction spanning SARS-CoV-2 ORFs that can be translated from the CUG initiation upstream the TRS-leader This table lists junction spanning SARS-CoV-2 ORFs that can be translated from the CUG initiation upstream the TRS-leader at each of the subgenomic RNAs.

Supplementary Table 4.

Novel SARS-CoV-2 ORFs that have been identified in our study This table lists all the SARS-CoV-2 translated ORFs identified in this study.

Supplementary Table 5.

Translation levels of SARS-CoV-2 ORFs This table lists all translated SARS-CoV-2 ORFs, canonical and newly identified, and their estimated translation levels based on ribosome profiling

Supplementary Table 6.

Multiple sequence alignment for canonical and novel SARS-CoV-2 ORFs in Sarbecoviruses This table includes links for annotated multiple sequence alignment (MSA) views of all SARS-CoV-2, canonical and novel, described in this study, using the CodAlignView tool [38]. The MSA includes SARS-CoV-2, SARS-CoV and 42 bat coronavirus genomes [30].

Peer Review File

Rights and permissions

Reprints and Permissions

About this article

Check for updates

Cite this article

Finkel, Y., Mizrahi, O., Nachshon, A. *et al.* The coding capacity of SARS-CoV-2. *Nature* **589,** 125–130 (2021). https://doi.org/10.1038/s41586-020-2739-1

Download citation

- Received: 15 May 2020
- Accepted: 01 September 2020
- Published: 09 September 2020
- Issue Date: 07 January 2021
- DOI: https://doi.org/10.1038/s41586-020-2739-1

Further reading

- **Will SARS-CoV-2 Infection Elicit Long-Lasting Protective or Sterilising Immunity? Implications for Vaccine Strategies (2020)**

  - David S. Kim
  - , Sarah Rowland-Jones
  - & Ester Gea-Mallorquí

  Frontiers in Immunology (2020)

- **Dynamically evolving novel overlapping gene as a factor in the SARS-CoV-2 pandemic**

  - Chase W Nelson
  - , Zachary Ardern
  - , Tony L Goldberg
  - , Chen Meng
  - , Chen-Hao Kuo
  - , Christina Ludwig
  - , Sergios-Orestis Kolokotronis
  - & Xinzhu Wei

  eLife (2020)

- **The Role of Type I Interferons in the Pathogenesis and Treatment of COVID-19**

  - Gideon Schreiber

  Frontiers in Immunology (2020)

- **Pervasive generation of non-canonical subgenomic RNAs by SARS-CoV-2**

  - Jason Nomburg
  - , Matthew Meyerson
  - & James A. DeCaprio

  Genome Medicine (2020)

- **A Novel In-Cell ELISA Assay Allows Rapid and Automated Quantification of SARS-CoV-2 to Analyze Neutralizing Antibodies and Antiviral Compounds**

  - Lara Schöler
  - , Vu Thuy Khanh Le-Trilling
  - , Mareike Eilbrecht
  - , Denise Mennerich
  - , Olympia E. Anastasiou
  - , Adalbert Krawczyk
  - , Anke Herrmann

- , Ulf Dittmer
- & Mirko Trilling

Frontiers in Immunology (2020)

Comments

By submitting a comment you agree to abide by our Terms and Community Guidelines. If you find something abusive or that does not comply with our terms or guidelines please flag it as inappropriate.

Download PDF

This article was downloaded by **calibre** from https://www.nature.com/articles/s41586-020-2739-1

- Article
- Published: 25 November 2020

Commensal-driven immune zonation of the liver promotes host defence

- Anita Gola ORCID: orcid.org/0000-0003-1431-1398[1 nAff9],
- Michael G. Dorrington[2 na1],
- Emily Speranza[1,3 na1],
- Claudia Sala ORCID: orcid.org/0000-0002-4889-1047[4],
- Rochelle M. Shih ORCID: orcid.org/0000-0002-3218-4479[1],
- Andrea J. Radtke[1],
- Harikesh S. Wong[1],
- Antonio P. Baptista[1,5,6],
- Jonathan M. Hernandez[7],
- Gastone Castellani[8],
- Iain D. C. Fraser[2] &
- Ronald N. Germain ORCID: orcid.org/0000-0003-1495-9143[1]

Nature **volume 589**, pages131–136(2021)Cite this article

- 7459 Accesses
- 1 Citations
- 130 Altmetric
- Metrics details

Subjects

- Chemokines
- Imaging the immune system

Abstract

The liver connects the intestinal portal vasculature with the general circulation, using a diverse array of immune cells to protect from pathogens that translocate from the gut[1]. In liver lobules, blood flows from portal triads that are situated in periportal lobular regions to the central vein via a polarized sinusoidal network. Despite this asymmetry, resident immune cells in the liver are considered to be broadly dispersed across the lobule. This differs from lymphoid organs, in which immune cells adopt spatially biased positions to promote effective host defence[2,3]. Here we used quantitative multiplex imaging, genetic perturbations, transcriptomics, infection-based assays and mathematical modelling to reassess the relationship between the localization of immune cells in the liver and host protection. We found that myeloid and lymphoid resident immune cells concentrate around periportal regions. This asymmetric localization was not developmentally controlled, but resulted from sustained MYD88-dependent signalling induced by commensal bacteria in liver sinusoidal endothelial cells, which in turn regulated the composition of the pericellular matrix involved in the formation of chemokine gradients. In vivo experiments and modelling showed that this immune spatial polarization was more efficient than a uniform distribution in protecting against systemic bacterial dissemination. Together, these data reveal that liver sinusoidal endothelial cells sense the microbiome, actively orchestrating the localization of immune cells, to optimize host defence.

Access through your institution
Change institution
Buy or subscribe

Access options

Subscribe to Journal

Get full journal access for 1 year

$199.00

only $3.90 per issue

Subscribe

All prices are NET prices.
VAT will be added later in the checkout.

Rent or Buy article

Get time limited or full article access on ReadCube.

from$8.99

Rent or Buy

All prices are NET prices.

Additional access options:

- Log in
- Access through your institution
- Learn about institutional subscriptions

Fig. 1: Kupffer cells become enriched around periportal areas in the liver during weaning.

Fig. 2: GF mice lack Kupffer cell periportal concentration.

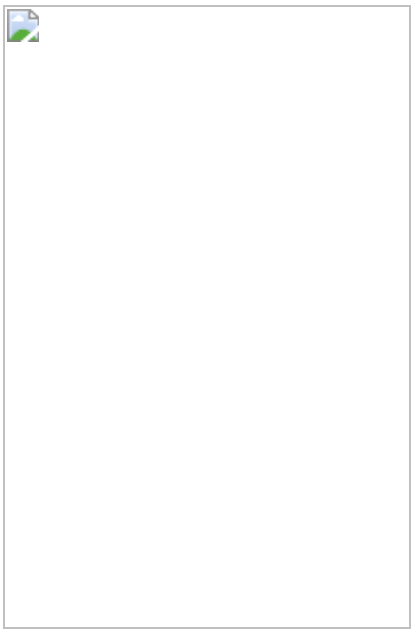

Fig. 3: Loss of LSEC MYD88 signalling results in Kupffer cell spatial disruption.

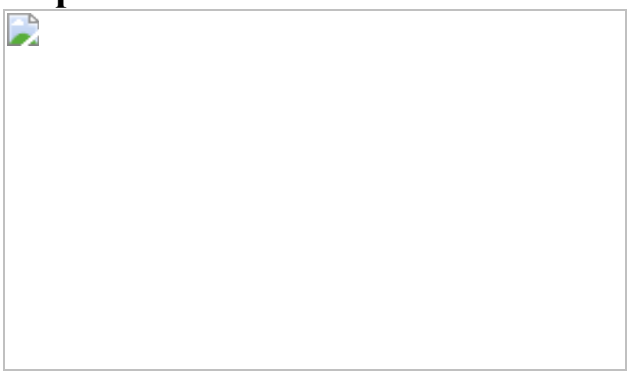

Fig. 4: The localization of Kupffer cells has a critical role in the prevention of pathogen dissemination.

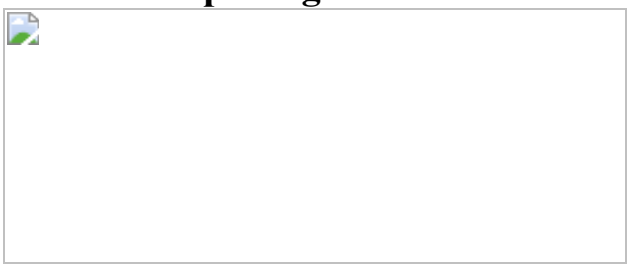

Data availability

RNA sequencing data that support the findings of this study have been deposited in the Gene Expression Omnibus database with the accession number GSE144087. Source data are provided with this paper.

Code availability

The modelling code can be accessed via GitHub at https://github.com/UniboDIFABiophysics/LiverBacteriaCaptureAssay.

References

1. 1.

   Kubes, P. & Jenne, C. Immune responses in the liver. *Annu. Rev. Immunol*. **36**, 247–277 (2018).

   CAS Article Google Scholar

2. 2.

   Kastenmüller, W., Torabi-Parizi, P., Subramanian, N., Lämmermann, T. & Germain, R. N. A spatially-organized multicellular innate immune response in lymph nodes limits systemic pathogen spread. *Cell* **150**, 1235–1248 (2012).

   Article Google Scholar

3. 3.

   Baptista, A. P. et al. The chemoattractant receptor Ebi2 drives intranodal naive CD4+ T cell peripheralization to promote effective adaptive immunity. *Immunity* **50**, 1188–1201 (2019).

   CAS Article Google Scholar

4. 4.

   Doi, Y. et al. Development of complementary expression patterns of E- and N-cadherin in the mouse liver. *Hepatol. Res*. **37**, 230–237 (2007).

   CAS Article Google Scholar

5. 5.

Braeuning, A. et al. Differential gene expression in periportal and perivenous mouse hepatocytes. *FEBS J*. **273**, 5051–5061 (2006).

CAS Article Google Scholar

6. 6.

Bouwens, L., Baekeland, M., De Zanger, R. & Wisse, E. Quantitation, tissue distribution and proliferation kinetics of Kupffer cells in normal rat liver. *Hepatology* **6**, 718–722 (1986).

CAS Article Google Scholar

7. 7.

Sleyster, E. C. & Knook, D. L. Relation between localization and function of rat liver Kupffer cells. *Lab. Invest*. **47**, 484–490 (1982).

CAS PubMed Google Scholar

8. 8.

Itoh, Y. et al. Functional heterogeneity of rat liver macrophages: interleukin-1 secretion and Ia antigen expression in contrast with phagocytic activity. *Liver* **12**, 26–33 (1992).

CAS Article Google Scholar

9. 9.

Gerner, M. Y., Kastenmuller, W., Ifrim, I., Kabat, J. & Germain, R. N. Histo-cytometry: a method for highly multiplex quantitative tissue imaging analysis applied to dendritic cell subset microanatomy in lymph nodes. *Immunity* **37**, 364–376 (2012).

CAS Article Google Scholar

10. 10.

MacParland, S. A. et al. Single cell RNA sequencing of human liver reveals distinct intrahepatic macrophage populations. *Nat. Commun*. **9**, 4383 (2018).

ADS Article Google Scholar

11. 11.

Geissmann, F. et al. Intravascular immune surveillance by CXCR6^{+} NKT cells patrolling liver sinusoids. *PLoS Biol*. **3**, e113 (2005).

Article Google Scholar

12. 12.

Benhamouche, S. et al. Apc tumor suppressor gene is the "zonation-keeper" of mouse liver. *Dev. Cell* **10**, 759–770 (2006).

CAS Article Google Scholar

13. 13.

Burke, Z. D. et al. Liver zonation occurs through a beta-catenin-dependent, c-Myc-independent mechanism. *Gastroenterology* **136**, 2316–2324 (2009).

CAS Article Google Scholar

14. 14.

Shiojiri, N. et al. Heterogeneous hepatocellular expression of glutamine synthetase in developing mouse liver and in testicular transplants of fetal liver. *Lab. Invest*. **72**, 740–747 (1995).

CAS PubMed Google Scholar

15. 15.

Schloss, P. D. et al. Stabilization of the murine gut microbiome following weaning. *Gut Microbes* **3**, 383–393 (2012).

Article Google Scholar

16. 16.

Mao, K. et al. Innate and adaptive lymphocytes sequentially shape the gut microbiota and lipid metabolism. *Nature* **554**, 255–259 (2018).

ADS CAS Article Google Scholar

17. 17.

Jacob, A. I., Goldberg, P. K., Bloom, N., Degenshein, G. A. & Kozinn, P. J. Endotoxin and bacteria in portal blood. *Gastroenterology* **72**, 1268–1270 (1977).

CAS Article Google Scholar

18. 18.

Lynch, R. W. et al. An efficient method to isolate Kupffer cells eliminating endothelial cell contamination and selective bias. *J. Leukoc. Biol*. **104**, 579–586 (2018).

CAS Article Google Scholar

19. 19.

Greenhalgh, S. N., Conroy, K. P. & Henderson, N. C. Cre-ativity in the liver: transgenic approaches to targeting hepatic nonparenchymal cells. *Hepatology* **61**, 2091–2099 (2015).

Article Google Scholar

20. 20.

Weber, M. et al. Interstitial dendritic cell guidance by haptotactic chemokine gradients. *Science* **339**, 328–332 (2013).

ADS CAS Article Google Scholar

21. 21.

Halpern, K. B. et al. Paired-cell sequencing enables spatial gene expression mapping of liver endothelial cells. *Nat. Biotechnol*. **36**, 962–970 (2018).

CAS Article Google Scholar

22. 22.

García-López, M. A. et al. CXCR3 chemokine receptor distribution in normal and inflamed tissues: expression on activated lymphocytes, endothelial cells, and dendritic cells. *Lab. Invest*. **81**, 409–418 (2001).

Article Google Scholar

23. 23.

Thomas, S. Y. et al. CD1d-restricted NKT cells express a chemokine receptor profile indicative of Th1-type inflammatory homing cells. *J. Immunol*. **171**, 2571–2580 (2003).

CAS Article Google Scholar

24. 24.

Groom, J. R. et al. CXCR3 chemokine receptor-ligand interactions in the lymph node optimize $CD4^+$ T helper 1 cell differentiation. *Immunity* **37**, 1091–1103 (2012).

CAS Article Google Scholar

25. 25.

Sakai, M. et al. Liver-derived signals sequentially reprogram myeloid enhancers to initiate and maintain Kupffer cell identity. *Immunity* **51**, 655–670 (2019).

CAS Article Google Scholar

26. 26.

Metzemaekers, M., Vanheule, V., Janssens, R., Struyf, S. & Proost, P. Overview of the mechanisms that may contribute to the non-redundant activities of interferon-inducible CXC chemokine receptor 3 ligands. *Front. Immunol*. **8**, 1970 (2018).

Article Google Scholar

27. 27.

Vanheule, V. et al. CXCL9-derived peptides differentially inhibit neutrophil migration in vivo through interference with glycosaminoglycan interactions. *Front. Immunol*. **8**, 530 (2017).

Article Google Scholar

28. 28.

Lämmermann, T. et al. Neutrophil swarms require LTB4 and integrins at sites of cell death in vivo. *Nature* **498**, 371–375 (2013).

ADS Article Google Scholar

29. 29.

Fernandez-Ruiz, D. et al. Liver-resident memory $CD8^+$ T cells form a front-line defense against malaria liver-stage infection. *Immunity* **45**, 889–902 (2016).

CAS Article Google Scholar

30. 30.

Gola, A. et al. Prime and target immunization protects against liver-stage malaria in mice. *Sci. Transl. Med*. **10**, eaap9128 (2018).

Article Google Scholar

31. 31.

Sörensen, I., Adams, R. H. & Gossler, A. DLL1-mediated Notch activation regulates endothelial identity in mouse fetal arteries. *Blood* **113**, 5680–5688 (2009).

Article Google Scholar

32. 32.

Li, W., Germain, R. N. & Gerner, M. Y. Multiplex, quantitative cellular analysis in large tissue volumes with clearing-enhanced 3D microscopy (C_e3D). *Proc. Natl Acad. Sci. USA* **114**, E7321–E7330 (2017).

CAS Article Google Scholar

33. 33.

Goddard, E. T., Fischer, J. & Schedin, P. A portal vein injection model to study liver metastasis of breast cancer. *J. Vis. Exp*. **118**, 54903 (2016).

Google Scholar

34. 34.

Pentecost, M., Kumaran, J., Ghosh, P. & Amieva, M. R. *Listeria monocytogenes* internalin B activates junctional endocytosis to accelerate intestinal invasion. *PLoS Pathog*. **6**, e1000900 (2010).

Article Google Scholar

35. 35.

Heymann, F. et al. Long term intravital multiphoton microscopy imaging of immune cells in healthy and diseased liver using CXCR6.Gfp reporter mice. *J. Vis. Exp*. **97**, 52607 (2015).

Google Scholar

36. 36.

Dobin, A. et al. STAR: ultrafast universal RNA-seq aligner. *Bioinformatics* **29**, 15–21 (2013).

CAS Article Google Scholar

37. 37.

Liao, Y., Smyth, G. K. & Shi, W. featureCounts: an efficient general purpose program for assigning sequence reads to genomic features. *Bioinformatics* **30**, 923–930 (2014).

CAS Article Google Scholar

38. 38.

McCarthy, D. J., Chen, Y. & Smyth, G. K. Differential expression analysis of multifactor RNA-seq experiments with respect to biological variation. *Nucleic Acids Res*. **40**, 4288–4297 (2012).

CAS Article Google Scholar

39. 39.

Sergushichev, A. A. An algorithm for fast preranked gene set enrichment analysis using cumulative statistic calculation. Preprint at https://doi.org/10.1101/060012 (2016).

40. 40.

Subramanian, A. et al. Gene set enrichment analysis: a knowledge-based approach for interpreting genome-wide expression profiles.

Proc. Natl Acad. Sci. USA **102**, 15545–15550 (2005).

ADS CAS Article Google Scholar

41. 41.

    Turner, A. B. R. spatstat: an R Package for analyzing spatial point patterns. *J. Stat. Softw*. **12**, 1–42 (2005).

    Google Scholar

42. 42.

    Wickham, H. *ggplot2: Elegant Graphics for Data Analysis* (Springer-Verlag, 2016).

Download references

Acknowledgements

We thank A. Luster and J. Lian for providing REX3 mice; E. Miao for providing (ΔintAB inlA^{m}) *Listeria* stocks; P. Brook for preliminary versions of the in silico bacterial capture model; Y. Belkaid and N. Bouladoux for GF mice; R. H. Adams for iCdh5-Cre mice; A. Martins for help with the RNA sequencing experiments; C. Chu for critical reading of the manuscript; and all members of the Laboratory of Immune Systems Biology for their comments during the course of these studies and input during preparation of the manuscript. A.P.B. is supported by a Marie Sklodowska-Curie Action (MSCA) fellowship. This research was supported by the Intramural Research Program of the NIAID (NIH).

Author information

Author notes

1. Anita Gola

Present address: Laboratory of Mammalian Cell Biology and Development, The Rockefeller University, New York, NY, USA

2. These authors contributed equally: Michael G. Dorrington, Emily Speranza

Affiliations

1. Lymphocyte Biology Section, Laboratory of Immune System Biology, National Institute of Allergy and Infectious Diseases, National Institutes of Health, Bethesda, MD, USA

   Anita Gola, Emily Speranza, Rochelle M. Shih, Andrea J. Radtke, Harikesh S. Wong, Antonio P. Baptista & Ronald N. Germain

2. Signaling Systems Section, Laboratory of Immune System Biology, National Institute of Allergy and Infectious Diseases, National Institutes of Health, Bethesda, MD, USA

   Michael G. Dorrington & Iain D. C. Fraser

3. Innate Immunity and Pathogenesis Section, Laboratory of Virology, National Institute of Allergy and Infectious Diseases, National Institutes of Health, Bethesda, MD, USA

   Emily Speranza

4. Department of Physics and Astronomy, University of Bologna, Bologna, Italy

   Claudia Sala

5. Laboratory of Immunoregulation and Mucosal Immunology, VIB-UGent Center for Inflammation Research, Ghent, Belgium

   Antonio P. Baptista

6. Department of Internal Medicine and Pediatrics, Ghent University, Ghent, Belgium

   Antonio P. Baptista

7. Metastasis Biology Section, Center for Cancer Research, National Cancer Institute, National Institutes of Health, Bethesda, MD, USA

   Jonathan M. Hernandez

8. Department of Experimental, Diagnostic and Specialty Medicine, University of Bologna, Bologna, Italy

   Gastone Castellani

Authors

1. Anita Gola
   View author publications

   You can also search for this author in PubMed Google Scholar

2. Michael G. Dorrington
   View author publications

   You can also search for this author in PubMed Google Scholar

3. Emily Speranza
   View author publications

   You can also search for this author in PubMed Google Scholar

4. Claudia Sala
   View author publications

   You can also search for this author in PubMed Google Scholar

5. Rochelle M. Shih
   View author publications

You can also search for this author in PubMed Google Scholar

6. Andrea J. Radtke
   View author publications

   You can also search for this author in PubMed Google Scholar

7. Harikesh S. Wong
   View author publications

   You can also search for this author in PubMed Google Scholar

8. Antonio P. Baptista
   View author publications

   You can also search for this author in PubMed Google Scholar

9. Jonathan M. Hernandez
   View author publications

   You can also search for this author in PubMed Google Scholar

10. Gastone Castellani
    View author publications

    You can also search for this author in PubMed Google Scholar

11. Iain D. C. Fraser
    View author publications

    You can also search for this author in PubMed Google Scholar

12. Ronald N. Germain
    View author publications

    You can also search for this author in PubMed Google Scholar

Contributions

A.G. conceptualized, designed and conducted most of the experiments, performed data analysis and prepared the manuscript. M.G.D. and I.D.C.F. helped with the in vitro and in vivo bacterial experiments. E.S. helped with RNA sequencing library preparation and performed RNA sequencing data analysis. C.S. and G.C. generated the in silico bacterial capture model. R.M.S. and A.J.R. performed the analysis on human samples, IBEX imaging and cleared liver sections. H.S.W. and A.P.B. provided discussion, data interpretation and help with statistical analyses. J.M.H. obtained human liver biopsies. R.N.G. designed the experiments, interpreted the data and prepared the manuscript. All authors helped to write and edit the manuscript.

Corresponding authors

Correspondence to Anita Gola or Ronald N. Germain.

Ethics declarations

Competing interests

The authors declare no competing interests.

Additional information

Peer review information *Nature* thanks Matteo Iannacone, Shalev Itzkovitz and the other, anonymous, reviewer(s) for their contribution to the peer review of this work.

Publisher's note Springer Nature remains neutral with regard to jurisdictional claims in published maps and institutional affiliations.

Extended data figures and tables

Extended Data Fig. 1 Kupffer cell MHCII expression and localization in mouse and human livers.

a, Representative IF image of F4/80$^+$, MHCII, Collagen IV, and E-cadherin expression in mouse liver lobule. (i-iii) Channel shown labelled in figures, CV highlighted by dashed circles in IFs. **b**, Scatter plot of KC MHCII Mean Fluorescence Intensity (MFI) and distance to the centre of CV vasculature (µm) (n = 3 mice, 2 lobules/mouse, each dot represents a KC). Linear regression model shown, intercept (m), p-value (Two-Tailed t-test) and R^2 indicated in figure. **c**, Representative IF human liver image of Kupffer cells (stained by CD163 and HLA-DR) and liver enzymes ASS1 and GS to identify the liver lobule (CV highlighted by dashed circles in IF images). **d**, Total number of KCs cells in PP and CV regions normalized to volume, each dot represents an ROI; Median shown. Two-tailed Mann–Whitney; *P = 0.0448. (n = 7 donors). Channels and CV as labelled in image. Source data

Extended Data Fig. 2 NKT cells show periportal enrichment, and are disrupted in *iCdh5-Myd88*$^{-/-}$ and *Cxcl9*$^{-/-}$ mice.

a, Representative IF image with CXCR6-GFP (NKT), E-cadherin, and CD1d, CV highlighted by dashed circles in IF images. **b**, Total number of NKT cells in PP and CV regions normalized to volume, each dot represents an ROI. n = 4 mice, Two-tailed Mann–Whitney, ****P < 0.0001; Median shown. **c**, Representative image from 2P-intravital movie of CXCR6-GFP animal showing E-Cadherin antibody injected intravenously i.v. and NKT cell positioning at time zero; Bottom: compiled NKT cell tracks. **d**, Representative ratio of total NKT cell numbers in CV to PP ROIs per frame over time. **e**, Total number of NKT cells in PP and CV regions normalized to volume for 2-P intravital movies, each dot represents an ROI. n = 3 mice, Two-tailed Mann–Whitney, ****P < 0.0001; Median shown. **f**, Ratio of total NKT cell numbers in CV to PP ROIs for 2-P intravital movies, each dot represents a frame. n = 3 mice. **g**, Representative IF image CXCR6$^+$ CD3$^+$ cells (NKT cells), and E-cadherin in iCdh5-MyD88$^{wt/wt}$, iCdh5-MyD88$^{fl/fl}$ and CXCL9$^{-/-}$ animals. **h**, **i**, Ratio of total NKT cells in PP and CV regions normalized to volume (**h**), and total number of cells per volume (**i**); each dot represents a lobule. n = 4 mice/condition, Kruskal–Wallis test, Dunn's multiple comparison test, ***P = 0.0002, **P = 0.0013, ns (not

significant) $P > 0.9999$; Median and quartile range shown. Channels and CV as labelled in image. Source data

Extended Data Fig. 3 Immunofluorescent images and total numbers of Kupffer cells in mice with distinct commensal microbiomes.

a, Total number of KCs normalized to volume in Alb^{Cre}-$\beta catenin^{wt/wt}$ and Alb^{Cre}-$\beta catenin^{fl/fl}$ animals, each dot represents a biological replicate, $n = 3$ mice/condition, Two-tailed Mann–Whitney test, ns p-value = 0.400; Median shown. **b**, Representative IF images of mouse livers at days (D) 3, 8, 13, 20, and 25 post-partum. At D3, GS synthetase expression is absent and E-cadherin is homogenously expressed throughout the liver lobule; by D8 both molecules show zonation. **c**, Same representative IF images of mouse livers at days (D) 3, 8, 13, 20, and 25 post-partum showing E-cadherin and $F4/80^+$ KCs (for quantification, see Fig. 1h). **d**, Total number of KCs normalized to volume at days (D) 3, 8, 13, 20, and 25 post-partum, each dot represent a biological replicate, $n = 5$ mice/time point. Kruskal–Wallis test with Dunn's multiple comparison: For D25 vs D3/D8/D13: ns p-value >0.9999, for D25 vs D20: ns p-value = 0.8492; Median shown. Channels and CV as labelled in image. **e**, Representative IF image showing normal germ-free animal liver lobule metabolic zonation depicting glutamine synthetase (GS), acetolactate synthase (ALS), argininosuccinate synthase 1 (ASS1) and Cytochrome P450 2E (Cyp2e1) expression, for comparison: see SPF zonation gradients in Fig. 1b. **f**–**k**, Representative IF images showing $F4/80^+$ KC distribution within mouse liver (insets showing $F4/80^+$ staining only) and total number of KCs normalized to volume in GF and SPF animals (each dot present a biological replicate) (**f**, **g**), $n = 5$ mice/condition; Two-Tailed Mann–Whitney test, ns p-value = 0.5159, Median shown; GF animals after cohousing with SPF animals (each dot present a biological replicate) (**h**–**i**), $n = 6$ mice/condition, Kruskal–Wallis test with Dunn's multiple comparison. For SPF vs D4/D14: ns p-value >0.9999, for SPF vs D2 ns p-value = 0.2650, for SPF vs D7 ns p-value = 0.5255; Median shown. SPF animals after antibiotic (ABX) treatment, (each dot presents a biological replicate) (**j**–**k**), $n = 6$ mice/condition, Kruskal–Wallis test with Dunn's multiple comparison. For SPF vs 3-wks: ns p-value = 0.8725, for

SPF vs 6-wks: ns p-value = 0.2936; Median shown. **l**, Representative IF image showing F4/80^{+} KC distribution of GF animals orally gavaged with LPS (two weeks post treatment), and PBS control animals (insets showing F4/80 staining only, CV highlighted by dashed circles in IFs). **m**, Ratio of total KC numbers in CV to PP ROIs, each dot represents a lobule. $n = 6$ mice/condition, Two-tailed Mann–Whitney test, ****$P < 0.0001$; Median and quartiles shown. **n**, Total number of KCs normalized to volume in global knockouts for MyD88, TRL4, TRIF and Caspase1/11 (each dot presents a biological replicate), $n = 4$ Caspase 1/11$^{-/-}$ mice, $n = 5$ MyD88$^{-/-}$ and WT mice, $n = 6$ TLR4$^{-/-}$ and TRIF$^{-/-}$ animals, Kruskal–Wallis test with Dunn's multiple comparison test. For WT vs TRIF$^{-/-}$/Caspase 1/11$^{-/-}$: ns p-value >0.9999, for WT vs MyD88$^{-/-}$: ns p-value = 0.0776, WT vs TLR4$^{-/-}$: ns p-value = 0.0524; Median shown. Channels shown labelled in figures, CV highlighted by dashed circles in IFs. Source data

Extended Data Fig. 4 iCdh5-Cre, Alb-Cre and LysM-Cre liver reporters: loss of MyD88 signalling in hepatocytes and Kupffer cells does not alter Kupffer cell localization.

a, Representative IF image showing iCdh5-Cre expression when crossed to a Rosa26-tdTomato reporter. **b**, Zoomed in image: iCdh5-Cre-tdTomato is predominantly found on CD138^{+} LSECs, but can also be seen on a small number of KCs. **c**, Percentage of total tdTomato^{+} KCs in iCdh5-Cre-tdTomato animals, each dot represents a biological replicate, $n = 3$ mice. **d**, MFI of tdTomato on tdTomato^{+} F4/80^{+} KCs and tdTomato^{+} LSECs from iCdh5-Cre-tdTomato (each dot represents a cell), $n = 3$ mice/condition, Two-tailed Mann–Whitney test, ****$P < 0.0001$; Median shown. **e**, **f**, Representative IF image showing F4/80^{+} KC distribution of Alb-MyD88$^{-/-}$ (**e**) and LysM-MyD88$^{-/-}$ (**f**) animals with littermate controls, CV highlighted by dashed circles in IFs. **g**, Ratio of total KC numbers in CV to PP ROIs, (each dot represents a lobule), $n = 4$ mice/condition, Kruskal–Wallis test with Dunn's multiple comparison test. For WT vs LysM^{Cre}-MyD88^{flfl-}: ns p-value >0.9999, for WT vs Alb^{Cre}-MyD88$^{fl/fl}$: ns p-value = 0.2082; Median shown. **h**, total KC numbers per volume; each dot represents a lobule. $n = 4$ mice/condition, Kruskal–Wallis test with Dunn's

multiple comparison test. For WT vs LysM^{Cre}-MyD88^{flfl-}: ns p-value = 0.0781, for WT vs Alb^{Cre}-MyD88$^{fl/fl}$: ns p-value = 0.0624; Median shown. Channels shown labelled in figures, CV highlighted by dashed circles in IFs. Source data

Extended Data Fig. 5 Sort strategy for LSEC populations and CXCL9 translation and protein expression in *iCdh5-Myd88*$^{wt/wt}$, *iCdh5-Myd88*$^{fl/fl}$ and *Cxcl9*$^{-/-}$ mice.

a, Representative IF image of CD117 expression around the CV on iCdh5-MyD88$^{wt/wt}$, Global MyD88$^{-/-}$ and iCdh5-MyD88$^{fl/fl}$ animals, $n = 2$ mice. CV highlighted by dashed circles in IFs. **b**, Representative flow-cytometry gating strategy for bulk RNA sequencing sort: cells were sorted on forward-side scatter, singlets and live. KCs were identified by expression of F4/80^{+} and Tim4^{+}. LSECs were identified by CD31^{+} and sorted into low, medium and high CD117 populations. **c**, Chemokine expression across the liver lobule as a correlate to CD117 in iCdh5-MyD88$^{wt/wt}$ animals. Statistical significance determined by edge-R glmLTR test, mean shown from 3 biological replicates; *p-values for: Cxcl9 = 0.009785, Ccl17 = 0.0147, Cxcl13 = 0.03433, Ccl24 = 0.01569, Ccl6 = 0.0004875. **d**, Representative IF image showing CXCL9-RFP expression on CD138^{+} LSECs in REX3 animals (Density plot of CXCL9 shown in Fig. 3a). **e**, Non-parametric estimate of the spatial intensity of KC, CXCL9, and CD138, (ρ(E-cadherin)) as a value of spatial covariate E-cadherin MFI, see Methods for details. $n = 3$ mice/condition. **f**, **g**, Log counts per million of CD117 (ns p-value = 0.9695) (**f**) and MyD88 (ns p-value = 1, ****P = 3.549e-23) (**g**) in LSECs and KCs. Statistical significance determined by edge-R glmLTR test, each dot represents a biological sample from sorted populations ($n = 3$ mice/condition). **h**, Chemokine expression across the liver lobule as a correlate to CD117 in iCdh5-MyD88$^{fl/fl}$ animals. In red are chemokines that are PP associated in WT animals. Statistical significance determined by edge-R glmLTR test; *p-values for: Cxcl11 = 0.01102, Ccl21a = 0.03187. **i**, Ratio of total KC numbers in CV to PP ROIs in global CCR2, CCR5, CCL5, CCL2, CX3CR1 knockout animals (each dot represents a lobule), $n = 4$ mice/condition for knockout animals, and $n = 3$ mice for WT controls. Kruskal–Wallis test with Dunn's multiple comparison test, for all

comparisons: ns p-value >0.9999, with the exception of WT vs CCL5$^{-/-}$: ns p-value = 0.3098; Median shown. Channels shown labelled in figures, CV highlighted by dashed circles in IFs. Source data

Extended Data Fig. 6 Expression of Kupffer cell putative markers in *iCdh5-Myd88*$^{wt/wt}$ and *iCdh5-Myd88*$^{fl/fl}$ mice.

a, Log counts per million of Cxcr3 in KCs and LSECs from MyD88$^{wt/wt}$ and iCdh5-MyD88$^{fl/fl}$ mice; biological replicates of sorted populations shown, statistical significance determined by edge-R glmLTR test; for all: ns p-value-values LSECs = 0.3191, and ns p-value-values KCs = 1. **b**–**d**, CXCR3 expression on KCs of WT, CXCR3$^{-/-}$ and CXCL9$^{-/-}$ mice as determined by flow-cytometry: Histogram of CXCR3 (**b**), quantification of CXCR3 MFI (**c**) and % of F4/80^{+} CXCR3^{+} of total F4/80^{+} cells (each dot represents a biological replicate) (**d**). n = 4 mice/group; Kruskal–Wallis test with Dunn's multiple comparison, *P = 0.0310, **P = 0.0089; Median shown. **e**, Representative IF image of Tim4, Clec4f and F4/80 expression in KCs of iCdh5-MyD88$^{wt/wt}$ and iCdh5-MyD88$^{fl/fl}$ animals. CV highlighted by dashed circles in IFs. **f**–**i**, Quantification of percent of Tim4^{+} Clec4f^{+} F4/80^{+} cells (ns p-value = 0.5) (**f**) and MFI of Tim4 (ns p-value = 0.7) (**g**), Clec4f (ns p-value = 0.4) (**h**), and F4/80 (ns p-value >0.9999) (**i**); n = 3 mice/condition, Two-tailed Mann–Whitney test. **j**, Log counts per million of Nr1h3, Id3, Clec4f, Ccr2, Spic, and Timd4 in KCs from MyD88$^{wt/wt}$ and iCdh5-MyD88$^{fl/fl}$ mice; biological replicates of sorted populations shown, statistical significance determined by edge-R glmLTR test; for all: ns p-value-values = 1. **k**, Percent of counts associated with cell cycle from RNASeq in KCs and LSECs from MyD88$^{wt/wt}$ and iCdh5-MyD88$^{fl/fl}$ mice, biological replicates shown, Two-Way Anova with Sidak MC test, ns p-value-value for KCs = 0.4710, for LSECs = 0.1591. Source data

Extended Data Fig. 7 RNA sequencing GAG pathway and histological ECM composition.

a, GSEA enrichment scores in relation to CD117 expression in LSECs from iCdh5-MyD88$^{wt/wt}$ (x-axis) and iCdh5-MyD88$^{fl/fl}$ (y-axis). Highlighted,

pathways enriched towards the PP regions of iCdh5-MyD88$^{wt/wt}$ disrupted in iCdh5-MyD88$^{fl/fl}$ animals (Top 10 pathways shown in Fig. 3k). **b**, GAG pathway enrichment score in iCdh5-MyD88$^{wt/wt}$ and iCdh5-MyD88$^{fl/fl}$. iCdh5-MyD88$^{wt/wt}$ show strong PP GAG enrichment, lost and/or disrupted in iCdh5-MyD88$^{fl/fl}$ animals. **c**, Representative IF image of Hyaluronic acid binding protein (HABP) detecting Hyaluronic acid (HA) in iCdh5-MyD88$^{wt/wt}$ and iCdh5-MyD88$^{fl/fl}$. **d**, Representative IF image of HS in iCdh5-MyD88$^{wt/wt}$ and iCdh5-MyD88$^{fl/fl}$. **e**, **f**, MFI of HS and HABP (respectively) in PP and CV ROIs of iCdh5-MyD88$^{wt/wt}$ and iCdh5-MyD88$^{fl/fl}$ animals, each dot represents an ROI; n = 4 iCdh5-MyD88$^{wt/wt}$ mice and n = 5 iCdh5-MyD88$^{fl/fl}$ animals, Two-Way ANOVA with Sidak multiple comparison test; Median shown. $^{**}P = 0.0011$, ns p-value-value = 0.0654 (**e**). $^{*}P = 0.0348$, ns p-value-value = 0.5972 (**f**). Channels shown labelled in figures. Source data

Extended Data Fig. 8 In vivo and in vitro capture of *L. monocytogenes* and malaria sporozoite spatial location after liver infection.

a, Representative IF image showing *L. monocytogenes-GFP* captured by KCs in iCdh5-MyD88$^{wt/wt}$ either in PP Region (E-cadherin^{+}) or CV Region (E-cadherin^{-}) two hours post i.v. administration. Quantification and experimental details shown in Fig. 4a. **b**, **c**, Percent of *L. monocytogenes* captured in liver, spleen and blood after portal vein injection in CXCR3$^{-/-}$ animals ($^{**}P = 0.0023$, $^{*}P = 0.0263$, ns p-value = 0.7585) (**b**) and CXCL9$^{-/-}$ animals ($^{***}P = 0.0001$, $^{*}P = 0.0102$, ns p-value = 0.209) (**c**); each dot represents a biological replicate, n = 4-8 animals/group, Two-way ANOVA with Sidak multiple; Median shown. **d**–**f**, In vitro bacteria capture assay of *L. monocytogenes-GFP* using KCs extracted from iCdh5-MyD88$^{wt/wt}$ and iCdh5-MyD88$^{fl/fl}$ animals. Representative flow cytometry histograms of infected and uninfected KCs at 4 °C and 37 °C showing *L. monocytogenes-GFP* intensity (**d**). Quantification of flow-cytometry data showing percent of KCs with bound *L. monocytogenes* at 4 °C (**e**) and 37 °C (**f**); each dot represents a biological replicate, n = 4 mice/condition; Two-tailed Mann–Whitney test, ns p-value = 0.3429; Median shown. **g**,

Representative examples of sporozoites (spz) locations one-day post liver infection in naïve animals; spz stained with anti-CSP antibody. **h**, **i**, Quantification of location of spz infection: % of total liver in WT mice that is E-cadherin$^+$, each dot represents a biological replicate, median shown (**h**); % of total spz either in E-cadherin$^+$ regions or outside E-cadherin$^+$ regions (**i**); n = 250 spz imaged, data pooled from 3 different mice, each dot represents a mouse (see Methods section regarding quantification); Two-tailed Mann–Whitney (ns p-value = 0.1000). Source data

Extended Data Fig. 9 In silico model of bacterial capture in sinusoidal network.

a, Example of the exponential distribution used to sample the KC locations along the sinusoid. The two histograms refer to two different values of the mean of the exponential distribution: $\lambda = 25$ (red- simulating a WT distribution) and $\lambda = 500$ (blue- simulating a KO distribution). **b**, Parameters used to constrain model simulations, obtained from analysing confocal images, mean number displayed (n = number of measurements made for each parameter, δ = standard deviation of measurements made). **c**, Illustrations of two example simulations in which the KC locations are sampled from an exponential distribution with mean $\lambda = 25$ (left) and $\lambda = 500$ (right). The top part of the graph corresponds to the PP region, the bottom part to the CV. White rectangles represent sinusoidal segments. Arrows schematically indicate the splitting and merging of vessels. Red rectangles symbolize KCs, while small coloured rectangles are representative of bacteria. The path of each bacterium is described by the string of rectangles of the same colour. All bacteria start their motion at the top of the graph (PP region) and only bacteria that are not successfully stopped by KCs reach the bottom (CV). In both simulations we show the path of 10 bacteria. **d**–**f**, Simulating varying KC distributions (λ) and KC bacterial binding probability in parameter space: the network's capturing capacity is proportional to increases of KC binding probability while inversely proportional to increases of λ values. Average percent of stopped bacteria as a function of KC binding probability (KC-BP - a probabilistic value of KC capture from 0-1), and of the mean of the exponential distribution λ. Results reported in a heat map in which the colour corresponds to the average percentage of stopped bacteria, as detailed by

the colour bar, rows correspond to KC-BP values and columns to different λ-values (**d**). Results reported as line graphs with average percentages of stopped bacteria reported and increasing values of KC binding probability (KC-BP) (**e**) or λ-values (**f**). Colour of each line corresponds to either changes of KC binding probability or λ-value, respectively.

Extended Data Fig. 10 Multiparameter, iterative staining (IBEX) of Prime and Target vaccinated animals.

a, Representative IF image of Prime and Target vaccinated animal showing expression of a diverse set of immune and non-parenchymal associated markers in relationship to E-cadherin acquired via IBEX staining (Channels shown labelled in figures). **b**, Ratio of total cell numbers in CV to PP ROIs, each dot represents a lobule (each dot represents a lobule); $n = 3$ mice/condition, Kruskal–Wallis test, Dunn's multiple comparison test; Median shown. KC vs Desmin: ns p-value = 0.3071, KC vs CD11c: ns p-value = 0.0549, KC vs Monocytes: ns p-value = 0.0510. **c**, Total number of Trm ($CD8^+$ $CD44^+$ $CXCR6^+$ $CD69^+$ T-cells) per volume in iCdh5-$MyD88^{wt/wt}$, iCdh5-$MyD88^{fl/fl}$ and $CXCL9^{-/-}$ animals (each dot represents a biological replicate). $n = 3$ mice/condition; Kruskal–Wallis test, Dunn's multiple comparison test; Median shown, ns p-value >0.9999. **d**, Ratio of Trm numbers in CV to PP ROIs, each dot represents a lobule. $n = 3$ mice/condition; Median shown, Kruskal–Wallis test, Dunn's multiple comparison test, $^{**}P = 0.0035$, ns p-value = 0.1275. Source data

Supplementary information

Supplementary Table 1

List of antibodies used for all immune-histochemistry and flow-cytometry experiments.

Reporting Summary

Supplementary Video 1

NKT cell patrolling behaviour in liver sinusoids. Tiled image of intravital video showing NKT cells migrating along the hepatic sinusoids of a CXCR6-GFP$^{-/+}$ animal i.v. injected with E-cadhering-A594 antibody. (20X magnification, frame rate 25hertz; movie plays twice).

Supplementary Video 2

Large volumetric C_e3D microscopy of mouse liver lobule. Ce3D-processed liver sample of LysM-tdTomato CXCR6-GFP dual reporter mice, E-cadherin (cyan) demarking the PP-regions and Collagen IV (gray) the liver sinusoids.

Supplementary Video 3

Visualization of multiparameter, iterative staining (IBEX) of Prime-target vaccinated animals. Single colour panels from iterative staining performed by IBEX, each panel is shown one at a time.

Source data

Source Data Fig. 1

Source Data Fig. 2

Source Data Fig. 3

Source Data Fig. 4

Source Data Extended Data Fig. 1

Source Data Extended Data Fig. 2

Source Data Extended Data Fig. 3

Source Data Extended Data Fig. 4

Source Data Extended Data Fig. 5

Source Data Extended Data Fig. 6

Source Data Extended Data Fig. 7

Source Data Extended Data Fig. 8

Source Data Extended Data Fig. 10

Rights and permissions

Reprints and Permissions

About this article

Check for updates

Cite this article

Gola, A., Dorrington, M.G., Speranza, E. *et al.* Commensal-driven immune zonation of the liver promotes host defence. *Nature* **589,** 131–136 (2021). https://doi.org/10.1038/s41586-020-2977-2

Download citation

- Received: 11 March 2020
- Accepted: 11 September 2020
- Published: 25 November 2020
- Issue Date: 07 January 2021

- DOI: https://doi.org/10.1038/s41586-020-2977-2

Further reading

- **Zones of immune defence in the liver**
  - Katrina Ray

  Nature Reviews Gastroenterology & Hepatology (2020)

Comments

By submitting a comment you agree to abide by our Terms and Community Guidelines. If you find something abusive or that does not comply with our terms or guidelines please flag it as inappropriate.

Access through your institution
Change institution
Buy or subscribe

This article was downloaded by **calibre** from https://www.nature.com/articles/s41586-020-2977-2

- Article
- Published: 18 November 2020

RNA nucleation by MSL2 induces selective X chromosome compartmentalization

- Claudia Isabelle Keller Valsecchi ORCID: orcid.org/0000-0003-4135-5927[1] [na1],
- M. Felicia Basilicata ORCID: orcid.org/0000-0002-1111-9459[1] [na1],
- Plamen Georgiev[1],
- Aline Gaub ORCID: orcid.org/0000-0002-3571-9547[1],
- Janine Seyfferth[1],
- Tanvi Kulkarni[1,2],
- Amol Panhale[1],
- Giuseppe Semplicio[1],
- Vinitha Manjunath[1],
- Herbert Holz[1],
- Pouria Dasmeh ORCID: orcid.org/0000-0002-4527-5302[3] &
- Asifa Akhtar ORCID: orcid.org/0000-0001-8973-6193[1]

Nature **volume 589**, pages137–142(2021)Cite this article

- 4868 Accesses
- 154 Altmetric
- Metrics details

Subjects

- Developmental biology
- Dosage compensation
- Fluorescence in situ hybridization
- Non-coding RNAs
- RNA

Abstract

Confinement of the X chromosome to a territory for dosage compensation is a prime example of how subnuclear compartmentalization is used to regulate transcription at the megabase scale. In *Drosophila melanogaster*, two sex-specific non-coding RNAs (roX1 and roX2) are transcribed from the X chromosome. They associate with the male-specific lethal (MSL) complex[1], which acetylates histone H4 lysine 16 and thereby induces an approximately twofold increase in expression of male X-linked genes[2,3]. Current models suggest that X-over-autosome specificity is achieved by the recognition of *cis*-regulatory DNA high-affinity sites (HAS) by the MSL2 subunit[4,5]. However, HAS motifs are also found on autosomes, indicating that additional factors must stabilize the association of the MSL complex with the X chromosome. Here we show that the low-complexity C-terminal domain (CTD) of MSL2 renders its recruitment to the X chromosome sensitive to roX non-coding RNAs. roX non-coding RNAs and the MSL2 CTD form a stably condensed state, and functional analyses in *Drosophila* and mammalian cells show that their interactions are crucial for dosage compensation in vivo. Replacing the CTD of mammalian MSL2 with that from *Drosophila* and expressing roX in *cis* is sufficient to nucleate ectopic dosage compensation in mammalian cells. Thus, the condensing nature of roX–MSL2^{CTD} is the primary determinant for specific compartmentalization of the X chromosome in *Drosophila*.

Access through your institution
Change institution
Buy or subscribe

Access options

Subscribe to Journal

Get full journal access for 1 year

$199.00

only $3.90 per issue

Subscribe

All prices are NET prices.
VAT will be added later in the checkout.

Rent or Buy article

Get time limited or full article access on ReadCube.

from$8.99

Rent or Buy

All prices are NET prices.

Additional access options:

- Log in
- Access through your institution
- Learn about institutional subscriptions

Fig. 1: *Drosophila* MSL2-CTD and roX2 RNA confer a condensed state.

Fig. 2: Selective compartmentalization by the MSL2-CTD is required for dosage compensation in vivo.

Fig. 3: roX2 RNA nucleation by a drosophilized MSL2 in mammalian cells.

Fig. 4: roX2-MSL2 nucleation elicits dosage compensation in mammalian cells.

Data availability

RNA-seq and ChIP–seq data have been deposited to the Gene Expression Omnibus under the accession number GSE129834. All other relevant data supporting the key findings of this study are available within the article and its Supplementary Information or from the corresponding author upon request.

References

1. 1.

   Meller, V. H. et al. Ordered assembly of roX RNAs into MSL complexes on the dosage-compensated X chromosome in *Drosophila*. *Curr. Biol*. **10**, 136–143 (2000).

   CAS PubMed Article PubMed Central Google Scholar

2. 2.

   Samata, M. & Akhtar, A. Dosage compensation of the X chromosome: a complex epigenetic assignment involving chromatin regulators and long noncoding RNAs. *Annu. Rev. Biochem*. **87**, 323–350 (2018).

   CAS PubMed Article PubMed Central Google Scholar

3. 3.

   Lucchesi, J. C. & Kuroda, M. I. Dosage compensation in *Drosophila*. *Cold Spring Harb. Perspect. Biol*. **7**, a019398 (2015).

   PubMed PubMed Central Article CAS Google Scholar

4. 4.

   Villa, R., Schauer, T., Smialowski, P., Straub, T. & Becker, P. B. PionX sites mark the X chromosome for dosage compensation. *Nature* **537**,

244–248 (2016).

ADS CAS PubMed Article PubMed Central Google Scholar

5. 5.

Alekseyenko, A. A. et al. A sequence motif within chromatin entry sites directs MSL establishment on the *Drosophila* X chromosome. *Cell* **134**, 599–609 (2008).

CAS PubMed PubMed Central Article Google Scholar

6. 6.

Valsecchi, C. I. K. et al. Facultative dosage compensation of developmental genes on autosomes in *Drosophila* and mouse embryonic stem cells. *Nat. Commun*. **9**, 3626 (2018).

ADS PubMed PubMed Central Article CAS Google Scholar

7. 7.

Bai, X., Alekseyenko, A. A. & Kuroda, M. I. Sequence-specific targeting of MSL complex regulates transcription of the roX RNA genes. *EMBO J*. **23**, 2853–2861 (2004).

CAS PubMed PubMed Central Article Google Scholar

8. 8.

Ilik, I. A. et al. Tandem stem-loops in roX RNAs act together to mediate X chromosome dosage compensation in *Drosophila*. *Mol. Cell* **51**, 156–173 (2013).

CAS PubMed PubMed Central Article Google Scholar

9. 9.

Kelley, R. L. et al. Expression of msl-2 causes assembly of dosage compensation regulators on the X chromosomes and female lethality in *Drosophila*. *Cell* **81**, 867–877 (1995).

CAS PubMed Article PubMed Central Google Scholar

10. 10.

Figueiredo, M. L. et al. Non-coding roX RNAs prevent the binding of the MSL-complex to heterochromatic regions. *PLoS Genet*. **10**, e1004865 (2014).

PubMed PubMed Central Article CAS Google Scholar

11. 11.

Hallacli, E. et al. Msl1-mediated dimerization of the dosage compensation complex is essential for male X-chromosome regulation in *Drosophila*. *Mol. Cell* **48**, 587–600 (2012).

CAS PubMed Article Google Scholar

12. 12.

Zheng, S. et al. Structural basis of X chromosome DNA recognition by the MSL2 CXC domain during *Drosophila* dosage compensation. *Genes Dev*. **28**, 2652–2662 (2014).

PubMed PubMed Central Article Google Scholar

13. 13.

Fauth, T., Müller-Planitz, F., König, C., Straub, T. & Becker, P. B. The DNA binding CXC domain of MSL2 is required for faithful targeting the Dosage Compensation Complex to the X chromosome. *Nucleic Acids Res*. **38**, 3209–3221 (2010).

CAS PubMed PubMed Central Article Google Scholar

14. 14.

Larson, A. G. & Narlikar, G. J. The role of phase separation in heterochromatin formation, function, and regulation. *Biochemistry* **57**, 2540–2548 (2018).

CAS PubMed Article Google Scholar

15. 15.

Roden, C. & Gladfelter, A. S. RNA contributions to the form and function of biomolecular condensates. *Nat. Rev. Mol. Cell Biol*. https://doi.org/10.1038/s41580-020-0264-6 (2020).

16. 16.

Kato, M. et al. Cell-free formation of RNA granules: low complexity sequence domains form dynamic fibers within hydrogels. *Cell* **149**, 753–767 (2012).

CAS PubMed PubMed Central Article Google Scholar

17. 17.

Meller, V. H. & Rattner, B. P. The roX genes encode redundant male-specific lethal transcripts required for targeting of the MSL complex. *EMBO J*. **21**, 1084–1091 (2002).

CAS PubMed PubMed Central Article Google Scholar

18. 18.

Kim, M., Faucillion, M.-L. & Larsson, J. RNA-on-X 1 and 2 in *Drosophila melanogaster* fulfill separate functions in dosage compensation. *PLoS Genet*. **14**, e1007842 (2018).

PubMed PubMed Central Article CAS Google Scholar

19. 19.

Apte, M. S. et al. Generation of a useful roX1 allele by targeted gene conversion. *G3 (Bethesda)* **4**, 155–162 (2014).

Article CAS Google Scholar

20. 20.

Straub, T. et al. Stable chromosomal association of MSL2 defines a dosage-compensated nuclear compartment. *Chromosoma* **114**, 352–364 (2005).

PubMed Article PubMed Central Google Scholar

21. 21.

Lin, Y. et al. Toxic PR poly-dipeptides encoded by the C9orf72 repeat expansion target LC domain polymers. *Cell* **167**, 789–802.e12 (2016).

CAS PubMed PubMed Central Article Google Scholar

22. 22.

Cheutin, T. et al. Maintenance of stable heterochromatin domains by dynamic HP1 binding. *Science* **299**, 721–725 (2003).

ADS CAS PubMed Article PubMed Central Google Scholar

23. 23.

Strom, A. R. et al. Phase separation drives heterochromatin domain formation. *Nature* **547**, 241–245 (2017).

ADS CAS PubMed PubMed Central Article Google Scholar

24. 24.

Schauer, T. *et al*. Chromosome topology guides the *Drosophila* dosage compensation complex for target gene activation. *EMBO Rep*. **18**, 1854–1868 (2017).

CAS PubMed Central Article Google Scholar

25. 25.

Toll-Riera, M., Radó-Trilla, N., Martys, F. & Albà, M. M. Role of low-complexity sequences in the formation of novel protein coding sequences. *Mol. Biol. Evol*. **29**, 883–886 (2012).

CAS PubMed Article PubMed Central Google Scholar

26. 26.

Bertrand, E. et al. Localization of ASH1 mRNA particles in living yeast. *Mol. Cell* **2**, 437–445 (1998).

CAS PubMed Article PubMed Central Google Scholar

27. 27.

Baron-Benhamou, J., Gehring, N. H., Kulozik, A. E. & Hentze, M. W. Using the lambdaN peptide to tether proteins to RNAs. *Methods Mol. Biol*. **257**, 135–154 (2004).

CAS PubMed PubMed Central Google Scholar

28. 28.

Quinn, J. J. et al. Rapid evolutionary turnover underlies conserved lncRNA-genome interactions. *Genes Dev*. **30**, 191–207 (2016).

CAS PubMed PubMed Central Article Google Scholar

29. 29.

McFarland, T. J. et al. Evaluation of a novel short polyadenylation signal as an alternative to the SV40 polyadenylation signal. *Plasmid* **56**, 62–67 (2006).

CAS PubMed Article PubMed Central Google Scholar

30. 30.

Flemr, M. & Bühler, M. Single-step generation of conditional knockout mouse embryonic stem cells. *Cell Rep*. **12**, 709–716 (2015).

CAS PubMed Article PubMed Central Google Scholar

31. 31.

Raja, S. J. et al. The nonspecific lethal complex is a transcriptional regulator in *Drosophila. Mol. Cell* **38**, 827–841 (2010).

CAS PubMed Article PubMed Central Google Scholar

32. 32.

Chelmicki, T. et al. MOF-associated complexes ensure stem cell identity and Xist repression. *eLife* **3**, e02024 (2014).

PubMed PubMed Central Article CAS Google Scholar

33. 33.

Groth, A. C., Fish, M., Nusse, R. & Calos, M. P. Construction of transgenic *Drosophila* by using the site-specific integrase from phage phiC31. *Genetics* **166**, 1775–1782 (2004).

CAS PubMed PubMed Central Article Google Scholar

34. 34.

Ramírez, F. et al. High-affinity sites form an interaction network to facilitate spreading of the MSL complex across the X chromosome in *Drosophila*. *Mol. Cell* **60**, 146–162 (2015).

PubMed PubMed Central Article CAS Google Scholar

35. 35.

Venken, K. J. T., He, Y., Hoskins, R. A. & Bellen, H. J. P[acman]: a BAC transgenic platform for targeted insertion of large DNA fragments in *D. melanogaster*. *Science* **314**, 1747–1751 (2006).

ADS CAS PubMed Article PubMed Central Google Scholar

36. 36.

Bischof, J., Maeda, R. K., Hediger, M., Karch, F. & Basler, K. An optimized transgenesis system for *Drosophila* using germ-line-specific phiC31 integrases. *Proc. Natl Acad. Sci. USA* **104**, 3312–3317 (2007).

ADS CAS PubMed Article PubMed Central Google Scholar

37. 37.

Chao, S. H. & Price, D. H. Flavopiridol inactivates P-TEFb and blocks most RNA polymerase II transcription in vivo. *J. Biol. Chem*. **276**, 31793–31799 (2001).

CAS PubMed Article PubMed Central Google Scholar

38. 38.

Kroschwald, S., Maharana, S. & Simon, A. Hexanediol: a chemical probe to investigate the material properties of membrane-less compartments. *Matters* https://doi.org/10.19185/matters.201702000010 (2017).

39. 39.

Johansen, K. M. et al. Polytene chromosome squash methods for studying transcription and epigenetic chromatin modification in *Drosophila* using antibodies. *Methods* **48**, 387–397 (2009).

CAS PubMed PubMed Central Article Google Scholar

40. 40.

Chlamydas, S. et al. Functional interplay between MSL1 and CDK7 controls RNA polymerase II Ser5 phosphorylation. *Nat. Struct. Mol. Biol*. **23**, 580–589 (2016).

CAS PubMed Article PubMed Central Google Scholar

41. 41.

Mendjan, S. et al. Nuclear pore components are involved in the transcriptional regulation of dosage compensation in *Drosophila*. *Mol. Cell* **21**, 811–823 (2006).

CAS PubMed Article PubMed Central Google Scholar

42. 42.

Yang, Z. & Nielsen, R. Codon-substitution models for detecting molecular adaptation at individual sites along specific lineages. *Mol. Biol. Evol*. **19**, 908–917 (2002).

CAS PubMed Article PubMed Central Google Scholar

43. 43.

Neyman, J. & Pearson, E. S. in *Breakthroughs in Statistics* (eds Kotz, S. & Johnson, N. L.) 73–108 (Springer, 1992).

44. 44.

Yang, Z. & dos Reis, M. Statistical properties of the branch-site test of positive selection. *Mol. Biol. Evol*. **28**, 1217–1228 (2011).

CAS PubMed Article PubMed Central Google Scholar

45. 45.

Arrigoni, L. et al. RELACS nuclei barcoding enables high-throughput ChIP-seq. *Commun. Biol*. **1**, 214 (2018).

PubMed PubMed Central Article CAS Google Scholar

46. 46.

Skene, P. J. & Henikoff, S. A simple method for generating high-resolution maps of genome-wide protein binding. *eLife* **4**, e09225 (2015).

PubMed PubMed Central Article CAS Google Scholar

47. 47.

Boehning, M. et al. RNA polymerase II clustering through carboxy-terminal domain phase separation. *Nat. Struct. Mol. Biol*. **25**, 833–840 (2018).

CAS Article Google Scholar

48. 48.

Langmead, B. & Salzberg, S. L. Fast gapped-read alignment with Bowtie 2. *Nat. Methods* **9**, 357–359 (2012).

CAS PubMed PubMed Central Article Google Scholar

49. 49.

Zhang, Y. et al. Model-based analysis of ChIP-Seq (MACS). *Genome Biol*. **9**, R137 (2008).

PubMed PubMed Central Article CAS Google Scholar

50. 50.

Ramírez, F. et al. deepTools2: a next generation web server for deep-sequencing data analysis. *Nucleic Acids Res*. **44**, W160–W165 (2016).

PubMed PubMed Central Article CAS Google Scholar

51. 51.

Quinlan, A. R. & Hall, I. M. BEDTools: a flexible suite of utilities for comparing genomic features. *Bioinformatics* **26**, 841–842 (2010).

CAS PubMed PubMed Central Article Google Scholar

52. 52.

Li, H. et al. The Sequence Alignment/Map format and SAMtools. *Bioinformatics* **25**, 2078–2079 (2009).

PubMed PubMed Central Google Scholar

53. 53.

Grüning, B. A. et al. The RNA workbench: best practices for RNA and high-throughput sequencing bioinformatics in Galaxy. *Nucleic Acids Res*. **45** (W1), W560–W566 (2017).

PubMed PubMed Central Article CAS Google Scholar

54. 54.

Robinson, J. T. et al. Integrative genomics viewer. *Nat. Biotechnol*. **29**, 24–26 (2011).

CAS PubMed PubMed Central Article Google Scholar

55. 55.

Bailey, T. L. & Elkan, C. Fitting a mixture model by expectation maximization to discover motifs in biopolymers. *Proc. Int. Conf. Intell. Syst. Mol. Biol*. **2**, 28–36 (1994).

CAS PubMed Google Scholar

56. 56.

Love, M. I., Huber, W. & Anders, S. Moderated estimation of fold change and dispersion for RNA-seq data with DESeq2. *Genome Biol*. **15**, 550 (2014).

PubMed PubMed Central Article CAS Google Scholar

57. 57.

The Gene Ontology Consortium. The Gene Ontology Resource: 20 years and still GOing strong. *Nucleic Acids Res*. **47**, D330–D338 (2019).

Article CAS Google Scholar

58. 58.

Piovesan, D. et al. MobiDB 3.0: more annotations for intrinsic disorder, conformational diversity and interactions in proteins. *Nucleic Acids Res*. **46**, D471–D476 (2018).

CAS PubMed Article Google Scholar

59. 59.

Mier, P. & Andrade-Navarro, M. A. dAPE: a web server to detect homorepeats and follow their evolution. *Bioinformatics* **33**, 1221–1223 (2017).

CAS PubMed PubMed Central Google Scholar

60. 60.

Hulsen, T., de Vlieg, J. & Alkema, W. BioVenn—a web application for the comparison and visualization of biological lists using area-proportional Venn diagrams. *BMC Genomics* **9**, 488 (2008).

PubMed PubMed Central Article CAS Google Scholar

61. 61.

Koulouras, G. et al. EasyFRAP-web: a web-based tool for the analysis of fluorescence recovery after photobleaching data. *Nucleic Acids Res*. **46** (W1), W467–W472 (2018).

CAS PubMed PubMed Central Article Google Scholar

62. 62.

Joshi, S. S. & Meller, V. H. Satellite repeats identify X chromatin for dosage compensation in *Drosophila melanogaster* males. *Curr. Biol*. **27**, 1393–1402.e2 (2017).

CAS PubMed PubMed Central Article Google Scholar

63. 63.

Patel, S. S., Belmont, B. J., Sante, J. M. & Rexach, M. F. Natively unfolded nucleoporins gate protein diffusion across the nuclear pore complex. *Cell* **129**, 83–96 (2007).

CAS PubMed Article PubMed Central Google Scholar

Download references

Acknowledgements

We thank the MPI-IE facilities for support: in particular, U. Bönisch for deep sequencing; D. Ryan and G. Renschler for bioinformatics; R. Pohlmeyer and the imaging facility during COVID19 curfew; J. Herman for help in creating the *Msl2* knock-in mES cells; W. Szymanski for mass spectrometry; C. Pessoa, U. Gündisch, A. Alexiadis and T. Stehle for technical support; U. Erdogdu and T. Rumpf for sharing reagents and visualizing the CXC domain structure, respectively; S. Hiller and T. Sharpe for advice on biophysical data and conducting SEC–MALS, respectively; G. Pyrowolakis, M. Carmo-Fonseca, V. Meller, A. Brand and M. Bühler for sharing antibodies, plasmids, fly stocks and the parental mES cells, respectively; M. Boehning and P. Cramer for the control protein for the in vitro FRAP experiment; and R. Sawarkar, N. Iovino, G. Renschler, M.

Samata, M. Shvedunova and K. Woolcock for input that helped to improve the manuscript. The mouse symbol was modified from an icon made by Freepik from www.flaticon.com. C.I.K.V. was supported by a Human Frontier Science Program long-term fellowship (000233/2014-L). This study was supported by the German Research Foundation (DFG) under Germany's Excellence Strategy (CIBSS – EXC-2189 – Project ID 390939984). This work was supported by the DFG under the CRC 992 (project A02) and CRC 1381 (project B3) awarded to A.A.

Author information

Author notes

1. These authors contributed equally: Claudia Isabelle Keller Valsecchi, M. Felicia Basilicata

Affiliations

1. Max Planck Institute of Immunobiology and Epigenetics, Freiburg im Breisgau, Germany

   Claudia Isabelle Keller Valsecchi, M. Felicia Basilicata, Plamen Georgiev, Aline Gaub, Janine Seyfferth, Tanvi Kulkarni, Amol Panhale, Giuseppe Semplicio, Vinitha Manjunath, Herbert Holz & Asifa Akhtar

2. Faculty of Biology, University of Freiburg, Freiburg im Breisgau, Germany

   Tanvi Kulkarni

3. Institute for Evolutionary Biology and Environmental Studies, University of Zurich, Zurich, Switzerland

   Pouria Dasmeh

Authors

1. Claudia Isabelle Keller Valsecchi
   View author publications

   You can also search for this author in PubMed Google Scholar

2. M. Felicia Basilicata
   View author publications

   You can also search for this author in PubMed Google Scholar

3. Plamen Georgiev
   View author publications

   You can also search for this author in PubMed Google Scholar

4. Aline Gaub
   View author publications

   You can also search for this author in PubMed Google Scholar

5. Janine Seyfferth
   View author publications

   You can also search for this author in PubMed Google Scholar

6. Tanvi Kulkarni
   View author publications

   You can also search for this author in PubMed Google Scholar

7. Amol Panhale
   View author publications

   You can also search for this author in PubMed Google Scholar

8. Giuseppe Semplicio
   View author publications

   You can also search for this author in PubMed Google Scholar

9. Vinitha Manjunath
View author publications

You can also search for this author in PubMed Google Scholar

10. Herbert Holz
View author publications

You can also search for this author in PubMed Google Scholar

11. Pouria Dasmeh
View author publications

You can also search for this author in PubMed Google Scholar

12. Asifa Akhtar
View author publications

You can also search for this author in PubMed Google Scholar

Contributions

C.I.K.V. conceptualized the study with M.F.B., P.G., P.D. and A.A. P.G. performed all *Drosophila* genetic experiments with the help of V.M. A.G. performed ChIP experiments and prepared polytene squashes. J.S. and H.H. assisted with the generation and analysis of mES cells. G.S. processed NGS data. T.K. and A.P. performed immunostainings and microscopy of the S2 cell hexanediol experiment. P.D. performed computational analyses on molecular evolution and fitted rate constants. C.I.K.V. and M.F.B. performed all other experiments and data analyses, and wrote the manuscript with input from all authors. C.I.K.V. and M.F.B. designed, coordinated and supervised the experiments. A.A. provided guidance and secured funding.

Corresponding author

Correspondence to Asifa Akhtar.

Ethics declarations

Competing interests

The authors declare no competing interests.

Additional information

Peer review information *Nature* thanks Justin Crocker, Richard Kriwacki and the other, anonymous, reviewer(s) for their contribution to the peer review of this work.

Publisher's note Springer Nature remains neutral with regard to jurisdictional claims in published maps and institutional affiliations.

Extended data figures and tables

Extended Data Fig. 1 Genome-wide analyses of dosage compensation upon loss of *msl* and *roX* genes.

a, H4K16ac ChIP–seq profiles were generated from wild-type male, wild-type female or homozygous mutant male L3 larvae. The $roX1^{SMC17A}$ $roX2^{\Delta}$ (abbreviated as *roX1 roX2*), mle^{9} (abbreviated as *mle*) and $msl\text{-}1^{L60}$ (abbreviated as *msl-1*) alleles were compared with controls. The chromatin was fragmented with MNase. Boxplots display the normalized coverage in the input (2-kb bins, n = 11,347 (chr2L), n = 12,083 (chr2R), n = 13,459 (chr3L), n = 15,624 (chr3R), n = 11,377 (chrX); replicates were merged for plotting). The relative coverage of the X chromosome shows that males and females were accurately separated. **b**, H4K16ac ChIP–seq as in **a**. The plots show the mean input-normalized $\log_2$[fold-change] enrichment at scaled X-linked gene bodies (first 0.6 kb unscaled, left), HAS (middle), and random regions (shuffled HAS positions, right). A Welch Two Sample t-test (two-tailed) for the enrichment of H4K16ac on X-linked gene bodies (n = 2,647) in mutant males compared with females revealed P-values of 3.86×10^{-87} (*roX1 roX2*), 2.57×10^{-54} (*mle*) and 0.025 (*msl-1*). A subset of the same

data are also shown in Fig. 1b. Also see Supplementary Data 4 for details on statistics. **c**, H4K16ac ChIP–seq as in **a**. Genome-browser snapshot showing the 1x sequencing depth normalized ChIP coverage on an X-linked region containing a HAS, whose position is highlighted with a diamond. **d**, H4K16ac ChIP–qPCR analyses of genotypes abbreviated as in **a**. The barplot shows the mean of $n = 3$ independent biological replicates/experiments ± s.e.m. on the indicated genes. Enrichment values were corrected over the input and expressed relative to the *Klg* gene (not shown for clarity of the panel). **e**, Cropped immunoblots of protein levels in nuclear extracts of male and female L3 larvae. Genotypes are wild-type (lanes 1 and 2), *msl-2::HA* (lanes 3 and 4) and $roX1^{SMC17A}$ $roX2^{\Delta}$/Y ; *msl-2::HA* (lane 5). For source data, see Supplementary Fig. 1. **f**, Schematic representation of the experimental setup for RNA-seq from dissected wing imaginal discs. The $msl\text{-}2^{227}$ (abbreviated as *msl-2*), $roX1^{SMC17A}$ $roX2^{\Delta}$ (abbreviated as *roX1 roX2*), mle^{9} (abbreviated as *mle*) and $msl\text{-}1^{L60}$ (abbreviated as *msl-1*) homozygous null mutant males were compared with control males. Data processing is described in Methods. **g**, RNA-seq as in **f**, MA-Plots showing normalized counts versus the $\log_2$[fold change] obtained with DESeq2. Differentially expressed (DE) genes (FDR < 0.05) are colored in red (upregulation) and blue (downregulation) and the number of DE genes is reported in each panel. **h**, RNA-seq as in **f**, Boxplots show the $\log_2$[fold-change] of all genes ($n = 265$) directly overlapping with HAS. The *P*-values were obtained by a two-sided Wilcoxon rank-sum test. **i**, RNA-seq as in **f**, Boxplots show the linear distance in kb to the closest HAS of all DE downregulated genes on the X chromosome scored in each mutant (*msl-2*: $n = 465$, *roX1 roX2*: $n = 430$, *mle*: $n = 632$, *msl-1*: $n = 777$ genes). This was compared with the distance to HAS obtained from the same number *n* of random X-linked genes (grey boxplots). The *P*-values were obtained by a two-sided Wilcoxon rank sum test. **j**, RNA-seq as in **f**, Barplot for the number of DE genes with respect to their location on the chromosomal arms. The *P*-values for overrepresentation of X-linked genes obtained from a one-sided Fisher's test are reported. **k**, RNA-seq as in **f**, Density plots of the $\log_2$[fold change] obtained with DESeq2 for genes on each of the indicated chromosomal arms. All genes were taken into account for the analyses, irrespective of whether they are scored as DE or not. **l**, RNA-seq as in **f**, Venn diagram showing the overlaps of the DE genes on

the X chromosome and autosomes, where the area is proportional to the number of genes in each group. For clarity of the panel, *mle* is not shown. **m**, RNA-seq as in **f**, Barplot showing the DE gene overlap. The plot illustrates whether DE genes were found exclusively in one particular mutant data set, or also in others. The results for the overlaps of DE genes are reported for up- versus downregulated and X chromosome and autosomes separately. **n**, MLE ChIP–qPCR analyses from separated male or female *msl-2*^{227}*/CyO-GFP* or *msl-2*^{227}*/msl-2*^{227} L3 larvae. The barplot shows the mean ± s.e.m. of $n = 3$ independent ($n = 2$ for male homozygous larvae due to limited sample availability) biological replicates/experiments on the indicated HAS or control regions (*odsh*, *Klg*). Enrichment values were corrected over the input and expressed relative to the mean of the non-target control regions (*odsh*, *Klg*). **o**, Cropped immunoblots of same genotypes as in **e**. MSL2 protein is not expressed in females[9]. For source data, see Supplementary Fig. 1. **p**, Immunofluorescence of polytene chromosome squashes from endogenously tagged *msl-2::HA* male (panel 1) and female (panel 2), as well as *roX1*^{SMC17A}*, roX2*$^{\Delta}$; *msl-2::HA* male salivary glands. MSL2-HA is shown in red, MOF in green and DAPI in blue. Panels 4 and 5 show the more frequent case of lost X chromosome enrichment for MSL2 with gain at the chromocentres accompanied by a homogenous, female-like staining of MOF. Panel 3 illustrates a rare example, where some X chromosome staining can be scored in *roX1 roX2* double nulls, however, the staining pattern is clearly distinct from wild-type. The latter staining is similar to what has been reported in[10,17] and we interpret it to be a consequence of an alternative mechanism that can drive MSL complex recruitment to the X[62]. Scale bars = 20 μm. **q**, MSL2-HA ChIP–qPCR analyses from wild-type *msl-2::HA* male, *msl-2::HA* female or homozygous mutant male L3 larvae abbreviated as in **f**. The barplot shows the mean of $n = 3$ independent biological replicates/experiments ± s.e.m. on the indicated HAS or control regions (*odsh*, *Ent2*). Enrichment values were corrected over the input and expressed relative to the mean of the non-target control regions (*odsh*, *Ent2*).

Extended Data Fig. 2 Computational and in vitro characterization of MSL2 CXC and CTD domains.

a, MSL2 ChIP–seq analyses (data published by[10]). Boxplots display the change in input-normalized ChIP enrichment difference in *roX1ex6 Df(1)roX2*[52] (abbreviated as *roX1 roX2*) versus wild-type on MSL2-enriched 1 kb bins, HAS (n = 267/26 on X/autosomes) or random regions. The random regions were generated by shuffling the enriched 1 kb bins. A negative value indicates a loss of enrichment in the mutant, while a gain is indicated by a positive value. The enrichment score was calculated using deepTools multibigwig summary. 1 kb bins with a score >0.7 in either genotype were classified as enriched (n = 1,893 enriched/144,916 total bins, of which n = 1,448 reside on X and n = 445 on autosomes). A Welch Two Sample t-test for the difference in enrichment of MSL2 at HAS in wild-type versus *roX1 roX2* revealed a P-value of 4.387×10^{-73}. **b**, as in **a**, Genome-browser snapshot of MSL2 ChIP–seq. Data normalization is described in Methods. **c**, Analysis of adult male viability in flies expressing transgenic roX2 (*tg1*, *tg2*, *tg3*) in a $roX1^{SMC17A}$ $roX2^{\Delta}$ background. The data was expressed relative to females obtained from the same cross. The barplot represents the mean ± s.e.m. with overlaid datapoints reflecting the results from n = 6 vials/crosses per genotype. Details on genotypes and nature of transgenes are provided in Methods and Supplementary Data 4. **d**, RT–qPCR analysis of the indicated genes in $roX1^{SMC17A}$ $roX2^{+}$ (bar 1) or $roX1^{SMC17A}$ $roX2^{\Delta}$; *roX2tg1/tg2/tg3* (bars 2–4, see Methods) or wild-type female (bar 5) L3 larvae. All genotypes additionally contained the *msl-2::HA* allele. The RNA level of each gene was normalized to *RpL32* and expressed relative to $roX1^{SMC17A}$ $roX2^{+}$ male flies. The barplot represents the mean ± s.e.m. of n = 5 larvae with overlaid datapoints reflecting the result from one individual larva. **e**, Representative coomassie-stained SDS–PAGE of the purified GST-CXC domains of *D. melanogaster* (Dmel), *D. virilis* (Dvir) and *H. sapiens* (Human). GST was used as negative control (−ctrl). For source data, see Supplementary Fig. 1. **f**, Biolayer interferometry (BLItz) experiments were conducted to quantify binding of the recombinant GST-tagged CXC proteins of different species as in **e** to the biotinylated ATGAGCGAGATG dsDNA (referred to as S12 in[12]). The barplots report the mean fitted K(on1) and K(off1) ± s.e.m. rate constants (left), the boxplots display the equilibrium KDs (right). Parameters were determined from two independent protein purifications. In each independent experiment (Dmel CXC n = 12, Dvir CXC n = 7, Human CXC n = 6), the

proteins were measured over a concentration range of at least 5 different dilutions. Only measurements at concentrations above 1 μM were taken into account for fitting using a 2:1 binding model (also see Methods). The *P*-values were obtained by a two-sided Wilcoxon rank sum test. **g**, as in **f**, Representative BLItz experiments with observed signals shown in grey and fitted in red-blue colour. **h**, Sequence alignment of the CTD of MSL2 in different mammalian and *Drosophila* species abbreviated as Dmel = *D. melanogaster*, Dsim = *D. simulans*, Dsec = *D. sechellia*, Dyak = *D. yakuba*, Dere = *D. erecta*, Dana = *D. ananassae*, Dpse = *D. pseudoobscura*, Dwil = *D. willistoni*, Dmoj = *D. mojavenis*, Dvir = *D. virilis*, Dgri = *D. grimshawi*. The numbering at the top refers to the relative amino-acid position, starting from the CTD. **i**, Evaluation of the poly-proline bias in the MSL2 CTD of *Drosophila* species abbreviated as in **h** compared to mammalian species. Prolines are indicated with a grey bar. The amino acid sequence of the *D. melanogaster* CTD is shown below, with significantly enriched low complexity regions by dAPE software shown in colour. **j**, Top, illustration of the published crystal structure of the MSL2 CXC domain in complex with DNA (PDB: 4RKH). Residues with signs of positive selection are colored in red, conserved residues in blue. Bottom, sequence alignment of the MSL2 CXC domains of different species abbreviated as in **e**. Residues with signs of positive selection (also see Supplementary Data 2) are colored in red, conserved residues in blue. **k**, Representative coomassie-stained SDS–PAGE of the purified *Drosophila* dCXC-CTD, as well as the *Drosophila* dCTD proteins. Purified His-Smt3 was used as negative control in several in vitro assays. For source data, see Supplementary Fig. 1. **l**, Biolayer interferometry (BLItz) experiments were conducted to quantify binding of *Drosophila* dCXC-CTD or dCTD proteins to the biotinylated dsDNA CGAATATGAGCGAGATGGATG (CES11D1). The BLItz experiments for the dCXC-CTD (20 and 10 μM) are shown in black/grey, while the dCTD (40 and 20 μM) is shown in blue. The two lines at each concentration indicate two independent measurements. **m**, Absorbance at 280 nm recorded during anion exchange chromatography conducted after the His-Talon purification of the dCXC-CTD construct. Two peaks were monitored, of which the second one corresponds to co-purifying nucleic acids. **n**, Absorbance at 280 nm recorded during gel filtration of the *Drosophila* dCXC-CTD and mammalian mCXC-CTD proteins. Final pooled fractions used for in vitro assays are indicated. **o**, Representative

example BLItz experiments of the recombinant *D. melanogaster* GST-dCXC and untagged dCXC-CTD protein binding to the CGAATATGAGCGAGATGGATG dsDNA (referred to as CES11D1 in[12]). The experimental signal is colored in grey and the fitted data overlaid in colour. The concentrations from top to bottom in the panels of the GST-dCXC proteins were (40, 16, 4, 2, 0.66, 0.33 μM) and dCXC-CTD (100, 75, 50, 37.5, 25, 10, 4, 1.5, 0.75 μM). Fitted rate constants from $n = 5$ (dCXC-CTD) or $n = 4$ (GST-dCXC) independent protein purifications are reported in Fig. 1i. Significance was evaluated with a two-sided Wilcoxon rank sum test, where the difference in equilibrium constant (K_{D1}) revealed a P-value of 1.26×10^{-7}, $n = 29$ (dCXC-CTD) versus $n = 21$ (GST-dCXC) measurements.

Extended Data Fig. 3 In vitro characterization of dCXC-CTD oligomerization and dCXC-CTD-roX2 droplets.

a, Size exclusion multiangle light scattering (SEC-MALS) experiment performed for the recombinant dCXC-CTD protein. Left, schematic representation of the experimental approach to determine the molar mass of a particle by SEC-MALS. Middle, normalized excess Rayleigh ratio (light scattering, red), normalized differential refractive index (blue) and molar mass (green dots) from SEC-MALS for the dCXC-CTD at three different concentrations with the elution volume displayed on the *x* axis. The 27.8 kDa dCXC-CTD exhibited a similar elution volume to the 66 kDa BSA monomer, suggesting that it has an unusually large hydrodynamic radius, consistent with parts of it being intrinsically disordered. Right, legend and table with weight-averaged molar mass determined from the SEC-MALS experiment. The loading concentrations of the samples were: 1) high concentration (50 μM, left) and 2) medium (15 μM, right) 3) low concentration (5 μM, right). The observed particle masses at high concentrations are higher than the calculated molar mass of the monomeric dCXC-CTD protein. **b**, Fluorescence confocal microscopy of 10 μM roX2 RNA spiked at 1:100 molar ratio with fluorescein-labelled roX2, which was mixed with recombinant dCXC-CTD protein at the indicated concentrations and conditions. The buffer was 25 mM MES, pH 6.5, 75 mM NaCl, 0.5 mM TCEP, 2.5% glycerol, 2.5% PEG-8000. In the lower panel, the buffer was

25 mM MES, pH 6.5, 75 mM NaCl, 0.5 mM TCEP, 10% PEG-8000. Scale bars = 20 μm. **c**, as in **b**, upon addition of 5% or 10% 1,6-hexanediol, which did not dissolve the roX2-dCXC-CTD particles over the observed time period of around 1 h. Scale bars = 20 μm. **d**, Average fluorescence intensity over time of bleached area of 10 μM roX2 RNA spiked at 1:100 molar ratio with fluorescein-labelled roX2 mixed with 10 μM recombinant dCXC-CTD protein. The buffer was 25 mM MES, pH 6.5, 75 mM NaCl, 0.5 mM TCEP, 2.5% Glycerol, 2.5% PEG-8000. Entire droplets were bleached and the recovery was recorded over two different time courses (long, 600 s and short, 85 s). For each time course, the black line represents the average of $n = 7$ FRAP experiments that were performed with 2 different protein purifications with the standard deviation shaded in grey. Data fitting and immobile fraction analysis was obtained with EasyFRAP (see Methods). Representative FRAP images (scale bars = 2 μm) of in vitro roX2-MSL2 (dCXC-CTD) droplets are shown below the data curve panels. **e**, Fast recovering FRAP control, MBP-Pol2(CTD), as described by[47]. 75 μM unlabelled protein was spiked at 1:100 molar ratio with Alexa488-labelled protein in 20 mM HEPES, pH 7.4, 220 mM NaCl, 0.2 mM TCEP, 2% Glycerol, 16% Dextran. The black line represents the average of $n = 10$ FRAP experiments with the standard deviation shaded in grey. The fitted $t_{1/2}$ recovery time was 5.5 ± 0.8 s.

Extended Data Fig. 4 In vivo dynamics of the MSL complex territory.

a, Schematic representation of the experimental setup to analyse in vivo dynamics of the MSL complex. *Drosophila* S2 cells or L3 larval imaginal discs were exposed to 5% of 1,6-hexanediol at the indicated time points. For the recovery experiment, 1,6-hexanediol is removed after 5 min and replaced with fresh growth media. The recovery times were 3.5 h in S2 cells and only 10 min in imaginal discs to avoid prolonged incubation of the inverted larval tissues ex vivo (see Methods). The treatments were stopped by fixation. **b**, The X chromosomal territory enrichment ratio by immunofluorescence is calculated by dividing the average intensity of the territory in one nucleus by the average intensity of an equally sized region elsewhere in the same nucleoplasm. Immobile fractions by 1,6-hexanediol were calculated as percent territory enrichment remaining after treatment. **c**, Quantification of hexanediol experiment in S2 cells as outlined in **a** with a recovery phase of 3.5 h see **f** for representative pictures. The dot plots represent mean ± s.e.m. percentage of nuclei with a rim localization (NUP153, left) or X chromosome territory (MSL1, right) of the total number of nuclei. Each dot represents the *n* fields of view that were evaluated ($n = 4$ for 0 min, 2 min and 5 min; $n = 3$ for recovery), the total number of analysed nuclei is reported for each experimental condition. The *P*-values were obtained by a Kruskal–Wallis test followed by a Dunn's statistical test for multiple comparisons. **d**, Quantification of hexanediol experiment in S2 cells as outlined in **a** with a recovery phase of 3.5 h see **f** for representative pictures. The territory enrichment ratio by intensity was determined as delineated in **b**. The bar plots show the mean ± s.e.m. with overlaid data points reflecting individual nuclei, $n = 117$ (0 min), $n = 116$ (2 min), $n = 99$ (5 min), $n = 103$ (recovery) for MSL1 and $n = 117$ (0 min), $n = 108$ (2 min), $n = 99$ (5 min), $n = 103$ (recovery) for H4K16ac. The *P*-values were obtained by a Kruskal–Wallis test followed by a Dunn's statistical test for multiple comparisons. **e**, Quantification of hexanediol experiment in *Drosophila* L3 larval imaginal discs as delineated in **a** with recovery phase of 10 min, see **g** for representative pictures. The territory enrichment ratio by intensity was determined as delineated in **b**, evaluated areas in territory and nucleoplasm were 0.384 μm^2 as of the smaller nuclear

size compared to S2 cells. The bar plots show the mean ± s.e.m. with overlaid data points reflecting individual nuclei. n = 120 (0 min), n = 115 (5 min), n = 123 (10 min) n = 109 (recovery) nuclei were counted from three (n = 3) imaginal discs/biological replicates for each condition. The P-values were obtained by a Kruskal–Wallis test followed by a Dunn's statistical test for multiple comparisons. **f**, Hexanediol experiment as outlined in **a**. Immunofluorescence was performed in S2 cells and H4K16ac (red), MSL1 (green), NUP153 (grey) were detected with antibodies, DAPI in blue. NUP153 serves as a control, as FG-nucleoporins are sensitive to 1,6-hexanediol[63]. The representative pictures are orthogonal projections of an entire z-stack with scale bars = 10 µm. The recovery experiment highlights that cell viability was not compromised by the treatment and cellular function was sustained during the recovery phase. **g**, Hexanediol experiment as outlined in **a**. Immunofluorescence was performed in imaginal discs from *msl-2::HA* flies (endogenously tagged). HA (MSL2, red), MSL1 (green), NUP153 (grey) were detected with antibodies, DAPI in blue. The representative pictures are single z-planes with scale bars = 10 µm. **h**, RT–qPCR analysis of the indicated genes from dissected wing imaginal discs with *msl-2*^{227} null alleles in homozygous or heterozygous (*CyO-GFP*) condition. The RNA level of each gene was normalized to *RpL32* and expressed relative to heterozygous males. The barplot represents the mean ± s.e.m. of n = 5 replicates with overlaid data points representing individual wing disc samples. **i**, RT–qPCR analysis of the indicated genes from dissected wing imaginal discs in females ectopically expressing *UAS-msl-2* or *UAS-ctrl* with *hh-Gal4*. The RNA level of each gene was normalized to *RpL32* and expressed relative to *UAS-ctrl*. The barplot represents the mean ± s.e.m. of n = 5 replicates with overlaid data points representing individual wing disc samples. **j**, RT–qPCR analysis of the indicated genes from male L3 larvae. Heterozygous and homozygous mutants of the *msl-1*^{L60} (abbreviated as *msl1-1*), *msl-2*^{227} (abbreviated as *msl-2), msl-3*^{083} (abbreviated as *msl-3*) alleles were analysed. The RNA level of each gene was normalized to *RpL32* and expressed relative to wild-type male flies. The barplot represents the mean ± s.e.m. of n = 5 larvae. **k**, as in **j**, but for the *msl-2*^{227} (abbreviated as *msl-2), mle*^{9} (abbreviated as *mle*) and *roX1*^{SMC17A}, *roX2*$^{\Delta}$ (abbreviated as *roX1, roX2*) and recombinants of these alleles.

Extended Data Fig. 5 Characterization of MSL2 hybrids in *Drosophila*.

a, Cropped immunoblots of total protein extracts of adult male fly heads expressing *msl-2* hybrid transgenes (*UAS-tg*). The genotype was *msl-2*^{227}/*msl-2*^{kmA} *; tub-Gal4/UAS-tg*. The MSL2* transgene refers to point mutations at I529T, N534P and T535G, which gave largely identical results to the *D. virilis* MSL2^{vCXC} hybrid construct (also see Supplementary Data 3). Because the CTD and RING hybrids displayed some defects in protein stability, we generated additional transgenic flies with two integrations for the CTD and CXC-CTD hybrids (indicated as 2× and 1×, also see Methods). This served to exclude the possibility that a particular assay is confounded by lower protein levels. For source data, see Supplementary Fig. 1. **b**, as in **a**, but for the heterozygous *msl-2*$^{227/kmA}$/*CyO-GFP; tub-Gal4/UAS-tg*-expressing male flies. The no transgene refers to *msl-2*$^{227/kmA}$/*CyO-GFP ; tub-Gal4/+* . **c**, as in **a**, but for the *msl-2*^{227}/*msl-2*^{kmA} *; tub-Gal4/UAS-tg*-expressing female flies. **d**, as in **a**, but for the *msl-2*^{227}/*msl-2*^{kmA} *; tub-Gal4/UAS-tg*-expressing male flies and with extracts prepared from L3 larvae. The lines with two integrations of the MSL2$^{mCXC-CTD}$ construct were created by recombining integrations at the VK33 and 68FB landing sites. **e**, Co-immunoprecipitations of Flag-tagged full-length MSL2^{WT}, MSL2 hybrids and an untagged control with cropped immunoblots for Flag and MSL1. Flag expression vectors driven by an inducible MtnA promoter were transiently transfected into S2 cells. Following selection with blasticidin, the protein was induced overnight by addition of copper sulfate to the culture media. Flag immunoprecipitations were conducted from nuclear extracts. For source data, see Supplementary Fig. 1. **f**, ChIP–qPCR analyses of His-Bio-His-tagged full-length MSL2 (MSL2^{WT}), MSL2 domain hybrids and an untagged control. Expression vectors driven by an inducible *MtnA* promoter were transfected into S2 cells. Following selection with Blasticidin, the protein was induced overnight by addition of copper sulfate to the culture media before formaldehyde fixation and ChIP (Streptavidin IP). The barplot shows the mean of n=3 independent biological replicates/experiments ± s.e.m. on the indicated HAS with overlaid data points. Enrichment values were corrected over the input and expressed relative to the control region (*odsh*). **g**,

H4K16ac ChIP–qPCR analyses of male L3 larvae expressing *msl-2* hybrid transgenes in *msl-2*^{227}/*msl-2*^{kmA} backgrounds. The barplot shows the mean of n = 3 independent biological replicates/experiments ± s.e.m. on the indicated genes. Enrichment values were corrected over the input and expressed relative to *Klg*, which does not display any H4K16ac enrichment in ChIP–seq. *CG42732, U6, U12, Klg* and *Intergenic* represent negative controls. **h**, Immunofluorescence of polytene chromosome squashes from male L3 larvae expressing Flag-tagged *msl-2* hybrid transgenes (MSL2^{WT} or MSL2^{mCXC}) in *msl-2*^{227}/*msl-2*^{kmA} background. MSL1 (green), Flag (red) and DAPI (blue) are shown, scale bars = 20 µm (left panel) and 10 µm (right panel). **i**, RT–qPCR analysis of the indicated genes from male L3 larvae of the following genotypes: *msl-2*$^{227/kmA}$/*CyO-GFP; tub-Gal4/+* (bar 1, abbreviated as het), *msl-2*^{227}/*msl-2*^{kmA}*; tub-Gal4/+* (bar 2), *msl-2*^{227}/*msl-2*^{kmA}*; tub-Gal4/UAS-tg* (MSL2^{WT}, bar 3, blue) or *msl-2*^{227}/*msl-2*^{kmA}*; tub-Gal4/UAS-tg* (MSL2^{mCXC}, bar 4, orange). The RNA level of each gene was normalized to the geometric mean of *RpL32, hh* and *ssp4* and expressed relative to *msl-2*$^{227/kmA}$/*CyO-GFP; tub-Gal4/+* flies. The barplot represents the mean ± s.e.m. of at least n = 4 larvae with overlaid datapoints representing individual larva. **j**, MEME motif analyses of *Drosophila* MSL2 ChIP peaks overlapping with HAS[6] or mouse MSL2 ChIP peaks[32] in mouse embryonic stem cells (mES cells) at transcription start sites (TSS ± 1 kb), within gene bodies (intragenic, 1 kb to transcription end site) or outside annotated genes (distal). For mammalian MSL2, only MACS2 peaks associated with differentially expressed genes in *Msl2*Δ mES cells[6] were analysed. The top scoring motif with respective E-value is reported in the panel. **k**, b-isox precipitation experiments were conducted from wild-type males (*msl-2::HA*, endogenously tagged) and *msl-2*^{227}/*msl-2*^{kmA} *; tub-Gal4/UAS-tg* (Flag-tagged MSL2^{WT} or MSL2^{mCTD} hybrid)-expressing female transgenic L3 larvae. Left, schematic representation of the experimental setup as in Fig. 2g. Right, cropped immunoblots of b-isox precipitation fractions. The HA blot was cropped to remove marker positions, the HA and Flag blots were obtained from 2 different gels loaded with the same extracts. For source data, see Supplementary Fig. 1.

Extended Data Fig. 6 ChIP–seq, expression and immunofluorescence analyses of MSL2 hybrids in *Drosophila*.

a, Cropped immunoblots of a fraction of input and immunoprecipitate of the Flag ChIP–seq samples generated from male L3 larvae expressing *msl-2* wild-type or hybrid transgenes with *tub-Gal4* in the *msl-2*^{227}/*msl-2*^{kmA} background. The MSL2^{mCTD} (2x) was used, all other transgenes are present in a single copy and have a C-terminal 3xFlag tag. RPB3 and histone H3 serve as loading and negative IP control. Blots were cropped at the vertical dashed line to remove extra lanes. Displayed bands were derived from the same gels. No bands were detectable in the ChIP samples for H3. For source data, see Supplementary Fig. 1. **b**, MSL2–Flag ChIP–seq as in **a**. Genome-browser snapshot on a selected X-chromosomal region showing the Flag ChIP–seq data (Input subtracted) obtained from MSL2 hybrids together with roX2 ChIRP[28], H3K36me3 and H4K16ac from male L3 larvae[6]. **c**, MSL2–Flag ChIP–seq analyses from transgenic L3 larvae as in **a**. Heatmaps show the normalized ChIP enrichment (Input subtracted) on HAS (top) and same number of randomly shuffled regions (bottom). The first four represent male samples, the last females. Biological replicates were merged for visualization. For the MSL2$^{mCXC\text{-}CTD}$ male only a single replicate of sufficient quality could be generated. **d**, MSL2–Flag ChIP–seq as in **a**. Heatmaps show the $\log_2$[fold-change] of the normalized MSL2^{mCTD} or MSL2^{mRING} ChIP enrichment versus the normalized wild-type MSL2^{WT} ChIP enrichment on all MACS2 peaks collectively called in each replicate and ChIP experiment (wild-type and all hybrids combined). Two unsupervised K-means clusters were generated, which separates the regions into gain of enrichment (top, red) and loss of enrichment (bottom, blue) in the hybrids. The signal is sorted by enrichment intensity within each cluster. Right, frequency of peaks per chromosome in the gain of enrichment group in comparison with the size of the *Drosophila* chromosomal arms. The gained peaks are almost exclusively found on autosomes. **e**, MSL2–Flag ChIP–seq as in **a**. MEME-ChIP was used to analyse motifs in peaks within the gain of enrichment group determined in **d**. No significant motifs were found by MEME, the top scoring motif from DREME with E-value is shown. **f**, as in **e**, showing the DREME motif and E-value that displayed the highest central distribution by Centrimo ($E = 5.3 \times 10^{-1}$). **g**, MSL2–Flag ChIP–seq as in **a**. Schematic representation of the motif search approach. FIMO was used to find the mMSL2 TSS, distal and intragenic motifs (Extended Data Fig. 5j) in the *Drosophila* genome. The identified motif

positions were intersected with the collective peaks list and analysed for overrepresentation in the gain or loss-group by a one-sided Fisher's exact test. The peak frequencies in each group are displayed on the right and revealed no statistically significant *P*-values. **h**, Immunofluorescence of Armadillo (green) and phosphorylated Histone H3 Ser28 (purple) in male wing imaginal discs from wild-type or *msl-2*^{227}*/msl-2*^{kmA} L3 larvae expressing the MSL2^{WT}, MSL2^{mCTD} (2x) or MSL2$^{mCXC\text{-}CTD}$ (2x) transgenes with *tub-Gal4*. DAPI in blue. The pictures are single *z*-planes with scale bars = 20 µm. **i**, Immunofluorescence of Armadillo (green) in male salivary glands from L3 larvae as in **h**. The pictures are single *z*-planes with scale bars = 100 µm, DAPI is shown in blue. **j**, RT–qPCR analysis of RNA levels of the indicated genes in homozygous *msl-2*^{227}*/msl-2*^{kmA} L3 larvae expressing MSL2 hybrids as in **h**. The RNA level of each gene was normalized to *RpL32* and expressed relative to *msl-2*$^{227/km}$*/CyO-GFP* heterozygous flies expressing MSL2^{WT}. For clarity of the panel, the results of the heterozygous flies are not shown. The barplot represents the mean ± s.e.m. with overlaid data points reflecting one individual larva (*n* analysed larvae reported for each bar). The selected genes are involved in cellular functions such as cell division (*Yippee*), cell adhesion and signalling (*arm*) or cell migration (*pico*). **k**, RT–qPCR analysis of roX2 in heterozygous *msl-2*$^{227/km}$*/CyO-GFP* or homozygous *msl-2*^{227}*/msl-2*^{kmA} male L3 larvae expressing the MSL2 hybrid transgenes (*tub-Gal4/UAS-tg*). The "no transgene" (no tg) control refers to *tub-Gal4/+* on the 3rd chromosome. All transgenes were present in a single copy. The RNA level of each gene was normalized to *RpL32* and expressed relative to the no transgene, *CyO-GFP* flies. The barplot represents the mean ± s.e.m. of at least 3 replicates with overlaid data points reflecting one individual larva.

Extended Data Fig. 7 Validation of mammalian reconstitution models.

a, Co-immunoprecipitations of Flag-tagged MSL2^{WT}, MSL2^{dCTD} or MSL2$^{dCXC\text{-}CTD}$ hybrid knock-in (also see Fig. 3a) and untagged parental control mES cell lines with cropped immunoblots for the MSL complex members MSL1 and MOF. RNA Pol2 serves as an input loading and negative immunoprecipitation control. Immunoprecipitations were

conducted from nuclear extracts. Blots were cropped at the vertical dashed line to remove extra lanes. Displayed bands were derived from the same gels. For source data, see Supplementary Fig. 1. **b**, RT–qPCR analysis of the mouse MSL2 target genes *Bex2*, *Phf8*, *Zfp185* and *Tsix* in parental (clone MF, $n = 4$), *Msl2*Δ (clone D12, $n = 4$), $MSL2^{WT}$ (clone D11, $n = 4$), $MSL2^{dCTD}$ (clone F4, $n = 4$) and $MSL2^{dCXC\text{-}CTD}$ (clone G2, $n = 3$) mES cells (also see Fig. 3a). The RNA level of each gene was normalized to *Hprt* and expressed relative to the parental cell line (MF). The barplot represents the mean ± s.e.m. with overlaid data points representing biological replicates. **c**, RNA-seq was conducted in $MSL2^{WT}$ (clone D11), knockout (*Msl2*Δ, clone D12) or hybrid ($MSL2^{dCTD}$, clone F4; $MSL2^{dCXC\text{-}CTD}$, clone G2)-expressing mES cells. In the scatterplot, each dot shows the $\log_2$[fold-change] of the RNA expression of a mouse gene in a given MSL-hybrid cell line versus the $MSL2^{WT}$ mES cells. Differentially expressed (DE) genes were colored in red (upregulation) or blue (downregulation), if the FDR from DESeq2 was <0.05 in any of the MSL2 hybrid cell lines. The Pearson correlation coefficient of the gene expression changes was calculated with the panel.cor function in R. **d**, RNA-seq as in **c**. Heatmap and dendrogram displaying the $\log_2$[fold-change] of the significantly (FDR < 0.05) DE genes in any of MSL2 hybrid versus the control ($MSL2^{WT}$) mES cells by RNA-seq. The $\log_2$[fold-change] of these genes in *Msl2*Δ knockout versus control ($MSL2^{WT}$) was plotted to compare whether DE genes in MSL2 hybrid expressing cells are also misregulated in the knockout. **e**, Cropped agarose gel of PCR products across the *Zfp185* locus from gDNA of parental and HAS knock-in clones derived from G2 ($MSL2^{dCXC\text{-}CTD}$ hybrid) as parental mES cell line (also see Supplementary Data 4) with primers binding outside both homology arms. This product was then re-amplified in a nested PCR for resolving the size shift introduced by replacing the 2 kb *Zfp185* region with 1.5 kb of HAS sequences. The original PCR product was analysed by Sanger sequencing to verify insertion of the HAS and deletion (data not shown). For source data, see Supplementary Fig. 1. **f**, RT–qPCR analysis of *Zfp185* and its two neighbouring genes, *Nsdhl* and *Pnma5*, the latter of which is also downregulated in *Msl2*Δ mES cells. *Bex2* and *Firre* are target genes at a different locus, *Rplp0* and *Tbp* serve as non-target controls. The *Zfp185* knock-in cell lines displayed with green bars are all derived from the

MSL2$^{dCXC-CTD}$ hybrid cell line (G2, blue). The clone IDs from top to bottom are D11 (MSL2^{WT}, black), G2 (MSL2$^{dCXC-CTD}$, blue), 444-A11, 444-C2, G2-F4, 376-28, 377-A4 and 377-D6. The RNA level of each gene is normalized to *Hprt* and expressed relative to the MSL2^{WT} cell line. The barplot represents the mean ± s.e.m. of at least $n = 4$ biological replicates. **g**, as in Fig. 3f, RT–qPCR analysis of the indicated genes in roX2 (exon 3)- or EGFP control-expressing cell lines that were derived from mES cell clones D11 (MSL2^{WT}), G2 (MSL2$^{dCXC-CTD}$), G2-F4 (MSL2$^{dCXC-CTD}$, *roX1* HAS at *Zfp185*), 444-C2 (MSL2$^{dCXC-CTD}$, *socs16D* HAS at *Zfp185*). The RNA level of each gene was normalized to *Hprt*. The barplot represents the mean with overlaid datapoints of biological replicates ($n = 2$ independently derived cell lines). **h**, RT–qPCR analysis of the indicated genes in mES cell clones D11 (MSL2^{WT}), G2 (MSL2$^{dCXC-CTD}$ hybrid) or G2-A5 that expresses roX2 (exon 3) from the *HBB-y* locus (see Fig. 4c and Supplementary Data 4). The RNA level of each gene was normalized to *Hprt*. The barplot represents the mean ± s.e.m. of at least $n = 2$ biological replicates. The *P*-values were obtained by a two-sided Wilcoxon rank-sum test.

Extended Data Fig. 8 Characterization of roX2 in hybrid and tethered MSL2-expressing mES cells.

a, Schematic representation of the experimental setup showing the RNA levels after transcription inhibition with flavopiridol at the indicated time points in cell lines D11 (MSL2^{WT}) and G2 (MSL2$^{dCXC-CTD}$ hybrid) expressing roX2 (random, single-copy integration). The RNA levels were determined by RT–qPCR, normalized to a spike that was added before RNA isolation and expressed relative to the 0 min control time point in the D11 (MSL2^{WT}) cell line. The line plot connects the mean at each time point ± s.e.m. of $n = 7$ (MSL2^{WT}) or $n = 5$ (MSL2$^{dCXC-CTD}$ hybrid) biological replicates. Nascent RNA levels decrease at timeframes correlating with the length of the analysed gene (for example, *Pgk1*: 16.6 kb, intron levels drop by 50% after around 15 min). mRNAs (for example, *Rplp0*, *Pgk1*), rRNA (RNA Polymerase I) or U6 snRNA (RNA Polymerase III) remain rather unaffected within the timeframe of 15 min. Total roX2 levels (0.5 kb) decrease by 50% within 15 min of flavopiridol inhibition,

pointing towards a rapid turnover (also see Fig. 3h). **b**, Cropped immunoblots comparing the Flag-tagged MSL2^{WT} (D11) with the MSL2$^{dCXC-\Delta CTD}$-3xFlag-His-λN cell line (clone 513-A6, abbreviated as MSL2Δ$^{\lambda N}$). The coomassie-stained gel, DHX9 and OCT3/4 serve as loading controls. For source data, see Supplementary Fig. 1. **c**, Representative RNA FISH pictures of roX2 RNA (red) and DAPI (light blue) in the MSL2$^{dCXC-CTD}$ hybrid mES cells (clone G2) with stably integrated roX2 (top) or the MSL2$^{dCXC-\Delta CTD}$-3xFlag-His-λN mES cells (clone 513-A6, abbreviated as MSL2Δ$^{\lambda N}$) with stably integrated 2×boxB-roX2 (bottom). The pictures are single *z*-planes with scale bars = 10 µm. **d**, Quantification of RNA FISH in **c** obtained from 3 independent hybridizations in 2 stable clones. Induction of the roX2 foci in mouse ESCs by either the drosophilized hybrid (MSL2$^{dCXC-CTD}$) or by ectopic tethering of the mouse MSL2 to roX RNA (MSL2Δ$^{\lambda N}$) is compared. Left, dot plots with centre line represent the mean ± s.e.m. foci frequency, where each overlaid data point represents the quantification result of a single tiled image. Each image was quantified as the number of cells that display a confined signal in the nucleus as % of all nuclei identified based on DAPI staining (% of nuclei with foci/total nuclei). The total number of quantified nuclei examined over all experiments was $n = 447$ or $n = 284$ cells and is displayed on top of the dot plot. Statistical significance was evaluated by a two-sided Wilcoxon rank-sum test. Right, boxplots representing the area of the roX2 foci obtained from orthogonal projection images. Overlaid data points represent individual foci ($n = 140$ and $n = 85$). The *P*-values were obtained with a two-sided Wilcoxon rank-sum test.

Extended Data Fig. 9 Validation of mammalian reconstitution models expressing roX2 from *Zfp185*.

a, Schematic representation of experimental outline to create mES cells with targeted integrations of *roX2* at mammalian loci to study induction of a local dosage compensation-like phenomenon. A scarless CRISPR strategy without integration of a selection cassette was used[30]. roX2-expressing cells were derived from the MSL2$^{dCXC-CTD}$ hybrid cell line (clone G2). *roX2* or shuffled *roX2* expression was driven by the *Pgk1* promoter. The *roX2* expression cassette is followed by 1.5 kb of *Drosophila* HAS (*roX1*,

socs16D) or control sequences: *odsh* (*Drosophila* non-target) and *Bscl2* (Mouse target). All cell lines are reported in Supplementary Data 4. **b**, Cropped agarose gel of PCR products across the *Zfp185* locus from gDNA of parental and *Pgk1* promoter-driven *roX2* knock-in clones derived from G2 ($MSL2^{dCXC\text{-}CTD}$) as parental mES cell line (also see Supplementary Data 4). The locus was amplified with primers in the *Pgk1* promoter and 3′ outside of the homology arm. The PCR product was analysed by Sanger sequencing to verify the insertions. The control PCR shown below each gel amplifies the *HBB-y* locus. For source data, see Supplementary Fig. 1. **c**, RNA FISH of roX2 (red), Huwe1 (white) and DAPI (blue) of the mES cells $MSL2^{dCXC\text{-}CTD}$ (G2), *Pgk1-roX2*-mCTRL (422-C9 (*Bscl2*)), *Pgk1-roX2-socs16D HAS* (424-B12). The pictures are single *z*-planes with scale bars = 5 µm, the hybridization was performed three times with similar results (also see Supplementary Note for technical information on RNA FISH). The co-localization with the X-linked Huwe1 RNA implies that these foci, which occur independently of the presence of HAS, correspond to transcripts at the targeted *Zfp185* locus. **d**, RNA FISH for roX2 upon exposure of mES cells to 3% 1,6-hexanediol for 3 or 10 min. mES cells express roX2 from *Zfp185* (cell line 419-D2), the MSL2-CTD is drosophilized ($MSL2^{dCXC\text{-}CTD}$ hybrid). Scale bars = 5 µm, the hybridization was performed once. Right, quantification of the roX2 foci areas (n = 27 (0 min), n = 20 (3 min), n = 59 (10 min)). Barplots show mean ± s.e.m. with overlaid data points representing individual foci. The P-values were obtained by a Kruskal–Wallis test followed by a Dunn's statistical test for multiple comparisons (see Extended Data Fig. 4a-g for response of the *Drosophila* MSL territory to 1,6-hexanediol treatment). **e**, RT–qPCR analysis of the indicated genes. The roX2 *Zfp185* knock-in cell lines are displayed with red shaded bars, shuffled roX2 with grey shaded bars, the wild-type mouse MSL2-expressing cell line (D11) in black and the $MSL2^{dCXC\text{-}CTD}$ hybrid cell line (G2) in blue. The RNA level of each gene was normalized to *Hprt* and expressed relative to the $MSL2^{WT}$ cell line. The barplot represents the mean ± s.e.m. of at least 3 biological replicates. The roX2 and shuffled roX2 RNA levels are expressed as a geometric mean over all cell lines, as these transcripts are not expressed in the $MSL2^{WT}$ cell line. All cell lines and RT–qPCR significance testing for *Pnma5* are listed in Supplementary Data 4. A subset of the same data (result for $MSL2^{WT}$,

D11; MSL2$^{dCXC-CTD}$, G2; 424-B12 (*roX2*) and 443-C3 (shuffled *roX2*) is shown in Fig. 4a. **f**, H4K16ac ChIP–qPCR analyses from MSL2^{WT} (D11), MSL2$^{dCXC-CTD}$ (G2) and *Pgk1-roX2*-HAS (424-B12, 421-B5, 419-C3)-expressing mES cells. The barplot with overlaid data points shows the mean of $n = 2$ independent experiments ($n = 1$ for MSL2^{WT}) at the indicated positions along the *Zfp185* locus. Enrichment values were calculated relative to input and serial dilutions performed to account for primer efficiency. The data are expressed as fold change enrichment over the *Intergenic 3* region (see Supplementary Data 4), which resides near the transcriptionally inactive *HBB-y* gene (for clarity not shown in panel).

Extended Data Fig. 10 Validation of mES cells expressing roX2 from *Bex2*, *HBB-y* and *Drosophila* tethering experiment.

a, Cropped agarose gel of PCR products across the *Bex2* locus from gDNA of parental and *Pgk1* promoter-driven *roX2* knock-in clones derived from G2 (MSL2$^{dCXC-CTD}$) as parental mES cell line (also see Supplementary Data 4). For source data, see Supplementary Fig. 1. **b**, RT–qPCR analysis of the indicated genes as in Fig. 4b. The RNA level of each gene was normalized to *Hprt* and expressed relative to the MSL2^{WT} cell line (arbitrary units for roX2, since it is not expressed in MSL2^{WT} cells). The barplot represents the mean ± s.e.m. of at least 3 biological replicates. **c**, as in **a**, but for cells with *roX2* integrated into the *HBB-y* locus. For source data, see Supplementary Fig. 1. **d**, RT–qPCR analysis of the indicated genes as in Fig. 4c. The barplot represents the mean ± s.e.m. RNA levels (normalized to *Hprt*) of at least 3 biological replicates. RNA levels represent arbitrary units. *HBB-bs* gene could only be detected in RT–qPCR from a mouse control cDNA, but not from the experimental mES cells. roX2 is not expressed in MSL2^{WT} cells. **e**, as in **b** but in *Msl3Δ* knockout cells derived from MSL2^{WT} (D11 ± *Msl3Δ*, black), MSL2$^{dCXC-CTD}$ (G2 ± *Msl3Δ*, blue) and MSL2$^{dCXC-CTD}$ + *roX2* (498-B6 ± *Msl3Δ* red) cells. roX2 in clone 498-B6 (red bars) is expressed from the *Bex2* locus (Fig. 4b). **f**, Cropped immunoblots of total protein extracts of adult male fly heads expressing MS2CP-tagged MSL2 transgenes (also see Fig. 4d) in comparison with wild-type control (*msl-2::HA*). All transgenes also contain a 2xHA-mCherry tag and were expressed with *tub-Gal4* in a heterozygous

msl-2$^{227/kmA}$/*CyO-GFP* background. To account for differences in protein stability, the MSL2Δ^{MS2CP} (86FB) and MSL2^{MS2CP} (VK33) transgenes are expressed from different landing sites. The star indicates the expected migration of the full-length fusion proteins, whereas the lower products correspond to degradation products. The experiment has been performed once. For source data, see Supplementary Fig. 1. **g**, Analysis of adult male viability in flies expressing transgenic MS2CP-tagged or untagged transgenes. The genotype was *roX1*$^{+}$*, roX2*$^{+}$; *msl-2*^{kmA}/*msl-2*^{227}*; tub-Gal4/UAS-msl-2* or respective heterozygous *CyO-GFP* control. The data was expressed relative to females obtained from the same cross. The barplot represents the mean ± s.e.m. with overlaid datapoints reflecting the results from each cross/vial (n = 5 for MSL2^{MS2CP}, n = 7 for MSL2Δ^{MS2CP}, n = 6 for MSL2^{WT}). Details on genotypes and nature of transgenes are provided in Methods. **h**, Transgenic flies expressing MS2CP-tagged MSL2 transgenes are ectopically tethered to MS2-loops tagged roX RNA (also see Fig. 4d–h, MSL2^{WT} = wild-type *D. melanogaster* transgene, MSL2^{MS2CP} = wild-type MS2CP-tagged and MSL2Δ^{MS2CP} = MSL2(1-520) MS2CP-tagged). The transgenes were expressed as *UAS-msl-2* versions in *act-Gal4, msl-2*$^{\Delta}$/*msl-2*^{227} transheterozygous null mutant backgrounds, where the X chromosome is *roX1*$^{+}$ *roX2*$^{+}$ (no loops) or *roX1*^{6xMS2}*, roX2*$^{\Delta}$ (with tethering, indicated with loops symbol). For cross setup and details see Methods. Immunofluorescence was performed in salivary glands and the *msl-2* transgenes were detected with HA antibodies (red), MSL1 is shown in green, DAPI in blue. The pictures are orthogonal projections of an entire stack with scale bars = 50 µm. **i**, as in **h** but in imaginal discs. *msl-2* transgenes were detected with HA antibodies (yellow), DAPI in blue. The representative pictures are single *z*-planes with scale bars = 10 µm. **j**, Top, schematic representation of the strategy to determine the territory enrichment ratio, which is calculated by dividing average intensity of the territory in one nucleus by the average intensity of an equally sized region elsewhere in the same nucleus. Bottom, quantification of **h**, density plots of the X-chromosome territory enrichment ratio. The number of quantified nuclei is MSL2^{WT} (no loops n = 22, with loops n = 24), MSL2^{MS2CP} (no loops n = 45, with loops n = 42) and MSL2Δ^{MS2CP} (no loops n = 37, with loops n = 37). The P-values were obtained with a two-sided Wilcoxon rank-sum test comparing the MSL2 enrichment in comparison with DAPI. DAPI

is equally dispersed within the nucleus and shows a territory enrichment ratio of 1 (= not enriched).

Supplementary information

Supplementary Note

Further explanation and discussion of ChIP-seq and RNA-seq data, Drosophila MSL complex members response to 1,6-hexanediol treatment in vivo, Analysis of MSL2 CXC-domain hybrids, Sequence evolution and in vitro properties of MSL2 domains, Hierarchy between roX2 and roX1, RNA FISH technical notes and Supplementary discussion.

Reporting Summary

Supplementary Figure 1

Uncropped gel pictures and immunoblots.

Supplementary Data 1

List of differentially expressed (DE) genes and GO-terms obtained in RNA-seq from dissected Drosophila wing imaginal discs.

Supplementary Data 2

Branch-site test results for MSL2 RING, CXC and CTD.

Supplementary Data 3

Individual results per cross regarding viability of male *msl-2* null mutants expressing MSL2 hybrids.

Supplementary Data 4

Related to Methods, table with primer sequences, plasmids, cell lines, HAS sequences, RNA FISH probes, Drosophila lines, Main Figure Drosophila genotypes and statistical testing.

Rights and permissions

Reprints and Permissions

About this article

Check for updates

Cite this article

Valsecchi, C.I.K., Basilicata, M.F., Georgiev, P. *et al.* RNA nucleation by MSL2 induces selective X chromosome compartmentalization. *Nature* **589,** 137–142 (2021). https://doi.org/10.1038/s41586-020-2935-z

Download citation

- Received: 10 May 2019
- Accepted: 04 September 2020
- Published: 18 November 2020
- Issue Date: 07 January 2021
- DOI: https://doi.org/10.1038/s41586-020-2935-z

Comments

By submitting a comment you agree to abide by our Terms and Community Guidelines. If you find something abusive or that does not comply with our

terms or guidelines please flag it as inappropriate.

Access through your institution
Change institution
Buy or subscribe

This article was downloaded by **calibre** from https://www.nature.com/articles/s41586-020-2935-z

| Section menu | Main menu |

- Article
- Published: 09 December 2020

Structure of mycobacterial ATP synthase bound to the tuberculosis drug bedaquiline

- Hui Guo[1,2] na1,
- Gautier M. Courbon[1,2] na1,
- Stephanie A. Bueler[1],
- Juntao Mai[3],
- Jun Liu[3] &
- John L. Rubinstein ORCID: orcid.org/0000-0003-0566-2209[1,2,4]

Nature **volume 589**, pages143–147(2021)Cite this article

- 4500 Accesses
- 1 Citations
- 108 Altmetric
- Metrics details

Subjects

- Bioenergetics
- Cryoelectron microscopy
- Enzyme mechanisms
- Tuberculosis

Abstract

Tuberculosis—the world's leading cause of death by infectious disease—is increasingly resistant to current first-line antibiotics[1]. The bacterium *Mycobacterium tuberculosis* (which causes tuberculosis) can survive low-energy conditions, allowing infections to remain dormant and decreasing their susceptibility to many antibiotics[2]. Bedaquiline was developed in 2005 from a lead compound identified in a phenotypic screen against *Mycobacterium smegmatis*[3]. This drug can sterilize even latent *M. tuberculosis* infections[4] and has become a cornerstone of treatment for multidrug-resistant and extensively drug-resistant tuberculosis[1,5,6]. Bedaquiline targets the mycobacterial ATP synthase[3], which is an essential enzyme in the obligate aerobic *Mycobacterium* genus[3,7], but how it binds the intact enzyme is unknown. Here we determined cryo-electron microscopy structures of *M. smegmatis* ATP synthase alone and in complex with bedaquiline. The drug-free structure suggests that hook-like extensions from the α-subunits prevent the enzyme from running in reverse, inhibiting ATP hydrolysis and preserving energy in hypoxic conditions. Bedaquiline binding induces large conformational changes in the ATP synthase, creating tight binding pockets at the interface of subunits a and c that explain the potency of this drug as an antibiotic for tuberculosis.

Access through your institution
Change institution
Buy or subscribe

Access options

Subscribe to Journal

Get full journal access for 1 year

$199.00

only $3.90 per issue

Subscribe

All prices are NET prices.
VAT will be added later in the checkout.

Rent or Buy article

Get time limited or full article access on ReadCube.

from$8.99

Rent or Buy

All prices are NET prices.

Additional access options:

- Log in
- Access through your institution
- Learn about institutional subscriptions

Fig. 1: Structure of the mycobacterial ATP synthase.

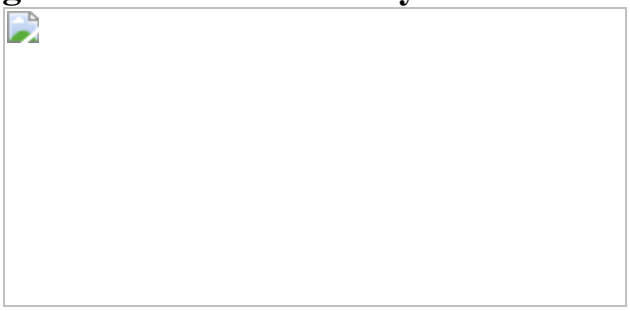

Fig. 2: Autoinhibition of ATP hydrolysis.

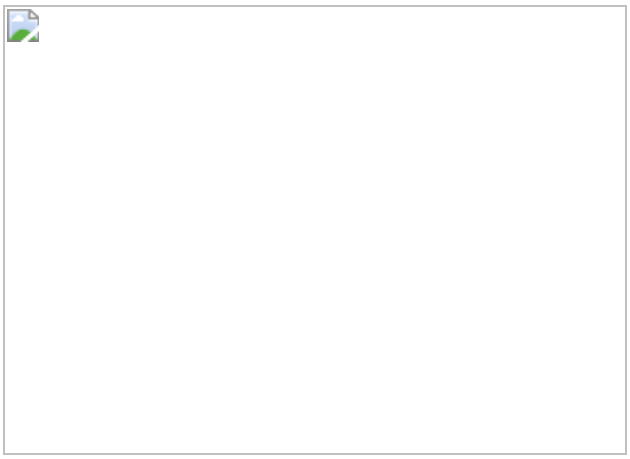

Fig. 3: Inhibition of mycobacterial ATP synthase by BDQ.

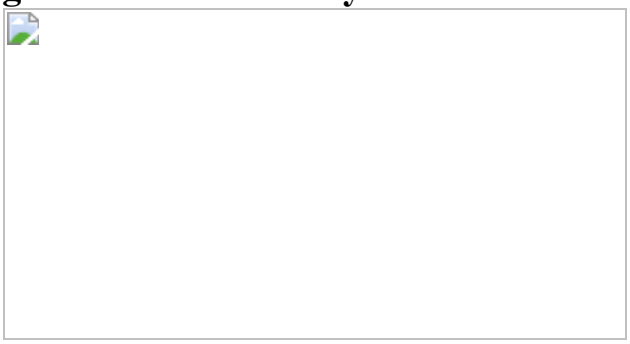

Fig. 4: Large-scale conformational changes and high-affinity binding of BDQ.

Data availability

Cryo-EM maps have been deposited in the Electron Microscopy Data Bank (EMDB) under accession numbers EMD-22311 to EMD-22322. Atomic models have been deposited in the Protein Data Bank under accession numbers 7JG5, 7JG6, 7JG7, 7JG8, 7JG9, 7JGA, 7JGB and 7JGC. Strains and plasmids are available from the corresponding author upon reasonable request.

References

1. 1.

   World Health Organization. *Global Tuberculosis Report 2019* (World Health Organization, 2019).

2. 2.

   Lu, P., Lill, H. & Bald, D. ATP synthase in mycobacteria: special features and implications for a function as drug target. *Biochim. Biophys. Acta* **1837**, 1208–1218 (2014).

   CAS Google Scholar

3. 3.

   Andries, K. et al. A diarylquinoline drug active on the ATP synthase of *Mycobacterium tuberculosis*. *Science* **307**, 223–227 (2005).

   ADS CAS Google Scholar

4. 4.

   Koul, A. et al. Diarylquinolines are bactericidal for dormant mycobacteria as a result of disturbed ATP homeostasis. *J. Biol. Chem.* **283**, 25273–25280 (2008).

   CAS PubMed PubMed Central Google Scholar

5. 5.

World Health Organization. *The Selection and Use of Essential Medicines* (World Health Organization, 2019).

6. 6.

Médecins Sans Frontières. MSF press release, https://www.msf.org.za/stories-news/press-releases/fix-patent-laws-campaign-launches-global-campaign-urging-johnson-johnson (2019).

7. 7.

McNeil, M. B., Ryburn, H. W. K., Harold, L. K., Tirados, J. F. & Cook, G. M. Transcriptional inhibition of the F1F0-type ATP synthase has bactericidal consequences on the viability of mycobacteria. *Antimicrob. Agents Chemother*. **64**, e00492-20 (2020).

CAS PubMed PubMed Central Google Scholar

8. 8.

Zhao, J., Benlekbir, S. & Rubinstein, J. L. Electron cryomicroscopy observation of rotational states in a eukaryotic V-ATPase. *Nature* **521**, 241–245 (2015).

ADS CAS PubMed PubMed Central Google Scholar

9. 9.

Guo, H., Suzuki, T. & Rubinstein, J. L. Structure of a bacterial ATP synthase. *eLife* **8**, e43128 (2019).

PubMed PubMed Central Google Scholar

10. 10.

Preiss, L. et al. Structure of the mycobacterial ATP synthase F_o rotor ring in complex with the anti-TB drug bedaquiline. *Sci. Adv*. **1**, e1500106 (2015).

ADS PubMed PubMed Central Google Scholar

11. 11.

Zhou, A. et al. Structure and conformational states of the bovine mitochondrial ATP synthase by cryo-EM. *eLife* **4**, e10180 (2015).

PubMed PubMed Central Google Scholar

12. 12.

Guo, H., Bueler, S. A. & Rubinstein, J. L. Atomic model for the dimeric FO region of mitochondrial ATP synthase. *Science* **358**, 936–940 (2017).

ADS CAS PubMed PubMed Central Google Scholar

13. 13.

Hahn, A., Vonck, J., Mills, D. J., Meier, T. & Kuhlbrandt, W. Structure, mechanism, and regulation of the chloroplast ATP synthase. *Science* **360**, eaat4318 (2018).

PubMed PubMed Central Google Scholar

14. 14.

Sobti, M. et al. Cryo-EM structures provide insight into how *E. coli* F_1F_o ATP synthase accommodates symmetry mismatch. *Nat. Commun*. **11**, 2615 (2020).

ADS CAS PubMed PubMed Central Google Scholar

15. 15.

Gajadeera, C. S. & Weber, J. *Escherichia coli* F_1F_o-ATP synthase with a b/δ fusion protein allows analysis of the function of the individual b subunits. *J. Biol. Chem*. **288**, 26441–26447 (2013).

CAS PubMed PubMed Central Google Scholar

16. 16.

Sobti, M. et al. Cryo-EM structures of the autoinhibited *E. coli* ATP synthase in three rotational states. *eLife* **5**, e21598 (2016).

PubMed PubMed Central Google Scholar

17. 17.

Abrahams, J. P., Leslie, A. G., Lutter, R. & Walker, J. E. Structure at 2.8 Å resolution of F_1-ATPase from bovine heart mitochondria. *Nature* **370**, 621–628 (1994).

ADS CAS PubMed PubMed Central Google Scholar

18. 18.

Shirakihara, Y. et al. Structure of a thermophilic F_1-ATPase inhibited by an ε-subunit: deeper insight into the ε-inhibition mechanism. *FEBS J*. **282**, 2895–2913 (2015).

CAS PubMed PubMed Central Google Scholar

19. 19.

Cingolani, G. & Duncan, T. M. Structure of the ATP synthase catalytic complex (F_1) from *Escherichia coli* in an autoinhibited conformation. *Nat. Struct. Mol. Biol*. **18**, 701–707 (2011).

CAS PubMed PubMed Central Google Scholar

20. 20.

Zhang, A. T., Montgomery, M. G., Leslie, A. G. W., Cook, G. M. & Walker, J. E. The structure of the catalytic domain of the ATP synthase from *Mycobacterium smegmatis* is a target for developing

antitubercular drugs. *Proc. Natl Acad. Sci. USA* **116**, 4206–4211 (2019).

CAS Google Scholar

21. 21.

Ragunathan, P. et al. The uniqueness of subunit α of mycobacterial F-ATP synthases: an evolutionary variant for niche adaptation. *J. Biol. Chem*. **292**, 11262–11279 (2017).

CAS PubMed PubMed Central Google Scholar

22. 22.

Lutter, R. et al. F_1F_o-ATP synthase from bovine heart mitochondria: development of the purification of a monodisperse oligomycin-sensitive ATPase. *Biochem. J*. **295**, 799–806 (1993).

CAS PubMed PubMed Central Google Scholar

23. 23.

Koul, A. et al. Diarylquinolines target subunit c of mycobacterial ATP synthase. *Nat. Chem. Biol*. **3**, 323–324 (2007).

MathSciNet CAS PubMed PubMed Central Google Scholar

24. 24.

Hards, K. et al. Bactericidal mode of action of bedaquiline. *J. Antimicrob. Chemother*. **70**, 2028–2037 (2015).

CAS PubMed PubMed Central Google Scholar

25. 25.

Hards, K. et al. Ionophoric effects of the antitubercular drug bedaquiline. *Proc. Natl Acad. Sci. USA* **115**, 7326–7331 (2018).

CAS PubMed PubMed Central Google Scholar

26. 26.

Haagsma, A. C. et al. Probing the interaction of the diarylquinoline TMC207 with its target mycobacterial ATP synthase. *PLoS ONE* **6**, e23575 (2011).

ADS CAS PubMed PubMed Central Google Scholar

27. 27.

Kundu, S., Biukovic, G., Grüber, G. & Dick, T. Bedaquiline targets the ε subunit of mycobacterial F-ATP synthase. *Antimicrob. Agents Chemother*. **60**, 6977–6979 (2016).

CAS PubMed PubMed Central Google Scholar

28. 28.

Lounis, N. et al. R207910 (TMC207): un nouvel antibiotique pour le traitement de la tuberculose. *Med. Mal. Infect*. **40**, 383–390 (2010).

CAS PubMed PubMed Central Google Scholar

29. 29.

Guillemont, J., Meyer, C., Poncelet, A., Bourdrez, X. & Andries, K. Diarylquinolines, synthesis pathways and quantitative structure–activity relationship studies leading to the discovery of TMC207. *Future Med. Chem*. **3**, 1345–1360 (2011).

CAS PubMed PubMed Central Google Scholar

30. 30.

Sutherland, H. S. et al. 3,5-Dialkoxypyridine analogues of bedaquiline are potent antituberculosis agents with minimal inhibition of the hERG channel. *Bioorg. Med. Chem*. **27**, 1292–1307 (2019).

CAS PubMed PubMed Central Google Scholar

31. 31.

Haagsma, A. C. et al. Selectivity of TMC207 towards mycobacterial ATP synthase compared with that towards the eukaryotic homologue. *Antimicrob. Agents Chemother*. **53**, 1290–1292 (2009).

CAS PubMed PubMed Central Google Scholar

32. 32.

Murphy, K. C. et al. ORBIT: a new paradigm for genetic engineering of mycobacterial chromosomes. *MBio* **9**, e01467-18 (2018).

PubMed PubMed Central Google Scholar

33. 33.

Vasanthakumar, T. et al. Structural comparison of the vacuolar and Golgi V-ATPases from *Saccharomyces cerevisiae*. *Proc. Natl Acad. Sci. USA* **116**, 7272–7277 (2019).

CAS PubMed PubMed Central Google Scholar

34. 34.

Kornberg, A. & Pricer, W. E. Jr. Enzymatic phosphorylation of adenosine and 2,6-diaminopurine riboside. *J. Biol. Chem*. **193**, 481–495 (1951).

CAS PubMed PubMed Central Google Scholar

35. 35.

Russo, C. J. & Passmore, L. A. Ultrastable gold substrates for electron cryomicroscopy. *Science* **346**, 1377–1380 (2014).

ADS CAS PubMed PubMed Central Google Scholar

36. 36.

Meyerson, J. R. et al. Self-assembled monolayers improve protein distribution on holey carbon cryo-EM supports. *Sci. Rep*. **4**, 7084 (2014).

PubMed PubMed Central Google Scholar

37. 37.

Marr, C. R., Benlekbir, S. & Rubinstein, J. L. Fabrication of carbon films with ∼ 500 nm holes for cryo-EM with a direct detector device. *J. Struct. Biol*. **185**, 42–47 (2014).

CAS PubMed PubMed Central Google Scholar

38. 38.

Tivol, W. F., Briegel, A. & Jensen, G. J. An improved cryogen for plunge freezing. *Microsc. Microanal*. **14**, 375–379 (2008).

ADS CAS PubMed PubMed Central Google Scholar

39. 39.

Punjani, A., Rubinstein, J. L., Fleet, D. J. & Brubaker, M. A. cryoSPARC: algorithms for rapid unsupervised cryo-EM structure determination. *Nat. Methods* **14**, 290–296 (2017).

CAS PubMed PubMed Central Google Scholar

40. 40.

Zheng, S. Q. et al. MotionCor2: anisotropic correction of beam-induced motion for improved cryo-electron microscopy. *Nat. Methods* **14**, 331–332 (2017).

CAS PubMed PubMed Central Google Scholar

41. 41.

Punjani, A., Zhang, H. & Fleet, D. J. Non-uniform refinement: adaptive regularization improves single particle cryo-EM reconstruction. Preprint at https://doi.org/10.1101/2019.12.15.877092 (2019).

42. 42.

Scheres, S. H. W. RELION: implementation of a Bayesian approach to cryo-EM structure determination. *J. Struct. Biol*. **180**, 519–530 (2012).

CAS PubMed PubMed Central Google Scholar

43. 43.

Zivanov, J., Nakane, T. & Scheres, S. H. W. A Bayesian approach to beam-induced motion correction in cryo-EM single-particle analysis. *IUCrJ* **6**, 5–17 (2019).

CAS PubMed PubMed Central Google Scholar

44. 44.

Ramírez-Aportela, E. et al. Automatic local resolution-based sharpening of cryo-EM maps. *Bioinformatics* **36**, 765–772 (2020).

PubMed PubMed Central Google Scholar

45. 45.

Pettersen, E. F. et al. UCSF Chimera—a visualization system for exploratory research and analysis. *J. Comput. Chem*. **25**, 1605–1612 (2004).

CAS Google Scholar

46. 46.

Emsley, P. & Cowtan, K. Coot: model-building tools for molecular graphics. *Acta Crystallogr. D* **60**, 2126–2132 (2004).

PubMed PubMed Central Google Scholar

47. 47.

Croll, T. I. ISOLDE: a physically realistic environment for model building into low-resolution electron-density maps. *Acta Crystallogr. D* **74**, 519–530 (2018).

CAS Google Scholar

48. 48.

Adams, P. D. et al. PHENIX: a comprehensive Python-based system for macromolecular structure solution. *Acta Crystallogr. D* **66**, 213–221 (2010).

CAS PubMed PubMed Central Google Scholar

49. 49.

Chen, V. B. et al. MolProbity: all-atom structure validation for macromolecular crystallography. *Acta Crystallogr. D* **66**, 12–21 (2010).

CAS Google Scholar

50. 50.

Barad, B. A. et al. EMRinger: side chain-directed model and map validation for 3D cryo-electron microscopy. *Nat. Methods* **12**, 943–946 (2015).

CAS PubMed PubMed Central Google Scholar

51. 51.

Goddard, T. D. et al. UCSF ChimeraX: meeting modern challenges in visualization and analysis. *Protein Sci*. **27**, 14–25 (2018).

CAS PubMed PubMed Central Google Scholar

Download references

Acknowledgements

We thank V. Kanelis for suggestions on the manuscript. H.G. was supported by an Ontario Graduate Scholarship for International Students. G.M.C. was supported by a W. P. Caven Memorial Fellowship. J.L.R. was supported by the Canada Research Chairs programme. This work was supported by Canadian Institutes of Health Research grant PJT162186 (J.L.R.) and PJT156261 (J.L.). Cryo-EM data were collected at the Toronto High-Resolution High-Throughput cryo-EM facility, supported by the Canada Foundation for Innovation and Ontario Research Fund.

Author information

Author notes

1. These authors contributed equally: Hui Guo, Gautier M. Courbon

Affiliations

1. Molecular Medicine Program, The Hospital for Sick Children, Toronto, Ontario, Canada

   Hui Guo, Gautier M. Courbon, Stephanie A. Bueler & John L. Rubinstein

2. Department of Medical Biophysics, The University of Toronto, Toronto, Ontario, Canada

   Hui Guo, Gautier M. Courbon & John L. Rubinstein

3. Department of Molecular Genetics, The University of Toronto, Toronto, Ontario, Canada

   Juntao Mai & Jun Liu

4. Department of Biochemistry, The University of Toronto, Toronto, Ontario, Canada

   John L. Rubinstein

Authors

1. Hui Guo
   View author publications

   You can also search for this author in PubMed Google Scholar

2. Gautier M. Courbon
   View author publications

   You can also search for this author in PubMed Google Scholar

3. Stephanie A. Bueler
   View author publications

   You can also search for this author in PubMed Google Scholar

4. Juntao Mai
   View author publications

   You can also search for this author in PubMed Google Scholar

5. Jun Liu
   View author publications

   You can also search for this author in PubMed Google Scholar

6. John L. Rubinstein
   View author publications

You can also search for this author in PubMed Google Scholar

Contributions

J.L.R. conceived the project and supervised the research. J.L. advised on *M. smegmatis* cell culture and chromosomal tagging strategies. S.A.B. prepared the 3×FLAG ORBIT payload plasmid and an *M. smegmatis* strain used in the initial stages of the project, with help from J.M. G.M.C. prepared the *M. smegmatis* strains used for structure determination and enzyme assays. G.M.C. and H.G. purified the protein, H.G. performed the cryo-EM and image analysis, and G.M.C. and H.G. constructed the atomic models. J.L.R., H.G. and G.M.C. wrote the manuscript and prepared figures with input from the other authors.

Corresponding author

Correspondence to John L. Rubinstein.

Ethics declarations

Competing interests

The authors declare no competing interests.

Additional information

Peer review information *Nature* thanks Clifton Barry, Damian Ekiert and the other, anonymous, reviewer(s) for their contribution to the peer review of this work. Peer reviewer reports are available.

Publisher's note Springer Nature remains neutral with regard to jurisdictional claims in published maps and institutional affiliations.

Extended data figures and tables

Extended Data Fig. 1 Workflow for cryo-EM image analysis for BDQ-free, BDQ-saturated and -washed *M. smegmatis* ATP synthase.

a, **b**, Example micrograph (**a**) and 2D class average images (**b**) for BDQ-saturated *M. smegmatis* ATP synthase. Example particles are circled in white. We collected 7,691 movies (including 1,435,679 particle images) for the drug-free condition, 7,589 movies (including 1,825,672 particle images) for the BDQ-saturated condition and 4,962 movies (including 1,865,961 particle images) for the BDQ-washed condition. **c**, **d**, Workflow for obtaining maps of the three rotational states (**c**) and F_O region (**d**).

Extended Data Fig. 2 Cryo-EM map validation.

a–**d**, Corrected Fourier shell correlation curves after gold-standard refinement, orientation distribution plots and local resolution maps are shown for maps of the entire complex from the BDQ-free dataset (**a**), BDQ-saturated dataset (**b**) and BDQ-washed dataset (**c**), as well as F_O-region maps from focused refinement (**d**).

Extended Data Fig. 3 Examples of model-in-map fit to demonstrate map quality.

a, **b**, Examples are shown from each subunit in the BDQ-free model (**a**) and BDQ-saturated model (**b**).

Extended Data Fig. 4 Comparison of subunits a and b–δ from different organisms.

a, The *Bacillus* PS3 subunit a is in grey and the *M. smegmatis* subunit a is in green. **b**, The *E. coli* subunit a is in purple and the *M. smegmatis* subunit a is in green. **c**, The N-terminal domain of the δ region of the b–δ fusion protein (right side, top) is substantially larger than the N-terminal domain of *Bacillus* PS3 δ-subunit (right side, middle), being composed of about 270 residues instead of about 170 residues. The extra sequence contributes

5 additional α-helices to the 6 found in the *Bacillus* PS3 δ-subunit, giving a total of 11 α-helices in the N-terminal domain of b–δ (Fig. 1b, bottom). *Mycobacterium smegmatis* b–δ and *Bacillus* PS3 δ also form different interactions with the N-terminal sequences of the α-subunits that help to attach the peripheral stalk to F_1 region (right side, red).

Extended Data Fig. 5 Two conformations of the α-extension are seen in rotational state 2.

Density for the α-extension in its predominant conformation is coloured pink, and the alternative conformation is coloured red.

Extended Data Fig. 6 The BDQ-washed structures are in the BDQ-saturated conformation.

Fit of the BDQ-saturated protein models in the BDQ-washed maps shows that the two preparations adopt the same conformation.

Supplementary information

Supplementary Table 1

Cryo-EM data collection, refinement and validation statistics. This file contains Supplementary Tables 2-4 and Supplementary Figures 1-2.

Reporting Summary

Peer Review File

Video 1

Release of the inhibitory α extension during ATP synthesis. The video shows interpolation between the different rotational states of the enzyme, including the alternative conformation of rotational state 2, which suggests the sequence of events that occur during release of the α-extension during

ATP synthesis and binding of the α-extension to subunit γ to inhibit ATP hydrolysis. The video may be viewed as a loop.

Video 2

Binding of BDQ to the mycobacterial ATP synthase. The video shows interpolation between the conformation of the ATP synthase in the BDQ-free and BDQ-bound states. BDQ in the leading, c-only, and lagging binding sites are coloured pink, yellow, and blue, respectively. Phe69 in subunit c and Phe221 in subunit a, which undergo large conformational changes upon drug binding, are shown as space-filling models. The video may be viewed as a loop.

Rights and permissions

Reprints and Permissions

About this article

Check for updates

Cite this article

Guo, H., Courbon, G.M., Bueler, S.A. *et al.* Structure of mycobacterial ATP synthase bound to the tuberculosis drug bedaquiline. *Nature* **589,** 143–147 (2021). https://doi.org/10.1038/s41586-020-3004-3

Download citation

- Received: 10 July 2020
- Accepted: 21 October 2020
- Published: 09 December 2020

- Issue Date: 07 January 2021
- DOI: https://doi.org/10.1038/s41586-020-3004-3

Further reading

- **Hit movie reveals how a tuberculosis drug halts ATP synthesis**
  - Valerie Mizrahi
  - & Clifton E. Barry III

  Nature (2021)

Comments

By submitting a comment you agree to abide by our Terms and Community Guidelines. If you find something abusive or that does not comply with our terms or guidelines please flag it as inappropriate.

Access through your institution
Change institution
Buy or subscribe

Associated Content

Nature | News & Views

Hit movie reveals how a tuberculosis drug halts ATP synthesis

- Valerie Mizrahi
- & Clifton E. Barry III

This article was downloaded by **calibre** from https://www.nature.com/articles/s41586-020-3004-3

- Article
- Published: 02 December 2020

Structure of the class D GPCR Ste2 dimer coupled to two G proteins

- Vaithish Velazhahan[1],
- Ning Ma[2],
- Gáspár Pándy-Szekeres[3,4],
- Albert J. Kooistra[3],
- Yang Lee ORCID: orcid.org/0000-0002-8040-3648[1],
- David E. Gloriam ORCID: orcid.org/0000-0002-4299-7561[3],
- Nagarajan Vaidehi ORCID: orcid.org/0000-0001-8100-8132[2] &
- Christopher G. Tate ORCID: orcid.org/0000-0002-2008-9183[1]

Nature **volume 589**, pages148–153(2021)Cite this article

- 4940 Accesses
- 1 Citations
- 56 Altmetric
- Metrics details

Subjects

- Cryoelectron microscopy
- Fungal biology

Abstract

G-protein-coupled receptors (GPCRs) are divided phylogenetically into six classes[1,2], denoted A to F. More than 370 structures of vertebrate GPCRs (belonging to classes A, B, C and F) have been determined, leading to a substantial understanding of their function[3]. By contrast, there are no structures of class D GPCRs, which are found exclusively in fungi where they regulate survival and reproduction. Here we determine the structure of a class D GPCR, the *Saccharomyces cerevisiae* pheromone receptor Ste2, in an active state coupled to the heterotrimeric G protein Gpa1–Ste4–Ste18. Ste2 was purified as a homodimer coupled to two G proteins. The dimer interface of Ste2 is formed by the N terminus, the transmembrane helices H1, H2 and H7, and the first extracellular loop ECL1. We establish a class D1 generic residue numbering system (CD1) to enable comparisons with orthologues and with other GPCR classes. The structure of Ste2 bears similarities in overall topology to class A GPCRs, but the transmembrane helix H4 is shifted by more than 20 Å and the G-protein-binding site is a shallow groove rather than a cleft. The structure provides a template for the design of novel drugs to target fungal GPCRs, which could be used to treat numerous intractable fungal diseases[4].

Access through your institution
Change institution
Buy or subscribe

Access options

Subscribe to Journal

Get full journal access for 1 year

$199.00

only $3.90 per issue

Subscribe

All prices are NET prices.
VAT will be added later in the checkout.

Rent or Buy article

Get time limited or full article access on ReadCube.

from$8.99

Rent or Buy

All prices are NET prices.

Additional access options:

- Log in
- Access through your institution
- Learn about institutional subscriptions

Fig. 1: Overall cryo-EM reconstruction of the Ste2–G-protein heterotrimer complex.

Fig. 2: The Ste2 dimer interface.

Fig. 3: |α-Factor-binding site.

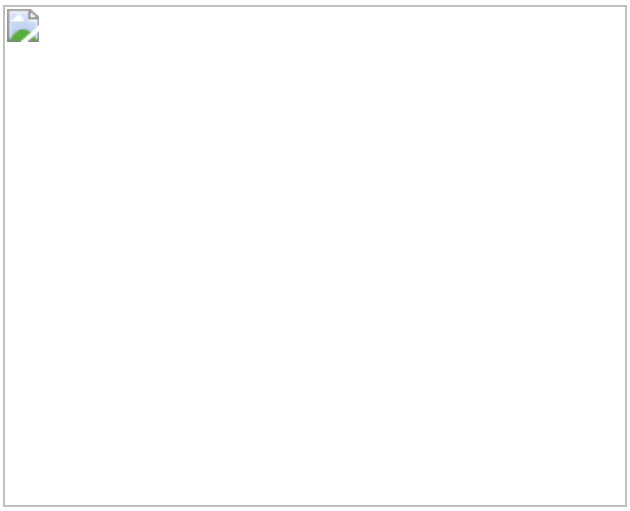

Fig. 4: G-protein-binding site.

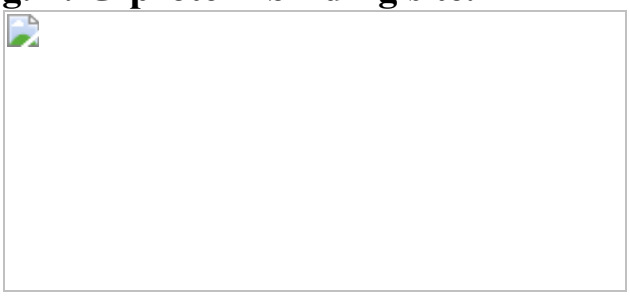

Fig. 5: Comparison of Ste2 with mammalian GPCRs.

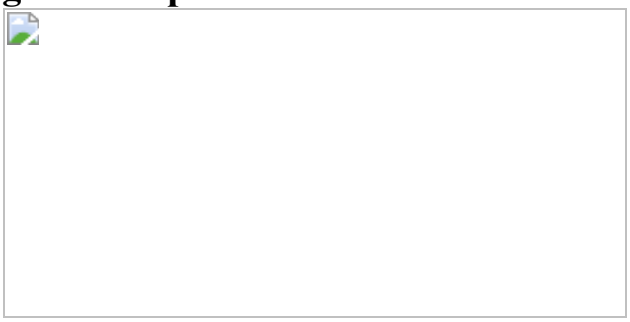

Data availability

The structure of the Ste2 dimer coupled to G proteins has been deposited in the Protein Data Bank (PDB) with accession code 7AD3, and the associated cryo-EM data has been deposited in the Electron Microscopy Data Bank (EMDB) with accession code EMDB-11720. The cryo-EM datasets eBIC Krios1, LMB Krios1 and LMB Krios2 are available from the Electron Microscopy Public Image Archive (EMPIAR; https://www.ebi.ac.uk/pdbe/emdb/empiar/) with the accession code EMPIAR-10550. There are no restrictions on data availability. Ste2

orthologue sequences and the generic residue numbering are available at https://gpcrdb.org/protein/ste2_yeast and the structure-based sequence alignments are available at https://gpcrdb.org/alignment/targetselection. Other structures discussed in this Article (with PDB codes 6G79, 3SN6, 6B3J, 7C7Q, 6D32, 6CMO and 6OFJ) are available at https://www.rcsb.org/.

References

1. 1.

   Attwood, T. K. & Findlay, J. B. Fingerprinting G-protein-coupled receptors. *Protein Eng*. **7**, 195–203 (1994).

   CAS PubMed Article Google Scholar

2. 2.

   Kolakowski, L. F., Jr. GCRDb: a G-protein-coupled receptor database. *Receptors Channels* **2**, 1–7 (1994).

   CAS PubMed Google Scholar

3. 3.

   García-Nafría, J. & Tate, C. G. Cryo-EM structures of GPCRs coupled to G_s, G_i and G_o. *Mol. Cell. Endocrinol*. **488**, 1–13 (2019).

   PubMed Article CAS Google Scholar

4. 4.

   Brown, N. A., Schrevens, S., van Dijck, P. & Goldman, G. H. Fungal G-protein-coupled receptors: mediators of pathogenesis and targets for disease control. *Nat. Microbiol*. **3**, 402–414 (2018).

   CAS PubMed Article Google Scholar

5. 5.

Van Dijck, P. et al. in *The Fungal Kingdom* (eds J. Heitman et al.) 417–439 (Wiley, 2017).

6. 6.

Burkholder, A. C. & Hartwell, L. H. The yeast α-factor receptor: structural properties deduced from the sequence of the *STE2* gene. *Nucleic Acids Res*. **13**, 8463–8475 (1985).

CAS PubMed PubMed Central Article Google Scholar

7. 7.

Xue, C., Hsueh, Y. P. & Heitman, J. Magnificent seven: roles of G protein-coupled receptors in extracellular sensing in fungi. *FEMS Microbiol. Rev*. **32**, 1010–1032 (2008).

CAS PubMed PubMed Central Article Google Scholar

8. 8.

Lee, B. K., Khare, S., Naider, F. & Becker, J. M. Identification of residues of the *Saccharomyces cerevisiae* G protein-coupled receptor contributing to alpha-factor pheromone binding. *J. Biol. Chem*. **276**, 37950–37961 (2001).

CAS PubMed Google Scholar

9. 9.

Nehmé, R. et al. Mini-G proteins: novel tools for studying GPCRs in their active conformation. *PLoS ONE* **12**, e0175642 (2017).

PubMed PubMed Central Article CAS Google Scholar

10. 10.

Isberg, V. et al. Generic GPCR residue numbers – aligning topology maps while minding the gaps. *Trends Pharmacol. Sci*. **36**, 22–31 (2015).

CAS PubMed Article Google Scholar

11. 11.

Overton, M. C., Chinault, S. L. & Blumer, K. J. Oligomerization, biogenesis, and signaling is promoted by a glycophorin A-like dimerization motif in transmembrane domain 1 of a yeast G protein-coupled receptor. *J. Biol. Chem*. **278**, 49369–49377 (2003).

CAS PubMed Article Google Scholar

12. 12.

Overton, M. C. & Blumer, K. J. G-protein-coupled receptors function as oligomers in vivo. *Curr. Biol*. **10**, 341–344 (2000).

CAS PubMed Article Google Scholar

13. 13.

Yesilaltay, A. & Jenness, D. D. Homo-oligomeric complexes of the yeast α-factor pheromone receptor are functional units of endocytosis. *Mol. Biol. Cell* **11**, 2873–2884 (2000).

CAS PubMed PubMed Central Article Google Scholar

14. 14.

Gehret, A. U., Bajaj, A., Naider, F. & Dumont, M. E. Oligomerization of the yeast α-factor receptor: implications for dominant negative effects of mutant receptors. *J. Biol. Chem*. **281**, 20698–20714 (2006).

CAS PubMed Article Google Scholar

15. 15.

Stoneman, M. R. et al. Quaternary structure of the yeast pheromone receptor Ste2 in living cells. *Biochim. Biophys. Acta Biomembr*. **1859**, 1456–1464 (2017).

CAS PubMed Article Google Scholar

16. 16.

Kim, S. et al. Transmembrane glycine zippers: physiological and pathological roles in membrane proteins. *Proc. Natl Acad. Sci. USA* **102**, 14278–14283 (2005).

ADS CAS PubMed Article Google Scholar

17. 17.

Mentesana, P. E. & Konopka, J. B. Mutational analysis of the role of N-glycosylation in α-factor receptor function. *Biochemistry* **40**, 9685–9694 (2001).

CAS PubMed Article Google Scholar

18. 18.

Wang, H. X. & Konopka, J. B. Identification of amino acids at two dimer interface regions of the α-factor receptor (Ste2). *Biochemistry* **48**, 7132–7139 (2009).

CAS PubMed Article Google Scholar

19. 19.

Abel, M. G., Zhang, Y. L., Lu, H. F., Naider, F. & Becker, J. M. Structure–function analysis of the *Saccharomyces cerevisiae* tridecapeptide pheromone using alanine-scanned analogs. *J. Pept. Res*. **52**, 95–106 (1998).

CAS PubMed Article Google Scholar

20. 20.

Naider, F. & Becker, J. M. The α-factor mating pheromone of *Saccharomyces cerevisiae*: a model for studying the interaction of peptide hormones and G protein-coupled receptors. *Peptides* **25**, 1441–1463 (2004).

CAS PubMed Article Google Scholar

21. 21.

Shenbagamurthi, P., Kundu, B., Raths, S., Becker, J. M. & Naider, F. Biological activity and conformational isomerism in position 9 analogues of the des-1-tryptophan,3-β-cyclohexylalanine-α-factor from *Saccharomyces cerevisiae*. *Biochemistry* **24**, 7070–7076 (1985).

CAS PubMed Article Google Scholar

22. 22.

Lee, Y. H., Naider, F. & Becker, J. M. Interacting residues in an activated state of a G protein-coupled receptor. *J. Biol. Chem*. **281**, 2263–2272 (2006).

CAS PubMed Article Google Scholar

23. 23.

Lee, B. K. et al. Tyr266 in the sixth transmembrane domain of the yeast α-factor receptor plays key roles in receptor activation and ligand specificity. *Biochemistry* **41**, 13681–13689 (2002).

CAS PubMed Article Google Scholar

24. 24.

Blumer, K. J. & Thorner, J. Beta and gamma subunits of a yeast guanine nucleotide-binding protein are not essential for membrane

association of the alpha subunit but are required for receptor coupling. *Proc. Natl Acad. Sci. USA* **87**, 4363–4367 (1990).

ADS CAS PubMed Article Google Scholar

25. 25.

García-Nafría, J. Cryo-EM structure of the serotonin 5-HT_{1B} receptor coupled to heterotrimeric G_o. *Nature* **558**, 620–623 (2018).

ADS PubMed PubMed Central Article CAS Google Scholar

26. 26.

Flock, T. et al. Universal allosteric mechanism for Gα activation by GPCRs. *Nature* **524**, 173–179 (2015).

ADS CAS PubMed PubMed Central Article Google Scholar

27. 27.

Dixit, G., Baker, R., Sacks, C. M., Torres, M. P. & Dohlman, H. G. Guanine nucleotide-binding protein (Gα) endocytosis by a cascade of ubiquitin binding domain proteins is required for sustained morphogenesis and proper mating in yeast. *J. Biol. Chem*. **289**, 15052–15063 (2014).

CAS PubMed PubMed Central Article Google Scholar

28. 28.

Mao, C. et al. Cryo-EM structures of inactive and active $GABA_B$ receptor. *Cell Res*. **30**, 564–573 (2020).

CAS PubMed Article Google Scholar

29. 29.

Ng, S. Y., Lee, L. T. & Chow, B. K. Receptor oligomerization: from early evidence to current understanding in class B GPCRs. *Front. Endocrinol. (Lausanne)* **3**, 175 (2013).

Article Google Scholar

30. 30.

Milasta, S. et al. Interactions between the Mas-related receptors MrgD and MrgE alter signalling and trafficking of MrgD. *Mol. Pharmacol*. **69**, 479–491 (2006).

CAS PubMed Article Google Scholar

31. 31.

Zhao, D. Y. et al. Cryo-EM structure of the native rhodopsin dimer in nanodiscs. *J. Biol. Chem*. **294**, 14215–14230 (2019).

CAS PubMed PubMed Central Article Google Scholar

32. 32.

Weis, W. I. & Kobilka, B. K. The molecular basis of G protein-coupled receptor activation. *Annu. Rev. Biochem*. **87**, 897–919 (2018).

CAS PubMed PubMed Central Article Google Scholar

33. 33.

Dror, R. O. et al. Activation mechanism of the β_2-adrenergic receptor. *Proc. Natl Acad. Sci. USA* **108**, 18684–18689 (2011).

ADS CAS PubMed Article Google Scholar

34. 34.

Warne, T., Edwards, P. C., Doré, A. S., Leslie, A. G. W. & Tate, C. G. Molecular basis for high-affinity agonist binding in GPCRs. *Science*

364, 775–778 (2019).

ADS CAS PubMed PubMed Central Article Google Scholar

35. 35.

Goddard, T. D. et al. UCSF ChimeraX: Meeting modern challenges in visualization and analysis. *Protein Sci*. **27**, 14–25 (2018).

CAS PubMed PubMed Central Article Google Scholar

36. 36.

García-Nafría, J., Watson, J. F. & Greger, I. H. IVA cloning: a single-tube universal cloning system exploiting bacterial in vivo assembly. *Sci. Rep*. **6**, 27459 (2016).

ADS PubMed PubMed Central Article CAS Google Scholar

37. 37.

Manahan, C. L., Patnana, M., Blumer, K. J. & Linder, M. E. Dual lipid modification motifs in G_α and G_γ subunits are required for full activity of the pheromone response pathway in *Saccharomyces cerevisiae*. *Mol. Biol. Cell* **11**, 957–968 (2000).

CAS PubMed PubMed Central Article Google Scholar

38. 38.

Hirschman, J. E. & Jenness, D. D. Dual lipid modification of the yeast Gγ subunit Ste18p determines membrane localization of Gβγ. *Mol. Cell. Biol*. **19**, 7705–7711 (1999).

CAS PubMed PubMed Central Article Google Scholar

39. 39.

Mastronarde, D. N. Automated electron microscope tomography using robust prediction of specimen movements. *J. Struct. Biol*. **152**, 36–51 (2005).

PubMed PubMed Central Article Google Scholar

40. 40.

Mastronarde, D. N. Advanced data acquisition from electron microscopes with serialEM. *Microsc. Microanal*. **24**, 864–865 (2018).

ADS Article Google Scholar

41. 41.

Zivanov, J., Nakane, T. & Scheres, S. H. W. Estimation of high-order aberrations and anisotropic magnification from cryo-EM data sets in RELION-3.1. *IUCrJ* **7**, 253–267 (2020).

CAS PubMed PubMed Central Article Google Scholar

42. 42.

Zheng, S. Q. et al. MotionCor2: anisotropic correction of beam-induced motion for improved cryo-electron microscopy. *Nat. Methods* **14**, 331–332 (2017).

CAS PubMed PubMed Central Article Google Scholar

43. 43.

Zhang, K. Gctf: Real-time CTF determination and correction. *J. Struct. Biol*. **193**, 1–12 (2016).

CAS PubMed PubMed Central Article Google Scholar

44. 44.

Ramlaul, K., Palmer, C. M., Nakane, T. & Aylett, C. H. S. Mitigating local over-fitting during single particle reconstruction with SIDESPLITTER. *J. Struct. Biol*. **211**, 107545 (2020).

PubMed PubMed Central Article Google Scholar

45. 45.

Ramlaul, K., Palmer, C. M. & Aylett, C. H. S. A local agreement filtering algorithm for transmission EM reconstructions. *J. Struct. Biol*. **205**, 30–40 (2019).

PubMed PubMed Central Article Google Scholar

46. 46.

Tan, Y. Z. et al. Addressing preferred specimen orientation in single-particle cryo-EM through tilting. *Nat. Methods* **14**, 793–796 (2017).

CAS PubMed PubMed Central Article Google Scholar

47. 47.

Kim, K. M. et al. Multiple regulatory roles of the carboxy terminus of Ste2p a yeast GPCR. *Pharmacol. Res*. **65**, 31–40 (2012).

CAS PubMed Article Google Scholar

48. 48.

Burnley, T., Palmer, C. M. & Winn, M. Recent developments in the CCP-EM software suite. *Acta Crystallogr. D* **73**, 469–477 (2017).

CAS Article Google Scholar

49. 49.

Adams, P. D. et al. PHENIX: a comprehensive Python-based system for macromolecular structure solution. *Acta Crystallogr. D* **66**, 213–

221 (2010).

CAS PubMed Article PubMed Central Google Scholar

50. 50.

Cowtan, K. The Buccaneer software for automated model building. 1. Tracing protein chains. *Acta Crystallogr. D* **62**, 1002–1011 (2006).

PubMed Article CAS Google Scholar

51. 51.

Moriarty, N. W., Grosse-Kunstleve, R. W. & Adams, P. D. electronic Ligand Builder and Optimization Workbench (eLBOW): a tool for ligand coordinate and restraint generation. *Acta Crystallogr. D* **65**, 1074–1080 (2009).

CAS PubMed Article Google Scholar

52. 52.

Long, F. et al. AceDRG: a stereochemical description generator for ligands. *Acta Crystallogr. D* **73**, 112–122 (2017).

CAS Article Google Scholar

53. 53.

Chen, V. B. et al. MolProbity: all-atom structure validation for macromolecular crystallography. *Acta Crystallogr. D* **66**, 12–21 (2010).

CAS PubMed Article Google Scholar

54. 54.

Barad, B. A. et al. EMRinger: side chain-directed model and map validation for 3D cryo-electron microscopy. *Nat. Methods* **12**, 943–946

(2015).

CAS PubMed PubMed Central Article Google Scholar

55. 55.

Amunts, A. et al. Structure of the yeast mitochondrial large ribosomal subunit. *Science* **343**, 1485–1489 (2014).

ADS CAS PubMed PubMed Central Article Google Scholar

56. 56.

Danev, R. & Baumeister, W. Cryo-EM single particle analysis with the Volta phase plate. *eLife* **5**, e13046 (2016).

PubMed PubMed Central Article Google Scholar

57. 57.

Kawate, T. & Gouaux, E. Fluorescence-detection size-exclusion chromatography for precrystallization screening of integral membrane proteins. *Structure* **14**, 673–681 (2006).

CAS PubMed Article Google Scholar

58. 58.

Hayashi, Y., Matsui, H. & Takagi, T. Membrane protein molecular weight determined by low-angle laser light-scattering photometry coupled with high-performance gel chromatography. *Methods Enzymol*. **172**, 514–528 (1989).

CAS PubMed Article Google Scholar

59. 59.

Cooley, R. B., O'Donnell, J. P. & Sondermann, H. Coincidence detection and bi-directional transmembrane signaling control a

bacterial second messenger receptor. *eLife* **5**, e21848 (2016).

PubMed PubMed Central Article Google Scholar

60. 60.

Grossfield, A. & Zuckerman, D. M. Quantifying uncertainty and sampling quality in biomolecular simulations. *Annu. Rep. Comput. Chem*. **5**, 23–48 (2009).

CAS PubMed PubMed Central Article Google Scholar

61. 61.

Monticelli, L., Sorin, E. J., Tieleman, D. P., Pande, V. S. & Colombo, G. Molecular simulation of multistate peptide dynamics: a comparison between microsecond timescale sampling and multiple shorter trajectories. *J. Comput. Chem*. **29**, 1740–1752 (2008).

CAS PubMed Article Google Scholar

62. 62.

Berendsen, H. J., van der Spoel, D. & van Drunen, R. GROMACS: a message-passing parallel molecular dynamics implementation. *Comput. Phys. Commun*. **91**, 43–56 (1995).

ADS CAS Article Google Scholar

63. 63.

Lee, J. et al. CHARMM-GUI input generator for NAMD, GROMACS, AMBER, OpenMM, and CHARMM/OpenMM simulations using the CHARMM36 additive force field. *J. Chem. Theory Comput*. **12**, 405–413 (2016).

CAS PubMed Article Google Scholar

64. 64.

Jo, S., Kim, T., Iyer, V. G. & Im, W. CHARMM-GUI: a web-based graphical user interface for CHARMM. *J. Comput. Chem*. **29**, 1859–1865 (2008).

CAS PubMed Article Google Scholar

65. 65.

Martyna, G. J., Klein, M. L. & Tuckerman, M. Nosé–Hoover chains: the canonical ensemble via continuous dynamics. *J. Chem. Phys*. **97**, 2635–2643 (1992).

ADS Article Google Scholar

66. 66.

Parrinello, M. & Rahman, A. Polymorphic transitions in single crystals: a new molecular dynamics method. *J. Appl. Phys*. **52**, 7182–7190 (1981).

ADS CAS Article Google Scholar

67. 67.

Darden, T., York, D. & Pedersen, L. Particle mesh Ewald: An $N\cdot\log(N)$ method for Ewald sums in large systems. *J. Chem. Phys*. **98**, 10089–10092 (1993).

ADS CAS Article Google Scholar

68. 68.

Bhattacharya, S. et al. Critical analysis of the successes and failures of homology models of G protein-coupled receptors. *Proteins* **81**, 729–739 (2013).

CAS PubMed PubMed Central Article Google Scholar

69. 69.

Paramo, T., East, A., Garzón, D., Ulmschneider, M. B. & Bond, P. J. Efficient characterization of protein cavities within molecular simulation trajectories: trj_cavity. *J. Chem. Theory Comput*. **10**, 2151–2164 (2014).

CAS PubMed Article Google Scholar

70. 70.

Waterhouse, A. M., Procter, J. B., Martin, D. M., Clamp, M. & Barton, G. J. Jalview Version 2—a multiple sequence alignment editor and analysis workbench. *Bioinformatics* **25**, 1189–1191 (2009).

CAS PubMed PubMed Central Article Google Scholar

71. 71.

Larsson, A. AliView: a fast and lightweight alignment viewer and editor for large datasets. *Bioinformatics* **30**, 3276–3278 (2014).

CAS PubMed PubMed Central Article Google Scholar

72. 72.

Zhang, Y. & Skolnick, J. TM-align: a protein structure alignment algorithm based on the TM-score. *Nucleic Acids Res*. **33**, 2302–2309 (2005).

CAS PubMed PubMed Central Article Google Scholar

73. 73.

Krissinel, E. Enhanced fold recognition using efficient short fragment clustering. *J. Mol. Biochem*. **1**, 76–85 (2012).

PubMed PubMed Central Google Scholar

Download references

Acknowledgements

V.V. was funded by a Gates Cambridge Scholarship. Work in the C.G.T. laboratory was funded by a grant from the European Research Council (EMPSI 339995), Sosei Heptares and core funding from the Medical Research Council (MRC U105197215). Work in the N.V. laboratory was funded by grants from the National Institutes of Health (R01-GM117923, R01-GM097261). Work in the D.E.G. laboratory was funded by Independent Research Fund Denmark | Natural Sciences (8021-00173B), Lundbeck Foundation (R163-2013-16327) and Novo Nordisk Foundation (NNF18OC0031226). D.E.G. is a member of the Integrative Structural Biology at the University of Copenhagen (ISBUC) cluster. We thank T. Nakane, P. Emsley, A. G. W. Leslie, S. Scheres, E. Miller, E. R. S. Kunji, P. Edwards, T. Warne and V. Chandrasekaran for discussions; and S. McLaughlin and C. Johnson from the Laboratory of Molecular Biology (LMB) biophysics facility, G. Cannone and G. Sharov from the LMB EM facility and J. Grimmett and T. Darling from the LMB scientific computing facility for technical support.

Author information

Affiliations

1. MRC Laboratory of Molecular Biology, Cambridge, UK

   Vaithish Velazhahan, Yang Lee & Christopher G. Tate

2. Department of Computational and Quantitative Medicine, Beckman Research Institute of the City of Hope, Duarte, CA, USA

   Ning Ma & Nagarajan Vaidehi

3. Department of Drug Design and Pharmacology, Universitetsparken 2, Copenhagen, Denmark

   Gáspár Pándy-Szekeres, Albert J. Kooistra & David E. Gloriam

4. Medicinal Chemistry Research Group, Research Center for Natural Sciences, Budapest, Hungary

   Gáspár Pándy-Szekeres

Authors

1. Vaithish Velazhahan
   View author publications

   You can also search for this author in PubMed Google Scholar

2. Ning Ma
   View author publications

   You can also search for this author in PubMed Google Scholar

3. Gáspár Pándy-Szekeres
   View author publications

   You can also search for this author in PubMed Google Scholar

4. Albert J. Kooistra
   View author publications

   You can also search for this author in PubMed Google Scholar

5. Yang Lee
   View author publications

   You can also search for this author in PubMed Google Scholar

6. David E. Gloriam
   View author publications

   You can also search for this author in PubMed Google Scholar

7. Nagarajan Vaidehi
   View author publications

You can also search for this author in PubMed Google Scholar

8. Christopher G. Tate
View author publications

You can also search for this author in PubMed Google Scholar

Contributions

V.V. performed receptor and G-protein engineering, expression, purification, complex formation, biophysical characterization, preparation of cryo-EM grids, cryo-EM data collection, data processing, structure determination and model building. N.M. performed the molecular dynamics simulations, and N.M. and N.V. analysed the molecular dynamics simulation trajectories. G.P.-S. developed the generic residue numbers and GPCRdb resources. A.J.K. analysed sequence conservation, structural mechanisms and co-supervised G.P.-S. Y.L. advised on cryo-EM data collection, data processing and model building. D.E.G. supervised G.P.-S. and A.J.K. and contributed to the design of residue numbering and GPCRdb resource. V.V. and C.G.T. carried out structure analysis and manuscript preparation. C.G.T. managed the overall project. The manuscript was written by V.V. and C.G.T., and included contributions from all authors.

Corresponding author

Correspondence to Christopher G. Tate.

Ethics declarations

Competing interests

C.G.T. is a shareholder in, consultant to, and member of the scientific advisory board of Sosei Heptares, who also partly funded this work.

Additional information

Peer review information *Nature* thanks Zhi-Jie Liu and the other, anonymous, reviewer(s) for their contribution to the peer review of this work. Peer reviewer reports are available.

Publisher's note Springer Nature remains neutral with regard to jurisdictional claims in published maps and institutional affiliations.

Extended data figures and tables

Extended Data Fig. 1 Purification, formation and biophysical characterization of the Ste2-G-protein heterotrimer complex.

a, FSEC trace of insect cells expressing wild-type Ste2-TEV-eGFP-His10 solubilized in different detergents. Ste2 migrated as a dimer in all tested detergents with an apparent molecular weight of around 380 kDa. The molecular weight standards used for calibration of the column are shown for reference. Results are representative of three independent experiments. **b**, SEC profiles of Ste2 and SDS–PAGE analysis of the eluted fractions. **c**, SEC profiles of Ste2–G-protein heterotrimer complex and SDS–PAGE analysis of the eluted fractions from the complex formation reaction (see Methods). **d**, SDS–PAGE analysis of the pooled and concentrated Ste2–G-protein complex along with the individual components used to form the complex. Experiments in **b**–**d** are representative of three independent purifications. **e**, Complex stability as analysed by SEC after incubation of the purified complex on ice for up to 15 days. This experiment was carried out once. **f**, Thermal stability as analysed by nanoscale differential scanning fluorimetry, which measures changes in the intrinsic fluorescence of the protein when subjected to thermal denaturation. The melting temperatures (T_m) of the Ste2–G-protein complex and the Ste2 dimer were calculated to be 51.2 °C and 55.0 °C, respectively. This experiment was performed once in two replicates. **g**, Representative 2D class averages of Ste2 imaged on a Titan Krios with the GIF Quantum K2 detector and a Volta Phase Plate[56] (VPP). All classes are consistent with a dimer and no monomer classes were observed. **h**, SEC–MALS analysis of the Ste2–mini-G-protein heterotrimer complex, Ste2–wild-type G-protein heterotrimer complex, Ste2 dimer and mini-G-protein heterotrimer complex. A large change in

refractive index that occurs at the end of the column volume due to the elution of salts and/or detergents present in the solvent is indicated as the solvent peak. Where indicated, chromatograms show signal from UV absorbance, light scattering and refractive index. The traces were normalized to the peak maxima. Calculated molar masses are depicted as traces. The molar masses of the protein components across the peak and the theoretical molar masses are indicated. SDS–PAGE analysis of the Ste2–mini-G-protein heterotrimer and Ste2–wild-type G-protein heterotrimer complexes are shown. The results are representative of three independent experiments, except the experiment with the Ste2 dimer, which was performed once. For gel source data (**b**–**d**, **h**), see Supplementary Fig. 1.

Extended Data Fig. 2 Cryo-EM single-particle reconstruction of the Ste2–G-protein heterotrimer complex.

a, A representative micrograph (defocus −2.0 μm) from the eBIC Krios1 dataset. **b**, Representative 2D class averages of the Ste2–G-protein heterotrimer complex determined using the initial set of particles from eBIC Krios1 dataset following 3D classification. Reconstructions with the detergent micelle are juxtaposed to indicate relative orientations. **c**, A representative 2D class average is shown from the final set of particles (eBIC Krios1 dataset) used to determine the model. Whereas one G protein is well-resolved, the second heterotrimeric G protein manifests as a poorly resolved density in the reference-free 2D averages (circled). **d**, The poorly resolved G-protein heterotrimer (orange circle) becomes apparent at lower contour levels and certain secondary structural features become visible when the map is low-pass-filtered to 8 Å. The contact between mini-$Gpa1_B$ and $Ste4_A$ of the adjacent mini-$Gpa1_A$ heterotrimer is indicated (pink circle) **e**, **g**, FSC curves of the reconstructions map 1 (**e**) and map 2 (**g**) (black lines) shows an overall resolution of 3.5 Å and 3.3 Å, respectively, using the gold standard FSC of 0.143. The directional 3D-FSC curves computed from the two half-maps are shown in colour. **h**, Local resolution estimation of the Ste2 dimer portion from map 2 as calculated by RELION. **f**, **i**, Local resolution estimation of the Ste2–G-protein heterotrimer complex from map 1 (**f**) and map 2 (**i**) as calculated by RELION. Map 2 shows a higher local

resolution in the Ste2 dimer, but the resolution is limited in the G-protein regions.

Extended Data Fig. 3 Flow chart of single-particle cryo-EM data processing.

Micrographs were collected from three independent sessions (between 24-h and 72-h long) on a Titan Krios with GIF Quantum K2. Each dataset was corrected separately for drift, beam-induced motion and radiation damage. After estimation of CTF parameters, particles were picked using a Gaussian blob and subjected to two rounds of 3D classification using an ab initio model as reference. The number of final particles from each round of 3D classification is shown. A representative 3D classification scheme (round 2) from the eBIC Krios1 dataset is shown. The initial set of best particles from the eBIC Krios1 dataset was refined and corrected for beam-tilt. Per-particle CTF estimation and Bayesian polishing was performed, detergent micelle signal was subtracted, and a 3D classification without alignment was performed. A model (map 1) with 96,611 particles was refined and achieved a global resolution of 3.5 Å. In parallel, the final set of particles from LMB Krios1 and LMB Krios2 were refined and corrected for beam-tilt, which was followed by per-particle CTF estimation and Bayesian polishing. The initial set of particles from eBIC Krios1 was combined with the final set of particles from LMB Krios1 and LMB Krios2. The combined set of particles was refined, anisotropic magnification correction was performed, and the particles were subjected to a 3D classification without alignment after subtraction of the signal from the detergent micelle and the G protein. After restoring the G-protein signal, a set of 131,266 particles was refined to a global resolution of 3.3 Å (map 2) with improved features in the Ste2 dimer region. Resolution of the models after refinements was calculated with the gold-standard FSC of 0.143 in RELION.

Extended Data Fig. 4 Cryo-EM map quality of the Ste2–mini-Gpa1–Ste4–Ste18 heterotrimer complex and model validation.

Unless stated otherwise, densities from map 1 were visualized using UCSF ChimeraX[35] (contour level 0.03) and encompass a carve radius of 2 Å

around the indicated region. **a**, Densities of transmembrane helices of $Ste2_A$ (contour level 0.045), α-$factor_B$, mini-$Gpa1_B$, dimer interface between $Ste2_A$ and $Ste2_B$, intracellular loops ICL1–3 and extracellular loops ECL1–3 are shown as a mesh. Densities of αN and α4–β6 are shown as representative densities from mini-$Gpa1_A$. Densities of Ste4 and Ste18 (contour 0.025) are shown as a mesh at a contour level of 0.01 and a carve radius of 2 Å. **b**, Two *N*-acetylglucosamine molecules were modelled attached to Asn25 of Ste_A and $Ste2_B$ and they contribute to the dimer interface (contour level 0.01 from map 2). Asn25 is a well-characterized glycosylation site in Ste2[17]. **c**, Densities for six ordered putative CHS molecules surrounding the dimer interface were visible and were modelled (contour level 0.01). Several other detergent or lipid acyl-chain densities were visible in the map before detergent micelle signal subtraction, but were left unmodelled. **d**, FSC of the refined model versus the map (green curve) and FSC_{work}/FSC_{free} validation curves (orange and blue curves, respectively).

Extended Data Fig. 5 Comparison of Ste2 with other classes of GPCRs.

Thirty-nine receptors in the active state were aligned using GESAMT[73] and then prototypical members of different classes were compared with Ste2. Both GESAMT[73] and TM-align[72] provided similar results. In all panels, Ste2 is shown in rainbow colouration and is compared with: **a**, β_2-adrenoceptor (class A; PDB ID: 3SN6); **b**, glucagon-like peptide receptor 1 (class B; PDB ID: 6B3J); **c**, $GABA_B$ receptor (class C, PDB ID: 7C7Q); **d**, smoothened (class F; PDB ID: 6D32).

Extended Data Fig. 6 Amino acid conservation of Ste2 and the CD1 numbering system.

a, The size of the letter is related to the degree of conservation from the aligned Ste2 orthologues (395 sequences). The CD1 numbering system is shown alongside the positions of the defining residue and Ballesteros–Weinstein number for class A GPCRs. Generic residue numbers use the

GPCRdb scheme, which uses the same reference positions as the Ballesteros–Weinstein scheme but corrects offsets due to helix bulges or constrictions. Two structurally important motifs in class A GPCRs (DRY and NPXXY) are depicted. **b**, The amino acid sequence of *S. cerevisiae* Ste2 is shown (coloured boxes) in relation to secondary structural elements. The CD1 number (for example, 5x50) is given adjacent to the amino acid residue number. Numbers in grey boxes represent the sequence conservation of the *S. cerevisiae* Ste2 residue at that position among Ste2 orthologues from 395 unique sequences. The light blue colour on the residue sequence numbers indicates residues predicted to be positioned in the lipid bilayer on the basis of structural superposition with the class B receptor GLP1R (PDB ID: 6B3J).

Extended Data Fig. 7 Amino acid residues forming the Ste2 dimer interface.

Contacts are shown as coloured squares with a digit representing the number of van der Waals interactions (≤3.9 Å) and hydrogen bonds.

Extended Data Fig. 8 Molecular dynamics simulations of the Ste2 dimer in the absence of G proteins and ligands.

a, Groove in the H1–H1 dimer interface. **b**, Heat map of the percentage of molecular dynamics snapshots that show residue contacts in the dimer interface in the EM structure and in the representative structure from molecular dynamics simulations in the absence of the ligands and G proteins. **c**, Top row, histograms of the standard deviation among 25 simulation runs (total 1.4 μs) for Ste2 dimer with G protein and α-factor. Bottom row, histograms of the standard deviation in $Ste2_A$ and $Ste2_B$ interface residue contacts among 5 simulation runs (total 5 μs) of the Ste2 dimer without G protein. **d**, Convergence of the five 1-μs simulations was tested by calculating the dot product among the top 5 weighted principal components (PCs) for the 5 simulations of Ste2 dimer without G protein or α-factor. The top weighted principal components (PC1 to PC5) from each run all show strong overlap (red squares) with at least one of the PCs from other runs. **e**, Cumulative variance of PCs show that the top five PCs

occupy more than 90% of the populations, and therefore they are sufficient to describe the motion of the complex.

Extended Data Fig. 9 Structural features of Ste2 and comparison with mammalian GPCRs.

a–c, Alignment of GPCRs was performed by GESAMT[73] (CCP4 suite of programs) in conjunction with 39 other G-protein- or arrestin-coupled GPCR structures (Fig. 5a). Ste2 is depicted in rainbow colouration and the adenosine A_{2A} receptor ($A_{2A}R$) is in grey. **a**, DRY motif showing the stacking (van der Waals contacts, yellow dashed lines) of the highly conserved Arg^{3x50} residue with $Phe^{H5.23}$ of the α-subunit of $G_{s.}$ **b**, The Pro^{5x50}-Ile^{3x40}-Phe^{6x44} motif provides a conserved packing of residues in the active state at the core of class A receptors. A similar role could be played by Leu^{5x35} and Val^{3x40} in Ste2. **c**, The NPXXY motif in class A GPCRs aligns with a conserved region in Ste2 receptors (see also Extended Data Fig. 6a), but Pro^{7x50} in Ste2 is not associated with a kink in H7 as it is in class A GPCRs. **d**, Conformational changes in the transmembrane α-helices observed during molecular dynamics simulations of the dimer without the G proteins or the ligands. **e**, Alignment of the active-state Ste2 (rainbow colouration) with the Ste2 conformation (grey) reached after molecular dynamics simulations in the absence of G protein and ligand. Gpa1 would not be able to couple to this new conformation owing to clashes with atoms in H2 (Ile80), H3 (Phe148, Gln149, Lys151, Val152, Thr155) and ICL2 (Gly156, Asp157, Asn158, Phe159). Clashes are defined as atoms (grey spheres) within 2 Å of atoms in Gpa1 coupled to the active state of Ste2. **f**, The position of the α-helical domain in Gpa1 distal to the dimer interface can be inferred from comparison with the structure of G_i (yellow) coupled to rhodopsin (PDB ID: 6CMO) after alignment with mini-Gpa1 (purple). The position in Gpa1 of the deletion of the α-helical domain (which also includes the ubiquitination domain) is indicated by the amino acid residues immediately before and after the deletion being shown as spheres. **g**, Superposition of G_o-coupled serotonin 5-HT_{1B} receptor (yellow) with $Ste2_A$ (blue). The Gpa1 heterotrimer is rotated by 58° (angle between the centre of masses of Gβ subunit of G_o heterotrimer and Ste4 of Gpa1

heterotrimer) perpendicular to the membrane plane, which creates sufficient space for two G-protein heterotrimers to simultaneously couple to the Ste2 dimer. **h**, Views of the intracellular surfaces of dimers from class D (Ste2), class A (rhodopsin; PDB ID: 6OFJ) and class C ($GABA_B$ receptor; PDB ID: 7C7Q). All receptors are in rainbow colouration.

Extended Data Table 1 Cryo-EM data collection and refinement statistics
Full size table

Supplementary information

Supplementary Figure 1

Uncropped SDS-PAGE gels. The Coomassie Blue-stained SDS PAGE gels used to generate the cropped panels in Extended Data Fig. 1 are depicted in full.

Reporting Summary

Peer Review File

Supplementary Table 1

Dimer interface. Previous published mutations of amino acid residues at the Ste2 dimer interface are listed, with associated changes in ligand binding and receptor signalling, and the literature source.

Supplementary Table 2

Ste2 conservation and source organisms. The conservation of amino acid residues in the Ste2 receptor is shown along with the list of all organisms containing Ste2 orthologues used in the analysis.

Supplementary Table 3

Ste2 mutations in the orthosteric binding site. Previous published mutations of amino acid residues at the Ste2 orthosteric binding site are listed, with associated changes in ligand binding and receptor signalling, and the literature source.

Supplementary Table 4

Mutations in α-factor. Previous published alterations of amino acid residues in α-factor are listed, with associated changes in ligand binding and receptor signalling, and the literature source.

Supplementary Table 5

G-protein mutations. Previous published mutations of amino acid residues in Gpa1 found at the receptor-G protein interface are listed, with associated changes in Ste2 signalling, and the literature source.

Rights and permissions

Reprints and Permissions

About this article

Check for updates

Cite this article

Velazhahan, V., Ma, N., Pándy-Szekeres, G. *et al.* Structure of the class D GPCR Ste2 dimer coupled to two G proteins. *Nature* **589,** 148–153 (2021). https://doi.org/10.1038/s41586-020-2994-1

Download citation

- Received: 03 July 2020
- Accepted: 25 September 2020
- Published: 02 December 2020
- Issue Date: 07 January 2021
- DOI: https://doi.org/10.1038/s41586-020-2994-1

Further reading

- **GPCRdb in 2021: integrating GPCR sequence, structure and function**

  - Albert J Kooistra
  - , Stefan Mordalski
  - , Gáspár Pándy-Szekeres
  - , Mauricio Esguerra
  - , Alibek Mamyrbekov
  - , Christian Munk
  - , György M Keserű
  - & David E Gloriam

  Nucleic Acids Research (2021)

Comments

By submitting a comment you agree to abide by our Terms and Community Guidelines. If you find something abusive or that does not comply with our terms or guidelines please flag it as inappropriate.

Access through your institution
Change institution
Buy or subscribe

This article was downloaded by **calibre** from https://www.nature.com/articles/s41586-020-2994-1

Amendments & Corrections

- **Publisher Correction: Subducting carbon** [11 December 2020]
  Publisher Correction •

Publisher Correction: Subducting carbon
Download PDF

- Publisher Correction
- Published: 11 December 2020

Publisher Correction: Subducting carbon

- Terry Plank ORCID: orcid.org/0000-0002-1665-0484[1] &
- Craig E. Manning[2]

Nature **volume 589**, pageE1(2021)Cite this article

- 887 Accesses
- 3 Altmetric
- Metrics details

Subjects

- Carbon cycle
- Geochemistry

The Original Article was published on 16 October 2019

Download PDF

Correction to: *Nature* https://doi.org/10.1038/s41586-019-1643-z Published online 16 October 2019

In the HTML version of this Review, the figures associated with all four Boxes were incorrectly assigned. The PDF version was correct. The Article has been corrected online.

Author information

Affiliations

1. Lamont-Doherty Earth Observatory, Columbia University, Palisades, NY, USA

   Terry Plank

2. University of California, Los Angeles, CA, USA

   Craig E. Manning

Authors

1. Terry Plank
   View author publications

   You can also search for this author in PubMed Google Scholar

2. Craig E. Manning
   View author publications

   You can also search for this author in PubMed Google Scholar

Corresponding author

Correspondence to Terry Plank.

Rights and permissions

Reprints and Permissions

About this article

Check for updates

Cite this article

Plank, T., Manning, C.E. Publisher Correction: Subducting carbon. *Nature* **589,** E1 (2021). https://doi.org/10.1038/s41586-020-3022-1

Download citation

- Published: 11 December 2020
- Issue Date: 07 January 2021
- DOI: https://doi.org/10.1038/s41586-020-3022-1

Comments

By submitting a comment you agree to abide by our Terms and Community Guidelines. If you find something abusive or that does not comply with our terms or guidelines please flag it as inappropriate.

Download PDF

This article was downloaded by **calibre** from https://www.nature.com/articles/s41586-020-3022-1